applied sciences

Special Issue Reprint

Sustainability in Geotechnics

Edited by
António Alberto Santos Correia and Paulo José da Venda Oliveira

mdpi.com/journal/applsci

MDPI

Sustainability in Geotechnics

Sustainability in Geotechnics

Editors

António Alberto Santos Correia
Paulo José da Venda Oliveira

MDPI

Basel • Beijing • Wuhan • Barcelona • Belgrade • Novi Sad • Cluj • Manchester

Editors

António Alberto Santos Correia
Department of Civil Engineering, CERES
University of Coimbra
Coimbra
Portugal

Paulo José da Venda Oliveira
Department of Civil Engineering, ISISE
University of Coimbra
Coimbra
Portugal

Editorial Office
MDPI AG
Grosspeteranlage 5
4052 Basel, Switzerland

This is a reprint of articles from the Special Issue published online in the open access journal *Applied Sciences* (ISSN 2076-3417) (available at: https://www.mdpi.com/journal/applsci/special_issues/4QUQOR576N).

For citation purposes, cite each article independently as indicated on the article page online and as indicated below:

Lastname, A.A.; Lastname, B.B. Article Title. *Journal Name* **Year**, *Volume Number*, Page Range.

ISBN 978-3-7258-2369-7 (Hbk)
ISBN 978-3-7258-2370-3 (PDF)
doi.org/10.3390/books978-3-7258-2370-3

Contents

About the Editors

António Alberto Santos Correia

António Alberto Santos Correia has a PhD in Civil Engineering and is an Associate Professor at the University of Coimbra, where he is also the coordinator of the Degree in Environmental Engineering. He is a member of the Research Centre on Chemical Engineering and Renewable Resources for Sustainability (CERES). He is a specialist in sustainable materials and solutions for engineering problems (binders, nanotechnology), ground improvement, and environmental problems (remediation of contaminated soils). He has worked as a geotechnical expert in 18 national projects, ranging from dams, slopes, and embankments to roads and industrial infrastructures. He has previously supervised 11 students/individual grants, 4 of which were PhD grants, and 30 MSc theses; he is currently supervising 3 PhD theses and 4 MSc theses. António Correia has published more than 100 scientific papers, 42 of which were in peer-reviewed international journals, and is the author of 1 book chapter and the editor of 12 books. He is the Associate Editor and member of the Editorial Board of the international journal *Soils and Rocks*. He is also a frequent reviewer for some international journals, including *Geotextiles and Geomembranes*, *Construction and Building Materials*, *Geotechnical and Geoenvironmental Engineering*, and *Soils and Rocks*, among others. António Correia is the General-Secretary of the Board of the Portuguese Commission for Ground Improvement and a Portuguese Delegate on the International Technical Committees TC211-Ground Improvement and TC101- Laboratory Testing. Other additional positions held by António Correia include the following: Member of the European Committee for Standardization (CEN) - TC 189 and International Organization for Standardization (ISO) TC 221; UC representative at the cluster Smart Waste Portugal; Ambassador of the Alliance Sustainable Development Goals (SDG) Portugal - United Nations Global Compact Network; and Geotechnical Specialist and Senior Fellow of the Portuguese Institution of Engineers. António Correia has also taken up a central role in science dissemination, organizing symposia, workshops, and conferences at various levels.

Paulo José da Venda Oliveira

Paulo José da Venda Oliveira graduated in Civil Engineering at the University of Coimbra (UC) in 1988. In 2001, he obtained his PhD in Engineering Science, specializing in Foundations and Geotechnics. Since 1988, he has taught geotechnics courses at the UC, currently holding the position of Associate Professor. His teaching career has progressed in degree, post-graduate, master's, and doctorate study courses. Additionally, he has participated in more than 90 master's degree and PhD boards. In terms of the transference of knowledge, he has performed numerous laboratory tests of soil mechanics and many technical studies concerning problems of slope instability, retaining walls, dams, foundations, embankments, etc. At present, he is a member of the Institute for Sustainability and Innovation in Structural Engineering (ISISE), which is a research unit funded by the Portuguese Science Foundation (FCT) rated as "Excellent". He has authored more than 150 scientific and technical papers, 46 of which are peer-reviewed publications in international journals (ISI/Scopus). He has supervised more than 40 master's degree and PhD dissertations. He is a frequent reviewer of more than 15 geotechnical journals, such as *Computers and Geotechnics*, *Geosynthetics International*, *Journal of Materials in Civil Engineering*, *Journal of Geotechnical and Geoenvironmental Engineering*, and *Geotechnique*, among others. He has supervised various research grants in the field of chemically stabilized soils and the biocementation of soils. His research activity is focused on geotechnics, from soil characterization to numerical modeling. During the last five years, his research interests

include numerical modeling of the behavior of stabilized soft soils, laboratory characterization of the monotonic and cyclic behavior of stabilized soft soils with binders (cement, lime, fly ash, slags, etc.), biopolymers (xanthan gum), and the use of enzymes (urease) to promote the biocementation process.

Preface

Human development and the development of societies have posed huge challenges to geotechnics. Since the adoption of the Sustainable Development Goals established in the United Nations Agenda 2030 (adopted in 2015), it has become imperative to seek sustainable solutions that respect the environment and contribute to the mitigation of climate change at an affordable cost, without compromising the safety and stability of structures. The geotechnical community has been facing up to these challenges by presenting innovative and sustainable solutions. New and smart materials, nature- and bio-based materials and technologies, the use of nanotechnology and artificial intelligence, advances in constitutive soil models through the integration of climate effects, and life-cycle assessment, among other topics, are examples of the most recent advances related to the sustainability of geotechnical works. All types of geotechnical works, such as embankments, deep and shallow foundations, retaining structures, tunnels, dams, and slopes, among others, benefit from such sustainable advances.

The aim of this Special Issue is not to provide an exhaustive summary of the latest advances in the field of sustainability in geotechnics, but rather to present some works considered innovative and whose practical application is already a reality or may occur in the near future. Therefore, this Special Issue entitled "Sustainability in Geotechnics" brings together sixteen papers (from among twenty-five submitted) that, not only for their scientific merit, address some of the current and future challenges in sustainability in geotechnics. The papers published cover a wide range of sustainable topics with a specific focus on the research, design, construction, and performance of sustainable geotechnical works. These works are expected to inspire the development of geotechnics, contributing to the future construction of more resilient and sustainable geotechnical structures.

Lastly, we would like to take this opportunity to acknowledge all of the authors who contributed to this Special Issue "Sustainability in Geotechnics". A special mention of thanks is also addressed to all of the reviewers for their valuable contributions and to the *Applied Sciences*/MDPI editorial team for the invitation and for all of the support given during the production of this Special Issue, especially Ms. Sara Zhan.

António Alberto Santos Correia and Paulo José da Venda Oliveira
Editors

applied sciences

MDPI

Editorial

Sustainability in Geotechnics

António Alberto S. Correia [1,*] and Paulo J. Venda Oliveira [2,*]

[1] Chemical Engineering and Renewable Resources for Sustainability (CERES), Department of Civil Engineering, University of Coimbra, 3030-788 Coimbra, Portugal
[2] Institute for Sustainability and Innovation in Structural Engineering (ISISE), Department of Civil Engineering, University of Coimbra, 3030-788 Coimbra, Portugal
* Correspondence: aalberto@dec.uc.pt (A.A.S.C.); pjvo@dec.uc.pt (P.J.V.O.)

The development of humans and societies has posed huge challenges to geotechnics. Since the adoption of the Sustainable Development Goals established in the United Nations Agenda 2030, adopted in 2015 [1], it has become imperative to seek sustainable solutions that respect the environment and contribute to the mitigation of climate change at an affordable cost, without compromising the safety and stability of geotechnical structures. Indeed, geotechnics is currently undergoing a transformative shift towards sustainability. Embracing sustainable practices in geotechnics involves integrating new and smart materials, nature- and bio-based materials and technologies, the use of nanotechnology and artificial intelligence, advances in constitutive soil models by integration of climate effects, and holistic design approaches that consider environmental, economic, and social implications throughout the life cycle assessment of geotechnical structures.

The Special Issue "Sustainability in Geotechnics" was launched with an invitation to authors from all over the world to address current and future sustainable solutions in geotechnics. Twenty-five manuscripts were submitted to this Special Issue, and sixteen were accepted for publication. Contributions were received from nine countries (Brazil, China, Japan, Norway, Poland, Portugal, Saudi Arabia, Slovakia, and the United Kingdom), representing three continents (America, Asia, and Europe); these papers address some of the emerging topics, focusing on the research, design, construction, and performance of sustainable geotechnical works.

The first three contributions deal with the recovery of mining tailings in geotechnics. Coelho and Camacho (Contribution 1) characterize iron ore tailings from a geotechnical perspective, studying their physical and identification (grain size and plasticity) properties, compaction behavior, and stress–strain properties under monotonic and cyclic triaxial undrained loading. The study highlights some particularly important characteristics of iron ore tailings such as a significant silty component that is responsible for the low plasticity observed, particles with an angular shape, their very high solid density, and their higher angle of friction and liquefaction resistance than common granular geomaterials. The results indicate that there is a high potential for mining tailings to be used in a wide variety of geotechnical applications. One such example is presented by Saldanha et al. (Contribution 2), where the potential use of iron ore tailings for replacing the conventional aggregates used in interlocking paving blocks for lightly trafficked pavements is explored. The study focuses not only on mechanical performance (in terms of compressive strength), but also on environmental performance through a life cycle assessment (cradle-to-gate), demonstrating the clear advantages of valorizing mining tailings. Correia et al. (Contribution 3) study sustainable ways of increasing the stability of mining tailing deposits, which is a current concern given the large number and size of such deposits. To this end, they propose the use of bio-stabilization techniques, combining the use of biopolymers (xanthan gum and carboxymethyl cellulose) with bioremediation (bio-stimulation and bioaugmentation). The results show that both polymers applied alone (albeit in low concentrations—1%) are effective sustainable stabilizers and an alternative to

Citation: Correia, A.A.S.; Venda Oliveira, P.J. Sustainability in Geotechnics. *Appl. Sci.* **2024**, *14*, 9037. https://doi.org/10.3390/app14199037

Received: 15 September 2024
Revised: 2 October 2024
Accepted: 4 October 2024
Published: 7 October 2024

Portland cement. Bioaugmentation was revealed to be an ineffective technique, while biostimulation combined with xanthan gum showed very good results in terms of unconfined compressive strength. Moreover, the study revealed that bio-based techniques, such as soil engineering techniques, are promising, offering environmentally friendly alternatives for sustainable soil stabilization and contributing to a greener and more sustainable future.

The fourth, fifth, sixth, and seventh contributions study sustainable ways of improving the mechanical behavior of different soils. The fourth and fifth contributions propose the use of bio-inspired techniques (enzymes and biopolymers) to replace the use of cement in soil stabilization, while the sixth contribution proposes a sustainable solution by partially replacing Portland cement with industrial by-products and/or biochars; the seventh contribution proposes the potential use of coarse aggregate crushing waste to improve the geotechnical properties of a silty sand soil. Mwandira et al. (Contribution 4) propose an innovative method that uses hybrid enzyme carriers (copper–carbonic anhydrase) to catalyze the bioprecipitation of calcium carbonate, aiming to increase the efficiency and sustainability of the biocementation process. Venda Oliveira and Reis (Contribution 5) study the effects of soil's organic matter content on the biostabilization induced by the biopolymer xanthan gum. The results showed a detrimental effect in terms of unconfined compressive strength and stiffness, as well as an increase in compressibility and primary consolidation time for organic matter contents higher than 5.5%. Hov et al. (Contribution 6) study viable alternatives (four biochars, including demolition wood and sewage waste, and five industrial by-products, including ashes and slags) as a partial replacement of Portland cement for the stabilization of three soils (a soft clay, a quick clay, and one peat). The results suggest that the stabilization effect of Portland cement combined with biochars increases with the increasing water content of the soils, while the opposite effect was observed for Portland cement combined with industrial by-products. Further studies should be carried out to establish the correlations between the mineralogical and chemical composition of these additives, as well as the mechanical performance of the stabilized soils. Abdullah et al. (Contribution 7) investigate the reusing of coarse aggregate crushing waste mixed with Portland cement to improve the geotechnical properties of soil when applied in road construction. It was found that a combination of 10% coarse aggregate crushing waste with 2% Portland cement increases the undrained shear strength, the California Bearing Ratio (CBR), and the P-wave velocity, making such a soil improvement approach almost carbon neutral.

Soares et al. (Contribution 8) propose a framework to assess soil liquefaction based on the ratio between the shear wave velocity and the peak undrained deviatoric stress. The authors state that such a ratio can be accurately used to define a boundary between liquefaction and strain hardening for sands and between strain softening and strain hardening for silty sands and silts. This tool has the potential to assess the liquefaction of in situ soils, including natural deposits or mine tailings, contributing to safer and more sustainable geotechnical structures.

The ninth and tenth contributions (Contributions 9 and 10, respectively) study the interaction of soil-sustainable reinforcement elements under monotonic and cyclical loading. The ninth contribution focuses on geogrids, while the tenth contribution focuses on wooden frame beams and bamboo anchor rods. Barajas et al. (Contribution 9) study the pullout apparatus scale (small and large) effect on the characterization of the soil–geogrid interface shear behavior. It was found that the pullout apparatus scale effect is small for confining stresses greater than or equal to 50 kPa, so the adoption of small-scale equipment is less material- and time-consuming, making it a more sustainable way of characterizing such interfaces. Yang et al. (Contribution 10) conducted a series of model tests in embankment slopes supported by wooden frame beams and bamboo anchor rods under train loadings complemented with three-dimensional numerical simulations. The stresses acting on the support/reinforcement elements depend on loading magnitude and frequency, as well as the slope depth. It was shown that this ecological and environmentally friendly support system is not only a sustainable solution, but also contributes to increasing slope stability.

Nguyen et al. (Contribution 11) propose a methodology to deal with uncertainty in the direct shear tests used to characterize the shear parameters of a soil reinforced with polyester fibers. The authors state that it is not recommended to carry out direct shear tests with only three specimens since different combinations of three specimens provide different shear strength parameters. Therefore, it is important to evaluate the uncertainty of the shear strength parameters by taking into account all the test procedures and material variability.

Wu et al. (Contribution 12) present a novel technique for constructing the protection and seepage control layer in Cemented Sand, Gravel and Rock (CSGR) dams. The advantages of this new method, integrated with dam body construction, were demonstrated in a case study, showing significant economic, environmental, and safety benefits, thus promoting sustainable dam construction.

Tinoco et al. (Contribution 13) use machine learning techniques, namely artificial neural networks and genetic algorithms combined with modern optimization processes, aiming to develop a slope classification system for rock and soil cuttings, as well as embankments based on visual features that are usually collected during routine inspection. This slope stability assessment tool can allow railway infrastructure management companies to collect less information to determine the stability level of their slope network (reducing costs without compromising safety issues), allowing for the strategic investment of the available budget on critical slopes. This approach is an important contribution to the efficient and sustainable management of geotechnical transportation infrastructures.

The last three contributions present case studies demonstrating the application of sustainability concepts in geotechnics. Pedro et al. (Contribution 14) postulate that one of the best solutions for improving sustainability in the construction sector is to improve the design and construction methods, thereby reducing material consumption. Such a strategy was applied to a real case of shaft construction, where it was demonstrated that optimizing the characteristics of the lining of the shaft can result in a reduction in CO_2 emissions by at least 50% without compromising the safety engineering requirements. Takahashi et al. (Contribution 15) investigate the long-term durability of cement-treated soil on an artificial island of Central Japan International Airport, where the pneumatic flow mixing method was first fully introduced; this method uses dredged soil rather than soil transported from cuttings, and uses small amounts of Portland cement, allowing it to be classified as a sustainable ground improvement method. The results showed negligible deterioration 20 years after construction, demonstrating that there is no need for energy or materials for repair, i.e., the cement-treated soil offers many environmental and economic benefits, and consequently increases sustainability. Kitazume (Contribution 16) presents the recent case histories of carbon-neutral activity using ground improvement technology in Japan. Some ways to reduce material consumption, with environmental, social, and economic benefits, can be implemented by promoting the recovery of industrial waste and by-products, as well as the development of new materials with negative emission technology such as biomass materials.

The integration of sustainable solutions in geotechnics is not merely a trend but a necessity for building a resilient and environmentally responsible future. By leveraging new and smart materials, nature- and bio-based materials and technologies, nanotechnology, artificial intelligence, advanced soil models, and life cycle assessment, geotechnical engineers can design and implement projects that meet the current and future demands of modern society while safeguarding our planet. As the scientific community continues to innovate and adopt these sustainable practices, the field of geotechnics will play a key role in shaping a sustainable and resilient built environment.

Funding: This research received no external funding.

Acknowledgments: The Guest Editors would like to acknowledge all the authors who contributed to this Special Issue, “Sustainability in Geotechnics”. A special mention of thanks is also addressed to the Applied Sciences/MDPI Editorial team for the invitation and for all the support given during the production of this Special Issue.

Conflicts of Interest: The authors declare no conflicts of interest.

List of Contributions

1. Coelho, P.; Camacho, D. The Experimental Characterization of Iron Ore Tailings from a Geotechnical Perspective. *Appl. Sci.* **2024**, *14*, 5033. https://doi.org/10.3390/app14125033.
2. Saldanha, R.B.; Menezes, M.F.L.; Bittar, R.J.; Consoli, N.C. Performance of Ore Sand as Aggregate for Interlocking Blocks. *Appl. Sci.* **2023**, *14*, 48. https://doi.org/10.3390/app14010048.
3. Correia, A.A.S.; Caldeira, J.B.; Branco, R.; Morais, P.V. Enhancing the Strength of Mine Residue Soil by Bioremediation Combined with Biopolymers. *Appl. Sci.* **2023**, *13*, 10550. https://doi.org/10.3390/app131810550.
4. Mwandira, W.; Purchase, D.; Mavroulidou, M.; Gunn, M.J. Synthesis and Utilisation of Hybrid Metal-Carbonic Anhydrase Enzyme Carrier System for Soil Biocementation. *Appl. Sci.* **2023**, *13*, 9494. https://doi.org/10.3390/app13179494.
5. Oliveira, P.J.V.; Reis, M.J.F.C.C. Effect of the Organic Matter Content on the Mechanical Properties of Soils Stabilized with Xanthan Gum. *Appl. Sci.* **2023**, *13*, 4787. https://doi.org/10.3390/app13084787.
6. Hov, S.; Paniagua, P.; Sætre, C.; Long, M.; Cornelissen, G.; Ritter, S. Stabilisation of Soft Clay, Quick Clay and Peat by Industrial By-Products and Biochars. *Appl. Sci.* **2023**, *13*, 9048. https://doi.org/10.3390/app13169048.
7. Abdullah, G.M.S.; El Aal, A.A.; Al Saiari, M.; Radwan, A.E. Sustainable Impact of Coarse Aggregate Crushing Waste (CACW) in Decreasing Carbon Footprint and Enhancing Geotechnical Properties of Silty Sand Soil. *Appl. Sci.* **2023**, *13*, 10930. https://doi.org/10.3390/app131910930.
8. Soares, M.; da Fonseca, A.V.; Ferreira, C.; Rios, S. Static Liquefaction Assessment Combining Shear Wave Velocity, Peak Strength and Soil Grading. *Appl. Sci.* **2023**, *13*, 8580. https://doi.org/10.3390/app13158580.
9. Barajas, S.R.; Pedroso, G.O.M.; Ferreira, F.B.; da Silva, J.L. Influence of Apparatus Scale on Geogrid Monotonic and Cyclic/Post-Cyclic Pullout Behavior in Cohesive Soils. *Appl. Sci.* **2024**, *14*, 5861. https://doi.org/10.3390/app14135861.
10. Yang, H.; Huang, G.; Wei, Z.; Jiang, X.; Cao, Z. A Study on the Dynamic Response of a Timber-Frame Beam–Bamboo Anchor-Supported Roadbed Slope under Train Load. *Appl. Sci.* **2024**, *14*, 2426. https://doi.org/10.3390/app14062426.
11. Nguyen, G.; Masarovičová, S.; Gago, F.; Grzybowska-Pietras, J. Application of Direct Shear Test to Analysis of the Rate of Soil Improvement with Polyester Fibres. *Appl. Sci.* **2024**, *14*, 4601. https://doi.org/10.3390/app14114601.
12. Wu, Y.; Jia, J.; Zheng, C.; Jia, B.; Wang, Y.; Baah, W.A. A New Method for Constructing the Protection and Seepage Control Layer for CSGR Dam and Its Application. *Appl. Sci.* **2024**, *14*, 5423. https://doi.org/10.3390/app14135423.
13. Tinoco, J.; Correia, A.G.; Cortez, P.; Toll, D. An Evolutionary Neural Network Approach for Slopes Stability Assessment. *Appl. Sci.* **2023**, *13*, 8084. https://doi.org/10.3390/app13148084.
14. Pedro, A.M.G.; Repsold, L.; e Sousa, J.A. Assessing the Sustainability of Alternative Shaft Construction Methods. *Appl. Sci.* **2024**, *14*, 4476. https://doi.org/10.3390/app14114476.
15. Takahashi, H.; Sato, I.; Morikawa, Y.; Ozawa, A. Long-Term Durability of Cement-Treated Soil Used in Offshore Airport Island Construction. *Appl. Sci.* **2023**, *13*, 8081. https://doi.org/10.3390/app13148081.
16. Kitazume, M. Recent Case Histories of Carbon-Neutral Activity Using Ground Improvement Technology in Japan. *Appl. Sci.* **2023**, *13*, 8985. https://doi.org/10.3390/app13158985.

Reference

1. *UN-A/RES/70/1*; Transforming Our World: The 2030 Agenda for Sustainable Development, in Resolution Adopted by the General Assembly on 25 September 2015. United Nations: New York, NY, USA, 2015.

applied sciences

MDPI

Article

The Experimental Characterization of Iron Ore Tailings from a Geotechnical Perspective

Paulo Coelho [1,*] and David Camacho [2]

[1] Research Centre for Territory, Transports and Environment (CITTA), Department of Civil Engineering, University of Coimbra, 3030-788 Coimbra, Portugal
[2] Department of Civil Engineering, University of Coimbra, 3030-788 Coimbra, Portugal; uc2018262946@student.uc.pt
* Correspondence: pac@dec.uc.pt

Featured Application: Iron ore tailings are amongst some of the most common and widely available types of mining waste. This paper focus on the geotechnical characterization of these materials in order to promote their potential applications as building materials in more sustainable geotechnical works, namely in embankments, employing the concept of circular economy.

Abstract: The mining industry produces large amounts of tailings which are disposed of in deposits, which neglects their potential value and represents important economic, social and environmental risks. Consequently, implementing circular economy principles using these unconventional geomaterials may decrease the wide-ranging impacts of raw material extraction. This paper presents an experimental characterization of iron ore tailings, which are the most abundant type of mining waste. The characterization includes various aspects of behavior that are relevant to different types of use as a building material, including physical and identification properties, compaction behavior and stress–strain properties under undrained monotonic and cyclic triaxial loading. The tailings tested can be described as low-plasticity silty sand materials with an average solids density of 4.7, a maximum dry unit weight close to 3 g/cm^3 and a higher angle of friction and liquefaction resistance than common granular materials. The experimental results highlight the particular features of the behavior of iron ore tailings and emphasize the potentially promising combination of high shear resistance and high density that favors particular geotechnical applications. Overall, the conclusions provide the basis for promoting the use of mining wastes in the construction of sustainable geotechnical works and underpin the advanced analysis of tailings storage facilities' safety founded on an open-minded geotechnical approach.

Keywords: iron ore tailings; geotechnical characterization; grain size distribution; plasticity; permeability; compaction behavior; shear strength; cyclic liquefaction

Citation: Coelho, P.; Camacho, D. The Experimental Characterization of Iron Ore Tailings from a Geotechnical Perspective. *Appl. Sci.* **2024**, *14*, 5033. https://doi.org/10.3390/app14125033

Academic Editor: Syed Minhaj Saleem Kazmi

Received: 3 May 2024
Revised: 5 June 2024
Accepted: 6 June 2024
Published: 9 June 2024

1. Introduction

Modern societies need increasing amounts of metal and mineral resources to sustain their development in a context of a growing and increasingly environmentally conscious global population, with the aim of achieving a conversion to a so-called low-carbon economy. However, clean energy technologies tend to use significantly more mineral and metal resources, which will necessarily intensify the demand for these commodities in the future. In fact, some experts consider that, to accomplish the desired global energy transition, the demand for metals such as nickel and cobalt may be almost 20 times higher in 2040 compared to 2020 [1]. But the case of iron ore is particularly relevant, as it is currently the most massively mined commodity, with its global production reaching about 2400 Mt in 2021 [2]. Furthermore, in 2019, iron ore accounted for almost 94% of all metals produced by the mining industry in the world, with 98% of which being used for steelmaking [3], making it the ideal mining waste to study from a circular economy perspective.

Unfortunately, the mining industry produces large amounts of waste, usually in the form of tailings that are disposed of in massive tailings storage facilities where their potential value as a construction material is neglected and which frequently pose important economic, social and environmental risks. In fact, the rock-to-metal ratio, which is an important measure of mining environmental impacts, is usually extremely high, with values in the range 10^5 to 10^6, in the case of gold, and values in the order of 10 in the case of iron ore often being reported [4]. Moreover, the metallic ore grades exploited through mining show an evident global tendency to decrease, because the higher-grade reserves have already been almost completely exploited [5]. As a result, the number and magnitude of tailings storage facilities in the world are expected to rise further. Consequently, an increase in the number of accidents involving these massive geotechnical structures has been observed during the last few decades, particularly in the case of the more failure-prone tailings dams. This problem is particularly serious in the case of iron ore tailings, with different failure mechanisms being identified from past events [6]. According to data collected by WMTF [7], which compiles the number of failures that have occurred in the past, at least 30 serious or very serious tailings dam failures are predicted to occur in the current decade (Figure 1). This distressing forecast suggests that the volume of mining waste produced must be reduced and that the safety of tailings storage facilities must be enhanced.

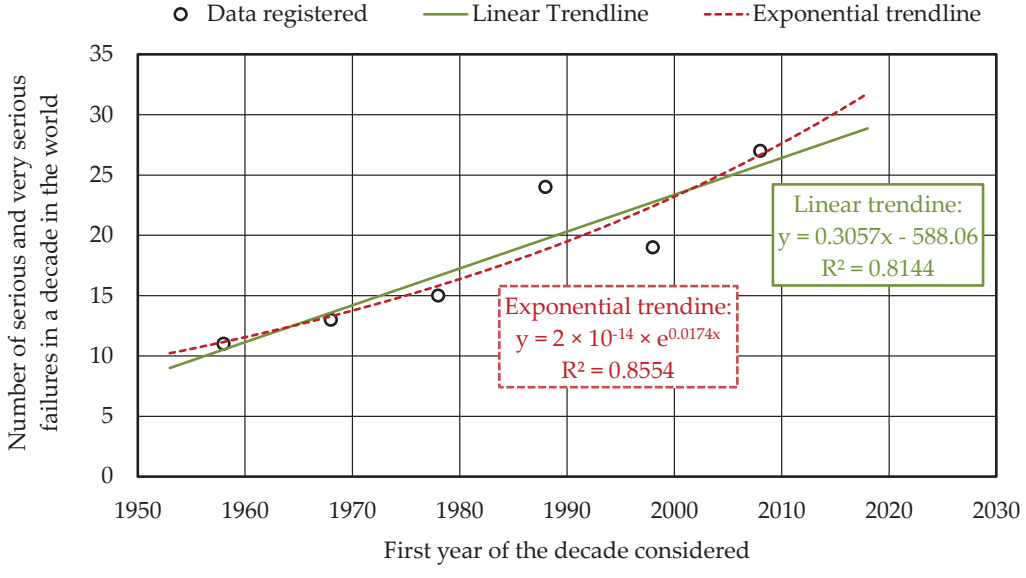

Figure 1. The number of serious and very serious tailings dam failures observed in the past in the world and predictions of similar failures in the future, based on data from WMTF [7].

Considering the volume of mining waste that is currently being generated, different principles of the circular economy could be applied to enhance mining waste management sustainability, including re-treating tailings within mine processing to enable the reuse and regeneration of materials [8]. This may be achieved in practice through the use of these unconventional geomaterials in geotechnical works in order to decrease the wide-ranging impacts of raw materials' extraction. In fact, the UN urges for further research on innovations in tailings' reuse, namely with respect to the potential to reuse at least part of the mining waste as an alternative to natural aggregates in construction [9]. Some attempts have been made to reuse tailings in construction, namely those resulting from iron ore mining, with the experimental results suggesting promising applications for the waste analyzed, which was processed by briquetting [10]. Using iron ore tailings in geotechnical

works can be even more attractive, due to the large volume of materials that are often required to build embankments, land reclamation works, etc. Yet, sustainable geotechnical applications require control of the environmental safety of the applications, namely through suitable physicochemical and ecotoxicological analysis that must be carried out, similarly to other unconventional geomaterials used in construction [11,12].

On the other hand, the safety of tailings dams and other tailings storage facilities must be enhanced in order to protect human life, the environment and the economy. In fact, as mining is currently trying to cope with falling ore grades, increasingly larger projects are required to manage growing amounts of tailings. This creates continuous pressure in tailings management, namely with respect to stability to avoid catastrophic failures and other short- and long-term problems [2]. Also, there is increasingly growing pressure from society to avoid the consequences of dramatic failures such as the 2019 Brumadinho tailings dam collapse, which is believed to be the most serious social and environmental disaster that affected Brazil [13]. In addition, at least three different outstanding international teams reached inconsistent conclusions with respect to the causes of failure [14–16], which suggests that the mechanical behavior of tailings is still poorly understood. But even if the Brumadinho tailings dam collapse did not seem to be caused by earthquake loading, many of these structures are built in seismically active areas and are prone to earthquake-induced liquefaction [17]. This complex phenomenon can cause dramatic failures in granular saturated geomaterials due to the reduction in effective stress induced by large excess pore pressure generation, with its analysis and mitigation requiring proper mechanical characterization [18] and advanced modeling tools incorporating the intricate nature of local earthquakes [19]. But even if excess pore pressure generation induced by static or cyclic loading plays a role in major failures of tailings dams [20], the behavior of tailings still requires further clarification due to their rather peculiar man-made origin [21].

Considering the relevant problem faced by the mining industry regarding the reduction in the volume and the enhancement of the safety of tailings storage facilities in a challenging environment, this paper focus on the experimental characterization of iron ore tailings, which are the most abundant type of mining waste produced in the world. Iron ore samples representing real tailings and compacted tailings were tested to assess the most relevant physical, identification and mechanical properties governing their performance under different conditions that may exist in the field, namely when used as a building material. The tailings tested can be described as low-plasticity silty sand materials with average solids density of 4.7, a maximum dry unit weight close to 3 g/cm^3 and an angle of friction and liquefaction resistance exceeding the values usually found in common granular materials. The experimental results highlight the particular features of the behavior of iron ore tailings and emphasize the potentially promising combination of high shear resistance and high density that favors particular geotechnical applications. The research outcome should contribute to improving our current understanding of the behavior of this unconventional geomaterial so that safer tailings storage facilities can be designed and alternative uses for iron ore tailings can be found in the field of geotechnical engineering.

2. Materials and Methods

The experimental characterization of iron ore tailings was carried out using a selected representative material from a Portuguese iron mine and by employing different tests to characterize the behavior of the material from diverse relevant geotechnical perspectives.

2.1. The Moncorvo Iron Mine

This research was based on tailings collected from an old tailings storage facility created during the operation of the Torre de Moncorvo iron mine, which lasted until the 1980s. The mine, whose activity was recently revived, is located in the NE region of Portugal (Figure 2).

Figure 2. Location of Torre de Moncorvo iron mine tailings storage facility (northeast Portugal).

Disturbed iron ore tailings were collected in order to prepare compacted and slurry-based reconstituted samples for geotechnical testing, as described below. The material was selected because it represents the most abundant type of mining waste available in the world and also because its properties are typical of other iron ore tailings storage facilities found in the world. Thus, the iron ore tailings selected were consistent with the research aims.

2.2. Experimental Methods

2.2.1. Sample Reconstitution to Replicate Tailings' Field Behavior

To more truthfully reproduce tailings' field depositional conditions and obtain uniform samples showing realistic geotechnical behavior under different testing conditions, the samples aiming to replicate the tailings' field behavior were prepared using the "slurry deposition method"—SDM [22]. The SDM was adapted to the material tested, using a water content that facilitated uniform mixing of the slurry while avoiding particle segregation, which was significantly encouraged by the differences in the sizes and densities of the grains found in the iron ore tailings. Sample reconstitution, carried out with a water content of 23%, involved 3 stages (Figure 3): (A) preparing a slurry with the particles forming the iron ore tailings, aleatorily selected using a riffle sample divider, with the desired water content (23%); (B) placing the slurry in a rigid mold, with a diameter of 11.5 cm and a height of 30 cm; (C) consolidating the slurry in a rigid mold, acting as a consolidometer, to the desired effective vertical stress (50 kPa) by successively increasing the vertical load by 10% every two days. In the end, samples were easily cut from the block to the required dimensions for testing, provided that vibrations were strictly avoided.

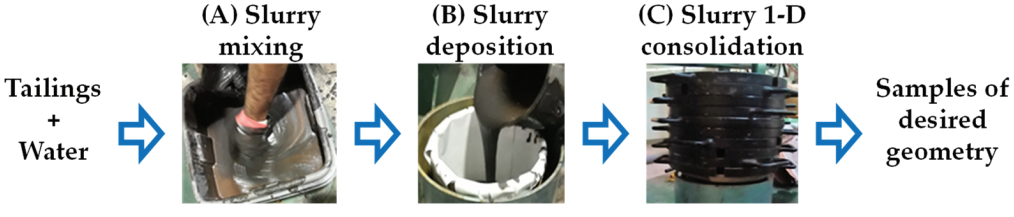

Figure 3. Slurry-based reconstitution method used to prepare the iron ore tailings samples, involving the following stages: (**A**) slurry uniformization through hand mixing at the desired water content; (**B**) the deposition of the slurry in a suitable mold; (**C**) slurry consolidation under the selected vertical load.

2.2.2. Physical and Identification Tests

The physical and identification tests were carried out on the tailings selected following mostly the ASTM standards, namely the Standard Test Method for Particle-Size Distribution

of Fine-Grained Soils Using the Sedimentation (Hydrometer) Analysis [23] (ASTM D7928-21), the Standard Test Method for Specific Gravity of Soil Solids by the Water Displacement Method [24] (ASTM D854-23) and the Standard Test Methods for Plastic Limit of Soils [25] (ASTM D4318-17^{e1}). Because the iron ore tailings used in the research had low plasticity, the determination of the liquid limit was carried out using the BS standards, namely BS 1377-2:2022 [26], as the determination was based on the cone penetrometer method (definitive method). In fact, this method is more suitable to determine the liquid limit of low-plasticity materials such as those used in this research.

2.2.3. Modified Proctor Test

The modified Proctor test was carried out following the ASTM standards relative to this test [27]: Standard Test Methods for Laboratory Compaction Characteristics of Soil Using Modified Effort—ASTM D1557-12(2021). This test was selected in order to assess the behavior of the unconventional geomaterial considered in the research, namely to verify if the material showed a compaction curve similar to the curves shown by conventional geomaterials and also to prepare a sample for testing under undrained triaxial compression. The results also shed further light on the opportunity of using the material as a building material in the construction of embankments and other geotechnical works.

2.2.4. Undrained Monotonic Triaxial Tests

The undrained monotonic shear stress–strain behavior of the iron ore tailings tested was determined through undrained monotonic triaxial compression tests carried out in accordance with the ASTM standards, namely the Standard Test Method for Consolidated Undrained Triaxial Compression Test for Cohesive Soils—ASTM D4767-11 [28]. All the samples tested were cylindrical with a height-to-diameter ratio of 2:1. The samples prepared by the SDM had a height of 76 mm and the samples prepared by compaction had a height of 200 mm.

2.2.5. Undrained Cyclic Triaxial Tests

The undrained cyclic shear-stress–strain behavior of the iron ore tailings tested was determined through undrained cyclic triaxial compression tests carried out in accordance with the ASTM standards, namely the Standard Test Method for Load Controlled Cyclic Triaxial Strength of Soil—ASTM D5311-11 [29]—adapted to the characteristics of the triaxial equipment available, which only permits low-frequency tests that are completely suitable to test the response of liquefiable materials under undrained cyclic loading. The samples tested were prepared by the SDM and had a cylindrical shape, with a height-to-diameter ratio of 2:1 and a height of 76 mm.

3. Results

Following the tests carried out, the results obtained are presented and discussed in this section, which is organized in accordance with the previous section, which defines the details of the tests carried out.

3.1. Sample Reconstitution to Replicate Tailings' Field Behavior

The iron ore tailings samples' reconstitution procedures resulted in a series of uniform samples with the required geometry for testing, as shown in Figure 4. After progressive consolidation of the slurry for a total of almost 3 weeks, the samples prepared through the SDM were relatively straightforward to remove from the consolidometer (Figure 4a) and cut to the desired geometry (Figure 4b). In fact, provided that the samples were not submitted to any form of vibration that would induce liquefaction, the samples were fairly consistent. The different samples were tested at different locations with respect to the grain size distribution, plasticity and specific gravity of soil solids, which confirmed that the reconstituted samples prepared with the described method had uniform compositions and coherent behavior at different locations [30].

(**a**) (**b**)

Figure 4. Results of the sample reconstitution: (**a**) final aspect of the reconstituted block; (**b**) final aspect of a sample cut from the block and ready for testing in a triaxial cell.

3.2. Physical and Identification Properties

The most relevant physical and identification properties of the reconstituted samples of iron ore tailings considered in this research were determined using the methodologies described in Section 2.2.2. The average values shown were obtained from 24 tests carried out for each of the properties determined.

3.2.1. Grain Size Distribution

Figure 5 represents the grain size distribution curve for the reconstituted iron ore tailings samples with sieve and sedimentation analysis, which is representative of the 24 tests performed. The results show that the tailings are composed of silt (51%) and sand (49%) in similar proportions, which is consistent with the results of similar tests carried out on samples collected from similar tailings storage facilities around the world. For example, the average values of D_{10} and D_{50}, which are close to 0.0145 mm and 0.059 mm, respectively, are within the intervals observed in the Yuhezhai iron ore tailings. In fact, in these iron ore tailings, the values of D_{10} and D_{50} were determined in the ranges of 0.005 to 0.051 and 0.030 to 0.120 for D_{10} and D_{50}, respectively [31]. The results also suggest that the grain size distribution of the tailings tested is fairly uniform, with a coefficient of uniformity (C_u) of 4.07. This value is also consistent with the range (3.11~8.82) observed in similar materials [31].

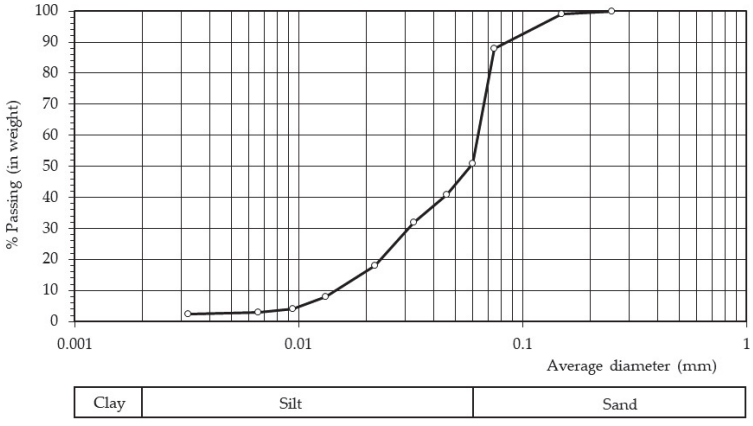

Figure 5. Grain size distribution curve of the reconstituted iron ore tailings samples.

3.2.2. Specific Gravity of Soil Solids

The specific gravity of soil solids (G) relative to the iron ore tailings tested was experimentally determined through the water displacement method [24]. The average value

obtained (G ≈ 4.7) is significantly higher than the values commonly obtained in conventional geotechnical materials (G ≈ 2.6~2.7), which is due to the fact that tailings still contain variable but significant amount of metals and minerals. In this case, the fact that iron particles have a density close to 8 results in a much higher value of G for the tailings particles, which also indicates that the tailings tested still incorporate significant amounts of iron. The fact that in some cases the values of G reported for similar materials are not so high derives from the fact that the efficiency levels of the methods used to separate the iron vary a lot amongst different mines. E.g., for the Yuhezhai iron ore tailings, the values of G reported are in the range 3.08 to 3.23 [31], which suggests a more efficient recovery of the iron ore. It should be noted that the tailings tested were produced about 50 years ago, in many cases involving manual selection of the natural rock during the beneficiation stage, which was undoubtedly an ineffective selection process.

3.2.3. Plasticity

The plasticity characteristics of the iron ore tailings tested, namely the plastic (w_P) and liquid (w_L) limits and the plasticity index (PI), were experimentally determined. The soil plastic limit was assessed through the soil hand rolling procedure defined by the ASTM standards [25]. The liquid limit was assessed through the cone penetrometer method (multipoint) defined by the BS standards, which is a more reproducible method that should not yield significant differences when compared to the alternative method employing the Casagrande apparatus [26].

The results obtained (Table 1) show that the tailings tested are slightly plastic, with a plasticity index of just 5%. These results are consistent with the grain size distribution and composition of the tailings tested but also with the values observed in other iron tailings storage facilities. For example, the values obtained fit into the ranges for the plastic (0∼19%) and liquid (0∼28%) limits, as well as for the plasticity index (0∼9%), measured in the Yuhezhai iron ore tailings [31].

Table 1. Average plasticity characteristics experimentally determined for the iron ore tailings tested.

Plastic Limit—w_P (%) [1]	**Liquid Limit—w_L (%)** [2]	**Plasticity Index—PI (%)**
15	20	5

[1] ASTM D4318—17^{e1} [25]; [2] BS 1377-2:2022 [26].

3.3. Modified Proctor Test

The compaction curve relative to the modified Proctor test for the iron ore tailings tested (Figure 6) was obtained following the procedures established by the ASTM standards [27]. The values of the optimum water content and the maximum dry unit weight were established as 8.95% and 2.99 g/cm^3, respectively.

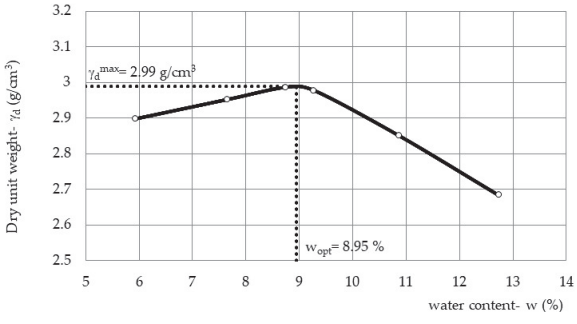

Figure 6. Compaction curve obtained for the iron ore tailings tested using the energy defined for the modified Proctor test.

The shape of the compaction curve, obtained with the modified Proctor test, is similar to the compaction curves usually found in conventional geomaterials, namely for those commonly employed in embankment construction. In fact, a peak is clearly defined in the curve relating the water content used in the compaction with the resulting dry unit weight. Also, the value of the optimum water content, which is about 60% of the plastic limit, is in line with the values observed in conventional geomaterials. For example, the optimum water content (w_{opt}) can be correlated with the liquid limit (w_L) as follows [32]:

$$w_{opt} = 0.3802 w_L + 2.4513 \quad (1)$$

Equation (1), where w_{opt} and w_L are given in %, predicts a value of 10.1% for the optimum water content (w_{opt}) of a geomaterial with a liquid limit (w_L) of 20%, which is fairly close to the value experimentally determined.

On the contrary, the value obtained for the maximum dry unit weight is much higher than the values commonly found in conventional geomaterials. For example, employing the database that was used to establish the correlation shown in Equation (1), the maximum dry unit weight ($\gamma_d{}^{max}$) can be correlated with the liquid limit (w_L) as follows [32]:

$$\gamma_d{}^{max} = 2.116 - 0.01008 w_L \quad (2)$$

Equation (2), where $\gamma_d{}^{max}$ is shown in g/cm^3 and w_L is given in %, predicts a value of 1.91 g/cm^3 for the maximum dry unit weight ($\gamma_d{}^{max}$) of a geomaterial with a liquid limit (w_L) of 20%, which is much lower than the value experimentally determined. However, it should be noted that the large database (126 different soils with different plasticity and grain size compositions) used for establishing these correlations is only composed of conventional geomaterials, with specific gravity of soil solids (G) varying between 2.58 and 2.85. However, the iron ore tailings tested have a much higher value of the specific gravity of soil solids (G), which is much higher than the range of values exhibited by the materials included in the database. As a result, the values cannot be directly compared and the correlation proposed in Equation (2) is not applicable to the unconventional material tested in this research.

3.4. Undrained Monotonic Triaxial Compression Tests

The stress–strain shear resistance response in the undrained monotonic triaxial compression (UMTC) of reconstituted samples representing field behavior, reconstituted through the SDM, was assessed through the behavior of isotropically consolidated samples to effective confining stresses of 50 and 200 kPa (Figure 7). The stress paths described by both samples (Figure 7a) under undrained triaxial compression indicate that, during the early loading stages, the samples show a tendency to contract until reaching a common line passing through the origin.

The so-called phase transformation line (PhTL) observed in Figure 7a marks the instant where the samples change from a contractive to a dilatant tendency, with the stress paths curving to the right-hand side of the plane p'-q and progressive shearing causing an increase in the effective confining stresses (p'). For a certain level of axial strain, the stress paths tend to follow another common line passing through the origin, which may possibly coincide with the so-called critical state line (CrSL).

During shearing, the stress–strain responses of the two samples also show similar features (Figure 7b). Until they come near to the PhTL, there is a fairly linear stress–strain response of the samples. But as the PhTL is crossed, the samples show decreasing stiffness and strains increase at a larger rate with the increase in shear stress. Finally, as the samples approach the CrSL, the samples show progressively increasing stiffness with strain. As expected, during all the described stages, the sample consolidated at higher effective confining stresses exhibits a stiffer response due to the well-known effect of p' on the stiffness of soils [18]. In fact, this well-known effect of p' on the stiffness of soils during shearing is also clear in the case of this unconventional geomaterial.

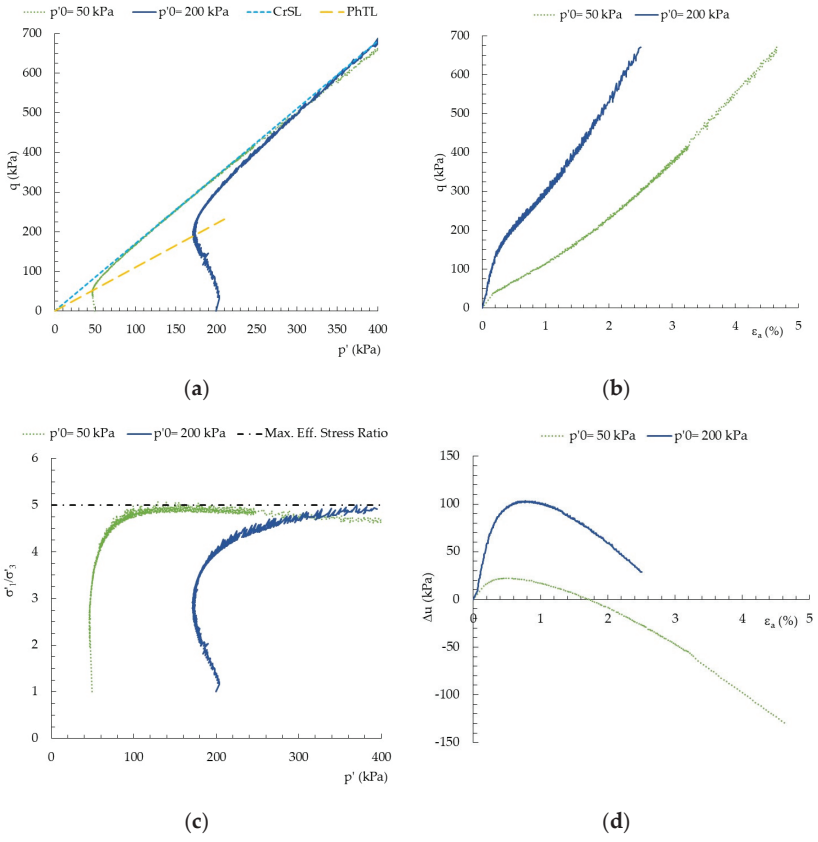

Figure 7. Stress–strain shear resistance response of slurry-based reconstituted samples isotropically consolidated to effective confining stresses of 50 and 200 kPa under undrained monotonic triaxial compression: (**a**) effective stress path; (**b**) stress–strain response; (**c**) variation in the effective stress ratio with p'; (**d**) variation in the excess pore pressure with axial strain.

Figure 7c reinforces some of the features of behavior previously described, namely with respect to the tendency for the effective stress ratio (σ'1/σ'3) to reach a similar and fairly constant value for the two samples tested, which is close to 5. This value corresponds to an effective friction angle of 42°, which is a fairly high value in comparison with a conventional soil with the characteristics of the tailings tested. Still, this value is within the range of values observed in the field, namely in Campo Grande iron ore tailings dam (Mariana/MG, Brazil), possibly due to the very important angularity of the grains formed by rock crushing and grinding, as shown by optical and electron microscope photographs [33]. It is also worth mentioning that the sample consolidated to a higher effective confining stress shows a higher initial tendency to contract, which results in a large reduction in p' during the earlier loading stages. This is a feature that is also typical of the behavior of granular soils under undrained monotonic shearing, which also tend to show a larger contractive tendency (responsible for higher excess pore pressure generation) when consolidated under larger effective confining stresses.

Figure 7d emphasizes the tendency of the samples to change their behavior from contractive to dilative during monotonic shearing, which is another feature of behavior that is also commonly shown by granular soils [18]. In the case of the undrained monotonic triaxial compression tests carried out, this tendency can be observed through the variation in the excess pore pressure with the axial strain imposed to the sample. In fact, as the PhTL

is crossed, both samples show an inversion of the initial tendency to generate positive excess pore pressure and progressive shear straining, inducing a significant reduction in the pore pressures to values that can be lower than the initial values. Once again, the effect of the effective confining stress on the behavior of the samples is notorious and similar to that observed in conventional granular geomaterials.

Overall, the qualitative response of the reconstituted iron ore tailings tested in undrained monotonic triaxial compression, representing the field behavior, is similar to that exhibited by other conventional geomaterials, namely granular soils. Still, the value of the effective friction angle observed in the tailings tested may exceed the values currently found in other geomaterials, possibly due to the significant angular nature of their industrially produced particles.

An additional triaxial test (Figure 8) was carried out to assess the stress–strain shear resistance response in the undrained monotonic triaxial compression (UMTC) of compacted samples, representing the behavior of the tested iron ore tailings, namely when used as a construction material for sustainable geotechnical works. The sample was compacted with the water content defined in Section 3.3, using the specific energy of the modified Proctor test. For the sake of comparison, the sample was isotropically consolidated to an effective confining stress of 50 kPa, which aimed to represent relatively shallow field conditions of iron tailings when used as a construction material, namely in embankment construction.

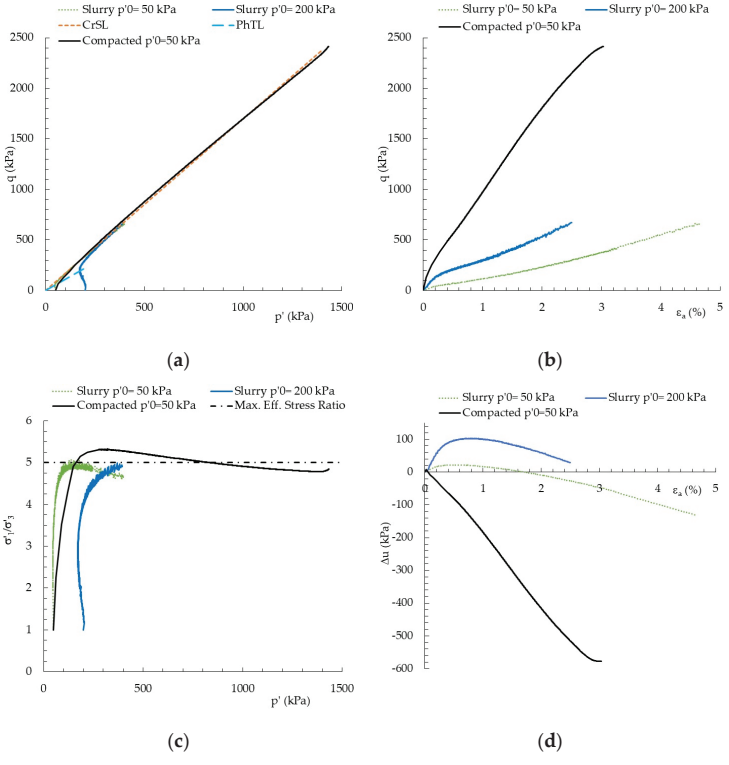

Figure 8. Stress–strain shear resistance response of isotropically consolidated compacted iron ore tailings and slurry-based reconstituted samples under undrained monotonic triaxial compression: (**a**) effective stress path; (**b**) stress–strain response; (**c**) variation in the effective stress ratio with p'; (**d**) variation in the excess pore pressure with axial strain.

The major features of behavior described with respect to the stress–strain shear resistance response of reconstituted samples representing field behavior (Figure 7) remain

qualitatively valid when the behavior of the compacted sample is observed (Figure 8). However, similarly to what is shown by conventional geotechnical materials under comparable conditions, significant differences can be observed when a compacted tailings sample is sheared in undrained monotonic triaxial compression. In fact, the compacted sample tends to exhibit a clear dilatant tendency from an early stage, as shown by the effective stress paths (Figure 8a) or by the variation in the excess pore pressure with the axial strain (Figure 8d).

But the most relevant and interesting aspect of behavior exhibited by the compacted tailings sample, from a geotechnical perspective with the aim of using tailings as a construction material, is the significant increase in the stiffness of the sample during undrained triaxial compression (Figure 8b). This is evident when comparing the stress–strain behavior of the compacted and slurry-based reconstituted samples isotopically consolidated for the same effective confining stress (50 kPa). In fact, the former sample shows very large reductions in the axial strains induced by shearing. These reductions in axial strain mount up to 94% and 89%, corresponding to increases in the deviatoric stress of 100 and 500 kPa, respectively. It is also noticeable that the maximum value of the effective stress ratio observed in the reconstituted samples ($\sigma'_1/\sigma'_3 \approx 5$) is exceeded for smaller strains in the compacted sample (Figure 8c).

3.5. Undrained Cyclic Triaxial Tests

The stress–strain-shear resistance response of reconstituted samples, prepared with the slurry-based method, in undrained cyclic triaxial compression, was assessed through the behavior of an isotropically consolidated sample to an effective confining stress of 200 kPa tested under cyclic shear loading of $\Delta q = \pm 200$ kPa (Figure 9).

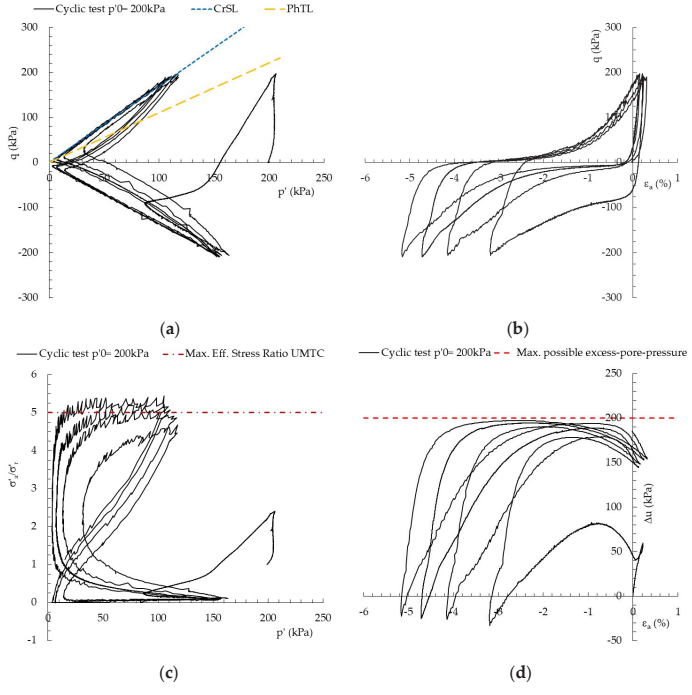

Figure 9. Stress–strain shear resistance response of a reconstituted sample isotropically consolidated to an effective confining stress of 200 kPa under undrained cyclic triaxial loading with $\Delta q = \pm 200$ kPa: (**a**) effective stress path; (**b**) stress–strain response; (**c**) variation in the effective stress ratio with p'; (**d**) variation in the excess pore pressure with axial strain.

The cyclic stress path described by the sample (Figure 9a) under undrained cyclic triaxial loading indicates that a very large tendency to contract is observed during the first cycle, due to the fact that the cyclic loading imposed is large and the stress path comes near to the PhTL. Like in undrained monotonic triaxial compression (Figure 7a), this line marks the instant where the sample changes from a contractive to a dilatant tendency in each loading cycle, with the stress path curving to the right-hand side of the plane p'-q with progressive shearing. And as cyclic loading progresses, the stress path defines a so-called butterfly shape that indicates the occurrence of cyclic liquefaction ($p' \approx 0$), as commonly observed in conventional geotechnical materials, especially in granular soils. The CrSL governs the position of the stress paths at this loading stages, namely in compression loading.

The stress–strain response of the sample during undrained cyclic shearing is also similar to that observed in conventional granular geomaterials (Figure 9b). In fact, as liquefaction looms, large axial strains accumulate in each cycle, namely in extension, and the progressive degradation of the iron ore tailings sample's stiffness occurs, even if during the initial parts of the unloading and reloading stages the stress–strain response is fairly rigid.

Another relevant aspect of stress–strain behavior (Figure 9b) is the large damping observed as cyclic loading progresses and liquefaction is observed, which reflects the substantial amount of energy dissipated in each cycle at this stage, as also commonly observed in conventional granular geomaterials.

Figure 9c reinforces some of the features of behavior previously described, namely with respect to the tendency for the effective stress ratio (σ'_a/σ'_r) to reach a similar and fairly constant value in specific parts of the loading stages in every cycle after liquefaction occurs. This value of σ'_a/σ'_r is in fact similar to the value observed in undrained monotonic triaxial compression, which is also close to 5. On the other hand, during other parts of the loading cycles, this ratio is close to zero, which results from the fact that, in this particular case, the value of σ'_a is close to zero. In other parts of the cycle, this ratio varies significantly while p' is practically zero.

Figure 9d highlights the tendency of the sample to change its behavior from contractive to dilative in each cycle, even if, overall, the excess pore pressure tends to increase during the cyclic test until reaching its maximum possible value, which is equal to the initial effective confining stress of the sample (200 kPa). This is another feature of behavior that is also commonly shown by granular soils, with the fact that the maximum excess pore pressure value was achieved so quickly being determined by the fact that the first peak loading cycle resulted in a close approach to the PhTL, which has a significant detrimental effect on the liquefaction resistance of more conventional geomaterials [19]. It should also be noted that the reversion of the contractive to dilatant tendency in each cycle occurs when the PhTL is crossed, which is also typically observed in conventional granular geomaterials.

Overall, the response of the iron ore tailings tested in undrained cyclic triaxial loading is similar to that exhibited by other conventional geomaterials, namely granular soils, with the PhTL and CrSL governing the behavior during most of the test, namely after liquefaction ($p' \approx 0$) is achieved.

The stress–strain shear resistance response of slurry-based reconstituted samples during the undrained cyclic triaxial compression of an isotropically consolidated sample to a similar effective confining stress of 200 kPa but tested under a significantly lower value of cyclic shear loading ($\Delta q = \pm 60$ kPa) is shown in Figure 10.

The major features of behavior previously described for the sample tested under a larger cyclic shear loading of $\Delta q = \pm 200$ kPa (Figure 9) remain valid, the main difference being the number of cycles required to reach liquefaction (Figure 10a). As expected, a significant reduction (70%) in the cyclic shear loading applied under similar conditions results in a significant increase in the number of cycles that the sample can sustain before reaching a state of near-zero effective stress, inducing large cyclic axial strains in each cycle.

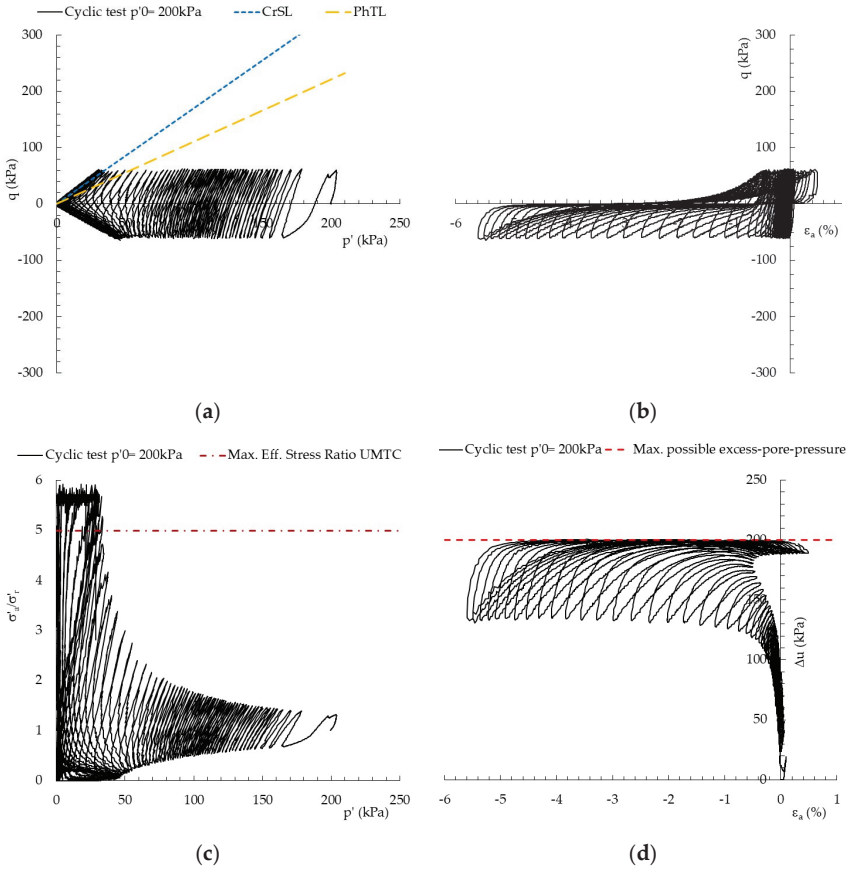

Figure 10. Stress–strain shear resistance response of a reconstituted sample isotropically consolidated to an effective confining stress of 200 kPa under undrained cyclic triaxial loading with Δq = ±60 kPa: (**a**) effective stress path; (**b**) stress–strain response; (**c**) variation in the effective stress ratio with p'; (**d**) variation in the excess pore pressure with axial strain.

In addition, the progression of cyclic axial strains in each cycle is considerably smaller, even after a state of near-zero effective stress is reached (Figure 10b). As the cyclic loading progresses and a state of near-zero effective stresses is reached, the maximum value of the effective stress ratio observed in each cycle increases up to values close to the maximum values observed in UMTC conditions. The fact that the maximum value previously observed is slightly exceeded may be due to the fact that the effective stress values compared are in some cases extremely low for significant periods of the loading/unloading stages, as clearly shown by the variation in the excess pore pressure with the axial strain (Figure 10d).

It can also be observed that, due to the smaller value of cyclic shear loading applied in this test (Δq = ±60 kPa), the temporary dilation periods observed in each cycle (Figure 10d) never cause a reduction in the excess pore pressure as large as in the test (Figure 9d) where a larger value of cyclic shear loading was applied (Δq = ±200 kPa). In fact, in this latter case, transient negative values of excess pore pressure were observed, namely at the peak of the extension stages in each loading cycle (Figure 9d).

4. Discussion

The results presented in detail in the previous section highlight the most relevant aspects of behavior of the iron ore tailings tested, which were collected from a Portuguese

iron mine located in Torre de Moncorvo. These tailings should be, at least qualitatively, representative of other iron ore tailings present in the world, as the extraction, beneficiation and depositional procedures used in iron mining around the world are fairly comparable.

Firstly, reconstituted samples were prepared based on the slurry deposition method, which tends to more effectively replicate the field depositional conditions observed in many tailings storage facilities, namely in tailings dams. Because these geotechnical structures are usually the most prone to failure, it was reasonable to select this reconstitution method to address tailings' mechanical properties, namely those that depend more on the conditions and structure of the samples and/or that are more relevant to stability analysis. In fact, this method results in uniform reconstituted samples that truly replicate field behavior [30], provided that the correct amount of water is used during reconstitution to avoid segregation. In addition, its use has been proven successfully, namely when preparing reconstituted samples with complex geometry [22], which is another advantage of the method.

With respect to the physical and identification properties, the iron ore tailings tested can be described as a transitional uniform material composed of very similar percentages of silt and sand, exhibiting limited but non-negligible plasticity (IP = 5). It is in fact the plasticity of these tailings that supports the use of the slurry deposition method. But because the difference between the liquid and the plastic limits is relatively small, the liquid limit could only be assessed using the cone penetrometer method (multipoint) defined by the BS standards [26]. But the most remarkable feature of the iron ore tailings tested is the unusually high values observed for the specific gravity of soil solids ($G \approx 4.7$), which considerably exceed the values commonly observed in conventional geotechnical materials ($G \approx 2.6$~2.7). Even if these values can vary more or less significantly depending on the amount of iron left in the tailings, which reflects the particular efficiency of the beneficiation process during mining that depends on the mine and on the historical period, the values of the specific gravity of soil solids and other index properties of iron tailings that are directly correlated (unit weight, e.g.,) tend to show values that are often much higher than those commonly found in soils. The value of G obtained in this case reflects the fact that the tailings tested were produced about 50 years ago and using fairly primitive manual selection procedures. Overall, the values obtained for the samples tested are comparable to those found in other mining sites, e.g., in Yuhezhai iron ore tailings [31]. Furthermore, except for the values of G, the values obtained fit into the ranges commonly observed in conventional geotechnical materials. This suggests that the experimental characterization of iron ore tailings should be established based on a geotechnical perspective, without overlooking the particular features of tailings' compositions.

But if iron ore tailings are to be used as a construction material in geotechnical works, the tailings are expected to be compacted in order to improve their mechanical behavior, except in very specific conditions of application. The results obtained show that the shape of the compaction curve is similar to that observed in the vast majority of conventional geomaterials, with the possible exception of uniform sands. In fact, the existence of a peak in the compaction curve defining the optimum water content (w_{opt}) and the maximum dry unit weight ($\gamma_d{}^{max}$) is clearly observed. In addition, the value of w_{opt} obtained (≈9%) is consistent with the ranges for conventional geotechnical materials with similar plasticity characteristics. That said, it is important to emphasize that the value of $\gamma_d{}^{max}$ resulting from the modified Proctor test (≈3 g/cm^3) is much higher than that commonly observed in conventional geomaterials. This should not be understood as an experimental error nor as a sign of an extremely dense material, as, in fact, the value obtained would be physically unacceptable if the density of solid particles (G) would be in the usual range. But as previously described, iron ore tailings can have G values much higher than usual (4.7, in this case), which justifies the higher values of $\gamma_d{}^{max}$ in compacted iron ore tailings.

Irrespective of the need to consider a particular use of iron ore tailings as a building material for geotechnical works or, as an alternative, to assess the stability of tailings storage facilities, the shear resistance of tailings, namely under undrained conditions, must be established. This is true both for static and cyclic loading conditions, with the

latter being particularly important when tailings storage facilities are built in seismically active regions, where earthquake loading can have dramatic consequences. Overall, the undrained monotonic and cyclic behaviors observed in the triaxial tests carried out as part of this research suggest that tailings observe the basic features of behavior established for conventional granular materials. In fact, the principles of CrSL and PhTL govern the undrained response of iron ore tailings under monotonic and cyclic triaxial loading.

In particular, in undrained monotonic compression carried out on samples prepared through the slurry-based method and potentially representing field conditions of some traditional tailings storage facilities, the effects of the effective confining stresses are clear both with respect to the increase in the contractive tendency during the early shearing stages (resulting in positive excess pore pressures in undrained tests) and also in the increase in the stiffness of the material at every loading stage. But even if in a fairly loose condition, both of the samples tested show a tendency to dilate as soon as the PhTL is reached. All these features of behavior are typically observed in sandy materials under similar loading conditions [18]. For larger axial strains, both samples follow stress paths corresponding to an effective angle of friction close to 42°, a value that exceeds what is commonly observed in conventional geomaterials but is within the values observed in iron ore tailings in the region of Minas Gerais, Brazil, where values between 26 and 45 were reported [33]. Once again, to explain this value, the particular characteristics of tailings must be examined in detail. In fact, natural soil particles with dimensions comparable to those found in tailings are created naturally and tend to suffer long processes of weathering that result in near spherically shaped particles. In contrast, tailings result from the mechanical crushing and grinding of rocks that tend to form particles with a much more angular shape, as observed in optical and electron microscope photographs, which justifies the fairly large value of effective angle of friction found in the experiments and in other tailings storage deposits in the world [33].

When compacted in order to simulate the conditions of tailings used as a building material or in alternative tailings storage facilities (dry stacking, e.g.,), the tailings' behavior is qualitatively comparable to that of the reconstituted samples in similar conditions. But, as observed in conventional geomaterials, the stress–strain response of the compacted tailings is much more rigid, at least partially as a result of the much clearer tendency to dilate from earlier loading stages. In fact, the axial strains induced by deviatoric stress increases that would be expected in the field under conceivable undrained loading conditions ($\Delta q \approx 100$~500 kPa) are considerably smaller. As a result, the undrained Young's Modulus (E_U) measured in the compacted sample rises from 11.6 to 252.1 MPa for a deviatoric stress increase of 100 kPa and rises from 13.3 to 119.0 MPa for a deviatoric stress increase of 500 kPa when compared to the non-compacted reconstituted samples.

Similarly, under undrained cyclic triaxial loading, the features of behavior are also typically observed in sandy materials under comparable loading conditions. In fact, not only does every cycle cause increasing excess pore pressure, but also, as p' approaches near-zero values, the typical butterfly shape shown by the cyclic effective stress patch is established. Once again, the cyclic behavior of the material is governed by the same lines observed in undrained monotonic loading: the CrSL and the PhTL. In addition, the level of cyclic loading applied in each cyclic test strongly affects the response of the material, namely with respect to the number of loading cycles needed to reach liquefaction. The stress–strain response of the sample during undrained cyclic shearing also fits the typical behavior of conventional granular geomaterials, with large axial strains accumulating in each cycle, namely in extension, as liquefaction occurs.

The behavior of the iron ore tailings tested under undrained cyclic loading can also be assessed through the progressive degradation of shear stiffness and variation in the damping ratio with increasing shear strain (Figure 11).

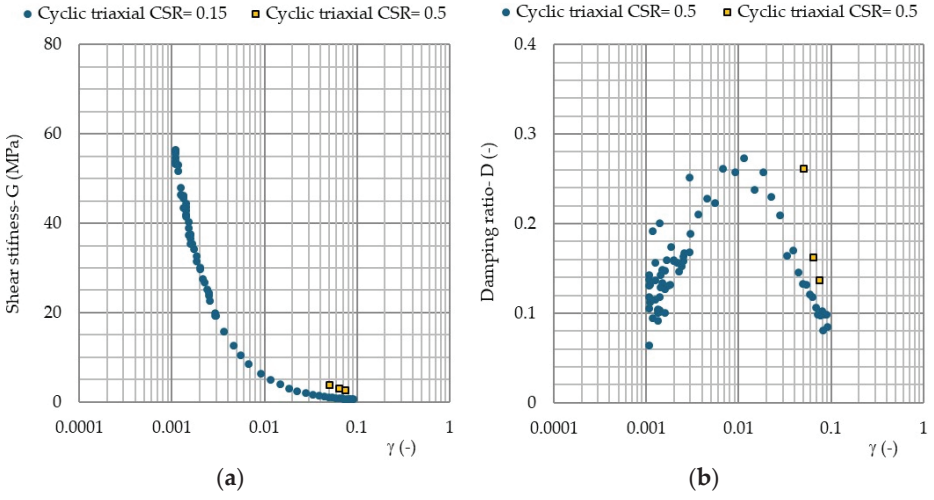

Figure 11. Analysis of the undrained cyclic triaxial tests on iron ore tailings with CSR values of 0.15 and 0.5: (**a**) shear stiffness degradation with shear strain; (**b**) damping variation with shear strain.

As observed in conventional geomaterials, significant degradation of the shear stiffness and large damping variations can be observed as the shear strain progressively increases with cyclic loading. The shear stiffness degradation with shear strain (Figure 11a) shows behavior similar to that observed in common geomaterials, namely in sands, where cyclic-induced liquefaction causes a progressive but massive reduction in the shear stiffness with shear strain. With respect to the damping variation with shear strain (Figure 11b), the initial behavior is consistent with that observed in common geomaterials, with a progressive increase in damping being observed in each cycle. But as shear strains increase above around 2%, the shapes of the hysteretic shear stress–shear strain curves deviate from the common shape used to calculate damping based on elastic considerations, and the damping values obtained show significant reductions. Clarification of whether this is a specific feature of tailings or results from an inappropriate estimation of real damping values due to the shape of the stress–strain curves requires further testing and analysis.

When assessing the liquefaction resistance of conventional granular geomaterials, when cyclically loaded in undrained conditions, it is common to represent the variation in the number of cycles required to reach liquefaction ($N_{Liquefaction}$) against the cyclic stress ratio (CSR = τ/σ'_{v0}) applied during the test, often assuming that liquefaction occurs when the double-amplitude axial strain measured in a cycle reaches 5% (5%DA). The results of the liquefaction resistance of the samples of iron ore tailings tested are plotted in Figure 12, with the results being compared with the liquefaction resistance of mineral sand tailings [34] and a natural sand, namely Sile sand [35], tested under fairly comparable conditions. The results show that the iron ore tailings tested have a liquefaction resistance that exceeds that of the mineral sand tailings presented for large values of CSR, but the resistance increase with decreasing CSR values is less pronounced. In addition, both tailings show higher liquefaction resistance than natural sands, including Sile sand (Figure 12), possibly due to the uncommon shape of non-natural tailings particles. Overall, the behavior observed, namely in terms of liquefaction resistance, is closer to that of sands, despite some plasticity of the tailings tested. This signals the need to address the possibility of earthquake-induced liquefaction occurrence in iron tailings, eventually considering energy-based methods that tend to more effectively explain the behavior of conventional granular geomaterials [19].

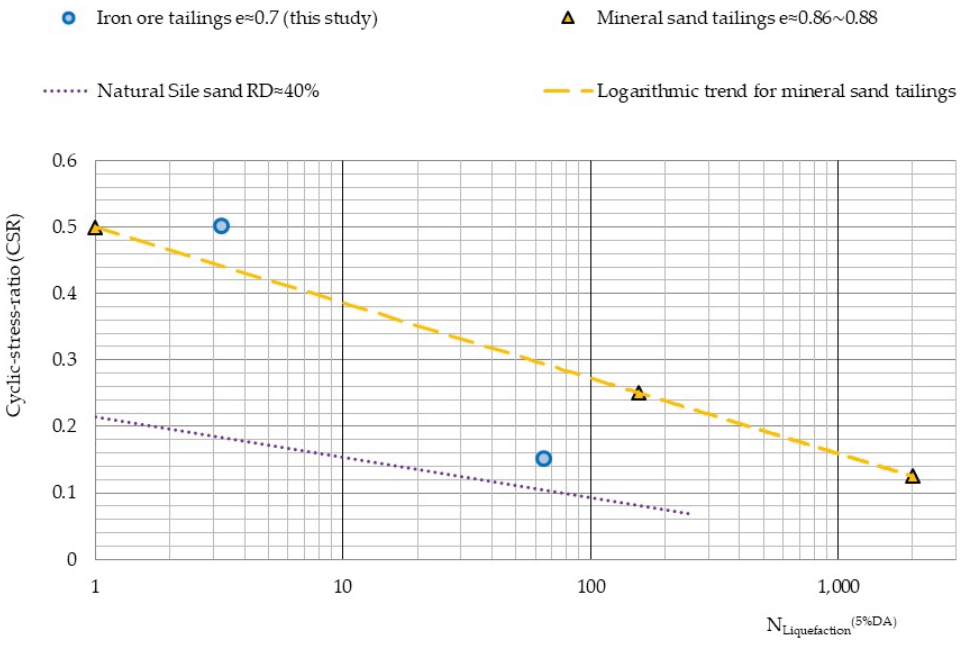

Figure 12. Liquefaction resistance (5%DA) of the tailings tested in comparison to other mineral sand tailings [34] and natural Sile sand [35].

Based on the results obtained, iron ore tailings seem to have promising behavior for application as a building material in the field of geotechnical engineering. In fact, the effectiveness of compaction in increasing the stiffness of tailings in undrained monotonic compression is quite promising and should be accompanied by a significant increase in the liquefaction resistance, similarly to what is observed in granular soils, where densification is a valuable liquefaction resistance measure [36]. In addition, the further light shed on the behavior of the tested unconventional geomaterial will support the more accurate analysis of existing and new tailings storage facilities, which will enhance the safety of these massive structures and reduce the possibility of dramatic consequences that result from their failure. But if tailings need to be assessed from a geotechnical perspective, they are not natural soils. Actually, a true understanding of tailings' behavior requires the solid and openminded interpretation of the results, where the specific nature of tailings must not be ignored, namely with respect to the composition and shape of its grains. In this case, apparently, too-large values of the effective angle of friction or the maximum dry unit weight look more reasonable when a detailed understanding of the particular features of tailings is achieved.

Nevertheless, a final but important recommendation must be issued, namely when considering the use of iron ore tailings as a sustainable building material. Indeed, sustainable geotechnical solutions can only be achieved when using unconventional geomaterials, particularly waste, if the environmental impacts of using these materials are fully under control. Therefore, real applications of iron ore tailings and other similar types of waste require previous analysis of their physicochemical and ecotoxicological properties to confirm the environmental safety of their use in the particular projected conditions [10,11].

5. Conclusions

The mining industry produces large amounts of valueless tailings with significant economic, social and environmental risks to society. Ensuring the safety of massive tailings storage deposits and implementing the principles of circular economy by using these

unconventional geomaterials in geotechnical works to reduce this problem and the wide-ranging impacts of raw materials' extraction is therefore a critical goal of the mining industry. This paper focuses on the experimental characterization of iron ore tailings, which are the most abundant type of mining waste produced in the world.

The results presented highlight the most relevant aspects of behavior of iron ore tailings, which behave as follows:

- They qualitatively behave like other conventional geomaterials with similar grain size composition, in the range of silts and sands, and low plasticity;
- They are distinct from natural soils, with the composition and shape of the grains more or less significantly affecting the values of some relevant properties;
- They exhibit compaction characteristics typical of conventional geomaterials, with large dry unit weights being a consequence of unusually high G values that result from the remaining presence of iron particles;
- They considerably benefit from the improvement induced by compaction, namely with respect to the stiffness and straining-induced dilation observed in undrained monotonic triaxial compression, with intrinsic shear resistance (ϕ') being high in any case;
- They present large shear stiffness degradation and large damping variations under undrained cyclic loading causing liquefaction, with the behavior strongly depending on the cyclic stress ratio applied;
- They show liquefaction resistance similar to other comparable tailings and possibly larger than natural sands.

Overall, iron ore tailings can be described as granular materials, with a significant silty component that is responsible for the low plasticity observed, combining higher effective shear resistance and very high maximum dry unit weight after compaction with some susceptibility to earthquake-induced liquefaction, as a result of the following characteristics of tailings particles:

- Large resistance which is due to the fact that tailings result from the mechanical crushing and grinding of rocks, which tend to form particles with an angular shape that considerably differs from the spherical shape of natural soils particles, as observed in optical and electron microscope photographs;
- Larger than expected values of the maximum dry unit weight which result from the presence of iron particles in the tailings.

The outcome of this research suggests that the characterization of iron ore tailings' behavior requires a geotechnical approach that does not overlook the particular and singular features of tailings particles shape and composition. Based on the results obtained, iron ore tailings seem to have promising behavior for applications as building materials in the field of geotechnical engineering. In fact, the consequences of the singularity of iron ore tailings grains with respect to the higher effective shear resistance and very high maximum dry unit weight after compaction should be explored for specific geotechnical applications where these unique properties are relevant. This includes applications where, namely after compaction, the following aspects apply:

- High shear resistance and stiffness, at least partially due to the uncommon shape of tailings particles, are required (e.g., embankments);
- Large unit weights, due to the presence of iron particles that result in unusually high G values, can be an advantage (e.g., sea shore protection).

Still, a note of caution must be issued with respect to the potential issues related to the earthquake-induced liquefaction susceptibility of these materials and the potential negative environmental impacts of their use as a building material. In fact, sustainable geotechnical solutions involving unconventional geomaterials, particularly waste, must be preceded by proper analysis to assess the environmental safety of their use in the particular projected conditions.

Author Contributions: The individual contributions to this paper were as follows: conceptualization, P.C.; methodology, P.C. and D.C.; software, P.C. and D.C.; validation, D.C.; formal analysis, P.C. and D.C.; investigation, D.C.; resources, P.C.; data curation, D.C.; writing—original draft preparation, P.C.; writing—review and editing, P.C. and D.C.; visualization, P.C. and D.C.; supervision, P.C.; project administration, P.C.; funding acquisition, P.C. All authors have read and agreed to the published version of the manuscript.

Funding: This research was funded by FCT—Foundation for Science and Technology—through the research grant PTDC/ECI-EGC/4147/2021.

Institutional Review Board Statement: Not applicable.

Informed Consent Statement: Not applicable.

Data Availability Statement: The original contributions presented in the study are included in the article; further inquiries can be directed to the corresponding author.

Acknowledgments: The authors acknowledge the contribution made to this research by the company responsible for Torre de Moncorvo's iron mine, Aethel Mining, Ltd., by providing access to the tailings storage facilities and authorizing sample collection.

Conflicts of Interest: The authors declare no conflicts of interest. The funders had no role in the design of the study; in the collection, analyses, or interpretation of data; in the writing of the manuscript; or in the decision to publish the results.

References

1. Komnitsas, K.; Lazos, I.; Eerola, T. Energy Transition Metals: Future Demand and Low-Carbon Processing Technologies. *Mater. Proc.* **2023**, *15*, 56. [CrossRef]
2. Mudd, G.M. Assessing the Availability of Global Metals and Minerals for the Sustainable Century: From Aluminium to Zirconium. *Sustainability* **2021**, *13*, 10855. [CrossRef]
3. Bhutada, G. All the Metals We Mined in One Visualization, Visual Capitalist. 2021. Available online: https://www.visualcapitalist.com/all-the-metals-we-mined-in-one-visualization/ (accessed on 20 April 2024).
4. Nassar, N.T.; Lederer, G.W.; Brainard, J.L.; Padilla, A.J.; Lessard, J.D. Rock-to-Metal Ratio: A Foundational Metric for Understanding Mine Wastes. *Environ. Sci. Technol.* **2022**, *56*, 6710–6721. [CrossRef] [PubMed]
5. Norgate, T.; Jahanshahi, S. Low grade ores-smelt, leach or concentrate. *Miner. Eng.* **2010**, *23*, 65–73. [CrossRef]
6. Otieno, F.; Shukla, S.K. An insight into failure of iron ore mine tailings dams. *Int. J. Min. Reclam. Environ.* **2022**, *37*, 127–147. [CrossRef]
7. WMTF. Estimate of World Tailings Portfolio, Data from the Organization World Mine Tailings Failures. Center for Science in Public Participation, Bozeman, Montana, USA. Available online: https://worldminetailingsfailures.org/ (accessed on 20 April 2024).
8. Zhou, L. Towards sustainability in mineral resources. *Ore Geol. Rev.* **2023**, *160*, 105600. [CrossRef]
9. Franks, D.M.; Keenan, J.; Hailu, D. Mineral security essential to achieving the Sustainable Development Goals. *Nat. Sustain.* **2023**, *6*, 21–27. [CrossRef]
10. Ardelean, E.; Socalici, A.; Lupu, O.; Bistrian, D.; Dobrescu, C.; Constantin, N. Recovery of Waste with a High Iron Content in the Context of the Circular Economy. *Materials* **2022**, *15*, 4995. [CrossRef] [PubMed]
11. Bandarra, B.S.; Mesquita, C.; Passos, H.; Martins, R.C.; Coelho, P.A.L.F.; Pereira, J.L.; Quina, M.J. An integrated characterisation of incineration bottom ashes towards sustainable application: Physicochemical, ecotoxicological, and mechanical properties. *J. Hazard. Mater.* **2023**, *455*, 131649. [CrossRef]
12. Bandarra, B.S.; Monteiro, L.; Veloso, G.; Abreu, P.; Sousa, H.; Martins, R.C.; Pereira, J.L.; Coelho, P.A.L.F.; Quina, M.J. Evaluation of MSW incineration bottom ash for environmentally safe geotechnical applications. *Constr. Build. Mater.* **2024**, *427*, 136011. [CrossRef]
13. Rotta, L.H.S.; Alcântara, E.; Park, E.; Negri, R.G.; Lin, Y.N.; Bernardo, N.; Mendes, T.S.G.; Filho, C.R.S. The 2019 Brumadinho tailings dam collapse: Possible cause and impacts of the worst human and environmental disaster in Brazil. *Int. J. Appl. Earth Obs. Geoinf.* **2020**, *90*, 102119. [CrossRef]
14. Robertson, P.K.; Melo, L.; Williams, D.; Wilson, G.W. Report of the Expert Panel on the Technical Causes of the Failure of Feijão Dam I, Vale, S.A., Brazil, 2019; 71p. Available online: https://bdrb1investigationstacc.z15.web.core.windows.net/assets/Feijao-Dam-I-Expert-Panel-Report-ENG.pdf (accessed on 20 April 2024).
15. CIMNE. *Computational Analyses of Dam I Failure at the Corrego de Feijao Mine in Brumadinho*; Final Report; International Centre for Numerical Methods in Engineering: Barcelona, Spain, 2021; 561p.
16. Zhu, F.; Zhang, W.; Puzrin, A.M. The slip surface mechanism of delayed failure of the Brumadinho tailings dam in 2019. *Commun. Earth Environ.* **2024**, *5*, 33. [CrossRef]

17. Verdugo, R.; Sitar, S.; Frost, J.D.; Bray, J.D.; Candia, G.; Eldridge, T.; Hashash, Y.; Olson, S.M.; Urzua, A. Seismic Performance of Earth Structures during the February 2010 Maule, Chile, Earthquake: Dams, Levees, Tailings Dams, and Retaining Walls. *Earthq. Spectra J.* **2012**, *28* (Suppl. 1), S75–S96. [CrossRef]
18. Azeiteiro, R.J.N.; Coelho, P.A.L.F.; Taborda, D.M.G.; Grazina, J.C.D. Critical State–Based Interpretation of the Monotonic Behavior of Hostun Sand. *ASCE J. Geotech. Geoenviron. Eng.* **2017**, *143*, 04017004. [CrossRef]
19. Azeiteiro, R.J.N.; Coelho, P.A.L.F.; Taborda, D.M.G.; Grazina, J.C.D. Energy-based evaluation of liquefaction potential under non-uniform cyclic loading. *Soil Dyn. Earthq. Eng.* **2017**, *92*, 650–665. [CrossRef]
20. Ishihara, K. Liquefaction and flow failure during earthquakes. *Géotechnique* **1993**, *43*, 351–415. [CrossRef]
21. Carrera, A.; Coop, M.; Lancellotta, R. Influence of grading on the mechanical behaviour of Stava tailings. *Géotechnique* **2011**, *61*, 935–946. [CrossRef]
22. Tastan, E.O.; Carraro, J.A.H. A New Slurry-Based Method of Preparation of Hollow Cylinder Specimens of Clean and Silty Sands. *Geotech. Test. J.* **2013**, *36*, 811–822. [CrossRef]
23. *D7928-21*; Standard Test Method for Particle-Size Distribution of Fine-Grained Soils Using the Sedimentation (Hydrometer) Analysis. ASTM: West Conshohocken, PA, USA, 2021.
24. *D854-23*; Standard Test Method for Specific Gravity of Soil Solids by the Water Displacement Method. ASTM: West Conshohocken, PA, USA, 2023.
25. *D4318-17^{e1}*; Standard Test Methods for Liquid Limit, Plastic Limit, and Plasticity Index of Soils. ASTM: West Conshohocken, PA, USA, 2018.
26. *BS 1377-2:2022*; Methods of Test for Soils for Civil Engineering Purposes—Classification Tests and Determination of Geotechnical Properties. BSI: London, UK, 2022.
27. *D1557-12(2021)*; Standard Test Methods for Laboratory Compaction Characteristics of Soil Using Modified Effort. ASTM: West Conshohocken, PA, USA, 2021.
28. *D4767-11*; Standard Test Method for Consolidated Undrained Triaxial Compression Test for Cohesive Soils. ASTM: West Conshohocken, PA, USA, 2011.
29. *D5311-11*; Standard Test Method for Load Controlled Cyclic Triaxial Strength of Soil. ASTM: West Conshohocken, PA, USA, 2011.
30. Coelho, P.A.L.F.; Camacho, D.; Gobbi, F.; Araújo Santos, L. Sample reconstitution for evaluating the cyclic liquefaction resistance of iron ore tailings. In Proceedings of the 20th International Conference on Soil Mechanics and Geotechnical Engineering, Sydney, Australia, 1–5 May 2021.
31. Hu, L.; Wu, H.; Zhang, L.; Zhang, P.; Wen, Q. Geotechnical Properties of Mine Tailings. *ASCE J. Mater. Civ. Eng.* **2017**, *29*, 04016220. [CrossRef]
32. Günaydın, O. Estimation of soil compaction parameters by using statistical analyses and artificial neural networks. *Environ. Geol.* **2009**, *57*, 203–215. [CrossRef]
33. Becker, L.D.B.; Cavalcanti, M.D.C.R.; Marques, A.A.M. Statistical Analysis of the Effective Friction Angle of Sand Tailings from Germano Dam. *Infrastructures* **2023**, *8*, 61. [CrossRef]
34. Cartwright, A. Investigating Cyclic Liquefaction in Transitional Tailings. Ph.D. Thesis, Department of Civil, Environmental & Geomatic Engineering, University College London, London, UK, April 2022.
35. Zeybek, A. Experimental and Empirical Studies to Evaluate Liquefaction Resistance of Partially Saturated Sands. *Appl. Sci.* **2023**, *13*, 81. [CrossRef]
36. Coelho, P.A.L.F.; Haigh, S.K.; Madabhushi, S.P.G. Centrifuge modelling of liquefaction of saturated sand under cyclic loading. In Proceedings of the International Conference on Cyclic Behaviour of Soils and Liquefaction Phenomena, Cyclic Behaviour of Soils and Liquefaction Phenomena, Bochum, Germany, 31 March–2 April 2004; pp. 349–354.

applied sciences

MDPI

Article

Performance of Ore Sand as Aggregate for Interlocking Blocks

Rodrigo Beck Saldanha [1], Mariana Figueira Lacerda Menezes [2], Rafael Jabur Bittar [3] and Nilo Cesar Consoli [1,*]

[1] Graduate Program in Civil Engineering, Universidade Federal do Rio Grande do Sul, Porto Alegre 90035-190, RS, Brazil; rodrigo.saldanha@ufrgs.br
[2] AGERA S.A., Nova Lima 34006-049, MG, Brazil; mariana.menezes@agera.com
[3] VALE S.A., Belo Horizonte 30380-403, MG, Brazil; rafael.bittar@vale.com
* Correspondence: consoli@ufrgs.br

Abstract: The search for alternatives that can replace conventional materials extracted from nature is crucial for environmental sustainability. This is especially the case for construction and geotechnical engineering, as this sector is a major consumer of the planet's natural resources. This paper explores the use of ore sand (OS) tailings with fine aggregate characteristics, which are generated during exploration of iron ore and usually stored in stacks, in terms of their potential for replacing conventional aggregates (gravel, natural sand, and limestone sand) used in interlocking paving blocks for light-traffic pavement. A comparative life cycle assessment (LCA, cradle-to-gate) approach was applied for aggregates in interlocking blocks produced using OS compared to blocks produced with conventional aggregates. The OS was able to replace 24wt% of conventional aggregates (100% limestone sand and 13.3% natural sand), while maintaining compressive-strength performance similar to that of the conventional block (35 MPa). For all eleven environmental-impact categories evaluated in the LCA, the block with OS has improved environmental performance compared to the conventional block. Through the creation and use of a scoring indicator (SI), it was possible to determine that the transport distance of the OS is a limiting factor for the environmental efficiency of the alternative block. Nonetheless, the incorporation of OS mitigates the impacts of block production on eutrophication, acidification, fresh water, human toxicity, and abiotic depletion. The use of tailings reduces the demand for natural resources, decreasing the environmental impact of production and promoting sustainable construction practices.

Keywords: ore sand; aggregates; interlocked block; tailings; life cycle assessment

Citation: Saldanha, R.B.; Menezes, M.F.L.; Bittar, R.J.; Consoli, N.C. Performance of Ore Sand as Aggregate for Interlocking Blocks. *Appl. Sci.* **2024**, *14*, 48. https://doi.org/10.3390/app14010048

Academic Editors: H.J.H. Brouwers, Paulo José da Venda Oliveira and António Alberto Santos Correia

Received: 13 October 2023
Revised: 30 November 2023
Accepted: 5 December 2023
Published: 20 December 2023

1. Introduction

The construction industry continues to grow due to housing shortages, the need for modern infrastructure and urbanization, and other factors. Its activity is responsible for a large demand for natural resources, contributing to the consumption of 4.27 billion tons of cement [1] and 50 billion tons of aggregates (gravel and sand) per year worldwide [2]. Sand and gravels are mined worldwide, with aggregates accounting for the largest volume of solid material extracted globally [3]. In Brazil, approximately 500 million tons of aggregates are consumed annually. These aggregates are mostly employed in cementitious materials used for construction and civil-engineering applications [4].

As a result, the search for alternative raw materials is essential to creating a more sustainable construction industry. Mine tailings can be a promising source of substitutes for natural raw materials, with a worldwide availability that can reach up to 60 billion tons [5]. All countries that conduct ore extraction generate mining waste. Brazil, India, China, and Australia are major producers of iron ore in the world and are consequently the largest sources of iron ore tailings [6]. It is estimated that in Western Australia, 632 million tons of iron ore tailings are produced per year [7]; in China, approximately 600 million tons are generated [8]; and in India, the data are not precise, but the amount is up to 20 million tons [9]. Around the world, this resource has been usually stockpiled behind dams, with

attendant latent environmental and social risks [10,11]. In the state of Minas Gerais (Brazil) alone, 290 million tons per year of tailings are generated from mining activity [12]. Iron ore mining generates large amounts of tailings (on the order of 0.48 tons for each 1.0 ton of iron ore concentrate), and this amount tends to increase with the depletion of the metal concentration in the deposits [13]. Studies have shown that iron ore tailings (IOTs), also called ore sand (OS), have characteristics that can enable them to be effectively used in construction as a substitute for natural sand [14].

Mine tailings have been studied in terms of their use as a fine aggregate for the production of concrete [15,16], geopolymers [17,18] ceramic materials [19,20], and pigments [21]. Along the same lines, mine tailings can be used for the production of interlocked blocks, which have been utilized on a large scale for paving in Brazil. The growth in the production of interlocked blocks is due to their reduced repair cost, easy installation and reusability; more than 90% of the blocks are reused. Vilaça et al. [13] systematized the recovery of iron ore tailings using the criteria of classification, potential, quantity/viability, and applicability for four possible uses: asphalt pavement; aggregate for pavers; aggregate for mortar; and aggregate for ceramic products. Through the critical index developed by the author, the use in block pavers allows for IOTs to be valued and used in symbiosis with industry.

Ravi et al. [22] investigated the properties of interlocking concrete block paver mixed with IOT as a partial replacement for cement. For M25 concrete, the addition of varying levels of iron ore tailings resulted in an increase in compressive strength with IOT levels from 5% to 15% and decrease in compressive strength for IOT levels from 15% to 25%. Santana Filho et al. [23] studied the use of IOTs as a fine aggregate in the production of interlocking concrete blocks, replacing natural aggregate in proportions from 10 to 80%. Physical analyses, environmental analyses (leaching and dissolution), and mechanical tests were performed. The authors concluded that IOTs can be technically and environmentally used for the production of precast concrete blocks. According to Brazilian standards (NBR 9781 [24]), the fundamental materials for the manufacture of interlocking blocks are binders, aggregates, and water, with the use of additives and pigments being allowed.

Despite the applicability of IOTs in construction, it is necessary to evaluate the environmental benefits of replacing aggregates with mining waste. For example, Saldanha et al. [25], verified that the use of IOTs as raw material in the production of sodium silicate for soil stabilization reduces environmental impacts because it avoids the extraction of natural sand. The focus of that work was on the production of sodium silicate using IOT as a source of silicates in the production of a binder. Garcia-Troncoso et al. [26] studied concrete produced with mining waste. Using life cycle analysis, the author examined the replacement of natural sand with tailings at different content levels (5% to 100%). A 3% reduction in the carbon footprint was found in the case of 100% replacement of sand by tailings. However, the environmental impact associated with the transportation of materials represents a possible restriction in the search for environmentally friendly concrete produced using waste [27].

Liu et al. [28] used IOTs as a cementitious composite to improve the mechanical properties of the composite while helping to reduce the environmental burden of production. These authors evaluation LCA in five impact categories: photochemical ozone-creation potential, acidification potential, global-warming potential, ozone-depletion potential and nitrification potential, and found that incorporation of IOTs into concrete reduces the environmental impact of production, which consolidates the possibility of achieving clean production with the use of IOTs to prepare cementitious composites. Nevertheless, that work is more focused on the mechanical and microstructural aspects of using tailings in concrete, with the LCA being used superficially. Gao et al. [29] also briefly evaluated the environmental impacts of using molybdenum mining tailings to replace fine aggregates in structural concrete. Additionally, in both studies, the life cycle assessment is focused on the completed concrete (cement and aggregates), not just the aggregates that compose the blend. A comparative LCA between aggregates highlights the environmental importance of using waste. In general, LCA studies of the use of IOT have focused mainly on cement

mortars. Evaluations of their use as an aggregate for interlocking blocks are still lacking. Brazil alone has the potential to consume around 2.5 million tons of ore sand per year as fine aggregate in the paving of its roads [23].

In this context, no studies were found that carried out a more focused environmental life cycle assessment for the replacement of conventional aggregates by ore tailings in interlocking concrete paving blocks, along with the influence and limits imposed by the transportation of the alternative aggregate for the production of this civil construction product. Hence, this study investigates the environmental impact of utilizing ore sand in constructing interlocking paver blocks and assesses how the distance from the source of tailings generation impacts the life cycle environmental footprint of these materials. The application of LCA to the construction sector is part of a wide effort to implement LCA as a decision-support tool for industry and policy [30]. Therefore, research on the mechanical feasibility of using mining tailings to replace natural resources and on their environmental impact (considering other relevant categories beyond CO_2 emissions) is key to developing more sustainable products.

The objective of this research is to assess sustainability by considering the environmental benefits of utilizing ore sand as a substitute for conventional aggregates (natural sand and limestone sand) in the production of interlocking concrete block pavement and to evaluate the impact of ore-sand transportation on environmental assessment. The compressive strength of both alternatives (conventional and ore-sand blocks) was evaluated and compared. A comparative life cycle assessment was carried out to assess eleven categories of environmental impacts and determine the environmental performance of the aggregates used in the production of the blocks. Using a proposed scoring indicator in conjunction with life-cycle impacts, it was possible to determine a maximum distance for the environmentally sustainable transportation of ore sand used in the production of interlocking concrete paving blocks.

2. Materials and Methods

2.1. Iron Ore Tailings

Ore sand (OS) was obtained from the Itabira complex in the state of Minas Gerais, which has potential to produce 130,000 tons of ore sand per year. Physical test data showed that the material has a specific gravity of 2.75, a unit mass of 1.49 g/cm^3, a fineness modulus of 0.5, and a water-absorption rate of 0.7%. The particle-size distribution indicated that the ore sand is considered a fine aggregate (0.06 mm < diameter < 0.2 mm), with 26% powdery material (<0.075 mm). Per the results of X-ray fluorescence tests, the OS is composed of 87.9% SiO_2, 10.25% Fe_2O_3 and 0.19% Al_2O_3. Its mineralogical composition (Figure 1) is largely quartz, hematite and illite. According to Zhang et al. [31], the compositions of mining tailings depend on the physical and chemical characteristics of the iron ore sources and are very specific to the extraction site. The grain-size distributions of the ore sand studied here and of the other aggregates used are shown in Figure 2. The D_{30}, curvature coefficient (C_c) and uniformity coefficient (C_u) for the materials used are, respectively, (i) ore sand D_{30} = 95, C_c = 0.9 and C_u = 2.6; (ii) limestone sand D_{30} = 90, C_c = 0.1 and C_u = 27.5; (iii) natural sand D_{30} = 280, C_c = 1.0 and C_u = 7.8; and (iv) gravel D_{30} = 1110, C_c = 1.1 and C_u = 2.6. The ore sand is well graded, with diameters varying over a short range, and more uniform than the limestone sand it replaced, promoting better filling of the voids in the mixture of gravel and natural sand.

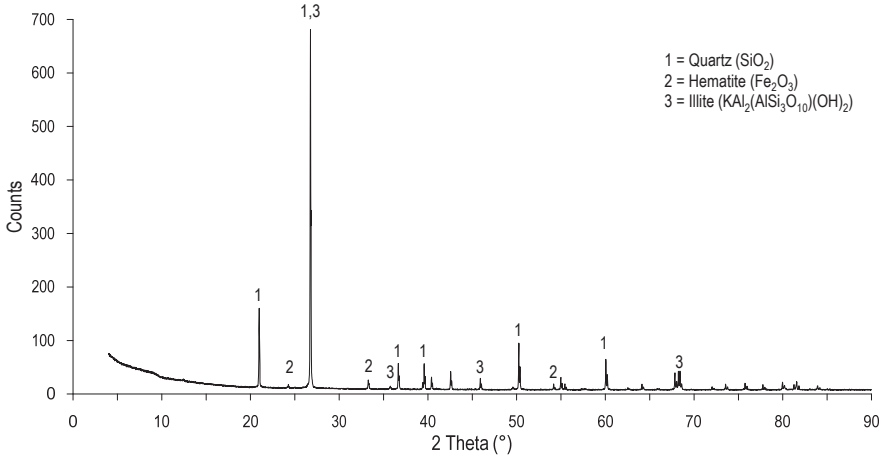

Figure 1. X-ray-diffraction results for the ore-sand sample.

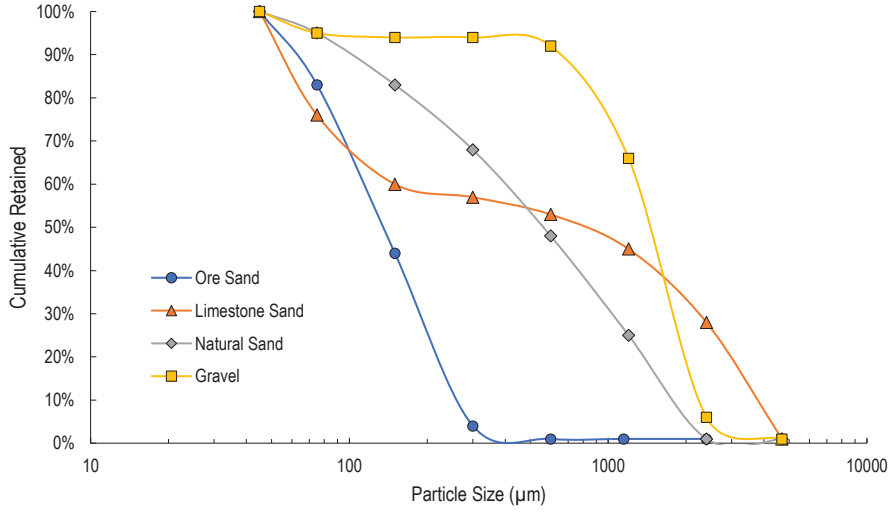

Figure 2. Particle-size distributions of the aggregates.

2.2. Production of Pavers

The relative amounts of components used by local companies were applied to the production of the traditional blocks. For the blocks constructed with OS, the proportion of aggregates was determined based on the ideal granulometry for block production. Pilot tests were performed in a block factory, where the ideal amount of aggregates to use in molding the blocks was determined. Based on these preliminary results, it was found that ore sand could replace 100% of the limestone sand and part of the natural sand (13.3%). The ordinary Portland cement (OPC) was the same for both blocks tested. This additive is a plasticizer. It was obtained in the regular market and used for all mixtures tested. This additive enables dry concrete to be produced with less water, improving the plasticity and lubricity of the compound. Table 1 shows the proportion of each material used for the production of interlocking blocks.

Table 1. Mix ratios used to produce 60,000 interlocking concrete blocks.

Material	Conventional Block		OS Block	
	Weight (t)	Percentage (wt%)	Weight (t)	Percentage (wt%)
Natural Sand *	98.2	51.4	85.1	44.5
Limestone Sand *	26.2	13.7	-	0.0
Gravel *	39.3	20.5	39.3	20.5
Ore sand *	-	0.0	39.3	20.5
Cement (OPC) *	27.5	14.4	27.5	14.4
Water	8.4	4	8.4	4
Plasticizer Additive	10.5	5	10.5	5

* Percentage relative to the dry mass (cement and aggregates).

The blocks were produced in a factory specialized in manufacturing these components. The mixing of the raw materials is automated, and the compaction of the dry concrete is finished in a hydraulic vibro-press. The produced pavers have a parallelepiped format with the dimensions 100 mm × 200 mm × 80 mm. After molding, the specimens were cured in a humid room (above 98% relative humidity). The compression test was performed after 15 and 28 days of curing, per the Brazilian standard [24]. For the strength test, standards require samples (blocks) to be saturated 24 h before the test, loading surfaces to be straight, auxiliary plates to be used, and loading to be carried out continuously at 550 kPa/s until complete rupture with equipment Class 1 (ISO 7500-1 [32]). Six replicate samples of each mixture were tested for conventional and OS block pavers. Interlocked paving blocks subject to light vehicle traffic must have an estimated minimum typical compressive strength of 35 MPa [24].

2.3. Life Cycle Assessment

The environmental assessment was conducted in accordance with ISO 14.040/14.044 [33,34] and encompassed four primary phases: (i) goal and scope determination, (ii) inventory analysis, (iii) impact assessment, and (iv) interpretation of results. LCA is a systematic method for assessing the environmental impacts of products or processes throughout their entire life cycle, from raw-material extraction to production, use, and end-of-life disposal or recycling. These standards provide a comprehensive methodology for conducting such assessments and offer a flexible framework that allows for customization to meet the specific needs of the LCA study.

The evaluation of environmental impact was carried out using the LCA software SimaPro version 9.3 [35]. The software was used to (i) assist in structuring the flowchart of processes established in the goal and scope of this work; (ii) access the life cycle inventory database to obtain inputs and outputs of raw materials, energy, emissions, and waste for all the analyzed processes that generate environmental impacts; and (iii) apply the CML 2001 life cycle impact assessment method, which quantifies impacts in categories.

2.3.1. Goal and Scope

The life cycle assessment compared the environmental impacts of two sets of aggregates for the production of 60,000 interlocking concrete blocks with the same load capacity (functional unit). The first alternative corresponds to a conventional block produced with natural aggregates (gravel, sand, and limestone sand), and the second alternative (ore sand block) was produced by partial replacement of natural aggregates with OS.

The LCA involved a cradle-to-gate analysis of the production of aggregates. The process of molding the blocks is the same for both mixtures; thus, the production process was not analyzed. Concrete blocks can have different applications (i.e., paving of roads and sidewalks, parking lots, and outside areas of houses); thus, the impacts related to use and end of life were not considered. The two systems studied are shown in Figure 3, and all emissions associated with energy and the production of raw materials are considered. The system for the ore sand block consists of (1) production of the gravel; (2) production of

the natural sand; (3) transport of gravel and natural sand; and (4) transport of IOT sand. The ore sand was considered a waste product and thus was considered not to have any environmental impact associated with its production. The system for conventional blocks consists of (1) production of the gravel; (2) production of the natural sand; (3) production of limestone sand; (4) transport of gravel, natural sand, and limestone sand.

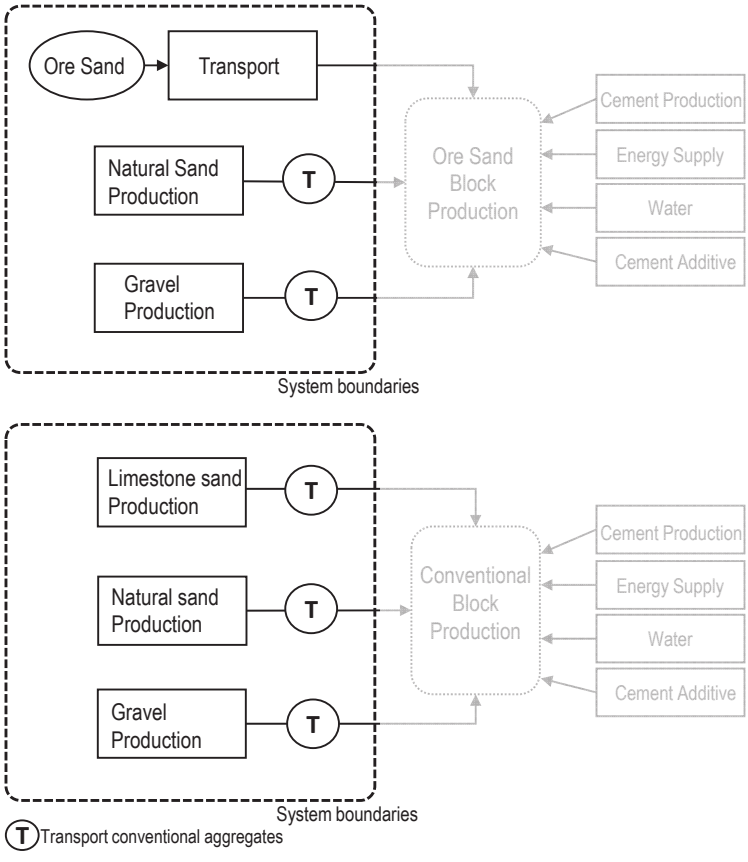

Figure 3. System boundary defined to produce interlocking blocks [35].

An assessment of the environmental impact of transporting ore sand was carried out to determine the influence of the transportation distance of this material on the production of the blocks. Six distances (50, 100, 200, 400, 800, and 1600 km) were established for truck and train conveyance. Trains are normally used in Brazil to transport mining materials. The average diesel consumption for road transport is 1.9×10^{-2} L_{diesel}/km.t, and the consumption for the freight rail system is 3.6×10^{-3} L_{diesel}/km.t. These data were obtained from local companies that transport this material. Calculations involving the transportation of conventional aggregates were based on the average distance traveled by these products to the block factory: 10 km for gravel and limestone sand and 60 km for natural sand. Transportation of such materials is usually carried out by truck.

2.3.2. Inventory Analysis

Life cycle inventory (LCI) enables the collection, structuring, and analysis of data associated with the inputs and outputs of raw materials, energy, emissions, and waste at all stages of a life cycle process. Secondary inventory data was obtained from the Ecoinvent

3.8 database [36] using SimaPro software and from the literature. Table 2 summarizes the inventory data employed in the calculations associated with the conventional block and the ore sand block used for evaluation. The data for natural sand were for extraction from rivers, which corresponds to 70% of the production of this material in Brazil [37]. There are no specific data regarding the production of limestone sand, but its production process is similar to that of gravel, with quarrying, crushing, and screening; consequently, the same data inventory used for gravel was used for limestone sand.

Table 2. Inventory process database for the IOT block and conventional block aggregates.

Process	Amount	Unit	Inventory Impact Data Source
Ore Sand Block			
Gravel	39.3	tons	Gravel, crushed {BR}—gravel production, crushed [38].
Transportation of Gravel	7.46 (10 km)	liters	Diesel, burned in building machine {GLO}—market [39].
Natural Sand	85.1	tons	Sand {BR}—sand-quarry operation, extraction from riverbed [40].
Transportation of Natural Sand	106.69 (66 km)	liters	Diesel, burned in building machine {GLO}—market [39].
Transportation of ore sand—freight train	7.07 (50 km) 14.4 (100 km) 28.27 (200 km) 56.54 (400 km) 113.09 (800 km) 226.18 (1600 km)	liters	Diesel, burned in building machine {GLO}—market [39].
Transportation of ore sand—freight truck	37.3 (50 km) 74.61(100 km) 149.22 (200 km) 298.43 (400 km) 596.86 (800 km) 1193.72 (1600 km)	liters	Diesel, burned in building machine {GLO}—market [39].
Conventional Block			
Gravel	39.3	tons	Gravel, crushed {BR}- gravel production, crushed [38].
Transportation of Gravel	7.46 (10 km)	liters	Diesel, burned in building machine {GLO}—market [39].
Natural Sand	98.2	tons	Sand {BR}—sand quarry operation, extraction from riverbed [40].
Transportation of Natural Sand	123.10 (66 km)	liters	Diesel, burned in building machine {GLO}—market [39].
Limestone Sand	26.2	tons	Gravel, crushed {BR}—gravel production, crushed [38].
Transportation of Limestone Sand	4.97 (10 km)	liters	Diesel, burned in building machine {GLO}—market [39].

{BR} = data for Brazil; {GLO} = data for World.

2.3.3. Impact Assessment

Life cycle assessment evaluates environmental effects based on LCI data, using methods and indicators that quantify the impact in different categories. The impact assessment was performed in SimaPro software. It applied the CML 2001 method [41] and involved the following impact categories: abiotic depletion, fossil-fuel depletion, global warming, ozone depletion, potential for human toxicity, potential for freshwater aquatic ecotoxicity, potential for marine aquatic ecotoxicity, potential for terrestrial ecotoxicity, photochemical oxidation, acidification, and eutrophication.

For the transport assessment, a scoring method (score indicator) was used. This method combines the results of the eleven impact categories obtained with the CML 2001 method into a single score, making it easier to compare the cumulative impacts across the different distances considered. The ratios between the results obtained in each impact category between the two blocks are metrics that compare the performance of the OS Block (V) to that of the conventional block (V_t). Higher proportions indicate a more significant difference between the products being compared. This evaluation format is commonly used in performance management, strategic planning, project evaluations, and evaluation of company goals [42].

All impact categories were given equal weight in the present analysis. The *Score Indicator* (*SI*) is the sum of the results of relative impact for each category (V/V_t) for each of the systems evaluated and divided by the number of impact categories assessed (n). The equation (Equation (1)) used is shown below:

$$SI = \frac{\sum_1^n \left(\frac{V}{V_t}\right)}{n} \quad (1)$$

where V is the value (result) of the impact category obtained for each distance variation, V_t is the value of the impact category for the target product (e.g., conventional block), and n is the number of impact categories evaluated.

3. Results

3.1. Compressive Strength of the Blocks

Figure 4 shows the results of compressive-strength tests for the compared blocks. The compressive strength of the block with IOT is similar to that of the conventional block. After 15 days of curing, the ore sand block presented a strength of 37.87 MPa. The Brazilian standard [24] establishes that this strength must be 80% (28 MPa) of the expected strength for light traffic paving. Both blocks meet this requirement. After 28 days of curing, the ore-sand block presented strength higher than that established in the standard (35 MPa) and higher than that of the conventional block. Therefore, the results meet the minimum requirements of the Brazilian standard, as well as of the requirements of the European and British standard BS EN 1338:2003 [43], the Indian standard IS 15658 [44], and the Egyptian standard ESS 4382 [45], which establish a strength of 30 MPa as the minimum acceptable. However, the American standard ASTM C936 [46] specifies a value of 50 to 55 MPa. A cone-shaped fracture with vertical crack [47] was identified in the compression tests for both blocks analyzed.

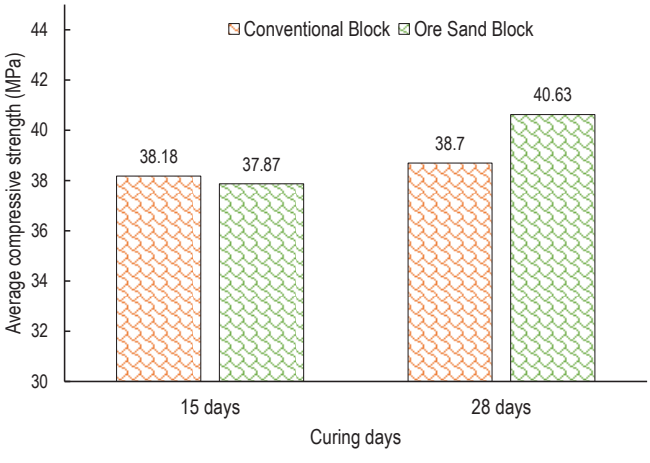

Figure 4. Comparison of the compressive strengths of the blocks.

The blocks constructed with ore sand were homogeneous and dense (Figure 5). The limestone sand has fine granulometry and works as a filler in the block. Thus, the total replacement of this material by ore sand that had finer granulometry and that was well graded and more uniform resulted in better packing, reducing the voids and resulting in better mechanical performance of the ore-sand blocks compared to the limestone-sand blocks [48,49]. According to Mendes Protasio et al. [50], ore sand reduces the porosity of the material by increasing the contact surface between the particles, promoting performance that is satisfactory and even superior compared to that of blocks made with natural sand.

The results obtained for mechanical strength show that the blocks have similar performance and can be considered products of the same standard category. They are therefore comparable in the environmental-performance assessment.

Figure 5. Visual aspect of the block produced using iron-ore sand.

3.2. Production Impacts

As part of the scope and goal of this work, the environmental impacts of the aggregates used to manufacture conventional paving blocks and paving blocks with the addition of ore sand were evaluated. With the data obtained from the life cycle inventory analysis of aggregate production (Table 2), it was possible to quantify the environmental impacts of block production in eleven impact categories using the CML 2001 method. Figure 6 shows the comparative results (highest result divided by the lowest) in each of the impact categories for aggregates used to manufacture 60,000 blocks (excluding impacts associated with transportation). As noted in Section 2.3, only the impacts of producing the aggregates (not of manufacturing the blocks) are considered because the latter process is the same regardless of the aggregates used. Table 3 shows the results obtained for the categories evaluated with the percentage reduction in impacts with the replacement of natural resources by ore sand. A reduction in impact was observed for all categories, with abiotic depletion having one of the highest reductions. This category accounts for minerals and resources used and is influenced mainly by the rate of resource extraction [38,40]. To minimize abiotic depletion, sustainable practices in the extraction and use of non-living resources need to be promoted. Such practices include reducing consumption via recycling and circular-economy practices, developing more efficient extraction and processing techniques, and promoting the use of alternative and renewable resources. The replacement of 100% of the limestone sand and 13.3% (98.2 t to 85.1 t) of the natural sand with iron ore tailings resulted in an average overall reduction of 30% in all environmental impacts compared to using conventional aggregates in the manufacture of interlocked blocks.

The graphical representation in Figure 6 illustrates the relative contributions of limestone sand, gravel, and natural sand to the impact categories assessed during the production of conventional and ore-sand blocks. These assessments follow the predefined limits established for life cycle assessment (goal and scope). The hotspots are the categories of abiotic depletion (fossil fuel), global warming and ozone depletion, which cause major impacts due to the extensive consumption of natural sand resources in manufacturing the blocks. These categories are related to the use and burning of fossil fuels in engines used in river dredging to obtain the sand, internal transportation from the river mine area to the port, and port processing operations [38]. The other eight categories are influenced by the extraction of gravel and limestone sand. Mining and crushing entail creating large exploitation areas where the outer layer of the soil is modified and the fauna and flora are eradicated, while also generating microparticles harmful to humans, among other negative effects [51,52]. Limestone sand with natural sand (used for the conventional block) contributes significantly in all categories evaluated. Using OS to replace these resources creates a reduction in such impacts ranging from 35% to 22%. The incorporation of waste

with a granulometry similar to that of natural sand and gravel is one way to improve the performance of the block with tailings. Despite the reduction in environmental impacts associated with the use of ore sand in blocks, it is still necessary to determine the environmental impact of the transportation of aggregates to the manufacturing site in order to determine the environmental impact of using the ore sand.

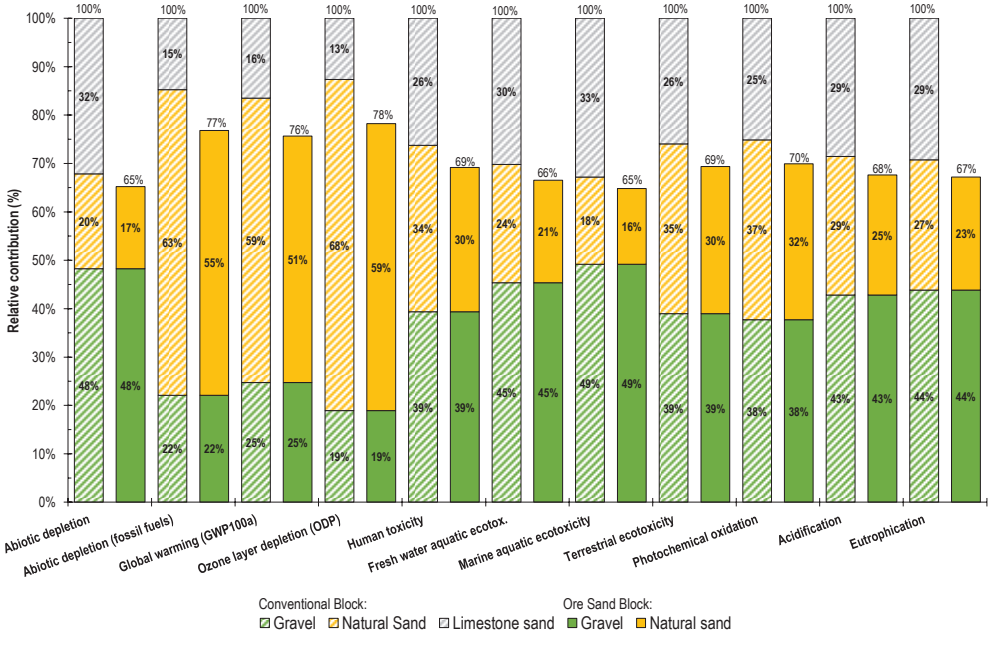

Figure 6. Relative contribution to environmental impacts by each aggregate type used in conventional blocks and ore-sand blocks (excluding impacts related to the transportation of aggregates).

Table 3. Environmental impacts of aggregates for the production of 60,000 blocks.

Impact Category	Unit	Conventional Block	OS Block	Reduction
Abiotic depletion	kg Sb eq	3.6×10^{-4}	2.3×10^{-4}	35%
Abiotic depletion (fossil fuels)	MJ	9.3×10^{3}	7.2×10^{3}	23%
Global warming (GWP100a)	kg CO_2 eq	7.2×10^{2}	5.5×10^{2}	24%
Ozone-layer depletion (ODP)	kg CFC-11 eq	1.1×10^{-4}	0.86×10^{-4}	22%
Human toxicity	kg 1,4-DB eq	9.2×10^{1}	6.4×10^{1}	31%
Freshwater aquatic ecotoxicity	kg 1,4-DB eq	5.9×10^{1}	3.9×10^{1}	33%
Marine aquatic ecotoxicity	kg 1,4-DB eq	1.7×10^{5}	1.1×10^{5}	35%
Terrestrial ecotoxicity	kg 1,4-DB eq	2.4×10^{-1}	1.7×10^{-1}	31%
Photochemical oxidation	kg C_2H_4 eq	1.8×10^{-1}	1.2×10^{-1}	30%
Acidification	kg SO_2 eq	1.1×10^{1}	0.77×10^{1}	32%
Eutrophication	kg PO_4 eq	2.7	1.8	33%

Sb (antimony); CFC (chlorofluorocarbons); DB (dichlorobenzene); C_2H_4 (ethylene); SO_2 (sulfur dioxide); PO_4 (phosphate).

3.3. Transportation Impacts

Within the predefined boundaries for life cycle assessment in this study, transportation is an important determinant of the environmental impact of aggregates used in the production of pavers. Figure 7 summarizes the impacts of production and transportation of the conventional aggregates, namely, natural sand, limestone sand, and gravel (detailed in Section 3.2). In this scenario, the environmental assessment includes the impact of the

transportation of conventional aggregates. The average contributions of transportation to diesel burning for the conventional and alternative blocks were 22.7% and 25.6%, respectively. Figure 8 and Table 4 show only the impact of transporting such aggregates according to their type and quantity (Table 2). The greatest impact comes from the transportation of natural sand due to the large amount needed and the distance of this resource from the block factory site, which together result in higher diesel consumption. Gravel and limestone are transported the same distance, but the amount of gravel needed is greater than the amount of limestone needed, so gravel has a greater impact. Among the materials used in the block manufactured with ore sand, the transportation of natural sand had the greatest impacts across all the categories evaluated.

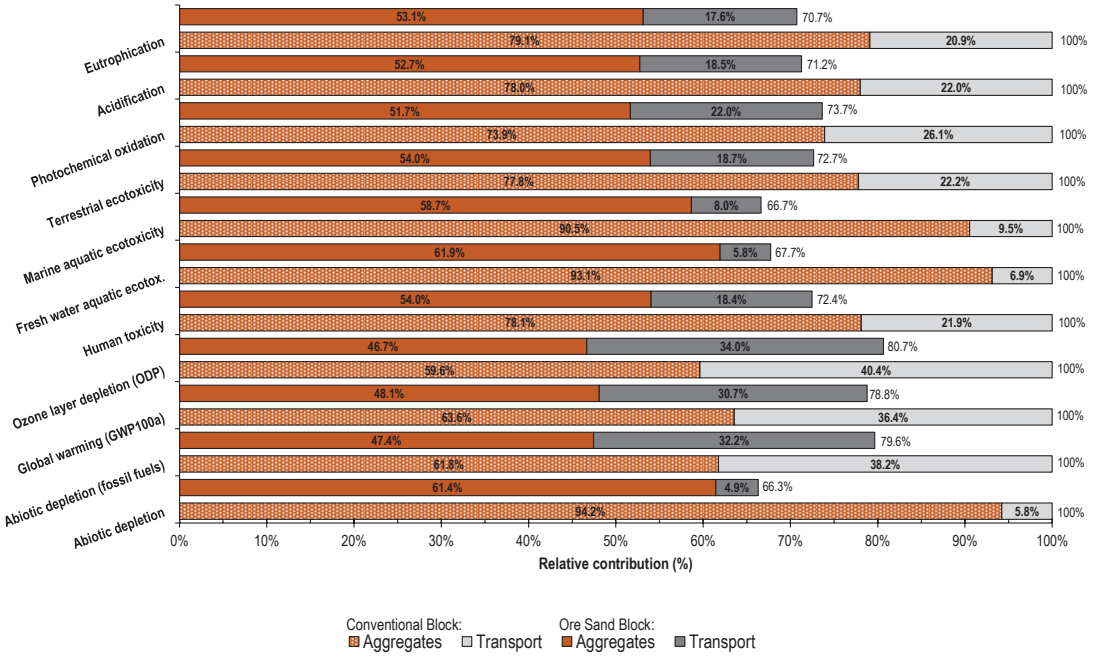

Figure 7. Environmental impact of the production and transportation of conventional aggregates (natural sand, limestone sand, and gravel).

To capture the complete environmental impact of the alternative block, it is essential to consider the transportation of ore sand from the storage or mining site to the block factory. More specifically, the break-even point, or the distance up to which the ore-sand block has a lower environmental impact than the conventional block considering the transportation of this waste, needs to be identified. Figures 9a and 10a show the impacts for different transportation distances for the block manufactured using ore sand (in combination with the transportation impacts for the block constructed with conventional aggregates) by train and truck, respectively. The overall impact for each distance was calculated using the Score Indicator.

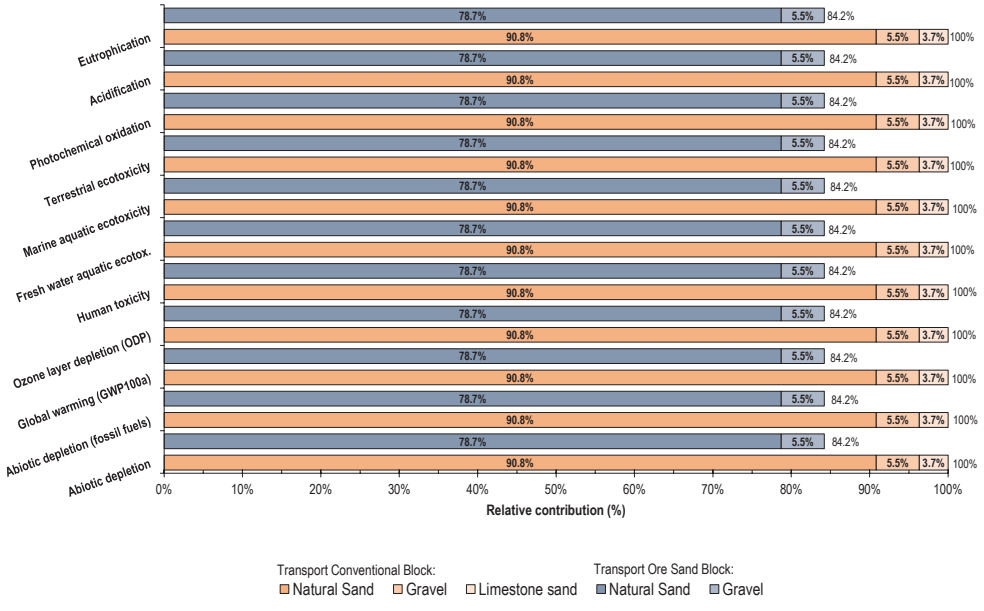

Figure 8. Contribution of conventional aggregates to transportation impacts.

Table 4. Environmental impact of the transportation of conventional aggregates (natural sand, limestone sand, and gravel) for the production of blocks.

Impact Category	Unit	Transport of Ordinary Aggregates	
		Conventional Block	Ore-Sand Block
Abiotic depletion	kg Sb eq	2.20×10^{-5}	1.86×10^{-5}
Abiotic depletion (fossil fuels)	MJ	5.77×10^{3}	4.86×10^{3}
Global warming	kg CO_2 eq	4.14×10^{2}	3.49×10^{2}
Ozone-layer depletion (ODP)	kg CFC-11 eq	7.40×10^{-5}	6.23×10^{-5}
Human toxicity	kg 1,4-DB eq	2.57×10^{1}	2.17×10^{1}
Fresh water aquatic ecotox.	kg 1,4-DB eq	4.33	3.65
Marine aquatic ecotox.	kg 1,4-DB eq	1.78×10^{4}	1.50×10^{4}
Terrestrial ecotox.	kg 1,4-DB eq	6.79×10^{-2}	5.72×10^{-2}
Photochemical oxidation	kg C_2H_4 eq	6.28×10^{-2}	5.29×10^{-2}
Acidification	kg SO_2 eq	3.20	2.70
Eutrophication	kg PO_4 eq	7.17×10^{-1}	6.04×10^{-1}

Sb (antimony); CFC (chlorofluorocarbons); DB (dichlorobenzene); C_2H_4 (ethylene); SO_2 (sulfur dioxide); PO_4 (phosphate).

For example, for the global-warming category, the conventional block generates 7.2×10^2 kg of CO_2 (Table 3) from the production of aggregates and an additional 4.14×10^2 kg of CO_2 (Table 4) from transportation, totaling 11.4×10^2 kg CO_2 (Vt). The block manufactured with ore sand generates 5.5×10^2 kg of CO_2 from the aggregates and 3.5×10^2 kg of CO_2 from transportation. Transporting ore sand (100 km) entails the burning of an additional 14.1 L of diesel, which generates 0.43×10^2 kg of CO_2 (3.06 kg CO_2/L), for a total of 9.4×10^2 kg CO_2 (V). The ratio between the two results (V/V_t) for this category is 0.82. This process was carried out for all impact categories. Next, the ratios were summed and divided by the number of categories (n). For 100 km, the *SI* result was 0.75; for 200 km it was 0.78, etc., as shown in Figure 9a.

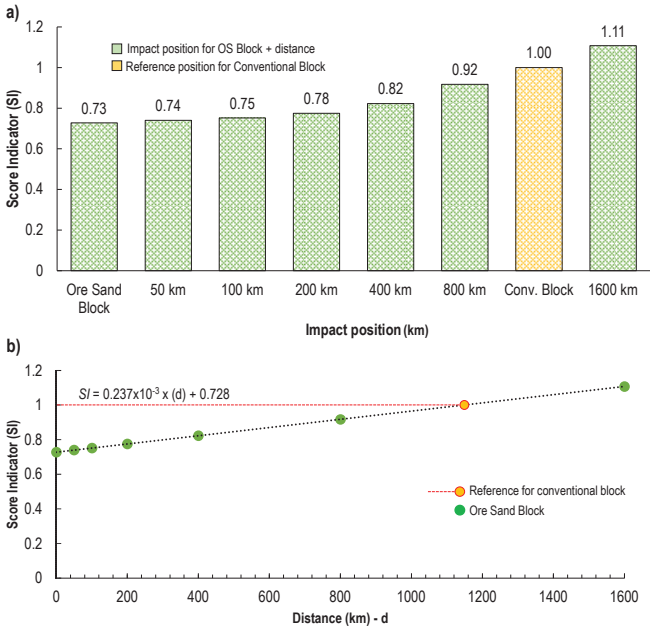

Figure 9. Environmental impact score for the ore sand block: (**a**) impact for different transportation distances for OS materials by train; (**b**) break-even point with the conventional block.

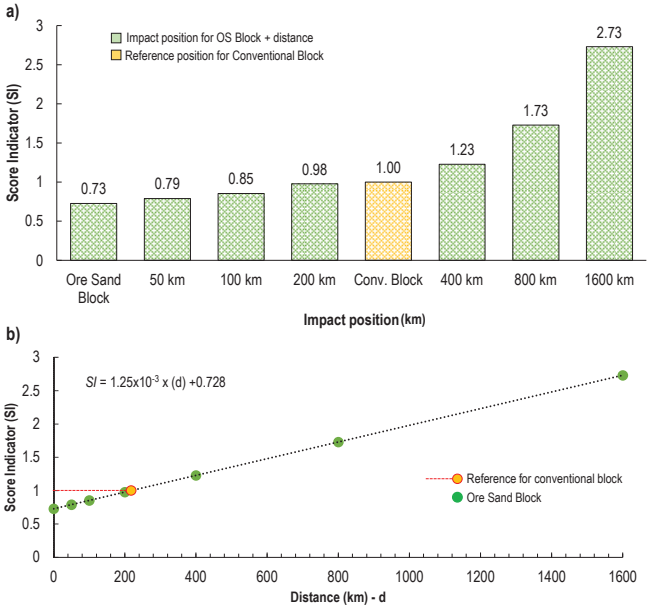

Figure 10. Environmental-impact score for the ore-sand block: (**a**) impact for different transportation distances for OS materials by truck; (**b**) point at which the ore-sand block breaks even with the conventional block.

At distance zero, the environmental impact of the conventional block is compared to the alternative paver block without ore-sand transportation. The environmental per-

formance of the paver measured by the Score Indicator at distance zero is 0.728 (~0.73), indicating reduced environmental impacts due to the use of ore sand in block production, as described in the previous section. Therefore, the OS block starts at an advantage over the conventional block, with an SI less than 1. This difference decreases when ore-sand transportation is considered.

For a transportation distance of 1,147 km by train and 217 km by truck for the ore sand, the alternative block has the same potential environmental impacts as the conventional block (Figures 9b and 10b) considering the impacts of the and production and transportation of all aggregates. These values were obtained by establishing linear functions (Equations (2) and (3), for train and truck transportation, respectively) connecting the transportation distance for the ore sand to the Score Indicator. This result means that the ore-sand block is a most sustainable alternative in comparison to traditional blocks only when OS is transported less than 1147 km by train or 217 km by truck. It is important to highlight that both distances entail the same diesel consumption (162.2 L), but trucks are less efficient than trains in terms of the distance travelled per liter. Golev et al. [5] verified this same trend, where transporting ore sand by train causes a lower environmental impact in greenhouse gas emissions compared to road transport. Each liter of diesel used for transportation contributes to the following environmental impacts (per unit): 1.63×10^{-7} kg Sb eq. (abiotic depletion); 4.26×10^{1} MJ (abiotic depletion—fossil fuels); 3.06 kg CO_2 eq. (global warming); 5.46×10^{-7} kg CFC-11 eq. (ozone-layer depletion); 1.90×10^{-1} kg 1,4-DB eq. (human toxicity); 3.20×10^{-2} kg 1,4-DB eq. (freshwater aquatic ecotox.); 1.31×10^{2} kg 1,4-DB eq. (marine aquatic ecotox.); 5.01×10^{-4} kg 1,4-DB eq. (terrestrial ecotox.); 4.64×10^{-4} kg C_2H_4 eq. (photochemical oxidation); 2.36×10^{-2} kg SO_2 eq. (acidification); and 5.29×10^{-3} kg PO_4 eq. (eutrophication) [35,39,41].

$$SI_{train} = 0.237 \times 10^{-3}(d) + 0.728 \left(R^2 = 1\right) \quad (2)$$

$$SI_{truck} = 1.25 \times 10^{-3}(d) + 0.728 \left(R^2 = 1\right) \quad (3)$$

4. Discussion

In assessing the environmental performance of only the aggregates used to manufacture the interlocking paver blocks, the ore-sand block has a significant environmental advantage over the conventional block and has similar load capacity. This difference is explained by the replacement of 24% of the aggregate (by mass) with IOTs (a leftover), which creates an alternative with a lower environmental footprint in all eleven impact categories. In the context of this work, from a materials point of view, the ore-sand block has an advantage over the conventional block. However, the iron-mining areas are strategically located for iron extraction, in contrast to the areas for commercial natural-sand extraction, which are typically situated close to block factories. This feature demonstrates the importance of the transportation analysis performed here for the environmental appraisal of this alternative solution. Transportation represented an average of 22.7% of the environmental impact across the eleven impact categories evaluated for blocks constructed with conventional aggregates. This finding highlights the fact that the transportation of materials is important in assessing environmental performance. Sjunnesson [53] identifies the main contributors to the total environmental burden of concrete over its life cycle as the raw materials and transportation.

The Score Indicator enabled a comparison of the impacts of different transportation distances for the leftover ore sand. As the distance increases, the consumption of diesel burned by rail or road transport increases. The increase in the burning of fossil fuel leads to increases in the several categories, all of which were considered to have the same weight in this work. Figure 11 shows that $SI = 1$ for the V/V_t ratio, which corresponds to the distance values obtained with Equation (2) (1147 km) and 3 (217 km) for both transportation types. This figure shows the categories (photochemical oxidation, ozone layer depletion, global

warming, and abiotic depletion-fossil fuels) that have an increase in impact ($V/V_t > 1$) in comparison to traditional blocks for distances above 1,147 km for train and 217 km for truck. However, for the other seven categories, the burning of diesel had a smaller impact compared to construction of conventional blocks ($V/V_t < 1$). The sum of the values (V/V_t) in the impact categories divided by the number of categories ($n = 11$) results in a value of 1.0, where the increase in certain categories is counterbalanced by categories with lower impacts compared to the conventional block. This result confirms that the equations developed from the SI were effective in determining the best distance for ore-sand transportation. The evaluation of several impact categories enhances the understanding of environmental trade-offs between analyzed systems [54,55]. Evaluating the performance of two products through the ratio of the impacts across environmental categories (V/Vt) is an established practice in life cycle assessment studies [56–58]. This approach provides an objective metric by which to identify categories with better or worse performance. Calculating category ratios simplifies complex environmental data, allowing for easier result interpretation through this metric.

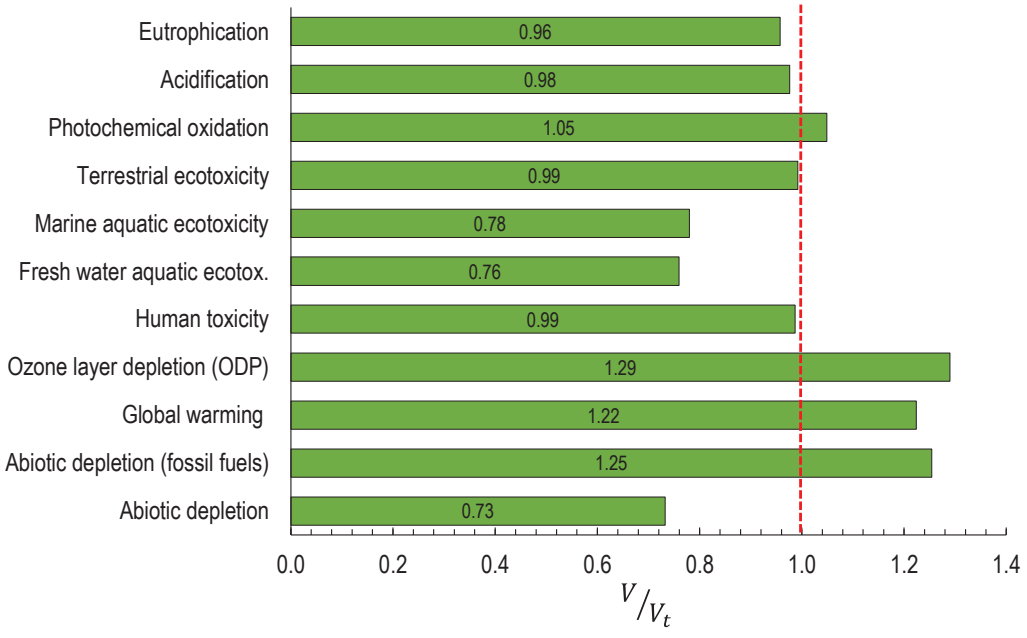

Figure 11. Relative impact of the evaluated categories for the OS block with transportation (V) compared to the conventional block (V_t). The red line delimits which category is higher and lower than the conventional block.

The Scoring Indicator used in this study proved to be a useful and efficient tool for determining the increase in impacts due to transportation. It provides an equation that supports decision-making regarding the distance allowed for incorporating ore sand into interlocking paving blocks. Alternative models, such as the normalization and ranking of environmental indicators for decision-making [59] and MIVES (Spanish Integrated Value Model for the Sustainability Assessment) [60], are applicable, although they are complex. However, the latter model allows for the inclusion of broader considerations from studies that incorporate assessments in the environmental, social, and economic fields.

Figure 12 shows the potential range for the distribution and use of ore sand in block production, according to the distances calculated. The distribution of this sand can reach up to nine states via rail network and can reach several cities around the iron-ore mining area

by road, enabling the production of an interlocking block with less environmental impact. Göswein et al. [27] conducted a study that employed a combination of LCA and geospatial analysis to assess the incorporation of fly ash and recycled construction waste into concrete in Portugal. Alzard et al. [61] also used a similar method to assess the environmental and economic impact of the transportation of construction waste to concrete plants in the United Arab Emirates. Estanqueiro et al. [62] emphasize the importance of regionalized (geography-specific) assessments, considering local production and transportation conditions to enhance accuracy.

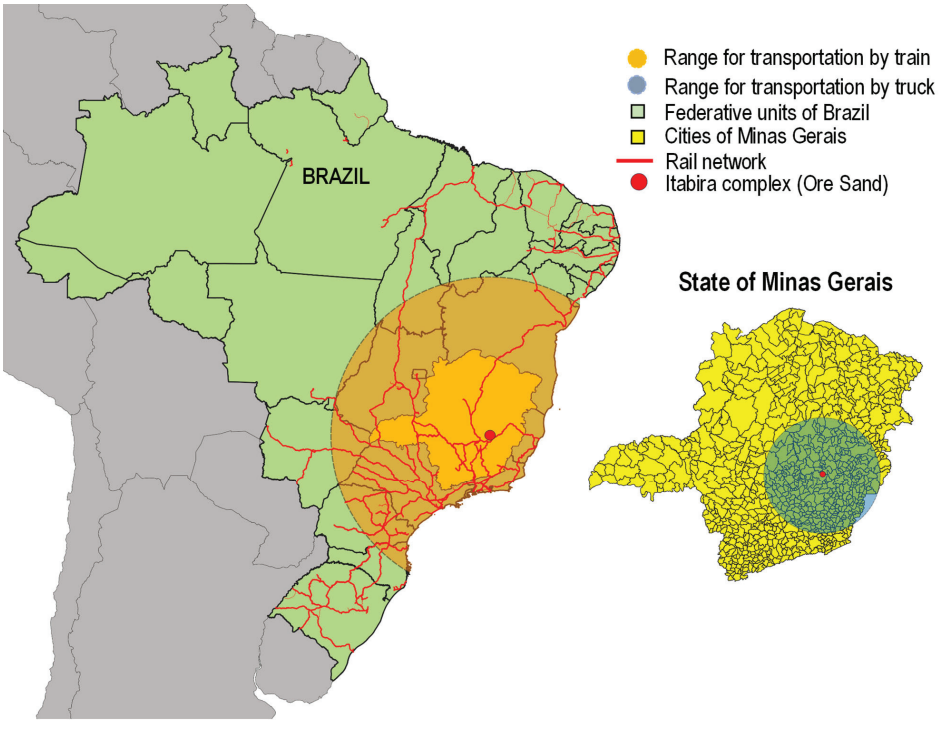

Figure 12. Potential distribution of ore sand for use in producing an environmentally friendly block (map created using QGIS software v3.14 [63] and data from IBGE [64]).

Future research should focus on evaluating: (i) the potential to replace the cement used in the production of blocks with ore sand, which produces the same mechanical behavior; (ii) replacing natural sand with other left-overs (e.g., bottom ash) and its impact on the LCA; (iii) analyzing transport by waterway; (iv) analyzing databases from other locations and processes; and (v) assess sustainability across environmental, social, and economic aspects, in alignment with the UN's Sustainable Development Goals.

5. Conclusions

Based on the objectives set and the findings of this research, the following conclusions can be drawn:

- The OS block has similar strength performance compared to the conventional block, meeting the established standard of 35 MPa.
- Ore sand is an environmentally sustainable alternative for use in the replacement of conventional aggregates used for the production of interlocked blocks. This study found an average reduction of 30% for the 11 impact categories compared to the traditional block.

- The transportation of conventional aggregates has a significant impact on the production of both blocks. It represents an average of 23.7% of the total impact for the ordinary block and 26% for the block produced with ore sand.
- Using the scoring indicator (SI), it was possible to establish that the transportation of ore sand for distances of 1147 km by rail and 217 km by road results in the same environmental impact for the ore-sand block as for the conventional block.
- Transportation distances shorter than those above make the block with ore sand more environmentally friendly than the conventional alternative. Over these distances, it is possible to reach other states in Brazil, as well as many cities (mostly inside the state of Minas Gerais) around the mining area that can supply other interlocking paving block factories.
- The LCA technique in association with *SI* proved to be a useful decision-making tool in defining the transport distance that makes it possible to manufacture an environmentally responsible block.

Within the limits set, this work offers an innovative LCA-based approach to evaluating the environmental performance of interlocking paving blocks constructed with ore sand as an aggregate and the limiting effects of transportation on their production. The incorporation of ore sand into the interlocking paving block confers environmental benefits to the product, increasing the environmental sustainability of the industry. The method presented can be adapted to different locations, allowing the determination of an environmentally safe distance between the tailings-generation site and the production sector.

Author Contributions: Conceptualization, R.B.S., M.F.L.M., R.J.B. and N.C.C.; methodology, R.B.S., M.F.L.M., R.J.B. and N.C.C.; validation, R.B.S. and M.F.L.M.; formal analysis, R.B.S. and M.F.L.M.; investigation, R.B.S. and M.F.L.M.; data curation, R.B.S. and M.F.L.M.; writing—original draft preparation, R.B.S., M.F.L.M., R.J.B. and N.C.C.; writing—review and editing, R.B.S., M.F.L.M., R.J.B. and N.C.C.; supervision, N.C.C.; project administration, N.C.C.; funding acquisition, N.C.C. All authors have read and agreed to the published version of the manuscript.

Funding: The authors wish to make explicit their appreciation to VALE S.A. (IAP-001247 and IAP-001466) and CNPq (Brazilian Research Council) for the support to the research group.

Institutional Review Board Statement: Not applicable.

Informed Consent Statement: Not applicable.

Data Availability Statement: The data presented in this study are available on request from the corresponding author. The data are not publicly available due to ethical considerations and potential future publications.

Conflicts of Interest: The authors declare that this study received funding from VALE S.A. The funder was not involved in the study design, collection, analysis, interpretation of data, the writing of this article or the decision to submit it for publication.

References

1. Global Cement Market. *Analysis by Production, by Consumption, Type (Blended, Portland and Others), by Application (Non-Residential and Residential), by Region, Size and Trends with Impact of COVID-19 and Forecast up to 2027*; Global Cement Market: Dublin, Ireland, 2022.
2. United Nations Environment Programme—UNEP. *Sand and Sustainability: Finding New Solutions for Environmental Governance of Global Sand Resources: Synthesis for policy makers*; United Nations Environment Programme: Nairobi, Kenya, 2019.
3. Peduzzi, P. Sand, rarer than one thinks. *Environ. Dev.* **2014**, *11*, 208–218. [CrossRef]
4. National Association of Aggregates Producers for Construction—ANEPAC 2019. Environmental Overview of Mining. Available online: https://www.anepac.org.br/ (accessed on 9 November 2022).
5. Golev, A.; Gallagher, L.; Velpen, A.V.; Lynggaard, J.R.; Friot, D.; Stringer, M.; Chuah, S.; Arbelaez-Ruiz, D.; Mazzinghy, D.; Moura, L.; et al. *Ore-Sand: A Potential New Solution to the Mine Tailings and Global Sand Sustain-Ability Crises: Final Report*; The University of Queensland: Brisbane, QLD, Australia; The University of Geneva: Geneva, Switzerland, 2022. [CrossRef]
6. United States Geological Survey—USGS. Mineral Commodity Summaries, Iron Ore. 2020. Available online: https://pubs.usgs.gov/periodicals/mcs2020/mcs2020-iron-ore.pdf (accessed on 5 September 2023).

7. Kuranchie, F.A.; Shukla, S.K.; Habibi, D. Electrical resistivity of iron ore mine tailings produced in Western Australia. *Int. J. Min. Reclam. Environ.* **2014**, *29*, 191–200. [CrossRef]
8. Han, F.; Li, L.; Song, S.; Liu, J. Early-age hydration characteristics of composite binder containing iron tailing powder. *Powder Technol.* **2017**, *315*, 322–331. [CrossRef]
9. Das, S.K.; Kumar, S.; Ramachandrarao, P. Exploitation of iron ore tailing for the development of ceramic tiles. *Waste Manag.* **2000**, *20*, 725–729. [CrossRef]
10. Dávila, R.B.; Fontes, M.P.F.; Pacheco, A.A.; Ferreira, M.S. Heavy metals in iron ore tailings and floodplain soils affected by the Samarco dam collapse in Brazil. *Sci. Total Environ.* **2020**, *709*, 136151. [CrossRef]
11. Armstrong, M.; Petter, R.; Petter, C. Why have so many tailings dams failed in recent years? *Resour. Policy* **2019**, *63*, 101412. [CrossRef]
12. Environmental State Foundation. *Mining Solid Waste Inventory, Base Year 2017*; Environmental State Foundation: Belo Horizonte, Brazil, 2017.
13. Vilaça, A.S.I.; Simão, L.; Montedo, O.R.K.; Novaes de Oliveira, A.P.; Raupp-Pereira, F. Waste valorization of iron ore tailings in Brazil: Assessment metrics from a circular economy perspective. *Resour. Policy* **2022**, *75*, 102477. [CrossRef]
14. Zhang, W.; Gu, X.; Qiu, J.; Liu, J.; Zhao, Y.; Li, X. Effects of iron ore tailings on the compressive strength and permeability of ultra-high-performance concrete. *Constr. Build. Mater.* **2020**, *260*, 119917. [CrossRef]
15. Han, G.; Zhang, J.; Sun, H.; Shen, D.; Wu, Z.; An, X.; Meye, S.M.; Huang, Y. Application of iron ore tailings and phosphogypsum to create artificial rockfills used in rock-filled concrete. *Buildings* **2022**, *12*, 555. [CrossRef]
16. Arbili, M.M.; Alqurashi, M.; Majdi, A.; Ahmad, J.; Deifalla, A.F. Concrete made with iron ore tailings as a fine aggregate: A step to-wards sustainable concrete. *Materials* **2022**, *15*, 6236. [CrossRef]
17. Wang, A.; Liu, H.; Hao, X.; Wang, Y.; Liu, X.; Li, Z. Geopolymer synthesis using garnet tailings from molybdenum mines. *Minerals* **2019**, *9*, 48. [CrossRef]
18. Opiso, E.M.; Tabelin, C.B.; Maestre, C.V.; Aseniero, J.P.J.; Arima, T.; Villacorte-Tabelin, M. Utilization of palm oil fuel ash (POFA) as an admixture for the synthesis of a gold mine tailings-based geopolymer composite. *Minerals* **2023**, *13*, 232. [CrossRef]
19. Li, X.; Wang, P.; Qin, J.; Liu, Y.; Qu, Y.; Liu, J.; Cao, R.; Zhang, Y. Mechanical properties of sintered ceramsite from iron ore tailings affected by two-region structure Constr. *Build. Mater.* **2020**, *240*, 117919. [CrossRef]
20. Chen, Y.; Zhang, Y.; Chen, T.; Liu, T.; Huang, J. Preparation and characterization of red porcelain tiles with hematite tailings Constr. *Build. Mater.* **2013**, *38*, 1083–1088. [CrossRef]
21. Carmignano, O.; Vieira, S.; Teixeira, A.P.; Lameiras, F.; Brandão, P.R.; Lago, R. Iron ore tailings: Characterization and applications. *J. Braz. Chem. Soc.* **2021**, *32*, 1895–1911. [CrossRef]
22. Ravi, K.; Kumar, A.; Prashanth, M.H.; Reddy, D.V. Experimental studies on iron-ore tailing based interlocking paver blocks. *Int. J. Earth Sci. Eng.* **2012**, *5*, 501–504.
23. Santana Filho, J.N.; Da Silva, S.N.; Silva, G.C.; Mendes, J.C.; Peixoto, R.A.F. Technical and environmental feasibility of interlocking concrete pavers with iron ore tailings from tailings dams. *J. Mater. Civ. Eng.* **2017**, *2017*, 29. [CrossRef]
24. *NBR 9781 2013*; Peças de Concreto Para Pavimentação—Especificação e Métodos de Ensaio. Brazilian Standards Organization: Rio de Janeiro, Brazil, 2013. (In Portuguese)
25. Saldanha, R.B.; Caicedo, A.M.L.; Tonini de Araújo, M.; Scheuermann Filho, H.C.; Moncaleano, C.J.; Silva, J.P.S.; Consoli, N.C. Potential use of iron ore tailings for binder production: A life cycle assessment. *Constr. Build. Mater.* **2023**, *365*, 130008. [CrossRef]
26. Garcia-Troncoso, N.; Baykara, H.; Cornejo, M.H.; Riofrio, A.; Tinoco-Hidalgo, M.; Flores-Rada, J. Comparative mechanical properties of conventional concrete mixture and concrete incorporating mining tailings sands. *Case Stud. Constr. Mater.* **2022**, *16*, e01031. [CrossRef]
27. Göswein, V.; Gonçalves, A.B.; Silvestre, J.D.; Freire, F.; Habert, G.; Kurda, R. Transportation matters—Does it? *GIS-based comparative environmental assessment of concrete mixes with cement, fly ash, natural and recycled aggregates. Resour. Conserv. Recycl.* **2018**, *137*, 1–10. [CrossRef]
28. Liu, K.; Wang, S.; Quan, X.; Jing, W.; Xu, J.; Zhao, N.; Liu, B.; Ying, H. Industrial byproduct iron ore tailings as ecofriendly materials in the utilization of cementitious composites. *Constr. Build. Mater.* **2023**, *372*, 130813. [CrossRef]
29. Gao, S.; Cui, X.; Kang, S.; Ding, Y. Sustainable applications for utilizing molybdenum tailings in concrete. *J. Clean. Prod.* **2020**, *266*, 122020. [CrossRef]
30. Hauschild, M.Z.; Rosenbaum, R.K.; Olsen, S.I. *Life Cycle Assessment*; Springer International Publishing: Cham, Switzerland, 2018; pp. 59–66. [CrossRef]
31. Zhang, N.; Tang, B.; Liu, X. Cementitious activity of iron ore tailing and its utilization in cementitious materials, bricks and concrete. *Constr. Build. Mater.* **2021**, *288*, 123022. [CrossRef]
32. *ISO 7500-1:2018*; Metallic Materials-Verification of Static Uniaxial Testing Machines Tension/Compression Testing Machines-Verification and Calibration of the Force-Measuring Systems. ISO: Geneva, Switzerland, 2018. ISO: Geneva, Switzerland, 2018.
33. *ISO 14040*; Environmental Management—Life Cycle Assessment—Principles and Framework. ISO: Geneva, Switzerland, 2006.
34. *ISO 14044*; Environmental Management—Life Cycle Assessment—Requirements and Guidelines. ISO: Geneva, Switzerland, 2006.
35. PR'e Consultants. Company History. Available online: https://www.pre-sustainability.com/aboutpre/company (accessed on 5 December 2022).

36. Wernet, G.; Bauer, C.; Steubing, B.; Reinhard, J.; Moreno-Ruiz, E.; Weidema, B. The Ecoinvent database version 3 (part I): Overview and methodology. *Int. J. Life Cycle Assess.* **2016**, *21*, 1218–1230. Available online: http://link.springer.com/10.1007/s11367-016-1087-8 (accessed on 4 December 2023).
37. Valverde, F.M. Agregados para construção civil. In *Sumário Mineral Brasileiro de 2006*; Departamento Nacional de Produção Mineral: Brasília, Brazil, 2006; pp. 37–42.
38. Silva, B.S. Gravel production, crushed, BR, Allocation, APOS 2021. Ecoinvent Database Version 3.8. Available online: https://ecoinvent.org/the-ecoinvent-database/data-releases/ecoinvent-3-8/ (accessed on 5 September 2023).
39. Kellenberger, D.; Materialprüf, E. Diesel, Burned in Building Machine, GLO, Allocation, APOS 2021. Ecoinvent DATABASE version 3.8. Available online: https://ecoinvent.org/the-ecoinvent-database (accessed on 5 September 2023).
40. Moranga, G. Sand Quarry Operation, Extraction from Riverbed, BR, Allocation, APOS 2021. Ecoinvent Database Version 3.8. Available online: https://ecoinvent.org/the-ecoinvent-database (accessed on 5 September 2023).
41. Guinee, J.B. *Handbook on Life Cycle Assessment: Operational Guide to the ISO Standards*; Kluwer Academic Publishers: Dordrecht, The Netherlands, 2001.
42. Shewhart, W.A.; Deming, W.E. *Statistical Method from the Viewpoint of Quality Control*; Courier Corporation: Mineola, NY, USA, 1986.
43. *BS EN 1338:2003*; Concrete Paving Blocks—Requirements and Test Methods; The British Standards (BSI) and The European Standard (CEN). European Committee for Standardization: Brussels, Belgium, 2003.
44. *BIS 15658*; Precast Concrete Blocks for Paving-Specification. Bureau of Indian Standards: New Delhi, India, 2006.
45. *ESS 4382*; Egyptian Standard, Concrete Interlocking Paving Units. ESS: Cairo, Egypt, 2004.
46. *ASTM C 936*; Standard Specification for Solid Concrete Interlocking Paving Units. ASTM: West Conshohocken, PA, USA, 2002.
47. Van Vliet, M.; Van Mier, J. Softening behaviour of concrete under uniaxial compression'. In *Fracture Mechanics of Concrete Structures*; Proceedings FRAMCOS-2; Wittmann, F.H., Ed.; AEDIFICATIO Publishers: Freiburg, Germany, 1995; pp. 383–396.
48. Zhao, S.; Fan, J.; Sun, W. Utilization of iron ore tailings as fine aggregate in ultra-high-performance concrete. *Constr. Build. Mater.* **2014**, *50*, 540–548. [CrossRef]
49. Kuranchie, F.A.; Shukla, S.K.; Habibi, D.; Mohyeddin, A. Utilisation of iron ore tailings as aggregates in concrete. *Cogent Eng.* **2015**, *2*, 1083137. [CrossRef]
50. Mendes Protasio, F.N.; Ribeiro de Avillez, R.; Letichevsky, S.; de Andrade Silva, F. The use of iron ore tailings obtained from the Germano dam in the production of a sustainable concrete. *J. Clean. Prod.* **2021**, *278*, 123929. [CrossRef]
51. Simion, I.M.; Fortuna, M.E.; Bonoli, A.; Gavrilescu, M. Comparing environmental impacts of natural inert and recycled construction and demolition waste processing using LCA. *J. Environ. Eng. Landsc. Manag.* **2013**, *21*, 273–287. [CrossRef]
52. Langer, W.H. *A General Overview of the Technology of in-Stream Mining of Sand and Gravel Resources, Associated Potential Environmental Impacts, and Methods to Control Potential Impacts*; US Department of the Interior: Washington, DC, USA; US Geological Survey: Reston, VA, USA, 2003.
53. Sjunnesson, J. Life Cycle Assessment of Concrete. Master's Thesis, Department of Technology and Society, Environmental and Energy Systems Studies, Lund University, Lund, Sweden, 2005.
54. Teillard, F.; Maia de Souza, D.; Thoma, G.; Gerber, P.J.; Finn, J.A. What does life-cycle assessment of agricultural products need for more meaningful inclusion of biodiversity. *J. Appl. Ecol.* **2016**, *53*, 1422–1429. [CrossRef]
55. McClelland, S.C.; Arndt, C.; Gordon, D.R.; Thomas, G. Type and number of environmental impact categories used in livestock life cycle assessment: A systematic review. *Livest. Sci.* **2018**, *209*, 39–45. [CrossRef]
56. Da Rocha, C.G.; Passuello, A.; Consoli, N.C.; Quiñónez Samaniego, R.A.; Kanazawa, N.M. Life cycle assessment for soil stabilization dosages: A study for the Paraguayan Chaco. *J. Clean. Prod.* **2016**, *139*, 309–318. [CrossRef]
57. Shan, X.; Zhou, J.; Chang, V.W.-C.; Yang, E.-H. Life cycle assessment of adoption of local recycled aggregates and green concrete in Singapore perspective. *J. Clean. Prod.* **2017**, *164*, 918–926. [CrossRef]
58. Tosti, L.; van Zomeren, A.; Pels, J.R.; Damgaard, A.; Comans, R.N.J. Life cycle assessment of the reuse of fly ash from biomass combustion as secondary cementitious material in cement products. *J. Clean. Prod.* **2020**, *245*, 118937. [CrossRef]
59. Van Hoof, G.; Vieira, M.; Gausman, M.; Weisbrod, A. Indicator selection in life cycle assessment to enable decision making: Issues and solutions. *Int. J. Life Cycle Assess.* **2013**, *18*, 1568–1580. [CrossRef]
60. Pons, O.; de la Fuente, A.; Aguado, A. The Use of MIVES as a Sustainability Assessment MCDM Method for Architecture and Civil Engineering Applications. *Sustainability* **2016**, *8*, 460. [CrossRef]
61. Alzard, M.H.; El-Hassan, H.; El-Maaddawy, T. Environmental and Economic Life Cycle Assessment of Recycled Aggregates Concrete in the United Arab Emirates. *Sustainability* **2021**, *13*, 10348. [CrossRef]
62. Estanqueiro, B.; Dinis Silvestre, J.; de Brito, J.; Duarte Pinheiro, M. Environmental life cycle assessment of coarse natural and recycled aggregates for concrete. *Eur. J. Environ. Civ. Eng.* **2016**, *22*, 429–449. [CrossRef]
63. lQGIS Development Team. QGIS Geographic Information System 2009. Open-Source Geospatial Foundation. Available online: http://qgis.org (accessed on 4 December 2023).
64. IBGE—Instituto Brasileiro de Geografia e Estatística. Geoscience Products. Brasília, DF. Available online: https://www.ibge.gov.br/geociencias/todos-os-produtos-geociencias.html (accessed on 8 September 2023).

applied sciences

MDPI

Article

Enhancing the Strength of Mine Residue Soil by Bioremediation Combined with Biopolymers

António A. S. Correia [1,*], Joana B. Caldeira [2], Rita Branco [3] and Paula V. Morais [3]

[1] University of Coimbra, CIEPQPF—Chemical Process Engineering and Forest Products Research Centre, Department of Civil Engineering, 3030-788 Coimbra, Portugal
[2] University of Coimbra, CEMMPRE—Centre for Mechanical Engineering, Materials and Processes, ARISE, Department of Life Sciences, 3000-456 Coimbra, Portugal; joanaritacaldeira@gmail.com
[3] University of Coimbra, CEMMPRE, ARISE, Department of Life Sciences, 3000-456 Coimbra, Portugal; rsrbranco@gmail.com (R.B.); pvmorais@uc.pt (P.V.M.)
* Correspondence: aalberto@dec.uc.pt; Tel.: +351-239-797-277 or +351-239-797-100

Abstract: Traditional soil stabilization methods are usually associated with high energy consumption, carbon emissions, and long-term environmental impact. Recent developments have shown the potential use of bio-based techniques as eco-friendly alternatives for soil stabilization. The present work studies the effects of the addition of the biopolymers xanthan gum (XG) or carboxymethyl cellulose (CMC) to a mine residue soil, combined or not with biostimulation and bioaugmentation techniques, in terms of compressive stress–strain behavior. Unconfined compressive strength (UCS) tests were performed on previously disturbed samples (two cycles of percolation, extraction and homogenization) to evaluate if the biostimulation and bioremediation remain active in a real adverse scenario. The results allowed for us to conclude that both biopolymers, when applied individually (with a content of 1%), are effective stabilizers (CMC allows for unconfined compressive strength increases of up to 109%), showing better results for CMC than Portland cement. The biostimulation of the autochthonous community of the mine residue soil was revealed to be a non-effective technique, even when combined with the biopolymers. However, good results were observed when the bioaugmentation was combined with xanthan gum, with unconfined compressive strength improvements of up to 27%. The study revealed that these bio-based techniques are promising soil engineering techniques, offering environmentally friendly alternatives for sustainable soil stabilization and contributing to a greener and more sustainable future.

Keywords: biopolymer; biostimulation; bioaugmentation; xanthan gum; carboxymethyl cellulose; unconfined compressive strength (UCS) test; stress-strain

Citation: Correia, A.A.S.; Caldeira, J.B.; Branco, R.; Morais, P.V. Enhancing the Strength of Mine Residue Soil by Bioremediation Combined with Biopolymers. *Appl. Sci.* **2023**, *13*, 10550. https://doi.org/10.3390/app131810550

Academic Editor: Fulvia Chiampo

Received: 31 July 2023
Revised: 15 September 2023
Accepted: 20 September 2023
Published: 21 September 2023

1. Introduction

The global population growth has presented significant socio-economic challenges, particularly in terms of resource consumption and infrastructure development. The exponential increase in population has led to an excessive need for natural resources, resulting in the large-scale production of mining waste and associated environmental liabilities and safety risks (e.g., contaminant leaching, acid mine waters, and the collapse of tailing dams). Additionally, the expansion of societies has required the construction of extensive infrastructures, often in areas characterized by soils with poor mechanical properties (low bearing capacity, high compressibility, or poor drainage characteristics) [1,2]. Both situations pose substantial engineering challenges that may be solved by ground improvement techniques.

Ground improvement is a crucial aspect of geotechnical engineering, aimed at improving the mechanical properties and durability of soils [3,4]. There is a wide range of ground improvement techniques for multiple applications. Within ground improvement techniques, soil stabilization has emerged as one of the most versatile and promising techniques, being applied all over the world [1,5,6]. Traditional soil stabilization methods

often rely on chemical binders, which have demonstrated significant advantages but also pose environmental concerns. These binders, such as cement and lime, have proven effective in enhancing soil strength, reducing permeability, and mitigating environmental hazards [7]. However, the use of these binders raises concerns due to their high energy consumption, carbon emissions, and long-term environmental impact [4,8–10]. To address these challenges, researchers have turned their attention to sustainable alternatives for soil stabilization. Indeed, recent developments in the field have explored the use of biopolymers and bioremediation techniques as eco-friendly alternatives to soil stabilization. Biopolymers, derived from natural sources, offer promising advantages in terms of their sustainability, biodegradability, and low environmental impact. Bio-techniques, such as biostimulation and bioaugmentation, utilize microbial activity to enhance soil properties and/or remediate contaminants.

Biopolymers, such as xanthan gum, guar gum, carboxymethyl cellulose, and chitosan, have gained attention in geotechnical engineering due to their unique properties and environmental compatibility. These biopolymers, derived from natural sources, exhibit an ability to improve soil strength, reduce permeability, and control erosion [4,11]. It is important to note that biopolymers differ in terms of their origins and specific characteristics [12]. The choice of biopolymer for soil stabilization depends, among others, on the type of soil and its compatibility with the biopolymer, biopolymer content, curing time, thermal treatment, and mixing methods [13]. The identification and efficient design of biopolymers for stabilized soil systems rely on the Armistead et al. [8] methodology: (1) a rapid membrane-enabled bio-mineral affinity screening approach, (2) supported by mineral binding characterization and complemented by geotechnical verification. Another aspect that should also be considered is the price of biopolymers, which can vary depending on factors such as production scale, purity, and market demand.

Here, some results are highlighted for two of the most widely used biopolymers in soil stabilization, xanthan gum and carboxymethyl cellulose, due to their potential suitability to stabilize acid mine residue soils [8].

Xanthan gum (XG) is an anionic polysaccharide biopolymer produced by the bacterium *Xanthomonas campestris* [9,14]. It is commonly used in various industries, including geotechnical engineering, where it is applied in contents ranging from 0.5 to 5% of the soil weight. XG forms a highly viscous gel when hydrated, coating soil particles and creating bonds between soil particles, namely clay particles, via electrostatic (ionic and hydrogen) interactions [4,9,12], promoting an increase in the shear strength and stiffness of the bio-stabilized soil [8,9,11,13], increasing the optimum water content and the plasticity characteristics (mainly the liquid limit) [13,15], reducing permeability [16], and enhancing erosion resistance [4,17]. The high molecular weight and long-chain structure of XG contribute to its effectiveness in soil stabilization. Regarding the mine residue soils, a very limited number of studies have been published on the subject. Studies from Chen et al. [17] and Bonal et al. [18] indicated that the addition of XG effectively reduced mine tailings/residue erosion. Nevertheless, it is not clear what effect the addition of XG to a mine residue soil has in terms of unconfined compressive strength and stiffness.

Carboxymethyl cellulose (CMC) is a biopolymer derived from cellulose, a major component of plant cell walls, and on wooden barks of trees [3]. CMC is widely used in various industries [19] due to its high water-retaining capacity, adhesion, ability to change the viscosity of the system [7], and film-forming properties. In soil stabilization, CMC acts as a binder and a water-retaining agent, filling the voids between soil particles and forming a cohesive matrix. These features result in reduced soil permeability and water infiltration rate [3,7,20], increased optimum water content and decreased maximum dry unit weight [10], and increased cohesion between particles, and therefore the strength and stiffness of the bio-stabilized soil [3,19–21], which promotes vegetation growth and increases soil erosion resistance [20], contributing to the enhancement of soil properties [20]. Regarding the effect of CMC in contaminated soils, a field assessment of CMC-bridged chlorapatite microparticles was performed by Li and co-authors [22], who demonstrated

the effectiveness, long-term stability, and mechanism of CMC in reducing the mobility of lead in contaminated soil, with the best results achieved at a CMC content of 0.5%. The effect of CMC on mine residue soils has not yet been studied, and its effect in terms of unconfined compressive strength and stiffness is unknown.

Bioremediation techniques offer another avenue for soil stabilization by harnessing the power of microbial activity to enhance soil properties and/or degrade contaminants. Biostimulation involves stimulating the native microbial population in soils by providing suitable growth conditions, such as nutrients or oxygen. This stimulation enhances microbial activity, leading to the degradation or transformation of contaminants or improvements in soil properties. Mendonça et al. [16] demonstrated a reduction in soil permeability using bacteria-produced biopolymers through biostimulation. On the other hand, bioaugmentation involves the introduction of specific microorganisms or microbial communities into the soil to remediate contaminants or improve soil properties. These microorganisms can degrade pollutants or transform them into less harmful substances, or induce the calcium carbonate precipitation that binds soil particles [4]. Su et al. [23] explored the combined application of CMC-stabilized nanosized Fe^0 and mixed anaerobic microorganisms for the enhanced stabilization of chromium (VI) in soil. The authors observed that CMC enhanced the dispersion of nanosized Fe^0 and at the same time promoted the activity of microorganisms.

Despite the research to date, there are still gaps in the knowledge regarding the application of these bio-techniques (biopolymers and bioremediation) to mine residue soils. In addition, the combined application of these two bio-techniques is a subject that has been less discussed but can bring technical benefits and therefore deserves to be studied. Thus, the novelty of the present work is to add to the existing knowledge about the compressive stress–strain behavior of a mine residue soil stabilized with a combination of two promising bio-techniques (biopolymers and bioremediation), contributing to a greener and more sustainable future.

The present work studies the impact of two bio-techniques on the compressive strength behavior of mine residue soil. The effects of the addition of the biopolymers XG or CMC to the soil, combined or not with the biostimulation and bioaugmentation techniques, will be studied in terms of compressive stress–strain behavior. To achieve such goals, the following experimental testing program was designed: (i) unconfined compressive strength (UCS) tests performed with the mine residue soil samples stabilized with the biopolymers applied in a content of 1%; (ii) UCS tests performed with the mine residue soil samples biostimulated (BS) or bioaugmentated (BA), combined or not with the addition of the two biopolymers. In both cases, the results are compared with the control (soil without biopolymer) and the addition of Portland cement (content of 1%).

2. Materials and Methods

2.1. Materials

The soil selected for this study came from a tungsten mine (Panasqueira mine, Fundão, Portugal), collected at Basin 1, as described in previous work [24], and stored at 4 °C until sample preparation. The soil is characterized by a grain size composition of sand, silt and clay content of 61.6%, 35.7%, and 2.7%, respectively (evaluated by the wet sieving method [25]), a porosity of 52.4% and a water content of 19% [25]. Table 1 summarizes the main metals identified in the soil, revealing toxicity. The mine residue soil microbiome contains different strains of bacteria (heterotrophic and facultative anaerobic); the most common are *Acinetobacter*, *Bacillus*, *Pseudomonas*, *Streptococcus*, *Cellulomonas* and *Rothia* [24].

Table 1. Main metals identified in the Panasqueira mine soil, Basin 1—results from XRF test (performed at Trace Analysis and Imaging Laboratory, University of Coimbra).

Si (%)	Al (%)	Fe (%)	K (%)	Pb (%)	As (%)	Ti (%)	Ca (%)	S (%)	W (%)	Ba (%)
38.7	24.2	16.4	10.8	4.3	1.4	1.4	0.9	0.4	0.3	0.3

The soil was stabilized with one of the following three stabilizers: biopolymer xanthan gum (Sigma-Aldrich, St. Louis, MO, USA), biopolymer sodium carboxymethyl cellulose (Sigma-Aldrich), and Portland cement type I 42.5 R (Cimpor, Coimbra, Portugal). Considering the biopolymer contents usually used in soil stabilization, as presented in the introduction, all stabilizers were added to the mine residue soil in a content of 1% of the dry unit weight of the soil.

The biostimulation of the native bacteria from the mine residue soil was performed with Reasoner's 2A broth (R2Ab) 10-fold diluted (culture media), which percolated through the samples in 2 cycles of 7 days each. For the bioaugmentation tests, the strain *Diaphorobacter polyhydroxybutyrativorans* B2A2W2 [26] was selected, which was grown in R2Ab medium for 48 h at 25 °C and 140 rpm. After centrifuging and washing steps, a bacterial suspension with an OD600 of approximately 1 was obtained and stored on ice until its use in the bioaugmentation tests.

2.2. Testing Program and Sample Preparation

Table 2 summarizes the experimental testing program.

Table 2. Experimental testing program.

Test ID	Biopolymer	Bio-Technique	Number of UCS Tests
control	No	no	2
cement	No		2
CMC	Yes		2
XG	Yes		2
BS—control	No	biostimulation	2
BS—cement	No		2
BS—CMC	Yes		2
BS—XG	Yes		2
BA—control	No	bioaugmentation	2
BA—cement	No		2
BA—CMC	Yes		2
BA—XG	Yes		2

CMC = carboxymethyl cellulose; XG = xanthan gum; BS = biostimulation; BA = bioaugmentation.

The laboratory testing program started with the homogenization of the mine residue soil. After air-drying the soil, a Proctor test [27] was performed to evaluate the optimum water content (19.5%) to be added to the soil to achieve the "best" compaction conditions. The wet mine residue soil sample was introduced in a PVC mold (76 mm height, 37 mm diameter) in three layers. For each layer, the sample was statically compacted with a steel bar 20 times; the surface of the first and second layers was scarified before the introduction of the next layer; the top surface was smoothed with a spatula. The samples were cured for seven days in a room with temperature (20 ± 2 °C) and humidity (95 ± 5%), which served as the control.

For the samples stabilized with biopolymer (XG or CMC) or Portland cement, the dry mass of each stabilizer was mixed with the wet mine residue soil and then introduced into the PVC mold following the previously described procedure.

For the bioaugmentated samples, a bacterial B2A2W2 suspension of approximately 5.0×10^7 cells per gram of the dry mine residue soil was added to the top layer, following the remaining part of the procedure described above.

For the BS and BA samples, the testing procedure can be summarized in the following steps: (i) mix all the materials and introduce the samples to the PVC mold, as described above; (ii) percolate the culture media R2Ab through the samples for 7 days; (iii) extract the sample from the PVC mold to undergo homogenization, followed by the re-introduction of the samples to the PVC mold, as described previously, and curing for 7 days; (iv) repeat steps (ii) and (iii). The extraction and homogenization steps, followed by the re-introduction

of the sample to the PVC mold, aim to evaluate if the tested bio-based techniques remain active in a real adverse scenario where the sample has been disturbed.

The percolation system is a constant head permeability test with the modifications proposed in [28]. The tests were performed under a constant head of 5 kPa.

Finally, the samples were extracted from the PVC mold and weighted, and UCS tests were performed to assess the stress–strain compressive behavior. The UCS test was carried out in a universal testing machine (Wykeham Farrance Tristar 5000 kg) under a constant axial strain rate of 1%/min, as stated in the standard [29]. The maximum uniaxial compressive strength ($q_{u\ max}$) of the samples is a fundamental design parameter obtained from the stress–strain curve [30], as well as the strain at failure (ε_f) and the undrained Young's modulus, defined for 50% of $q_{u\ max}$ ($E_{u\ 50}$).

3. Results

Table 3 summarizes the results from the UCS tests that were performed, namely, the parameters obtained from the stress–strain curves ($q_{u\ max}$, ε_f and $E_{u\ 50}$) that allow for a characterization of the compressive behavior in terms of strength and stiffness. In general, the variability of the unconfined compressive strength results is less than ±15% of the average value [31], with some discrepancies explained by the experimental nature of the study. In the following figures, only the stress–strain curve of one of the two UCS tests is presented for clarity in the discussion of the results.

Table 3. UCS results.

	$q_{u\ max}$		ε_f		$E_{u\ 50}$	
Test ID	**(kPa)**	**Average**	**(%)**	**Average**	**(MPa)**	**Average**
Control—T1	110.23	106.18	1.235	1.15	11.78	11.58
Control—T2	102.13		1.073		11.38	
Cement—T1	165.27	175.48	1.388	1.58	14.10	12.51
Cement—T2	185.68		1.773		10.93	
CMC—T1	241.08	221.82	4.074	4.58	6.27	5.24
CMC—T2	202.55		5.087		4.22	
XG—T1	190.51	167.76	3.983	4.08	5.01	4.58
XG—T2	145.01		4.186		4.14	
BS_Control—T1	103.48	78.09	4.431	5.22	3.07	2.40
BS_Control—T2	52.70		6.016		1.73	
BS_Cement—T1	75.83	85.38	6.911	5.92	1.51	2.21
BS_Cement—T2	94.94		4.932		2.92	
BS_CMC—T1	47.20	47.28	4.581	4.56	1.44	1.49
BS_CMC—T2	47.35		4.530		1.55	
BS_XG—T1	118.85	99.99	3.657	3.70	4.57	4.40
BS_XG—T2	81.13		3.742		4.23	
BA_Control—T1	104.70	102.66	5.191	3.66	2.61	4.32
BA_Control—T2	100.61		2.121		6.03	
BA_Cement—T1	142.75	142.82	5.249	5.04	3.42	3.94
BA_Cement—T2	142.88		4.839		4.46	
BA_CMC—T1	62.75	62.76	4.228	3.91	1.96	2.11
BA_CMC—T2	62.78		3.593		2.26	
BA_XG—T1	158.66	130.48	4.960	3.93	5.12	4.41
BA_XG—T2	102.29		2.891		3.71	

CMC = carboxymethyl cellulose; XG = xanthan gum; BS = biostimulation; BA = bioaugmentation.

3.1. Effect of the Stabilizers Applied Individually

From Figure 1 and Table 3, the addition of the applied individually stabilizers is shown to have a tremendous impact on the stress–strain compressive behavior of the mine residue soil. The addition of Portland cement (the most common binder used in soil stabilization) enhanced the maximum unconfined compressive strength significantly, whereas stiffness

was enhanced only slightly. However, the addition of any of the biopolymers (XG or CMC) promoted significant changes in the stress–strain behavior, increasing the compressive strength and the strain at failure. Comparing both biopolymers, the CMC exhibits a better performance than XG, which may be explained by the higher viscosity induced by the CMC [14], conferring a higher adhesion/cohesion between particles. Indeed, in the case of CMC, the strength more than doubled the control value and is above the cement value, while for the case of XG, the results can be compared with the samples stabilized with cement, in agreement with the findings of Armistead et al. [8]. These results clearly show the good performance of both biopolymers, and their ability to be used as stabilizers in mine residue soils. The stress–strain curves also showed that the samples stabilized with biopolymers exhibit a more ductile behavior, characterized by a higher strain at failure. This means that the bio-stabilized material can deform as the compressive strength is mobilized, avoiding catastrophic failure without previous warning.

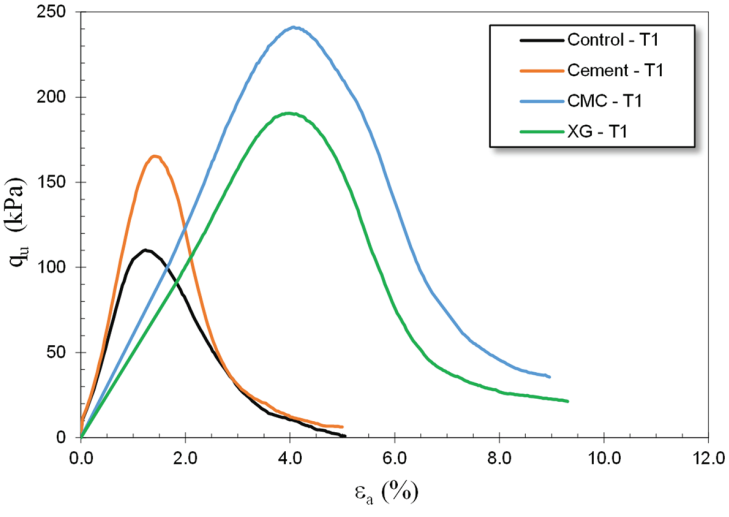

Figure 1. UCS results—effect of the stabilizers applied individually (CMC = carboxymethyl cellulose; XG = xanthan gum).

3.2. Effect of the Biostimulation and Bioaugmentation Techniques

Figures 2 and 3 and Table 3 summarize the results from the UCS tests performed with the mine residue soil samples that were biostimulated (BS, Figure 2a) or bioaugmentated (BA, Figure 2b), whether or not they were combined with the addition of the two biopolymers (XG or CMC). In both cases, the results are compared with the control (soil without biopolymer but BS or BA) and with the addition of Portland cement combined with BS and BA. Figure 2 also includes the results of the UCS tests of the individually applied stabilizers to assist in the interpretation and discussion of the results. Figure 3 illustrates the variation between the unconfined compressive strength ($q_{u\,max}$) and undrained Young's modulus defined for 50% of $q_{u\,max}$ ($E_{u\,50}$) for all the tested samples, representing the average values, the variability regarding the average value and the increase or decrease in the respective control value.

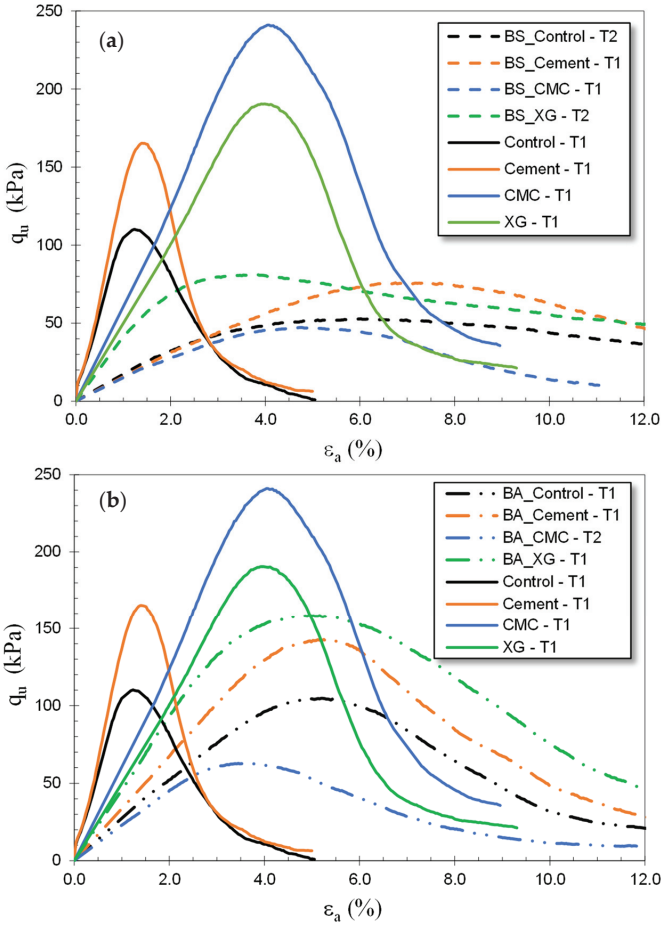

Figure 2. UCS results—effect of two different bio-techniques: (**a**) biostimulation (BS); (**b**) bioaugmentation (BA). (CMC = carboxymethyl cellulose; XG = xanthan gum).

In general, it may be concluded that the biostimulation of the native bacteria produces worse results than the bioaugmentation technique. Indeed, independently of the combination of biostimulation and any of the studied stabilizers, the results are always below the control test (Control), revealing that biostimulation after two percolation cycles is not effective. Moreover, no substantial difference was observed between the biostimulated samples, even when combined with any of the stabilizers, which supports the conclusion that this technique is not effective for this particular mine residue soil.

However, in the case of the bioaugmentation technique, the stress–strain compressive behavior is characterized by a higher strain at failure, inducing a more ductile behavior, and by an unconfined compressive strength that is higher than the control values (control and BA-control) for the stabilizers XG (BA-XG) and Portland cement (BA-cement). The poor performance of the biopolymer CMC (BA-CMC) may be due to the combination of percolation cycles and the extraction and homogenization steps, where some of the bonds promoted by the CMC seemed to be washed and/or destroyed, suggesting that CMC shows a poor mechanical behavior over time. Another possible explanation is the degradation of the biopolymer CMC by the bacteria, which needs to be confirmed. The best unconfined compressive strength result obtained with the biopolymer XG (BA-XG) is supported by the studies of Soldo and Miletić [9], Bozyigit et al. [11] and Ni et al. [13].

Moreover, Bozyigit et al. [11] observed that the addition of XG to soil promoted a significant increase in the unconfined compressive strength over time (up to three years), i.e., the XG exhibits a very good performance and stability over time. Thus, it may be concluded that despite the disturbance associated with the percolation, extraction and homogenization steps, the biopolymer XG continues to be active, and is able to stabilize the mine residue soil. Comparing the samples containing Portland cement, it may be seen that the percolation, extraction and homogenization steps induced the destruction of a great majority of the cementitious bonds responsible for the enhancement of the mechanical properties of the cement-stabilized soil. This justifies the lower unconfined compressive strength of the BA-cement sample compared to the cement sample. However, it is known that the Portland cement develops cementitious bonds (due to hydrated reactions) over long periods, during months or even years [32], justifying the increase in the unconfined compressive strength of the sample BA-cement when compared to the control sample (BA-control). Thus, it may be concluded that Portland cement remains active in the presence of the bioaugmentation technique.

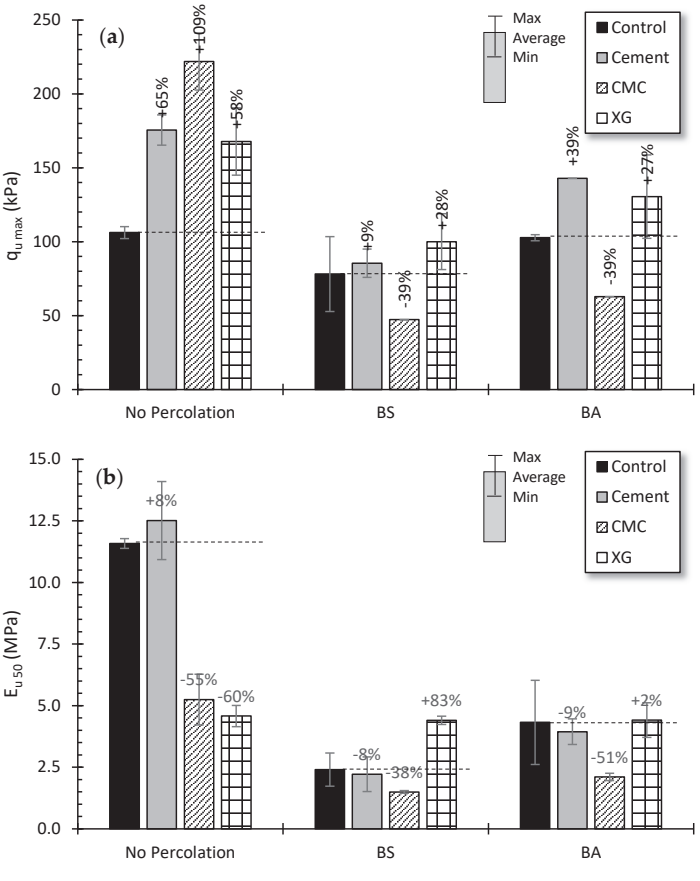

Figure 3. UCS results—the impact of the bio-techniques in terms of: (**a**) $q_{u\,max}$; (**b**) $E_{u\,50}$. (CMC = carboxymethyl cellulose; XG = xanthan gum; BS = biostimulation; BA = bioaugmentation).

4. Conclusions

Based on the UCS tests performed on previously disturbed samples (two cycles of percolation, extraction and homogenization) of mine residue soil stabilized with Portland cement, or with the biopolymers XG and CMC, applied individually or combined with the biostimulation and bioaugmentation techniques, allowed for the following conclusions:

- Both biopolymers (XG and CMC), when applied individually, are effective stabilizers of the mine residue soil, showing better CMC results in terms of unconfined compressive strength than Portland cement when applied with the same content (1% of the dry unit weight of the soil);
- The biostimulation of the autochthonous community of the mine residue soil was revealed to be a non-effective technique, even when combined with the biopolymers or with the Portland cement;
- The bioaugmentation of the mine residue soil with the bacterial strain *Diaphorobacter polyhydroxybutyrativorans* B2A2W2, when combined with the biopolymer xanthan gum (XG), exhibited a good performance in terms of stress–strain compressive behavior, even after the samples were disturbed. Improvements in the unconfined compressive strength of up to 27% were observed compared to the respective control test.

Through further research and application, these bio-techniques have the potential to revolutionize soil engineering practices, offering environmentally friendly alternatives for sustainable soil stabilization, and contributing to a greener and more sustainable future.

Author Contributions: Conceptualization, A.A.S.C. and P.V.M.; methodology, A.A.S.C. and P.V.M.; validation, A.A.S.C., J.B.C. and P.V.M.; formal analysis, A.A.S.C., J.B.C., R.B. and P.V.M. investigation, J.B.C.; resources, A.A.S.C. and P.V.M.; data curation, A.A.S.C. and J.B.C.; writing—original draft preparation, A.A.S.C.; writing—review and editing, J.B.C., R.B. and P.V.M.; supervision, A.A.S.C. and P.V.M.; project administration, A.A.S.C. and P.V.M.; funding acquisition, P.V.M. All authors have read and agreed to the published version of the manuscript.

Funding: This research was funded by FEDER funds through the program COMPETE—Programa Operacional Factores de Competitividade and by national funds through FCT—Fundação para a Ciência e Tecnologia, under the projects UID/EMS/00285/2020, UIDB/00102/2020, and LA/P/0112/2020, by the Project ERA-MIN-2019_67-Reviving and by BIORECOVER Horizon2020 under grant agreement No 821096, supported under Horizon 2020 the European Union's Framework for Research and Innovation. Joana B. Caldeira was supported by a PhD research grant (2022.13542.BD) from FCT/MCTES through national funds.

Institutional Review Board Statement: Not applicable.

Informed Consent Statement: Not applicable.

Data Availability Statement: Some or all data, models, or code generated or used during the study are available from the corresponding author upon reasonable request.

Acknowledgments: The authors would like to express their thanks to CIMPOR for supplying the Portland cement used in the research.

Conflicts of Interest: The authors declare no conflict of interest.

References

1. Correia, A.A.S.; Venda Oliveira, P.J.; Lemos, L.J.L. Strength assessment of chemically stabilised soft soils. *Proc. Inst. Civ. Eng. Geotech. Eng.* **2019**, *172*, 218–227. [CrossRef]
2. Venda Oliveira, P.J.; Correia, A.A.S.; Lemos, L.J.L. Numerical prediction of the creep behaviour of an unstabilised and a chemically stabilised soft soil. *Comput. Geotech.* **2017**, *87*, 20–31. [CrossRef]
3. Sujatha, E.R.; Kannan, G. An Investigation on the Potential of Cellulose for Soil Stabilization. *Sustainability* **2022**, *14*, 6277. [CrossRef]
4. Chang, I.; Lee, M.; Tran, A.T.P.; Lee, S.; Kwon, Y.-M.; Im, J.; Cho, G.-C. Review on biopolymer-based soil treatment (BPST) technology in geotechnical engineering practices. *Transp. Geotech.* **2020**, *24*, 100385. [CrossRef]
5. Correia, A.A.S.; Venda Oliveira, P.J.; Teles, J.M.N.P.C.; Pedro, A.M.G. Strength of a stabilised soil reinforced with steel fibres. *Proc. Inst. Civ. Eng. Geotech. Eng.* **2017**, *170*, 312–321. [CrossRef]

6. Kitazume, M.; Terashi, M. *The Deep Mixing Method*; CRC Press: Boca Raton, FL, USA, 2013.
7. Ghorab, H.Y.; Hassan, A.H.E.; Ahmed, H.E.D.H. Stabilization of the swelling soil for earth construction. *Cem.-Wapno-Beton Cem. Lime Concr.* **2020**, *25*, 198–207. [CrossRef]
8. Armistead, S.J.; Rawlings, A.E.; Smith, C.C.; Staniland, S.S. Biopolymer Stabilization/Solidification of Soils: A Rapid, Micro-Macro, Cross-Disciplinary Approach. *Environ. Sci. Technol.* **2020**, *54*, 13963–13972. [CrossRef] [PubMed]
9. Soldo, A.; Miletić, M. Study on Shear Strength of Xanthan Gum-Amended Soil. *Sustainability* **2019**, *11*, 6142. [CrossRef]
10. Ojuri, O.O.; Ramdas, V.; Aderibigbe, E.A.; Williams, C.G.; Ramchuran, S.; Al-Nageim, H. Improving strength and hydraulic characteristics of regional clayey soils using biopolymers. *Case Stud. Constr. Mater.* **2022**, *17*, e01319. [CrossRef]
11. Bozyigit, I.; Javadi, A.; Altun, S. Strength properties of xanthan gum and guar gum treated kaolin at different water contents. *J. Rock Mech. Geotech. Eng.* **2021**, *13*, 1160–1172. [CrossRef]
12. Kwon, Y.M.; Chang, I.; Cho, G.C. The Effect of Pore Fluid Chemistry on the Behavior of Xanthan Gum-Treated Kaolinite. In *Geotechnical Engineering in the XXI Century: Lessons Learned and Future Challenges*; IOS Press: Amsterdam, The Netherlands, 2019; pp. 2388–2395.
13. Ni, J.; Li, S.S.; Ma, L.; Geng, X.Y. Performance of soils enhanced with eco-friendly biopolymers in unconfined compression strength tests and fatigue loading tests. *Constr. Build. Mater.* **2020**, *263*, 120039. [CrossRef]
14. Khatami, H.; O'Kelly, B.C. Prevention of bleeding of particulate grouts using biopolymers. *Constr. Build. Mater.* **2018**, *192*, 202–209. [CrossRef]
15. Ni, J.; Hao, G.L.; Chen, J.-Q.; Ma, L.; Geng, X.-Y. The Optimisation Analysis of Sand-Clay Mixtures Stabilised with Xanthan Gum Biopolymers. *Sustainability* **2021**, *13*, 3732. [CrossRef]
16. Mendonça, A.; Morais, P.V.; Pires, A.C.; Chung, A.P.; Venda Oliveira, P.J. Reducing Soil Permeability Using Bacteria-Produced Biopolymer. *Appl. Sci.* **2021**, *11*, 7278. [CrossRef]
17. Chen, R.; Ding, X.; Lai, H.; Zhang, L. Improving dust resistance of mine tailings using green biopolymer. *Environ. Geotech.* **2021**, *8*, 382–391. [CrossRef]
18. Bonal, N.S.; Prasad, A.; Verma, A.K. Use of biopolymers to enhance the geotechnical properties of coal mine overburden waste. *Géotechnique Lett.* **2020**, *10*, 179–185. [CrossRef]
19. Ma, H.; Ma, Q. Experimental Studies on the Mechanical Properties of Loess Stabilized with Sodium Carboxymethyl Cellulose. *Adv. Mater. Sci. Eng.* **2019**, *2019*, 9375685. [CrossRef]
20. Yang, Q.-W.; Pei, X.-J.; Huang, R.-Q. Impact of polymer mixtures on the stabilization and erosion control of silty sand slope. *J. Mt. Sci.* **2019**, *16*, 470–485. [CrossRef]
21. Zinchenko, A.; Sakai, T.; Morikawa, K.; Nakano, M. Efficient stabilization of soil, sand, and clay by a polymer network of biomass-derived chitosan and carboxymethyl cellulose. *J. Environ. Chem. Eng.* **2022**, *10*, 107084. [CrossRef]
22. Li, Z.; Gong, Y.; Zhao, D.; Deng, H.; Dang, Z.; Lin, Z. Field assessment of carboxymethyl cellulose bridged chlorapatite microparticles for immobilization of lead in soil: Effectiveness, long-term stability, and mechanism. *Sci. Total Environ.* **2021**, *781*, 146757. [CrossRef]
23. Su, M.; Yin, W.; Liu, L.; Li, P.; Fang, Z.; Fang, Y.; Chiang, P.; Wu, J. Enhanced Cr(VI) stabilization in soil by carboxymethyl cellulose-stabilized nanosized Fe0 (CMC-nFe0) and mixed anaerobic microorganisms. *J. Environ. Manag.* **2020**, *257*, 109951. [CrossRef] [PubMed]
24. Chung, A.P.; Coimbra, C.; Farias, P.; Francisco, R.; Branco, R.; Simão, F.V.; Gomes, E.; Pereira, A.; Vila, M.C.; Fiúza, A.; et al. Tailings microbial community profile and prediction of its functionality in basins of tungsten mine. *Sci. Rep.* **2019**, *9*, 19596. [CrossRef] [PubMed]
25. *BS-1377-2*; Methods of Test for Soils for Civil Engineering Purposes. Part 2: Classification Tests. British Standards Institution: London, UK, 1990.
26. Rito, B.; Almeida, D.; Coimbra, C.; Vicente, D.; Francisco, R.; Branco, R.; Weigand, H.; Morais, P.V. Post-measurement compressed calibration for ICP-MS-based metal quantification in mine residues bioleaching. *Sci. Rep.* **2022**, *12*, 16007. [CrossRef] [PubMed]
27. *BS-1377-4*; Methods of Test for Soils for Civil Engineering Purposes. Compaction-Related Tests. British Standards Institution: London, UK, 1990.
28. Correia, A.A.S.; Matos, M.P.S.R.; Gomes, A.R.; Rasteiro, M.G. Immobilization of Heavy Metals in Contaminated Soils—Performance Assessment in Conditions Similar to a Real Scenario. *Appl. Sci.* **2020**, *10*, 7950. [CrossRef]
29. *BS-1377-7*; Methods of Test for Soils for Civil Engineering Purposes. Shear Strength Tests (Total Stress). British Standards Institution: London, UK, 1990.
30. Tinoco, J.; Correia, A.A.S.; Venda Oliveira, P.J.; Correia, A.G.; Lemos, L.J.L. A Data-driven Approach for qu Prediction of Laboratory Soil-cement Mixtures. *Procedia Eng.* **2016**, *143*, 566–573. [CrossRef]
31. *EN-206-1*; Concrete—Part 1: Specification, Performance, Production and Conformity. European Committee for Standardization: Bruxelles, Belgium, 2007.
32. Taylor, H. *Cement Chemistry*, 2nd ed.; Thomas Telford: London, UK, 1997.

applied sciences

MDPI

Article

Synthesis and Utilisation of Hybrid Metal-Carbonic Anhydrase Enzyme Carrier System for Soil Biocementation

Wilson Mwandira [1], Diane Purchase [2], Maria Mavroulidou [1,*] and Michael J. Gunn [1]

[1] Division of Civil and Building Services Engineering, London South Bank University, 103 Borough Road, London SE1 0AA, UK; mwandiw2@lsbu.ac.uk (W.M.); gunnm@lsbu.ac.uk (M.J.G.)
[2] Department of Natural Sciences, Middlesex University, The Burroughs, London NW4 4BT, UK; d.purchase@mdx.ac.uk
* Correspondence: mavroum@lsbu.ac.uk; Tel.: +44-2078157646

Abstract: Biocementation is an emerging nature-inspired method of producing eco-friendly cement for soil stabilization. This paper used the bovine-derived carbonic anhydrase (CA) enzyme to catalyse the bioprecipitation of $CaCO_3$ in a fine-grained soil and thus to biocement the soil. To increase the efficiency of the CA, an innovative copper–carbonic anhydrase (CA) hybrid was fabricated. This study is a proof-of-concept of the potential application of these enzyme carriers for soil biocementation. The hybrid carriers are aimed to enhance the stability, recovery and reusability of the enzyme used in the biocementation process. The results showed that the fabricated copper phosphate-based inorganic hybrid was stable throughout the duration of the tests (2 months) and under a wide range of pH and temperatures. Its enzymatic activity was enhanced compared to the free CA enzyme and it was proved suitable for soil biocementation. This was further confirmed by the SEM analysis. Additionally, the treated soil with the formulated hybrid carrier showed improved unconfined compressive strength, especially when the carriers were implemented into the soil by mixing. The material analysis by Raman spectroscopy confirmed calcium carbonate as the primary precipitate, consistent with soil biocementation. Overall, this innovative method of delivery of enzymes with enhanced stability and activity shows promise that, upon further development, it can be successfully used to increase the efficiency and sustainability of the biocementation process.

Keywords: carbonic anhydrase; enzyme carriers; ground improvement; biocementation; CO_2 capture

Citation: Mwandira, W.; Purchase, D.; Mavroulidou, M.; Gunn, M.J. Synthesis and Utilisation of Hybrid Metal-Carbonic Anhydrase Enzyme Carrier System for Soil Biocementation. *Appl. Sci.* **2023**, *13*, 9494. https://doi.org/10.3390/app13179494

Academic Editors: Paulo José da Venda Oliveira and António Alberto Santos Correia

Received: 6 July 2023
Revised: 12 August 2023
Accepted: 19 August 2023
Published: 22 August 2023

1. Introduction

Biocementation has recently emerged as a nature-inspired method of producing eco-friendly cement, with a reduced environmental impact and carbon footprint compared to Portland cement [1–4]. The process of biocementation uses organic and inorganic compounds to produce mechanically robust biomaterials [5]. Most biocementation studies use carbonates to biocement soils. The carbonates formed can store carbon permanently in the ground and potentially reduce the amount of CO_2 accumulation in the atmosphere [6]. Biocementation can be realised by different pathways, such as urea hydrolysis [7], denitrification [8], carbonic anhydrase [9] and methane oxidation [10] amongst others, or by a combination of processes [11].

The most common biocementation techniques to date are microbially induced calcium carbonate precipitation (MICP) or enzyme-induced calcium carbonate precipitation (EICP) [2,12,13]. MICP can have limitations for in situ applications in fine-grained soils, if precultured bacteria are injected in the soil to increase the bacteria population favourable for biocementation (bioaugmentation). This is because of the relatively large size of bacteria compared to that of the pore throats in fine-grained soils [14] (bacterial cells have cell sizes ranging usually from 0.5 to 3 μm). Additionally, living microorganisms are difficult to handle, as they are sensitive to environmental conditions [15,16]. EICP was therefore

proposed to overcome these problems associated with MICP. In EICP, free enzymes derived from microbes or plant sources have been suggested and used as a catalyst to produce biocement [2,17,18]. The use of free enzymes facilitates the injection of biocementation treatments in fine-grained soils with narrow pore-throat sizes and bypasses the complexity of controlling living organisms in situ. However, EICP also comes with limitations, as the use of free enzymes in soils entails different challenges. These are linked predominantly to: (a) the stability of the enzyme once released into the ground; (b) the limited enzyme supply (as there is no generation of more enzymes from the soil bacteria, unlike when microbial biocementation is used) and (c) the poor reusability of the enzyme, which increases treatment costs.

Previous studies for different applications have addressed these challenges by immobilizing the enzymes using suitable enzyme carriers. For example, enzyme carriers have been used in bioconcrete [19] or for CO_2 capture in bioreactors [20]. In CO_2 capture applications, hybrid enzyme–metal nanoflower carriers have been extensively used to achieve higher enzyme activity and stability [21]. The term "nanoflower" is used because the structure formed resembles a small flower.

The formation of enzyme–inorganic hybrid nanoflowers comprises a four-step mechanism, namely (a) the coordination, (b) coprecipitation, (c) self-assembly and (d) size growth of the hybrid nanoflower carriers [22]. The process was demonstrated in previous studies, where metal ions were shown to react with phosphate ions to form the first crystals. Once the crystal is created, the metal ion complexes with the enzyme, producing a "nanoflower". Previous studies have shown that the formation process of nanoflower enzyme carriers by encapsulation, adsorption and covalent attachment to flower-like structures is efficient and that the carriers are stable [23–26].

Because of these advantages, the present study combined an inorganic metal ion and carbonic anhydrase (CA) enzyme to fabricate a stable enzyme carrier based on the hybrid enzyme–metal nanoflower method. The study is a proof-of-concept of the hybrid nanoflower technique for soil biocementation using the CA pathway, for concurrent CO_2 absorption and soil stabilisation.

The CA biocementation pathway adopted in this study is proposed as an innovative, eco-friendly, sustainable soil stabilisation method that can consume CO_2 from the atmosphere or use captured CO_2 to precipitate $CaCO_3$, which binds together (i.e., biocements) soil particles. In this multi-step chemical process, CA catalyses the precipitation of calcite. The aqueous CO_2 (aq) formed (Equation (1)) reacts with water to form H_2CO_3 (Equation (2)). The absorption of CO_2 in an aqueous medium entails the conversion of CO_2 (aqueous) to HCO_3 (Equation (3)). CA enzyme can substantially increase the rate of CO_2 mineralization by CA-catalysed hydration of CO_2 to HCO_3. This CO_2 -derived HCO_3 can be mineralized to metal carbonates that can be stored as CO_2 minerals or used in value-added chemicals and other products/materials (adhesives, sealants, food additives, pharmaceuticals, paints, coatings, paper, cement and construction materials [26]).

$$CO_2\ (g) \leftrightarrow CO_2\ (aq) \tag{1}$$

$$CO_2\ (aq) + H_2O\ (l) \leftrightarrow H_2CO_3\ (aq) \tag{2}$$

To form a biocement via biomineral precipitates, the metal ion, e.g., Ca^{2+}, reacts with $CO_3{}^{2-}$ (Equation (5)), forming calcium carbonate, where the CA enzyme provides nucleation sites.

$$H_2CO_3(aq) \leftrightarrow H^+ + HCO_3{}^-\ (aq) \tag{3}$$

$$HCO_3{}^- \leftrightarrow H^+ + CO_3{}^{2-} \tag{4}$$

$$Ca^{2+} + CO_3{}^{2-} \leftrightarrow CaCO_3\ (s) \downarrow \tag{5}$$

Due to the simplicity of the process, CA-mediated mineralization has become one of the most popular ways of CO_2 conversion and utilization. There are many examples in the literature, demonstrating that stabilized and immobilized CA drastically enhances CO_2 mineralization and retains most of its CO_2 mineralization capacity after many cycles of $CaCO_3$ mineralization for faster and more efficient CO_2 conversion and utilization (see, e.g., [26,27]). Thus, a major industrial application of hybrid delivery systems is for carbon capture and storage (CCS) and carbon conversion and utilisation (CCU) technologies, where a basic requirement for the success of the processes is the adequate transfer of CO_2 from the gas phase to the aqueous phase. This critical requirement can be addressed by the use of the CA enzyme, whose active site contains hydroxide-bound Zn^{2+} for catalysis of the interconversion between CO_2 and bicarbonate. However, a major challenge for the industrial implementation of CA is the poor stability of CA at high temperatures, in alkaline pH, or in the presence of high salt concentrations. Thus, producing robust CAs is essential; CA immobilization in hybrid nano-carriers is one way of addressing this challenge, while also enabling the easier recovery and reuse of enzymes, lowering the cost of CA per ton of captured/utilized CO_2. Furthermore, immobilization and stabilization of CA in nanostructured materials, allows CA to be placed together closely with other CO_2-converting enzymes; this way CO_2 captured by CA can be transferred to other enzymes in order to improve the kinetics of CO_2 conversion. CA immobilization and stabilization in nanostructured materials also allows for the combination of immobilized CA with CO_2-converting microorganisms. Overall, the immobilization of CA with nanostructured carriers gives promise for the development of highly stable and reusable CA for the faster and more efficient CO_2 conversion and utilization [28].

Inspired by the literature covering CCC and CCU, this paper aims to assess, for the first time, the feasibility of using immobilized CA in hybrid carriers, as an efficient enzyme delivery system for soil biocementation applications by EICP. The supply of the enzyme through the hybrid carrier aims to overcome challenges of the EICP biocementation method linked to enzymatic stability and supply issues. This would be a useful advancement in improving the EICP technique, while also proposing a method of mineralizing CO_2 in the process, which could create a carbon sink. Also, in view of the proposed electrokinetic implementation of the treatments by the authors to address treatment delivery under existing infrastructure [29], it seems practical to use the same electrokinetic system in situ for the recovery of the hybrid carriers for future reuse.

The particular novelty of our experimental (laboratory) research is therefore the synthesis and study of the performance of a stable metal–organic hybrid enzyme carrier aimed for biocementation applications in soil stabilization; this is investigated for the first time. The research is unique and different from previous studies on hybrid nanoflower carriers, which did not consider soil biocementation applications. It is also innovative compared to other biocementation studies as: (a) it proposes the novel enzyme delivery system for biocementation applications; (b) it aims to produce biocement to stabilize soils while capturing CO_2 at the same time, thus contributing to the net-zero targets of the construction industry; this is unlike most other biocementation studies, based on the ureolytic route.

The following sections present the synthesis and utilisation of a metal–organic hybrid carrier based on the principle of nanoflower synthesis for the delivery and stabilisation of CA enzymes with enhanced enzymatic activity.

2. Materials and Methods

2.1. Materials Used

The soil used in this study was a sandy silty clay sampled from the Prickwillow site of the East Anglia railway network (East Cambridgeshire, Eastern England X/Y co-ordinates: 559,276, 282,290). Soil samples from the railway embankment were obtained by rotary drilling method. Undisturbed soil samples were collected using tube samplers. Figure 1 shows the particle size distribution of the soil from 1.2 to 2.2 m depth, which was used in this study. Table 1 shows some basic physicochemical characteristics of the soil.

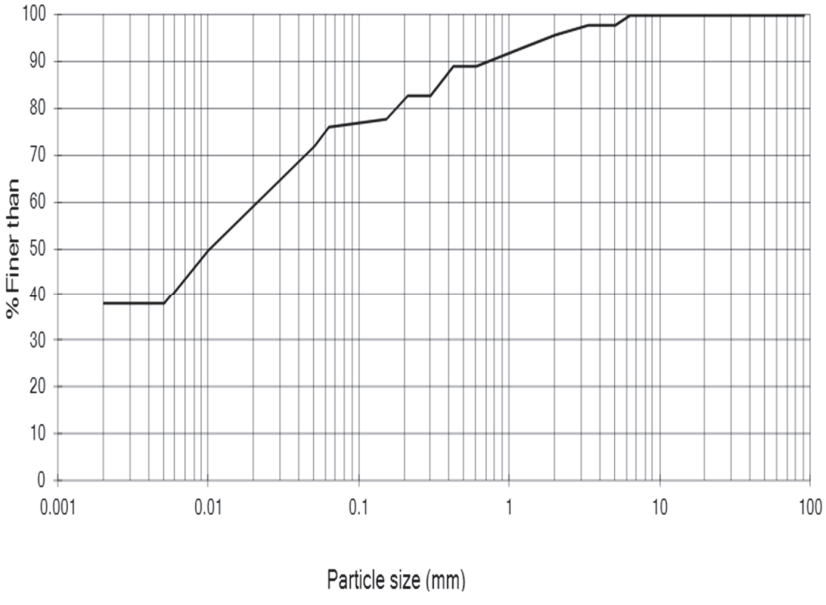

Figure 1. Particle size distribution of the soil used in this study.

Table 1. Basic physicochemical properties of a sandy silty clay soil from Prickwillow, East Anglia.

Property	Value	Test/Standard
Liquid limit: % *w*/*w*	63	Cone penetrometer; BS 1377-2: 1990 [30]
Plastic limit: % *w*/*w*	33	BS 1377-2: 1990 [30]
Plasticity index: % *w*/*w*	30	BS 1377-2: 1990 [30]
Gravel content (%)	4	BS 1377-2: 1990 [30]
Sand content (%)	20	BS 1377-2: 1990 [30]
Silt content (%)	37	BS 1377-2: 1990 [30]
Clay content (%)	39	BS 1377-2: 1990 [30]
Soil classification	CH	BS 1377-2: 1990 [30]
Organic matter content: % *w*/*w*	3.9	Loss of ignition: ASTM D2974-14 [31]
Moisture content: % *w*/*w*	47.5	BS EN ISO 17892: Part 1: 2014 [32]
In situ bulk density (g/cm^3)	1.78	BS EN ISO 17892: Part 2: 2014 [33]
pH	7.7	BS ISO 10390:2005 [34]
Natural $CaCO_3$ content (%)	4.82	ASTM D4373-21 [35]
Undrained shear strength, S_u (kPa)	5.5	Unconfined compression test BS EN ISO 17892-7:2018 [36]

For the synthesis of the enzyme carrier, copper sulphate, manganese sulphate, cobalt sulphate, titanium sulphate, calcium chloride, sodium bicarbonate, 4-nitrophenyl acetate (p-NPA) and carbonic anhydrase (CA) from bovine erythrocytes (E.C.4.2.1.1) were obtained from Sigma-Aldrich. Ultra-pure water was used to formulate stock solutions of these salts.

2.2. Synthesis of Metal–CA and Measurement of CA Activity

The metal–CA hybrid carrier assay was synthesised according to the Duan research group's protocol, which produced hybrid nanoflower carriers for CO_2 capture [25]. Briefly, the procedure used was the following: 0.6 mL of metal phosphate solution (Ti, Co, Mn, Cu, Ca and Zn) of 120 mM was added into 100 mL of phosphate-buffered saline (PBS, 0.1 M, pH 7.4) solution containing 10 mg of CA and was incubated at 4 °C for 2.5 days, as illustrated in Figure 2. The red and blue dots in Figure 2 represent phosphate and metal ions, respectively, in the reaction. The activity of the CA enzyme was determined spectrophotometrically by mixing p-nitrophenyl acetate (p-NpA) hydrolysis at room temperature in

a reaction mixture (1.35 mL) containing freshly prepared 3 mM p-nitrophenyl acetate in phosphate buffer (0.13 M and pH 7.2). Activity for p-NpA hydrolysis was determined using a method that Armstrong and the group proposed in 1966 [37]. The reaction proceeded for 5 min, and the change to A_{348} per minute was measured. Then, the CA activity was characterised by the amount of p-nitrophenol produced per unit of time, and enzyme activity was expressed in terms of U (see Equation (6)):

$$\text{CA activity}\left(\frac{\text{U}}{\text{mL}}\right) = \frac{(A_{348}\text{T} - A_{348}\text{B}) \times 1000}{5 \times Volume} \quad (6)$$

where A_{348}T is the final reading of absorbance; A_{348}B is the initial uncatalysed reaction at a wavelength of 348 nm; and 1 U (μmol/min) is defined as the amount of the enzyme that catalyses the conversion of one micromole of substrate per minute.

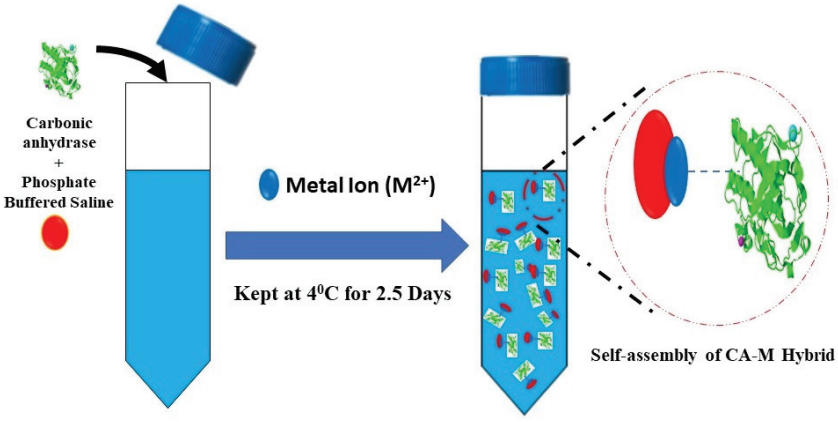

Figure 2. Schematic representation of nanoflower of CA–metal synthesis.

2.3. Effect of pH and Temperature on the Stability of CA and CA-Cu

The activity of the CA and CA-Cu was determined at various reaction pH ranges and temperatures. For the thermal stability investigation, the temperature in the incubator shaker was maintained at 5, 10, 15, 25, 37, 50 and 60 °C under the constant pH of the PBS buffer (pH = 7.4), whereas the study of the stability of the enzyme at different pH values (pH 7, 8, 9, 10 and 11) was performed at room temperature.

2.4. Bioprecipitation Testing and CO_2 Capture Ability

Bioprecipitation experiments in a total volume of 30 mL were conducted using cementation solution (i.e., sodium bicarbonate ($NaHCO_3$) and calcium chloride ($CaCl_2$)) with either free CA or Cu-CA hybrid carriers. Water was used as the control medium. The composition of each system is shown in Table 2. Each bioprecipitation experiment was conducted in a conical flask at 25 °C, 120 rpm, and the investigation lasted for 24 h. Precipitation experiments were conducted in triplicate.

2.5. Characterisation Analysis

2.5.1. Aqueous Chemistry Measurements

The pH and conductivity of each system were monitored using a Hanna Instruments (Bedfordshire, UK) HI 9813-6N Waterproof pH/EC/TDS Temperature Meter. The total amount of bioprecipitate formed in each system was measured by discarding the supernatant after centrifuging, and the biomineral was dried and weighed.

Table 2. Experimental conditions for bioprecipitation and CO_2 capture ability.

	Water (mL)	CA (mL)	CA-Cu (mL)	$CaCl_2$ (mL)	$NaHCO_3$ (mL)
Bioprecipitation					
Control	10	0	0	10	10
Free CA enzyme	0	10	0	10	10
Cu-CA hybrid carrier	0	0	10	10	10
CO_2 capture ability					
Control	100	0	0	100	0
Free CA enzyme	0	100	0	100	0
Cu-CA hybrid carrier	0	0	100	100	0

2.5.2. SEM and Raman Analysis

The microstructure of the biomineral formed was analysed using scanning electron microscopy (SEM) with Thermo Scientific Pharos FEG-SEM (ThermoFisher Scientific, Waltham, MA, USA) with high vacuum mode, 15 KV acceleration voltage; elemental analysis was performed with an energy dispersive X-ray detector (EDS). Raman spectroscopy (LabRAM ARAMIS confocal Raman microscope Horiba Jobin-Yvon, Villeneuve d'Ascq, France) with 633 nm laser (1% power), 50X objective, 100 μm pinhole, 600 L/mm grating was used.

2.5.3. Calcium Carbonate Content Measurement

The $CaCO_3$ content was determined using the acid-washing technique. This technique measured the oven-dried mass at 105 °C before and after an acid wash in a 2 M solution of HCl. The difference between the two masses was taken as the calcium carbonate mass.

2.6. Biocementation Experiments Design

The biocementation treatments were implemented in the soil using two different methods: injection and mixing. The injection was executed in two stages: in the first stage, the synthesised hybrid enzyme carrier was injected into cylindrical soil specimens of 50-mm diameter and 100-mm length; then, the cementation solution of $CaCl_2$ and $NaHCO_3$ (0.1 M) with a pH = 8.5 was injected at the top of the soil specimens at a rate of 3 mL/min and was allowed to percolate by gravity. For the mixing method, the treatments were implemented by hand mixing for 3 min using different mixing ratios of $CaCl_2$, $NaHCO_3$ and water, CA and CA-Cu hybrid enzyme carrier, as shown in Table 3. The molarity of the cementation solution used was based on prior optimisation conducted for bioprecipitation. A set of control specimens (untreated soil) was also prepared for comparison purposes, as shown in Table 3. The unconfined compressive strength testing (UCS) of the 50 mm diameter and 100 mm length soil specimens was measured using a Multiplex 50–48-kN loading frame. The axial load was applied at a constant rate of 1%/min.

Table 3. Experimental conditions for biocementation treatment by injection and mixing.

Treatment Option	Description	Sandy Silty Clay Soil(g)	$CaCl_2$/$NaHCO_3$ (M)	Sterile Distilled Water (mL)	CA Enzyme (mL)	CA-Cu Enzyme (mL)	Curing Time (Day)
Injection	Control	300	0.0/0.1/0.2/0.5	1.5 P.V	0	0	7
	CA Only	300	0.0/0.1/0.2/0.5	0	1.5 P.V		7
	CA-Cu	300	0.0/0.1/0.2/0.5	0	0	1.5 P.V	7
Mixing	Control	300	0.0/0.1/0.2/0.5	50	0	0	7
	CA Only	300	0.0/0.1/0.2/0.5	0	50	0	7
	CA-Cu	300	0.0/0.1/0.2/0.5	0	0	50	7

All experiments were performed in triplicate ($n = 3$) to reduce the experimental errors and confirm the variability and validity of the results.

3. Results and Discussion

3.1. Synthesis of Hybrid Enzyme–Metal Carriers

The synthesis results of hybrid enzyme–metal carriers are shown in Figure 3a–f for the different morphologies of the metal tested, including Ti, Co, Mn, Cu, Ca and Zn. Based on the morphology of the carriers (which were flower-shaped), these will be referred to as 'nanoflowers' for simplicity, as in previous investigations [38,39]. However, in this study, the sizes of the carriers were of the order of several microns. As observed from the SEM images, only the copper nanoflowers were successfully formed; the other metal ions tested failed to produce flower-shaped hybrid carriers [21]. The shape of nanoflowers is essential as it contributes to the high surface-to-volume ratio of the flowers, thus enhancing surface adsorption for accelerating the kinetics of reactions [40]. Despite changing the pH, metal concentration, and enzyme concentration, no flower-shaped carriers were observed when using other metal ions. Several previous studies have also alluded to the failure to develop nanoflowers and have concluded that the formation of nanoflowers is sensitive to experimental conditions [40–42]. It could therefore be postulated that the optimal conditions for nanoflower formation were not met. This could probably be due to two critical factors in nanoflower synthesis: medium environment [43] and surface chemistry of the enzyme biomolecules [44]. As reported, these two parameters are essential for the organic–inorganic hybrid nucleation, growth and assembly. Thus, the results in the following sections and discussion are based on only the copper hybrid carrier (CA-Cu), whose morphology shown in Figure 3d was similar to that reported by previous studies [21,25].

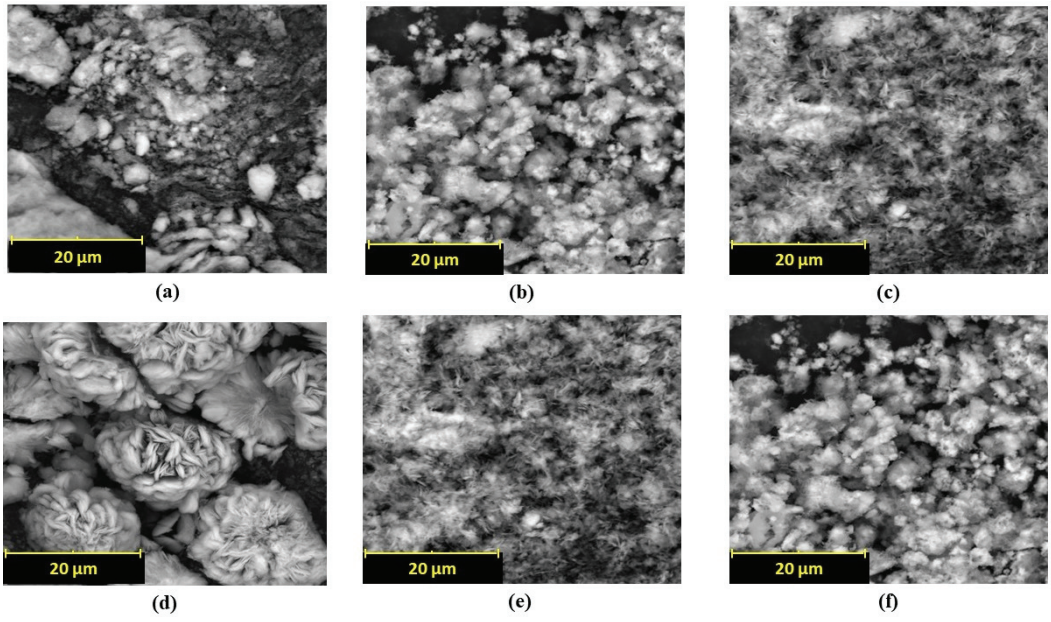

Figure 3. SEM images of (**a**)Ti-CA hybrid carriers, (**b**) Co-CA hybrid carriers, (**c**) Mn-CA hybrid carriers, (**d**) Cu-hybrid carriers, (**e**) Ca-CA hybrid carriers, (**f**) Zn–CA hybrid carriers.

Figure 4a–d shows the flower-like structures for the Cu-CA hybrid, confirmed by SEM images. These showed good dispersity of the petals with three-dimensional microstructures. Specifically, the hybrid "nanoflowers" presented a unified structural morphology like a "Dahlia pinnata", as depicted in the final image of Figure 4d. Since the inceptive

investigations of new nanomaterials in the mid-2000s, different organic–inorganic nanomaterials have been created with different metal ions and organic components exhibiting different morphologies [45]. Previous studies have confirmed that nanoflower morphology is affected by the concentration of reactants and solvent conditions. Thus, there is a plethora of different nanoflower morphologies as can be attested in the literature [23,40]. Different morphologies of each type of nanoflower have different applications, discussed in the Introduction and Discussion sections.

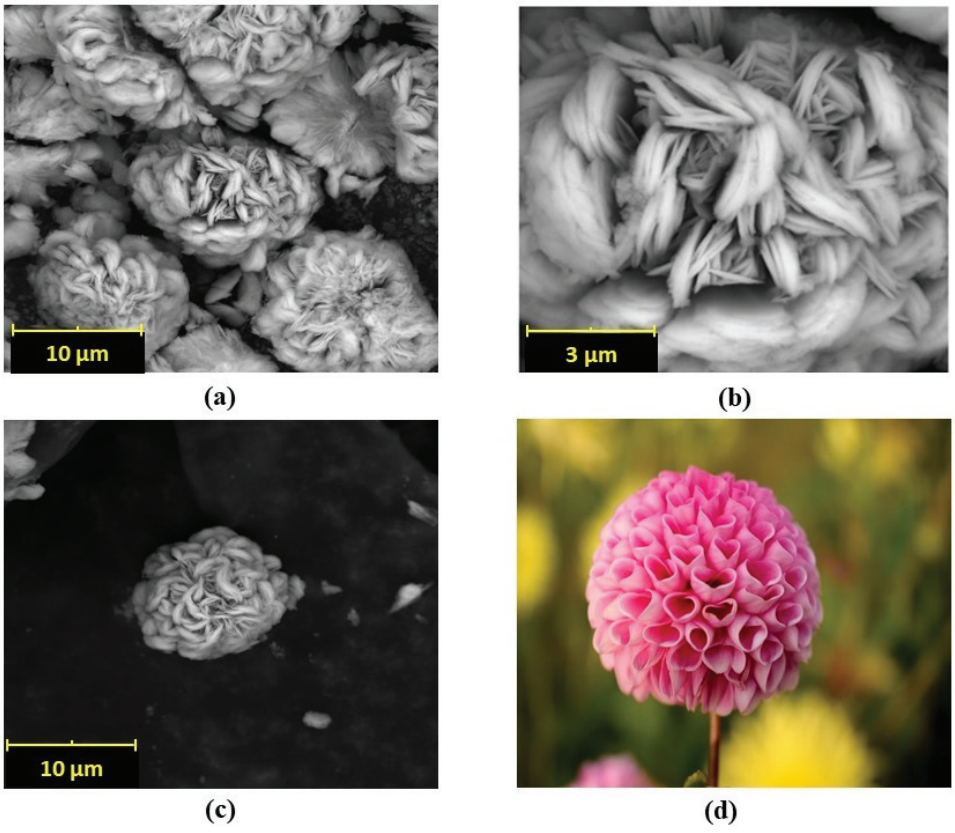

Figure 4. (**a**–**c**) SEM images of Cu-CA hybrid nanoflower at different magnifications (coloured photograph courtesy of public resources in the network), (**d**) a "Dahlia pinnata" flower.

3.2. Stability of CA-Cu and CO_2 Capture Ability

We compared the relative activity of both the free and immobilised enzyme. The relative enzyme activity is the ratio of the retained activity of an immobilised CA or a free enzyme and was investigated over 60 days. The results in Figure 5 showed that the immobilised enzyme efficiency was 95%. Previous studies presented similar findings for the immobilised CA [46,47]. In our study, the free CA enzyme lost 34% of its initial activity within 7 days when incubated in PBS (pH 7.4) at room temperature. Conversely, CA-Cu hybrid carriers maintained 94% of their initial activity under the same conditions even after one month (Figure 5a). Thus, the immobilisation strategy lowers enzyme deactivation so that enzymes can be used for extended periods, as previously reported [48]. The increased stability of the CA-Cu is crucial as it is an essential factor in biocementation.

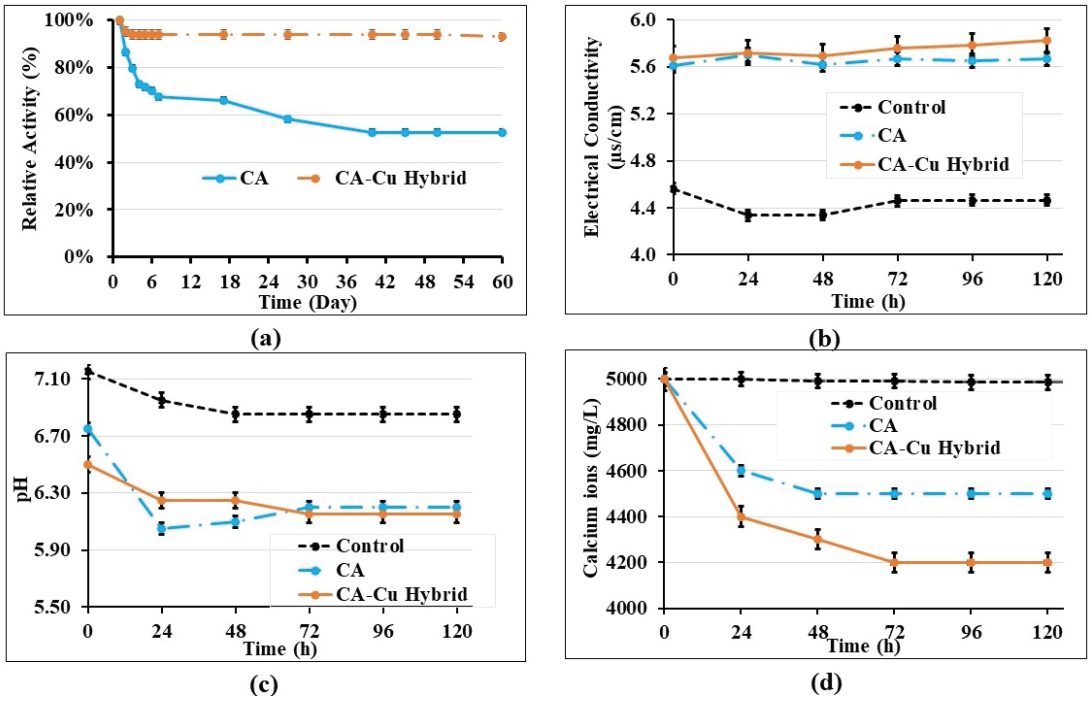

Figure 5. (**a**) Stability of CA and CA-Cu hybrid over time, (**b**) electrical conductivity changes over time, (**c**) pH changes over time, (**d**) change curve of calcium concentration.

The pH stability of the free CA and immobilized CA-Cu was assessed after incubating at specified pH values. pH is a critical factor in biocementation, as it controls the precipitation and dissolution of biominerals; the enzyme is therefore required to be stable in the alkaline range where calcite bioprecipitation occurs [19]. Figure 6a shows the relative activity of the CA enzyme (free or immobilized) compared to the initial activity of the enzyme, under different pH values. From Figure 6a, it can be seen that when the incubation pH increased, the free enzyme lost its activity steadily but still preserved about 85% of its stability at pH > 9. On the other hand, the immobilized CA was even more stable retaining about 92% of its original activity at pH > 9. Similar results from the literature also showed that the CA enzyme remained stable and maintained its secondary structure for pH values of 7.0–11.5 [49].

The activity of the free and immobilised CA enzyme was also measured under different temperatures; the results are presented in Figure 6b in terms of the relative activity of the enzyme compared to its initial activity. The free enzyme lost approximately 30% of its activity at temperatures higher than 50 °C. The activity loss of the CA-Cu at the same temperature range was only 10%. Overall, the activity of the immobilized CA was minimally affected for a wide temperature range until around 40 °C, when a more notable activity loss started. Previous studies also found that immobilised CA enzyme had a higher thermal stability/activity than the free CA enzyme and that the optimal temperature for CA immobilized within polyurethane foam was 40 °C [50]. Other studies of thermostable CA found it to be active in the temperature range 0–100 °C, with an optimal temperature of approximately 80 °C [51]. Despite the difference in optimal temperature observed in the two papers, it can be concluded that CA enzymes can operate at wide temperature ranges. This finding is important, as in biocementation it is critical that the enzyme remains stable at different soil temperatures. In our study, we investigated temperature ranges from 5 to 60 °C; we found the immobilised enzyme to lose only up to 10% of its initial

activity within this temperature range; moreover, only a 1–2% activity loss was observed for temperatures up to 35 °C. The foundation soil temperature commonly ranges between 10 and 24 °C. Therefore, the CA and CA-Cu enzymes would suit ground improvement applications in most world regions, while contributing to climate change mitigation by converting CO_2 into calcium carbonate. Comparing the proposed method to using bacteria for biocementation, cultivation of the latter could be challenging if in situ temperatures and pH were unsuitable for bacterial growth and survival.

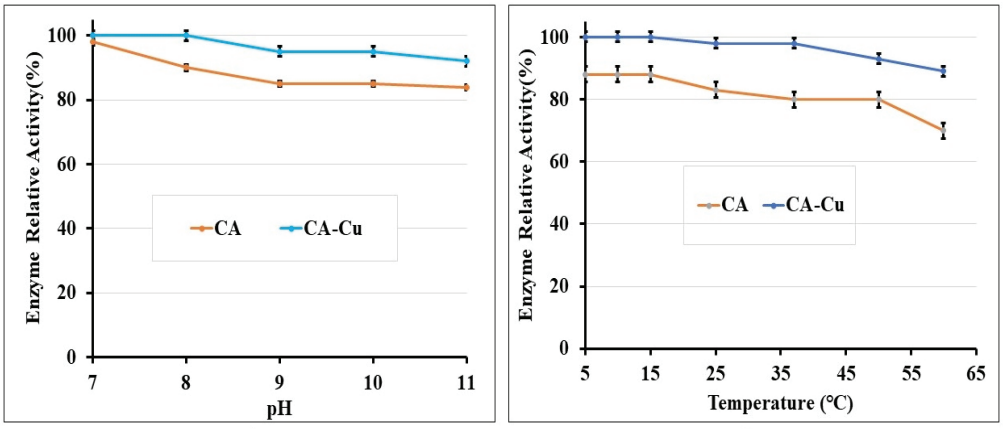

Figure 6. (**a**) Stability of CA and CA-Cu hybrid under different pH; (**b**) Stability of CA and CA-Cu hybrid under different temperatures.

To understand the CO_2 capture of the synthesised CA-Cu and free CA, the water chemistry was investigated, and the pH (Figure 5b), electrical conductivity (Figure 5c) and calcium ion content (Figure 5d) were determined. As shown in Figure 5b, CA-Cu and free CA systems showed an increased electrical conductivity compared to the water-only system. This difference in electrical conductivity is due to the CO_2-H_2O system, whereupon CO_2 dissolution in the water, there is the formation of HCO_3^- leading to increased conductivity. In the control samples with water only, the electrical conductivity and pH remained relatively the same, as in the water-only system, the dissolution of CO_2 in water was limited. Consistently with what was previously reported, the results of the present study showed that immobilised CA is more stable over time and contributes to CO_2 capture and precipitation [40,52]. Bioprecipitation is confirmed by the reduction in calcium ion content as the CA captures CO_2 from the atmosphere and forms biominerals. Conversely, the water-only system did not show any changes in calcium concentration (Figure 5d) as no precipitate was observed.

Enzyme immobilisation has been used in industrial biotechnology to reduce costs [20,53]. Thus, this study postulated that the proposed method would reduce the costs of biocementation, as the immobilisation process is inexpensive and could allow large amounts of recoverable and reusable enzyme to be prepared for large-scale biocementation. Although, arguably, the hybrid carrier synthesis would incur some extra costs compared to the use of free enzymes, in the longer term, the savings coming from the reuse of the hybrid carriers (which are recoverable and can maintain their activity at various temperatures and pH conditions for a long time) would outweigh the synthesis costs.

3.3. Bioprecipitation in Liquid Batches

A bioprecipitation experiment in liquid batches was conducted to attest calcite formation using the synthesised CA-Cu nanoflower with a calcium source. The bioprecipitation results showed the distinct difference in morphology between precipitates from chemical

reactions without enzyme and enzyme-promoted bioprecipitation, as shown in Figure 7a–c. The chemical reaction between $CaCl_2$ and $NaHCO_3$ without enzymes showed a combination of spherical and cubic morphology of calcite at different equimolar concentrations. However, different morphologies were seen in both free CA and CA-Cu nanoflower bioprecipitation. Generally, the reaction proceeds slowly at low equimolar concentrations forming mainly amorphous and irregular unidentifiable crystals seen in either the CA or the CA-Cu nanoflower case. The difference is, however, that the CA-Cu nanoflower had nanoflower co-precipitate together with the calcite, as seen in Figure 7c. Calcite is the most stable form of calcium carbonate compared to vaterite and aragonite. The findings are consistent with the study by Li et al. on the calcium carbonate induced by carbonic anhydrase, which also revealed calcite formation after 24 h of bioprecipitation [54].

The results from Raman's spectroscopy identified the precipitates as calcite (Figure 8) (see the matching signals of the three superimposed spectra in Figure 8, which include those of calcite mineral). The peaks corresponded to the lattice vibration of calcite and the in-plane bending vibration peak of the carbonate group of calcites at approximately 716 cm^{-1} and were therefore identified as calcite. For Raman spectroscopy, the peak at 288 cm^{-1} arises from the vibrations of the CO_3^{2-} groups that involve rotatory oscillations of those groups. The results thus indicate that both the free CA and the Cu-CA carrier enzymes can be used to biocement soil due to calcite production, as previously reported [55]. This result suggests that Cu-CA hybrid carriers can be a good alternative to the free-enzyme catalysing calcite precipitation for soil biocementation.

3.4. Biocementation of Fine-Grained Soil Using CA-Cu Nanoflower

3.4.1. Unconfined Compressive Strength

Figures 9 and 10 show the fine-grained soil specimens after treatment with cementation solution, free CA and CA-Cu using injection and mixing, respectively. Table 4 summarises the results of each case for the control, CA and CA-Cu. According to the results, the maximum UCS of the biocemented soil increased by 85% for CA only, whereas for CA-Cu hybrid carrier mixed in the soil it increased by 319% compared to the control. On the other hand, the injection method showed a 116% increase for CA only and only a 38% increase for the CA-Cu nanoflower. Although this study aimed to use injection as a preferred method for nanoflowers, the results indicate the difficulty in injecting the CA-Cu into the fine-grained soil due to the size of the hybrid carrier, compared to the narrow pore throats in the soil matrix. This is reflected in the lower UCS values achieved and is confirmed by the non-uniform calcite precipitation in the specimen discussed later. Another possible reason for the observed UCS values upon injection is the rapid reaction of the CA enzyme involved in bioprecipitation. As shown in Figure 5d, the bioprecipitation process occurs spontaneously due to the action of the CA enzyme and the reaction is completed quickly. The rapid reaction naturally caused bioclogging of the top surfaces of the soil column, restricting the movement of both enzymes and the cementation solution. This severe bioclogging was observed in all CA-Cu cases; hence, the lower UCS values of the specimens treated by injection in Figure 9, as the treatments appear to have biocemented only the top surfaces of the soil specimens. Namely, in Figure 9, a thin layer of crust is seen to have formed on the top of all treated soil specimens (whether the treatment was caused by chemical reaction without enzymes (Figure 9a), chemical reaction with CA enzymes (Figure 9b) or CA-Cu carriers (Figure 9c) and for all solution molarities used); this crust was identified as calcium carbonate (see Figure 8). This biocement crust reduces the soil permeability on the top of the soil specimen by clogging the soil pores; it thus prevents the ingress of further treatments. Similar results have been frequently reported in previous studies for both the EICP and MICP processes. These studies have also shown the formation of a water-impermeable and high-strength crust layer on the soil surface (usually sandy soils) rather than a more uniform biocementation of the soil at further depth [56–59].

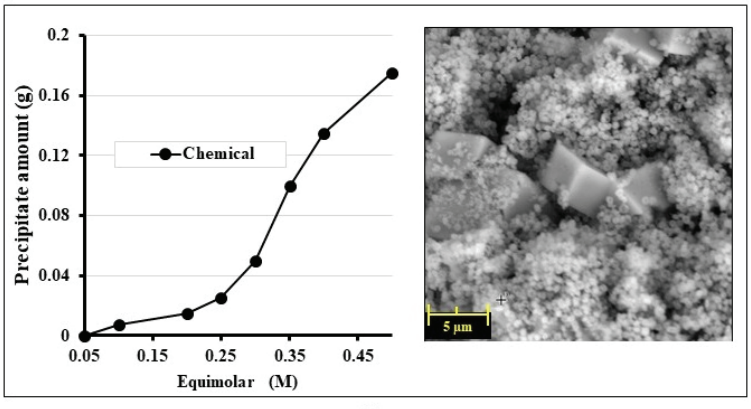

(a)

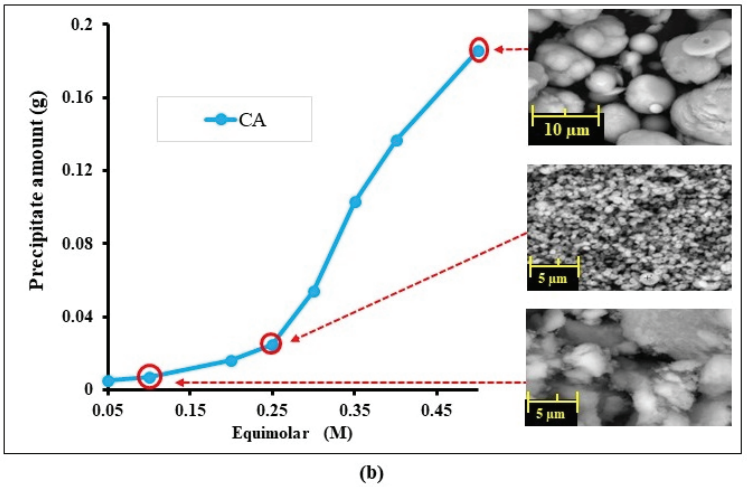

(b)

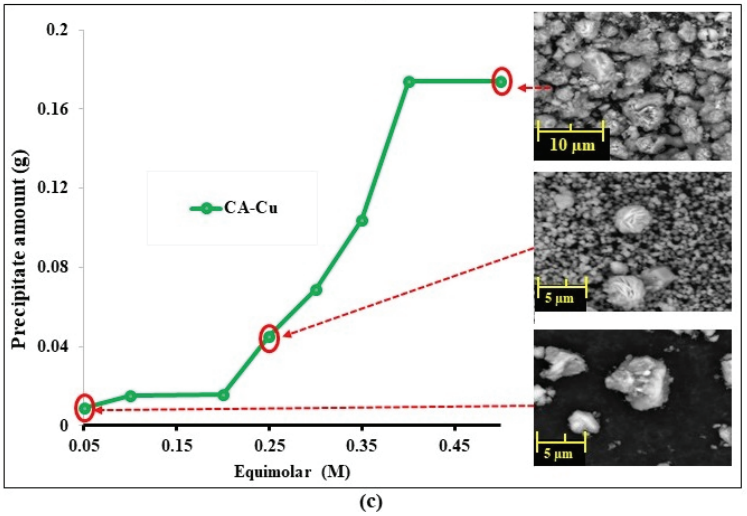

(c)

Figure 7. Bioprecipitation at different equimolar concentrations of $CaCl_2$ and $NaHCO_3$ (**a**) chemical reaction without enzyme, (**b**) carbonic anhydrase (CA) enzyme only, (**c**) CA-Copper nanoflower.

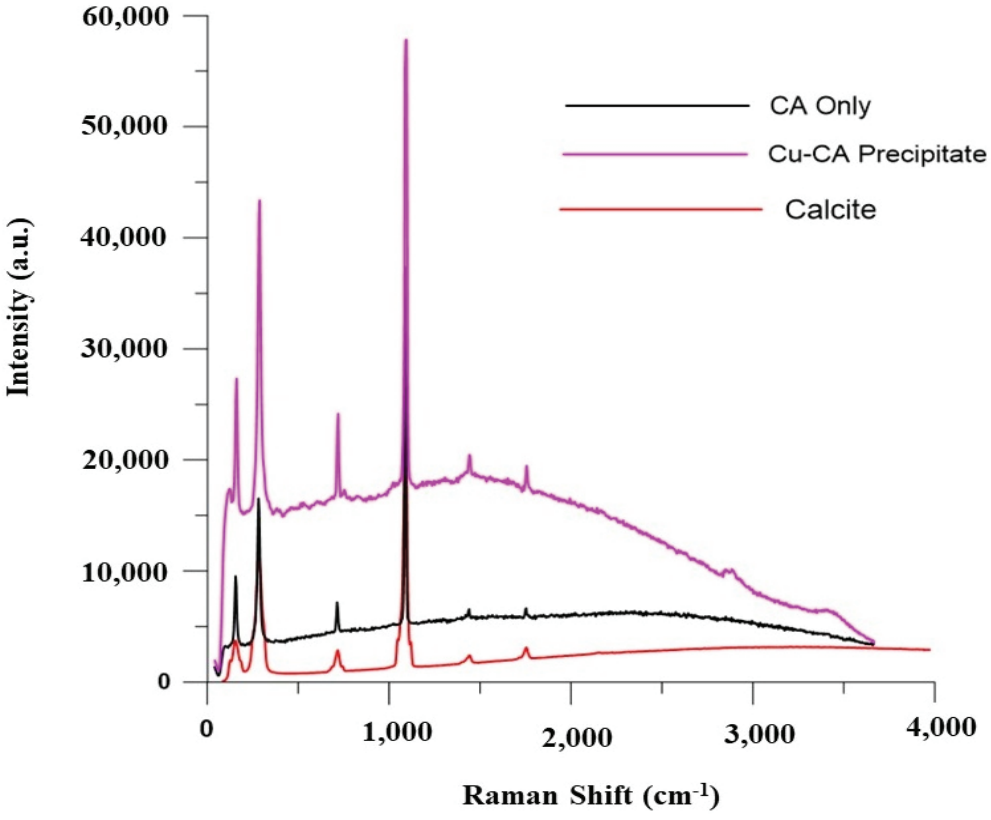

Figure 8. Raman spectroscopy of CA and CA-Cu hybrid carrier bioprecipitate (a.u. stands for 'arbitrary units').

Comparatively, the mixing method (Figure 10) was superior to the injection method (Figure 9), according to the results of this study. This was evidenced (a) by the higher strengths achieved as reported earlier; (b) by the absence of a localized biocement crust on the surface (as opposed to the injection method); (c) by an observed more uniform soft-rock-like consistency throughout the soil sample. Generally, the results showed that the synthesized CA-Cu enzyme was highly effective in biocementing the soil. Specifically, the CA-Cu carriers yielded over 300% increase in UCS compared to the control, when treatments were implemented by mixing; conversely, with the injection method a 38% increase was obtained using CA-Cu carriers. Mixing was therefore still the best way of treating fine-grained soil investigated in this study and this is consistent with the literature [38,39]. As shown in Figure 1, the investigated soil consisted of 39% clay. This is why it was difficult to treat the specimens by injecting enzyme carriers of a size of several microns. Thus, unless the size of the hybrid carrier is reduced and the injection sequence optimized, mixing would be the preferred method of implementation, if the desired outcome is a uniform biocementation throughout a soil sample/layer, instead of encapsulation or bioclogging by crust formation on the soil surface.

The UCS results in this study were compared to previous EICP studies using the urease enzyme. In [13,60], UCS values of approximately 4500 kPa and 4000 kPa were reported, using, respectively, urease enzymes extracted from soybeans and watermelon seeds. It is worth noting that these studies used a different soil type (sand), so the strength values cannot be directly comparable. Moreover, these studies used the ureolytic pathway of biocementation that has been widely investigated and optimised by

many researchers [2–4,61–64]. Thus, despite the lower UCS values recorded in this study, the CA immobilisation and formation of the nanoflower would be a valuable method to stabilise an enzyme for biocementation, as demonstrated.

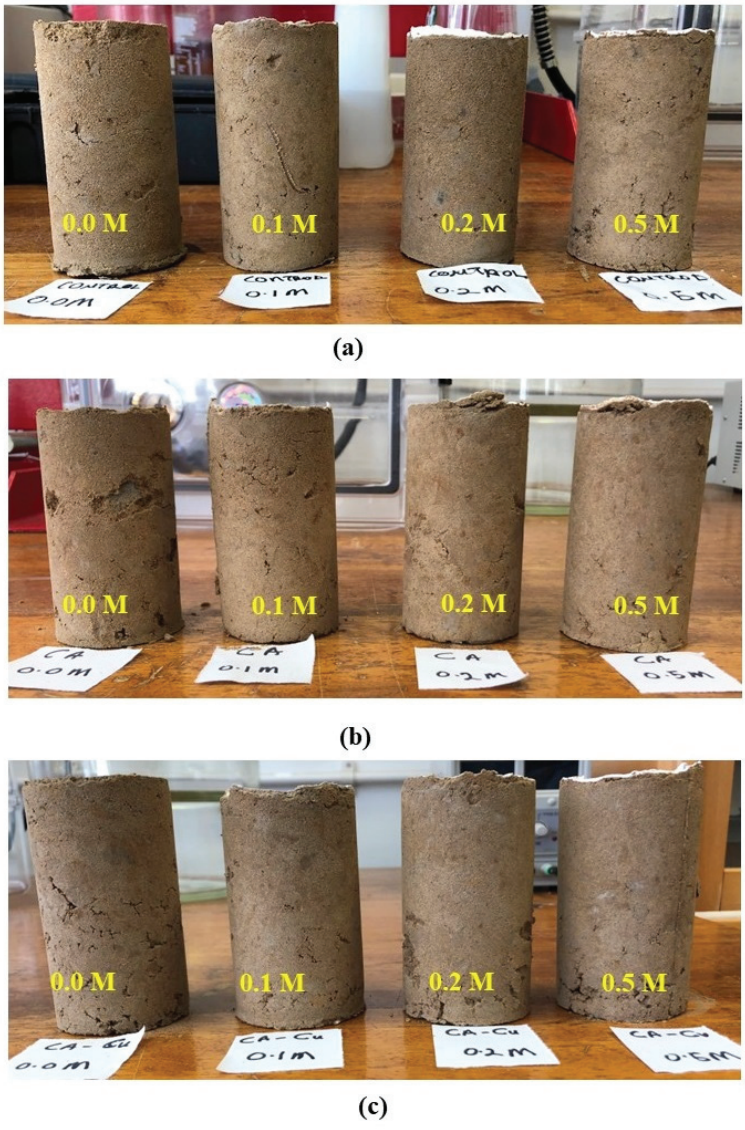

Figure 9. The typical appearance of the specimens biocemented by injection (**a**) control, (**b**) biocemented by CA only, and (**c**) biocemented by CA-Cu nanoflower.

3.4.2. Calcium Carbonate Content

The precipitated calcium carbonate was measured as it is a critical factor in the increase in the strength of biocemented soil. As with the previously reported results on calcium carbonate distribution for biocementation by injection [65], the amount of calcium carbonate was non-uniform throughout the specimens. High amounts of $CaCO_3$ were observed at the top, compared to the middle and bottom sections of the specimens. This is due to a significantly high reaction rate at the top, leading to bioclogging so that only the upper

soil layers are biocemented. Due to the size of the hybrid carriers, this study did not overcome the uniformity problem; however, had nano-sized carriers been produced, the uniformity challenge could have been addressed. Conversely, the mixing method yielded better uniformity of treatment, with $CaCO_3$ contents ranging between 6% and 10% for the treated samples. As observed, the optimal CA-Cu mixing ratio is 0.1 M, yielding higher UCS and $CaCO_3$ content than a 0.2 M or 0.5 M mixing ratio. Similarly, in most other cases, 0.2 M solutions give higher $CaCO_3$ content and UCS than 0.5 M solutions. Similar observations have been reported in urease enzyme reactions where a highly concentrated solution was undesirable [66].

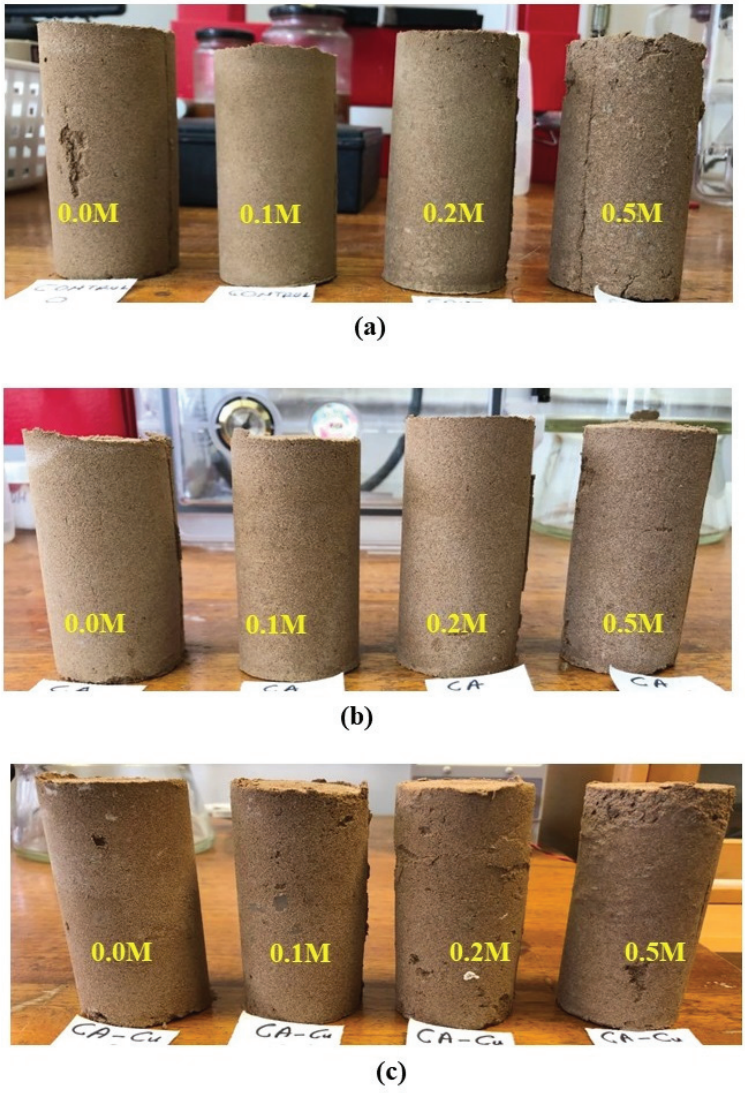

Figure 10. The typical appearance of the specimens biocemented by mixing (**a**) control, (**b**) biocemented by CA only, and (**c**) biocemented by CA-Cu nanoflower.

Table 4. Comparison of the UCS and calcium carbonate content.

Treatment	Test Category	$CaCl_2/NaHCO_3$(g)	CA Enzyme Concentration (mg/mL)	q_u, (kPa)	Average $CaCO_3$ (%)	Moisture Content (%)
Mixing	Control	0.0 M	0	11	5%	30
		0.1 M	0	100	6%	30
		0.2 M	0	108	6%	30
		0.5 M	0	108	7%	30
	CA Only	0.0 M	0.1	109	5%	30
		0.1 M	0.1	92	6%	30
		0.2 M	0.1	200	7%	30
		0.5 M	0.1	189	9%	30
	CA-Cu Nano-flower	0.0 M	0.1	11	5%	30
		0.1 M	0.1	453	10%	30
		0.2 M	0.1	387	9%	30
		0.5 M	0.1	219	8%	30
Injection	Control	0.0 M	0	11	5%	30
		0.1 M	0	34	5%	30
		0.2 M	0	58	6%	30
		0.5 M	0	11	6%	30
	CA Only	0.0 M	0.1	11	5%	30
		0.1 M	0.1	44	6%	30
		0.2 M	0.1	125	12%	30
		0.5 M	0.1	11	5%	30
	CA-Cu Nano-flower	0.0 M	0.1	11	5%	30
		0.1 M	0.1	80	6%	30
		0.2 M	0.1	60	7%	30
		0.5 M	0.1	34	5%	30

Figure 11 shows the SEM results of the biocemented soil. The microphotographs show that the untreated soil had no crystal of $CaCO_3$. Conversely, for the treated specimens, typical $CaCO_3$ crystals on the surface and between particles are observed, consistent with the biocementation mechanism reported in the literature [40,41].

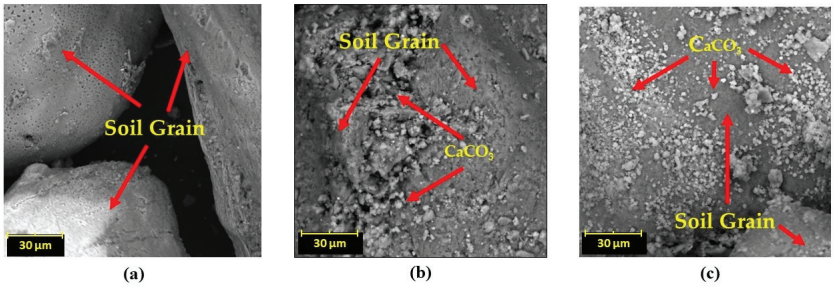

Figure 11. The SEM images of EICP biocemented-treated specimens (**a**) control, (**b**) biocemented by CA only, and (**c**) biocemented by CA-Cu nanoflower.

4. Discussion

4.1. Anticipated Advantages for Practical Applications

This proof-of-concept study investigated an innovative delivery method of enzymes for biocementation via EICP. The method was applied to a fine-grained soil. For this type of soil, MICP can be a challenge due to the pore throat size compared to bacteria size, and for this reason, EICP was suggested instead. Notably, EICP could also use ex situ produced enzyme by the action of bacteria. However, the main challenge of using free enzymes is the cost of the purified enzyme [67] and its stability in high temperatures and extreme pH conditions [68,69]. The study was conducted to address the stability of the enzyme during EICP treatment using a cheap and easy-to-control protocol. The results were encouraging, as the hybrid carrier enabled the enzyme to maintain 94% of its activity over the study period. This is very promising, as the desired advantage of the proposed delivery method is precisely the long-term stability of the synthesized nanoflowers [25,40,70]. The long-term stability of synthesized nanoflowers can be further investigated at bench scale and field conditions in future research. Such studies can then be used for educated estimates of the cost of the technique in an industrial scale environment, and its overall sustainability in comparison with other soil stabilization methods currently used.

Another advantage is the possibility of recovering and reusing the nanoflower. Reuse and recovery contribute to the sustainability of materials used and the circular economy [71,72]. Therefore, practical ways of recovering the nanoflowers in situ merit further investigation. Moreover, researchers can explore the cost comparison between the suggested and traditional EICP/MICP treatment methods for field applications after establishing ways of nanoflower recovery. As mentioned in the Introduction, for the planned future research by the authors, the recovery of the carriers through an electrokinetic setup will be considered.

Due to their versatility and other advantages discussed in the Introduction, nanoflowers have been used in various biomedical and environmental science applications such as to capture and store or convert and utilize CO_2, to diagnose disease biomarkers, biosensors, catalysts, and the therapeutic process along with wastewater remediation and gas sensing [22]. The results from our study proved the hybrid carriers for biocementation for the first time. They indicated that they could play a significant role in enhancing the stability and efficiency of enzymes used for biocementation. The proposed methodology in this study could be thus used for a number of civil and environmental engineering applications of biocementation, such as manufacturing biobricks, enhancing the stability of earthworks and foundation soils, preventing erosion, suppressing dust contamination, or encapsulating and stabilizing pollutants in the soil. Finally, the synthesis of hybrid carriers for other enzymes such as urease [73] or asparaginase [74], which can promote biocementation, could be investigated in future studies.

4.2. Limitations of the Presented Experimental Work

Currently, the nanoflowers synthesised in this study were less than 15 μm (see Figure 12). Compared to bacteria whose size could reach 5–6 μm, the macro flowers are too large to penetrate the fine-graded soil as originally desired. This is a limitation of the current work. However, the literature using this type of enzyme carrier for different applications shows that nano-sized carriers can be produced. The successful synthesis of nano-sized carriers of this type requires further experimental work and an improved protocol, as it is sensitive to temperature, pH, buffer solution and metal concentration changes, whose effects should be evaluated further [23,46]. For applying EICP technology in large-scale geotechnical applications, achieving the economical usage of enzymes is essential; the costs of the method at this scale are yet to be determined. Another limitation of this work is that the CO_2 captured by the method was not quantitatively measured. This information is of importance to further assess the benefits of the technique in terms of CO_2 absorption.

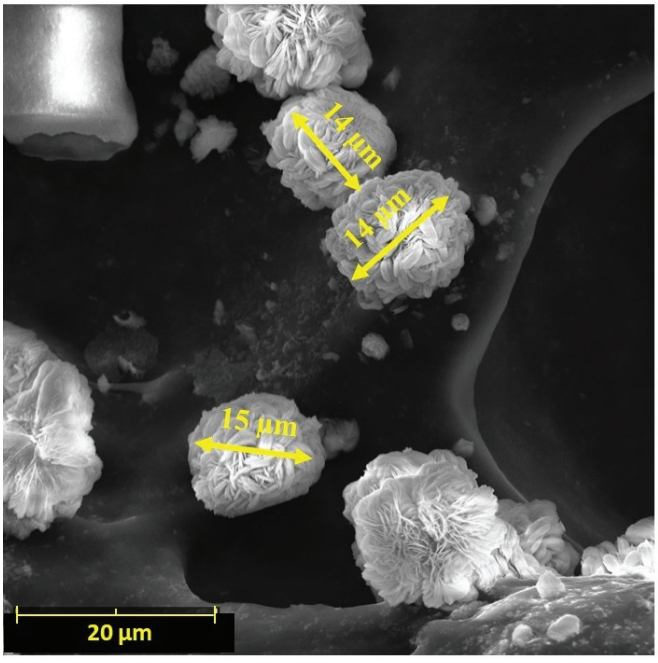

Figure 12. SEM image showing the length of CA-Cu hybrid carriers synthesized in this study.

5. Conclusions

In this study, we investigated the delivery of immobilized carbonic anhydrase (CA) enzyme in hybrid carriers, as one possible way to overcome the challenges of enzyme instability in the EICP biocementation process. A series of laboratory tests were conducted to fabricate a copper phosphate-based inorganic hybrid enzymatic delivery system that is stable and suitable for biocementation with enhanced enzyme activity and efficiency. The key developments and findings from the study are as follows:

i. The study achieved the synthesis and utilization of inorganic hybrid enzyme carriers with the morphological structure of flowers to biocement soil.
ii. The results showed that the bovine carbonic anhydrase enzyme enhanced the CO_2 hydration reaction, resulting in a bioprecipitation reaction and calcium carbonate production. This calcium carbonate was identified as calcite.
iii. The immobilized CA enzyme effectively promoted the absorption of CO_2 into the calcium carbonate, which can be used for biocementation with concurrent CO_2 sequestration.
iv. It was demonstrated that the immobilised CA enzyme was very stable over long periods of time and within a wide range of pH and temperatures. This result has significant implications for biocementation, as the improved enzyme stability would be helpful in various soil conditions, such as variable temperatures and pH, encountered during ground improvement. The fact that the stability was preserved over months also demonstrates that the hybrid carrier system can promote the reusability of the enzymes.
v. The carriers were successfully used in the soil to achieve biocementation. Their capability as a practical enzyme delivery alternative was demonstrated.
vi. Unconfined compressive strength values of fine-grained soil increased significantly upon implementation of the carriers, especially when mixing was used as a treatment implementation method.

vii. The scanning electron microscope micrographs and Raman spectroscopy confirmed calcite as the primary precipitate formed, which can act as a bonding agent between soil particles to biocement soils.

Thus, the carrier delivery system shows promise that upon further development, enzyme immobilisation can successfully be used for soil biocementation to increase the efficiency and overall sustainability of the EICP process.

Author Contributions: W.M., D.P., M.M. and M.J.G., carried out the experiment and analysed the results; W.M., M.M. and D.P. wrote the manuscript with support from M.J.G.; D.P., M.M. and M.J.G. supervised the project; M.M., D.P. and M.J.G. conceived the original idea. All authors have read and agreed to the published version of the manuscript.

Funding: The European Commission funded this work under the Horizon 2020 Marie Skłodowska-Curie Individual Fellowships Grant Number 101025184 Project NOBILIS (Grant holder: London South Bank University).

Institutional Review Board Statement: Not applicable.

Informed Consent Statement: Not applicable.

Data Availability Statement: Data sharing does not apply to this article.

Acknowledgments: The authors thank Dr Leonardo Pantoja-Muñoz for conducting the SEM-EDS and Raman analyses, Matthew Billing for conducting the XRD analyses and Alejandra Gonzalez for the technical assistance.

Conflicts of Interest: The authors declare no conflict of interest.

References

1. De Jong, J.T.; Soga, K.; Kavazanjian, E.; Burns, S.; van Paassen, L.A.; Al Qabany, A.; Aydilek, A.; Bang, S.S.; Burbank, M.; Caslake, L.F.; et al. Biogeochemical processes and geotechnical applications: Progress, opportunities and challenges. *Géotechnique* **2013**, *63*, 287–301. [CrossRef]
2. Venda Oliveira, P.J.; Freitas, L.D.; Carmona, J.P.S.F. Effect of Soil Type on the Enzymatic Calcium Carbonate Precipitation Process Used for Soil Improvement. *J. Mater. Civ. Eng.* **2016**, *29*, 04016263. [CrossRef]
3. Safdar, M.U.; Mavroulidou, M.; Gunn, M.J.; Garelick, J.; Payne, I.; Purchase, D. Innovative methods of ground improvement for railway embankment peat fens foundation soil. *Géotechnique* **2021**, *71*, 985–998. [CrossRef]
4. Safdar, M.U.; Mavroulidou, M.; Gunn, M.J.; Purchase, D.; Gray, C.; Payne, I.; Garelick, J. Towards the Development of Sustainable Ground Improvement Techniques—Biocementation Study of an Organic Soil. *Circ. Econ. Sustain.* **2022**, *2*, 1589–1614. [CrossRef]
5. Wang, Z.; Su, J.; Ali, A.; Yang, W.; Zhang, R.; Li, Y.; Zhang, L.; Li, J. Chitosan and carboxymethyl chitosan mimic biomineralization and promote microbially induced calcium precipitation. *Carbohydr. Polym.* **2022**, *287*, 119335. [CrossRef]
6. Robles-Fernández, A.; Areias, C.; Daffonchio, D.; Vahrenkamp, V.C.; Sánchez-Román, M. The Role of microorganisms in the nucleation of carbonates, environmental implications and applications. *Minerals* **2022**, *12*, 1562. [CrossRef]
7. Graddy, C.M.; Gomez, M.G.; DeJong, J.T.; Nelson, D.C. Native bacterial community convergence in augmented and stimulated ureolytic MICP biocementation. *Environ. Sci. Technol.* **2021**, *55*, 10784–10793. [CrossRef]
8. Gao, Y.; Wang, L.; He, J.; Ren, J.; Gao, Y. Denitrification-based MICP for cementation of soil: Treatment process and mechanical performance. *Acta Geotech.* **2022**, *17*, 3799–3815. [CrossRef]
9. Jin, P.; Zhang, S.; Liu, Y.; Zhang, W.; Wang, R. Application of Bacillus mucilaginosus in the carbonation of steel slag. *Appl. Microbiol. Biotechnol.* **2021**, *105*, 8663–8674. [CrossRef]
10. Ganendra, G.; Wang, J.; Ramos, J.A.; Derluyn, H.; Rahier, H.; Cnudde, V.; Ho, A.; Boon, N. Biogenic concrete protection driven by the formate oxidation by Methylocystis parvus OBBP. *Front. Microbiol.* **2015**, *6*, 786. [CrossRef]
11. Dhami, N.K.; Mukherjee, A.; Reddy, M.S. Micrographical, minerological and nano-mechanical characterisation of microbial carbonates from urease and carbonic anhydrase producing bacteria. *Ecol. Eng.* **2016**, *94*, 443–454. [CrossRef]
12. Arpajirakul, S.; Pungrasmi, W.; Likitlersuang, S. Efficiency of microbially-induced calcite precipitation in natural clays for ground improvement. *Constr. Build. Mater.* **2021**, *282*, 122722. [CrossRef]
13. Shu, S.; Yan, B.; Ge, B.; Li, S.; Meng, H. Factors affecting soybean crude urease extraction and biocementation via Enzyme-Induced carbonate precipitation (EICP) for soil improvement. *Energies* **2022**, *15*, 5566. [CrossRef]
14. Song, C.; Elsworth, D.; Zhi, S.; Wang, C. The influence of particle morphology on microbially induced $CaCO_3$ clogging in granular media. *Mar. Georesour. Geotechnol.* **2021**, *39*, 74–81. [CrossRef]
15. Sun, X.; Miao, L.; Tong, T.; Wang, C. Study of the effect of temperature on microbially induced carbonate precipitation. *Acta Geotech.* **2019**, *14*, 627–638. [CrossRef]

16. Mortensen, B.M.; Haber, M.J.; DeJong, J.T.; Caslake, L.F.; Nelson, D.C. Effects of environmental factors on microbial induced calcium carbonate precipitation. *J. Appl. Microbiol.* **2011**, *111*, 338–349. [CrossRef]
17. Cui, M.; Lai, H.; Hoang, T.; Chu, J. One-phase-low-pH enzyme induced carbonate precipitation (EICP) method for soil improvement. *Acta Geotech.* **2021**, *16*, 481–489. [CrossRef]
18. Almajed, A.; Lateef, M.A.; Moghal, A.A.B.; Lemboye, K. State-of-the-art review of the applicability and challenges of microbial-induced calcite precipitation (MICP) and enzyme-induced calcite precipitation (EICP) techniques for geotechnical and geoenvironmental applications. *Crystals* **2021**, *11*, 370. [CrossRef]
19. Castro-Alonso, M.J.; Montañez-Hernandez, L.E.; Sanchez-Muñoz, M.A.; Macias Franco, M.R.; Narayanasamy, R.; Balagurusamy, N. Microbially induced calcium carbonate precipitation (MICP) and its potential in bioconcrete: Microbiological and molecular concepts. *Front. Mater.* **2019**, *6*, 126. [CrossRef]
20. Sirisha, V.L.; Jain, A.; Jain, A. Chapter Nine—Enzyme Immobilization: An Overview on Methods, Support Material, and Applications of Immobilized Enzymes. *Adv. Food Nutr. Res.* **2016**, *79*, 179–211. [CrossRef]
21. Lee, S.W.; Cheon, S.A.; Kim, M.I.; Park, T.J. Organic–inorganic hybrid nanoflowers: Types, characteristics, and future prospects. *J. Nanobiotechnol.* **2015**, *13*, 54. [CrossRef] [PubMed]
22. Liu, Y.; Ji, X.; He, Z. Organic-inorganic nanoflowers: From design strategy to biomedical applications. *Nanoscale* **2019**, *11*, 17179–17194. [CrossRef] [PubMed]
23. Ge, J.; Lei, J.; Zare, R.N. Protein-inorganic hybrid nanoflowers. *Nat. Nanotechnol.* **2012**, *7*, 428–432. [CrossRef] [PubMed]
24. Cipolatti, E.P.; Silva, M.J.A.; Klein, M.; Feddern, V.; Feltes, M.M.C.; Oliveira, J.V.; Ninow, J.L.; de Oliveira, D. Current status and trends in enzymatic nanoimmobilization. *J. Mol. Catalysis. B Enzym.* **2014**, *99*, 56–67. [CrossRef]
25. Duan, L.; Li, H.; Zhang, Y. Synthesis of hybrid nanoflower-based carbonic anhydrase for enhanced biocatalytic activity and stability. *ACS Omega* **2018**, *3*, 18234–18241. [CrossRef]
26. Kim, H.S.; Hong, S.-G.; Woo, K.M.; Teijeiro Seijas, V.; Kim, S.; Lee, J.; Kim, J. Precipitation-based nanoscale enzyme reactor with improved loading, stability, and mass transfer for enzymatic CO_2 conversion and utilization. *ACS Catal* **2018**, *8*, 6526–6536. [CrossRef]
27. Gadikota, G. Carbon mineralization pathways for carbon capture, storage and utilization. *Commun. Chem.* **2021**, *4*, 23. [CrossRef]
28. Talekar, S.; Jo, B.H.; Dordick, J.S.; Kim, J. Carbonic anhydrase for CO_2 capture, conversion and utilization. *Curr. Opin. Biotechnol.* **2022**, *74*, 230–240. [CrossRef]
29. Safdar, M.U.; Mavroulidou, M.; Gunn, M.J.; Purchase, D.; Payne, I.; Garelick, J. Electrokinetic biocementation of an organic soil. *Sustain. Chem. Pharm.* **2021**, *21*, 100405. [CrossRef]
30. *BS 1377:1990*; Methods of Test for Soils for Civil Engineering Purposes. Classification Tests. BSI: London, UK, 1990.
31. *ASTM D2974—14*; Standard Test Methods for Moisture, Ash, and Organic Matter of Peat and Other Organic Soils. ASTM International: West Conshohocken, PA, USA, 2014.
32. *BS EN ISO 17892*; Part 2: 2014 Geotechnical Investigation and Testing—Laboratory Testing of Soil—Part 1: Determination of Bulk Density. BSI: London, UK, 2014.
33. *BS EN ISO 17892*; Part 1: 2014 Geotechnical Investigation and Testing—Laboratory Testing of Soil—Part 1: Determination of Water Content. BSI: London, UK, 2014.
34. *BS ISO 10390:2005*; Soil Quality. Determination of pH. BSI: London, UK, 2005.
35. *ASTM D4373-21*; Standard Test Method for Rapid Determination of Carbonate Content of Soils. ASTM International: West Conshohocken, PA, USA, 2021.
36. *BS EN ISO 17892-7:2018*; Geotechnical Investigation and Testing. Laboratory Testing of Soil-Unconfined Compression Test. BSI: London, UK, 2018.
37. Armstrong, J.M.; Myers, D.V.; Verpoorte, J.A.; Edsall, J.T. Purification and properties of human erythrocyte carbonic anhydrases. *J. Biol. Chem.* **1966**, *241*, 5137–5149. [CrossRef]
38. Chakraborty, A.; Samriti; Ruzimuradov, O.; Gupta, R.K.; Cho, J.; Prakash, J. TiO_2 nanoflower photocatalysts: Synthesis, modifications and applications in wastewater treatment for removal of emerging organic pollutants. *Environ. Res.* **2022**, *212*, 113550. [CrossRef]
39. Wang, Q.; Chen, Y.; Zhu, R.; Luo, M.; Zou, Z.; Yu, H.; Jiang, X.; Xiong, X. One-step synthesis of Co(OH)F nanoflower based on micro-plasma: As an effective non-enzymatic glucose sensor. *Sens. Actuators B Chem.* **2020**, *304*, 127282. [CrossRef]
40. Shende, P.; Kasture, P.; Gaud, R.S. Nanoflowers: The future trend of nanotechnology for multi-applications. *Artif. Cells Nanomed. Biotechnol.* **2018**, *46* (Suppl. 1), 413–422. [CrossRef]
41. Dastjerdi, R.; Hashemikia, S. Mechanisms and guidelines on the sustainable engineering of self-assembling; nanostars and nanoflowers. *J. Clean. Prod.* **2021**, *312*, 127570. [CrossRef]
42. Gupta, T.; Samriti; Cho, J.; Prakash, J. Hydrothermal synthesis of TiO_2 nanorods: Formation chemistry, growth mechanism, and tailoring of surface properties for photocatalytic activities. *Mater. Today Chem.* **2021**, *20*, 100428. [CrossRef]
43. Li, Y.; Fei, X.; Liang, L.; Tian, J.; Xu, L.; Wang, X.; Wang, Y. The influence of synthesis conditions on enzymatic activity of enzyme-inorganic hybrid nanoflowers. *J. Mol. Catal. B Enzym.* **2016**, *133*, 92–97. [CrossRef]
44. Shao, P.; Shen, Y.; Ye, J.; Zhao, J.; Wang, L.; Zhang, S. Shape controlled ZIF-8 crystals for carbonic anhydrase immobilization to boost CO_2 uptake into aqueous MDEA solution. *Sep. Purif. Technol.* **2023**, *315*, 123683. [CrossRef]
45. Kharisov, B.I. A Review for Synthesis of Nanoflowers. *Recent Pat. Nanotechnol.* **2008**, *2*, 190–200. [CrossRef]

46. Ren, S.; Chen, R.; Wu, Z.; Su, S.; Hou, J.; Yuan, Y. Enzymatic characteristics of immobilized carbonic anhydrase and its applications in CO2 conversion. *Colloids Surf. B Biointerfaces* **2021**, *204*, 111779. [CrossRef]
47. Patel, S.K.S.; Otari, S.V.; Chan Kang, Y.; Lee, J. Protein–inorganic hybrid system for efficient his-tagged enzymes immobilization and its application in l -xylulose production. *RSC Adv.* **2017**, *7*, 3488–3494. [CrossRef]
48. Zhang, M.; Zhang, Y.; Yang, C.; Ma, C.; Tang, J. Enzyme-inorganic hybrid nanoflowers: Classification, synthesis, functionalization and potential applications. *Chem. Eng. J.* **2021**, *415*, 129075. [CrossRef]
49. Idrees, D.; Shahbaaz, M.; Bisetty, K.; Islam, A.; Ahmad, F.; Hassan, M.I. Effect of pH on structure, function, and stability of mitochondrial carbonic anhydrase VA. *J. Biomol. Struct. Dyn.* **2017**, *35*, 449–461. [CrossRef] [PubMed]
50. Kanbar, B.; Ozdemir, E. Thermal stability of carbonic anhydrase immobilized within polyurethane foam. *Biotechnol. Prog.* **2010**, *26*, 1474–1480. [CrossRef] [PubMed]
51. Luca, V.D.; Vullo, D.; Scozzafava, A.; Carginale, V.; Rossi, M.; Supuran, C.T.; Capasso, C. An α-carbonic anhydrase from the thermophilic bacterium Sulphurihydrogenibium azorense is the fastest enzyme known for the CO_2 hydration reaction. *Bioorg. Med. Chem.* **2013**, *21*, 1465–1469. [CrossRef] [PubMed]
52. Giri, A.; Pant, D. CO_2 management using carbonic anhydrase producing microbes from western Indian Himalaya. *Bioresour. Technol. Rep.* **2019**, *8*, 100320. [CrossRef]
53. Fasim, A.; More, V.S.; More, S.S. Large-scale production of enzymes for biotechnology uses. *Curr. Opin. Biotechnol.* **2021**, *69*, 68–76. [CrossRef]
54. Li, W.; Chen, W.; Zhou, P.; Zhu, S.; Yu, L. Influence of initial calcium ion concentration on the precipitation and crystal morphology of calcium carbonate induced by bacterial carbonic anhydrase. *Chem. Eng. J.* **2013**, *218*, 65–72. [CrossRef]
55. Pan, L.; Li, Q.; Zhou, Y.; Song, N.; Yu, L.; Wang, X.; Xiong, K.; Yap, L.; Huo, J. Effects of different calcium sources on the mineralization and sand curing of $CaCO_3$ by carbonic anhydrase-producing bacteria. *RSC Adv.* **2019**, *9*, 40827–40834. [CrossRef]
56. Almajed, A.; Tirkolaei, H.K.; Kavazanjian, E.; Hamdan, N. Enzyme Induced Biocementated Sand with High Strength at Low Carbonate Content. *Sci. Rep.* **2019**, *9*, 1135. [CrossRef]
57. Wani, K.M.N.S.; Mir, B.A. An Experimental Study on the Bio-cementation and Bio-clogging Effect of Bacteria in Improving Weak Dredged Soils. *Geotech. Geol. Eng.* **2021**, *39*, 317–334. [CrossRef]
58. Chu, J.; Ivanov, V.; Naeimi, M.; Stabnikov, V.; Liu, H. Optimization of calcium-based bioclogging and biocementation of sand. *Acta Geotech.* **2014**, *9*, 277–285. [CrossRef]
59. Stabnikov, V.; Naeimi, M.; Ivanov, V.; Chu, J. Formation of water-impermeable crust on sand surface using biocement. *Cem. Concr. Res.* **2011**, *41*, 1143–1149. [CrossRef]
60. Dilrukshi, R.; Nakashima, K.; Kawasaki, S. Soil improvement using plant-derived urease-induced calcium carbonate precipitation. *Soils Found.* **2018**, *58*, 894–910. [CrossRef]
61. Cui, M.; Zheng, J.; Zhang, R.; Lai, H. Soil bio-cementation using an improved 2-step injection method. *Arab. J. Geosci.* **2020**, *13*, 1270. [CrossRef]
62. Whiffin, V.S. Microbial $CaCO_3$ Precipitation for the Production of Biocement. Ph.D. Thesis, Murdoch University, Perth, Australia, 2004; pp. 1–162. Available online: http://researchrepository.murdoch.edu.au/399/2/02Whole.pdf (accessed on 1 June 2023).
63. Abo-El-Enein, S.A.; Ali, A.H.; Talkhan, F.N.; Abdel-Gawwad, H.A. Utilization of microbial induced calcite precipitation for sand consolidation and mortar crack remediation. *HBRC J.* **2012**, *8*, 185–192. [CrossRef]
64. Neupane, D.; Yasuhara, H.; Kinoshita, N.; Unno, T. Applicability of Enzymatic Calcium Carbonate Precipitation as a Soil-Strengthening Technique. *ASCE J. Geotech. Geoenviron. Eng.* **2013**, *139*, 2201–2211. [CrossRef]
65. Gowthaman, S.; Yamamoto, M.; Nakashima, K.; Ivanov, V.; Kawasaki, S. Calcium phosphate biocement using bone meal and acid urease: An eco-friendly approach for soil improvement. *J. Clean. Prod.* **2021**, *319*, 128782. [CrossRef]
66. Phua, Y.J.; Røyne, A. Bio-cementation through controlled dissolution and recrystallization of calcium carbonate. *Constr. Build. Mater.* **2018**, *167*, 657–668. [CrossRef]
67. Poźniak, G.; Krajewska, B.; Trochimczuk, W. Urease immobilized on modified polysulphone membrane: Preparation and properties. *Biomaterials* **1995**, *16*, 129–134. [CrossRef]
68. Ahenkorah, I.; Rahman, M.M.; Karim, M.R.; Beecham, S.; Saint, C. A Review of Enzyme Induced Carbonate Precipitation (EICP): The Role of Enzyme Kinetics. *Sustain. Chem.* **2021**, *2*, 92–114. [CrossRef]
69. Zhang, S.; Zhang, Z.; Lu, Y.; Rostam-Abadi, M.; Jones, A. Activity and stability of immobilized carbonic anhydrase for promoting CO_2 absorption into a carbonate solution for post-combustion CO_2 capture. *Bioresour. Technol.* **2011**, *102*, 10194–10201. [CrossRef] [PubMed]
70. Liang, S.; Wu, X.; Xiong, J.; Zong, M.; Lou, W. Metal-organic frameworks as novel matrices for efficient enzyme immobilization: An update review. *Coord. Chem. Rev.* **2020**, *406*, 213149. [CrossRef]
71. Ghufran, M.; Khan, K.I.A.; Ullah, F.; Nasir, A.R.; Al Alahmadi, A.A.; Alzaed, A.N.; Alwetaishi, M. Circular Economy in the Construction Industry: A Step towards Sustainable Development. *Buildings* **2022**, *12*, 1004. [CrossRef]
72. Norouzi, M.; Chàfer, M.; Cabeza, L.F.; Jiménez, L.; Boer, D. Circular economy in the building and construction sector: A scientific evolution analysis. *J. Build. Eng.* **2021**, *44*, 102704. [CrossRef]

73. Khodadadi Tirkolaei, H.; Javadi, N.; Krishnan, V.; Hamdan, N.; Kavazanjian, E. Crude Urease Extract for Biocementation. *J. Mater. Civ. Eng.* **2020**, *32*, 04020374. [CrossRef]
74. Li, M.; Fu, Q.; Zhang, Q.; Achal, V.; Kawasaki, S. Bio-grout based on microbially induced sand solidification by means of asparaginase activity. *Sci. Rep.* **2015**, *5*, 16128. [CrossRef] [PubMed]

applied sciences

MDPI

Article

Effect of the Organic Matter Content on the Mechanical Properties of Soils Stabilized with Xanthan Gum

Paulo J. Venda Oliveira [1,*] and Maria J. F. C. C. Reis [2]

[1] Department of Civil Engineering, ISISE, ARISE, University of Coimbra, 3030-788 Coimbra, Portugal
[2] Department of Civil Engineering, University of Coimbra, 3030-788 Coimbra, Portugal
* Correspondence: pjvo@dec.uc.pt; Tel.: +351-239-797-271

Abstract: The aim of this paper is to study the effect of the organic matter (OM) content on the effectiveness of the soil stabilization process using the biopolymer xanthan gum. Five different artificial soils with an organic matter content in the range of 1.5 to 7.7% are subjected to unconfined compressive strength (UCS) and oedometer tests to evaluate their strength, stiffness and compressibility, respectively. These results are complemented by an analysis of SEM images. The results from the UCS tests show a positive effect of the stabilization process in terms of strength and stiffness in a range of an OM content of 1.5 to 5.5%, but a detrimental effect for a higher OM content (7.7%) is observed. Due to the hydration of the biopolymer's hydrogels, the compressibility tends to increase in specimens stabilized with xanthan gum. This effect is amplified for higher OM contents. The results of oedometer tests also show that the stabilization with xanthan gum brings about a significant decrease in the coefficient of consolidation, inducing an increase in the primary consolidation time.

Keywords: xanthan gum; organic soils; soil stabilization

Citation: Oliveira, P.J.V.; Reis, M.J.F.C.C. Effect of the Organic Matter Content on the Mechanical Properties of Soils Stabilized with Xanthan Gum. *Appl. Sci.* **2023**, *13*, 4787. https://doi.org/10.3390/app13084787

Academic Editor: Tiago Miranda

Received: 14 March 2023
Revised: 1 April 2023
Accepted: 8 April 2023
Published: 11 April 2023

1. Introduction

The construction of many civil engineering structures (such as buildings, ports, airports, bridges, tunnels, among others) on/in problematic soils with poor mechanical behavior requires the implementation of improvement methods to enhance these soils' characteristics, in order to increase the strength and/or decrease the compressibility. One of the most common techniques used to improve a soil's properties is chemical stabilization, which consists of a mixture of the natural soil with binders, such as quicklime, fly ash, blast furnace granulated slag and cement (which is the most used), among others. The use of cement is associated with a significant ecological footprint, since: (i) the cement industry is responsible for about 2.6% of the global CO_2 emissions [1]; (ii) the use of cement in soil stabilization induces an increase in the pH of the soil treated, which has a negative impact on the natural microbiome and on the vegetation's development [2]; and (iii) the material produced by the cement-based soil stabilization is irreversible [2], which is not an advantage for construction in an environmentally sensitive area.

To reduce the environmental impact of the use of cement, some alternative techniques have been investigated in the last few years, such as the reuse of materials in the construction industry [3], and the use of biodegradable [4,5] and bio-based materials, among others. One of the most studied bio-based methods consists of the precipitation of calcium carbonate that behaves as a bio-cement. When this material is deposited in the porous spaces of the soil, it creates bonds between the soil particles, inducing an improvement in the mechanical properties of the composite material [6–14]. This methodology presents two variants, microbial-induced calcium carbonate precipitation [7,15] and enzyme-induced calcium carbonate precipitation [7–10,15,16]; in the former, bacteria are added to the soil to produce enzymes, while in the latter, the enzymes are added directly to the soil.

The use of biopolymers (biodegradable polysaccharides produced by living organisms) has emerged as an alternative to the bio-based methodologies, which are also associated

with a low ecological footprint. Among the several types of biopolymers studied to solve geotechnical problems (casein and sodium caseinate salt, guar, cationic e-polylysine, gellan, agar, chitosan, curdlan and β-Glucan, Persian gum [17], Zein biopolymer [18], etc.), xanthan gum (XG) is one of the biopolymers most investigated in geotechnical engineering, mainly due to the significant reduction in its market price in the last years [5] and to its ability to mitigate some soil weaknesses; in particular, it:

(i) Decreases the soil's erosion [19], and in parallel promotes the growth of the vegetation, which also contributes to erosion mitigation [20];
(ii) Decreases the permeability coefficient of the treated soil [21–26] due to the hydration of the XG hydrogels, which decreases the soil's porosity and consequently makes the flow of water in the porous space difficult;
(iii) Improves the mechanical properties of the treated soils, such as sands [23,27], silty sands [28,29], clayed soils [19,27,30], bentonite, kaolinite [26,27,31,32], and residual soils [33,34];
(iv) Some one-dimensional compression tests with a bentonite and a kaolinite stabilized with XG show a decrease in the compressibility after the stabilization with xanthan gum [31]. However, it should be emphasized that not all the results published are consistent with each other; indeed, results of a soft marine soil [30], kaolinite clay [35], sandy soil [23], and silt sand [29] show an increase in the compressibility after stabilization with XG. In terms of the coefficient of consolidation (Cv), results of the treatment of a marine soft soil [30], high plastic soil [36], and kaolinite clay [35] with XG promotes a significant reduction in the Cv; i.e., the stabilization with XG prolongs the time required to the end of the primary consolidation. Additionally, the coefficient of secondary compression of a kaolinite clay increases after the stabilization with xanthan gum [35];
(v) Increases the pH value [34] and the plasticity index [19,26,34], and decreases the specific gravity [34];
(vi) Changes the compaction characteristics, namely, it increases the optimum moisture content and decreases the maximum dry density of a tropical residual soil [34], a dispersive soil [37], and a kaolinite clay [26];
(vii) Increases the undrained shear strength of a kaolinite clay, but decreases the undrained shear strength of a montmorillonite clay [38];
(viii) Decreases the cumulative variation in moisture loss and mass loss in freeze–thaw tests [36];
(ix) Decreases the swelling potential of a high plastic soil [36].

Some research works indicate that the effectiveness of XG in stabilizing soils results from the contribution of two effects: (i) the aggregation of the soil particles due to the deposition of the XG in the voids; and (ii) the bonds established between the XG (hydrogen bonding) and the surfaces of the soil particles, mainly when they are electrically charged, as it occurs in clayed soils [2,27]. These two effects justify the greater effectiveness of the XG in stabilizing clays than coarse-grained soils, since in clays, both effects are cumulative in strengthening the soil. Nevertheless, in coarse-grained soils the improvement of the mechanical properties is only due to the deposition of the XG in the porous space of the soil, inducing the generation of a network of XG fibers, similar to micro-reinforcement of the soil, as illustrated in Figure 1 for a silty sand.

Some experiments with specimens of silty sand submitted to curing in humid conditions indicate that the stabilization with XG is potentiated for a curing time of 7–14 days and for an XG content of approximately 1% [29]. For a curing time of less than 3 days, a detrimental effect of the stabilization with XG was observed [29].

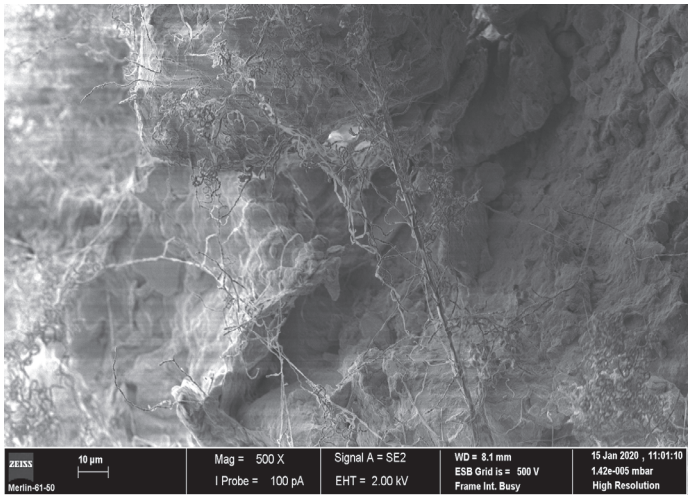

Figure 1. SEM image of a non-organic silty sand stabilized with 2% of XG.

Although xanthan gum is a biodegradable biopolymer, which is naturally associated with a progressive loss of its properties with elapsed time, some experimental results show a high stability over time in strengthening the soils in dry environments. Indeed, the benefit of XG strengthening such soils tends to grow with curing time [23,27,29,31,37], and even in the long-term (until 730 days) no traces of biodegradability in a sand-XG mixture were observed [27]. On the other hand, the evolution over time of the permeability coefficient (in saturated conditions) did not show results totally consistent with a great stability over time. In fact, the results of Bouazza et al. [22] reveal a decrease in the permeability coefficient of a sandy-XG mixture during the curing time, while the opposite was observed in a clayed soil [24] and a sandy soil [23]. Additionally, the results of Mendonça et al. [25] show a decrease in the permeability coefficient of a sandy soil during the first 14 days of curing time, followed by a slight increase in the permeability coefficient for higher curing times, which may be the consequence of some biodegradability and/or some dehydration of the biopolymer's hydrogels over time [25,32].

Some previous research has described the efficiency of the treatment of soils with xanthan gum, namely concerning the effect of several factors (such as soil type, curing time, content of XG, among others) on the strengthening, plasticity [30,32] and the permeability coefficient. However, not only is the number of studies about the compressibility of water-soil-XG mixtures in the bibliography limited, there is also a lack of research concerning the effect of the organic matter content on the effectiveness of water-soil-XG mixtures, both in terms of the mechanical properties and of the compressibility characteristics. The main objective and the novelty of this work is to contribute to filling these gaps in the scientific knowledge. Thus, the present study intends to analyze the effectiveness of the use of XG to stabilize five soils, in terms of mechanical properties and compressibility, each with a different organic matter content (1.5, 2.4, 4.1, 5.5 and 7.7%) but a constant particle size distribution. This study is based on the experimental results obtained from unconfined compression strength (UCS) and one-dimensional compression (oedometer) tests, where the behavior of non-stabilized soils is compared with the behavior obtained after stabilization with XG (Table 1). Additionally, images obtained from scanning electron microscopy (SEM) of some specimens are also considered in the analysis.

Table 1. Testing program. Number of UCS and oedometer tests carried out.

Organic Matter Content (%)	Xanthan Gum Content (%)	Curing Time (Days)	UCS Tests (N)	Oedometer Tests (N)
1.5	0.0 [1]	—	3	2
	1.0 [2]	14	3	2
2.4	0.0 [1]	—	3	2
	1.0 [2]	14	3	2
4.1	0.0 [1]	—	3	2
	1.0 [2]	14	3	2
5.5	0.0 [1]	—	3	2
	1.0 [2]	14	3	2
7.7	0.0 [1]	—	3	2
	1.0 [2]	14	3	2

[1] Non-stabilized specimen; [2] Specimen stabilized with 1% of xanthan gum.

2. Materials and Methods

2.1. Characteristics of the Soils

Table 2 presents the main physical and chemical properties of the five soils used in the experimental work. The reference soil is a natural alluvial soft soil collected in the "Baixo Mondego" area, located in central Portugal. This is an organic soil (OM = 7.7%) with a low pH (3.6) and with a grain size distribution composed predominantly of sand (57%), classified as OH (ASTM D2487-00), i.e., an organic soil with high plasticity. These characteristics affect the behavior of the soil, which exhibits a low undrained shear strength (c_u < 25 kPa), high compressibility and high plasticity (w_L = 71%; w_P = 44.3%) [39–41].

Table 2. Physical and chemical properties of the soils tested.

Property	Organic Matter Content (%)				
	1.5	2.4	4.1	5.5	7.7 [1]
Grain size distribution:					
Clay (%)	23	23	23	23	23
Silt (%)	57	57	57	57	57
Sand (%)	20	20	20	20	20
Specific gravity, G	–	–	–	–	2.32
Liquid limit, w_L (%)	36.3	40.9	46.6	54.1	71.0
Plastic limit, w_P (%)	15.3	33.1	33.2	33.0	44.3
Plasticity index, PI (%)	21.0	7.8	13.4	21.1	26.7
Liquidity index	1.09	1.09	1.09	1.09	1.09
Soil classification, USCS [2]	CL	CL	OL	OH	OH
Chemical composition					
pH (BSI337-3)	–	–	–	–	3.6
SiO_2 (%)	–	–	–	–	62
Al_2O_3 (%)	–	–	–	–	16
Fe_2O_3 (%)	–	–	–	–	4.8

[1] Natural organic soil; [2] (ASTM D2487-00).

The reference soil was used to prepare the remaining four artificial soils with five different OM contents, as described in the following sections. Therefore, the five soils used in the experiments have the same grain size distribution. The results presented in Table 2 show the increase in the plasticity (w_L and w_P) for the higher OM content [42], which matches with other studies [43–46].

2.2. Characteristiques of the Biopolymer (Xanthan Gum)

The xanthan gum (XG) is a commercial biopolymer produced by the Xanthomonas campestris bacterium and available in powdered form. It is a heteropolysaccharide, composed of glucose, mammose and glucuronic acid [47]; it is usually used as a thickening

agent, since when in contact with water it generates viscous hydrogels which promotes an increase in the viscosity [22,30]. XG is active under a wide range of temperature (10°–80°) and pH values (1–13), which promotes its use in agriculture, food and the pharmaceutical industry, cosmetics, drilling lubrication, industrial oils and enhanced oil recovery, among others [22,47].

2.3. Specimen Preparation and Testing

To mitigate the variability usually observed in natural soils, the present work uses remolded samples which maintain the organic matter content, mineralogical composition and grain size distribution composition of the natural soil; but the intrinsic structure of the natural soil is totally destroyed during the remolding process.

The preparation of the soil used for testing started by sifting the natural soil through a 2.36 mm mesh sieve to remove the larger particles and some shell residues. The OM content of a certain amount of "natural" soil (OM = 7.7%) was destroyed by loss-on-ignition at 400 °C, which was then used to prepare the specimens with different OM contents (1.5–5.5%). The specimens of the soils with the different OM contents were prepared in accordance with the following actions (Figure 2):

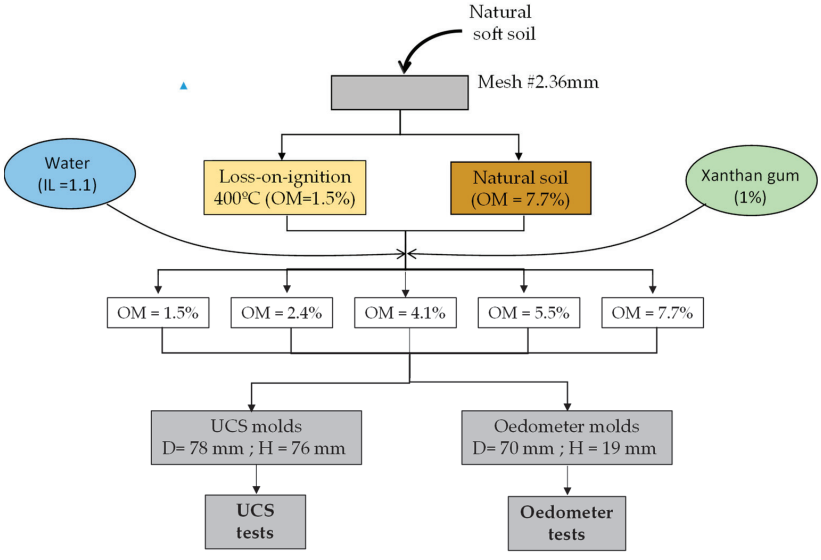

Figure 2. Flow chart of the specimen preparation.

(i) This soil subjected to loss-on-ignition at 400 °C (with an OM content of 1.5%) was mixed with the "natural" soil (OM = 7.7%) in different amounts to obtain the samples of artificial soil with the desired OM content, between 1.5% (lower OM) and 7.7% (natural OM). Naturally, the process of adjustment of the OM content had some iterations, with the re-evaluation and eventual re-adjustment of the OM content;

(ii) In the case of the stabilized samples, an XG content of 1% (ratio of the dry weight of XG to the dry weight of the soil) in powder form was added to the dry artificial soil and mixed well;

(iii) The artificial soil (with the required OM content), with or without XG, was mixed with the distilled water, to obtain a liquidity index of 1.1, during the time necessary to obtain a homogeneous soil-water-XG paste;

(iv) The mixture was introduced into the UCS molds (38 mm in diameter, 76 mm height) and oedometer molds (70 mm in diameter, 19 mm height) in 3 layers and 1 layer, respectively;

(v) Each layer was subjected to tapping (10 times) to remove air bubbles and compacted with 100 kPa for 10 s;

(vi) A superficial scarification of the previous layer was performed to improve the connection between two successive layers in the molds;
(vii) Based on the results of Venda Oliveira and Cabral [29], the stabilized specimens were stored in a plastic bag during 14 days of curing time (only stabilized specimens) inside a room with controlled temperature (20 ± 2 °C) and humidity (95 ± 5%), in order to reduce the suction phenomenon. The unstabilized specimens were not submitted to a curing time;
(viii) After that, the specimens were removed from the molds, both surfaces were trimmed and the quality of the samples was analyzed visually;
(ix) The specimens with the required quality were accepted for testing (UCS and oedometer tests);
(x) The oedometer ring (polished stainless steel) was coated with a thin film of grease prior to the oedometer tests to minimize the friction between it and the soil;
(xi) The oedometer ring was assembled with the specimen, and they were saturated by immersion;
(xii) The displacement transducers (both tests) and the load cell (UCS tests) were set up and adjusted;
(xiii) The UCS and oedometer tests were carried out. The vertical displacement (both tests) and the vertical pressure (UCS test) were recorded by an automatic data acquisition system;
(xiv) A strain controlled test was used in the UCS tests under a strain rate of 1%/min (ASTM2166-05);
(xv) In accordance with ASTM D2435-04, stress increments with a load ratio of 2 were applied in the loading path of the oedometer tests, while in the unloading path a load ratio of 4 was used during the time required to the end of the primary consolidation. The coefficient of consolidation (Cv) was evaluated using Casagrande's methodology.

For each condition tested, the UCS tests were repeated three times and the oedometer tests were duplicated, which ensured the quality and reproducibility of the tests carried out (Table 1). The conformity/compliance criterion used for the UCS tests states that the results must be within the range ±10% of the average value, which is a more demanding requirement than the ±15% specified in the standard EN-206-1 (2007).

Additionally, in order to study the repercussions of the factors studied on the microstructure, SEM images were analyzed.

3. Results and Discussion

3.1. UCS Tests

The stress-strain curves of the UCS tests for the unstabilized and stabilized specimens for the various organic matter contents are compared in Figure 3. Despite some scattering, the results clearly indicate a beneficial impact concerning the stabilization with 1% of XG for an OM content in the range of 1.5–5.5%, manifested by a significant increase in strength and stiffness. On the other hand, for a higher OM content (7.7%), a detrimental consequence of the stabilization with XG was observed, indicated by the decrease in mechanical properties (strength and stiffness). Moreover, for the range of OM content of 1.5–5.5%, the results also show that the stabilization with XG tends to decrease the ductility of the stress-strain behavior; in fact, the stabilized soil shows a peak strength followed by a decrease, while a continuous increase in the strength is seen for the unstabilized soil, which is characteristic of ductile behavior. In contrast, stabilized samples with an OM content of 7.7% show clear ductile stress-strain behavior, both for the unstabilized and stabilized soils.

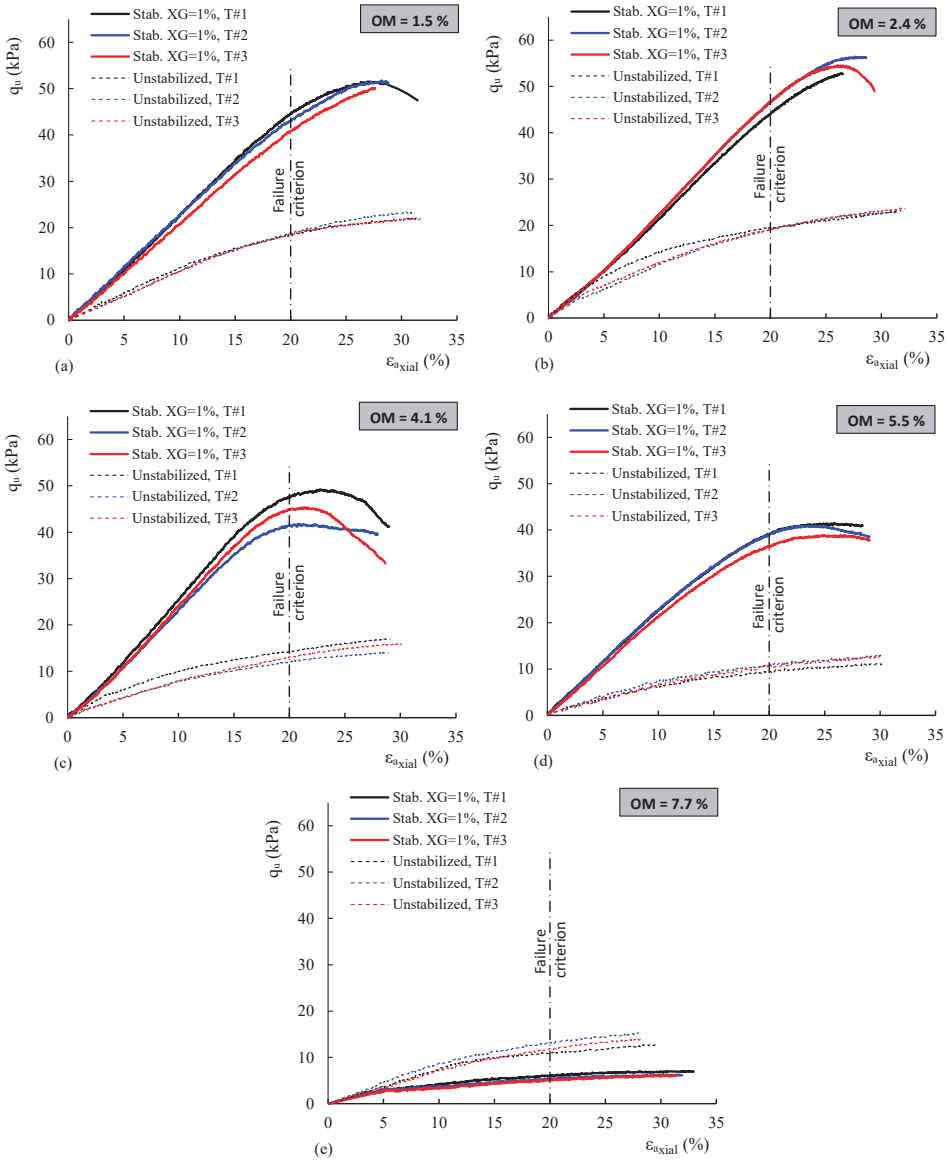

Figure 3. UCS tests. Effect of organic matter content on the stress-strain behavior: (**a**) OM = 1.5%; (**b**) OM = 2.4%; (**c**) OM = 4.1%; (**d**) OM = 5.5%; (**e**) OM = 7.7%.

Considering the ductile stress-strain behavior exhibited by the majority of the samples tested, a failure criterion that corresponds to an axial strain (ε_{ax}) of 20% is used to quantify the unconfined compressive strength (q_u). The evolution of q_u with the OM content, depicted in Figure 4a, highlights the features previously described, namely, a significant increase in the unconfined compressive strength with positive gains between +131% and +270%, for soils with an OM content of 1.5% and 5.5%, respectively. The opposite of this behavior is seen for the soil with an OM content of 7.7%, described by a loss of strength higher than 50% after stabilization with XG.

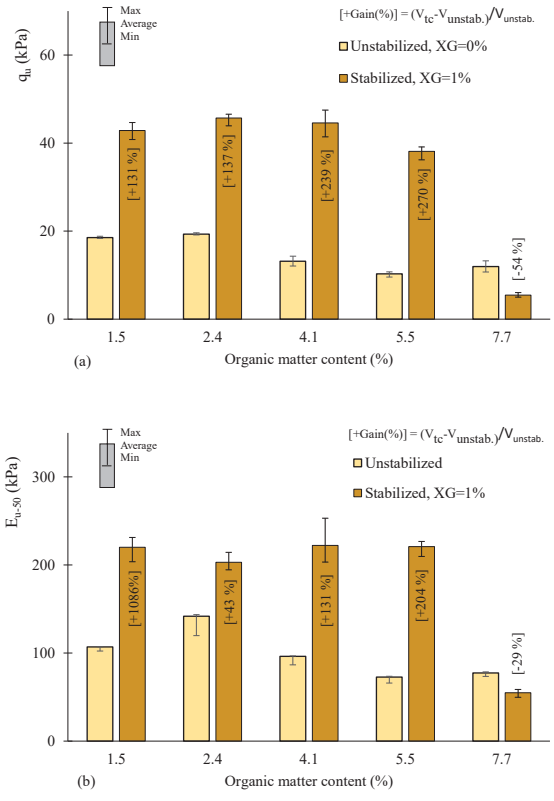

Figure 4. UCS tests. Effect of OM on the evolution of: (**a**) q_u; (**b**) $E_{u\text{-}50}$.

The evolution of the secant modulus at $0.5q_u$ (E_{u50}) with the OM content (Figure 4b) matches with the trend observed in Figure 4a for qu. In fact, the stabilization with XG induced a significant gain of stiffness (from about 109 to 204%) for OM contents in the range of 1.5–5.5%, while for an OM content of 7.7% a reduction of 29% was obtained.

These results indicate that the process of stabilization with XG can be used successfully for soils with a low organic matter content (less than 5.5%), but is counterproductive for higher values of OM content (7.7%). Indeed, after a certain threshold value of OM content (7.7%), the OM that exists in the soil tends to coat the soil particle and partially fill the voids. This prevents the creation of a network of micro-fibers of XG that would create bonds between the soil particles. Simultaneously, the hydration of the biopolymer's hydrogels that exist in the soil's porous spaces seems to promote a reduction in the friction between the soil particles, inducing a decrease in the mechanical properties of the stabilized soil. The SEM image of the stabilized soil with an OM content of 7.7% (Figure 5b) confirms a greater coating of the soil particles with OM than that observed with a stabilized soil with an OM content of 1.5% (Figure 5a). Thus, the increase in the OM content makes it difficult to establish a network of bonds, similar to the micro-reinforcement observed in a stabilized non-organic silty sand (Figure 1).

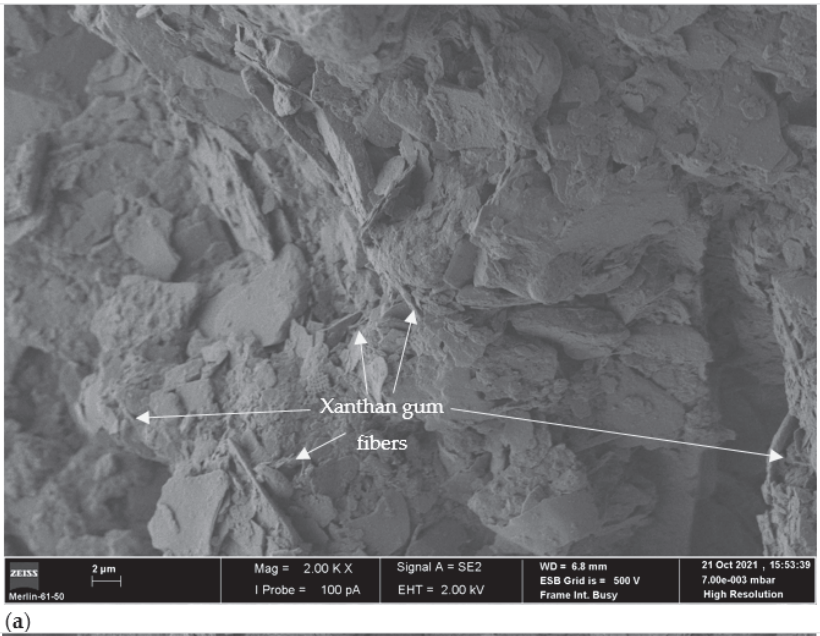

(**a**)

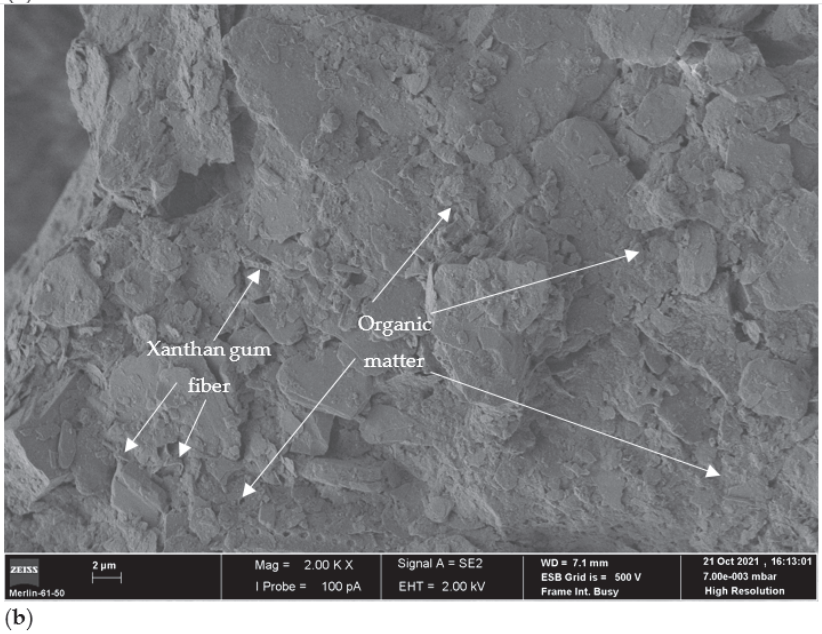

(**b**)

Figure 5. SEM images (2000X) of soil stabilized with 1% of XG for an OM content of: (**a**) 1.5%; (**b**) 7.7%.

3.2. Oedometer Tests

The e-logσ'_v curves obtained from the one-dimensional compression (oedometer) tests for the five different organic matter contents are illustrated in Figure 6. Despite some scattering in terms of the evaluation of the void ratio, in qualitative terms there were some similarities in the curves; mainly:

(i) a progressive increase in the compressibility with the increase in the vertical stress.
(ii) The increase in the void ratio with the OM content, which agrees with the findings of Venda Oliveira et al. [48].
(iii) The upward movement of the e-logσ'v curves after the stabilization with XG due to the hydration of the biopolymer's hydrogels, which induces an increase in the void ratio; this tendency matches with the results of Venda Oliveira et al. [29].

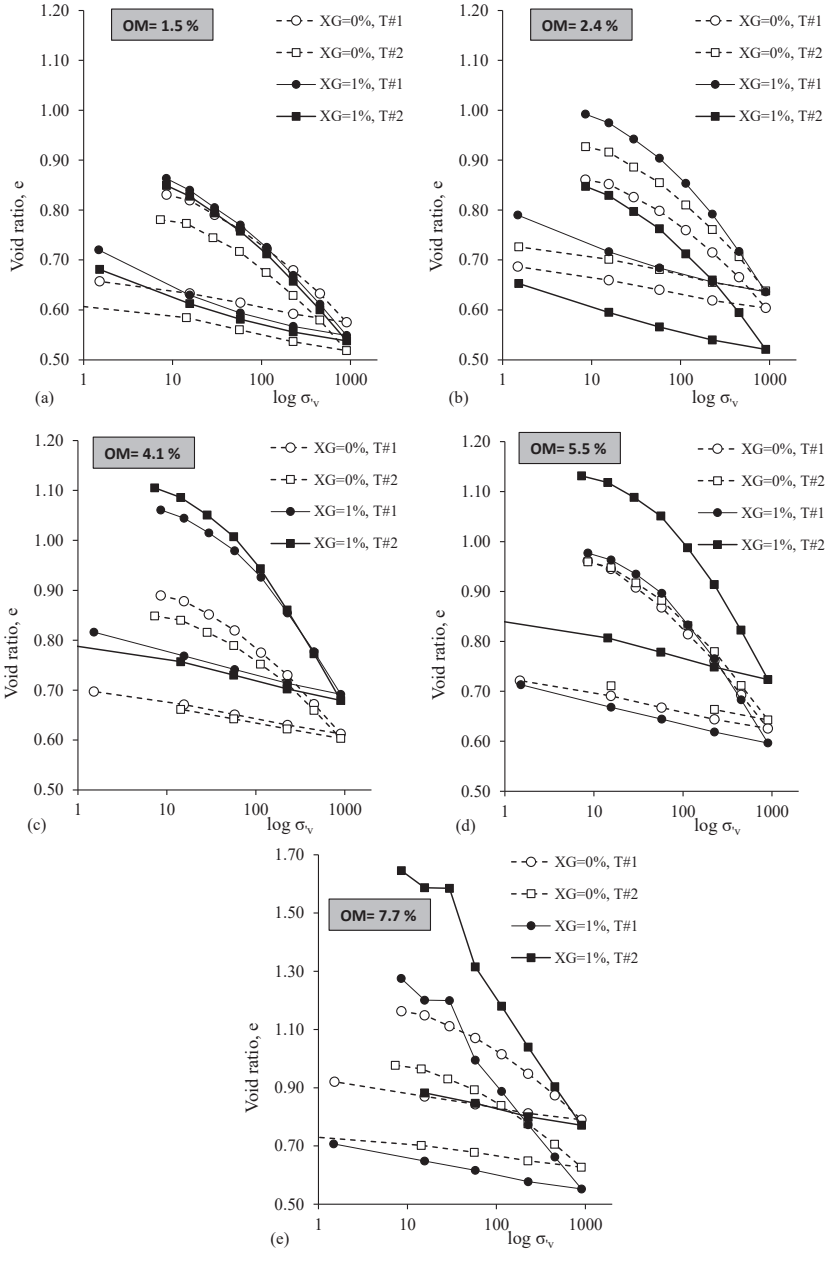

Figure 6. Oedometer tests. Effect of organic matter content on the e-logσ'$_v$ behavior. (**a**) OM = 1.5%; (**b**) OM = 2.4%; (**c**) OM = 4.1%; (**d**) OM = 5.5%; (**e**) OM = 7.7%.

Figure 7 highlights the effect of the OM content on the initial void ratio and on the change in the void ratio during compression ($\Delta e_{compression}$) and swelling ($\Delta e_{swelling}$). These results clearly show the increase in the initial void ratio after the stabilization of the soil with XG, and this effect is enhanced with the increase in the OM content. In fact, this behavior can be explained by two cumulative factors—the high ability of the organic matter to retain water, and the hydration of the hydrogels of the XG when water is present—which together potentiate a high void ratio for a stabilized soil with a high OM content. Figure 7 also demonstrates that the change in the void ratio (both in compression and swelling) increases after stabilization with XG; although, as expected, with a greater variation for the compression paths than for the swelling paths. Additionally, in the compression paths the Δe increases with the OM content, while in the swelling path the Δe is negligible in relation to the change in the OM content. Figure 8 illustrates the effect of the variation in the OM content on the compression index (Cc) and the swelling index (Cs). Naturally, the tendency observed by C_c and C_s corroborates the features described concerning the evolution of $\Delta e_{compression}$ and $\Delta e_{swelling}$ in Figure 7. Indeed, Cc increases after the stabilization of the soil and this effect is amplified for higher OM contents. Moreover, Cs is relatively unaffected by the organic matter content, increasing slightly for the stabilized soil.

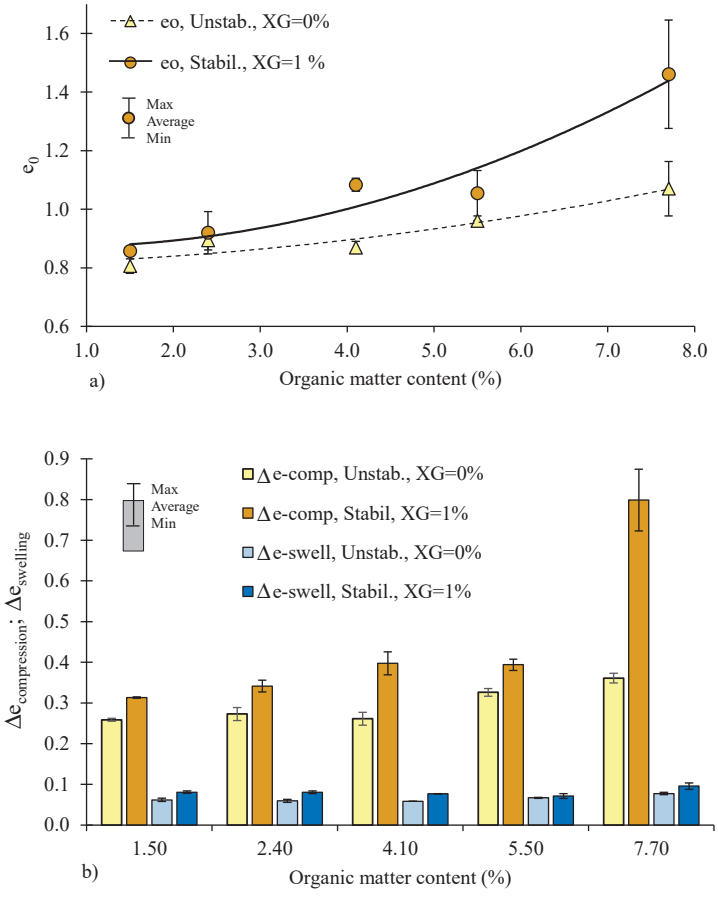

Figure 7. Oedometer tests. Effect of organic matter content on the: (**a**) initial void ratio, (**b**) variation of void ratio during compression (9.0 to 902 kPa) and swelling (902 to 1.5 kPa).

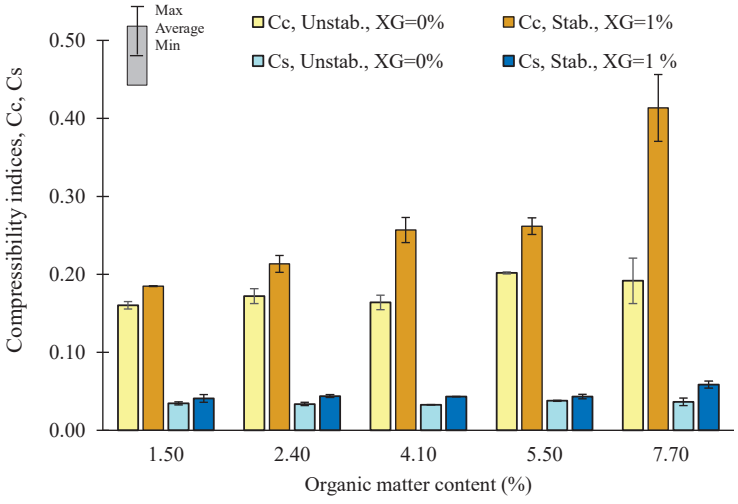

Figure 8. Oedometer tests. Effect of organic matter content on the compressibility indices, Cc and Cs.

The effect of the stabilization process and the variation in the organic matter content on the coefficient of consolidation (Cv) evaluated for the vertical stress increment between 450 and 900 kPa is presented in Figure 9. In line with other research work [39,48,49], the Cv of the unstabilized soil decreases with the increase in OM content, which corresponds to an increase in the primary consolidation time. This behavior is fundamentally due to the significant ability of the OM to absorb water, which induces a higher void ratio and a higher compressibility. On the other hand, the stabilization process induces a significant decrease in the Cv, which is related to the capacity of the biopolymers to retain water, due to the hydration of the hydrogels. This means that the stabilization of a soil with XG prolongs the time required to complete primary consolidation.

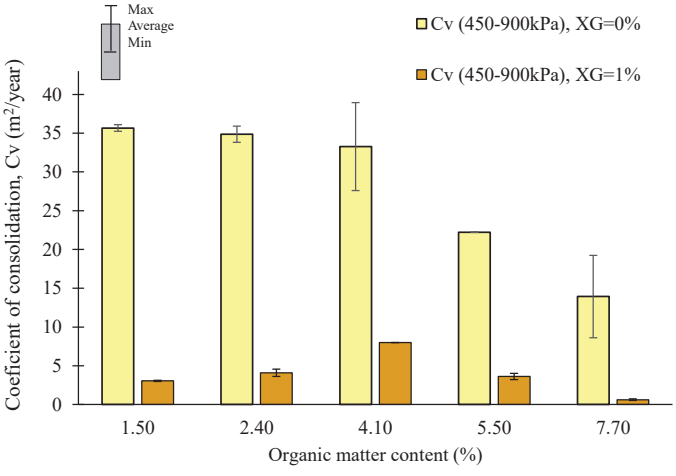

Figure 9. Oedometer tests. Effect of organic matter content on the coefficient of consolidation (Cv) during the increments in compression stress (405 to 900 kPa).

4. Main Conclusions

Considering the experimental results of the unconfined compressive strength (UCS) tests and one-dimensional compression (oedometer) tests concerning the consequences of changes in the organic matter (OM) content (from 1.5% to 7.7%) on the behavior of

unstabilized and stabilized soils with a content of 1% of the biopolymer xanthan gum during 14 days of curing time, the following conclusions were reached:

(i) For an OM content in the range of 1.5–5.5%, there is a positive impact resulting from the stabilization with XG on the mechanical properties, with a significant increase in strength (from 130% to 270%) and stiffness (from 109% to 204%). Moreover, the stabilization with XG induces a decrease in the ductility of the stress-strain behavior characterized by a loss of strength after the peak;
(ii) There is a detrimental impact of the stabilization with XG in terms of mechanical properties for an OM content of 7.7%, while the stress-strain behavior remains ductile. These results seem to indicate that this OM content is sufficient to coat the soil particles, which prevents bonds (i.e., a micro-reinforcement network) being established between the soil particles and the XG, and simultaneously the hydration of the biopolymer hydrogels tends to minimize the friction between the soil particles;
(iii) The stabilization of the soil with XG induces an increase in the initial void ratio; this effect is enhanced by the increase in the OM content, which reflects the effect of two cumulative factors, the ability of the organic matter to retain water, and the hydration of the hydrogels of the XG in the presence of water;
(iv) The stabilization with XG increases the change in the void ratio both in compression (i.e., Cc) and swelling (i.e., Cs), with more significant effects in terms of compression; this behavior is amplified with the increase in the OM content;
(v) In compression, the increase in the OM content induces an increase in the change in the void ratio (i.e., the Cc). The void ratio variation (and the Cs) is negligible for the swelling relative to the change in OM content;
(vi) The coefficient of consolidation (Cv) of the unstabilized soil decreases with the increase in OM content, which is due to the significant ability of the OM to absorb water;
(vii) The stabilization process induces a significant decrease in the Cv, which is related to the considerable capacity of the biopolymers to retain water, due to the hydration of the hydrogels.

Considering the results obtained in this work, it is expected that this technique can be used to improve the properties of the soils with low/medium organic matter content (lower than 5%). Considering that biodegradability is inherent in the use of these bio-based materials, it is expected that this methodology is suitable to apply in provisory works, mainly when a high level of sustainability is required. In this type of work, the biodegradability of the materials used can be a favorable issue, since it annuls all the traces of the work in long term.

Author Contributions: Conceptualization, P.J.V.O.; Investigation: M.J.F.C.C.R.; writing—original draft preparation, M.J.F.C.C.R. and P.J.V.O.; writing—review and editing, P.J.V.O.; supervision, P.J.V.O.; funding acquisition, P.J.V.O. All authors have read and agreed to the published version of the manuscript.

Funding: This work was partly financed by FCT/MCTES (project PTDC/ECI-CON/28382/2017) and through national funds (PIDDAC) under the R&D Unit Institute for Sustainability and Innovation in Structural Engineering (ISISE), under reference UIDB/04029/2020, and under the Associate Laboratory Advanced Production and Intelligent Systems ARISE under reference LA/P/0112/2020.

Institutional Review Board Statement: Not applicable.

Informed Consent Statement: Not applicable.

Data Availability Statement: No new data were created or analyzed in this study. Data sharing is not applicable to this article.

Acknowledgments: This work had the support of the lab technician J.A. Lopes, Department of Civil Engineering, University of Coimbra.

Conflicts of Interest: The authors declare no conflict of interest.

References

1. IPCC. *Climate Change 2022—Mitigation of Climate Change, IPCC AR6 WG III. Working Group III Contribution to the Sixth Assessment Report of the Intergovernmental Panel on Climate Change*; IPCC: Geneva, Switzerland, 2022.
2. Chang, I.; Im, J.; Cho, G.C. Introduction of microbial biopolymers in soil treatment for future environmentally-friendly and sustainable geotechnical engineering. *Sustainability* **2016**, *8*, 251. [CrossRef]
3. Gomes, C.; Lopes, M.L.; Venda Oliveira, P.J. Stiffness parameters of municipal solid waste. *Bull. Eng. Geol. Environ.* **2014**, *73*, 1073–1087. [CrossRef]
4. Nugent, R.; Zhang, G.; Gambrell, R. Effect of exopolymers on the liquid limit of clays and its engineering implications. *Transp. Res. Rec.* **2009**, *2101*, 34–43. [CrossRef]
5. Mendonça, A.; Morais, P.V.; Pires, A.C.; Chung, A.P.; Venda Oliveira, P.J. A Review on the Importance of Microbial Biopolymers Such as Xanthan Gum to Improve Soil Properties. *Appl. Sci.* **2021**, *11*, 170. [CrossRef]
6. Al Qabany, A.; Soga, K. Effect of chemical treatment used in MICP on engineering properties of cemented soils. *Géotechnique* **2013**, *63*, 331–339. [CrossRef]
7. Venda Oliveira, P.J.; Costa, M.S.; Costa, J.N.P.; Nobre, M.F. Comparison of the ability of two bacteria to improve the behaviour of a sandy soil. *J. Mater. Civ. Eng.* **2015**, *27*, 06014025. [CrossRef]
8. Venda Oliveira, P.J.; Freitas, L.D.; Carmona, J.P.S.F. Effect of Soil Type on the Enzymatic Calcium Carbonate Precipitation Process Used for Soil Improvement. *J. Mater. Civ. Eng.* **2016**, *29*, 04016263. [CrossRef]
9. Venda Oliveira, P.J.; Neves, J.P.G. Effect of Organic Matter Content on Enzymatic Biocementation Process Applied to Coarse-Grained Soils. *J. Mater. Civ. Eng.* **2019**, *31*, 04019121. [CrossRef]
10. Venda Oliveira, P.J.; Rosa, J.A.O. Confined and unconfined behaviour of a silty sand improved by the enzymatic biocementation method. *Transp. Geotech.* **2020**, *24*, 100400. [CrossRef]
11. Lin, H.; Suleiman, M.T.; Brown, D.G.; Kavazanjian, E., Jr. Mechanical behaviour of sands treated by microbially induced carbonate precipitation. *J. Geotech. Geoenviron. Eng.* **2016**, *142*, 04015066. [CrossRef]
12. van Paassen, L.A.; Ghose, R.; van der Linden, T.J.M.; van der Star, W.R.L.; van Loosdrecht, M.C.M. Quantifying biomediated ground improvement by ureolysis: Large-scale biogrout experiment. *J. Geotech. Geoenviron. Eng.* **2010**, *136*, 1721–1728. [CrossRef]
13. Mortensen, B.M.; Haber, M.J.; DeJong, J.T.; Caslake, L.F.; Nelson, D.C. Effects of environmental factors on microbial induced calcium carbonate precipitation. *J. Appl. Microbiol.* **2011**, *111*, 338–349. [CrossRef] [PubMed]
14. Yasuhara, H.; Neupane, D.; Hayashi, K.; Okamura, M. Experiments and predictions of physical properties of sand cemented by enzymatically-induced carbonate precipitation. *Soils Found.* **2012**, *52*, 539–549. [CrossRef]
15. Jiang, N.J.; Soga, K. The applicability of microbially induced calcite precipitation (MICP) for internal erosion control in gravel–sand mixtures. *Geotechnique* **2016**, *67*, 42–55. [CrossRef]
16. Carmona, J.P.S.F.; Venda Oliveira, P.J.; Lemos, L.J.L.; Pedro, A.M.G. Improvement of a sandy soil by enzymatic $CaCO_3$ precipitation. *ICE—Geotech. Eng.* **2018**, *171*, 3–15. [CrossRef]
17. Ghasemzadeh, H.; Farzaneh, M. Application of novel Persian gum hydrocolloid in soil stabilization. *Carbohydr. Polym.* **2020**, *246*, 116639. [CrossRef]
18. Babatunde, Q.O.; Byun, Y.-H. Soil Stabilization Using Zein Biopolymer. *Sustainability* **2023**, *15*, 2075. [CrossRef]
19. Muguda, S.; Hughes, P.N.; Augarde, C.E.; Perlot, C.; Walter, B.A.; Gallipoli, D. Cross-linking of biopolymers for stabilizing earthen construction materials. *Build. Res. Inf.* **2022**, *50*, 502–514. [CrossRef]
20. Chang, I.; Prasidhi, A.K.; Im, J.; Shin, H.D.; Cho, G.C. Soil treatment using microbial biopolymers for anti-desertification purposes. *Geoderma* **2015**, *253–254*, 39–47. [CrossRef]
21. Khachatoorian, R.; Petrisor, I.G.; Kwan, C.C.; Yen, T.F. Biopolymer plugging effect: Laboratory-pressurized pumping flow studies. *J. Pet. Sci. Eng.* **2003**, *38*, 13–21. [CrossRef]
22. Bouazza, A.; Gates, W.P.; Ranjith, P.G. Hydraulic conductivity of biopolymer-treated silty sand. *Géotechnique* **2009**, *59*, 71–72. [CrossRef]
23. Cabalar, A.F.; Wiszniewski, M.; Skutnik, Z. Effects of Xanthan Gum Biopolymer on the Permeability, Odometer, Unconfined Compressive and Triaxial Shear Behaviour of a Sand. *Soil Mech. Found. Eng.* **2017**, *54*, 356–361. [CrossRef]
24. Dehghan, H.; Tabarsa, A.; Latifi, N.; Bagheri, Y. Use of Xanthan and guar gums in soil strengthening. *Clean Technol. Environ. Policy* **2019**, *21*, 155–165. [CrossRef]
25. Mendonça, A.; Morais, P.V.; Pires, A.C.; Chung, A.P.; Venda Oliveira, P.J. Reducing Soil Permeability Using Bacteria-Produced Biopolymer. *Appl. Sci.* **2021**, *11*, 7278. [CrossRef]
26. Sujatha, E.R.; Atchaya, S.; Sivasaran, A.; Keerdthe, R.S. Enhancing the geotechnical properties of soil using xanthan gum—An eco-friendly alternative to traditional stabilizers. *Bull. Eng. Geol. Environ.* **2021**, *80*, 1157–1167. [CrossRef]
27. Chang, I.; Im, J.; Prasidhi, A.K.; Cho, G.C. Effects of Xanthan gum biopolymer on soil strengthening. *Constr. Build. Mater.* **2015**, *74*, 65–72. [CrossRef]
28. Lee, S.; Chung, M.; Park, H.M.; Song, K.-I.; Chang, I. Xanthan gum Biopolymer as Soil-Stabilization Binder for Road Construction Using Local Soil in Sri Lanka. *J. Mater. Civ. Eng.* **2019**, *31*, 06019012. [CrossRef]
29. Venda Oliveira, P.J.; Cabral, D.J.R. Behaviour of a silty sand stabilized with xanthan gum under unconfined and confined conditions. *ICE—Ground Improv.* **2023**, *176*, 3–13. [CrossRef]

30. Kwon, Y.-M.; Chang, I.; Lee, M.; Cho, G.C. Geotechnical engineering behaviour of biopolymer-treated soft marine soil. *Geomech. Eng.* **2019**, *17*, 453–464. [CrossRef]
31. Latifi, N.; Horpibulsuk, S.; Meehan, C.L.; Abd Majid, M.Z.; Tahir, M.M.; Mohamad, E.T. Improvement of problematic soils with biopolymer-an environmentally friendly soil stabilizer. *J. Mater. Civ. Eng.* **2017**, *29*, 04016204. [CrossRef]
32. Chang, I.; Kwon, Y.-M.; Im, J.; Gye-Chun Cho, G.C. Soil consistency and interparticle characteristics of Xanthan gum biopolymer–containing soils with pore-fluid variation. *Can. Geotech. J.* **2019**, *56*, 1206–1213. [CrossRef]
33. Chang, I.; Jeon, M.; Cho, G.C. Application of microbial biopolymers as an alternative construction binder for earth buildings in underdeveloped countries. *Int. J. Polym. Sci.* **2015**, *2015*, 326745. [CrossRef]
34. Sulaiman, H.; Taha, M.R.; Rahman, N.A.; Taib, A.M. Performance of soil stabilized with biopolymer materials—Xanthan gum and guar gum. *Phys. Chem. Earth* **2022**, *128*, 103276. [CrossRef]
35. Kwon, Y.-M.; Chang, I.; Cho, G.-C. Consolidation and swelling behavior of kaolinite clay containing xanthan gum biopolymer. *Acta Geotech.* **2023**, 1–17. [CrossRef]
36. Hamza, M.; Nie, Z.; Aziz, M.; Ijaz, N.; Akram, O.; Fang, C.; Ghani, M.U.; Ijaz, Z.; Noshin, S.; Madni, M.F. Geotechnical behavior of high-plastic clays treated with biopolymer: Macro–micro-study. *Environ. Earth Sci.* **2023**, *82*, 91. [CrossRef]
37. Reddy, J.J.; Varaprasad, B.J.S. Long-term and durability properties of xanthan gum treated dispersive soils—An eco-friendly material. *Mater. Today Proc.* **2021**, *44*, 309–314. [CrossRef]
38. Chang, I.; Kwon, Y.-M.; Cho, G.-C. Effect of Pore–Fluid Chemistry on the Undrained Shear Strength of Xanthan Gum Biopolymer-Treated Clays. *J. Geotech. Geoenviron. Eng.* **2021**, *147*, 06021013. [CrossRef]
39. Venda Oliveira, P.J.; Correia, A.A.S.; Garcia, M.R. Effect of organic matter content and curing conditions on the creep behaviour of an artificially stabilized soil. *J. Mater. Civ. Eng.* **2012**, *24*, 868–875. [CrossRef]
40. Correia, A.A.S. Applicability of Deep Mixing Technique to Portuguese Soft Soils. Ph.D. Thesis, University of Coimbra, Coimbra, Portugal, 2011. (In Portuguese)
41. Vieira, A.F.V. Effect of Organic Matter Content on the Creep Reduction by Preloading: Laboratorial Analysis. Master's Thesis, University of Coimbra, Coimbra, Portugal, 2016. (In Portuguese)
42. Reis, M.J.F.C.C. Effect of Organic Matter Content on the Behaviour of Soils Stabilized with the Biopolymer Xanthan Gum. Master's Thesis, University of Coimbra, Coimbra, Portugal, 2021. (In Portuguese)
43. Venda Oliveira, P.J.; Correia, A.A.S.; Garcia, M.R. Effect of stress level and binder composition on secondary compression of an artificially stabilized soil. *J. Geotech. Geoenviron. Eng.* **2013**, *139*, 810–820. [CrossRef]
44. Bennett, R.H.; Lehman, L.; Hulbert, M.H.; Harvey, G.R.; Bush, S.A.; Forde, E.B.; Crews, P.; Sawyer, W.B. Interrelationship of organic carbon and submarine sediment geotechnical properties. *Mar. Geotechnol.* **1985**, *6*, 61–98. [CrossRef]
45. Booth, J.S.; Dahl, A.G. A note on the relationships between organic matter and some geotechnical properties of marine sediment. *Mar. Geotechnol.* **1986**, *6*, 281–297. [CrossRef]
46. Coelho, P.A.L.F. Geotechnical Characterization of Soft Soils. Study of the Experimental Site of Quinta do Foja. Master's Thesis, University of Coimbra, Coimbra, Portugal, 2000. (In Portuguese)
47. García-Ochoa, F.; Santos, V.E.; Casas, J.A.; Gómez, E. Xanthan gum: Production, recovery, and properties. *Biotechnol. Adv.* **2000**, *18*, 549–579. [CrossRef] [PubMed]
48. Venda Oliveira, P.J.; Vieira, A.F.V.; Correia, A.A.S. Effect of organic matter content on creep mitigation by preloading. *ICE—Geotech. Eng.* **2017**, *170*, 305–311. [CrossRef]
49. Thiyyakkandi, S.; Annex, S. Effect of organic content on geotechnical properties of Kuttanad clay. *Electron. J. Geotech. Eng.* **2011**, *16*, 1653–1663.

applied sciences

MDPI

Article

Stabilisation of Soft Clay, Quick Clay and Peat by Industrial By-Products and Biochars

Solve Hov [1,2,*], Priscilla Paniagua [1,2], Christian Sætre [3,4], Mike Long [5], Gerard Cornelissen [6,7] and Stefan Ritter [8]

[1] Geotechnics and Natural Hazards, Norwegian Geotechnical Institute, 7034 Trondheim, Norway; priscilla.paniagua@ngi.no
[2] Department of Civil and Environmental Engineering, Norwegian University of Technology and Science, 7491 Trondheim, Norway
[3] Environment and Rock Engineering, Norwegian Geotechnical Institute, 7034 Trondheim, Norway; christian.setre@ngi.no
[4] Department of Geosciences, University of Oslo, 0313 Oslo, Norway
[5] School of Civil Engineering, University College Dublin, D04 V1W8 Dublin, Ireland; mike.long@ucd.ie
[6] Sustainable Geosolutions, Norwegian Geotechnical Institute, 0484 Oslo, Norway; gerard.cornelissen@ngi.no
[7] Faculty of Environmental Science and Natural Resources, Norwegian University of Life Sciences, 1433 Ås, Norway
[8] Onshore Foundations, Norwegian Geotechnical Institute, 0484 Oslo, Norway; stefan.ritter@ngi.no
* Correspondence: solve.hov@ngi.no; Tel.: +47-458-46-968

Abstract: The stabilisation of soft soils using the traditional binders cement and quicklime are known to emit large amounts of carbon dioxide. To reduce this carbon footprint, substitutes such as industrial by-products have been thoroughly tested as viable alternatives for soil stabilisation. However, recent research has also shown that biochar from biomass pyrolysis can in some instances have a positive stabilisation effect and even result in a carbon-negative footprint. This paper presents a laboratory study to investigate the stabilisation effect of five industrial by-products and four types of biochar on three natural Norwegian soils: two clays with low and high water contents and one peat with a very high water content. The soils and binders were characterised by their mineralogical and chemical compositions. The biochars had varying stabilisation effects on the clays when combined with cement, with some negative stabilisation effects, whilst the effect was very beneficial in the peat, with a strength increase of up to 80%. The industrial by-products showed opposite results, with beneficial effects in the clays and a strength increase of up to 150%, but negative stabilisation effects in the peat. Correlating the mineralogical and chemical compositions to stabilisation effects was found to be challenging.

Keywords: soil stabilisation; clay; peat; industrial by-products; biochar; shear strength; stiffness

Citation: Hov, S.; Paniagua, P.; Sætre, C.; Long, M.; Cornelissen, G.; Ritter, S. Stabilisation of Soft Clay, Quick Clay and Peat by Industrial By-Products and Biochars. *Appl. Sci.* **2023**, *13*, 9048. https://doi.org/10.3390/app13169048

Academic Editors: Paulo José da Venda Oliveira and António Alberto Santos Correia

Received: 15 June 2023
Revised: 18 July 2023
Accepted: 25 July 2023
Published: 8 August 2023

1. Introduction

Soil stabilisation is used extensively throughout the world to improve soil characteristics. One application of soil stabilisation involves the improvement of engineering properties of thick soft soil deposits, typically referred to as deep soil stabilisation or deep mixing, to enable the development and construction of buildings, roads, railways and other land use. Deep soil stabilisation is performed by mixing a binder into the soil, whereupon chemical reactions strengthen the soil matrix. Traditionally, cement (CEM) and quicklime (QL) have been the preferred binders. However, their production is well known to emit considerable amounts of carbon dioxide (CO_2). Globally, cement production alone contributes to approximately 8% of global anthropogenic CO_2 emissions [1,2]. To the best of the authors' knowledge, there is no estimation of the total CO_2 emissions generated from the deep soil stabilisation of soft soil deposits. However, it is safe to assume that it is considerable.

There are major research efforts being made across the world to decrease CO_2 emissions in the soil stabilisation industry as well as in the cement and concrete industries. One way of achieving this is to substitute CEM and QL with alternative binder types and, since society is creating large amounts of unused industrial by-products (IBPs), these could be a potential substitute. IBPs often come in the form of ashes from the combustion of the original waste product. In the soil stabilisation industry, research and testing on a laboratory scale have been conducted using a wide variety of IBPs, e.g., cement kiln dust [3–5], lime kiln dust [6,7], fly ash [8–10], bottom ash [11], gypsum [12,13], ground-granulated blast-furnace slag (GGBS) [14–18] and ladle slag [12]. In addition, other binders or additives have been studied, such as biopolymers [19,20], geopolymers [21], fibres [22], reactive magnesia [5], colloidal silica [23] and natural or synthetic zeolites [24,25]. These studies have illustrated the potential to reduce emissions when using IBPs. However, despite all the research efforts, it is difficult to establish a common framework for their stabilisation effect. This might be attributed to the fact that IBPs can differ considerably in their composition and to the high variability of soils in terms of, e.g., grain size distribution, mineralogical composition, water content, organic content, etc. It is, therefore, vital that studies on the stabilisation effect of different IBPs in different countries and regions continue to be performed.

Recently, there has also been increased interest and research on the use of biochar as an alternative binder. Biochar is manufactured by the pyrolysis of biomass, i.e., combustion in an inert atmosphere (i.e., the absence of oxygen), resulting in a non-biodegradable carbonaceous material with typical carbon contents exceeding 75%. It is characterised by a high porosity and large surface area and, hence, a high water-absorption capacity [26,27], and has several potential benefits, including soil fertility improvement and contaminant immobilisation [28]. Recent studies have also shown that biochar in mixtures with cement can have a positive stabilisation effect in soils [27,29–39], meaning that it can be used as an alternative binder along with its carbon sequestration potential. Since 1.0 kg of biochar contains a minimum of approximately 0.75 kg of carbon (C), it can sequester over ~2.7 kg of CO_2eq as no decomposition or erosion takes place in low permeable thick clay deposits. This amount of sequestered carbon is substantial, considering that corresponding CO_2eq emissions for CEM and QL, as examples, are approximately 0.65 kg and 1.0 kg CO_2eq, respectively, per kg binder [6]. To make a CEM-biochar-based binder climate neutral, i.e., resulting in net zero CO_2eq emissions, one thus needs only to replace approximately 20–30% of the CEM with biochar.

This paper presents results from a laboratory study where five different IBPs and four different biochars were used to stabilise three soft Norwegian soils: a soft, low-sensitive clay from Onsøy [40], located in southern Norway; a quick clay; and a peat, both from Tiller-Flotten [41,42], located in mid-Norway. All binders and soils were characterised by their composition and mineralogy, and the potential for soil stabilisation was investigated by strength and stiffness testing.

The purpose of this study was to investigate if and how the stabilisation effects of the IBPs and biochars differed for the different soil types and whether the stabilisation effect could be correlated to the binder and soil compositions. As few studies compare several types of IBPs and biochars in both clay and peat, the results presented herein give new insights into how their effectiveness can vary. This study shows that the differences can be considerable and highlights the importance of taking both the type of binder and the type of soil into consideration. It is believed that the results can also provide valuable guidance for further testing.

2. Materials and Methods

2.1. Natural Soils

The soft, low-sensitive Onsøy clay was sampled from the Norwegian GeoTest Site (NGTS) located outside of the city of Fredrikstad in southern Norway [40]. The sample depth was approximately 5–8 m. The clay had a bulk density (ρ_b) of 1.5–1.6 t/m^3, natural

water content (w) of 60–80%, sensitivity of 5–9, organic content of 3–4%, plasticity index (I_p) of 40–50%, and liquidity index (I_L) of approximately 0.9–1.0. The clay content was approximately 60–70%, the remaining being predominantly quartz silt grains.

The Tiller-Flotten quick clay was sampled from a depth of 9–13 m at the NGTS test site outside of Trondheim, mid-Norway [41]. The quick clay had a ρ_b of 1.75–1.85 t/m^3, w of 40–45%, sensitivity of 150–250, organic content of <1%, I_p of approximately 10–15%, and I_L of approximately 1.5–2.0. The clay content was similar to that of Onsøy, with the remaining being mostly quartz silt grains.

The peat was sampled from a depth of 1–1.5 m at the NGTS site at Tiller-Flotten [41,42]. The peat had a w of approximately 800–1000% and a ρ_b close to 1.0 t/m^3. The degree of humification according to the von Post classification [43] was determined at H2–H3, i.e., a very low degree of humification with insignificant or very slight decomposition with an identifiable plant structure. The sampling depth was approximately 1.5 m.

2.2. Binders

A Portland cement of type CEM I 52.5 R (EN 197-1 [44]), produced by Norcem at Brevik, near Porsgrunn, Norway, was used. The CEM I cement was chosen to avoid any content of fly ash or slag that could interact with the biochars and IBPs.

Four different types of biochars (BCs) were used, all produced in a full-scale microwave-assisted pyrolysis (MAP) unit with a residence time of ~20 min. The reactor temperature was approximately 470–600 °C. The four biochars were as follows:

- BC1: originated from demolition wood, i.e., wood panels, furniture and composite wood materials, which hence contained some metals and glue remains.
- BC2: originated from municipal sewage which had been sedimented to a bottom sludge and thereafter left to decay for some time. Approximately 39 wt.% of limestone ($CaCO_3$) was added for hygenisation and workability before the sludge was used for biochar production.
- BC3: originated from sewage and food waste. To speed up the sedimentation, iron chloride ($FeCl_3$) was added for flocculation. The bottom sludge was used to produce the biochar.
- BC4: originated from garden waste, i.e., branches, leaves and grass, but also contained some soil and sand.

The five types of IBPs included two types of bioashes, one paper-sludge ash and two ladle slags:

- The bioashes were one fly ash (FA) and one bottom ash (BA) obtained from the Bergene Holm's combustion plant at Brandval, near Kongsvinger, Norway. This plant is a grate-fire combustion plant where the boiler temperature is 1000–1200 °C. The resulting fly and bottom ash account for approximately 10% and 90%, respectively, of the total ash generated. The biomass consisted of a mixture of ~35–40% dry wood chips and ~60–65% bark. Bioash is mostly used for agricultural purposes [45]; however, a few studies have also been made on soil stabilisation [46–51].
- One type of paper-sludge ash (PSA) was used, originating from the Norske Skog factory at Skogn, mid-Norway, where paper production and recycling is performed. A mixture of ~58% biofuel (demolition wood), ~25% deinked pulp sludge, ~14% bio sludge and ~3% plastic/juice cartons, etc., was combusted at a temperature of approximately 850 °C. In this study, fly ash from the combustion was used. PSA has been used as an alternative binder in both mortars and concrete [52–54] and in soil stabilisation [55–61].
- The two ladle slags originated from Celsa Steel Services, where the recycling of steel is carried out to produce reinforcement steel bars. Both electric arc furnace slag and steelmaking slag are generated from different stages of the melting process. The ladle slags used herein were a mixture of these slags and were extracted from two different locations: at the melt shop (LS1), i.e., a fresh ladle slag, and from an intermediate repository (LS2). Since LS is cooled rather slowly, it develops a high crystallinity and

thus possesses relatively low hydraulic reactivity compared to GGBS [62]. LS can be alkali-activated using, e.g., sodium hydroxide, sodium silicate ('waterglass'), QL, CEM or reactive magnesia [63–65], albeit somewhat less effectively than GGBS [65,66]. LS has also been used for research purposes in soil stabilisation [12,67–71].

All biochars and IBPs were ground and sieved to a <1 mm fraction and dried before being used for soil stabilisation. Figure 1 shows the IBPs and an example of one biochar.

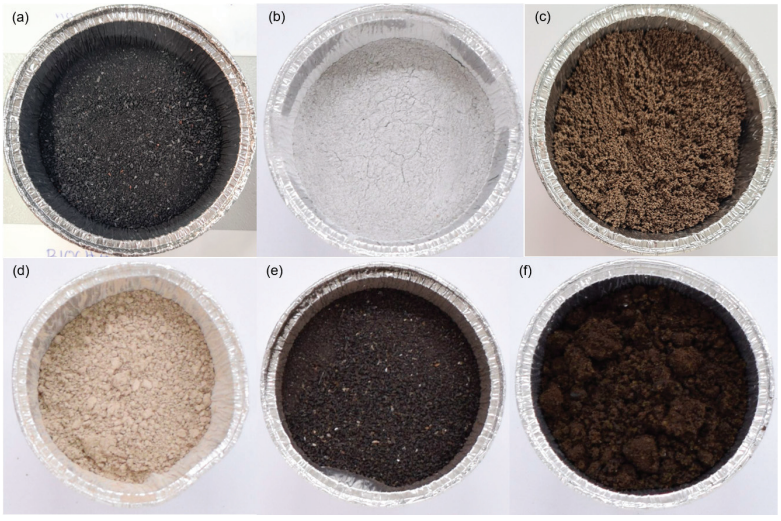

Figure 1. Photographs of selected biochars and IBPs: (**a**) biochar (BC3), (**b**) ladle slag (LS1), (**c**) ladle slag (LS2), (**d**) paper sludge ash (PSA), (**e**) bioash (BA) and (**f**) bioash (FA).

2.3. Microstructural and Compositional Analyses

Water contents (w) and particle densities (ρ_s) were determined according to ISO 17892-1 and -3, respectively. The ρ_s was determined using the fluid pycnometer with moist specimens. Two separate determinations were made and an average value was calculated if the difference was <0.03 t/m^3. These analyses were performed at the geotechnical laboratory at the Norwegian Geotechnical Institute (NGI).

Specific surface area (SFA) determinations were made by the adsorption of gas and calculated according to the Brunauer–Emmett–Teller (BET) theory [72]. The SFA analyses were performed by Nemko Norlab in Norway.

Thermogravimetric analyses (TGA) were performed on samples dried at 105 °C prior to analyses which were then, from room temperature, exposed to a temperature increase rate of 10 °C/min in a nitrogen atmosphere [73,74]. The TGA was performed at SINTEF in Norway.

X-ray fluorescence (XRF) analyses of major elements were performed using a PANalytical Axios 4 kW equipped with a rhodium X-ray tube on fused glass beads. The material was mixed with a lithium borate flux and heated to 1000 °C. X-ray diffraction (XRD) analyses were made on whole rock, i.e., not sieved, and were hand-mortared prior to the analyses. The analyses were made with a BRUKER D8 Advance using CuKα radiation (40 kV/40 mA). Scans were acquired on a rotating disk using 2.5° Soller slits and a fixed divergence slit (0.6 mm) in the range of 3 to 75° 2Θ with a step size of 0.02° 2Θ and a 1 s count time. Mineral identifications were performed using the BRUKER Diffrac.EVA ver. 5.2 software, Crystallographic Open Database (COD) and International Centre for Diffraction Data (ICDD) databases. Mineral quantification was conducted using Rietveld modelling with the TOPAS 5.0 software. The XRF and XRD analyses were performed by X-ray Mineral Services, UK.

2.4. Geotechnical Testing

The preparation of stabilised soil specimens was performed by first remoulding the natural clays and peat until they were visually considered homogeneous, whereupon the dry binder mixture was added and homogenised for ~3–5 min. The soil–binder mixtures were then moulded in plastic cylinders (diameter 54 mm; height 100 mm) using a rodding technique, i.e., tamping or pushing a rod onto the material to minimise the air content [75,76]. Three replicate samples from each mixture were produced and cured for 28 days in the sealed cylinders at a room temperature of approximately 20 °C [77]. Unconfined compression (UC) tests were then performed with a strain rate of ~3.7%/min. From the UC tests, the strength was interpreted as the maximum shear stress (τ_{max}), which is typically used in Nordic practice instead of the unconfined compressive strength ($\tau_{max} = UCS/2$). Stiffness was interpreted as secant Young's modulus (E_{50}) up to 50% of the peak stress.

Table 1 shows the complete laboratory strength testing programme. Based on the results from previous research [27,29,46], different binder quantities (α) and combinations were used for the clays and peat and for the IBPs and biochars. For the clays stabilised with IBPs, mixtures of 50 wt.% CEM and 50 wt.% IBP were used, with a total α of 60 kg/m^3. For comparison, specimens with 100% CEM were also prepared with α of 30 and 60 kg/m^3. For clays and biochar (BC), mixtures of 33 wt.% CEM and 67 wt.% BC were prepared with α of 150 kg/m^3, i.e., 50 kg/m^3 of CEM and 100 kg/m^3 of BC. For comparison, specimens with 100% CEM with α of 50 kg/m^3 were prepared.

Table 1. Laboratory strength testing programme. Mixtures were designated by binder quantity of CEM and binder quantity of biochar or IBP. For example, CEM-30/BC4-30 denotes a mixture of 30 kg of CEM and 30 kg of BC4 per m^3 of natural soil, i.e., a total binder quantity of 60 kg/m^3. For all mixtures, three replicate specimens were prepared.

Binder		Onsøy Clay	Tiller-Flotten Clay	Peat
Cement	CEM I	CEM-30 CEM-50 CEM-60	CEM-30 CEM-50 CEM-60	CEM-100
Sludge	PSA	CEM-30/PSA-30	CEM-30/PSA-30	CEM-100/PSA-200
Bioash	FA	CEM-30/FA-30	CEM-30/FA-30	CEM-100/FA-200
	BA	CEM-30/BA-30	CEM-30/BA-30	CEM-100/BA-200
Ladle slag	LS1	CEM-30/LS1-30	CEM-30/LS1-30	CEM-100/LS1-200
	LS2	CEM-30/LS2-30	CEM-30/LS2-30	CEM-100/LS2-200
Biochar	BC1	CEM-50/BC1-100	CEM-50/BC1-100	CEM-100/BC1-200
	BC2	CEM-50/BC2-100	CEM-50/BC2-100	CEM-100/BC2-200
	BC3	CEM-50/BC3-100	CEM-50/BC3-100	CEM-100/BC3-200
	BC4	CEM-50/BC4-100	CEM-50/BC4-100	CEM-100/BC4-200

For the peat specimens, all mixtures were prepared with 33 wt.% CEM and 67 wt.% IBP or BC with a total α of 300 kg/m^3. Again, for comparison, specimens with 100% CEM with α of 100 kg/m^3 were prepared.

To further investigate the stabilisation effect of the IBPs and biochars, testing according to the 'strength activity index' (SAI) [78] was performed, although not using the same recipe and geometry as specified in the ASTM standard due to available laboratory equipment. Specimens with mixtures of 12.5 wt.% water, 25 wt.% dry binder and 62.5 wt.% clean quartz sand were manufactured. One reference specimen with 100% CEM was prepared, followed by mixtures where 20% of the CEM was replaced with the respective IBP and biochar. Thus, in total, 10 mixtures were prepared, all moulded in cylinders (diameter 54 mm; height 100 mm) and cured for 14 days before being subjected to UC tests.

3. Results

3.1. The Characterisation of Natural Soils and Binders

Results from the w, ρ_s and SFA determinations are shown in Table 2. The w of the Tiller-Flotten quick clay (42%) was lower than that of the Onsøy clay (73%); however, the SFA was similar for both clays. The IBPs and biochars exhibited a large variation in w, although all were dried prior to being mixed with the natural soils. The PSA, BA, LS1 and BC2 had a $w \approx 0\%$ (Table 2). The biochars had varying w, ρ_s and SFA. The high SFA of the biochars BC1, BC2 and BC3 was expected [26,27].

Table 2. Results of water content, particle density and specific surface area (SFA) determinations. Note that the water contents for the IBPs and biochars were determined after receiving the binders in the laboratory. Before mixing with the soil, all IBPs and biochars were dried.

Material		Water Content [%]	Particle Density [t/m^3]	SFA [m^2/g]
Natural soils	Tiller-Flotten quick clay	42	2.85	23.26
	Tiller-Flotten peat	886	~1.45	1.28
	Onsøy clay	73	2.7	25.24
Cement	CEM I	~0	2.55	1.54
Sludge	PSA	~0	2.68	3.9
Bioash	FA	42.5	2.85	3.0
	BA	~0	2.69	0.5
Ladle slag	LS1	~0	3.02	0.8
	LS2	19.8	2.99	11.0
Biochar	BC1	98.4	1.61	38.5
	BC2	~0	2.44	54.8
	BC3	35.5	2.34	51.3
	BC4	85.3	1.67	5.3

The results of the compositional (XRF) and phase (XRD) analyses are shown in Tables 3–5. In general, the compositions were similar to those of previously published results. For example, the two ladle slags had high contents of SiO_2 and CaO [65,79]. The PSA also showed similar compositions as those reported in the literature, albeit with somewhat lower CaO contents [53]. The BC2 was particularly high in CaO because of the addition of limestone to the sludge prior to pyrolysis. Similarly, the BC3 contained a high amount of Fe_2O_3 because of the addition of iron chloride in the sedimentation process. This also resulted in higher particle densities compared to BC1 and BC4 (Table 2).

Bassanite ($Ca(SO_4) \bullet 0.5H_2O$) was identified in the CEM I sample at a concentration of 7.2% (Table 5). Bassanite was unexpected, but the chemical composition favoured the phase with sulphur and calcium at reasonable levels (Table 3). It was expected to find C_3A ($3CaO \bullet Al_2O_3$), a common constituent in cement, but no compelling evidence was present in the diffractograms. The high amorphous content (Table 5) made it difficult to argue for an aluminium-containing phase (C_2A) instead of a calcium–sulphate phase.

Results from the TGA for the natural soils are plotted in Figure 2, together with their respective derivative differential thermogravimetry (DTG) values. The clays displayed DTG peaks at approximately 480 °C for the Onsøy clay and 590 °C and 670 °C for the Tiller-Flotten clay, corresponding to the dehydroxylation of clay minerals such as illite and chlorite. The Tiller-Flotten clay also contained 2.1% calcite (Table 4), which was most likely reflected by the peak at approximately 590 °C. The TGA on peat naturally exhibited a high weight loss due to the high organic content, as could also be observed concerning the high LOI and amorphous contents in the XRF and XRD analyses, respectively. Overall, the results agree with both XRF and XRD as well as previous studies [40,41].

Table 3. Results of major element X-ray fluorescence analyses (XRF). All values in per cent. ND = not determined as abundance was below the detection limit.

Material		Al_2O_3	SiO_2	CaO	MgO	SO_3	K_2O	Fe_2O_3	Na_2O	LOI
Natural soils	Tiller-Flotten quick clay	16.97	51.04	3.22	5.86	0.02	4.05	9.28	2.01	5.6
	Tiller-Flotten peat	1.17	1.28	0.24	0.23	<0.01	0.10	0.38	0.03	96.4
	Onsøy clay	17.55	53.18	1.00	3.38	0.02	4.79	8.38	2.35	7.5
Cement	CEM I	4.58	18.79	61.05	2.40	3.94	0.87	3.30	0,34	2.6
Sludge	PSA	6.8	18.1	42.8	2.8	6.3	0.5	3.5	ND	16.3
Bioash	FA	2.2	4.3	36.5	3.9	2.2	7.4	0.4	ND	35.2
	BA	3.4	10.9	57.2	4.8	1.2	3.5	1.3	ND	8.0
Ladle slag	LS1	6.6	33.2	47.1	7.1	3.2	ND	1.8	ND	0.0
	LS2	6.9	25.5	43.7	7.5	1.7	ND	3.2	ND	9.7
Biochar	BC1	1.3	3.2	3.2	ND	0.7	0.5	0.8	ND	87.1
	BC2	8.2	9.5	32.8	0.8	2.2	0.3	6.3	ND	32.2
	BC3	10.1	16.5	4.1	0.4	2.8	0.7	24.9	ND	32.4
	BC4	2.9	12.2	4.7	0.4	0.5	1.1	2.3	ND	74.5

Table 4. Results of whole rock X-ray diffraction analyses (XRD) of natural soils, showing clay minerals in crystalline phase and amorphous phase separately. All values in per cent.

Material		Illite + Mica	Chlorite	Quartz	K-Feldspar	Plagioclase	Amphibole	Calcite	Others [1]	Amorphous
Natural soils	Tiller-Flotten quick clay	30.5	14.3	13.2	5.6	17.7	7.3	2.1	-	9.3
	Tiller-Flotten peat	1.2	-	0.3	-	-	-	-	-	98.6
	Onsøy clay	30.2	10.9	14.3	5.3	11.6	2.5	-	0.7	24.6

[1] Onsøy clay: halite (0.6%) and pyrite (0.1%).

Table 5. Results of X-ray diffraction analyses (XRD) of cement and industrial by-products, showing minerals in crystalline phase and amorphous separately. All values in per cent.

Material		C_2S [2]	C_3S [3]	C_4AF [4]	Calcite	Portlandite	Quartz	Merwinite	CaO-Lime	Others [1]	Amorphous
Cement	CEM I	8.1	47.4	10.2	-	-	-	-	-	7.2	27.2
Sludge	PSA	-	-	-	19.4	2.3	12.9	13.7	4.8	4.8	42.2
Bioash	FA	-	-	-	48.5	3.8	-	-	-	13.1	32.5
	BA	-	-	13.3	0.1	6.9	-	-	16.0	3.8	59.9
Ladle slag	LS1	-	-	-	-	-	-	20.5	-	42.3	37.2
	LS2	-	-	-	-	4.8	-	11.7	-	24.1	59.4
Biochar	BC1	-	-	-	1.3	-	0.6	-	-	0.6	97.5
	BC2	-	-	-	35.3	-	3.1	-	-	6.6	55.0
	BC3	-	-	-	-	-	6.4	-	-	10.0	83.7
	BC4	-	-	-	2.6	-	7.5	-	-	11.1	78.9

[1] CEM I: bassanite (7.2%). PSA: anhydrite (3.7%), rutile (1.1%). FA: fluorapatite (8.3%), arcanite (2.7%), thenardite (1.3%), hematite (0.8%). BA: magnesite (1.4%), periclase (2.4%). LS1: Calcio-olivine (25.9%), larnite (1.2%), gehlenite (9.3%), clinoenstatite (5.9%). LS2: calcio-olivine (18.9%), gehlenite (2.7%), zeolite (2.5%). BC1: rutile (0.6%). BC2: illite+mica (2.4%), K-feldspar (1.6%), plagioclase (2.6%). BC3: K-feldspar (2.8%), plagioclase (4.3%), magnetite (2.9%). BC4: illite+mica (1.7%), K-feldspar (3.7%), plagioclase (4.8%), amphibole (0.8%), dolomite (0.1%). [2] C_2S = di-calcium silicate (belite), $2CaOSiO_2$. [3] C_3S = tri-calcium silicate (alite), $3CaOSiO_2$. [4] C_4AF = tetra-calcium alumino ferrite (felite), $4CaOAl_2O_3\ Fe_2O_3$.

For the Tiller-Flotten peat, a DTG peak was observed between temperatures of 220–350 °C, caused by the dehydration of the organic content in the peat. A high weight loss in this temperature range indicated that the peat had a low degree of humification, e.g., a large number of intact fibres and leaves [73], which was coherent with the von Post classification of H2-H3. The TGA further showed a continuous weight loss at higher temperatures, which is typical for peat due to its rather complex composition [80].

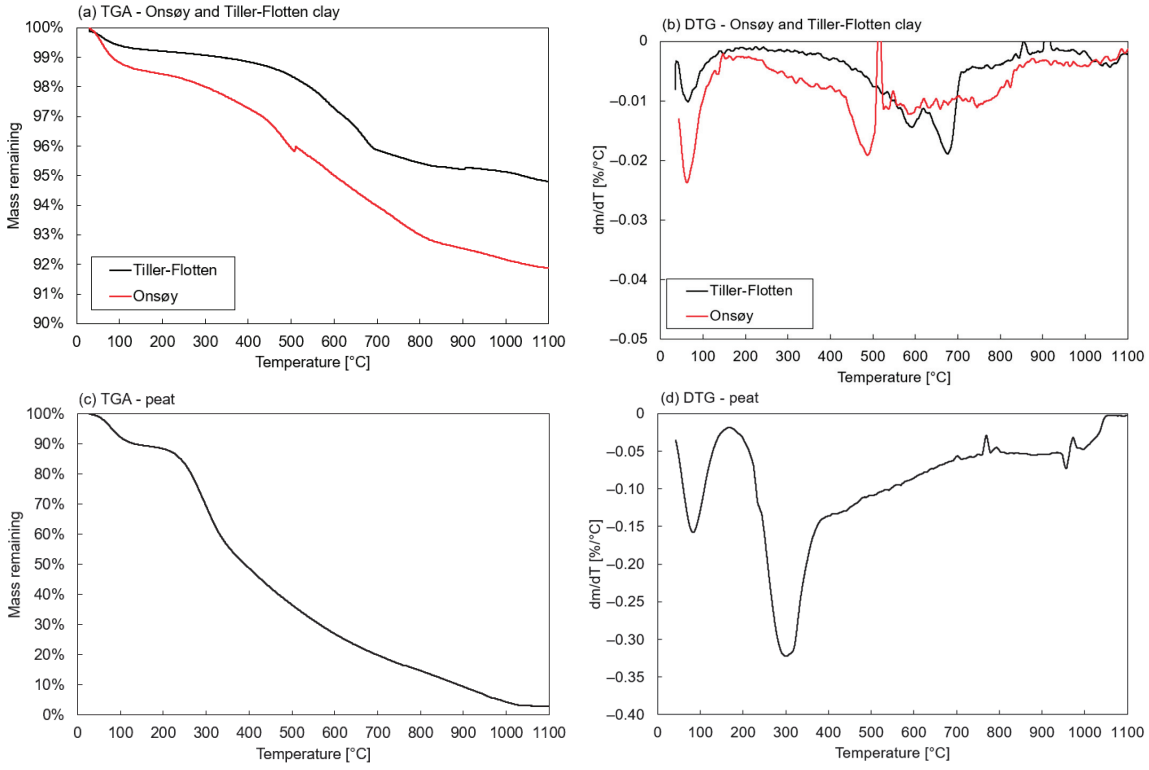

Figure 2. Results from thermogravimetric analyses on natural soils: (**a**,**b**) Onsøy and Tiller-Flotten clay, (**c**,**d**) peat.

TGA and DTG results for the CEM, IBPs and biochars are shown in Figure 3. The FA and LS2, in particular, had a high weight loss in the temperature range of approximately 40–120 °C as the free and adsorbed water evaporated, in line with the high water content determinations. The BA and LS2 showed additional weight loss at temperatures of 380–480 °C, i.e., dehydration of $Ca(OH)_2$. These also had the highest content of portlandite, as shown by the XRD analyses. At temperatures of 700–800 °C, the FA and PSA exhibited weight loss due to the decomposition of $CaCO_3$. Again, this was observed in the XRD analyses with high calcite contents. Two outlying results were identified: a weight increase for the PSA at temperatures of 380–630 °C and for LS1 at temperatures of 900–1050 °C. A possible reason for this might be baseline drift during the TGA tests; however, despite this, it should be of no particular relevance to the stabilisation effect of the binders. In general, the TGA and DTG analyses of the IBPs were similar to those found in the literature [54,61,65,69,81].

The TGA and DTG results for the biochar showed similar characteristics as those for the peat, i.e., a gradual weight loss over a large temperature range. This was expected since they had relatively similar compositions, as observed in the XRF analyses. One exception was the BC2, which exhibited a DTG peak at temperatures of 700–800 °C, i.e., decomposition of the $CaCO_3$ due to the high calcite content, as was observed in the XRD analysis.

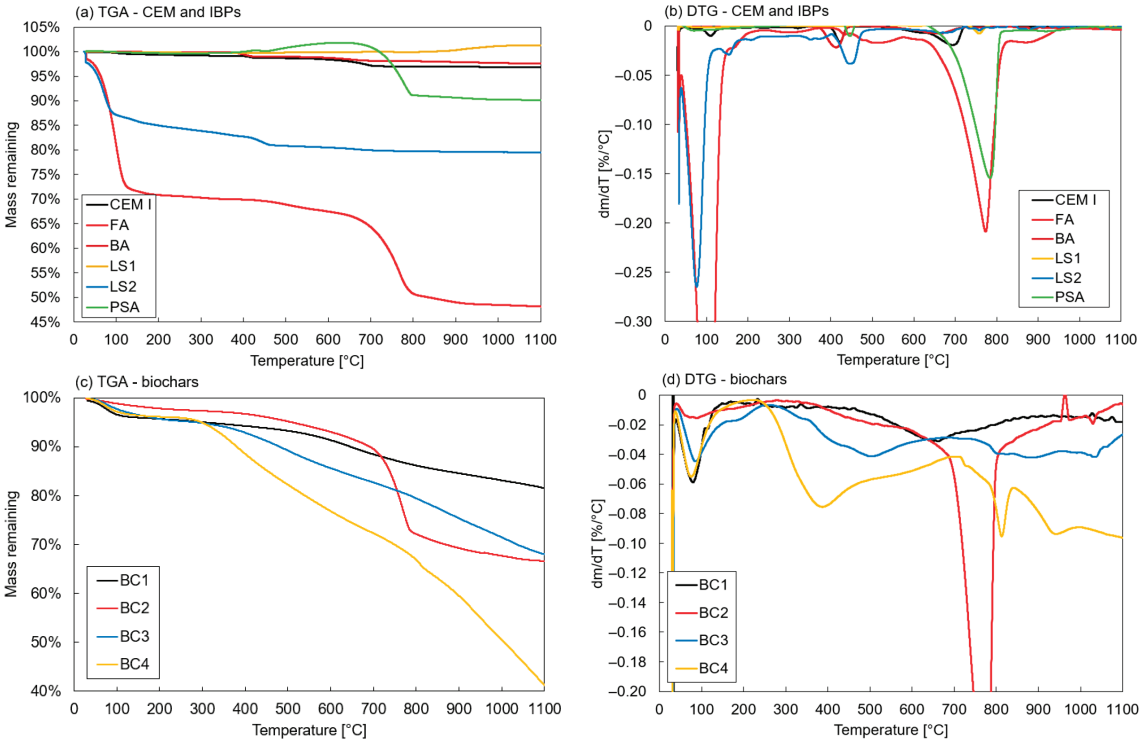

Figure 3. Results from thermogravimetric analyses of binders: (**a**,**b**) CEM and IBPs, (**c**,**d**) biochars.

3.2. Stabilisation Effect

Figure 4 shows results from the UC tests, i.e., strength and stiffness for the stabilised specimens cured at 28 days. The stabilised Onsøy clay (see Figure 4a) obtained τ_{max} values ranging between 50 and 100 kPa, except for CEM as a single binder with α of 60 kg/m^3, i.e., CEM-60, which reached almost 200 kPa. Adding 100 kg/m^3 of biochar had varying stabilisation effects. Biochars BC2 and BC3 had negative stabilisation effects on the strength development, whilst BC1 and BC4 had positive stabilisation effects. The same differences were also observed for E_{50} (see Figure 4b). The stabilisation effect of adding the calcium-based IBPs also varied. However, all IBPs had positive stabilisation effects with increased strength. The PSA and BA in particular seemed to give a relatively high strength and stiffness contribution.

The Tiller-Flotten clay (see Figure 4c,d) showed a considerably greater strength development, where τ_{max} ranged from just below 200 kPa up to approximately 550 kPa. However, for the Tiller-Flotten clay, all biochars had a negative stabilisation effect, although to a lesser degree for BC1 and BC4. For the IBPs, the same pattern as that for the Onsøy clay was observed, i.e., the PSA and BA had the highest stabilisation effect.

The results for the stabilised peat are shown in Figure 4e,f. All biochars, especially BC1 and BC4, had a positive stabilisation effect with an increased τ_{max} compared to CEM as a single binder. The effect of adding IBPs, however, reduced the strength considerably, except for LS1 and LS2. The same pattern was obtained for stiffness E_{50}.

The average relationships between stiffness E_{50} and strength τ_{max}, often referred to as the rigidity index, are plotted in Figure 5. For the clays, the ratio E_{50}/τ_{max} was generally between 200 and 400, equivalent to E_{50}/UCS between ~100 and ~200, which is in line with other studies [29,82,83]. The CEM and PSA stabilised specimens deviated from this (CEM-30/PSA-30), where the ratio E_{50}/τ_{max} was ~90, i.e., considerably lower

than that for the other IBPs. It was further observed that specimens stabilised with biochar in general had a lower ratio E_{50}/τ_{max} compared to CEM as a single binder and CEM combined with IBPs. This implies that stabilisation with biochar improves stiffness to a lesser degree than strength. For the peat specimens, the ratio E_{50}/τ_{max} varied between ~40 and ~100, independent of IBP or biochar, in line with previous studies on biochar in peat [27]; however, there was also an exceptionally low ratio for the CEM-PSA-specimen, where E_{50}/τ_{max} was ~13.

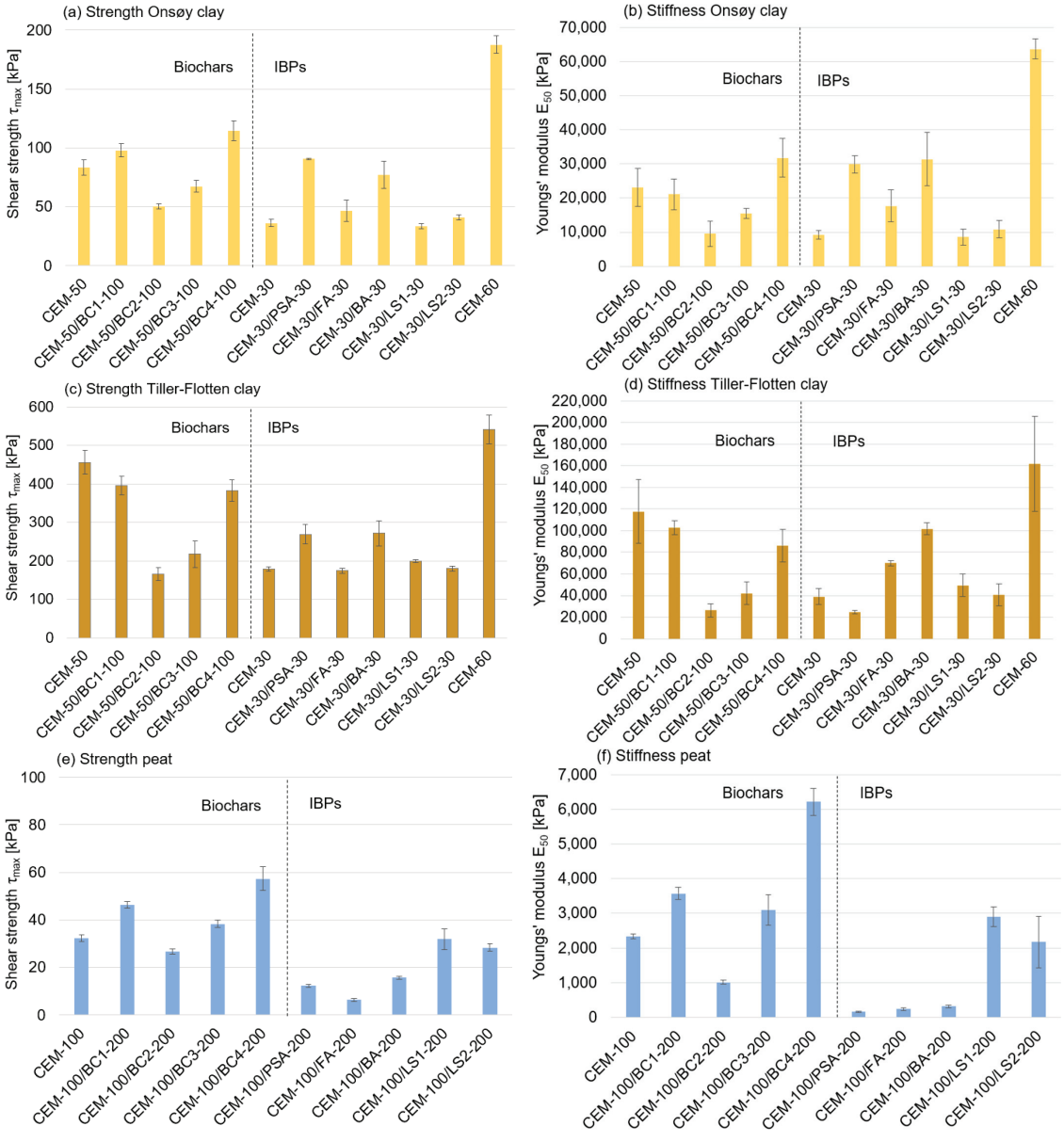

Figure 4. Results of shear strength (τ_{max}) and stiffness Youngs' modulus (E_{50}) from UC tests for the (**a**,**b**) Onsøy clay, (**c**,**d**) Tiller-Flotten clay and (**e**,**f**) peat. Error bars show the standard deviation.

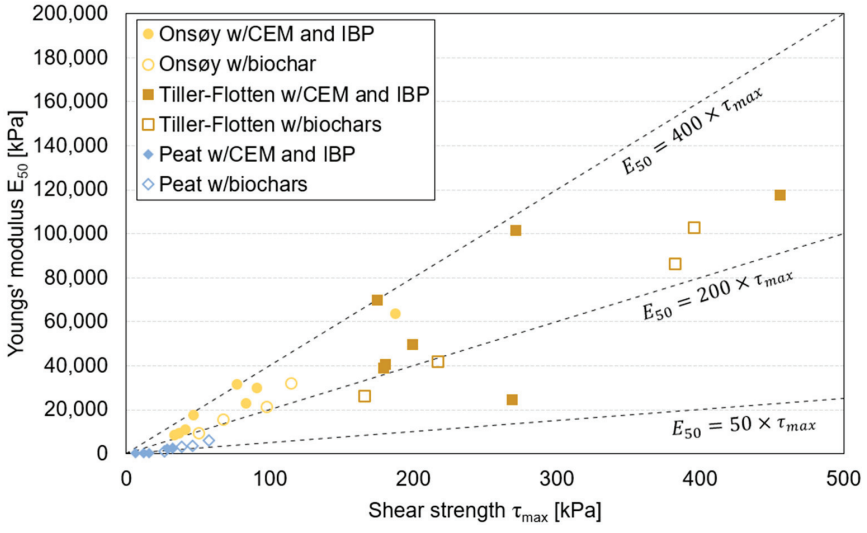

Figure 5. Relationship between shear strength (τ_{max}) and stiffness Youngs' modulus (E_{50}). Average values for the three replicate specimens for each mixture. Points denoted 'w/CEM and IBP' show mixtures with both CEM as a single binder and CEM and IBP in combination.

The results from the strength activity index (SAI) are shown in Figure 6. All biochars and IBPs reduced the strength but to various degrees, ranging from ~70% reduced strength for BC4, BA and FA to ~90% reduced strength for BC3. On average, the strength reduction was 81% for the biochars compared to 73% for the IBPs. This difference was very much affected by the low reduction for BC3 (93%). It should, however, be noted that the variation for each mixture was relatively large, as shown by the error bars.

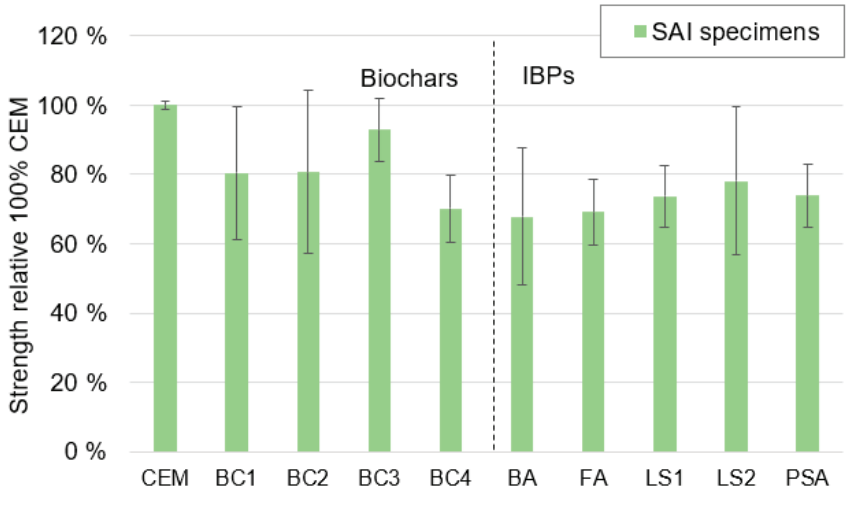

Figure 6. Results of the strength activity index (SAI) for 100% CEM and mixtures where 20% of the CEM was replaced with biochar or IBPs. Error bars show coefficients of variation.

4. Discussion

4.1. Stabilisation Effect for Different Binders in Clays

To further analyse the comparative stabilisation effects of biochars and IBPs, the relative strengths for both the Onsøy and the Tiller-Flotten clays when the biochars and IBPs were added to CEM are plotted in Figure 7. It was observed that most of the biochars had a negative effect on strength development (see Figure 7a), apart from BC1 and BC4 in the Onsøy clay, where the strength increase was ~20–40%. Notably, BC1 and BC4 also had the least negative effect in the Tiller-Flotten clay, where the strength only decreased ~15%. The largest negative effect was observed for BC2, where the strength in the Tiller-Flotten clay decreased by a considerable ~65%.

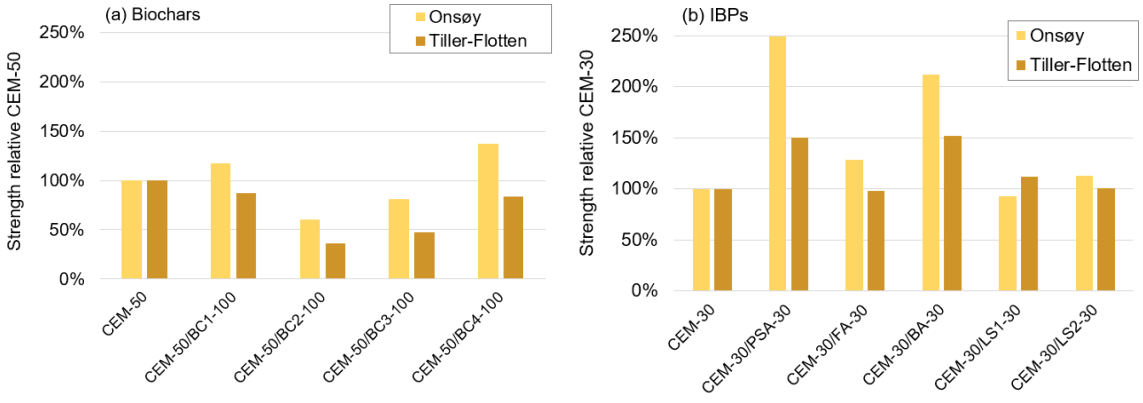

Figure 7. Average strength of mixtures of biochars and IBPs relative to mixtures with 100% CEM as a binder for the Onsøy and Tiller-Flotten clays, (**a**) biochars, and (**b**) IBPs.

These results indicate that the use of biochar in the stabilisation of clays results in relatively few benefits, which can be expected since it does not contain any calcium-based cementitious properties. However, previous tests have revealed positive stabilisation effects on the Tiller-Flotten clay [29], although with a different type of biochar. Notably, the stabilisation effect of biochar in soils has been observed to be highly dependent on the type of biochar and its properties such as SFA, water content and grain size distribution, and the resulting stabilisation effect thus varies greatly [37,84].

Research on mortars, concrete and asphalt has also shown that biochar can be beneficial as a substitution or additive, although negative effects also have been reported [85–89]. In those cases where the biochar has shown positive effects, this has mostly been attributed to the water retention properties of biochar. This reduces water evaporation during curing, reduces microcracking and provides a continuous source of water for the cement hydration occurring over time [85,86]. In addition, the micropores of the biochar can provide space for the cementitious compounds resulting from pozzolanic reactions [90,91]. Whether a positive or negative effect is obtained depends on the biochar content in relation to the cement content, the water saturation of biochar prior to mixing and the grain size distribution. Generally, finer-grained and pre-soaked biochar is preferred in cement mortar mixtures [38]. Typically, positive effects have been reported for biochar contents up to ~2–3%, beyond which, a negative effect is often observed, especially if the content is over ~10% [88,92].

How these findings translate to soil stabilisation has thus far not been properly investigated. As clays typically have a large amount of water readily available for cement hydration, the potential benefits from water retention properties might be lower compared to those from mortars and cement. On the other hand, biochar could enable densification in clays with high porosity and, thus, both the initial porosity and amount of biochar per unit volume of clay would affect the stabilisation effect. Previous tests on soils have shown

that an optimal amount of biochar can be found [29,38], which should be studied further with the soils used herein.

Another important parameter that highly affects the stabilisation effect is the binder uniformity, i.e., the distribution of binder in the soil that is obtained after mixing. The higher binder uniformity of calcium-based binders such as CEM and QL was observed to be beneficial [93]. How these results apply to biochar is not known and, although it could be assumed to have the same effect, this effect must be studied further.

Based on simple linear regression analyses, there appeared to be no correlations between the stabilisation effect and the mineralogical or chemical oxide compositions of the biochars as shown by the XRD and XRF analyses. For example, BC2 contained a considerable amount of CaO in a calcite mineral structure, originating from the addition of limestone to the sludge prior to pyrolysis. However, this had no stabilisation effect since the CaO was not available for pozzolanic reactions with the CEM. This was also observed previously when QL and calcite ($CaCO_3$) were used for the stabilisation of Tiller-Flotten clay [6].

The stabilisation effects of the calcium-based IBPs are shown in Figure 7b. Most of the IBPs had a positive stabilisation effect. However, there are a few exceptions where no effect was observed, specifically for FA, LS1 and LS2. Ladle slags in general are known for their relatively low effectiveness and often need to be alkali-activated [65,94], which appears not to have been achieved with the added quantity of CEM. The BA and PSA performed well, with an increased strength of 50% to 150%. This indicates that the CaO in these binders was available for chemical reactions with pozzolans in the binder or soil. In fact, CaO in free-form in the BA and PSA at 16% and 4.8%, respectively, was also noted by the XRD analyses (Table 5). However, these contents were not directly proportional to the relative strength increase.

Typically, for calcium-based products such as the ashes and ladle slags used herein, the CaO-content is correlated to the amount of cementitious products obtained in the soil–binder mixture. This, however, depends on the amount of CaO available for chemical reactions with the soil particles, also referred to as the active or free CaO content. This should be considered in further work.

4.2. The Stabilisation Effect for Different Binders in Peat

Figure 8 shows the stabilisation effect of the biochars and IBPs in the peat. Here, biochar was observed to be far more effective compared to the IBPs, with a strength increase of up to 80% for BC4. These results are similar to previous findings on peat stabilisation [27,31,95]. The stabilisation effect can possibly be attributed to the water retention (high absorption capacity) of the biochar and densification [32,96]. This could be a larger effect in peat with a very high water content and high porosity compared to clays with considerably lower porosity, as indicated by the water content determinations (Table 2).

In contrast to their positive stabilisation effect on clay, most of the IBPs had a negative effect on the strength of the peat. Adding PSA, FA and BA to CEM yielded strengths that were only ~20–50% of that for CEM as a single binder. The reason for this is not known. LS1 and LS2 had a lesser negative effect, with equivalent values of ~88–98%. Here, a possible explanation is that the ladle slags were activated by the higher amount of CEM than that in the clays and hence gave a cementitious contribution by pozzolanic reactions, similar to the effects of GGBS [13,97].

4.3. The Strength Difference between the Onsøy and Tiller-Flotten Clays

The absolute strength difference between the Onsøy and Tiller-Flotten clays was noticeable. The strength values for the Tiller-Flotten clay were ~3–6 times higher than those for the Onsøy clay and ~3.7 times higher on average. For CEM as a single binder, the strength was ~2.9 times higher. It was noted that the deviations were similar between the two clays, which might reflect the fact that the specimen quality was

similar for both clays. The strength difference is, therefore, believed not to be caused by, for example, differences in specimen quality. Further, based on previous research on similar types of clays, these differences seem too large to be explained by differences in, for example, the organic content alone, which was 3–4% for the Onsøy clay and <1% for the Tiller-Flotten clay [13,83]. Previous research has also shown that a lower liquidity index could imply a higher strength [98], but the opposite effect was observed herein as the liquidity indices were approximately 0.9–1.0 and 1.5–2.0 for the Onsøy and Tiller-Flotten clays, respectively.

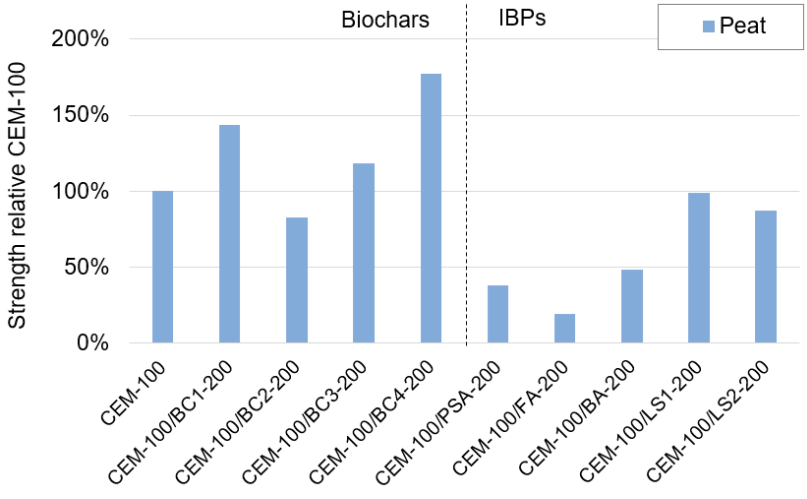

Figure 8. Strength of mixtures of biochars and IBPS relative to mixtures with 100% CEM as a binder for the peat.

Moreover, the difference cannot be explained by the differences in the water content relative to the binder quantity. This is typically analysed by using the water–binder ratio, i.e., the weight ratio between the water in the soil to the total α added during stabilisation [6,99,100]. With a w of ~42% and ~73% for the Tiller-Flotten and Onsøy clays, respectively, this corresponds to a content of water of approximately 530 l/m^3 and 660 l/m^3, respectively, which results in water–binder ratios of ~9 and ~11, respectively. Previous research on water–binder ratios vs. strength testing on Norwegian soils [6,82] indicates that the strength difference should only be approximately 20%, i.e., this does not explain the large strength differences between the two clays studied herein.

The strength differences between the two clays were also difficult to assess based on the compositional analyses. In addition, since previous studies have shown large strength differences between stabilised clays from different geographical regions without a satisfactory explanation [6,82,83,101], there is a need for further studies on this topic.

5. Conclusions

Four biochars (BCs) and five industrial by-products (IBPs) were characterised and tested for stabilisation effects on three natural Norwegian soils: the Onsøy and Tiller-Flotten clays and peat. The following conclusions were made:

- Two of the biochars (BC1 and BC4) had beneficial stabilisation effects (i.e., strength and stiffness) on the Onsøy clay with a relatively high water content (~73%). All four biochars had negative stabilisation effects on the Tiller-Flotten clay with a relatively low water content (~42%); however, BC1 and BC4 had the least negative effect.

- Almost all of the IBPs had positive stabilisation effects on the two clays. The greatest effect was observed with the paper sludge ash (PSA) and bottom ash (BA). The ladle slags (LS1 and LS2) had a negligible effect on strength and stiffness development.
- Three biochars (BC1, BC3 and BC4) had a positive stabilisation effect on the peat. Three IBPs had negative stabilisation effects, whilst the ladle slags LS1 and LS2 again had a negligible effect.
- The stiffness-to-strength ratios (E_{50}/τ_{max}) of most of the mixtures ranged between 200 and 400, except for all peat samples, which had E_{50}/τ_{max} values of approximately 50. The low E_{50}/τ_{max} values also applied to some mixtures with biochar and all PSA-stabilised specimens.

The varying results in strength for the biochars are believed to depend on the biochar characteristics such as grain size and water absorption capacity in relation to the porosity and water content of the soil. The results indicate that the stabilisation effect of the biochars increases with increasing water content of the soil; however, this has not been investigated in detail. Further research on biochar in soft soil stabilisation is needed as the climate mitigation potential is considerable.

No apparent correlation between stabilisation effect and the chemical composition of the biochars or IBPs was observed. This highlights the difficulty in predicting strength development based on chemical and mineralogical compositions alone and stresses the importance of performing laboratory testing.

The need for further studies is noted. In particular, further research should investigate the observed large strength and stiffness differences when stabilising different clays. In addition, further studies are needed to explain the effects of, for example, the grain size distribution of IBPs and biochars and the effects of the binder uniformity of biochar on the stabilisation effect.

Author Contributions: Conceptualization, S.R. and P.P.; methodology, S.R., C.S. and P.P.; software, S.H.; validation, S.H., P.P. and M.L.; formal analysis, S.H. and C.S.; investigation, S.H.; resources, S.R., P.P., G.C. and M.L.; data curation, S.H.; writing—original draft preparation, S.H.; writing—review and editing, S.H., P.P., S.R., G.C., C.S. and M.L.; visualization, S.H.; supervision, P.P.; project administration, S.R.; funding acquisition, S.R. and G.C. All authors have read and agreed to the published version of the manuscript.

Funding: This research was funded by the Research Council of Norway, grant number 328767 'GOAL—Green Soil Stabilisation'.

Institutional Review Board Statement: Not applicable.

Informed Consent Statement: Not applicable.

Data Availability Statement: All data are available from the corresponding author upon reasonable request.

Acknowledgments: The authors are grateful to Ingrid Peikli and Geir Wold Åsli at the NGI geotechnical laboratory in Oslo for performing many of the laboratory tests presented herein. The authors are also grateful to the staff at Nemko Norlab, SINTEF and X-ray Mineral Services for performing several of the characterisation investigations. The authors are especially grateful to Jonathan Wilkins at X-ray Mineral Services for contributing to the interpretation of the XRF and XRD analyses. The contributions from the industrial partners Norske Skog Skogn, Bergene Holm, Lindum and Celsa Steel Services are appreciated. The authors appreciate the valuable comments from the anonymous reviewers, which improved the quality of the manuscript.

Conflicts of Interest: The authors declare no conflict of interest.

References

1. Andrew, R.M. Global CO_2 emissions from cement production, 1928–2018. In *Earth System Science Data*; Copernicus GmbH: Göttingen, Germany, 2019; Volume 11, pp. 1675–1710. [CrossRef]
2. Gao, T.; Shen, L.; Shen, M.; Chen, F.; Liu, L.; Gao, L. Analysis on differences of carbon dioxide emission from cement production and their major determinants. *J. Clean. Prod.* **2015**, *103*, 160–170. [CrossRef]

3. Miller, G.A.; Azad, S. Influence of soil type on stabilization with cement kiln dust. *Constr. Build. Mater.* **2000**, *14*, 89–97. [CrossRef]
4. Yoobanpot, N.; Jamsawang, P.; Horpibulsuk, S. Strength behavior and microstructural characteristics of soft clay stabilized with cement kiln dust and fly ash residue. *Appl. Clay Sci.* **2017**, *141*, 146–156. [CrossRef]
5. Jegandan, S.; Liska, M.; Osman, A.A.M.; Al-Tabbaa, A. Sustainable binders for soil stabilisation. *Proc. Inst. Civ. Eng. Ground Improv.* **2010**, *163*, 53–61. [CrossRef]
6. Hov, S.; Paniagua, P.; Sætre, C.; Rueslåtten, H.; Størdal, I.; Mengede, M.; Mevik, C. Lime-cement stabilisation of Trondheim clays and its impact on carbon dioxide emissions. *Soils Found.* **2022**, *1*, 62. [CrossRef]
7. Ramírez, A.L.; Korkiala-Tanttu, L. Stabilisation of Malmi soft clay with traditional and low-CO_2 binders. *Transp. Geotech.* **2023**, *38*, 100920. [CrossRef]
8. Mypati, V.N.K.; Saride, S. Feasibility of Alkali-Activated Low-Calcium Fly Ash as a Binder for Deep Soil Mixing. *J. Mater. Civil. Eng.* **2022**, *34*, 04021410. [CrossRef]
9. Sharma, A.K.; Sivapullaiah, P.V. Strength development in fly ash and slag mixtures with lime. *Proc. Inst. Civ. Eng. Ground Improv.* **2016**, *169*, 194–205. [CrossRef]
10. Sukmak, P.; Horpibulsuk, S.; Shen, S.L. Strength development in clay-fly ash geopolymer. *Constr. Build. Mater.* **2013**, *40*, 566–574. [CrossRef]
11. Wu, J.; Deng, Y.; Zhang, G.; Zhou, A.; Tan, Y.; Xiao, H. A Generic Framework of Unifying Industrial By-products for Soil Stabilization. *J. Clean. Prod.* **2021**, *25*, 321. [CrossRef]
12. Xu, B.; Yi, Y. Soft Clay Stabilization Using Three Industry Byproducts. *J. Mater. Civil. Eng.* **2021**, *33*, 06021002. [CrossRef]
13. Åhnberg, H.; Johansson, S.-E.; Pihl, H.; Carlsson, T. Stabilising effects of different binders in some Swedish soils. *Proc. Inst. Civ. Eng. Ground Improv.* **2003**, *7*, 9–23. [CrossRef]
14. James, R.; Kamruzzaman, A.H.M.; Haque, A.; Wilkinson, A. Behaviour of lime—Slag-treated clay. *Proc. Inst. Civ. Eng. Ground Improv.* **2008**, *161*, 207–216. [CrossRef]
15. Wang, X.; Zhang, Z.; Song, Z.; Li, J. Engineering properties of marine soft clay stabilized by alkali residue and steel slag: An experimental study and ANN model. *Acta Geotech.* **2022**, *17*, 5089–5112. [CrossRef]
16. Wilkinson, A.; Haque, A.; Kodikara, J. Stabilisation of clayey soils with industrial by-products: Part, A. *Proc. Inst. Civ. Eng. Ground Improv.* **2010**, *163*, 149–163. [CrossRef]
17. Wilkinson, A.; Haque, A.; Kodikara, J. Stabilisation of clayey soils with industrial by-products: Part B. *Proc. Inst. Civ. Eng. Ground Improv.* **2010**, *163*, 165–172. [CrossRef]
18. Yi, Y.; Gu, L.; Liu, S.; Puppala, A.J. Carbide slag-activated ground granulated blastfurnace slag for soft clay stabilization. *Can. Geotech. J.* **2015**, *52*, 656–663. [CrossRef]
19. Armistead, S.J.; Smith, C.C.; Staniland, S.S. Sustainable biopolymer soil stabilisation: The effect of microscale chemical characteristics on macroscale mechanical properties. *Acta Geotech.* **2022**, *18*, 3213–3227. [CrossRef]
20. Soldo, A.; Miletić, M.; Auad, M.L. Biopolymers as a sustainable solution for the enhancement of soil mechanical properties. *Sci. Rep.* **2020**, *1*, 10. [CrossRef]
21. Voottipruex, P.; Teerawattanasuk, C.; Sramoon, W.; Meepon, I. Stabilization of Soft Clay Using Perlite Geopolymer Activated by Sodium Hydroxide. *Int. J. Geosynth. Ground Eng.* **2022**, *8*, 5. [CrossRef]
22. Correia, A.A.S.; Venda Oliveira, P.J.; Custódio, D.G. Effect of polypropylene fibres on the compressive and tensile strength of a soft soil, artificially stabilised with binders. *Geotext. Geomembr.* **2015**, *43*, 97–106. [CrossRef]
23. Zhao, M.; Liu, G.; Zhang, C.; Guo, W.; Luo, Q. State-of-the-art of colloidal silica-based soil liquefaction mitigation: An emerging technique for ground improvement. *Appl. Sci.* **2020**, *10*, 15. [CrossRef]
24. Ahmadi Chenarboni, H.; Hamid Lajevardi, S.; MolaAbasi, H.; Zeighami, E. The effect of zeolite and cement stabilization on the mechanical behavior of expansive soils. *Constr. Build. Mater.* **2021**, *272*, 121630. [CrossRef]
25. Eyo, E.U.; Ngambi, S.; Abbey, S.J. Performance of clay stabilized by cementitious materials and inclusion of zeolite/alkaline metals-based additive. *Transp. Geotech.* **2020**, *23*, 100330. [CrossRef]
26. Sørmo, E.; Silvani, L.; Thune, G.; Gerber, H.; Schmidt, H.P.; Smebye, A.B. Waste timber pyrolysis in a medium-scale unit: Emission budgets and biochar quality. *Sci. Total Environ.* **2020**, *718*, 137335. [CrossRef]
27. Ritter, S.; Paniagua, P.; Hansen, C.B.; Cornelissen, G. Biochar amendment for improved and more sustainable peat stabilisation. *Proc. Inst. Civil. Eng. Ground Improv.* 2022, *ahead of print*. [CrossRef]
28. Jeffery, S.; Bezemer, T.M.; Cornelissen, G.; Kuyper, T.W.; Lehmann, J.; Mommer, L. The way forward in biochar research: Targeting trade-offs between the potential wins. *GCB Bioenergy* **2015**, *1*, 1–13. [CrossRef]
29. Ritter, S.; Paniagua, P.; Cornelissen, G. Biochar in Quick Clay Stabilization: Reducing Carbon Footprint and Improving Shear Strength. *Proc. Geo-Congr.* **2023**, 15–24. [CrossRef]
30. GuhaRay, A.; Guoxiong, M.; Sarkar, A.; Bordoloi, S.; Garg, A.; Pattanayak, S. Geotechnical and chemical characterization of expansive clayey soil amended by biochar derived from invasive weed species Prosopis juliflora. *Innov. Infrastruct. Solut.* **2019**, *4*, 44. [CrossRef]
31. Lau, J. Static and Dynamic Performance of Biochar Enhanced Cement Stabilised Peat. Ph.D. Thesis, University of Cambridge, Cambridge, UK, 2018.
32. Lau, J.; Biscontin, G.; Berti, D. Effects of biochar on cement-stabilised peat soil. *Proc. Inst. Civ. Eng. Ground Improv.* **2021**, *176*, 76–87. [CrossRef]

33. Pardo, G.S.; Sarmah, A.K.; Orense, R.P. Mechanism of improvement of biochar on shear strength and liquefaction resistance of sand. *Geotechnique* **2019**, *69*, 471–480. [CrossRef]
34. Pardo, G.S.; Orense, R.P.; Sarmah, A.K. Cyclic strength of sand mixed with biochar: Some preliminary results. *Soils Found.* **2018**, *58*, 241–247. [CrossRef]
35. Vincevica-gaile, Z.; Teppand, T.; Kriipsalu, M.; Krievans, M.; Jani, Y.; Klavins, M. Towards sustainable soil stabilization in peatlands: Secondary raw materials as an alternative. *Sustainability* **2021**, *13*, 6726. [CrossRef]
36. Lu, S.G.; Sun, F.F.; Zong, Y.T. Effect of rice husk biochar and coal fly ash on some physical properties of expansive clayey soil (Vertisol). *Catena* **2014**, *114*, 37–44. [CrossRef]
37. Zong, Y.; Chen, D.; Lu, S. Impact of biochars on swell–shrinkage behavior, mechanical strength, and surface cracking of clayey soil. *J. Plant Nutr. Soil. Sci.* **2014**, *177*, 920–926. [CrossRef]
38. William, J.; Latifi, N.; Vahedifard, F. Effects of Biochar Amendment on Mechanical Properties of Buckshot Clay. In Proceedings of the IFCEE 2018: Innovations in Ground Improvement for Soils, Pavements, and Subgrades, Orlando, FL, USA, 5–10 March 2018; pp. 125–134.
39. Sadasivam, Y.; Reddy, K. Shear strength of waste-wood biochar and biochar-amended soil used for sustainable landfill cover systems. In Proceedings of the 15th Pan-American Conference on Soil. Mechanics and Geotechnical Engineering, Buenos Aires, Argentina, 15–18 November 2015; pp. 745–752.
40. Gundersen, A.S.; Hansen, R.C.; Lunne, T.; L'Heureux, J.S.; Strandvik, S.O. Characterization and engineering properties of the NGTS Onsøy soft clay site. *AIMS Geosci.* **2019**, *5*, 665–703. [CrossRef]
41. L'Heureux, J.S.; Lindgård, A.; Emdal, A. The Tiller-Flotten research site: Geotechnical characterization of a very sensitive clay deposit. *AIMS Geosci.* **2019**, *5*, 831–867. [CrossRef]
42. Long, M.; Paniagua, P.; Grimstad, G.; Trafford, A.; Degago, S.; L'Heureux, J.S. Engineering properties of Norwegian peat for calculation of settlements. *Eng. Geol.* **2022**, *308*, 106799. [CrossRef]
43. von Post, L.; Granlund, E. *Peat Resources in Southern Sweden*; Swedish Geological Survey: Uppsala, Sweden, 1926. (In Swedish)
44. *EN 197-1:2011*; Cement Part 1: Composition, Specifications and Conformity for Common Cements. European Committe for Standardization: Brussels, Belgium, 2011.
45. Silva, F.C.; Cruz, N.C.; Tarelho, L.A.C.; Rodrigues, S.M. Use of biomass ash-based materials as soil fertilisers: Critical review of the existing regulatory framework. *J. Clean. Prod.* **2019**, *214*, 112–124. [CrossRef]
46. Paniagua, P.; Ritter, S.; Moseid, M.; Okkenhaug, G. Bioashes and steel slag as alternative binders in ground improvement of quick clays. In Proceedings of the Geo-Congress 2023, Los Angeles, CA, USA, 26–29 March 2023. [CrossRef]
47. Jafarbiglookarami, A. Alternative Binders for Improvement of Soft Soils—A Geoenvironmental Approach. Master's Thesis, Norwegian University of Science and Technology, Trondheim, Norway, 2021.
48. Liu, Y.; Chang, C.W.; Namdar, A.; She, Y.; Lin, C.H.; Yuan, X. Stabilization of expansive soil using cementing material from rice husk ash and calcium carbide residue. *Constr. Build. Mater.* **2019**, *221*, 1–11. [CrossRef]
49. Okagbue, C.O. Stabilization of Clay Using Woodash. *J. Mater. Civ. Eng.* **2007**, *19*, 14–18. [CrossRef]
50. Nath, B.D.; Sarkar, G.; Siddiqua, S.; Rokunuzzaman, M.; Islam, M.R. Geotechnical Properties of Wood Ash-Based Composite Fine-Grained Soil. *Adv. Civil. Eng.* **2018**, *2018*, 9456019. [CrossRef]
51. Ayobami, A.B. Performance of wood bottom ash in cement-based applications and comparison with other selected ashes: Overview. *Resour. Conserv. Recycl.* **2021**, *166*, 105351. [CrossRef]
52. Azrizal, M.F.; Noorsuhada, M.N.; Latif, M.F.; Arshad, M.F.; Sulaiman, H. The properties of wastepaper sludge ash and its generic applications. *J. Phys. Conf. Ser.* **2019**, *1349*, 012087. [CrossRef]
53. Zmamou, H.; Leblanc, N.; Levacher, D.; Kubiak, J. Recycling of high quantities of wastepaper sludge ash for production of blended cements and alternative materials. *Environ. Technol. Innov.* **2021**, *23*, 101524. [CrossRef]
54. Bai, J.; Chaipanich, A.; Kinuthia, J.M.; O'Farrell, M.; Sabir, B.B.; Wild, S. Compressive strength and hydration of wastepaper sludge ash–ground granulated blastfurnace slag blended pastes. *Cem. Concr. Res.* **2003**, *33*, 1189–1202. [CrossRef]
55. Baloochi, H.; Aponte, D.; Barra, M. Soil Stabilization Using Waste Paper Fly Ash: Precautions for Its Correct Use. *Appl. Sci.* **2020**, *10*, 8750. [CrossRef]
56. Mavrouhdou, M.; Ziniatis, A.; Gray, C.; Ebad, Z.; del Rosario, J.; Kanak, S. Alternative calcium-based chemical stabilisers for ground improvement: Paper Sludge Ash treatment of London Clay. In Proceedings of the 15th International Conference on Environmental Science and Technology, Rhodes, Greece, 31 August–2 September 2017.
57. Mavroulidou, M. Use of waste paper sludge ash as a calcium-based stabiliser for clay soils. *Waste Manag. Res. J. A Sustain. Circ. Econ.* **2018**, *36*, 1066–1072. [CrossRef] [PubMed]
58. Bujulu, P.M.S.; Sorta, A.R.; Priol, A.; Emdal, A. Potential of wastepaper sludge ash to replace cement in deep stabilization of quick clay. In Proceedings of the "Characterization and Improvement of Soils and Materials" Session of the 2007 Annual Conference of the Transportation Association of Canada, Saskatoon, SK, Canada, 14–17 October 2007; pp. 1–16.
59. Bujulu, P.M.S. Deep-Mix Stabilization of Quick Clay: A Potential Area for Utilization of Wastepaper Sludge Ash. Ph.D. Thesis, Norwegian University of Science and Technology, Trondheim, Norway, 2008.
60. Rahmat, M.N.; Kinuthia, J.M. Effects of mellowing sulfate-bearing clay soil stabilized with wastepaper sludge ash for road construction. *Eng. Geol.* **2011**, *117*, 170–179. [CrossRef]
61. Rahmat, N. Soil Stabilization Utilising Wastepaper Sludge Ash. Ph.D. Thesis, University of Glamorgan, Pontypridd, UK, 2004.

62. Pinheiro, C.; Rios, S.; Viana da Fonseca, A.; Fernández-Jiménez, A.; Cristelo, N. Application of the response surface method to optimize alkali activated cements based on low-reactivity ladle furnace slag. *Constr. Build. Mater.* **2020**, *264*, 120271. [CrossRef]
63. Yi, Y.; Li, C.; Liu, S. Alkali-Activated Ground-Granulated Blast Furnace Slag for Stabilization of Marine Soft Clay. *J. Mater. Civil. Eng.* **2015**, *27*, 04014146. [CrossRef]
64. Yi, Y.; Liska, M.; Jin, F.; Al-Tabbaa, A. Mechanism of reactive magnesia—Ground granulated blastfurnace slag (GGBS) soil stabilization. *Can. Geotech. J.* **2016**, *53*, 773–782. [CrossRef]
65. Najm, O.; El-Hassan, H.; El-Dieb, A. Ladle slag characteristics and use in mortar and concrete: A comprehensive review. *J. Clean. Prod.* **2021**, *288*, 125584. [CrossRef]
66. Manso, J.M.; Losañez, M.; Polanco, J.A.; Gonzalez, J.J. Ladle Furnace Slag in Construction. *J. Mater. Civ. Eng.* **2005**, *17*, 5. [CrossRef]
67. Xu, B.; Yi, Y. Stabilisation/solidification of lead-contaminated soil by using ladle furnace slag and carbon dioxide. *Soils Found.* **2022**, *62*, 101205. [CrossRef]
68. Xu, B.; Yi, Y. Soft clay stabilization using ladle slag-ground granulated blastfurnace slag blend. *Appl. Clay Sci.* **2019**, *178*, 105136. [CrossRef]
69. Brand, A.S.; Singhvi, P.; Fanijo, E.O.; Tutumluer, E. Stabilization of a clayey soil with ladle metallurgy furnace slag fines. *Materials* **2020**, *13*, 4251. [CrossRef]
70. Manso, J.M.; Ortega-López, V.; Polanco, J.A.; Setién, J. The use of ladle furnace slag in soil stabilization. *Constr. Build. Mater.* **2013**, *40*, 126–134. [CrossRef]
71. Espinosa, A.; Revilla-Cuesta, V.; Lopez-Ausin, V.; Serrano-Lopez, V.; Fiol, F. Study of clayey soils stabilized with ladle furnace slag as alternative binder for use in road works. *Key Eng. Mater.* **2022**, *929*, 187–192. [CrossRef]
72. Brunauer, S.; Emmet, P.H.; Teller, E. Adsorption of Gases in Multimolecular Layers. *J. Am. Chem. Soc.* **1938**, *60*, 309–319. [CrossRef]
73. Plante, A.F.; Fernández, J.M.; Leifeld, J. Application of thermal analysis techniques in soil science. *Geoderma* **2009**, *153*, 1–10. [CrossRef]
74. Mitchell, J.; Soga, K. *Fundamentals of Soil Behavior*, 3rd ed.; John Wiley & Sons Inc.: Hoboken, NJ, USA, 2005.
75. Kitazume, M.; Grisolia, M.; Leder, E.; Marzano, I.P.; Correia, A.A.S.; Venda Oliveira, P.J.; Åhnberg, H.; Andersson, M. Applicability of molding procedures in laboratory mix tests for quality control and assurance of the deep mixing method. *Soils Found.* **2015**, *55*, 761–777. [CrossRef]
76. Hov, S.; Falle, F.; Paniagua, P. Optimization of Laboratory Molding Techniques for Nordic Dry Deep Mixing. *ASTM Geotech. Test. J.* **2022**, *1*, 45. [CrossRef]
77. Bache, B.K.; Wiersholm, P.; Paniagua, P.; Emdal, A. Effect of Temperature on the Strength of Lime–Cement Stabilized Norwegian Clays. *J. Geotech. Geoenvironmental. Eng.* **2022**, *148*, 04021198. [CrossRef]
78. *ASTM C311-07*; Standard Test Methods for Sampling and Testing Fly Ash or Natural Pozzolans for Use in Portland-Cement Concrete. ASTM International: West Conshohocken, PA, USA, 2022.
79. Setién, J.; Hernández, D.; González, J.J. Characterization of ladle furnace basic slag for use as a construction material. *Constr. Build. Mater.* **2009**, *23*, 1788–1794. [CrossRef]
80. Zhang, W.; Henschel, T.; Söderlind, U.; Tran, K.Q.; Han, X. Thermogravimetric and Online Gas Analysis on various Biomass Fuels. In *Energy Procedia*; Elsevier: Amsterdam, The Netherlands, 2017; pp. 162–167. [CrossRef]
81. Ashraf, M.S.; Ghouleh, Z.; Shao, Y. Production of eco-cement exclusively from municipal solid waste incineration residues. *Resour. Conserv. Recycl.* **2019**, *149*, 332–342. [CrossRef]
82. Paniagua, P.; Bache, B.K.; Karlsrud, K.; Lund, A.K. Strength and stiffness of laboratory-mixed specimens of stabilised Norwegian clays. *Proc. Inst. Civ. Eng. Ground Improv.* **2022**, *175*, 150–163. [CrossRef]
83. Hov, S.; Larsson, S. Strength and Stiffness Properties of Laboratory-Improved Soft Swedish Clays. *Int. J. Geosynth. Ground Eng.* **2023**, *9*, 11. [CrossRef]
84. Sadasivam, B.Y.; Reddy, K.R. Engineering properties of waste wood-derived biochars and biochar-amended soils. *Int. J. Geotech. Eng.* **2015**, *9*, 521–535. [CrossRef]
85. Zhang, Y.; He, M.; Wang, L.; Yan, J.; Ma, B.; Zhu, X. Biochar as construction materials for achieving carbon neutrality. *Biochar* **2022**, *4*, 59. [CrossRef]
86. Gupta, S.; Kua, H.W. Effect of water entrainment by pre-soaked biochar particles on strength and permeability of cement mortar. *Constr. Build. Mater.* **2018**, *159*, 107–125. [CrossRef]
87. Chen, L.; Zhang, Y.; Labianca, C.; Wang, L.; Ruan, S.; Poon, C.S. Carbon-negative cement-bonded biochar particleboards. *Biochar* **2022**, *4*, 58. [CrossRef]
88. Danish, A.; Ali Mosaberpanah, M.; Usama Salim, M.; Ahmad, N.; Ahmad, F.; Ahmad, A. Reusing biochar as a filler or cement replacement material in cementitious composites: A review. *Constr. Build. Mater.* **2021**, *300*, 124295. [CrossRef]
89. Dixit, A.; Gupta, S.; Pang, S.D.; Kua, H.W. Cement Replacement and Improved Hydration in Ultra-High Performance Concrete Using Biochar. In Proceedings of the 3rd International Conference on the Application of Superabsorbent Polymers (SAP) and Other New Admixtures Towards Smart Concrete, Skukuza, South Africa, 25–27 November 2019; pp. 222–229. [CrossRef]
90. Yang, X.; Wang, X.Y. Hydration-strength-durability-workability of biochar-cement binary blends. *J. Build. Eng.* **2021**, *42*, 103064. [CrossRef]
91. Wang, Y.S.; Wang, X.Y. Multi-characterizations of the hydration, microstructure, and mechanical properties of a biochar–limestone calcined clay cement (LC3) mixture. *J. Mater. Res. Technol.* **2023**, *24*, 3691–3703. [CrossRef]

92. Gupta, S.; Kua, H.W.; Pang, S.D. Biochar-mortar composite: Manufacturing, evaluation of physical properties and economic viability. *Constr. Build. Mater.* **2018**, *167*, 874–889. [CrossRef]
93. Larsson, S. State of Practice Report—Execution, monitoring and quality control. In Proceedings of the International Conference on Deep Mixing: Best Practice and Recent Advances, Stockholm, Sweden, 23–25 May 2005; pp. 732–785.
94. Marinho, B.; Santos, M.; Franco De Carvalho, M.; Mendes, J.C.; Brigolini, J.; Peixoto, F. Ladle Furnace Slag as Binder for Cement-Based Composites. *J. Mater. Civ. Eng.* **2017**, *29*, 04017207. [CrossRef]
95. Hernandez-Martinez, F.G.; Al-Tabbaa, A.; Medina-Cetina, Z.; Yousefpour, N. Stiffness and Strength of Stabilized Organic Soils—Part I/II: Experimental Database and Statistical Description for Machine Learning Modelling. *Geosciences* **2021**, *11*, 243. [CrossRef]
96. Berti, D.; Biscontin, G.; Asce, A.M.; Lau, J. Effect of Biochar Filler on the Hydration Products and Microstructure in Portland Cement–Stabilized Peat. *J. Mater. Civ. Eng.* **2021**, *33*, 04021263. [CrossRef]
97. Timoney, M.J.; Mccabe, B.A.; Bell, A.L. Experiences of dry soil mixing in highly organic soils. *Proc. Inst. Civ. Eng. Ground Improv.* **2012**, *165*, 3–14. [CrossRef]
98. Correia, A.A.S.; Venda Oliveira, P.J.; Lemos, L.J.L. Strength assessment of chemically stabilised soft soils. *Proc. Inst. Civ. Eng. Geotech. Eng.* **2019**, *172*, 218–227. [CrossRef]
99. Kitazume, M.; Terashi, M. *The Deep Mixing Method*; Taylor & Francis Group: London, UK, 2013.
100. Horpibulsuk, S.; Rachan, R.; Suddeepong, A. State of the art in strength development of soil-cement columns. *Proc. Inst. Civ. Eng. Ground Improv.* **2012**, *165*, 201–215. [CrossRef]
101. Åhnberg, H.; Pihl, H. *Type of Lime and Its Effect on Stabilisation Effect*; Swedish Deep Stabilization Research Centre: Linköping, Sweden, 1997. (In Swedish)

applied sciences

MDPI

Article

Sustainable Impact of Coarse Aggregate Crushing Waste (CACW) in Decreasing Carbon Footprint and Enhancing Geotechnical Properties of Silty Sand Soil

Gamil M. S. Abdullah [1], Ahmed Abd El Aal [1], Mabkhoot Al Saiari [2,3] and Ahmed E. Radwan [4,*]

[1] Civil Engineering Department, College of Engineering, Najran University, Najran 61441, Saudi Arabia; gmabdullah@nu.edu.sa (G.M.S.A.); akahmed@nu.edu.sa (A.A.E.A.)
[2] Advanced Materials and Nano Technology Research Centre, Najran University, Najran 61441, Saudi Arabia; mamalsaiari@nu.edu.sa
[3] Empty Quarter Research Unit, Chemistry Department, Faculty of Science and Art at Sharurah, Najran University, Najran 61441, Saudi Arabia
[4] Faculty of Geography and Geology, Institute of Geological Sciences, Jagiellonian University, Gronostajowa 3a, 30-387 Kraków, Poland
* Correspondence: ahmed.radwan@uj.edu.pl or radwanae@yahoo.com

Abstract: People are forced to use all types of soil, especially bad soils, as infrastructure demands grow. Different procedures must be used to ameliorate these poor soils, which are fragile during building. Natural resource depletion and the rising costs of available materials force us to consider alternative supplies. For several years, researchers have investigated the use of by-products from industry and associated approaches to improve the qualities of various soils. Coarse Aggregate Crushing Waste (CACW) is a waste product that results from the primary crushing of aggregates. Massive amounts of CACW are produced in the business, posing serious issues from handling to disposal. As a result, the widespread use of CACW for diverse purposes has been recommended in the civil engineering profession to address these concerns. Because some natural resources, such as gravel, are nonrenewable, it is vital to decrease their consumption and replace them with recycled, cost-effective, and ecologically acceptable alternatives. This research aimed to investigate the possibility of reusing CACW to improve the geotechnical properties of silty sand (SM) soil available in the Najran region. In this research, soil samples were collected from Najran city and subjected to a variety of lab experiments to determine their characterization. Mixes were designed for a parent soil with a range of percentages of CACW with/without 2% cement. The designed mixes were examined through a set of lab tests to obtain the optimum design for use in road construction. The findings of the tests showed that the optimum dosage is 10% CACW with 2% cement, raising the undrained shear strength of silty sand soil by 323%, CBR by 286%, and P-wave by 180%. The durability tests show that soil mixed with 10% CACW and 2% cement fulfills the requirements and stays within the 14% weight loss limit imposed by the Portland Cement Association (PCA). The microscopic investigation results confirmed the outcomes obtained by macro tests. As a result, the carbon footprint values decrease when CAWA is added, making this treatment approach almost carbon neutral. This study clarifies the long-term effects of CACW on improving the geotechnical characteristics of silty sand soil in the Najran Region of the Kingdom of Saudi Arabia and other comparable soils globally.

Keywords: aggregate waste materials; geotechnical properties; ultrasonic waves; Najran area

Citation: Abdullah, G.M.S.; Abd El Aal, A.; Al Saiari, M.; Radwan, A.E. Sustainable Impact of Coarse Aggregate Crushing Waste (CACW) in Decreasing Carbon Footprint and Enhancing Geotechnical Properties of Silty Sand Soil. *Appl. Sci.* **2023**, *13*, 10930. https://doi.org/10.3390/app131910930

Academic Editors: Paulo José da Venda Oliveira and António Alberto Santos Correia

Received: 31 August 2023
Revised: 28 September 2023
Accepted: 29 September 2023
Published: 2 October 2023

1. Introduction

There is a great deal of demand in Saudi Arabia's construction industry to create the country's essential infrastructure because of the country's fast-expanding population and industrialization. The most recently constructed infrastructure is located in arid

areas, mostly on brittle soils. These soils require chemical and/or mechanical stabilization techniques. Lime and Portland cement are often used for their chemical stability. For this function, various additional materials are also used, including Coarse Aggregate Crushing Waste (CACW). Due to the depletion of natural resources and the rising cost of accessible materials, it is critical to investigate alternative sources of supply because it is a critical issue in construction projects, particularly highways.

Because of the increased volume of waste materials in the environment in recent years, which has led to environmental contamination, the recycling of industrial waste materials in ground improvement applications has become increasingly important. Due to the growing amount of trash produced in nature, researchers have begun to utilize waste materials in a variety of sectors in order to limit the amount of industrial waste that is disposed of in nature [1–5]. Waste materials can be used in a variety of civil engineering applications [6,7]. Cement, which is widely utilized in practically all civil engineering projects, is made from natural resources such as chalk or limestone that have been heated to extremely high temperatures, utilizing enormous amounts of natural energy.

Industrial waste has been employed as aggregate or cement in concrete manufacturing in recent years [8]. Waste materials have also been employed in geotechnical engineering applications for soil improvement [1–7]. Researchers are currently faced with substantial difficulty in developing novel waste materials that may be employed as cement substitute materials in various civil engineering applications. Coarse aggregate crushing waste (CACW) dust appears to be one of the potential waste products for substituting cement in many engineering projects [9,10]. It is an environmentally benign and cost-effective material [11,12].

The by-product of the construction industry, with rising demand in the construction sector, is CACW. It is dumped in enormous quantities at crusher plants and quarry sites [13]. A non-plastic substance with good shear strength and no carbon emissions is CACW. Stone dust has a huge specific surface area due to its fine nature. Stone dust's physical characteristics, chemical make-up, and mineralogy differ depending on the parent rock type but are consistent with the quarry on-site [14]. CACW is a commercial by-product that results from the first stage of crushing aggregates [15]. These are fine aggregates made from particles smaller than 4 mm in diameter [16].

The rock type, where it came from, and how it was processed all affect the stone dust's quality. Every year, 1430 companies at various plants create 1.48 billion tons of stone dust globally. This huge quantity of stone dust and the large numbers of companies' plants reflect the need for good handling of this waste in a good manner and as an environmental issue. The wealthy nations of the world are extremely interested in and have had success using recycled aggregates. For instance, the USA has many years of experience manufacturing concrete. Over 20 million tons of concrete refuse are currently treated annually [17]. A normal rock generates between 400 and 500,000 tons of aggregate annually on average [18]. About 20 to 25 percent of this is wasted material [19]. The annual production of quarry by-products in India is about 200 million tons [20]. From quarry locations, mined boulders and blasted rocks are hauled into a crusher bin and fed to crushers [18]. However, because there was not enough water for the pozzolanic reactions between the soil and lime, adding too much lime had a negative impact on the strength of the soil. According to [21], cement kiln dust by itself is insufficient for efficient soil stabilization.

Due to its significant location on the southern border of the Kingdom of Saudi Arabia, its large diversity of economic resources (Najran granite, industrial aggregates), and the current rapid expansion of civilization, the Najran area is a significant region in Saudi Arabia. The idea of conducting research to address difficulties that had arisen in the community as a result of the recent spreading of civilization in the area was significantly motivated by the establishment of Najran University in the city of Najran ten years ago. The foundation bed often consists of silt and clay. Many authors have conducted geotechnical studies for a variety of reasons, such as characterizing geohazards [22–24], identifying geotechnical parameters [25], and delineating subsurface rock types, weak zones, and/or

clay layers. Significant amounts of industrial by-products (CACW) have also been produced as a result of industrialization.

They considered producing soil amendment material from some of the leftover coal. However, based on our observations, inter-sectoral cooperation has already helped the South African mining industry make rather efficient use of the recovered resources across the varied variety of ores that frequently contain many distinct metals [26] presented their attempts at using quarry wastes as fertilizer for growing tea crops. Moreover, [27,28] decomposed and eliminated organic and inorganic waste in soils through the vermicomposting process using earthworms. To adhere to environmental regulations, a lot of resources are used to dispose of the garbage. As a result, it is necessary to evaluate an alternative option for using waste products to improve silty sand soil. These options can meet the demands of both the economy and the environment. Although some research has been conducted to determine whether cement could be used to stabilize poor soils all over the world, more studies are required to determine whether these industrial by-products could be used to stabilize soil. In addition, there is a great need to reduce cement use through the efficient use of industrial waste products to lessen the greenhouse effect and environmental issues. The research above shows that silty sand soils are extremely variable materials with a reduced "natural" strength capacity, which causes a number of construction challenges when used [29] considered the processing of several minerals and materials found in soils and used by various companies in various parts of the world in 2022.

The primary purpose of this research is to investigate the potential of reusing CACW to enhance the geotechnical properties of silty sand soil in the Najran region.

2. Research Methodology

The goal of this study is to determine how to improve the geotechnical properties of the silty sand soil that is readily available in the Najran area for use in road applications by reusing coarse aggregate crushing waste (CACW). The process used to accomplish this goal is divided into four stages: (i) material collection and characterization; (ii) laboratory experimentation; (iii) analysis of the laboratory test results and comparison of the results with native soils and (iv) research on the materials' durability and environmental effects (Figure 1).

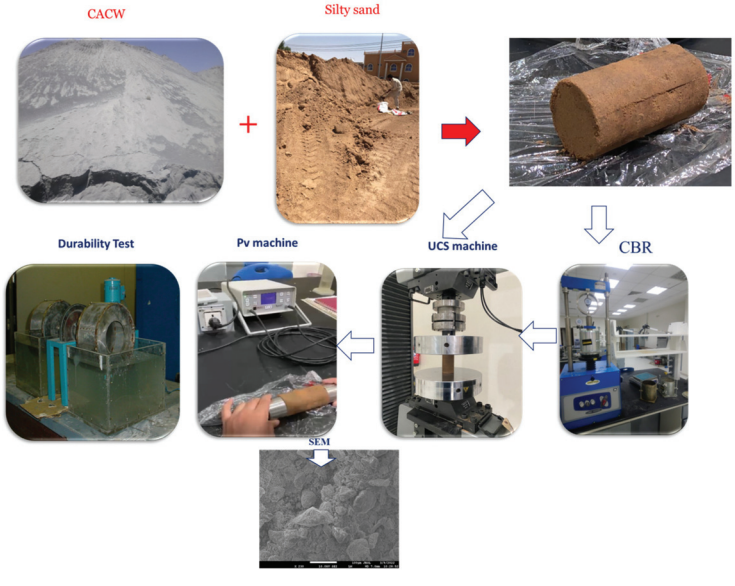

Figure 1. Diagram illustrating the experimental work.

3. Experimental Work

3.1. Materials

Samples of silty sand soil were collected from a location located in Najran City, Kingdom of Saudi Arabia. The methodology for collecting soil samples and conducting laboratory experiments for characterization consists of two stages. The first stage includes collecting two bags weighing 50 kg from a site on King AbdulAziz Street close to Jareer Library and then transporting them to the soil laboratory in the civil engineering department at Najran University. This quantity is considered sufficient to construct three lab samples for each designed mix. In the second stage, the soil was first air-dried for seven days in the open air before being properly blended for homogeneity. It was then pulverized with a plastic hammer and sieved with an ASTM sieve No. 4 after that. Finally, the crushed soil was oven-dried for 48 h at 70 °C to ensure moisture content elimination and then kept in a closed barrel until testing. The samples were then subjected to basic characterization such as grain size distribution, specific gravity, and Atterberg's limits. The CACW stabilizer samples were collected from coarse aggregate crushing quarries located in Habuna governorate (about 63 km from Najran city) in the Najran region and subjected to grain size analysis and specific gravity determination as well. The CACW samples were taken from the same quarries as the aggregates. There is a huge amount of silty sand soil in Saudi Arabia and all over the world, so similar laboratory tests can be applied. Table 1 summarizes the Chemical composition of the stabilizer.

Table 1. Chemical composition of CACW.

Element	Composition Range (%)
SiO2	45–77
Al_2O_3	15–20
CaO	3–15
Fe_2O_3	6–16
K_2O	3–5
MgO	1–4
Na_2O	0–3
P_2O_3	0–0.04
TiO_2	0–2.33

3.2. Soil Characterization

To examine the engineering characteristics and mineralogical phases of the soil specimens from the Najran area (Figure 2), primary characterization studies were carried out in accordance with ASTM standards. Specific gravity, Atterberg limits, and grain size distribution were used to classify the soil during the preliminary studies. The mineralogical composition of the soil was further assessed using XRD (X-ray diffraction) and SEM (scanning electron microscopy). According to [30], the specific gravity was calculated. A pair of "disturbed" specimens were used in the experiment and each specimen was put through ASTM sieve No. 4 before being used. The specific gravity was calculated using the average of both specimens. On specimens passing ASTM sieve No. 40, liquid and plastic limits were evaluated using [31]. All soil specimens were subjected to the [32] grain size distribution test.

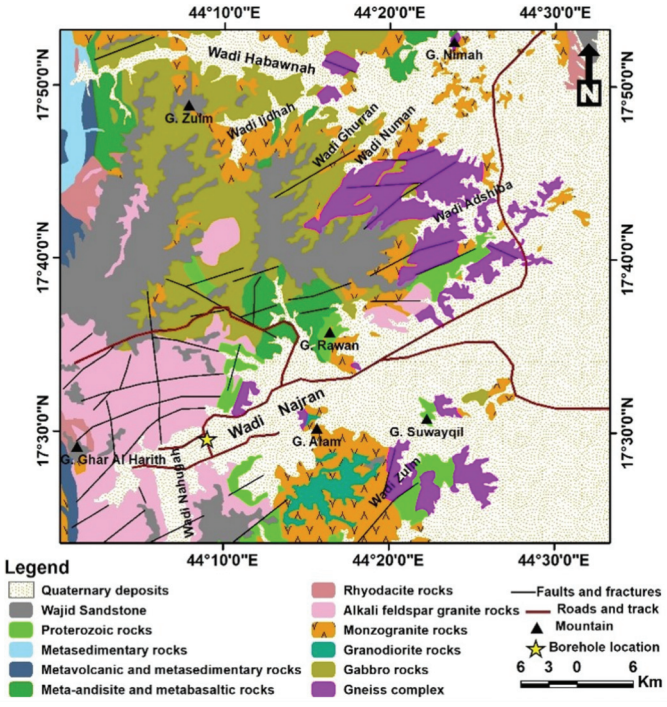

Figure 2. Geologic map for the study area modified after [33].

According to [25], a material's mineralogical distribution can be used to anticipate how it will behave and react in different situations. The mineralogical investigation employed only ten grams of the examined soil. The mineralogical compositions of the soil specimens were determined using SEM with Field- Electron (Tescan Lyra-3) and Powder X-ray Diffraction techniques (Ultima IV). The secondary electron mode was used for SEM. Before the experiments, the samples were covered with gold (Au) to boost their conductivity. In addition, the elemental compositions of the soil were measured using a dispersive energy X-ray (EDX) test and a scanning electron microscope (SEM) for all samples. Scanning electron microscopy (SEM) can be used to analyze the microstructural characteristics and the elemental composition of the carbonate samples, according to [28].

Soil specimens were ground into a powder using an agate mortar pestle for XRD examination. The specimens were then compressed into sample holders and inserted into the apparatus for examination. The powder method of X-ray diffraction is utilized, and the Powder XRD Ultima IV is the brand and model of the equipment used.

The sample's crystals are organized in an arbitrary manner. A monochromatic (of a single wavelength) X-ray beam strikes a crystal. X-rays that hit the parallel surfaces that make up the crystal will reflect at an angle because of this, as shown by Miller indices (jkl). A series of reflections can be seen, depending on the type of minerals in the soil. The crystals in the sample are arranged in a random pattern. By comparing the intensity and angle of incidence with those of standard minerals, it is possible to determine the type and number of minerals present in the sample. The diffraction pattern is contrasted with normative diffraction patterns created by the Joint Committee of Powder Diffraction Standards (JCPDS) for various stages.

3.3. Tests and Methods

The procedure used to design soil-CACW mixes with or without containing 2% cement was as follows: A Hobort mixer with a capacity of 0.3 m^3 was filled with the necessary

amount of soil. The percentage of CACW (5%, 10%, 15%, and 20%) by the dry weight of the soil sample was added to the mixer. In the case of adding cement, 2% of Portland cement was added to the dry weight of the soil sample. Finally, the percent of water content determined by the dry weight of the soil samples was added, and the mixer was operated continuously to obtain a homogeneous mix after about three minutes of mixing.

To evaluate the designed mixes of silty sand soil with various percentages of CACW additive for road construction, specified mechanical tests should be followed. First, the mixes were subjected to a modified Proctor compaction test in order to obtain the optimum percentage of CACW and attain the maximum dry density. Thereafter, the mixes were further examined using ultrasonic pulse velocity (UPV), unconfined compressive strength (UCS), and the California bearing ratio (CBR) test. Following the trend of the results of these tests, we can conclude that the best percentage of CACW enhances the geotechnical engineering properties of silty sand soil. Based on the results of previous tests, the passed mix will continue to be subjected to the durability test. The advantages of these tests are that they can give a clear picture of the long-term engineering performance of the mixes of CACW-silty sand soil in the pavement structure as a material in the subbase or subgrade layers. The following sections briefly describe the procedure of each test.

3.3.1. Modified Proctor Compaction Test

The aim of the compaction test is to identify compaction-related parameters, particularly the optimal moisture content at which the soil reaches its maximum dry density. For a certain compaction technique, this test illustrates a link between dry density and water content. Several compaction testing methodologies are employed, depending on the grain size distribution of the soil material. As seen in the example below, the study employed the modified Proctor compaction test [34]. The procedure used to compact soil-CACW mixes containing 2% cement was as follows: A Hobort mixer with a capacity of 0.3 m^3 was filled with the necessary amount of soil. The finished result was homogeneous after about three minutes of mixing, during which water was added. The modified Proctor compaction test's large mold was compacted at five levels. There were 25 blows per layer. Triple specimens were used and tested under each condition, and the average of the results was reported.

3.3.2. Ultrasonic Pulse Velocity (UPV)

In line with [35], measurements of ultrasonic pulse velocity (UPV) were made to assess the homogeneity and structural integrity of diverse compacted soils. The longitudinal wave velocities were calculated using the pulse transmission method, which entails connecting two piezoelectric sensors positioned on opposite faces of a sample with a diameter of 6 cm and a length of 12 cm. The velocity of the ultrasonic waves was determined using a standard meter (Matest Company located in Italy). A viscoelastic gel was added to the sample's flat surface. The samples were positioned between the transmitter and receiver, and until a constant velocity was measured, the faces of the transducers were firmly pressed against the compacted dirt samples. The UPV is measured using the pulse transmission method using a Panametrics Pulser-Receiver (Model 5058 PR) and an Agilent DSO-X-2014A Digital Storage Oscilloscope (100 MHz) manufacturered by Matest Company, Treviolo, Bergamo, Italy. Triple specimens were used and tested under each condition, and the average of the results was reported.

3.3.3. Unconfined Compressive Strength (UCS)

The UCS test is performed to find the undrained shear strength and stress-strain features of undisturbed, remolded, and/or compacted specimens. This test is appropriate for soils with some cohesiveness, as long as the sample is not allowed to expel water while being loaded. After eliminating the restriction provided by the mold walls for compacted samples, the soil sample must preserve its intrinsic strength. The preferred test for determining the strength of soils is the unconfined compressive strength (UCS) test. This test is normally performed using an unconfined compression machine with a variable

maximum load. The UCS test is conducted in accordance with [36]. The UCS test is usually carried out for a period of 1, 3, 7, 14, 28, 90, and so on to track the influence of alterations in the mineralogical composition of stabilized products as time and environmental exposure increase. In this research, no treatment stabilizers are used, so we performed our test after 7 days for all types of soil samples. As recommended by [36], samples utilized in this study with a height-to-diameter (h/d) ratio of 2 were taken from a cylindrical mold with a height of 4 in. (101.6 mm) and a diameter of 2 in. (50.8 mm). The split-type mold was utilized to ensure that the samples extruded were as perfect as possible, as were the edges of the specimens. Triple specimens were used and tested under each condition, and the average of the results was reported.

3.3.4. California Bearing Ratio (CBR) Test

In the structural design and assessment of pavements, the California Bearing Ratio (CBR) of the materials used in the base and sub-base courses has been widely used. Because of its simplicity and usefulness, the exam is well-known around the world. As a result, the test can be easily adapted by engineers to assess materials for use in road construction and to experimentally determine the soil strength under regulated water content and density circumstances. In this test, the force necessary for a standard-area plunger to pierce a soil sample is determined. The pressure that must be applied to pierce a standard layer of crushed rock at the same depth is divided by the measured pressure. The ASTM Standard [37] outline the CBR test for laboratory-prepared specimens. Soaked CBR tests were carried out in this study in accordance with [37] to imitate field situations in which the soil is flooded with water, which can come from either groundwater or rainwater permeating the layers. All of the soil specimens were subjected to soaking CBR tests, similar to UCS testing, to determine their CBR correlation with the P-wave results. Triple specimens were used and tested under each condition, and the average of the results wasreported.

4. Results and Discussion

4.1. Characterization of Soil and Stabilizer

CACW's external characteristics vary depending on the topography. CACW exhibits mineralogy and morphological changes when analyzed using scanning electron microscopy (SEM) and X-ray diffraction. Magma is the source of the intrusive igneous rock known as granite. Its main colors are white, pink, or gray. Minerals, including feldspar, quartz, mica, and amphibole, are the major components of these rocks. Depending on the region, the CACW produced by aggregate crushing plants and granite quarries has a different physical appearance. Plants for crushing aggregate produce CACW. The majority of fines are classified as fine aggregate with a particle size less than 4 mm in diameter and pass through the No. 200 screen. The chemical makeup of CACW is a significant material property that is essential to stability. Location, rock formation, and type of rock accessible all affect how it varies.

4.1.1. Composition of CACW

The composition of a CACW is shown in Table 1, which gives an approximation of the amounts of different chemical components [38].

4.1.2. Grain Size Distribution of Soil and CACW

Through a series of geotechnical tests, including specific gravity, Atterberg limits, and sieve analysis, the fundamental geotechnical characterization of the soil employed in this study was determined. According to the results of the specific gravity test, the soil has a value of 2.67. Contrarily, the findings of the Atterberg test indicate that the soil is non-plastic, which prevents us from rolling it to a thread with a diameter of 3.18 mm and from calculating the number of blows required to reach the liquid limit. The findings of the sieve analysis are shown in Figure 3. According to the figure, 2.3% of the soils pass through

sieve No. 200, and these soils are categorized as silty sand "SM" according to USCS and A-3 as well as the AASHTO soil classification system.

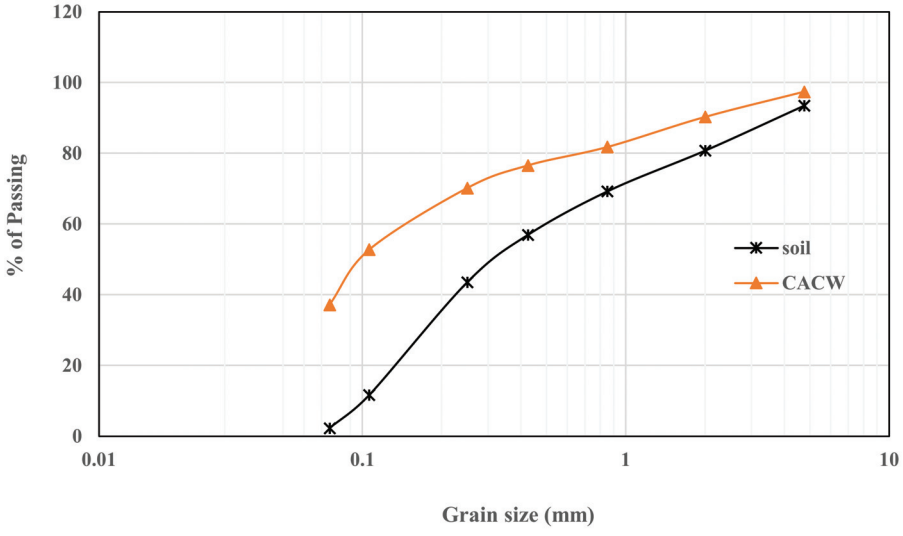

Figure 3. Chart of grain size distribution of soil and CACW.

4.1.3. CAWA as a Sustainable Material

CACW is taken from the foreshore using a process called "waste mining". Globally, mining produces between 47 and 59 billion tons of material. The use of CACW in a building leads to unacceptably large-scale waste mining, which is a result of the expansion of development activities. The sources of distinctive sand that are still present are running dry. High-quality sand may be transported over long distances, which has an impact on the economy. Therefore, a partial or complete material replacement is necessary to maintain the structural quality. The industry has financial and environmental costs as a result of the massive volume of CACW that is dumped. The excessive mining of river sand, which has negative environmental implications, can be avoided by using CACW [39]. Some geotechnical applications for CACW include embankments, backfills, materials for paving roads, fillers for underground cavities, materials for barrier walls, and sub-base.

4.2. Effect of CAWA on the Geotechnical Properties

4.2.1. Modified Proctor Compaction Test Results

The maximum dry density (MDD) values of the CACW-soil mixes with the addition of 2% cement were in the range of 2.123–2.256 g/cm^3, as shown in Figure 4. Considering the effect of CACW on the maximum dry density, it was observed that the effect of CACW on the maximum dry density was significant. The maximum dry density increased from 2.123 for plain soil to 2.174 and 2.256 g/cm^3 for the 5 and 10% addition of CACW, respectively. Thereafter, the maximum dry density decreased to 2.231 and 2.211 g/cm^3 with the further addition of 15% and 20% of CACW, respectively. This means that the addition of 10% of CACW filled the soil voids and enabled the production of extra-dense samples with robust strength characteristics, while at 10 and 20% of CACW, a decrease in the maximum dry density of the mix was detected (Figure 4).

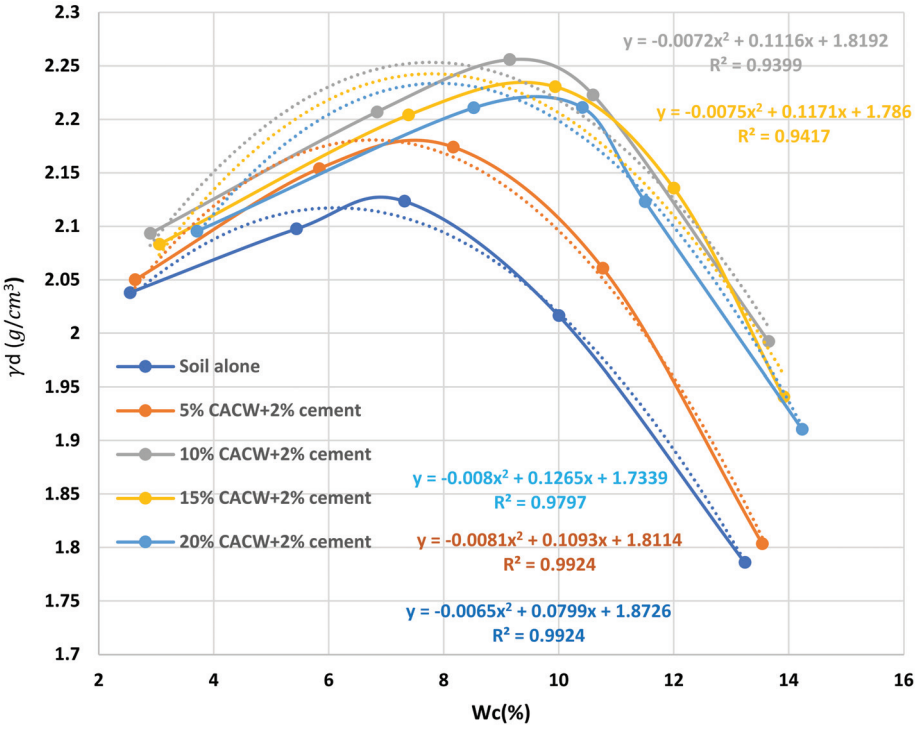

Figure 4. The relationship between dry density and moisture content of soil−CAWA−2% cement mixes.

The high concentration of CACW, which was more than that required to fill the pore space in the soil-CACW mixture, may be responsible for the reduction obtained with 15 and 20% CACW. The density of samples did not improve as the WMD proportion rose above 10%. Instead, a decrease in the sample density was found.

The influence of CACW content with 2% cement addition on the optimal moisture content (OMC) and the maximum dry density (MDD) is shown in Figure 5. The data in the figure clearly show that the increase in CACW percent was predominantly associated with an increase in the OMC. Due to the large surface area of CACW particles (i.e., high fineness) compared to soil; this behavior is expected, as it raises the water demand and, as a result, increases the optimal moisture content [40] (Figure 5).

According to the dependencies shown in Figures 4 and 5, mathematical models for calculating and predicting the output parameters under consideration, which can be obtained in the course of regression analysis, are given as follows:

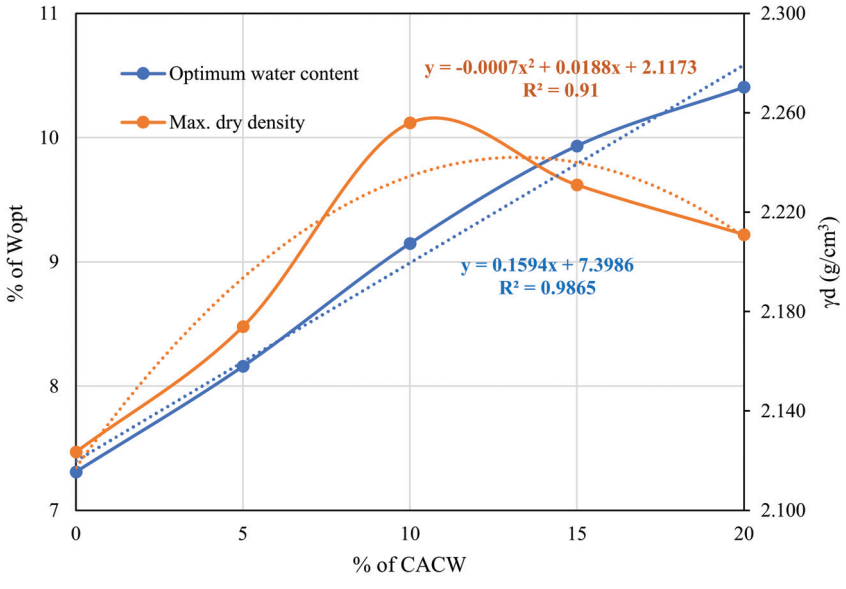

Figure 5. Impact of adding CAWA on the optimum moisture content and maximum dry density.

Y denotes the maximum dry density and x denotes water content in Figure 4;

$$\text{For soil alone } y = -0.0065x^2 + 0.0799x + 1.8726 \; R^2 = 0.9924 \quad (1)$$

$$\text{For soil + 5\% CACW + 2\% cement } y = -0.0081x^2 + 0.1093x + 1.8114 \; R^2 = 0.9924 \quad (2)$$

$$\text{For soil + 10\% CACW + 2\% cement } y = -0.0072x^2 + 0.1116x + 1.8192 \; R^2 = 0.9399 \quad (3)$$

$$\text{For soil + 15\% CACW + 2\% cement } y = -0.0075x^2 + 0.1171x + 1.786 \; R^2 = 0.9417 \quad (4)$$

$$\text{For soil + 20\% CACW + 2\% cement } y = -0.008x^2 + 0.1265x + 1.7339 \; R^2 = 0.9797 \quad (5)$$

Similarly, y represents the maximum dry density, and x represents the CACW percentage in Figure 5:

$$y = -0.0007x^2 + 0.0188x + 2.1173 \; R^2 = 0.91 \quad (6)$$

where y represents the optimum water content of the mix and x represents the CACW percentage in Figure 5 as well:

$$y = 0.1594x + 7.3986 \; R^2 = 0.9865 \quad (7)$$

4.2.2. Ultrasonic Pulse Velocity (UPV)

After 7 days of curing, UPV tests were conducted on four separate samples (i.e., 0, 5, 10, 15, and 20% of CACW). The CACW had a substantial influence on the improvement in ultrasonic pulse velocities, as seen in Figure 6. It can be shown that samples with

10% CACW had greater UPV values than those with other CACW fractions; however, specimens with 15% and 20% CACW had a slight decrease in UPV values. The sample with 10% CACW in the soil mixture performed better than the other mixes in terms of UPV. This finding is consistent with the research's earlier findings. The maximum UPV values were found at 10% of CACW due to the highest maximum dry density at the same percentage as indicated in the previous section. The improvement in UPV values is seen as a respectable indication of good densification in the soil-CACW mixture, particularly with 10% CACW and the soil-5% CACW-2% cement mixture as well. Greater UPV values are another excellent sign that the specimen's structure has been homogenized, as this enables the applied waves to pass through the specimens more quickly and leads to greater UPV values. CACW, a finely graded granular material, has demonstrated its capability to operate as a good filler material by producing well-homogeneous mixtures and increasing particle bonding. Figure 6 shows that specimens with CACW greater than 10% had lower UPV values than those with 10% WMD. This demonstrated that 10% CACW is the ideal proportion for filling the pore space in the specimen and maintaining the continuity of the grain-to-grain connections.

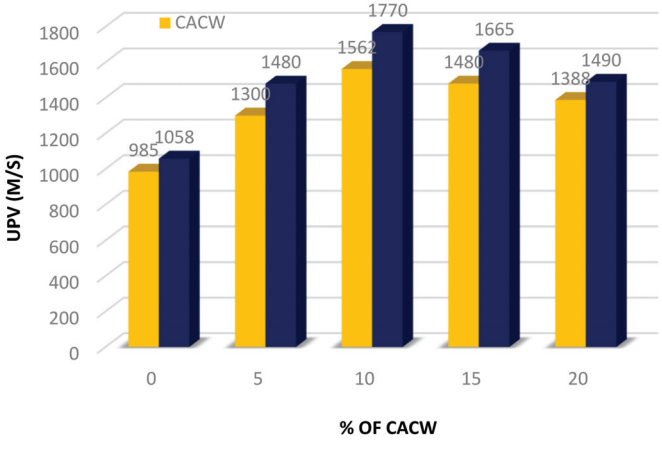

Figure 6. Effects of the addition of CACW on Ultrasonic pulse velocity at different mixes of CACW.

As stated before, with a 10% CACW replacement, the specimens' maximum dry density was increased, and the ultrasonic pulse velocity of the mixtures was increased. This was owing to the mixtures' more homogeneous and uniform structures, which hastened the passage of ultrasonic waves in the mixtures, resulting in higher UPV values. The extra amount of CACW in the combination caused a more porous structure, which resulted in a reduction in the UPV of the specimens with a further increase in CACW replacement (Figure 6). The same trend is observed with a higher value of ultrasonic pulse velocity, as seen in Figure 6 when 2% cement is added to the mix.

4.2.3. Results of California Bearing Ratio (CBR) Tests

It is critical to obtain CBR values for the materials used in a subgrade of pavement structure or subbase layer in order to evaluate their effectiveness under traffic loading. Soaked CBR tests on specimens of silty sand soil treated with varying proportions of CACW were undertaken to imitate the poorest field circumstances. The experiment was conducted three times, and the average is shown in Figure 7. From the figure, it is clear that when 10% of CACW is added, the CBR value increases from 21% to 40%. When the percentage of CACW increased to 15%, the CBR value dropped from 40% to 25%. The value of the CBR has dropped by roughly 37.5 percent. Additionally, the decrease in CBR value, which went from 25% to 18% when CACW addition increased from 15% to 20%, is strongly connected

with the rise in CACW percentage. This is because when CACW concentrations rise, more water is absorbed during the soaking phase, leading to an increase in fine materials, which in turn, causes a loss in strength and consequently lower CBR values. The same trend is observed with a higher value of CBR, as seen in Figure 7 when 2% of cement was added to the mix. It is worth noting that during the soaking period, the swelling was tracked and recorded, and the results showed that the soaked CBR specimens had no swelling. It can be deduced that adding 10% CACW with 2% cement to the soaked CBR value produced the greatest value, i.e., 60% and that it may be utilized as a subbase layer in the construction of high-traffic loading highways in compliance with standards. The process of filling and densification introduced by 10% CACW in the soil structure provides this strength, as seen in Figure 7. As one can see, the CACW powder acts as a void filler, forming a dense structure beneath the loading plunger of the CBR machine; furthermore, since its ratio is low (10%), water absorption is also low, enhancing the soil-CACW mixture's resistance to penetration and resulting in a higher CBR rating of 40%, which reached 60% when 2% of cement was added to the mix.

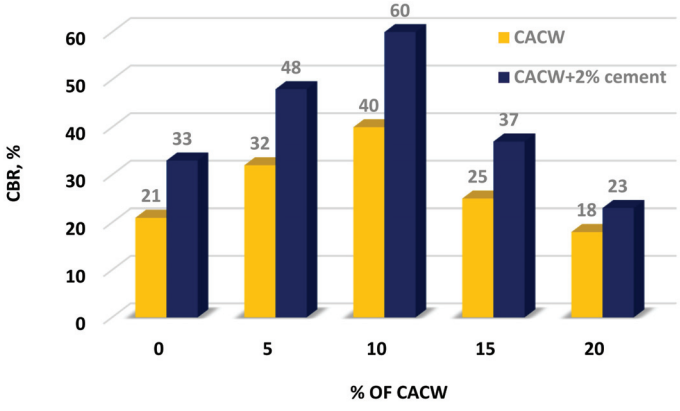

Figure 7. Effect of addition CACW on the soaked CBR value.

4.2.4. Results of Unconfined Compression Strength Tests

The specimens underwent an unconfined compression test to ascertain their compressive strength after 7 days of curing. As demonstrated in Figure 8, the addition of CACW to all mixes produced results that were better than the UCS value of the control specimen (soil only). With 10% CACW substitution, the greatest UCS value was attained. Figure 8 demonstrates that, in comparison to UCS values achieved with 10% CACW replacement, CACW replacement at a higher percentage than 10% led to lower UCS values. After a 7-day curing period, the UCS values of the specimens treated with 0, 5, 10, 15, and 20% CACW were 430, 735, 897, 827, and 795 KPa, respectively. The optimum concentration of CACW required to improve the compressive strength of the combinations was 10%. This suggested that for completely filling the pore space and producing efficient soil-binder reactions, 10% CACW with 2% cement is the optimal dosage. At a proportion above this cutoff, CACW completely fills all pore spaces, and extra CACW congregates on the grains in soil-binder mixtures. As a result, the amount of contact surface area required for chemical reactions was reduced. The same trend is observed when 2% cement is added to the soil-CACW mixes with higher values of UCS. The UCS values of the specimens treated with 0, 5, 10, 15, and 20% of CACW in addition to 2% of cement were 680, 1035, 1390, 1120, and 1090 KPa, respectively, after a 7-day curing period. These results are consistent with those obtained earlier from UPV and CBR tests. Figure 8 depicts the impact of various CACW percentages on UCS, and as can be observed from the graph, 10% CACW resulted in the greatest UPV and UCS values, as previously reported. When the CACW percentage was 10% higher than expected, both the UPV and the UCS values decreased.

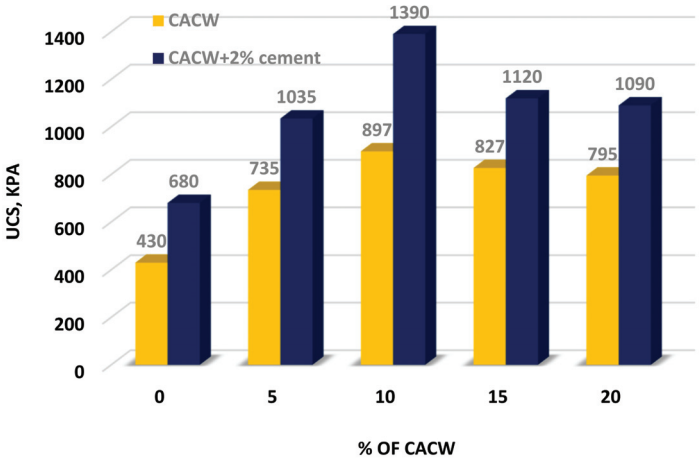

Figure 8. Effect of CACW addition on UCS.

In the construction of rigid pavement, the USA Army Corps of Engineers (USACE) has recommended a minimum 7-day qu of 1380 kPa (200 psi) for subbase and subgrade and 3450 kPa (500 psi) for base course layers, according to the ACI Committee 230 Report [33]. However, these values are 1725 kPa (250 psi) and 5175 kPa (750 psi), respectively, for the construction of flexible pavement. Based on this criterion, only soil mixes with 10% CACW and 2% Portland cement pass the ACI requirements for use in subgrade and subbase layers in rigid pavement construction. Thereafter, this mix (soil-10% CACW-2% cement) will be further evaluated for durability criteria.

The *p*-values and statistical results that support the trends described in Figure 8 are shown in Table 2. Based on the statistical results presented, it is seen that the differences are statistically significant since the *p*-values are very small compared to the reference *p*-value (i.e., 0.05). This indicates there is significant evidence against the null hypothesis.

Table 2. *t*-test: Paired two samples for means for UCS results.

% CACW		2% C + CACW
Mean	736.8	1063
Variance	32,829.2	64,595
Observations	5	5
Pearson Correlation	0.959028	
Hypothesized Mean Difference	0	
df	4	
t Stat	−7.64721	
P (T <= t) one-tail	0.000786	
t Critical one-tail	2.131847	
P (T <= t) two-tail	0.001571	
t Critical two-tail	2.776445	

4.3. Developed Research Methodology

Based on the research results shown in Figures 6–8 a method of introducing CACW-stabilized soil comprises the steps:

1. Introducing the CACW additive with the optimum percentage of CACW, i.e., 10%, that shows the highest values of UPV, CBR, and UCS in the dry silty sand soil.
2. Adding the corresponding optimum water content (9.2%) and operating the mixer such that a CACW-soil mix forms.

3. Introducing the Portland cement (2%) into the mixer and operating the mixer such that the cement-CACW stabilized soil forms.
4. Constructing specimens for durability tests and microscopic investigation
5. Comparing the results with the rigid and flexible pavement layer structure requirements and making a decision.

5. Durability Tests (Wetting and Drying)

Temperature and moisture can cause cycles of wetness and dryness, or freezing and thawing. To withstand physical stresses under cyclical environmental loading and various exposure situations, stabilized soils must be robust and sustain stability and durability. The water table's rise and fall, agricultural water use, septic tanks, leaks from surrounding utilities, and seasonal variations in rainfall all contribute to these soaking and drying cycles. These circumstances subject the stabilized soils to tensile and compressive stresses, which cause weight loss and/or volume change [41]. In this study, the durability of stabilized soils was evaluated using the proposed slake durability test and the standard [42,43]. The salke test was initially utilized for rock testing, but [44] recently adapted it to handle stabilized soil specimens of particular sizes. Triple specimens were used and tested under each condition, and the average of the results was reported.

5.1. Standard Durability Test [42]

For durability tests, silty sand soil samples stabilized with 10% CACW and 2% cement were created. The mold was 4 in. (101.6 mm) in diameter and 4.6 in. (116.8 mm) in height for the soil samples. Each specimen underwent six stages of compression to achieve its modified Proctor's maximum dry density. To attain the modified Proctor's maximum dry density, fewer blows were required. 39 strikes were determined to be the appropriate number after numerous tests were conducted for each layer. All samples were extruded from the molds after compaction. For each blend, four samples were created. These samples were chosen to indicate weight loss in two cases and volume change in two additional cases. The volume change samples' height and diameter were noted. At 23 °C and 100% relative humidity in the lab, all samples were cured for seven days. The samples were moved to an oven and held there for 42 h at 71 °C after spending five hours at room temperature in a water tank. For stabilized soils, this procedure equals one cycle of wetting and drying. At the end of this cycle, the specimens designated for volume change were weighed and dimensioned using a vernier caliper. The other two specimens were brushed with a standard brush with two strokes and a force of about 3 Ib (1.36 kg). To apply the 3 Ib. (1.36 kg) force, each sample was balanced on a balance, and it was brushed while being observed on the balance scale. Weighing the samples both before and after brushing was performed. The remaining 11 cycles were measured similarly, subjecting each specimen to 12 cycles in accordance with [42]. At the end of each cycle, the respective specimens' weight reduction and volume change were noted. After 12 cycles, the samples were dried at 110 °C to a constant weight. The two equations below [42] were used to compute the volume decrease and weight reduction as a result:

(1) Change of Volume (V_c):

$$Vc\ (\%) = \left[\frac{Vi - Vf}{Vi}\right] \times 100 \tag{8}$$

(2) Weight loss (W_l):

$$Wl(\%) = \left[\frac{Wi - Wf}{Wi}\right] \times 100 \tag{9}$$

In which, Vc is the change in sample volume after n cycles; Vi = the first volume of the sample (cm^3); Vf = the last volume of the sample (cm^3), whereas W_l = the loss of weight of

the sample after *n* cycles; *Wi* = initially computed oven-dry weight and *Wf* = last adjusted oven-dry weight.

It is also significant to note that the oven-dry weight was altered, and this weight may now be determined using the following equation [42]:

$$\text{Oven-dry weight adjusted} = \text{C/D} \times 100$$

In which C is the weight after drying in an oven at 230 °F (110 °C), D is the percent of water left on the sample plus 100.

5.2. Durability Using Slake Test

This test's primary objective is to determine how durable rocks are [43]. A 500-g sample of rock particles is weighed in a drum with a 2-mm stainless steel screen. The drum has a diameter of 140 mm and a length of 100 mm. 20 revolutions per minute are used to rotate the drum while it is half submerged in water. The amount of weight lost after 10 min of spinning indicates how durable the rock is. For the stabilized soil samples used in this investigation, this test was adopted and modified [44,45]. The drum was resized to 152.4 mm (6 inches) in length and 304.8 mm (12 inches) in diameter. The number of revolutions was altered to account for the change in dimensions so that the soil samples could go the same distance as the stone part in the first examination. Instead of 10 min, the revolution duration was cut to 4.6 min. A total trip distance of 88 m under the revised setup would be comparable to the original test. Figure 8 depicts the setup for the slake durability test.

Two additional samples were compacted using 10% CACW and 2% cement. These samples underwent the same wet and dry rounds as the materials tested using the [42] durability test when they were evaluated using the modified Slake durability apparatus. Before being weighed, the sample's surface was cleaned using a dry absorbent towel after slaking. It was possible to determine the weight reduction for each sample by comparing the weight before and after each cycle of laziness. After 12 cycles, the specimens were dried in the oven at 110 °C to determine the amount of volume change and loss of weight using the [42] formulas that were previously discussed.

5.3. Durability Test Results

The two durability tests' results show that for the [42] and slake tests, respectively the average weight losses of the evaluated mixes after 12 cycles are 8% and 10%. The findings demonstrate that the highest weight loss for the combinations did not go above the 14% maximum allowed weight loss for cement-soil mixtures specified by the [46]. A comparison of the durability test results showed that, for all the evaluated samples, the amount of weight drop recorded by the slake durability testing was consistently greater than the one obtained by [42]. This conclusion is consistent with findings made public by [6,35]. Figure 9 shows the durability tests for specimens and used equipment. The underlying mechanism for the improved durability is attributed to the high-density mixtures formed using a 10% CACW additive, which plays a filler role in the mix voids and increases the interlocking of the soil grains, which in turn increases the shear strength of the CACW-silty sand mixes. This result confirms the trend obtained through the previously mentioned tests (i.e., compaction, UCS, UPV, and CBR). Moreover, the microscopic analysis shows the dense mix formed at 10% CACW additive.

The quantitative statistical analysis of the durability results is presented in Table 3. The *p*-values and statistical results support the significant differences between the two test methods. Based on the statistical results presented, it is seen that the differences are statistically significant since the *p*-values are very small compared to the reference *p*-value (i.e., 0.05). This indicates there is significant evidence against the null hypothesis.

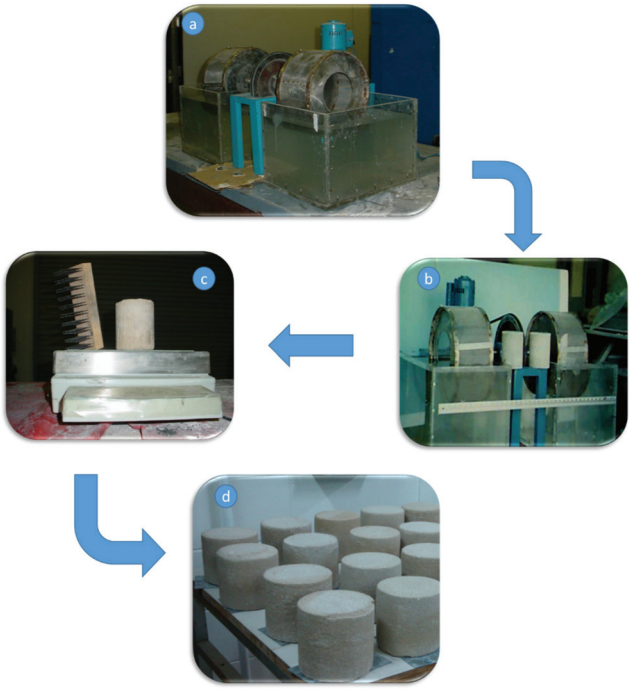

Figure 9. Durability using Modified Slake test: (**a**,**b**) slake test machine, (**c**) specimen with standard brush (**d**) speciemns after testing [44,45].

Table 3. *t*-test: Paired two sample for means for durability test results.

	Standard Durability of Soil + 10% CACW + 2% C	Slake Durability of Soil + 10% CACW + 2% C
Mean	8.333333	10
Variance	1.166667	0.9
Observations	6	6
Pearson Correlation	0.634335	
Hypothesized Mean Difference	0	
df	5	
t Stat	−4.66252	
P (T <= t) one-tail	0.00276	
t Critical one-tail	2.015048	
P (T <= t) two-tail	0.00552	
t Critical two-tail	2.570582	

5.4. Microscopic Investigation

By using an SEM Hitachi S 3700, the morphology of the silt and soil and admixtures was examined. With reference to Figures 10 and 11a–e, it is evident from the micrograph that silty sand, lime, and stone dust underwent pozzolanic reactions, resulting in stone dust and lime particles accumulating over the silty sand soil and generating the various cementitious compounds.

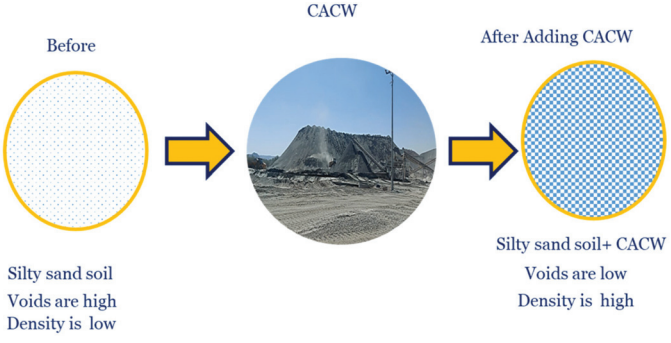

Figure 10. Effect of CACW addition on voids and density.

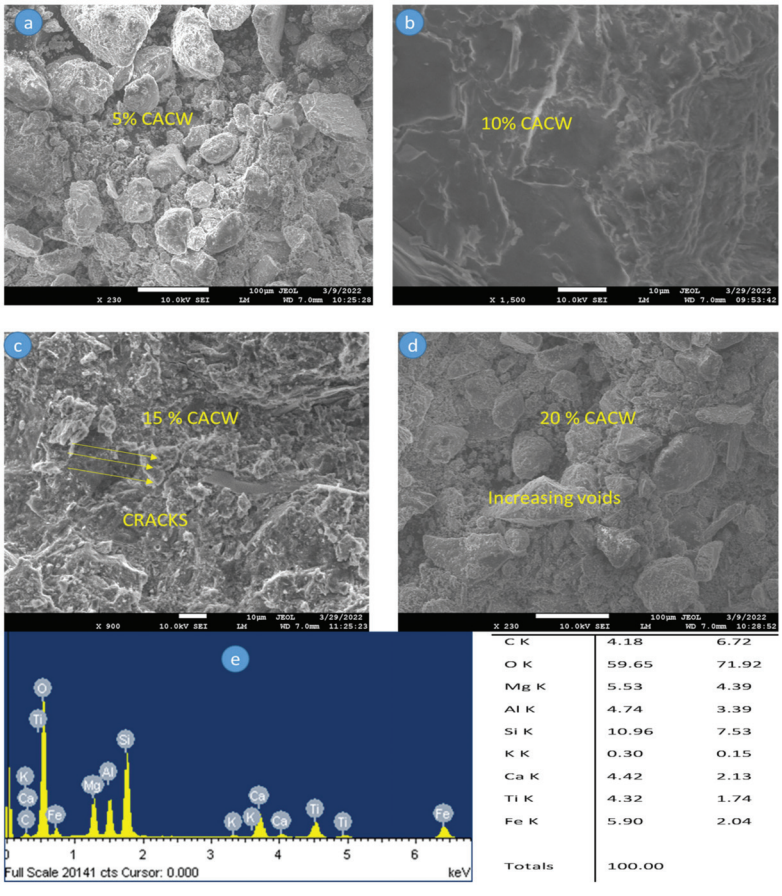

Figure 11. (**a**–**d**): SEM images illustrating the effect of CACW addition at 5, 10, 15 and 20%, respectively, (**e**) is EDX to illustrate the composition of soil and CACW, yellow arrows refered to minor cracks at 15% of CACW.

The SEM micrograph of silty sand soil stabilized with the optimal dose of 10% CACW and 2% cement in Figure 11b shows a significant amount of the white fibrous cloth-like cementing gel, C-S-H, coating the sand and/or silt particles. This improved the UCS of the stabilized silty sand soil. The system contains discrete sand and/or silt grains. Both direct

interactions between particles and connectors are visible. The stabilized soil matrix had weight proportions of 4.18, 5.53, 10.96, 4.42, 0.30, and 5.90% for C, Mg, Si, Ca, K, and Fe, according to EDX results.

To keep soil stable, various fundamental stabilizing mechanisms are in operation. The direct cementitious effects of Portland cement strengthen sandy materials since they are less plastic and volumetrically unstable (as measured by their bearing capacity, unconfined compressive strength, etc.). In this case, the main reaction takes place when the C_3S and C_2S in cement combine with water to form calcium silicate hydrate. Cementation is considerably enhanced by the concentration of available alkali in solution [47]. By combining soil, cement, and water, cement stabilizes soils [12]. The size has been reduced. The resultant mixture is a novel building material that is heat, water, and frost resistant. Stabilized soils can be used for canal lining, building foundations, road paving, and other purposes.

The two most important phases for stabilizing soil are the calcium silicate phases (C_3S and C_2S). These two phases aid in the formation of calcium silicate hydrate, or C-S-H, which acts as a binder in the soil matrix. By making calcium available for cation exchange, flocculation, and agglomeration when those phases are hydrated, calcium hydroxide stabilizes the clayey soil [17,48]. Everywhere soil is used to make pavements, it is first dumped in a loose state and then compacted using rolling or vibrating machinery until the required amount of compaction is obtained. A technique for controlling soil compaction on the site is provided by field moisture-density tests. The soil's field compaction is the sole purpose of the moisture-density test. The assumption is that a soil's stability increases along with its dry density.

5.5. Environmental Impact Evaluation

In the building business, sustainability has been emphasized in terms of the substitution of natural materials with waste or ecologically friendly resources. The construction sector, which may need to deploy cost-cutting and green products, may profit from this work. In addition to conserving currently used resources, the usage of these abundantly available waste materials will help mitigate their possibly harmful environmental effects. CAWA is a wonderful material that is sustainable and has a low embodied energy level. For a particular scenario, a reduction in the consumption of locally available resources equals an offset to the quantity of CO_2 generated as a result of adding CACW to native soil. As a result, adding CAWA reduces the carbon footprint values, making this treatment strategy nearly carbon neutral.

- Dynamic studies using CACW-stabilized soil can be used to investigate future rail and road applications.
- It is possible to test the stability of embankments and the endurance of highways built with soils treated with CACW.
- It is planned to test the results obtained from this work in future projects operated by the city authorities.

6. Conclusions and Recommendations for Future Work

The current paper discussed the use of CACW and clarified how it affects silty sand soils with various mineralogies in terms of their engineering characteristics. The viability of soils supplemented with CACW in the presence of an additional stabilizer (2% cement) has been evaluated. Discussion is held over the effectiveness of CACW as a backfill and paving material. Each soil engineering property improvement caused by the addition of CACW has a mechanism that is detailed. The principal results of this paper are as follows:

1. The improvement in the corresponding maximum dry density and shear strength causes an increase in soaked CBR values.
2. Adding a small amount of additive (10%) to CACW improves the engineering properties of silty sand soils. This addition causes a net reduction in pore volume, aids in the quick development of dense mixes, and significantly increases compressive strength.

3. The test findings showed that the optimum dosage is 10% CACW with 2% cement, raising the undrained shear strength of silty sand soil by 323%, CBR by 286%, and P-wave by 180%.
4. The durability tests reveal that soil containing 10% CACW and 2% cement satisfies the specifications and stays within the 14% weight loss limit imposed by the Portland Cement Association (PCA).
5. For subgrade and subbase layers, only silty sand soil stabilized with 10% CACW and 2% cement is suitable, in accordance with the durability findings and strength criteria. The other, on the other hand, is applicable to other field activities, such as enhancing the carrying capacity of sandy marl soil on pavements and low to moderately high-rise buildings.
6. The microscopic investigation results confirmed the outcomes obtained by macro tests.
7. This study clarifies the long-term effects of CACW on improving the engineering properties of silty sand soil in the Najran Region of the Kingdom of Saudi Arabia and other comparable soils globally. The general implications of this research and its prospective benefits are those for improving the geotechnical qualities of silty sand soils for road pavement applications and enhancing the bearing capacity under foundations and embankments.
8. The authors recommend addressing the effects of adding CACW to other kinds of soil, such as clayey soils, which are distributed over large areas of Najran city as well as many other places overall in the Kingdom of Saudi Arabia.

Author Contributions: Conceptualization, G.M.S.A., A.A.E.A., M.A.S. and A.E.R.; methodology, G.M.S.A., A.A.E.A., M.A.S. and A.E.R.; software, G.M.S.A., A.A.E.A., M.A.S. and A.E.R.; writing—original draft preparation, G.M.S.A., A.A.E.A., M.A.S. and A.E.R.; writing—review and editing, G.M.S.A., A.A.E.A., M.A.S. and A.E.R.; visualization, G.M.S.A., A.A.E.A., M.A.S. and A.E.R.; supervision, G.M.S.A., A.A.E.A., M.A.S. and A.E.R.; funding acquisition, G.M.S.A. and A.E.R. All authors have read and agreed to the published version of the manuscript.

Funding: The authors are thankful to the Deanship of Scientific Research at Najran University for funding this work under the General Research Funding program grant code (NU/DRP/SERC/12/47). Radwan is thankful to the Priority Research Area Anthropocene under the program "Excellence Initiative—Research University" at the Jagiellonian University in Kraków.

Data Availability Statement: Data supporting the findings of this study are available from the corresponding author upon reasonable request.

Acknowledgments: The authors are thankful to the Deanship of Scientific Research at Najran University for funding this work under the General Research Funding program grant code (NU/DRP/SERC/12/47). Radwan is thankful to the Priority Research Area Anthropocene under the program "Excellence Initiative—Research University" at the Jagiellonian University in Kraków. Authors would like also to thank Bn Harkil for Granite rock for their logistic support during the research.

Conflicts of Interest: The authors hereby declare that they have no conflict of interest.

References

1. Abdullah, G.M.; Wahhab, H.I.A.-A. Evaluation of foamed sulfur asphalt stabilized soils for road applications. *Constr. Build. Mater.* **2015**, *88*, 149–158. [CrossRef]
2. Abdullah, G.M.S.; Al-Abdul Wahhab, H.I. Stabilisation of soils with emulsified sulphur asphalt for road applications. *Road Mater. Pavement Des.* **2019**, *20*, 1228–1242. [CrossRef]
3. Abdullah, G.M.S. Performance of Enhanced Problematic Soils in Roads Pavement Structure: Numerical Simulation and Laboratory Study. *Sustainability* **2023**, *15*, 2595. [CrossRef]
4. Abdullah, G.M.S.; Abd El Aal, A. Assessment of the reuse of Covid-19 healthy personal protective materials in enhancing geotechnical properties of Najran's soil for road construction: Numerical and experimental study. *J. Clean. Prod.* **2021**, *320*, 128772. [CrossRef]
5. Abdullah, G.M. Using Plaxis 2D finite element modeling to assess bearing capacity of Sultana's soil in Najran Region, Kingdom of Saudi Arabia. Mater. *Today Proc.* **2021**, *49*, 2679–2687. [CrossRef]
6. Abdullah, G. Stabilization of Eastern Saudi Soils Using Heavy Fuel Oil Fly Ash and Cement Kiln Dust. Master's Thesis, King Fahd University of Petroleum & Minerals, Dhahran, Saudi Arabia, 2009.

7. Abdullah, G. Modeling the Behavior of Sulfur Modified Foamed and Emulsified Asphalt Soils Mixes for Local Road Applications. Ph.D. Thesis, King Fahd University of Petroleum & Minerals, Dhahran, Saudi Arabia, 2014.
8. Ashfaq, M.; Heera Lal, M.; Moghal, A.A.B. Static and Dynamic Leaching Studies on Coal Gangue. In *Sustainable Environmental Geotechnics*; Reddy, K.R., Agnihotri, A.K., Yukselen-Aksoy, Y., Dubey, B.K., Bansal, A., Eds.; Lecture Notes in Civil Engineering; Springer International Publishing: Cham, Switzerland, 2020; pp. 261–270.
9. Moghal, A.A.B.; Lateef, M.A.; Mohammed, S.A.S.; Lemboye, K.; C. S. Chittoori, B.; Almajed, A. Efficacy of Enzymatically Induced Calcium Carbonate Precipitation in the Retention of Heavy Metal Ions. *Sustainability* **2020**, *12*, 7019. [CrossRef]
10. Putra, H.; Yasuhara, H.; Kinoshita, N.; Hirata, A. Optimization of Enzyme-Mediated Calcite Precipitation as a Soil-Improvement Technique: The Effect of Aragonite and Gypsum on the Mechanical Properties of Treated Sand. *Crystals* **2017**, *7*, 59. [CrossRef]
11. Amulya, G.; Moghal, A.A.B.; Almajed, A. A State-of-the-Art Review on Suitability of Granite Dust as a Sustainable Additive for Geotechnical Applications. *Crystals* **2021**, *11*, 1526. [CrossRef]
12. Mohamedsalih, M.A.; El Aal, A.K.A.; Radwan, A.E.; Abdullah, G.M.S.; Al Saiari, M. Feasibility of Najran rocks crushing waste as manufactured sand in the sustainable concrete industry in the Kingdom of Saudi Arabia. *Int. J. Geotech. Eng.* **2023**, *17*. [CrossRef]
13. Suits, L.; Sheahan, T.; Soosan, T.; Sridharan, A.; Jose, B.; Abraham, B. Utilization of quarry dust to improve the geotechnicalproperties of soils in highway construction. *Geotech. Test. J.* **2005**, *28*, 11768. [CrossRef]
14. Sridharan, A.; Soosan, T.G.; Jose, B.T.; Abraham, B.M. Shear strength studies on soil-quarry dust mixtures. *Geotech. Geol. Eng.* **2006**, *24*, 1163–1179. [CrossRef]
15. Birch, W.; Datson, H. Reducing the Environmental Effects of Aggregate Quarrying: Dust, Noise & Vibration. 2008. Available online: https://miningandblasting.files.wordpress.com/2009/09/blast_dust_and_noise_control.pdf (accessed on 5 November 2021).
16. Saghafi, B.; Al Nageim, H.; Atherton, W. Mechanical behavior of a new base material containing high volumes of limestone waste dust, PFA, and APC residues. *J. Mater. Civ. Eng.* **2013**, *25*, 450–461. [CrossRef]
17. Tayeh, B.A.; Akeed, M.H.; Qaidi, S.; Abu Bakar, B. Influence of sand grain size distribution and supplementary cementitious materials on the compressive strength of ultrahigh-performance concrete. *Case Stud. Constr. Mater.* **2022**, *17*, e01495. [CrossRef]
18. Kumar, D.S.; Hudson, W.R. Use of Quarry Fines for Engineering and Environmental Applications. 1992. Available online: https://library.ctr.utexas.edu/digitized/iacreports/1992_specrsrch_natlstoneassoc.pdf (accessed on 1 October 2021).
19. Kumrawat, N.; Ahirwar, S.K. Performance analysis of black cotton soil treated with calcium carbide residue and stone dust. *Int. J. Eng. Res. Sci. Technol.* **2014**, *3*, 202–209. Available online: http://www.ijerst.com/currentissue.php (accessed on 15 July 2021).
20. Antonov, G.I.; Nedosvitii, V.P.; Semenenko, O.M.; Kulik, A.S.; Gerashchuk, Y.D.; I'chenko, N.V.; Poltavets, L.K. Use of dolomite dust for manufacturing stabilized dolomite refractories. *Refract. Ind. Ceram.* **1997**, *38*, 238–243. [CrossRef]
21. Al-Homidy, A.A.; Dahim, M.H.; El Aal, A.K.A. Improvement of geotechnical properties of sabkha soil utilizing cement kiln dust. *J. Rock Mech. Geotech. Eng.* **2017**, *9*, 749–760. [CrossRef]
22. Bellanova, J.; Calamita, G.; Giocoli, A.; Luongo, R.; Macchiato, M.; Perrone, A.; Uhlemann, S.; Piscitelli, S. Electrical resistivity imaging for the characterization of the Montaguto landslide (southern Italy). *Eng. Geol.* **2018**, *243*, 272–281. [CrossRef]
23. Fajana, A.O. Geohazard characterization of subsurface materials using integrated geophysical methods for post foundation studies: A case study. *Model. Earth Syst. Environ.* **2020**, *7*, 403–415. [CrossRef]
24. Shi, S.; Bu, L.; Li, S.; Xiong, Z.; Xie, X.; Li, L.; Zhou, Z.; Xu, Z.; Ma, D. Application of comprehensive prediction method of water inrush hazards induced by unfavourable geological body in high risk karst tunnel: A case study. *Geomat. Nat. Hazards Risk* **2017**, *8*, 1407–1423. [CrossRef]
25. El Aal, A.K.A.; Rouaiguia, A. Determination of the Geotechnical Parameters of Soils Behavior for Safe Future Urban Development, Najran Area, Saudi Arabia: Implications for Settlements Mitigation. *Geotech. Geol. Eng.* **2019**, *38*, 695–712. [CrossRef]
26. Malyukova, L.S.; Martyushev, N.V.; Tynchenko, V.V.; Kondratiev, V.V.; Bukhtoyarov, V.V.; Konyukhov, V.Y.; Bashmur, K.A.; Panfilova, T.A.; Brigida, V. Circular Mining Wastes Management for Sustainable Production of *Camellia sinensis* (L.) O. Kuntze. *Sustainability* **2023**, *15*, 11671. [CrossRef]
27. Ratnasari, A.; Syafiuddin, A.; Mehmood, M.A.; Boopathy, R. A review of the vermicomposting process of organic and inorganic waste in soils: Additives effects, bioconversion process, and recommendations. *Bioresour. Technol. Rep.* **2023**, *21*, 101332. [CrossRef]
28. El-Aal, A.K.A.; Salah, M.K.; Khalifa, M.A. Acoustic and strength characterization of Upper Cretaceous dolostones from the Bahariya Oasis, Western Desert, Egypt: The impact of porosity and diagenesis. *J. Pet. Sci. Eng.* **2019**, *187*, 106798. [CrossRef]
29. Stander, H.-M.; Harrison, S.T.; Broadhurst, J.L. Using South African sulfide-enriched coal processing waste for amelioration of calcareous soil: A pre-feasibility study. *Miner. Eng.* **2022**, *180*, 107457. [CrossRef]
30. *ASTM D854-14*; Standard Test Methods for Specific Gravity of Soil Solids by Water Pycnometer. ASTM International: West Conshohocken, PA, USA, 2014. Available online: www.astm.org (accessed on 27 September 2023). [CrossRef]
31. *ASTM D4318-17e1*; Standard Test Methods for Liquid Limit, Plastic Limit, and Plasticity Index of Soils. ASTM International: West Conshohocken, PA, USA, 2017; ASTM D424-54(1971) Standard Method of Test for Plastic Limit (Withdrawn 1982). Available online: www.astm.org (accessed on 27 September 2023). [CrossRef]
32. *ASTM D422-63(2007)e2*; Standard Test Method for Particle-Size Analysis of Soils (Withdrawn 2016). ASTM International: West Conshohocken, PA, USA, 2007. Available online: www.astm.org (accessed on 27 September 2023). [CrossRef]
33. El-Aal, A.A.; Abdullah, G.M.; Metwaly, W.M.A.; AbdelMaksoud, K.M. Geological and archeological heritage resources assessment of the Najran Province; towards the 2030 vision of Saudi Arabia. *Resour. Policy* **2023**, *85*, 104061. [CrossRef]

34. *ASTM D1557-12e1*; Standard Test Methods for Laboratory Compaction Characteristics of Soil Using Modified Effort (56,000 ft-lbf/ft3 (2,700 kN-m/m3)). ASTM International: West Conshohocken, PA, USA, 2012. Available online: www.astm.org (accessed on 27 September 2023). [CrossRef]
35. *ASTM C597-16*; Standard Test Method for Pulse Velocity Through Concrete. ASTM International: West Conshohocken, PA, USA, 2016. Available online: www.astm.org (accessed on 27 September 2023). [CrossRef]
36. *ASTM D2166/D2166M-16*; Standard Test Method for Unconfined Compressive Strength of Cohesive Soil. ASTM International: West Conshohocken, PA, USA, 2016. Available online: www.astm.org (accessed on 27 September 2023). [CrossRef]
37. *ASTM D1883-16*; Standard Test Method for California Bearing Ratio (CBR) of Laboratory Compacted Soils. ASTM International: West Conshohocken, PA, USA, 2016. Available online: www.astm.org (accessed on 27 September 2023). [CrossRef]
38. *ASTM C 289 ASR*; Aggregates Chemical Method. ASTM: West Conshohocken, PA, USA, 2017.
39. Sanjay, M.; Sindhi, P.R.; Vinay, C.; Ravindra, N.; Vinay, A. Crushed rock sand—An economical and ecological alternative to natural sand to optimize concrete mix. *Eng. Mater. Sci.* **2016**, *8*, 345–347.
40. Bonavetti, V.; Donza, H.; Menéndez, G.; Cabrera, O.; Irassar, E.F. Limestone filler cement in low w/c concrete: A rational use of energy. *Cem. Concr. Res.* **2003**, *33*, 865–871. [CrossRef]
41. Al-Ayedi, E.S. Chemical Stabilization of Al-Qurayyah Eastern Saudi Sabkha Soil. Master's Thesis, Department of Civil Engineering, King Fahd Univesity of Petroleum and Minerals, Dhahran, Saudi Arabia, 1996.
42. *ASTM D 559*; Standard Test Methods for Wetting and Drying. ASTM: West Conshohocken, PA, USA, 1996.
43. Goodman, R.E. *Introduction to Rock Mechanics*, 1st ed.; John Wiley and Sons: New York, NY, USA, 1980.
44. Aiban, S.A.; Al-Abdul Wahhab, H.; Al-Amoudi, O.S.B. *Identification, Evaluation, and Improvement of Eastern Saudi Soils for Constructional Purposes, Progess Report No.2*; King AbdulAziz City for Science and Technology: Riyadh, Saudi Arabia, 1995.
45. Aiban, S.A.; Al-Abdul Wahhab, H.; Al-Amoudi, O.S.B. *Identification, Evaluation, and Improvement of Eastern Saudi Soils for Constructional Purposes, Progess Report No.3*; King AbdulAziz City for Science and Technology: Riyadh, Saudi Arabia, 1995.
46. Ahmad, H.R. Characterization and Stabilization of Eastern Saudi Marls. Ph.D. Thesis, King Fahd University of Petroleum & Minerals, Dhahran, Saudi Arabia, 1995.
47. Helmuth, R.A. *Fly Ash in Cement and Concrete*; SP040; Portland Cement Association: Skokie, IL, USA, 1987.
48. Wang, L. Cementitious Stabilization of Soils in the Presence of Sulfate. Ph.D. Thesis, Louisiana State University, Baton Rouge, LA, USA, 2002.

applied sciences

MDPI

Article

Static Liquefaction Assessment Combining Shear Wave Velocity, Peak Strength and Soil Grading

Marisa Soares [1], António Viana da Fonseca [2], Cristiana Ferreira [2] and Sara Rios [2,*]

[1] Scottish Power, 320 St. Vincent Street, Glasgow G2 5AD, UK; m.soares@scottishpower.com
[2] CONSTRUCT-GEO, Faculty of Engineering (FEUP), University of Porto, Rua Dr. Roberto Frias, s/n, 4200-465 Porto, Portugal; viana@fe.up.pt (A.V.d.F.); cristiana@fe.up.pt (C.F.)
* Correspondence: sara.rios@fe.up.pt

Abstract: A large set of undrained compression triaxial tests was carried out on different types of cohesionless soils, from sands to silty sands and silts. Shear wave velocity measurements were also carried out. These tests exhibit distinct state transitions ranging from flow liquefaction to strain softening or strain hardening. With the purpose of defining a framework to assess soil liquefaction, it was found that the ratio between the shear wave velocity (V_{S0}) and the peak undrained deviatoric stress (q_{peak}), V_{S0}/q_{peak}, could be accurately used to define a boundary between liquefaction and strain hardening for sands and between strain softening and strain hardening for silty sands and silts. Since this ratio is a function of the tested material, the prediction of these boundaries can be made as a function of soil grading, namely via the coefficient of uniformity, C_U. Despite not being regarded as a strong geomechanical parameter, C_U is easily determined from a grain-size distribution test and has an empirically proven correlation with critical state parameters.

Keywords: liquefaction; shear wave velocity; peak undrained deviatoric stress; soil grading; coefficient of uniformity

Citation: Soares, M.; Viana da Fonseca, A.; Ferreira, C.; Rios, S. Static Liquefaction Assessment Combining Shear Wave Velocity, Peak Strength and Soil Grading. *Appl. Sci.* **2023**, *13*, 8580. https://doi.org/10.3390/app13158580

Academic Editors: Paulo José da Venda Oliveira and António Alberto Santos Correia

Received: 30 June 2023
Revised: 19 July 2023
Accepted: 22 July 2023
Published: 25 July 2023

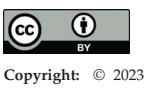

1. Introduction

Static liquefaction has been identified in several tailings dam failures [1–3] where loose saturated soils are deposited. These accidents resulted in severe consequences in terms of casualties, damages, environmental impacts and serious disruptions in the raw materials supply. The increasing number of these accidents has prompted more research in this area aimed at enhancing the design of these geotechnical structures and contributing to their sustainable construction and exploration. A large number of these facilities are immobilized and have to be removed (decommissioned) due to the high levels of failure probability. This condition demands for particularly sensitive deconstruction techniques that require a very accurate knowledge of the consequences of the necessary interventions on these highly unstable materials.

The assessment of soil liquefaction potential using laboratory techniques was initiated by Casagrande in 1936 [4], who proposed the critical void ratio line (CVR), nowadays known as the critical state line (CSL), as a boundary separating liquefiable from non-liquefiable soils. Later, Been and Jefferies (1985) [5] proposed the state parameter, ψ, assuming the existence of a unique CSL. This parameter is usually correlated, for static liquefaction assessment purposes, with the brittleness index, I_B, which measures the normalized degree of strain softening of a contractive soil using the peak and minimum shear strengths, $\sigma'_{d(peak)}$ and $\sigma'_{d(min)}$, respectively (e.g., [6–8]). Despite being widely consistent, both parameters are dependent on the soil type. Moreover, the state parameter also requires the previous laboratory determination of the position of the CSL. Nevertheless, in order to provide a universal framework, ref. [7] after [9], proposed the normalization of the state parameter as a ratio between ψ and the slope of the CSL, λ (ψ/λ).

Shear wave velocities were also used to assess soil liquefaction potential (especially cyclic liquefaction), which was initiated by Stokoe et al. (1988) [10] and later adapted by [11] through the correlation of the normalized small-strain shear wave velocity with the cyclic resistance ratio, CRR.

In the case of static liquefaction, the combination of both strength and stiffness measurements, using the seismic cone penetrometer test (SCPTU), for example, was found to effectively predict liquefaction response as it has a good correlation with the state parameter [12–14]. This combination also has the advantage of distinguishing between recent and/or aged or cemented deposits [15]. Its successful combination was already somewhat expected as both variables are controlled by the confining stress, void ratio, stress history, soil structure and geological age [16–18] and are also correlated with critical state parameters, which governs soil liquefaction response.

Schnaid et al. (2013) [19] used triaxial compression and extension tests with bender elements to develop a framework for the assessment of static liquefaction on gold tailings, showing that peak undrained deviatoric stress and shear wave velocity are correlated.

More recently, Riveros and Sadrekarimi (2021) [20] used the normalized shear wave velocity to distinguish between liquefiable and non-liquefiable soils, proposing an empirical method to evaluate the onset of instability and the post-liquefaction strength of tailings using shear wave velocity. However, it is assumed that this relationship is still soil-dependent, as demonstrated by [21]. Doygun et al. (2019) [22] shows that shear wave velocity in granular soils is significantly affected by the uniformity coefficient and fines content, which affect liquefaction potential [23]. Moreover, Santamarina and Cho (2004) [24] and Cho et al. (2006) [25] demonstrated that particle size and shape can be correlated with different critical state parameters as the macro scale behavior of the soil results from particle-level interactions.

This study aims to evaluate the applicability of the correlations between peak undrained deviatoric stress and shear wave velocity to assess the static liquefaction potential in different soils. The aim is to discuss its range of application and limitations depending on particle size, based on experimental evidence. This is very important to expand the methodologies for liquefaction assessment.

2. Material Properties

During this research, five materials were studied: (1) Osorio sand, a uniformly graded sand from Brazil, well-documented in past research (e.g., [26,27]); (2) a silt, artificially produced from grinding Osorio sand; (3) a silty sand (designated as "mixture"), artificially produced by mixing soils 1 and 2; (4) Algeria sand and (5) Coimbra sand, two uniformly graded sands, also well-documented in the literature (e.g., [28–31]).

The results obtained for these materials were presented and compared with the study previously published by [19] on gold tailings.

Table 1 summarizes the main gradation characteristics of these materials, including the fines content (*FC*), the coefficients of uniformity and shape, C_U and C_C, and the specific gravity. The fines are non-plastic as the fine fraction is silt and not clay. The maximum and minimum void ratios are also presented for the three sands, but not for the finer materials as the standards of these tests (for instance, [32]) are not applicable to soils with high fines content.

Table 1. Gradation characteristics of the materials.

Material	G_s	D_{50}	D_{100}	C_U	C_C	*FC* (%)	e_{max}	e_{min}	ASTM Classification
Gold tailings *	2.94	0.044	0.841	10.0	1.35	70	(1)	(1)	silt with sand
Osorio sand	2.65	0.190	0.420	1.9	1.00	4	0.85	0.57	non-plastic uniform fine sand
Silt	2.65	0.017	0.106	9.6	1.47	99.85	(1)	(1)	well-graded silt
Mixture	2.65	0.110	0.425	32.4	2.60	40	(1)	(1)	well-graded silty sand
Algeria sand	2.69	0.310	0.850	1.76	0.97	0	0.89	0.531	poorly graded sand
Coimbra sand	2.66	0.360	1.000	2.13	1.37	0	0.81	0.48	poorly graded sand

* results from Schnaid et al. (2013) [19]; (1) no information.

2.1. Gold Tailings

The particle size distribution of the gold tailings (Figure 1), determined at the Geotechnical Laboratory of FEUP (LabGeo), reveals a well-graded soil classified as a silt with sand according to the Unified Soil Classification System [33]. The specific gravity, G_s, also determined at LabGeo, is 2.94. The grains are generally sub-angular and angular with uneven edges, as shown in Figure 2.

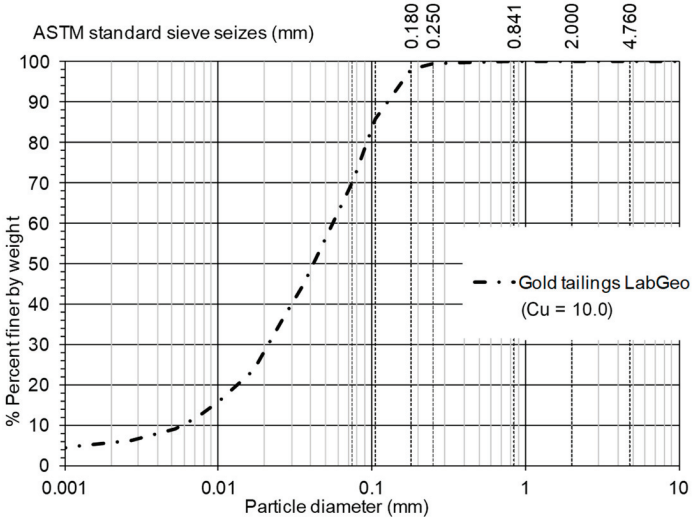

Figure 1. Grading curve and coefficient of uniformity of gold tailings determined at LabGeo [34].

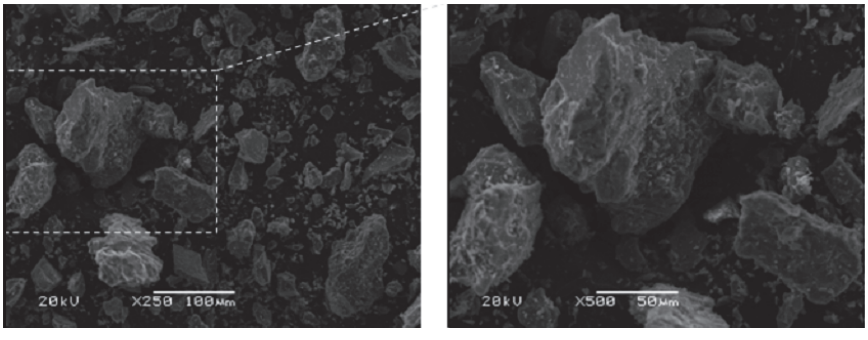

Figure 2. Grain shape of gold tailings—microstructural analysis [35].

2.2. Osorio Sand

Osorio sand is a siliceous fine sand from the region of Osorio near Porto Alegre in southern Brazil, with a specific gravity of 2.65 [26]. This soil is classified as a non-plastic uniform fine sand according to the Unified Soil Classification System [33]. Grain size distribution results are provided in Figure 3a (dashed line) and evidence a material with a minimum amount of fines (<4%).

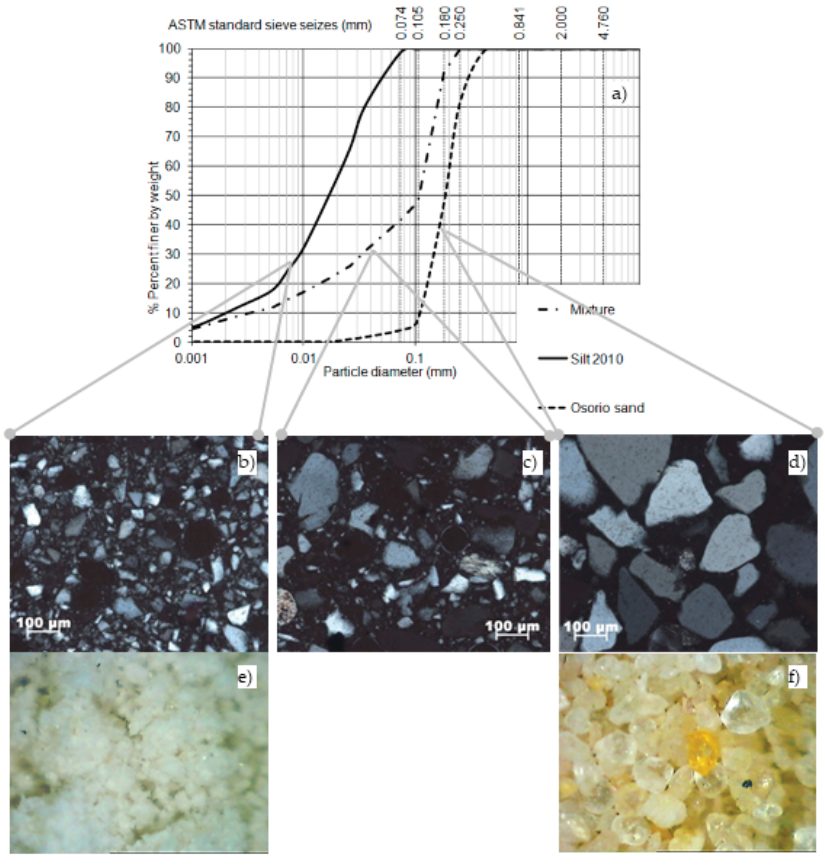

Figure 3. Comparison of the grading curves of the silt, Osorio sand and the mixture (all of them determined at LabGeo at FEUP) [34] (**a**) with the images of the corresponding grains: (**b**,**e**) for the silt, (**c**) for the mixture, and (**d**,**f**) for Osorio sand.

The coefficients of uniformity and curvature of C_U = 1.9 and C_C = 1.0, respectively, characterize this as a uniformly graded sand (Figure 3a, dashed line). Microscopic analysis of particle shape enabled the identification of generally rounded to sub-rounded grains, with a few sub-angular grains, as previously reported by other authors (e.g., [26]) (Figure 3d,f).

2.3. Silt

The silt is obtained from grinding Osorio sand, being a siliceous silt with a minor amount of sand (99.85% silt; <1% sand), as shown in Figure 3a (solid line). The coefficients of uniformity and curvature of this soil are C_U = 9.6 and C_C = 1.47, respectively, revealing a well-graded silt.

2.4. Mixture

The mixture of the two previous materials results in a silty sand (60% sand; 40% silt), which has also been independently studied. This material was produced with the purpose of obtaining a material with an intermediate particle size distribution between Osorio sand and silt. Its specific gravity of 2.65 is necessarily identical to that of the original sand and silt. The coefficients of uniformity and curvature, C_U = 32.4 and C_C = 2.6, indicate a well-graded silty sand according to the Unified Soil Classification System [33]. From the observation of

microscopic photographs, the grains are classified as generally sub-angular to angular with uneven edges, created by the grinding process (Figure 3c).

2.5. Algeria Sand

Algeria sand is a siliceous medium sand, with coefficients of uniformity and curvature of 1.76 and 0.97, revealing a poorly graded sand according to the Unified Soil Classification System [33] (Figure 4). Algeria sand is predominantly quartz sand with a minimal amount of feldspars. As shown in Figure 5, the grains are generally relatively spherical.

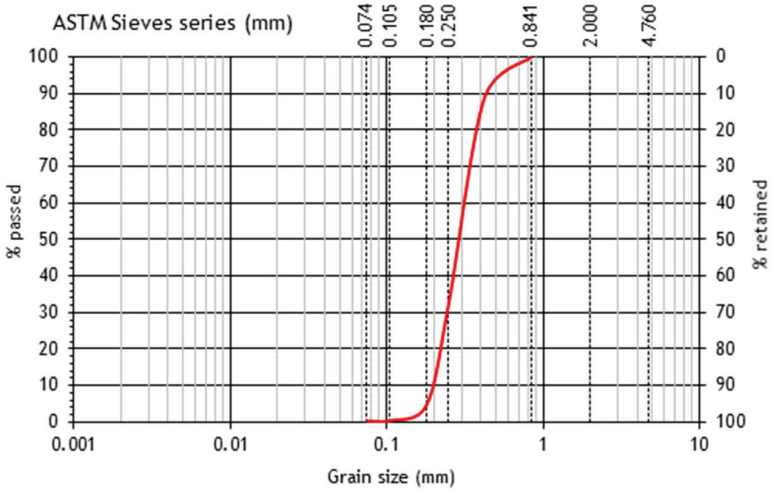

Figure 4. Grading curve and coefficient of uniformity of Algeria sand.

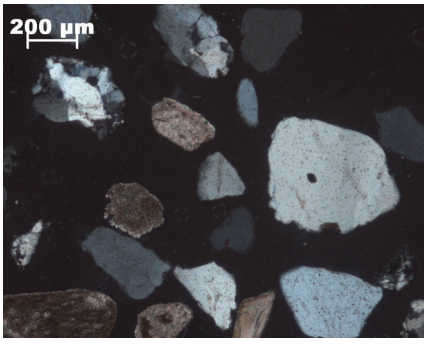

Figure 5. Grain shape of Algeria sand [31].

2.6. Coimbra Sand

Coimbra sand is a predominantly siliceous sand, artificially prepared from a quarry. The coefficients of uniformity and shape are C_U = 2.13 and C_C= 1.37, respectively, consistent with a poorly graded sand classification according to the Unified Soil Classification System [33] (Figure 6). The minimum and maximum void ratios correspond to e_{min} = 0.48 and e_{max} = 0.81, and the grains are generally sub-angular (Figure 7).

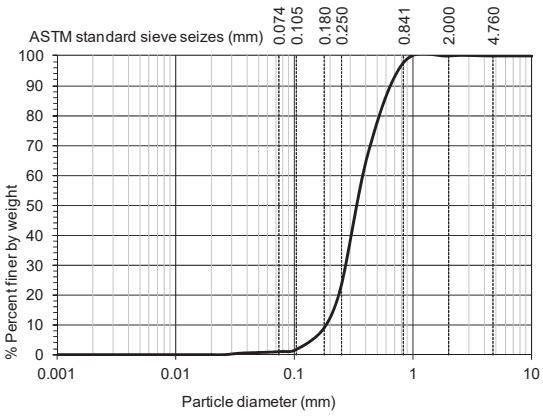

Figure 6. Grading curve and coefficient of uniformity of Coimbra sand [34].

Figure 7. Grain shape of Coimbra sand.

3. Specimen Preparation and Testing Conditions

The specimens were tested at different void ratios, but usually reconstituted to very loose conditions, and a wide range of confining pressures, aiming to evaluate their influence on liquefaction susceptibility. The reconstituted specimens were prepared by moist tamping with a water content of 5% for all uniformly graded sands (Osorio, Algeria and Coimbra sand), 11.5% for the silt and gold tailings [35] and 8.75% for the mixture (an intermediate value between 11.5% and 5%). These values were obtained by testing different tamping moisture contents, with the purpose of achieving a high void ratio. The moist tamping procedure was selected since [31] showed that inherent anisotropy created by specimen preparation with moist tamping or funnel dry pluviation did not significantly interfere with the liquefaction susceptibility of Coimbra sand.

It is also an effective, easy and relatively quick reconstitution technique that does not segregate soil particles (as opposed to the dry funnel pluviation technique), allowing the operator to control the final density much more readily [36]. The moist tamping reconstitution technique, used in this research, is described in detail in [37].

A large set of strain and stress-controlled triaxial tests were performed to study the static liquefaction potential of these soils. Thirty-eight undrained isotropically consolidated triaxial compression tests (CIU) are presented and discussed in this paper, together with twelve CIU triaxial tests published by [19]. The results of those tests are presented in Tables 2–7, where the test ID indicates the first letter of the soil (G for gold tailings, O for Osorio, S for silt, M for mixture, A for Algeria and C for Coimbra), followed by CU (undrained compression) and test number. Each triaxial test was carried out following the typical stages: percolation, saturation, consolidation and shear. In the initial stage, the specimens were percolated with de-aired water in a volume no less than twice the

initial voids volume and saturated by back-pressuring at constant effective stresses prior to undergoing the consolidation and shearing stages. A minimum Skempton's B parameter of 0.97 was ensured prior to the consolidation stage for most specimens. The specimen saturation was often verified by a *P*-wave velocity around 1500 m/s, measured by bender–extender elements.

Table 2. Set of results of CIU compression triaxial tests performed on gold tailings.

Test ID	σ'_{h0} (kPa)	σ'_{v0} (kPa)	V_{s0} (m/s)	G_0 (kPa)	V_{s1} (m/s)	p'_{peak} (kPa)	q_{peak} (kPa)	V_{s0}/q_{peak}	Behavior
GCU_1	15	15	75	8199	121	9.5	4.5	16.56	Liquefaction
GCU_2	22	22	85	10,699	125	13.5	7.2	11.84	Liquefaction
GCU_3	30	30	97	13,706	130	17.1	8.7	11.10	Liquefaction
GCU_4	50	50	113	19,335	135	27.3	14.0	8.09	Liquefaction
GCU_5	60	60	130	25,914	149	32.7	19.8	6.59	Liquefaction
GCU_6	75	75	131	26,004	141	43.9	29.8	4.39	Strain softening
GCU_7	100	100	156	37,159	156	56.5	37.4	4.17	Strain softening
GCU_8	200	200	173	46,487	145	114.2	98.7	1.75	Strain softening
GCU_9	600	600	279	127,731	178	391.1	410.7	0.68	Strain hardening
GCU_10	800	800	291	142,062	174	463.2	511.4	0.57	Strain hardening
GCU_11	1000	1000	316	169,304	179	658.7	734.7	0.43	Strain hardening
GCU_12	1200	1200	339	189,210	180	891.5	1059.3	0.32	Strain hardening

Table 3. Set of results of CIU compression triaxial tests performed on Osorio sand.

Test ID	σ'_{h0} (kPa)	σ'_{v0} (kPa)	V_{s0} (m/s)	G_0 (kPa)	V_{s1} (m/s)	p'_{peak} (kPa)	q_{peak} (kPa)	V_{s0}/q_{peak}	Behavior
OCU_1	50	50	184	49,913	219	35.8	21.0	8.79	Liquefaction
OCU_2	25	25	153	35,056	217	17.7	8.7	17.66	Liquefaction
OCU_3	100	100	221	72,218	220	63.0	42.5	5.20	Liquefaction
OCU_4	199	199	264	103,230	222	127.7	86.0	3.07	Liquefaction
OCU_5	299	299	298	134,685	227	193.0	140.7	2.12	Strain hardening
OCU_6	600	600	370	205,636	237	403.2	266.3	1.39	Strain hardening
OCU_7	600	600	365	200,484	233	386.0	253.4	1.44	Strain hardening
OCU_8	1200	1200	365	201,677	196	773.7	555.3	0.66	Strain hardening

Table 4. Set of results of CIU compression triaxial tests performed on the silt.

Test ID	σ'_{h0} (kPa)	σ'_{v0} (kPa)	V_{s0} (m/s)	G_0 (kPa)	V_{s1} (m/s)	p'_{peak} (kPa)	q_{peak} (kPa)	V_{s0}/q_{peak}	Behavior
SCU_1	15	15	73	7738	117	10.3	3.5	20.73	Liquefaction
SCU_2	30	30	91	12,552	124	19.3	12.8	7.12	Liquefaction
SCU_3	50	50	110	18,518	131	27.6	15.8	6.99	Liquefaction
SCU_4	101	101	127	24,680	126	58.1	38.8	3.27	Liquefaction
SCU_5	20	20	80	9363	119	14.7	5.2	15.24	Liquefaction
SCU_6	50	50	105	16,790	125	32.9	21.1	5.01	Liquefaction
SCU_7	99	99	140	30,417	141	59.7	36.5	3.85	Strain softening
SCU_8	201	201	168	44,367	141	115.2	78.3	2.15	Strain softening
SCU_9	699	699	276	122,377	170	575.2	635.0	0.43	Strain hardening
SCU_10	1199	1199	287	134,019	154	1097.2	1252.8	0.23	Strain hardening

Table 5. Set of results of CIU compression triaxial tests performed on the mixture.

Test ID	σ'_{h0} (kPa)	σ'_{v0} (kPa)	V_{s0} (m/s)	G_0 (kPa)	V_{s1} (m/s)	p'_{peak} (kPa)	q_{peak} (kPa)	V_{s0}/q_{peak}	Behavior
MCU_1	25	25	78	9690	111	16.4	8.0	9.70	Liquefaction
MCU_2	402	909	239	98,593	138	582.0	568.5	0.42	Strain softening
MCU_3	298	298	182	56,164	139	145.6	115.0	1.59	Strain softening
MCU_4	399	399	208	72,689	147	252.9	178.0	1.17	Strain softening

Table 6. Set of results of CIU compression triaxial tests performed with Algeria sand.

Test ID	σ'_{h0} (kPa)	σ'_{v0} (kPa)	V_{s0} (m/s)	G_0 (kPa)	V_{s1} (m/s)	p'_{peak} (kPa)	q_{peak} (kPa)	V_{s0}/q_{peak}	Behavior
ACU_1	23	23	138	27,790	200	17.6	9.1	15.21	Liquefaction
ACU_2	31	31	134	26,072	180	22.0	14.5	9.27	Liquefaction
ACU_3	99	99	168	41,743	169	70.3	45.3	3.71	Liquefaction
ACU_4	400	400	280	117,327	198	248.2	255.9	1.10	Strain hardening
ACU_5	1001	1001	411	253,963	231	540.4	536.9	0.77	Strain hardening
ACU_6	529	529	343	181,709	226	369.4	369.0	0.93	Strain hardening

Table 7. Set of results of CIU compression triaxial tests performed with Coimbra sand.

Test ID	σ'_{h0} (kPa)	σ'_{v0} (kPa)	V_{s0} (m/s)	G_0 (kPa)	V_{s1} (m/s)	p'_{peak} (kPa)	q_{peak} (kPa)	V_{s0}/q_{peak}	Behavior
CCU_1	100	100	177	49,037	177	57.7	43.4	4.07	Liquefaction
CCU_2	100	100	162	41,244	162	65.2	32.2	5.02	Liquefaction
CCU_3	201	201	218	76,508	183	121.4	87.3	2.50	Liquefaction
CCU_4	400	400	282	129,778	199	241.1	178.0	1.58	Liquefaction
CCU_5	92	92	182	51,490	186	64.0	22.4	8.13	Liquefaction
CCU_6	79	79	166	43,121	176	56.3	27.4	6.06	Liquefaction
CCU_7	498	498	293	137,588	196	327.9	161.5	1.82	Liquefaction
CCU_8	596	596	314	159,104	201	394.3	195.2	1.61	Liquefaction
CCU_9	400	400	313	159,317	221	282.1	350.7	0.89	Strain softening
CCU_10	1242	1242	372	224,325	198	471.8	463.5	0.80	Strain softening

Volumetric strains were systematically evaluated and recorded using internal/local transducers (inductive hall-effect calipers) to measure axial and radial deformation until the end of the saturation phase and complementarily monitored by a volume change gauge during the consolidation and shear stages. In addition, the tests presented in this paper were carried out on triaxial apparatuses equipped with bender–extender elements (for *S*- and *P*-wave velocity measurements) at the pedestal and cap. When excited, the transmitting bender element vibrates in a direction perpendicular to the length of the element producing a shear wave, which is registered in the other bender, located at the other end of the specimen. The shear wave velocity, Vs_0, is then calculated from the ratio between the tip-to-tip travelling distance (d) and the travel time (t), based on the first wave arrival method (described in [38]), according to Equation (1):

$$V_{S0} = \frac{d}{t} \tag{1}$$

The shearing stage was applied under both strain-control and stress-control on "Bishop–Wesley" stress-path cells and classical triaxial cells, respectively, up to at least 20% axial strain, until the critical state or "true" liquefaction was reached. The undrained tests were typically sheared with a strain rate of 0.05 mm/min while the ones carried out on the "Bishop–Wesley" cells required an initial stress rate specifically determined to enable shearing during less than one day. Despite the occurrence of bulging or excessive deformation, thus creating a complex distribution of stresses and strains inside the sample, the steady state was often reached for strains lower than 20% due to its "natural" proximity to the critical state line. It should be noted that the steady state line is classically defined under constant pore water pressure and constant shear stress conditions with increasing shear strain. On the other hand, liquefaction onset occurred at a very low shear strain and therefore no bulging or excessive deformation affected the phenomenon.

Membrane penetration tends to underestimate the pore pressure for loose specimens ($e > e_c$) and to overestimate the pore pressure of dense specimens ($e < e_c$). According to [39], this effect should be corrected only if the D_{20} of the soil is higher than twice the membrane thickness. As none of the tested soils have a D_{20} higher than 0.8 mm, this effect was considered negligible and therefore not taken into account.

Membrane rigidity may have a restraining effect, mainly for low confining pressures and when barreling occurs, over-predicting soil strength. Both deviator and mean effective stresses were corrected for the membrane effect, according to the European standard [40].

4. Liquefaction Assessment Based on Stiffness/Strength Parameters

4.1. Definition of the Critical State Lines

Following numerous studies published on soil liquefaction assessment (e.g., [6–8,41]), it is recognized that the state parameter, ψ, has a significant influence on liquefaction instability. For that purpose, this study initiated with the determination of the steady state line (SSL) for all the distinct soils (SSL is defined as the ultimate state achieved under undrained conditions, whilst CSL is defined as the ultimate state achieved under drained conditions).

Results obtained from both drained and undrained triaxial tests performed with Osorio sand are shown in Figure 8, where there are four different plots, including the stress–strain curves, the q-p' and the e-log p' paths followed by each triaxial test, as well as the identification of the SSL and CSL. For simplicity, only the plots associated with this soil are included. Any further reference to the other soils can be found in [34]. Similarly, further details concerning the other triaxial tests, namely non-CIU, are provided in [34]. The tables presented in this paper refer only to CIU triaxial tests.

However, it was perceived that the state parameter per se could not be used to accurately determine the limit beyond which soils exhibit a stable behavior if it is based on a linear CSL obtained from drained tests at low confining stresses or undrained tests at medium stresses. Figure 9 shows, as an example, the critical and steady state lines obtained for the mixture while Figure 10 summarizes this idea, showing a sketch of the distinct ultimate state conditions.

Additionally, the stress ratio at critical state ($M = q/p'$) was obtained for the different soils and compared to the particle morphology classified in a qualitative way (Table 8). From these results, it is observed that Osorio sand, which has rounded particles, has a lower critical state friction angle (related with $M = \frac{6\sin\phi}{3-\sin\phi}$) than the silt, which shows more angular particles due to the grinding of Osorio sand. This is expected as particle angularity improves the interlocking of the particles.

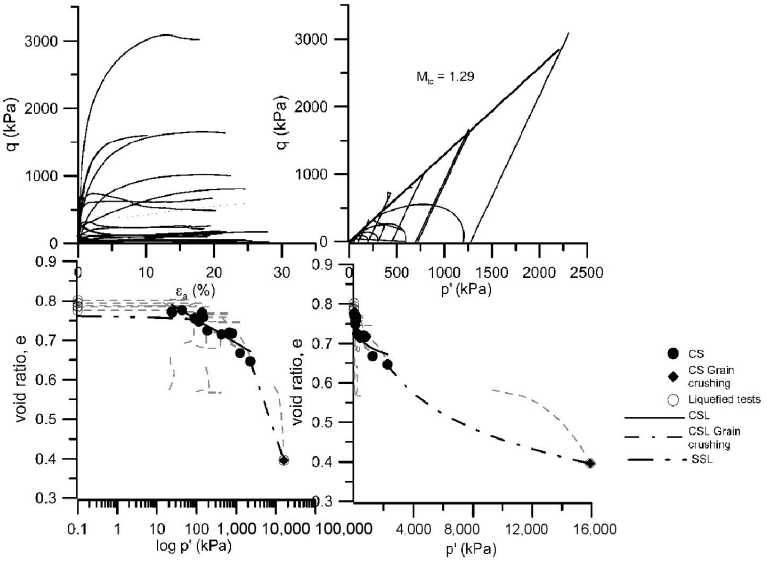

Figure 8. Critical state and steady states lines of Osorio sand.

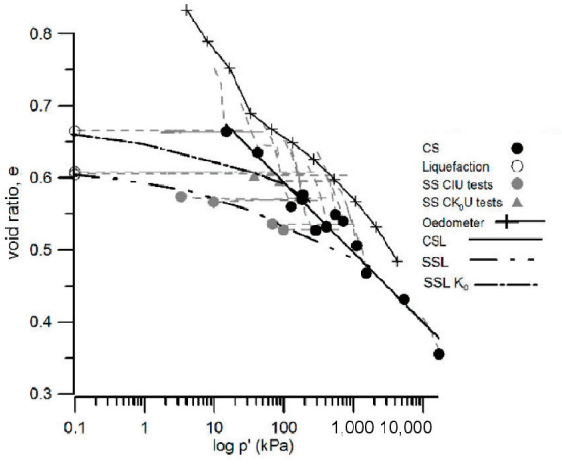

Figure 9. Critical and steady state lines of the mixture.

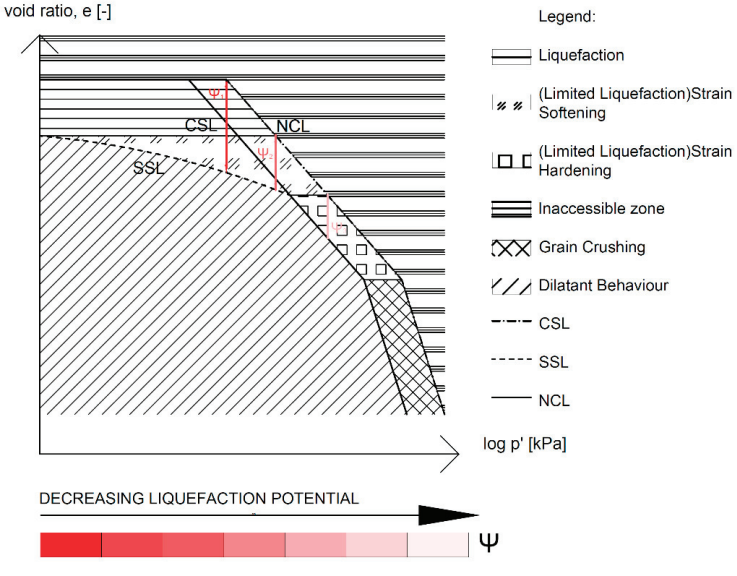

Figure 10. Normal state line, critical state line and steady state line for sands and silts; undrained shear strength of soils delimited in a diagram e-log p'; measurement of liquefaction potential through the state parameter ψ.

Table 8. M values compared with soil morphology.

Material	M Values	Particle Morphology
Gold tailings	1.49	sub-angular and angular
Osorio sand	1.29	rounded to sub-rounded grains
Silt	1.46	angular particles due to grinding
Mixture	1.38	angular particles due to grinding
Algeria sand	1.28	grains are generally relatively spherical
Coimbra sand	1.25	sub-angular

4.2. Definition of the Instability Line

The *loci* in the p'-q-e space of the onset of liquefaction (identified by the peak undrained deviatoric stress) define the instability line ("IL"), as suggested by [42]. Figure 11 shows the IL for all the soils under study. It is interesting to note the strong correlation coefficient (R^2) obtained, despite involving different types of soils with different M values.

According to some published works (namely [43,44]), the IL is shown to be dependent on the initial confining stress and the initial void ratio (e.g., [45]). However, this effect might be a result of the relative positioning of the initial state of the soil in the p'-q-e space, with reference to the IL. Such a fact could explain the strong correlation observed between the ILs obtained for the six different soils presented in Figure 11.

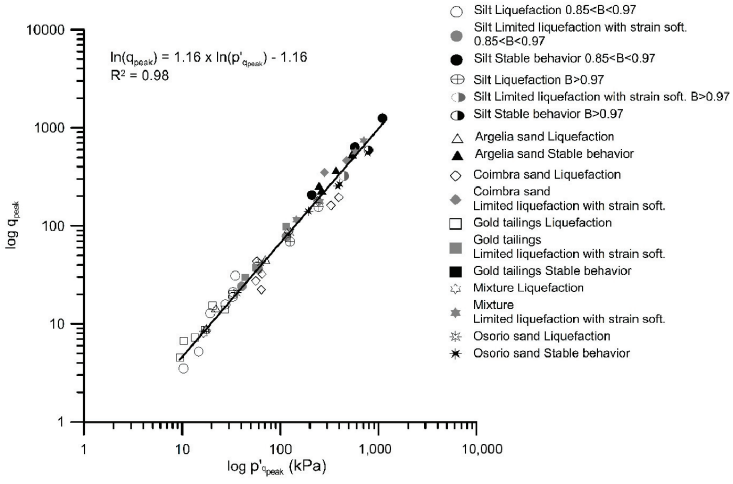

Figure 11. Instability line of all soils on a log–log scale.

4.3. Liquefaction Assessment

Whilst the state parameter ψ has the limitations previously mentioned, both stiffness (expressed by the shear wave velocity, Vs_0) and the peak undrained deviatoric stress ($q_{peak} = \sigma_V - \sigma_H$) are controlled (although differently) by the void ratio, mean stress state, contractiveness and soil structure. For this reason, these parameters were found to be particularly useful for predicting soil behavior [19].

The peak deviatoric stress occurs before the onset of complete (q_{ult} = 0 kPa) or partial (q_{ult} > 0 kPa) instability. It should be noted that "complete" or "true" liquefaction is achieved when a null mean effective stress is reached whilst "partial instability" is typically achieved by specimens which exhibit strain hardening and/or strain softening after reaching the phase transformation line and therefore always exhibit an ultimate deviatoric stress. A sketch comparing these distinct behaviors is shown in Figure 10.

V_{S0} is the shear wave velocity, measured after consolidation and prior to shearing. The respective normalized parameters q_1 and V_{S1} have been defined as follows:

$$q_1 = \left(\frac{q_{peak}}{p_a}\right)\left(\frac{p_a}{\sigma'_{v0}}\right)^{0.5} = \left(\frac{q_{peak}}{p_a}\right)\left(\frac{1+2K_0}{3}\right)^{0.5}\left(\frac{p_a}{\sigma'_m}\right)^{0.5} \quad (2)$$

$$V_{S1} = V_{S0}\left(\frac{p_a}{\sigma'_{v0}}\right)^{0.25} = V_{S0}\left(\frac{1+2K_0}{3}\right)^{0.25}\left(\frac{p_a}{\sigma'_m}\right)^{0.25} \quad (3)$$

where p_a is the atmospheric pressure (approximately 100 kPa), K_0 is the coefficient of earth pressure at rest, σ'_m is the mean effective confining pressure $\left(\sigma'_m = \frac{\sigma'_{V0}+2*\sigma'_{H0}}{3}\right)$ and σ'_{v0} is the vertical effective stress.

Figure 12 correlates q_1 and the ratio V_{S0}/q_{peak} for all the studied materials in a single plot, showing that it is possible to define the boundaries between true liquefaction and strain softening for finer materials as well as between true liquefaction and strain hardening for uniformly graded sands. The adopted symbols aim to distinguish true liquefaction (open symbols) from a strain softening behavior (grey symbols) and from a stable behavior, characterized by strain hardening (black symbols). This figure clearly distinguishes the boundaries of soil behavior, which correspond to the ratios for true liquefaction triggering provided in Table 9 for the soils under study. As shown in Figure 12, it is clear that low V_{S0}/q_{peak} and high q_1 correspond to a stable condition. This framework is particularly suitable for predicting liquefaction potential, overcoming the limitations of other approaches.

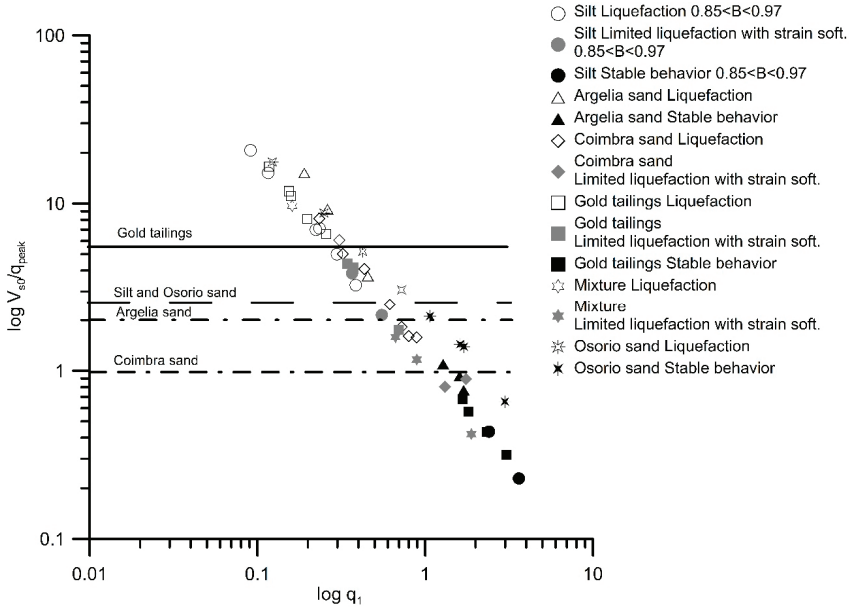

Figure 12. Correlation between the normalized peak undrained deviatoric stress and the ratio between shear wave velocity and peak undrained deviatoric stress.

Table 9. V_{s0}/q_{peak} ratios for true liquefaction triggering for the different tested materials.

Material	V_{s0}/q_{peak}	
	True Liquefaction Triggering	Behavior Limiting Boundary *
Gold tailings	>5 to 6	>0.8 to 1
Osorio sand	>2 to 3	>2 to 3
Silt	>2 to 3	>0.5
Mixture	>2 to 10 #	>0.2 #
Algeria sand	>2	>2
Coimbra sand	>1	>1

* between strain softening and strain hardening for finer soils and between true liquefaction and strain hardening for monogranular sands; # due to limited V_S data, there is greater uncertainty for this soil.

Figure 13 shows that stability increases both with increasing shear wave velocity, V_{s0}, (or stiffness) and with increasing peak undrained deviatoric stress, q_{peak}, for all soils. Thus, stability increases with both increasing V_{s1} and q_1, reflecting greater contact between grains, due to the dual effect of the increase in confining pressure and the decrease in the void ratio.

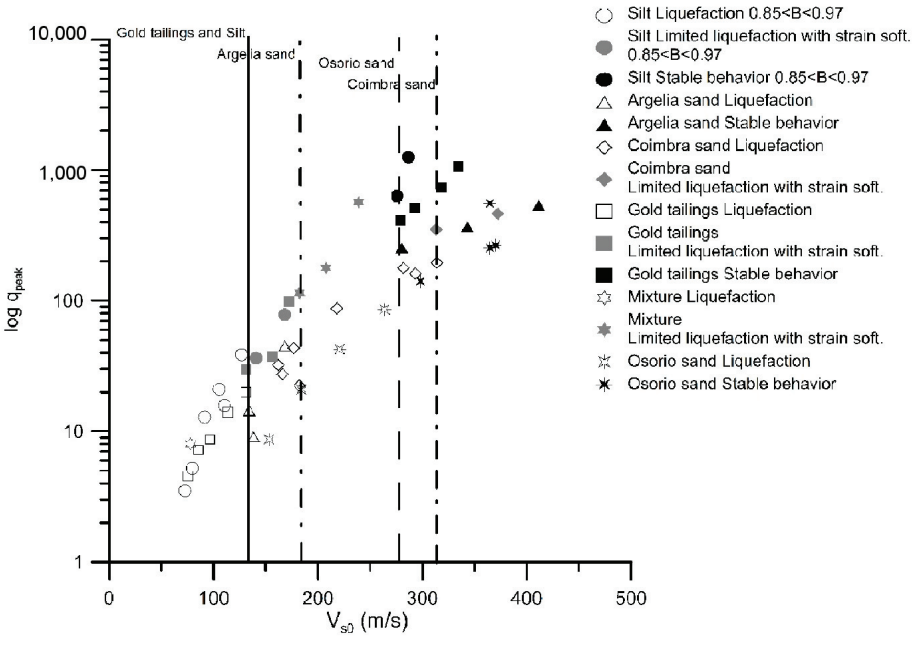

Figure 13. Peak undrained deviatoric stress as a function of the shear wave velocity.

From both Figures 12 and 13, further conclusions can be drawn. For instance, Figure 12 indicates that among the three sands, Algeria sand is the most stable one since the V_{s0} boundary separating liquefaction from a stable behavior is obtained for low V_{s0}. This is believed to be associated with the greater roundness of its particles. On the contrary, Coimbra sand is the soil with higher brittleness due to its highly meta-stable structure created by the small contact bridges between its angular grains. It can also be observed that both Coimbra sand and the mixture can only reach full stability (i.e., a strain hardening behavior) for very high initial confining stresses (and/or low void ratios), as stability was not verified within the wide range of confining pressures applied during the triaxial tests (Table 7). Finally, both the gold tailings and the silt are the least prone to liquefaction, yet this was not reflected in a higher stability, since these soils display a strain softening behavior within a wide range of shear wave velocities.

Despite the robust correlations obtained with the laboratory results, good reasoning must be applied since a strong statistical correlation exists between both variables (i.e., between V_{s0}/q_{peak} and q_1). In fact, a higher relevance should be given to the limiting effects of V_{s0}/q_{peak} when distinguishing liquefiable and non-liquefiable conditions than the correlation between V_{s0}/q_{peak} and q_1, particularly under laboratory conditions.

Making use of the same parameters, a different approach may be adopted. This framework derives from a concept based on the simplified procedure proposed by [46], initially adopted for cyclic conditions [47], as shown in Figure 14. In this case study, instead of the cyclic resistance ratio (CRR), the normalized peak undrained deviatoric stress under monotonic conditions, $q_{peak}/(2\sigma'_h)$, is taken (Equation (4)). Although this chart was initially proposed for determining the cyclic resistance of sands with low fines content, an analogy can be made to identifying the boundary that separates liquefiable from non-liquefiable conditions. It should also be pointed out that Andrus and Stokoe's equation was not corrected for fines content, instead it was decided to adjust both the b and V_{s1}* parameters. The main disadvantage of this framework is the existence of distinct boundaries, specific to each soil, which in this case, are a function of b and V_{s1}*. Table 10 summarizes these values for the studied soils, where it becomes clear that b is around 3.0 but V_{s1}* varies between

150 and 240 depending on the soil type. This is also observed in Figure 14 where the lines have approximately the same shape but their vertical asymptotes move to the right with increasing instability potential.

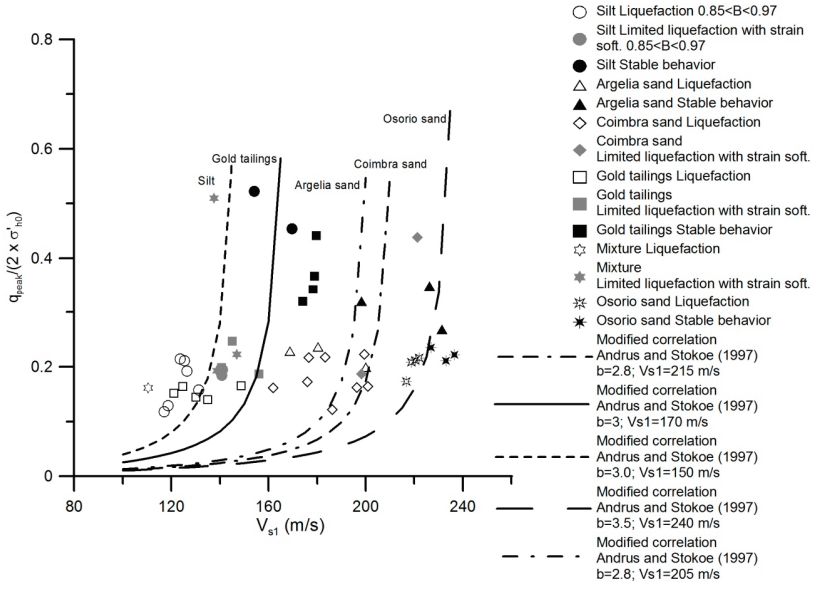

Figure 14. Normalized peak deviatoric stress versus normalized shear wave velocity—simplified procedure to evaluate static liquefaction [46].

$$\frac{q_{peak}}{2.\sigma'_h} = a\left(\frac{(V_{S1})}{100}\right)^2 + b\left(\frac{1}{V_{s1}^* - (V_{S1})} - \frac{1}{V_{S1}^*}\right) \quad (4)$$

Table 10. V_{s1}* and b fitting values for Equation (4).

Material	b	V_{s1}*
Gold tailings	3.0	170
Osorio sand	3.5	240
Silt	3.0	150
Algeria sand	2.8	205
Coimbra sand	2.8	215

In order to overcome the dispersion of the limiting ratios, given by V_{S0}/q_{peak}, with the type of soil, a new framework is proposed.

4.4. Effect of Soil Type

It is known that soil liquefaction is mainly a function of the contractiveness of the soil, which is affected, in the first place, by relative density. Relative density, in turn, is affected by the grain size distribution, shape of the grains and specific gravity. For this case study, specific gravity was not an issue since most soils have similar values, except the gold tailings, which have a very distinct G_s value of 2.94. The challenge was to find a parameter that could take into account not only grain size distribution but also indirectly consider the shape of the grains. Ref. [48] studied the effect of soil grading on the undrained shear strength of sands, considering C_U as an effective parameter to control shear resistance only for pure sand samples. Instead, the aim of this research was to define a single parameter for any soil type. Following this study, the coefficient of uniformity (C_U) was found to be

the most suitable parameter to correlate with the proposed ratios, as shown in Figure 15. Despite not being directly related to particle shape, C_U can evaluate soil dispersion by considering particle diameter, which is highly related to potential fabric configuration. Following these studies, this research found the coefficient of uniformity to be a reliable measure of the liquefaction potential. Figure 15 illustrates the new approach for predicting soil liquefaction potential for any type of soil, using C_U as a soil identifier.

In order to construct the graph in Figure 15, the correlations needed to be consistent for all the soils. For that, the adopted limiting V_{s0}/q_{peak} ratios were those between strain softening and strain hardening for finer soils (gold tailings, silt and mixture) and between true liquefaction and strain hardening for uniformly graded sands (Osorio sand, Argelia sand and Coimbra sand) since they typically do not exhibit strain softening, as summarized in Table 8. For the case of the mixture, the ratios provided were considered indicative due to the limited V_S measurements in the undrained compression triaxial tests carried out so far.

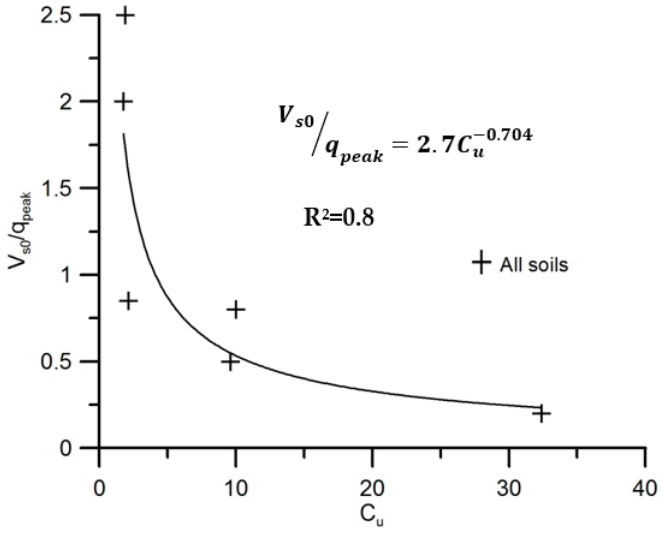

Figure 15. Correlation between the coefficient of uniformity (C_U) and the ratio of shear wave velocity to peak deviatoric stress (V_{s0}/q_{peak}) defining the limiting boundary between strain softening and strain hardening behavior.

Still, as with most correlations, this framework does have a limitation. According to this approach, soils with a better grading are likely to be more resistant to soil liquefaction. However, in the case of gap-graded specimens, which display a high C_U (similar to well-graded soils), the V_{s0}/q_{peak} ratio would be expected to be high due to the high liquefaction potential (e.g., [49]). This would go against the trend displayed in Figure 15. In any case, natural soils are generally not gap-graded.

Although more data are needed to confirm this trend, these promising results suggest that the limiting boundary between liquefaction or strain softening and strain hardening defined in terms of the V_{s0}/q_{peak} ratio can be related grain size measured by the uniformity coefficient.

5. Conclusions

The results obtained from this laboratorial research expand the liquefaction assessment framework proposed by [19]. From this research, the ratio between the normalized shear wave velocity and the peak strength, V_{s0}/q_{peak}, proved to be a very good and reliable parameter for soil liquefaction assessment in different types of soils. The association between properties relative to both small and large strain levels, which are controlled

(although differently) by the void ratio, mean stress state, contractiveness and soil structure, results in different functions of the same variables. Hence, these two measurements, as a ratio, can be useful in predicting not only liquefaction but also other relevant soil properties such as compressibility or cementation.

The boundary between strain hardening and strain softening soil behaviors measured by the V_{s0}/q_{peak} ratio was found to be a function of the coefficient of uniformity, C_U. The correlation obtained between both parameters provided a reliable framework, independent of soil type, for the assessment of static soil liquefaction.

Further investigations involving distinct stress paths and distinct K_0 consolidation conditions, among other factors, are necessary to evaluate if the observed correlation between V_{s0}/q_{peak} and C_U is limited to specific conditions.

However, in the authors' opinion, the potential of this framework goes beyond laboratory assessment and can also be applied to in situ data, namely via the seismic piezocone, by using a similar stiffness/stress ratio, known as the rigidity index, G_0/q_c. Therefore, this can be an important tool to assess the liquefaction potential of in situ soils, including natural deposits or mine tailings, contributing to safer and sustainable geotechnical structures.

Author Contributions: Conceptualization, Resources, A.V.d.F.; Investigation and writing, M.S.; Review & editing, C.F. and S.R.; Supervision, A.V.d.F. All authors have read and agreed to the published version of the manuscript.

Funding: The support of the Portuguese Foundation for Science and Technology (FCT) is also acknowledged through grant SFRH/BPD/120470/2016. This work was also financially supported by base funding—UIDB/04708/2020 of the CONSTRUCT—Instituto de I&D em Estruturas e Construções, funded by national funds through FCT/MCTES (PIDDAC).

Institutional Review Board Statement: Not applicable.

Informed Consent Statement: Not applicable.

Data Availability Statement: Data not available.

Acknowledgments: The authors would like to thank Fernando Schnaid for his cooperation during this research.

Conflicts of Interest: The authors declare no conflict of interest.

Nomenclature

C_C	coefficient of shape C_U
CIU	isotopically consolidated undrained triaxial test
CRR	cyclic resistance ratio
CSL	critical state line
C_U	coefficient of uniformity
CVR	critical void ratio line
e_{max}	maximum void ratio
e_{min}	minimum void ratio
G_0	small-strain shear modulus (MPa)
G_s	specific gravity
I_B	brittleness index
IL	instability line
K_0	at rest coefficient of Earth's pressure
p_a	atmospheric pressure (approximately 100 kPa)
q_c	CPT tip cone resistance (MPa)
q_{peak}	peak undrained deviatoric stress (kPa)
SSL	steady state line
V_{S0}	shear wave velocity prior to shear stage (m/s)
V_{S0}/q_{peak}	ratio between the shear wave velocity (V_{S0}) and the peak undrained deviatoric stress
V_{S1}	normalized small-strain shear wave velocity (m/s)

$\sigma'_{d(min)}$	minimum shear strength (kPa)
$\sigma'_{d(peak)}$	peak shear strength (kPa)
σ'_m	mean effective confining pressure (kPa)
σ'_{v0}	vertical effective stress (kPa)
ψ	state parameter, measured with reference to the CSL
ψ_{SSL}	state parameter, measured with reference to the SSL

References

1. Morgenstern, N.R.; Vick, S.G.; Viotti, C.B.; Watts, B.D. Fundão Tailings Dam Review Panel: Report on the Immediate Causes of the Failure of Fundao dam. 2015. Available online: https://pedlowski.files.wordpress.com/2016/08/fundao-finalreport.pdf (accessed on 29 September 2021).
2. Jefferies, M.; Morgenstern, N.R.; Van Zyl, D.V.; Wates, J. *Report on NTSF Embankment Failure*; Technical Report; Valley Operations for Ashurst Operations: South Orange, NSW, Australia, 2019; Available online: https://www.newcrest.com/sites/default/files/2019-10/190417_Report%20on%20NTSF%20Embankment%20Failure%20at%20Cadia%20for%20Ashurst.pdf (accessed on 21 July 2023).
3. Arroyo, M.; Gens, A. Computational Analyses of Dam I Failure at the Corrego de Feijao Mine in Brumadinho. Final Report from CIMNE to Vale S.A. 2021. Available online: http://www.mpf.mp.br/mg/sala-de-imprensa/noticias-mg/desastre-da-vale-relatorio-elaborado-por-universidade-da-espanha-aponta-causas-do-rompimento-da-barragem-em-brumadinho-mg (accessed on 21 July 2023).
4. Casagrande, A. Characteristics of cohesionless soils affecting the stability of slopes and earth fills. *J. Boston Soc. Civ. Eng.* **1936**, *23*, 13–32.
5. Been, K.; Jefferies, M.G. A state parameter for sands. *Géotechnique* **1985**, *35*, 99–112. [CrossRef]
6. Uthayakumar, M.; Vaid, Y. Static liquefaction of sands under multiaxial loading. *Can. Geotech. J.* **1998**, *35*, 273–283. [CrossRef]
7. Jefferies, M.G.; Been, K. Soil liquefaction. In *A Critical State Approach*; Taylor & Francis: Oxfordshire, UK, 2006.
8. Sadrekarimi, A.; Olsen, S. Yield strength ratios, critical strength ratios and brittleness of sandy soils from laboratory tests. *Can. Geotech. J.* **2011**, *48*, 493–510. [CrossRef]
9. Hird, C.C.; Hassona, F.A.K. Some factors affecting the liquefaction and flow of saturated sands in laboratory tests. *Eng. Geol.* **1990**, *28*, 149–170. [CrossRef]
10. Stokoe, K.H.I.; Roesset, J.M.; Bierschwale, J.G.; Aouad, M. Liquefaction potential of sands from shear wave velocity. In Proceedings of the 9th World Conference on Earthquake Engineering, Tokyo, Japan, 2–9 August 1988; Volume 3, pp. 213–218.
11. Tokimatsu, K.; Kuwayama, S.; Tamura, S. Liquefaction potential evaluation based on Rayleigh wave investigation and its comparison with field behavior. In Proceedings of the 2nd International Conference on Recent Advances in Geotechnical Earthquake Engineering and Soil Dynamics, St. Louis, MI, USA, 14 March 1991; Volume 1, pp. 357–364.
12. Eslaamizaad, S.; Robertson, P.K. Evaluation of settlement of footings on sand from seismic in-situ tests. In Proceedings of the 50th Canadian Geotechnical Conference, Ottawa, ON, Canada, 20–22 October 1997; BiTech Publishers: Richmond, BC, Canada; Volume 2, pp. 755–764.
13. Schnaid, F. Geocharacterization and engineering properties of natural soils by in situ tests. In Proceedings of the 16th International Conference on Soil Mechanics and Geotechnical Engineering, Osaka, Japan, 12–15 September 2005; Volume 1, pp. 3–45.
14. Schnaid, F.; Yu, H.S. Theoretical interpretation of the seismic cone test in granular soils. *Géotechnique* **2007**, *57*, 265–272. [CrossRef]
15. Schneider, J.A.; Moss, R.E.S. Linking cyclic stress and cyclic strain based methods for assessment of cyclic liquefaction triggering in sands. *Géotechnique Lett.* **2011**, *1*, 31–36. [CrossRef]
16. Hardin, B.O. The nature of stress-strain behavior of soils. In Proceedings of the Earthquake Engineering and Soil Dynamics Conference (ASCE), Pasadena, CA, USA, 19–21 June 1978; Volume 1, pp. 3–90.
17. Lo Presti, D.C.; Shibuya, S.; Rix, G.J. Innovation in soil testing. In Proceedings of the 2nd International Conference on Pre-Failure Deformation Characteristics of Geomaterials (IS Torino 99), Rotterdam, The Netherlands, 28–30 September 1999; Jamiolkowski, M., Lancellota, R., Lo Presti, D.C.F., Eds.; Volume 2, pp. 1027–1076.
18. Viana da Fonseca, A.; Coop, M.R.; Fahey, M.; Consoli, N. The interpretation of conventional and non-conventional laboratory tests for challenging geotechnical problem. In *Deformation Characteristics of Geomaterials*; IOS Press: Amsterdam, The Netherlands, 2011; Volume 1, pp. 84–119.
19. Schnaid, F.; Bedin, J.; Viana da Fonseca, A.; Costa-Filho, L.d.M. Stiffness and strength governing the static liquefaction of tailings. *J. Geotech. Geoenviron. Eng.* **2013**, *139*, 2136–2144. [CrossRef]
20. Riveros, G.A.; Sadrekarimi, A. Static liquefaction behaviour of gold mine tailings. *Can. Geotech. J.* **2021**, *58*, 889–901. [CrossRef]
21. Yang, Z.; Liu, X.; Guo, L.; Cui, Y.; Liu, T.; Shi, W.; Ling, X. Effect of silt/clay content on shear wave velocity in the Yellow River Delta (China), based on the cone penetration test (CPT). *Bull. Eng. Geol. Environ.* **2022**, *81*, 28. [CrossRef]
22. Doygun, O.; Brandes, H.G.; Roy, T.T. Effect of Gradation and Non-plastic Fines on Monotonic and Cyclic Simple Shear Strength of Silica Sand. *Geotech. Geol. Eng.* **2019**, *37*, 3221–3240. [CrossRef]
23. Zhao, J.; Zhu, Z.; Liu, J.; Zhong, H. Damping Ratio of Sand Containing Fine Particles in Cyclic Triaxial Liquefaction Tests. *Appl. Sci.* **2023**, *13*, 4833. [CrossRef]
24. Santamarina, J.C.; Cho, G.C. Soil behaviour: The role of particle shape. In Proceedings of the Skempton Conference, Advances in Geotechnical Engineering: The Skempton Conference, London, UK, 29–31 March 2004; pp. 604–617.

25. Cho, G.; Dodds, J.; Santamarina, J.C. Particle shape effects on packing density, stiffness, and strength: Natural and crushed sands. *J. Geotech. Geoenviron. Eng.* **2006**, *132*, 591–602. [CrossRef]
26. Consoli, N.C.; Heineck, K.S.; Coop, M.R.; Viana da Fonseca, A.; Ferreira, C. Coal bottom ash as a geomaterial: Influence of particle morphology on the behavior of granular materials. *Soils Found.* **2007**, *47*, 361–373. [CrossRef]
27. Consoli, N.; Viana da Fonseca, A.; Cruz, R.C.; Heineck, K.S. Fundamental parameters for the stiffness and strength control of artificially cemented sand. *J. Geotech. Geoenvironmental Eng.* **2009**, *135*, 1347–1353. [CrossRef]
28. Santos, J.A.; Gomes, R.C.; Lourenço, J.C.; Marques, F.; Coelho, P.; Azeiteiro, R.; Santos, L.A.; Marques, V.; Viana da Fonseca, A.; Soares, M.; et al. Coimbra sand round robin tests to evaluate liquefaction resistance. In Proceedings of the 15th World Conference on Earthquake Engineering, Lisboa, Portugal, 24–28 September 2012.
29. Viana da Fonseca, A.; Rocha, A.; Tahar, G. Liquefaction assessment charts on state and waves' velocities from static and cyclic triaxial tests on "Les Dunes" sands from Algier. In Proceedings of the 5th International Conference on Earthquake Geotechnical Engineering, Santiago, Chile, 10–13 January 2011.
30. Viana da Fonseca, A.; Soares, M. Effect of principal stress rotation on cyclic liquefaction. In Proceedings of the 2nd International Conference on Performance-Based Design in Earthquake Geotechnical Engineering, Taormina, Italy, 28–30 May 2012; pp. 441–454.
31. Viana da Fonseca, A.; Soares, M. Critical state soil mechanics assessment of instability and liquefaction locus of a sandy soil from Coimbra. In Proceedings of the XVII Brasilian Conference on Soil Mechanics and Geotechnical Engineering, Goiânia, Brasil, 9–13 September 2014.
32. *ASTM D4254*; Standard Test Methods for Minimum Index Density and Unit Weight of Soils and Calculation of Relative Density. American Society of Testing Materials: West Conshohocken, PA, USA, 2016.
33. *ASTM D2487*; Standard Practice for Classification of Soils for Engineering Purposes (Unified Soil Classification System). American Society of Testing Materials: West Conshohocken, PA, USA, 2017.
34. Soares, M. Evaluation of Soil Liquefaction Potential Based on Laboratory Data. Major Factors and Limit Boundaries. Ph.D. Thesis, University of Porto, Porto, Portugal, 2014.
35. Bedin, J. Study of the Geomechanical Behavior of Tailings. Ph.D. Thesis, Federal University of Rio Grande do Sul, Porto Alegre, Brazil, 2010.
36. Viana da Fonseca, A.V.; Cordeiro, D.; Molina-Gómez, F. Recommended procedures to assess critical state locus from triaxial tests in cohesionless remoulded samples. *Geotechnics* **2021**, *1*, 95–127. [CrossRef]
37. Soares, M.; Viana da Fonseca, A. Factors affecting steady state locus in triaxial tests. *Geotech. Test. J.* **2016**, *39*, 1056–1078. [CrossRef]
38. Viana da Fonseca, A.; Ferreira, C.; Fahey, M. A framework interpreting bender element tests, combining time-domain and frequency-domain methods. *ASTM Geotech. Test. J.* **2009**, *32*, 91–107. [CrossRef]
39. Nicholson, P.G.; Seed, R.B.; Anwar, H.A. Elimination of membrane compliance in undrained triaxial testing. I. Measurement and evaluation. *Can. Geotech. J.* **1993**, *30*, 727–738. [CrossRef]
40. CEN. *Standard on Geotechnical Investigation and Testing—Laboratory Testing of Soil—Part 9: Consolidated Triaxial Compression on Water Saturated Soil*; Technical Report; Comité Européen de Normalisation: Brussels, Belgium, 2004.
41. Bedin, J.; Schnaid, F.; Viana da Fonseca, A. Gold tailings liquefaction using critical state soil mechanics concepts. *Géotechnique* **2012**, *62*, 263–267. [CrossRef]
42. Lade, P.V. Instability, shear banding, and failure in granular materials. *Int. J. Solids Struct.* **2002**, *39*, 3337–3357. [CrossRef]
43. Lade, P.V.; Yamamuro, J.A. Stability of granular materials in post peak softening regime. *J. Eng. Mech.* **1993**, *119*, 128–144. [CrossRef]
44. Lade, P.V.; Yamamuro, J.A. Effects of nonplastic fines on static liquefaction of sands. *Can. Geotech. J.* **1997**, *34*, 918–928. [CrossRef]
45. Chu, J.; Leong, W.K.; Loke, W.L.; Wanatowski, D. Instability of loose sand under drained conditions. *J. Geotech. Geoenvironmental Eng.* **2012**, *138*, 207–216. [CrossRef]
46. Andrus, R.D.; Stokoe, K.H. Liquefaction Resistance Based on Shear Wave Velocity. In Proceedings of the National Center for Earthquake Engineering Research (NCEER) Workshop on Evaluation of Liquefaction Resistance of Soils, New York, NY, USA, 31 December 1997; Youd, T.Y., Idriss, I.M., Eds.;
47. Soares, M.; Bedin, J.; Silva, J.; Viana da Fonseca, A. Monotonic and cyclic liquefaction assessment on silty soils by triaxial tests with bender elements. In Proceedings of the International Conference on Advances in Geotechnical Engineering, Perth, Australia, 7–9 November 2011.
48. Bayat, E.; Bayat, M. Effect of grading characteristics on the undrained shear strength of sand: Review with new evidences. *Arab. J. Geosci.* **2013**, *6*, 4409–4418. [CrossRef]
49. Igwe, O.; Fukuoka, H.; Sassa, K. The effect of relative density and confining stress on shear properties of sands with varying grading. *Geotech. Geol. Eng.* **2012**, *30*, 1207–1229. [CrossRef]

applied sciences

MDPI

Article

Influence of Apparatus Scale on Geogrid Monotonic and Cyclic/Post-Cyclic Pullout Behavior in Cohesive Soils

Sergio Rincón Barajas [1], Gabriel Orquizas Mattielo Pedroso [2,*], Fernanda Bessa Ferreira [3,*] and Jefferson Lins da Silva [1]

[1] São Carlos School of Engineering, University of São Paulo (USP), São Carlos 13563-120, Brazil; srinconbarajas@gmail.com (S.R.B.); jefferson@sc.usp.br (J.L.d.S.)
[2] Faculty of Engineering and Sciences of Guaratinguetá, São Paulo State University (UNESP), Guaratinguetá 12516-410, Brazil
[3] CONSTRUCT, Faculty of Engineering, University of Porto, R. Dr. Roberto Frias, 4200-465 Porto, Portugal
* Correspondence: gabriel.pedroso@unesp.br (G.O.M.P.); fbf@fe.up.pt (F.B.F.); Tel.: +55-12-3123-2829 (G.O.M.P.)

Abstract: Geosynthetics have increasingly been applied to geotechnical engineering works due to their numerous advantages, including cost-effectiveness and their significant role in sustainable development. When geosynthetics are used as reinforcement in earth structures, such as embankments, retaining walls and bridge abutments, soil–geosynthetic interface shear behavior is a critical parameter involved in the design. This paper presents a series of monotonic and cyclic/post-cyclic pullout tests carried out to examine the apparatus scale effect on the pullout response of a geogrid embedded in two different soils. To assess the small-scale equipment feasibility, comparisons were made between pullout test parameters derived from small- and large-scale equipment. The test results indicate that, under a low confining stress of 25 kPa, using a smaller-sized apparatus results in lower values of geogrid pullout resistance and maximum mobilized shear stress, but higher values of confined tensile stiffness at low strains. On the other hand, as the confining stress increases (i.e., 50 kPa and 100 kPa), the difference between the results becomes less significant and similar trends are observed regardless of the equipment type. Adopting small-scale equipment enables obtaining soil–reinforcement interaction parameters using test procedures that are less time-consuming than those associated with large-scale pullout tests. However, proper scale effect correction factors may be considered for more consistent estimates of the interface strength parameters under low normal stress values.

Keywords: pullout test; reinforced soil; geogrid; cyclic loading; apparatus scale

Citation: Barajas, S.R.; Pedroso, G.O.M.; Ferreira, F.B.; Lins da Silva, J. Influence of Apparatus Scale on Geogrid Monotonic and Cyclic/Post-Cyclic Pullout Behavior in Cohesive Soils. *Appl. Sci.* **2024**, *14*, 5861. https://doi.org/10.3390/app14135861

Academic Editors: Paulo José da Venda Oliveira, António Alberto Santos Correia and Syed Minhaj Saleem Kazmi

Received: 29 April 2024
Revised: 25 June 2024
Accepted: 2 July 2024
Published: 4 July 2024

1. Introduction

Geosynthetics have been widely used as a reinforcement material in geotechnical structures, such as roadways, railways, steep slopes, embankments and retaining walls, with the function of improving the mechanical behavior of the surrounding soils or aggregates [1–3]. Several benefits, including the reliability, cost-effectiveness and contribution towards sustainability have led to the increasing use of geosynthetics in civil infrastructure projects worldwide. In particular, the role of geosynthetics in sustainable infrastructure development and circular economy has been well recognized and highlighted in recent years. For instance, these materials facilitate energy and resource savings by accelerating the construction process, minimizing on-site excavation, reducing the need to transport bulky materials, extending infrastructure longevity and decreasing maintenance requirements. They can replace or reduce the use of other construction materials, such as sand and aggregates, thus attenuating the adverse environmental impacts from natural resource extraction. In addition, they often enable the use of locally available low-quality soils (such as cohesive soils) or recycled aggregates (e.g., construction and demolition waste) as

alternative fill materials, in which case they significantly contribute towards reducing the amount of waste directed to landfills [4].

The geosynthetic reinforcement mechanism is mainly dependent upon the interaction developed at the soil–geosynthetic interfaces. The interaction between the soil and reinforcement redistributes stresses within the soil mass, increasing the stability of the reinforced structure, and decreasing horizontal deformations.

These redistributions of stress within the reinforced soil depend on the soil properties, the reinforcement characteristics, and the interaction between components. It is essential to identify the interaction mechanism and the most suitable test for its characterization [5]. Various experimental techniques have been developed to enhance the comprehension of the interaction between soils and geosynthetics. Among these methods are the direct shear test, pullout test, in-soil tensile test and ramp test. From these, the direct shear and pullout tests stand out as the most frequently used. The direct shear test assesses the interaction at the interface when the soil mass slides on the surface of the reinforcement. In contrast, the pullout test is applicable when the reinforcement is pulled out from the soil mass [6].

In the past several decades, different researchers have analyzed the interface mechanism between the geosynthetic and surrounding soil. Direct shear interface tests have been investigated by the authors of [5,7,8]. The pullout response has been studied experimentally by considering various influential factors such as box and specimen size, sleeve length, active length, test speed, soil characteristics and geosynthetic properties [9–19], as well as using analytical and numerical methods [20–23]. Apart from high-quality (i.e., granular) soils, the pullout behavior of geosynthetics in alternative backfill materials, such as cohesive and residual soils or recycled aggregates, has also been the subject of significant research [23–26].

In some structures, the geosynthetic reinforced soil is exposed to repeated or cyclic loads, which may be induced by compaction, road or railway traffic, wave loading and earthquakes. The understanding of the cyclic behavior of such reinforced soil structures is crucial for the design and performance. Reports of soil–geosynthetic interaction under cyclic loading conditions are available in [27–35].

The pullout resistance of geosynthetic reinforcements in granular soils can be evaluated by a theoretical relationship proposed by [36] and represented by Equation (1), where (P_R) is the geosynthetic pullout resistance per unit width, (L_R) is the geosynthetic length in the anchorage zone, (σ_n) is the effective normal stress at the reinforcement level, (f_b) is the soil–reinforcement pullout interaction coefficient and (ϕ) is the soil friction angle.

$$P_R = 2L_R\sigma_n f_b \tan\phi \quad (1)$$

In the absence of information concerning the soil friction angle to be considered in Equation (1), the pullout resistance of geosynthetics can be expressed in terms of the pullout interface's apparent coefficient of friction, $\mu_{S/GSY}$ (Equation (2)) [14]:

$$P_R = 2L_R\sigma_n\mu_{S/GSY} \quad (2)$$

To account for the non-linearity of the pullout force along the length of extensible reinforcements, a scale effect correction factor (α) was introduced by Berg et al. [2] (Equation (3)):

$$P_R = 2L_R\sigma_n F^*\alpha \quad (3)$$

where F^* is the pullout resistance factor.

In fact, the interface shear strength is not uniformly mobilized over the length of extensible geosynthetic reinforcements. The scale effect correction factor (α) accounts for the non-linear stress decrease throughout the reinforcement length and the development of progressive failure and depends mainly on the strain-softening of the soil and the reinforcement extensibility and length [2]. In the experimental data, which are lacking, the recommended values are 1.0 for metallic reinforcements, 0.8 for geogrids and 0.6 for geotextiles.

The pullout resistance factor (F^*) may be determined through laboratory or field pullout tests using the backfill material intended for the project. However, if such data are unavailable, a conservative estimate of F^* for geosynthetic materials can be obtained considering $F^* = 2/3 \tan \phi$ [2].

Pullout tests have been extensively used to assess the interface mechanism and analyze the reinforced soil structure parameters. However, several factors can influence the results of pullout tests. The experimental and numerical data on the apparatus scale effect suggest that the apparatus size is susceptible to influencing the results of pullout tests [9–11]. Palmeira and Milligan [9] and Palmeira [6] verified that pullout test results are influenced by boundary conditions and friction coefficients between soil and geogrid can be overestimated in small-scale tests. This effect can be minimized by the lubrication of the internal face of the box frontal wall. Lopes and Ladeira [11] observed that pullout apparatus with lower height resulted in stiffer interface response and higher maximum pullout load. Moreover, they noted a minimal impact of box height for heights exceeding the geosynthetic length. The authors recommended that the soil sample height should exceed 0.6 m.

A small pullout box was developed by Teixeira et al. [15] to evaluate the strength of individual geogrid ribs (i.e., longitudinal and transverse ribs). Moreover, the same equipment was used to evaluate the unsaturated soil conditions by Portelinha et al. [37] and Marques and Lins da Silva [38]. Kakuda [39] compared the results from monotonic tests using small- and large-scale equipment and concluded that the shear stress and interaction coefficient values were practically concomitant. Kakuda [39] and Sugimoto et al. [13] evaluated the effect of the size of the geogrid and the internal width of the equipment and concluded that as the specimen width approaches the internal dimensions of the box, the pullout force tends to a constant value. Therefore, for the analyzed geogrids, the authors recommended using twelve longitudinal elements.

The test method described in the ASTM D6706 [40] standard considers using large-scale equipment and is intended to be a performance test simulating design or as-built conditions [40]. Large-scale tests are considered to yield more reliable results compared to small-scale tests, because they better replicate the physical structure of a reinforced soil mass, while allowing for a better distribution of stresses and strains on the geosynthetic, potentially due to a scale effect [6]. On the other hand, the reduced dimensions of small-scale test boxes may interfere with the soil–reinforcement interaction, thus potentially casting doubt on the reliability of the results. However, as reported by Kakuda [39], adopting measures to minimize boundary effects of the small-scale equipment has led to obtaining pullout shear resistance and interface coefficients close to those from monotonic large-scale pullout tests when fine soils are used. Nevertheless, limited studies have previously compared the pullout behavior of geosynthetics derived from small- and large-scale equipment and further research is still required for a better understanding of the apparatus scale effect under different experimental conditions. In such earlier studies, geosynthetic specimens with distinct length/width ratios have generally been used, which may have jeopardized the comparison of results. Additionally, to the best of the authors' knowledge, no previous study has evaluated the influence of apparatus scale on the geogrid pullout behavior under both monotonic and cyclic/post-cyclic loading conditions.

Considering that the conventional pullout tests using large-scale devices have several inconveniences, such as the high cost, long execution time and complexity of the assembly, it is important to assess the feasibility of using small-scale equipment for geosynthetic pullout testing. Given this, a series of pullout tests have been carried out to evaluate the influence of apparatus scale on the pullout response of a geogrid subjected to different confining stresses and varying loading conditions (i.e., monotonic, cyclic and post-cyclic). The use of small-scale equipment to estimate soil–geosynthetic interface strength parameters would represent significant benefits, including the easier and faster test assembly, as well as the possibility of obtaining a larger amount of data using less resources.

2. Materials and Methods

2.1. Test Materials

Two soils (A and B) were used in the current pullout testing program. Both materials were collected close to São Carlos (São Paulo, Brazil). Soil A consists of tropical soil, classified as high-plasticity silt (MH), as per the Unified Soil Classification System (USCS). This material was used in the first three layers of compacted material inside each pullout box. The other soil (soil B) consists of a clayey sand (SC) and was used above the geogrid in the top layers. The particle size distribution of these soils is presented in Figure 1. It is noteworthy that soil A includes about 65% fines, with D_{50} = 0.007 mm and D_{85} = 0.25 mm. On the other hand, soil B has less fines (20%), with D_{50} = 0.15 mm and D_{85} = 0.4 mm.

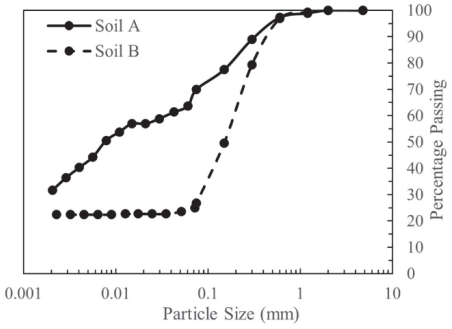

Figure 1. Particle size distribution curves of soils A and B.

The shear strength parameters of soils A and B were determined using triaxial load tests conducted at identical relative compaction and moisture conditions as the specimens used for the pullout tests. Consolidated drained (CD) triaxial tests were performed to characterize soil B, whereas consolidated undrained (CU) triaxial tests were conducted on soil A. These tests followed the recommendations of the ASTM D4767 and ASTM D7181 standards [41,42]. Table 1 summarizes the main physical properties of these soils.

Table 1. Soil characteristics.

Property	Unit	Soil A	Soil B
Classification (USCS)	-	MH	SC
Specific gravity, GS	-	2.913	2.646
Liquid limit, w_L	%	55	16
Plastic limit, w_P	%	32	-
Maximum dry unit weight, $\gamma_{d,máx}$	g/cm^3	1.626	1.983
Optimum water content, w_{op}	%	22.75	9.24
Friction angle, ϕ	°	27	31
Cohesion, c	kPa	66.27	34.64

The choice of different materials was made taking into account the distribution of induced interfacial shear stresses in the soil mass around the geosynthetic, and the study presented by Abdi et al. [43] and Abdi et al. [44], which reported that the inclusion of high-quality sand around the reinforcement can effectively improve the strength and deformative response of reinforced clay. With this in mind, while the bottom layer (soil A) has low mobilization of interface shearing resistance, the upper layer (soil B) provides a layer of frictional material above the geosynthetic reinforcement, potentially contributing to enhanced interface shear strength.

The reinforcement tested was an extruded flexible biaxial polypropylene (PP) geogrid (GGR) coated with polyvinyl chloride (PVC). Table 2 summarizes the main properties of

the geogrid. The aperture size of this particular geogrid takes into account the size of the small pullout box.

Table 2. Geogrid properties.

Property	Unit	Value
Polymer	-	PP
Thickness	mm	1.05
Mean grid size	mm	45 × 45
Short-term tensile strength	kN/m	43.24
Elongation at maximum load	%	5.75
Secant stiffness at 5% strain	kN/m	523

2.2. Pullout Test Devices

According to the ASTM pullout test standard [40], the large-scale pullout test box should have minimum dimensions of 610 mm in length, 460 mm in width and 305 mm in height. Additionally, the width of the box should be determined as the greater of 20 times the D_{85} of the soil or 6 times its maximum particle diameter, while ensuring the length is greater than 5 times the maximum aperture size of the geosynthetic. The box must provide a minimum depth of 150 mm above and below the geosynthetic, whereby the soil depth above and below the geosynthetic is at least 6 times the D_{85} of the soil and 3 times its maximum particle diameter. Finally, the box should allow for a minimum embedment length of 610 mm beyond the sleeve, as well as a geosynthetic length-to-width ratio not lower than 2.0.

The large pullout box (LB) utilized herein (Figure 2) consists of a rigid steel box, reinforced with U-shaped steel beams, which was first developed by Teixeira [45]. Its dimensions are 1500 mm long, 700 mm wide and 480 mm high. As can be observed, the box exceeds the dimensions prescribed by ASTM D6706 [40]. The system can apply a tensile force of up to 60 kN to the reinforcement. For normal load application, an airbag is used, providing a uniform surcharge that replicates field conditions [45].

(**a**) (**b**)

Figure 2. Large-scale pullout test apparatus: (**a**) overall view; (**b**) inextensible wires fixed along the GGR.

The boundary effects generated by the inner walls of the box can affect the measured pullout resistance value. As mentioned by Palmeira and Milligan [9], one of the options to reduce such effects consists of leaving a minimum distance of 150 mm between the geosynthetic and each pullout box wall. Additionally, Palmeira and Milligan [9] recommended using a metallic sleeve at the level of the reinforcement to mitigate the frictional effects at the front wall, as its implementation causes the point of application of the pullout force to be transferred inside the soil mass, as illustrated in Figure 2.

The small pullout box (SB) consists of a rigid steel box with inner dimensions of 245 mm in length, 300 mm in width and 145 mm in height, as shown in Figure 3. These

dimensions closely resemble those of a large-scale direct shear test apparatus and are approximately half of the minimum dimensions indicated by ASTM D6706 [40]. The upper surface of the box features a reaction cap attached to a pressure-controlled air bag used for applying the normal load. Positioned in the rear region is a support for the attachment of four tell-tales, which are linked to the geosynthetic by inextensible wires. The small box was originally developed by Teixeira et al. [15] to investigate the individual geogrid ribs. However, a comparison between the results from both devices considering the monotonic and cyclic pullout response of geosynthetic reinforcements to evaluate the associated scale effects had not yet been performed.

(**a**) (**b**)

Figure 3. Small-scale pullout test apparatus: (**a**) overall view; (**b**) inextensible wires over the GGR length.

In the case of the small-scale equipment, keeping a significant distance between the sidewalls of the box and the reinforcement or the inclusion of a metallic sleeve is not possible due to the limited dimensions of the box. Therefore, to reduce the sidewall friction, a different solution proposed by Palmeira and Milligan [9] was adopted, which consisted of installing two geomembranes on each wall, lubricated with graphite calcium grease, as shown in Figure 3. In order to use the same load application system in both pieces of equipment and to be able to establish the respective comparisons, an adaptation support for the small equipment in the large box was designed.

The displacements of the geogrid were measured using inextensible wires fixed to the geogrid. To reduce friction, the wires were protected by nylon tubes with an internal diameter of 2 mm, which were placed along the reinforcement length. Furthermore, two total pressure cells were installed 10 mm above the geogrid to evaluate the development of localized normal stresses.

For the large-scale equipment, the displacements were recorded by five different tell-tales nominated T1, T2, T3, T4 and T5 and two linear variable differential transformers (LVDT) with a maximum capacity of 50 mm and denominated L1 and L2 (Figure 4a). All points T1 to T5 were spaced 45 mm longitudinally. On the other hand, for the small box, the geogrid displacements were measured by four different tell-tales nominated T1, T2, T3 and T4 (Figure 4b). For consistency, all points were spaced 45 mm in the longitudinal direction, similar to the large-scale equipment.

Regarding the size of the geogrid specimens, a constant relationship was considered between the width and length of the specimens in the confined region for each piece of equipment. The ratio between the width and length in the confined region was limited by the size of the small-scale equipment. The dimensions were defined considering a distance of 20 mm between the side walls of the box and the geogrid, as well as a distance of 30 mm between the back wall and the reinforcement. Thus, the size of the geogrid specimen inside the small-scale equipment was defined as 215 mm $\times$ 260 mm, resulting in a ratio of 1.21, as shown in Figure 4. Considering the same ratio of 1.21 for the large-scale equipment and following the ASTM D6706 [46] recommendation of a 150 mm minimum distance between

the geosynthetic and the box sidewalls, a length of 250 mm and a width of 300 mm were adopted, resulting in a similar confined length in both types of equipment.

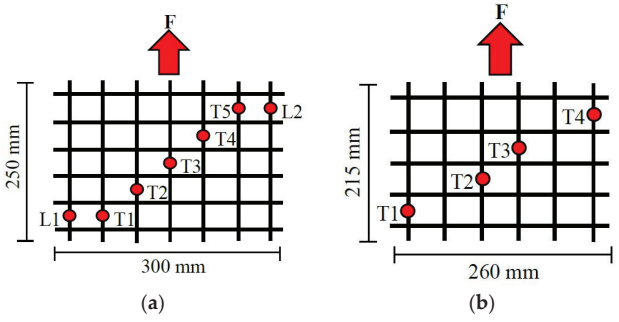

Figure 4. Measured points of GGR displacement: (**a**) large equipment; (**b**) small equipment.

2.3. Test Procedures

The large-scale pullout testing program was conducted in accordance with recommendations of the ASTM D6706 standard [46] and procedures adopted by Teixeira et al. [15]. The soils used were initially homogenized at their optimum moisture content. Then, the appropriate mass of soil for each layer was separated, considering both the target dry unit weight and the desired thickness of each layer. The compaction was carried out by utilizing a manual hammer with a 120 mm square base and 40 N weight. The hammer was dropped from a height of 450 mm to ensure proper compaction. The soil was compacted in six layers, each with a thickness of 80 mm. After the initial three layers were compacted, the geogrid specimen was attached to the clamp and placed at mid-height. As mentioned earlier, the initial three layers consisted of soil A. Once the geogrid was positioned, soil B was compacted in the upper portion of the box, following the same procedures used for the initial layers. An airbag was then fixed over the soil surface at the top plate, and a uniform distribution pressure was administered via a pneumatic system, regulated by a controlled compressor, as shown in Figure 5.

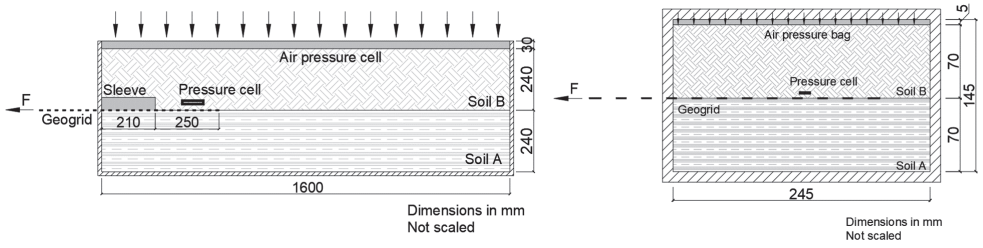

Figure 5. Schematic profile view: (**a**) small equipment; (**b**) large equipment.

For the small-scale equipment, the soil was mixed with the required water to attain the desired moisture content. Subsequently, it was compacted in the pullout box to the prescribed density in four layers, each with a thickness of 35 mm. The compaction was performed using a manual hammer with a 20 mm square base and 10 N weight, dropped from a height of 100 mm. The compaction procedures resulted in a consistent soil density for both types of equipment. Furthermore, the relative compaction varied from 96% to 102% of the standard proctor maximum dry unit weight.

A servo-hydraulic control system, powered by an electric pump, was used to apply the pullout force to the reinforcement. Programmable software controls the system speed, displacement and applied load throughout the test. The pullout clamp has reinforcement ribs along their sides, and the tightening is performed by clamping the screws, which

immobilizes the specimen throughout its width and minimizes the differential slips, as shown in Figure 6. The clamping system can be placed inside or outside the test box, as reported by Moraci and Recalcati [14].

(**a**) (**b**)

Figure 6. Clamping system: (**a**) clamp apparatus; (**b**) installed clamp system.

Initially, monotonic pullout tests were performed at a constant displacement rate of 4.0 mm/min until pullout or rupture of the geogrid was achieved. The displacement rate used in this study for geosynthetic pullout testing is different from that recommended by ASTM D6706 [40]. However, as reported by the authors of [39], the use of displacement rates of 1.0, 2.0 and 4.6 mm/min in this equipment did not lead to a high variability of results. A displacement rate of 4.0 mm/min was adopted herein to enable the comparison of the test results with those from other studies carried out using the same equipment, in which this particular rate of displacement has commonly been used.

After the monotonic pullout evaluation, the cyclic load limits were estimated, and the load amplitude was defined as 20% of the monotonic maximum pullout resistance value. This load amplitude was defined based on Razzazan et al. [47] and Garcia and Lodi [34], which concluded that for high amplitude values (80%), the geogrid breakage tends to occur before the end of cycles, and amplitude values ranging from 20% to 40% seem to lead to similar results.

In the cyclic/post-cyclic test procedure, the system was first loaded at a lower limit estimated according to ASTM D7499 [46], corresponding to 0.9 kPa for a confinement stress of 25 kPa and 3.6 kPa for a confinement stress of 100 kPa. Then, 10,000 loading cycles were applied to the reinforcement. The cyclic pullout load followed a haversine shape with a 0.5 s applied load period followed by a 0.5 s rest period in each load cycle, thus resulting in a frequency of 1 Hz. The number of load cycles was selected based on Razzazan et al.'s work [47], which showed that the increment in the number of cycles from 30 to 250 caused only slight changes in the peak pullout resistance. Therefore, a higher number of loading cycles were imposed herein. After the cyclic loading stage, the pullout test proceeded under monotonic loading conditions (post-cyclic loading stage) until pullout or tensile failure of the geogrid was reached.

3. Results

As mentioned previously, the test program consisted of assessing the equipment scale effect on the pullout response of the geosynthetics. First, the results of monotonic tests are presented. These tests were performed under applied vertical pressures of 25, 50 and 100 kPa, for both small- and large-scale equipment. Afterwards, the analyses were presented for the cyclic/post-cyclic tests. The post-cyclic tests were performed under 25 and 100 kPa applied vertical pressures for both types of equipment.

It is noteworthy that the vertical pressure was monitored by total pressure cells installed 10 mm above the reinforcement level. Prior to the beginning of the test, the vertical pressure was increased until it reached the prescribed value (25, 50 or 100 kPa), and

then kept constant for 8 min. Observations indicated that immediately after the start of the test, there was a deconfinement of the soil due to the dilatancy effect, followed by an increase in the vertical pressure due to the rearrangement of soil particles. Throughout the test, the total pressure cells reached an equilibrium state, with values stabilizing close to the required vertical pressure.

3.1. Monotonic Loading Conditions

In this study, the geogrid pullout resistance (P_R) was evaluated considering the effective area of the geogrid and the average force values, as recommended by Ochiai et al. [12]. The influence of the pullout test apparatus scale was verified through monotonic tests at three applied normal stresses (σ_n). Table 3 presents a summary of these test results, displaying the maximum pullout resistance (P_R), the corresponding frontal geogrid displacement (u_{PR}), the confined stiffness at 2% strain ($J_{C2\%}$), the maximum shear stress (τ_i) and the pullout interface apparent coefficient of friction ($\mu_{s/GSY}$).

Table 3. Summary of monotonic test results.

Test	P_R (kN/m)	u_{PR} (mm)	$J_{C2\%}$ (kN/m)	τ_i (kPa)	$\mu_{s/GSY}$	σ_n (kPa)	Equipment
1	15.68	27.16	725	36.47	1.46	25	SB
2	22.19	25.55	779	51.61	1.03	50	SB
3	27.57	15.82	838	64.12	0.64	100	SB
4	20.90	28.07	632	41.81	1.67	25	LB
5	26.70	20.05	686	53.40	1.06	50	LB
6	28.93	8.19	852	59.73	0.58	100	LB

Figure 7 presents the comparison between the pullout force versus geogrid displacement from the small box (Figure 7a) and large box (Figure 7b) at 50 kPa applied normal stress. From Figure 7a, it is observed that the displacement values from tell-tales T1 to T3 were similar for the small-scale equipment, even though they were installed at different locations along the geogrid length. Conversely, the displacements recorded in the large-scale tests varied considerably throughout the whole reinforcement length. The longer the distance from the rear edge, the higher the displacement values, as shown in Figure 7b. Although different instruments (tell-tales and LVDTs) were used in the large-scale equipment, the results of pairs L1–T1 and L2–T5 were quite consistent.

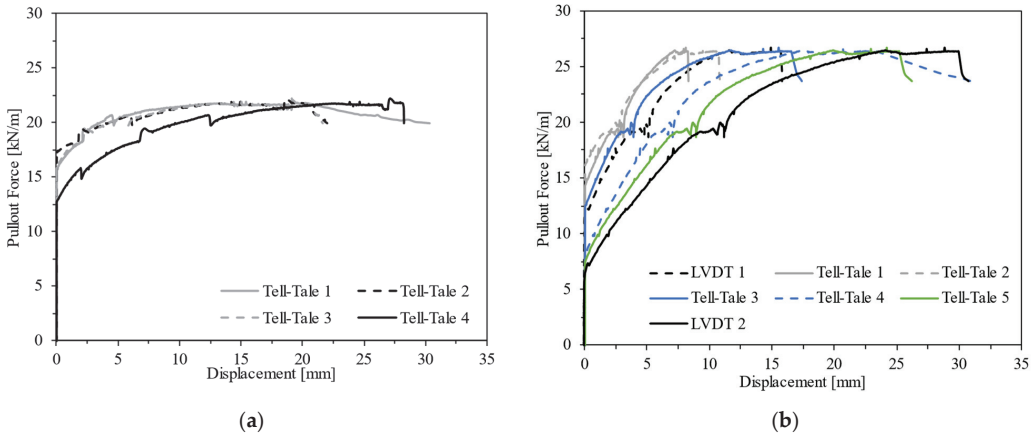

Figure 7. Displacement instrumentation response: (**a**) small box (σ_n = 50 kPa); (**b**) large box (σ_n = 50 kPa).

Figure 8 illustrates the influence of equipment scale on the pullout resistance of the geogrid for different applied normal stresses. When comparing the measured pullout resistance at lower applied normal stresses (25 and 50 kPa), it becomes apparent that the use of the large box led to significant increases in the maximum pullout resistance of 33.29% and 20.32%, respectively. However, for the tests performed under 100 kPa, the pullout resistance obtained from the large box exceeded that from the small box by only 4.9%. These results suggest that increasing the applied normal stress leads to a convergence of the values of pullout resistance estimated from both types of equipment.

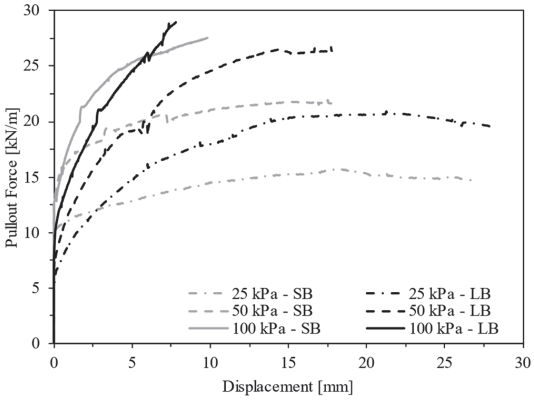

Figure 8. Monotonic pullout force versus frontal displacement of geogrid in small (SB) and large (LB) pullout boxes.

In pullout tests involving extensible geosynthetic reinforcements, the shear stress mobilized along the interface is non-uniform. It is dependent upon the reinforcement confined stiffness (extensibility) and the mobilized shear stresses over the active length of the reinforcement [14,16,48]. The active length corresponds to the confined geosynthetic length over which the mobilization of interaction mechanisms takes place, which can be determined based on the displacements recorded in discrete locations over the specimen length during the test. The experimental interpretation can be simplified by using Equation (4), as proposed by Cardile et al. [16]. This equation replaces the actual shear stress mobilized along the interface by an equivalent uniform average shear stress distribution (τ_{AL}) that can be expressed as the ratio between the applied pullout force (P_R) and the double active length of the geosynthetic (L_A):

$$\tau_{AL} = \frac{P_R}{2L_A} \tag{4}$$

Figure 9 illustrates the maximum shear stress mobilized in the pullout tests (i.e., at the moment of achieving maximum pullout resistance), as determined by Equation (4), plotted against the applied normal stress, as well as the respective linear best-fit lines. By adopting the Mohr–Coulomb failure criteria, the interface strength parameters, specifically the friction angle (δ) and apparent cohesion (c_a), were determined. Comparing the parameters derived from both types of equipment, it can be observed that the friction angle increases (from 13° to 19°), while the apparent cohesion decreases (from 38.6 to 30.2 kPa) when the small pullout box is used. Additionally, it is noted that the maximum pullout shear stress values are relatively similar, particularly under 50 kPa confining stress, indicating a different trend from that observed for the pullout resistance results.

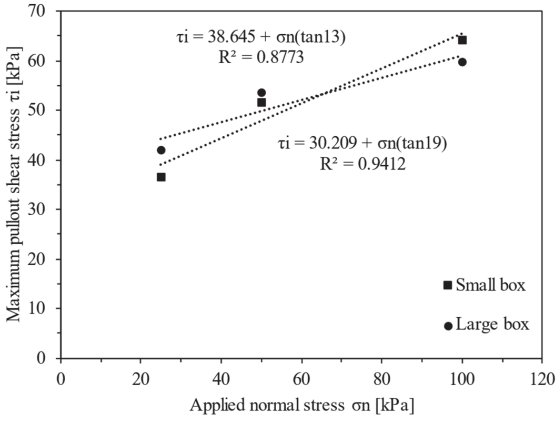

Figure 9. Evolution of maximum pullout shear stress with applied normal stress.

The geogrid stiffness is an important parameter for several reinforcement applications, including reinforced soil structures and pavement design. The design methods of reinforced pavement base, such as that developed by Giroud and Han [49], for example, use the unconfined stiffness (J_N) for designing the base layer. As the reinforcement is under confined conditions in the field, the confined tensile stiffness (J_C) that can better represent the actual geogrid stiffness under field conditions was obtained in this study from the pullout test results.

While the pullout test may not be the optimal method for this purpose, the criterion for assessing the confined stiffness was established as the ratio of the pullout force to the deformation of the geosynthetic between two designated measurement points, as defined in Equation (5):

$$J_C = \frac{P_R}{\left(\frac{X_i - X_{i+1}}{d}\right)} \quad (5)$$

where d represents the original distance between two adjacent measurement points, and X_i denotes the displacement of the i_{th} geogrid measurement point starting from the geogrid front end. For the purpose of this study, as shown in Table 3, analyses of confined tensile stiffness were conducted at 2% strain, considering the intermediate tell-tales (tell-tales T2–T3) for both types of equipment. Additionally, Figure 10 depicts the evolution of confined stiffness with increasing geogrid strain values.

The same method and test apparatus were previously used by Marques and Lins da Silva [38] to determine the confined stiffness. Similarly, refs. [14,16] adopted a comparable approach. Despite variations in equipment and materials, the stiffness curves presented in this study exhibited the same order of magnitude as those obtained by Cardile et al. [16].

Figure 10 indicates that, under lower normal stresses, the smaller box resulted in higher confined stiffness values, particularly for small strains (<2%). However, at a 2% strain, both types of equipment showed similar results. Specifically, for confining stresses of 25 and 50 kPa, the confined tensile stiffness decreased by 12.8% and 11.9%, respectively, when the larger box was utilized. However, a different behavior was observed under higher confining stress (100 kPa), where the influence of equipment scale was less significant, and both types of equipment presented relatively similar confined tensile stiffness values. Additionally, the confined tensile stiffness tended to increase with the confining stress, as also shown in Table 3.

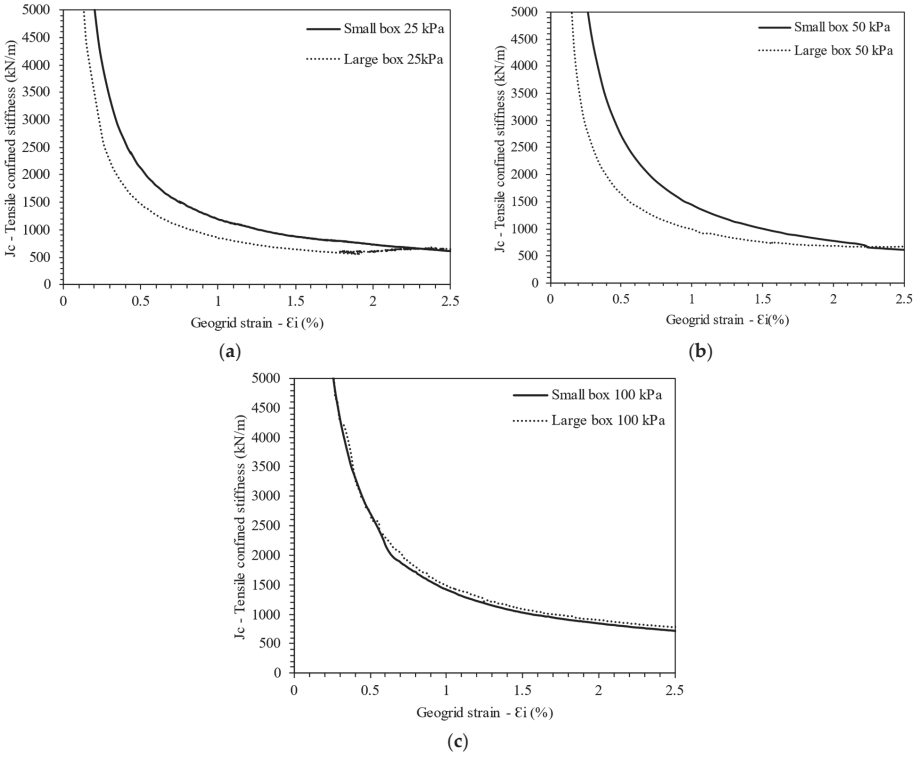

Figure 10. Confined tensile stiffness as a function of geogrid strain: (**a**) σ_n = 25 kPa; (**b**) σ_n = 50 kPa; and (**c**) σ_n = 100 kPa.

3.2. Cyclic/Post-Cyclic Loading Conditions

The cyclic/post-cyclic pullout behavior of the geogrid was evaluated through tests conducted under 25 kPa and 100 kPa confining pressures. Figure 11 shows the variation of P_R as a function of the geogrid frontal displacement based on the monotonic and cyclic/post-cyclic tests. As expected, at the commencement of cyclic loads, large frontal displacement occurs, leading to the mobilization of a significant portion of friction and bearing resistance; therefore, for high normal stress, during the post-cyclic loading stage, the pullout resistance is lower than that achieved under monotonic loading. This degradation of pullout capacity after cyclic loading is consistent with the findings of previously related research [28,29,31,35].

The cumulative frontal displacement of the geogrid during cyclic loading was similar for both types of equipment (Figure 11). Higher cumulative cyclic displacement was measured for the lower normal stress of σ_n = 25 kPa (Figure 11a). Under higher normal stress (Figure 11b), a premature failure of the geogrid in tension (tensile failure) occurred in the small-scale test in the post-cyclic stage. Conversely, when the large-scale equipment was used, the failure was attributed to sliding along the interface. It can also be observed that the displacement of the geogrid at maximum pullout force generally increased in the post-cyclic test, in comparison to that measured under monotonic loading conditions. This trend held true except for when the geogrid underwent tensile failure in the test under σ_n = 100 kPa (Figure 10b).

Table 4 indicates the values of maximum pullout resistance (P_R), the ratio of the maximum post-cyclic shear stress to the maximum shear stress attained in the comparable monotonic pullout test (τ_{cyc}/τ_{mon}), and the peak pullout interface apparent coefficient of friction ($\mu_{s/GSY}$) for the post-cyclic tests. It can be observed that, under the lower normal stress, no degradation of pullout resistance upon cyclic loading (reflected by the τ_{cyc}/τ_{mon} ratio) was observed; rather, the mobilized shear stress increased slightly. Conversely, under

the higher normal stress, lower values of pullout resistance and mobilized shear stress were obtained under post-cyclic conditions.

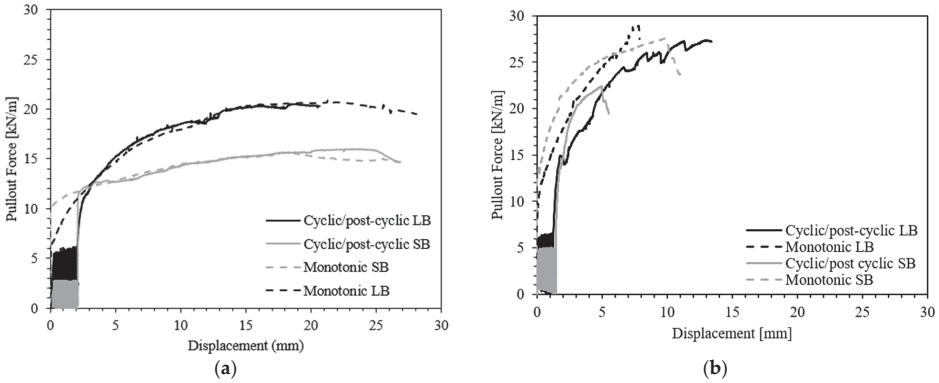

Figure 11. Post-cyclic pullout resistance: (**a**) σ_n = 25 kPa; (**b**) σ_n = 100 kPa.

Table 4. Summary of cyclic/post-cyclic test results.

Test	P_R (kN/m)	τ_{cyc}/τ_{mon} (kPa)	$\mu_{s/GSY}$	σ_n (kPa)	Equipment
1	15.98	1.12	1.48	25	SB
2	20.50	1.06	1.64	25	LB
3	22.39	0.95	0.60	100	SB
4	27.35	0.97	0.55	100	LB

Figure 12 shows the variation in $\mu_{s/GSY}$ as a function of the applied normal stress. The results refer to the two pieces of equipment used, and the different loading conditions adopted (monotonic or cyclic/post-cyclic). For all the test conditions examined, it can be observed that the $\mu_{s/GSY}$ decreases as the applied normal stress increases. This behavior can be explained due to the soil dilatancy effects at the interface [14]. Moreover, for σ_n = 25 kPa, the $\mu_{s/GSY}$ values obtained from the small pullout box exceeded those from the large box, regardless of the loading conditions. However, for higher normal stresses (σ_n = 50 and 100 kPa), the differences between the $\mu_{s/GSY}$ values associated with distinct equipment types were less significant. Except for the small box test under σ_n = 25 kPa, the μs/GSY values attained under monotonic loading conditions exceeded those reached under post-cyclic loading.

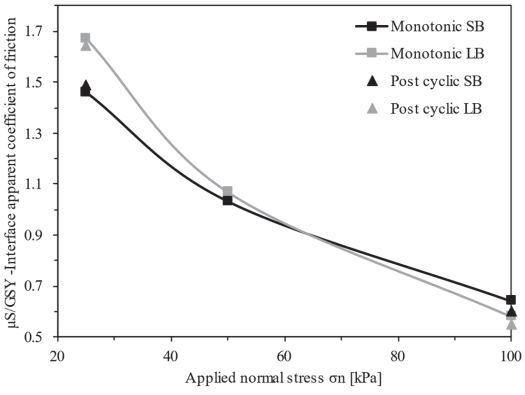

Figure 12. Comparison of interface apparent coefficient of friction ($\mu_{s/GSY}$) under monotonic and post-cyclic loading conditions.

4. Discussion

As previously mentioned, the evolution of displacements recorded by tell-tales T1 to T3 in the small box equipment for σ_n = 50 kPa was rather similar, as shown in Figure 6a. This indicates that only the front geogrid section underwent significant elongation during the load transfer phase of the pullout test and sliding occurred without significant deformation over the back half of the reinforcement. As shown in Figure 7b, for the large box, the instrumentation data revealed a non-linear distribution of shear stress over the whole geogrid length, where displacement values decreased with the distance from the loaded edge. These findings are in agreement with the studies of Cardile et al. [16] and Ferreira et al. [25], in which the geosynthetic deformation in the confined region was found to be more significant in the frontal zone and less significant towards the rear end. However, as mentioned, significant deformation occurred over the whole geogrid length in the large-scale test prior to the pullout phase, as opposed to the small-scale test. This occurrence may be associated with the fact that the specimen width was considerably lower than the pullout box width in the case of the large-scale tests. Previous studies have shown that when the reinforcement specimens are narrower than the pullout box, the non-dilating zone in the soil surrounding the specimen behaves as a restrain against soil dilation in the dilating zone (i.e., above and below the reinforcement), which generates shear stresses at the border between the two zones leading to an increase in the effective normal stress at the soil–reinforcement interface [14]. In turn, higher normal stresses induce a progressive mobilization of the interaction mechanisms at the interface, resulting in a more significant non-linear displacement distribution along the reinforcement length [16], as well as higher pullout resistance values (Figure 8).

As reported before, for lower applied normal stresses, when comparing the confined tensile stiffness at low strain values (less than 2%) for different types of equipment, a significant variability was identified (Figure 10a,b). This may be due to the different reinforcement mobilization (i.e., active length) in the distinct testing boxes. Despite this variability under lower strains, the confined stiffness values at 2% strain (or higher) showed reasonable agreement. Conversely, under a higher normal stress of 100 kPa, the confined stiffness values were similar for both types of equipment over the whole range of available strain values. This is likely associated with the fact that, under the higher normal stress, the deformation of the geogrid specimen tested in the small box extends to sections located further away from the clamp, resulting in similar deformations on the central section of the reinforcement (between tell-tales T2 and T3) in both tests, and hence similar confined stiffness values.

Table 5 presents the ratios between the results obtained from small and large equipment (SB/LB), expressed in terms of the maximum pullout resistance (P_R), maximum shear stress (τ_i) and pullout interface apparent coefficient of friction ($\mu_{s/GSY}$) for both monotonic and cyclic/post-cyclic loading conditions.

Table 5. Ratios between the results from small and large equipment (SB/LB).

Monotonic	σ_n = 25 kPa	σ_n = 50 kPa	σ_n = 100 kPa
P_R	0.75	0.83	0.95
τ_i	0.87	0.97	1.07
$\mu_{s/GSY}$	0.87	0.97	1.11
Cyclic/post-cyclic	σ_n = 25 kPa		σ_n = 100 kPa
P_R	0.78		0.94
τ_i	0.92		1.06
$\mu_{s/GSY}$	0.91		1.10

In Table 5, it can be concluded that for lower applied normal stress (σ_n = 25 kPa) and regardless of the loading conditions, the apparatus scale influences the measured pullout resistance, which is in accordance with the results reported by Palmeira and Milligan [9].

Higher values of pullout resistance are reached when the large box is used. However, as the normal stress increases, the ratio between the results from different equipment becomes closer to unity, such that a satisfactory agreement is attained for σ_n = 100 kPa. This corroborates that the increase in normal stress diminishes the scale effect, and consistent results are obtained from both test devices under higher confining pressures. The results in Table 5 also show that, under post-cyclic loading conditions, the effect of apparatus scale on the pullout resistance values follows the same trend as that observed under monotonic loading.

Compared to the pullout resistance, the values of maximum shear stress and apparent coefficient of friction were less influenced by the size of equipment and loading conditions. This can be justified by using the same specimen width-to-length ratio (1.21) for all the tests. Moreover, considering the ASTM pullout test standard guidelines regarding the equipment dimensions in relation to soil particle size, it becomes evident that the use of relatively fine soils in this study contributed to attenuating the apparatus scale effect. Kakuda [39] performed monotonic tests comparing both types of equipment with different boundary conditions, geogrids, specimen size ratio and soil properties, and a similar pattern for the shear stress was also verified. Nevertheless, additional studies involving different geosynthetics and fill materials would be useful to determine whether the obtained conclusions can be generalized.

5. Conclusions

This study evaluated the apparatus scale effect on the pullout response of a geogrid in cohesive soils through monotonic and cyclic/post-cyclic pullout tests subjected to different applied normal stresses. Based on the obtained results, the following conclusions can be highlighted:

- In general, in the small-scale tests, no significant deformation occurred over the back half of the reinforcement, as opposed to the large-scale tests, where the geogrid displacements decreased progressively with the distance to the front end, showing a progressive mobilization of the interaction mechanisms at the interface.
- Particularly under lower applied normal stresses, the geogrid pullout resistance was considerably influenced by the apparatus scale and higher values were reached in the large-scale tests. However, the scale effect became less prominent when the applied normal pressure increased. Under post-cyclic loading conditions, the effect of apparatus scale on the pullout resistance values followed the same trend as that observed under monotonic loading.
- Despite the variability for the pullout resistance, the maximum shear stresses obtained from both types of equipment showed reasonable agreement.
- Under normal stresses of 25 and 50 kPa, the geogrid's confined stiffness at low strains (<2%) derived from the small-scale tests exceeded that from the large-scale equipment. However, under a higher normal stress (100 kPa), the values of confined tensile stiffness obtained from both equipment types were consistent.
- The pullout interface's apparent coefficient of friction ($\mu s/GSY$) decreased with increasing normal stress. While for σ_n = 25 kPa, the $\mu s/GSY$ values obtained from the small-scale tests exceeded those from the large pullout box, under higher normal stresses, the differences between the $\mu s/GSY$ values associated with different test devices were not significant.

The inclusion of geosynthetics in civil infrastructure projects enables significant energy and natural resource savings, thus addressing the global sustainability requirements. Furthermore, the assessment of soil–geosynthetic interaction parameters using small-scale pullout test equipment represents significant benefits, including a reduced consumption of resources, reduced cost, and an easier and faster test assembly, in comparison to conventional large-scale tests. The presented results highlight the importance of the scale effect in pullout tests, while also considering the influence of the applied normal stress. When the pullout resistance is estimated on the basis of small-scale pullout tests, proper scale effect

correction factors may be considered for more consistent estimates of the soil–geosynthetic interface strength parameters.

Author Contributions: S.R.B.: Data curation, writing—original draft preparation, methodology, resources and conceptualization; G.O.M.P.: conceptualization, writing—original draft preparation, review and editing; F.B.F.: formal analysis, writing—original draft preparation, review and editing; J.L.d.S.: resources, project administration, supervision and writing—review and editing. All authors have read and agreed to the published version of the manuscript.

Funding: This research was funded by: Process 405594/2022-4. CNPq/FNDCT/MCTI 15/2022—Desempenho de pavimentos estabilizados com geossintéticos: uma abordagem experimental e numérica; Grant No. 2021.03625.CEECIND/CP1679/CT0002 with DOI 10.54499/2021.03625 accessed on 3 August 2024. CEECIND/CP1679/CT0002 from the Stimulus of Scientific Employment, Individual Support (CEECIND)—4th Edition, provided to F.B.F. by Fundação para a Ciência e Tecnologia (FCT); and Base Funding—UIDB/04708/2020 with DOI 10.54499/UIDB/04708/2020 (https://doi.org/10.54499/UIDB/04708/2020) accessed on 3 August 2024 of the CONSTRUCT—Instituto de I&D em Estruturas e Construções—funded by national funds through the FCT/MCTES (PIDDAC).

Data Availability Statement: The datasets generated for this study are available on request to the corresponding author.

Acknowledgments: The authors are indebted to the following institutions that supported the research activities reported in this paper in different ways: National Council for Scientific and Technological Development (CNPq), the University of São Paulo (USP) and CAPES—Brazilian Ministry of Education.

Conflicts of Interest: The authors declare no conflicts of interest. The funders had no role in the design of the study; in the collection, analyses, or interpretation of data; in the writing of the manuscript; or in the decision to publish the results.

References

1. Göbel, C.H.; Weisemann, U.C.; Kirschner, R.A. Effectiveness of a Reinforcing Geogrid in a Railway Subbase under Dynamic Loads. *Geotext. Geomembr.* **1994**, *13*, 91–99. [CrossRef]
2. Berg, R.; Christopher, B.; Samtani, N. *Design and Construction of Mechanically Stabilized Earth Walls and Reinforced Soil Slopes—Volume I*; Fhwa: Washington, DC, USA, 2009.
3. Byun, Y.H.; Tutumluer, E. Local Stiffness Characteristic of Geogrid-Stabilized Aggregate in Relation to Accumulated Permanent Deformation Behavior. *Geotext. Geomembr.* **2019**, *47*, 402–407. [CrossRef]
4. Touze, N. Healing the World: A Geosynthetics Solution. *Geosynth. Int.* **2021**, *28*, 1–31. [CrossRef]
5. Vieira, C.S.; Lopes, M.L.; Caldeira, L.M. Sand-Geotextile Interface Characterisation through Monotonic and Cyclic Direct Shear Tests. *Geosynth. Int.* **2013**, *20*, 26–38. [CrossRef]
6. Palmeira, E.M. Soil-Geosynthetic Interaction: Modelling and Analysis. *Geotext. Geomembr.* **2009**, *27*, 368–390. [CrossRef]
7. Fox, P.J.; Kim, R.H. Effect of Progressive Failure on Measured Shear Strength of Geomembrane/GCL Interface. *J. Geotech. Geoenviron. Eng.* **2008**, *134*, 459–469. [CrossRef]
8. Hsieh, C.W.; Chen, G.H.; Wu, J.H. The Shear Behavior Obtained from the Direct Shear and Pullout Tests for Different Poor Graded Soil-Geosynthetic Systems. *J. GeoEngin.* **2011**, *6*, 15–26. [CrossRef]
9. Palmeira, E.M.; Milligan, G.W.E. Scale and Other Factors Affecting the Results of Pull out Tests of Grids Buried in Sand. *Geotechnique* **1989**, *39*, 511–524. [CrossRef]
10. Farrag, K.; Acar, Y.B.; Juran, I. Pull-Out Resistance of Geogrid Reinforcements. *Geotext. Geomembr.* **1993**, *12*, 133–159. [CrossRef]
11. Lopes, M.L.; Ladeira, M. Influence of the Confinement, Soil Density and Displacement Rate on Soil-Geogrid Interaction. *Geotext. Geomembr.* **1996**, *14*, 543–554. [CrossRef]
12. Ochiaif, H.; Otani, J.; Hayashic, S.; Hirai, T. The Pull-Out Resistance of Geogrids in Reinforced Soil. *Geotext. Geomembr.* **1996**, *14*, 19–42. [CrossRef]
13. Sugimoto, M.; Alagiyawanna, A.M.N.; Kadoguchi, K. Influence of Rigid and Flexible Face on Geogrid Pullout Tests. *Geotext. Geomembr.* **2001**, *19*, 257–277. [CrossRef]
14. Moraci, N.; Recalcati, P. Factors Affecting the Pullout Behaviour of Extruded Geogrids Embedded in a Compacted Granular Soil. *Geotext. Geomembr.* **2006**, *24*, 220–242. [CrossRef]
15. Teixeira, S.H.C.; Bueno, B.S.; Zornberg, J.G.; Asce, M. Pullout Resistance of Individual Longitudinal and Transverse Geogrid Ribs. *J. Geotech. Geoenviron. Eng.* **2007**, *133*, 37–50. [CrossRef]
16. Cardile, G.; Moraci, N.; Calvarano, L.S. Geogrid Pullout Behaviour According to the Experimental Evaluation of the Active Length. *Geosynth. Int.* **2016**, *23*, 194–205. [CrossRef]

17. Mirzaalimohammadi, A.; Ghazavi, M.; Roustaei, M.; Lajevardi, S.H. Pullout Response of Strengthened Geosynthetic Interacting with Fine Sand. *Geotext. Geomembr.* **2019**, *47*, 530–541. [CrossRef]
18. Ferreira, F.B.; Vieira, C.S.; Lopes, M.D.L. Pullout Behavior of Different Geosynthetics—Influence of Soil Density and Moisture Content. *Front. Built Environ.* **2020**, *6*, 12. [CrossRef]
19. Vieira, C.S.; Ferreira, F.B.; Pereira, P.M.; Lopes, M.D.L. Pullout Behaviour of Geosynthetics in a Recycled Construction and Demolition Material—Effects of Cyclic Loading. *Transp. Geotech.* **2020**, *23*, 100346. [CrossRef]
20. Perkins, S.W.; Cuelho, E.V. Soil-Geosynthetic Interface Strength and Stiffness Relationships from Pullout Tests. *Geosynth. Int.* **1999**, *6*, 321–346. [CrossRef]
21. Palmeira, E.M. Bearing Force Mobilisation in Pull-out Tests on Geogrids. *Geotext. Geomembr.* **2004**, *22*, 481–509. [CrossRef]
22. Chen, C.; McDowell, G.R.; Thom, N.H. Investigating Geogrid-Reinforced Ballast: Experimental Pull-out Tests and Discrete Element Modelling. *Soils Found.* **2014**, *54*, 1–11. [CrossRef]
23. Abdi, M.R.; Zandieh, A.R. Experimental and Numerical Analysis of Large Scale Pull out Tests Conducted on Clays Reinforced with Geogrids Encapsulated with Coarse Material. *Geotext. Geomembr.* **2014**, *42*, 494–504. [CrossRef]
24. Sukmak, K.; Sukmak, P.; Horpibulsuk, S.; Chinkulkijniwat, A.; Arulrajah, A.; Shen, S.L. Pullout Resistance of Bearing Reinforcement Embedded in Marginal Lateritic Soil at Molding Water Contents. *Geotext. Geomembr.* **2016**, *44*, 475–483. [CrossRef]
25. Ferreira, F.B.; Vieira, C.S.; Lopes, M.L.; Carlos, D.M. Experimental Investigation on the Pullout Behaviour of Geosynthetics Embedded in a Granite Residual Soil. *Eur. J. Environ. Civ. Eng.* **2016**, *20*, 1147–1180. [CrossRef]
26. Vieira, C.S.; Pereira, P.; Ferreira, F.; de Lurdes Lopes, M. Pullout Behaviour of Geogrids Embedded in a Recycled Construction and Demolition Material. Effects of Specimen Size and Displacement Rate. *Sustainability* **2020**, *12*, 3825. [CrossRef]
27. Raju, D.M.; Fannin, R.J. Monotonic and Cyclic Pull-out Resistance of Geogrids. *Geotechnique* **1997**, *47*, 331–337. [CrossRef]
28. Moraci, N.; Cardile, G. Influence of Cyclic Tensile Loading on Pullout Resistance of Geogrids Embedded in a Compacted Granular Soil. *Geotext. Geomembr.* **2009**, *27*, 475–487. [CrossRef]
29. Cardile, G.; Pisano, M.; Moraci, N. The Influence of a Cyclic Loading History on Soil-Geogrid Interaction under Pullout Condition. *Geotext. Geomembr.* **2019**, *47*, 552–565. [CrossRef]
30. Nayeri, A.; Fakharian, K. Study on Pullout Behavior of Uniaxial HDPE Geogrids Under Monotonic and Cyclic Loads. *Int. J. Civ. Eng.* **2009**, *7*, 211–223.
31. Moraci, N.; Cardile, G. Deformative Behaviour of Different Geogrids Embedded in a Granular Soil under Monotonic and Cyclic Pullout Loads. *Geotext. Geomembr.* **2012**, *32*, 104–110. [CrossRef]
32. Ferreira, F.; Vieira, C.; De Lurdes Lopes, M. Cyclic and Post-Cyclic Shear Behaviour of a Granite Residual Soil—Geogrid Interface. *Procedia Eng.* **2016**, *143*, 379–386. [CrossRef]
33. Koshy, N.; Unnikrishnan, N. Geosynthetics Under Cyclic Pullout and Post-Cyclic Monotonic Loading. *Int. J. Geosynth. Ground Eng.* **2016**, *2*, 13. [CrossRef]
34. Garcia, G.F.N.; Lodi, P.C. Post-Cycling Interface Strength Test of Geogrids. *Int. J. Civ. Eng.* **2020**, *18*, 827–834. [CrossRef]
35. Ferreira, F.B.; Vieira, C.S.; Lopes, M.L.; Ferreira, P.G. HDPE Geogrid-Residual Soil Interaction under Monotonic and Cyclic Pullout Loading. *Geosynth. Int.* **2020**, *27*, 79–96. [CrossRef]
36. Jewell, R.A. Reinforcement Bond Capacity. *Geotechnique* **1990**, *40*, 513–518. [CrossRef]
37. Portelinha, F.H.M.; Pereira, V.R.G.; Correia, N.S. Small-Scale Pullout Test of a Geogrid-Reinforced Unsaturated Soil with Suction Monitoring. *Geotech. Test. J.* **2018**, *41*, 787–804. [CrossRef]
38. Marques, G.S.; Lins da Silva, J. Interaction Between a Lateritic Soil and a Non-Woven Geotextile in Different Moisture Conditions. *Front. Built Environ.* **2020**, *6*, 116. [CrossRef]
39. Kakuda, F.M. Geogrid Pullout Tests Using Reduced Scale Equipment. Master's Thesis, University of São Paulo, São Carlos, SP, Brazil, 2006. (In Portuguese).
40. *ASTM D6706-01*; Standard Test Method for Measuring Geosynthetic Pullout Resistance in Soil. ASTM International: West Conshehawken, PA, USA, 2021.
41. *ASTM D4767-11*; Standard Test Method for Consolidated Undrained Triaxial Compression Test for Cohesive Soils. ASTM International: West Conshehawken, PA, USA, 2020.
42. *ASTM D7181-20*; Standard Test Method for Consolidated Drained Triaxial Compression Test for Soils. ASTM International: West Conshehawken, PA, USA, 2020.
43. Abdi, M.R.; Sadrnejad, A.; Arjomand, M.A. Strength Enhancement of Clay by Encapsulating Geogrids in Thin Layers of Sand. *Geotext. Geomembr.* **2009**, *27*, 447–455. [CrossRef]
44. Abdi, M.R.; Arjomand, M.A. Pullout Tests Conducted on Clay Reinforced with Geogrid Encapsulated in Thin Layers of Sand. *Geotext. Geomembr.* **2011**, *29*, 588–595. [CrossRef]
45. Teixeira, H.S.C. Construction and Calibration of a Large Pullout Test Device. Master's Thesis, University of São Paulo, São Carlos, SP, Brazil, 1999. (In Portuguese).
46. *ASTM D7499/D7499M-09*; Standard Test Method for Measuring Geosynthetic-Soil Resilient Interface Shear Stiffness. ASTM International: West Conshehawken, PA, USA, 2014.
47. Razzazan, S.; Keshavarz, A.; Mosallanezhad, M. Pullout Behavior of Polymeric Strip in Compacted Dry Granular Soil under Cyclic Tensile Load Conditions. *J. Rock Mech. Geotech. Eng.* **2018**, *10*, 968–976. [CrossRef]

48. Wang, Z.; Jacobs, F.; Ziegler, M. Visualization of Load Transfer Behaviour between Geogrid and Sand Using PFC2D. *Geotext. Geomembr.* **2014**, *42*, 83–90. [CrossRef]
49. Giroud, J.P.; Asce, M.; Han, J. Design Method for Geogrid-Reinforced Unpaved Roads. I. Development of Design Method. *J. Geotech. Geoenv. Eng.* **2004**, *130*, 775–786. [CrossRef]

applied sciences

MDPI

Article

A Study on the Dynamic Response of a Timber-Frame Beam–Bamboo Anchor-Supported Roadbed Slope under Train Load

Hui Yang [1,2,†], Gang Huang [2,*], Zhenzhen Wei [2,*], Xueliang Jiang [1,2,†] and Zhengyi Cao [3]

[1] School of Civil Engineering and Engineering Management, Guangzhou Maritime University, Guangzhou 510725, China; yanghui-dd@163.com (H.Y.); iamjxl@163.com (X.J.)
[2] School of Civil Engineering, Central South University of Forestry and Technology, Changsha 410018, China
[3] Nuclear Industry Jinhua Survey and Design Institute Co., Ltd., Jinhua 321000, China; caozhengyi215@163.com
* Correspondence: hg19970412@163.com (G.H.); weizhenzhen0826@163.com (Z.W.); Tel.: +86-19198013952 (G.H.)
† These authors contributed equally to this work as co-first author.

Abstract: In order to investigate the dynamic response of embankment slopes supported by wooden frame beams and bamboo anchor rods under train loading, this study conducted model tests on embankment slopes supported by wooden frame beams and bamboo anchor rods and carried out three-dimensional numerical simulations of the slopes. This study focused on analyzing the effects of train loading frequency, the peak value difference, and the peak value of the soil pressure on the embankment slopes. This study also analyzed the horizontal displacement of the slope surface, the internal forces in the support structure, and the slope safety factor. The results indicated the following: (1) The increase in loading frequency from 2 Hz to 3 Hz resulted in a significant increase in dynamic soil pressure, with a smaller increase observed upon further frequency increments. Moreover, increasing the load or peak value difference led to an overall increase in the maximum dynamic soil pressure. (2) Under various loading conditions, the axial force in the top anchor rod was significantly greater than that in the middle anchor rod. Additionally, the axial force in the rod body exhibited a pattern of larger forces near the anchorage end and smaller forces near the anchor head. The location of the maximum bending moment in the anchor rod transitioned from the anchor head to the anchorage end as the slope depth increased. The bending moment of the anchor rod increased with the loading frequency but decreased with an increase in the peak value, showing a minor influence from the upper and lower peak values. (3) With the presence of this support system, the slope safety factor increased by 20.13%. A noticeable reduction in the horizontal displacement of the slope surface was observed, with the greatest reduction in the top slope area, followed by the slope angle.

Keywords: bamboo anchor; timber-frame beam; roadbed slope; slope support; dynamic response

Citation: Yang, H.; Huang, G.; Wei, Z.; Jiang, X.; Cao, Z. A Study on the Dynamic Response of a Timber-Frame Beam–Bamboo Anchor-Supported Roadbed Slope under Train Load. *Appl. Sci.* **2024**, *14*, 2426. https://doi.org/10.3390/app14062426

Academic Editors: Paulo José da Venda Oliveira and António Alberto Santos Correia

Received: 20 January 2024
Revised: 6 March 2024
Accepted: 11 March 2024
Published: 13 March 2024

1. Introduction

The integration of environmentally friendly and ecologically sound support structures, which also ensure slope safety and reliability, has been a recent and current focal point of research among scholars. As a consequence of this, the emergence of "vegetation for slope protection" technology [1] has been garnering attention. Wu Hongwei [2] investigated the interactions among vegetation, the atmosphere, and soil. They discovered that vegetation not only reinforces the soil through its root system but also enhances soil suction through transpiration, thereby increasing soil shear strength and augmenting slope stability. Furthermore, Wang Yibing et al. [3] studied the hydraulic characteristics of reinforced clay slopes using vegetation combined with vegetation reinforcement strips. Their findings revealed that these reinforcement strips not only provided better reinforcement but also

suppressed surface soil cracking. Der-Guey Lin et al. [4] established a three-dimensional numerical root model consisting of an inverted t-shaped rootstock and limiting hairy roots based on the actual root morphology in order to study the shear strength characteristics of the soil root system in Makino bamboo forests and successfully applied it to the numerical simulation of in situ uprooting tests of the soil root system.

This paper proposes a vegetation slope protection method that uses the combined support of live stumps and bamboo anchors [5,6]. Addressing the initial stage of live stump root development, a stage in which it fails to provide deep-root anchorage and shallow-root reinforcement to the slope [7,8], temporary support is applied to the roadbed slope using bamboo anchors and wooden frame beams. Previous studies have conducted experiments and three-dimensional numerical simulations on the use of wooden frame beam–bamboo anchor support systems under static loading conditions for slope protection. Yang H et al. [9] introduced an ecological slope-protection method—bamboo anchor wooden frame beams for initial support and indoor physical model experiments were conducted. Results indicated that under static loading, horizontal displacement initially occurred at the slope crest, but, ultimately, the horizontal displacement at the slope base exceeded that at the crest. Zhu Y et al. [10] performed indoor model experiments on four different forms of support using wooden frame beam–bamboo anchor systems for slope protection. The experiments demonstrated the significant effectiveness of the wooden frame beam–bamboo anchor support system, and optimizing the spacing between bamboo anchors and wooden frame beams enhanced its supportive effects. Jiang X et al. [11] conducted indoor model experiments applying static loads at the slope crest using the wooden frame beam–bamboo anchor support system. The study focused on the force characteristics of bamboo anchors and wooden frame beams and the slope surface displacement on cohesive soil slopes under this support.

Yan S. et al. [12] established a numerical model for roadbed slope under dynamic loading and verified its effectiveness through experiments. The results indicate that the maximum displacement of the roadbed slope increases with the amplitude of dynamic loading but decreases with an increase in load frequency. Ye S et al. [13] developed a dynamic response model for prestressed anchor beam-reinforced slopes, analyzing the dynamic soil pressure distribution, displacement of the frame-anchor structure, and the axial force distribution in the anchors. Gnanendran C. T. et al. [14] conducted small-scale physical model experiments to investigate the effect of dynamic loading frequency on the strip foundation at the crest of slopes. They found that cyclic loading can enhance the bearing capacity of the foundation soil. However, as the dynamic loading frequency increases, the increment in bearing capacity diminishes, leading to increased non-elastic deformations of the slope in both inclined and vertical directions. Qiu H. Z. et al. [15] used finite element software to study the dynamic response of excavation slopes under vehicle loading. They observed that, as the load position moves closer to the support structure, the displacement and deformation of the support structure increase, along with increased axial forces in the anchors. Additionally, with an increase in loading frequency, the deformation of the support structure increases, while the axial forces in the anchors decrease.

The majority of the aforementioned studies have focused on model experiments and three-dimensional numerical simulations of roadbed slopes under static loading. However, investigating the dynamic response of roadbed slopes under train loading holds significant research significance. This paper targets the support of roadbed slopes using bamboo anchors and wooden frame beams, employing a model experiment approach. It aims to explore the dynamic response of roadbed slopes supported by wooden frame beams and bamboo anchors under train loading. This research aims to provide a reference basis for studying the dynamic response of roadbed slopes under the combined support of live stumps and bamboo anchors.

2. Model Test Program

2.1. Model Box

The dimensions of the model box are 300 cm (net length) × 150 cm (net width) × 200 cm (net height). To mitigate boundary effects during hydraulic fatigue loading of the model box, thick high-density polyethylene black foam boards, approximately 5 cm in thickness, are adhered to the inner sides of the model box as energy-absorbing materials. The model box is illustrated in Figure 1.

Figure 1. Model box.

2.2. Determination of Similarity Relations

According to dimensional analysis [16], the similarity ratio between the model box and the physical quantities related to the actual slope is controlled. Utilizing dimensional matrices and the principle of dimensional homogeneity, the similarity constants for various physical quantities are derived. The main physical quantities are shown in Table 1.

Table 1. Similarity relationship.

Physical Quantities	Similarities	Similarity Constants
Geometric dimensions l	C_l	7
Elastic modulus E	C_E	1
Density ρ	C_ρ	1
Dynamic loading P	$C_P = (C_l)^2 C_\rho$	49
Internal friction angle φ	C_φ	1
Cohesion c	$C_c = C_E$	1
Poisson ratio μ	C_μ	1
Dynamic displacements u	$C_u = C_l$	7
Stress σ	$C_\sigma = C_E$	1
Time t	$C_t = (C_l)(C_\rho)^{1/2}(C_E)^{-1/2}$	7

2.3. Test Parameters

Prior to conducting indoor slope model experiments, relevant parameter tests were performed on the test materials. The optimum moisture content for red clay and sand-mixed red clay (at a ratio of 3:1) was found to be 13.5% and 12.5%, respectively, while their respective maximum dry densities were 1.87 g/cm^3 and 1.97 g/cm^3. Tensile tests were conducted on bamboo anchors and wooden frame beams to measure their elastic moduli and Poisson's ratios. The main test parameters are presented in Table 2.

Table 2. Test parameters.

Material Names	Model Types	Elastic Modulus (MPa)	Poisson Ratio	Capacity (kN/m^3)	Cohesion (kN/m^2)	Internal Friction Angle (°)
Bamboo Anchors	Elasticity	12,500	0.28	7.8	-	-
Wooden frame beam	Elasticity	14,300	0.36	9.6	-	-
Clay	Moorcullen	65	0.32	17.8	12	18.5
Clay (sand mixing)	Moorcullen	68	0.35	18.0	10	16

2.4. Strain Gauge Arrangement

As shown in Figure 2, the arrangement of strain gauges on the bamboo anchors is depicted. Prior to the slope test, strain gauges were placed at intervals of 10 cm, 22.5 cm, 35 cm, 47.5 cm, and 60 cm from the anchor head. The measurement points, numbered from 1 to 5, correspond sequentially from the thinner end (anchor head) to the thicker end (anchor tip). The total length of the bamboo anchor is 70 cm.

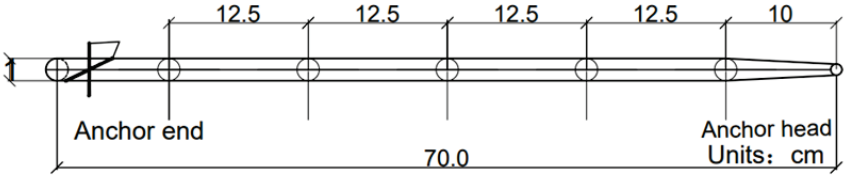

Figure 2. Bamboo anchor strain gauge measurement point arrangement.

As shown in Figure 3, the arrangement of strain gauges on the wooden frame beam is illustrated. Seven strain gauges were affixed to each of the first row's horizontal beams and middle vertical beams. For the horizontal beams, starting from the second span, strain gauges were applied at intervals of 12.5 cm, labeled from left to right as measurement points H1 to H7. For the vertical beams, starting from the first span, strain gauges were attached at intervals of 16.33 cm, labeled from top to bottom as measurement points S1 to S7.

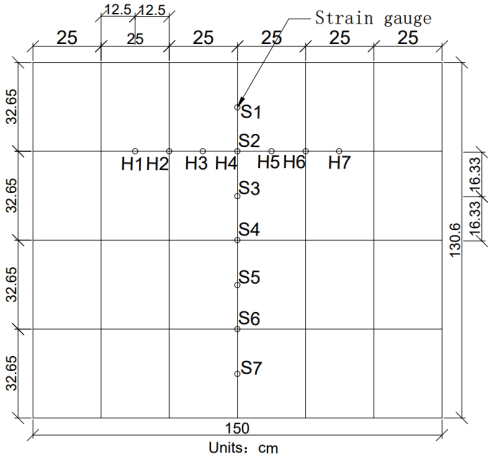

Figure 3. Arrangement of strain gauge measurement points for wood frame beams.

2.5. Slope Physical Model

The experiment consisted of two sets, divided into the original unsupported slope and the slope reinforced with three rows of bamboo anchors and wooden frame beams. As

illustrated in Figure 4, the soil in the experiment was divided into five layers from bottom to top. The bottom layer represented the foundation soil to simulate the base soil of the slope. The second layer comprised red clay typical of Hunan Province. The third layer represented the bottom layer of the subgrade, filled with a mixture of sand and red clay (in a 3:1 ratio). The fourth layer simulated the surface layer of the subgrade, also filled with the same mixture of sand and red clay. The fifth layer was the ballast layer, mainly consisting of crushed stones beneath the railway track. The slope ratio of the soil slope was 1:1, with the foundation layer being 20 cm high, the embankment layer 100 cm high, the bottom layer of the subgrade 27 cm high, the surface layer of the subgrade 9 cm high, and the slope ratio of the subgrade layer was 4%. The ballast layer was 6 cm high, with a slope ratio of 1:1.75. The total height of the slope was approximately 160 cm, with a length of around 250 cm and a width of about 140 cm. The average compactness of each layer, as measured in the experiment, met the requirements specified in the "Design Specifications for Heavy-duty Railways".

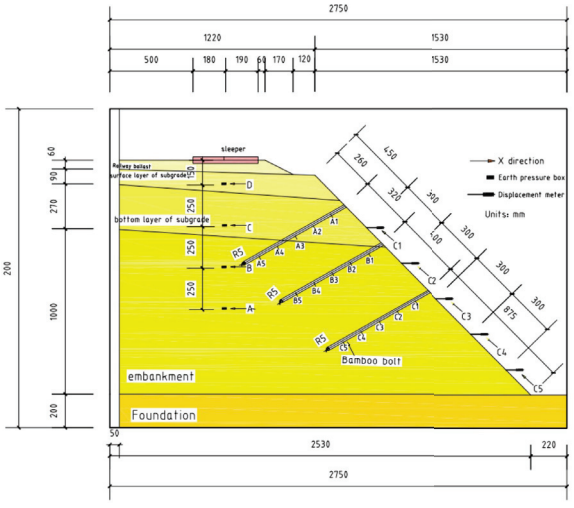

Figure 4. Indoor slope model.

The vertical soil pressure cells—labeled D, C, B, and A—were placed vertically downward from the loading point at the crest of the slope at distances of 15 cm, 40 cm, 65 cm, and 90 cm, respectively. Electronic displacement transducers denoted as C1 to C5 were installed parallel to the ground surface from the crest to the slope toe. The slope soil was compacted near its optimum moisture content, and, as indicated in Figure 5, electronic displacement transducers were mounted on the slope surface and connected to the Donghua data acquisition instrument. Strain gauges were attached to both the bamboo anchors and wooden frame beams, buried within the slope, and connected to the IMC data acquisition instrument. Different sinusoidal train loads were applied to the sleepers at the crest of the slope under varying working conditions, and relevant experimental data were collected during this process.

2.6. Loading Scheme Design

Taking into account various traffic load parameters [17,18], vehicle speed factors, and the effect of the vehicle's load, the train load was considered to be a sinusoidal waveform for loading the railway embankment slope. The specific application process of load in the test process is through the hydraulic fatigue machine to simulate the train load in the form of cyclic load applied to the railroad sleeper, in the thick steel plate of the railroad sleeper pad, in the steel plate on the placement of the distribution beam, and in a hydraulic fatigue

machine actuator, to apply the load to ensure the train load uniformity of the role of the rails on the sleeper. Considering model similarity ratios and the dynamic stress response of the train load, following the Railway Subgrade Design Code, the four 250 kN axle loads were converted into distributed loads and then scaled to the model. The peak value of the dynamic load was calculated as follows:

$$P_d = \frac{P_j}{d \times C_L} \times l \times (1.4 + i) = \frac{250}{1.4 \times 7} \times 0.6 \times (1.4 + 0.5) = 29.1 \text{ kN}$$

Figure 5. Wooden frame beam–bamboo anchor slope model test front.

The parameters are defined as follows: P_d is the peak load applied to the model; P_j is the static load; d is the spacing between axles; C_L is the model similarity ratio; l represents 0.6, the longitudinal length of the model track; 1.4 stands for the live load combination factor; and i represents the design impact coefficient set at 0.5. The specific experimental conditions for each scenario are presented in Table 3 below.

Table 3. Loaded working condition table.

Work Conditions	Frequency (Hz)	Lower Peak (kN)	Peak Difference (kN)	Upper Peak (kN)
1	2	15	14.1	29.1
2	3	15	14.1	29.1
3	4	15	14.1	29.1
4	3	12.24	14.1	26.65
5	3	17.76	14.1	31.86
6	3	20.52	14.1	34.62
7	3	15	11.1	25.1
8	3	15	17.1	32.1
9	3	15	20.1	35.1

3. Analysis of Slope Model Test Results

3.1. The Variation Law of Vertical Dynamic Ground Pressure

As depicted in Figure 6a,b, Figure 6a illustrates the vertical dynamic soil pressure curve at a loading frequency of 2 Hz, while Figure 6b displays the maximum dynamic soil pressure under various loading frequencies. When the loading frequency ranges between 2 and 4 Hz, the vertical dynamic soil pressure exhibits a similar sinusoidal pattern in correlation with the crest load. The dynamic soil pressure gradually decreases with increased burial depth, and as the burial depth increases, the peak values of the soil pressure curves become progressively closer to each other. At a loading frequency of 2 Hz, the maximum dynamic soil pressure at point D slightly surpasses that at point C. When the loading frequency is raised to 3 Hz, there is a noticeable increase in the maximum dynamic soil pressure at all measurement points. However, as the loading frequency

continues to increase to 4 Hz, the rate of increase in the maximum soil pressure at each point slows down.

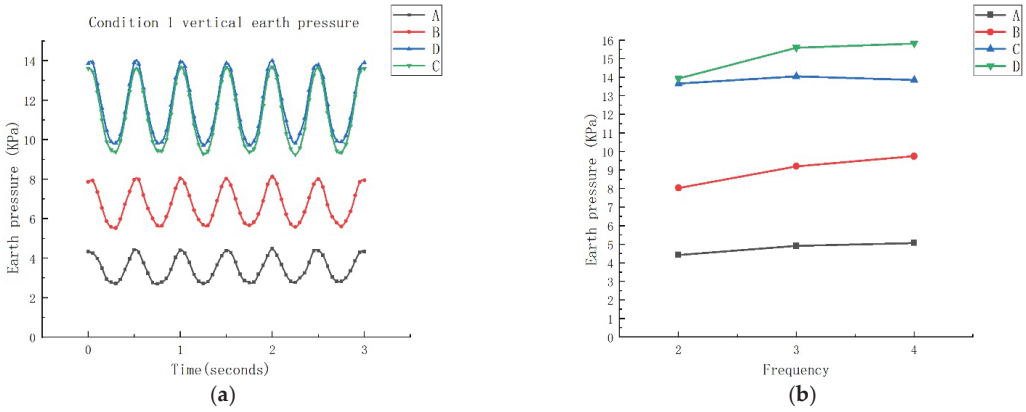

Figure 6. Vertical dynamic ground pressure at different loading frequencies. (**a**) Vertical dynamic ground pressure at 2 Hz; (**b**) Maximum dynamic ground pressure at different loading frequencies.

Figure 7 illustrates the maximum vertical dynamic soil pressure under various peak-to-peak loadings. With the increase in the peak-to-peak loading, the maximum dynamic soil pressure at points A to D initially experiences a sharp rise. Additionally, for shallower burial depths, the increment in pressure is more significant. Subsequently, while the maximum soil pressure at each point continues to increase with the rise in peak-to-peak loading, the rate of increase at each point diminishes.

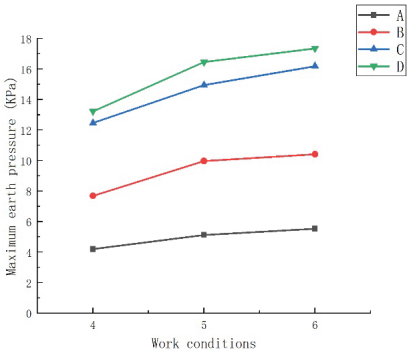

Figure 7. Maximum vertical dynamic ground pressure with different up and down peaks.

Figure 8 displays the maximum vertical dynamic soil pressure under constant amplitude differential loading. With the increase in the upper peak value, the increments at points A to D are 1, 1.5, 2.5, and 3 kPa, respectively. The curves representing the maximum dynamic soil pressure at each measurement point consistently maintain the lower peak value while adhering to the observed pattern of increment in the upper peak value.

The vertical dynamic soil pressure curves exhibit a sinusoidal pattern similar to crest loading across all loading conditions. The maximum dynamic soil pressure at each measurement point increases with depth, indicating that in model experiments, stress diffusion may become more apparent as the slope depth increases. Additionally, a significant portion of the force might dissipate due to friction between the slope and the model box. Hence, in engineering practice, as the burial depth decreases, the accuracy of soil pressure calculations tends to improve. When the frequency increased from 2 Hz to 3 Hz, there was a

substantial increase in soil pressure; however, with a further increase to 4 Hz, the increase in soil pressure was comparatively smaller. The increase in load also demonstrated a positive correlation with soil pressure, whether it was an increase in peak-to-peak values or peak value differentials, resulting in a continual increase in maximum dynamic soil pressure.

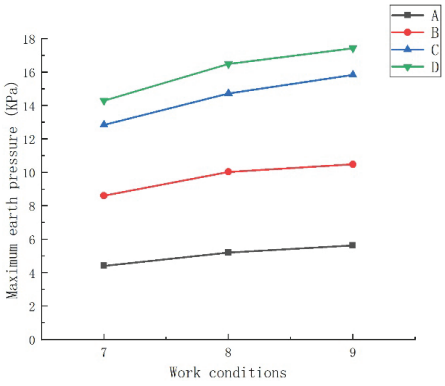

Figure 8. Maximum vertical ground pressure with different peak differences.

3.2. The Law of Change of Horizontal Displacement of Slope Surface

As shown in Figure 9, under the effect of crest loading at 2 Hz, the maximum horizontal displacement of the slope surface varied at different points. At points C1 and C2, the maximum horizontal displacement decreased. Particularly, at point C1, the reduction was at its most significant, decreasing from an outward protrusion of 1.3 mm to 0.1 mm, marking a reduction of nearly 92%. At point C3, the maximum horizontal displacement of the slope surface slightly increased, from a slight inward depression to 0.1 mm. However, at points C4 and C5, there was only a minimal change in the maximum horizontal displacement of the slope surface.

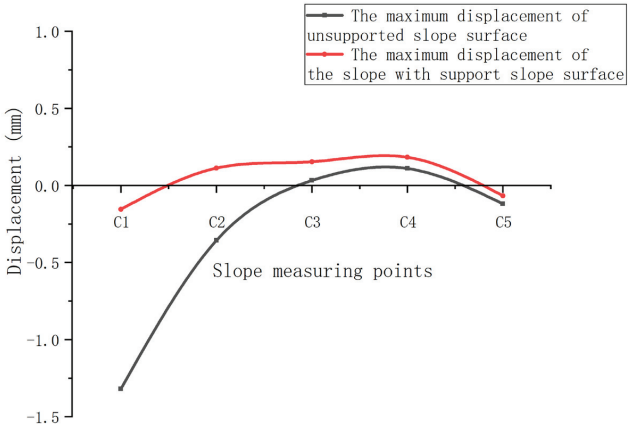

Figure 9. Maximum horizontal displacement of slope surface at 2 Hz loading frequency.

As depicted in Figure 10, under the effect of crest loading at 3 Hz, the maximum horizontal displacement of the slope surface exhibited varying trends at different measurement points. At points C1 and C2, the maximum horizontal displacement of the slope surface decreased. Specifically, at these points, the displacement reduced from the outward protrusion of 0.4 mm and 0.1 mm to 0.2 mm and 0.05 mm, respectively, marking a reduction of nearly 50% at both locations. Conversely, at points C3 and C4, the maximum horizontal

displacement of the slope surface increased. At these points, the displacement shifted from an inward depression of 0.05 mm and 0.02 mm to 0.2 mm. However, at point C5, there was no significant change in the maximum horizontal displacement of the slope surface.

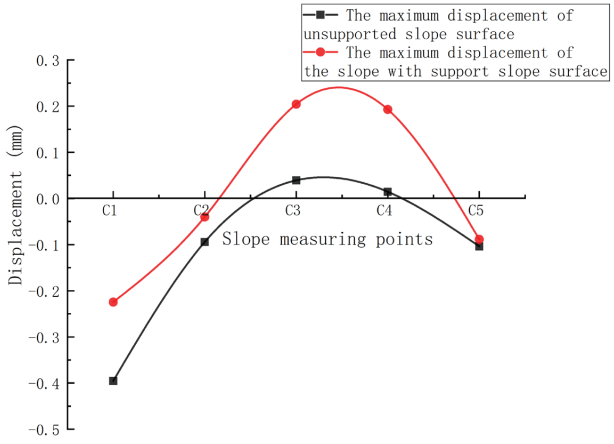

Figure 10. Maximum horizontal displacement of slope surface with loading frequency 3 Hz.

As shown in Figure 11, under the effect of crest loading at 4 Hz, the maximum horizontal displacement of the slope surface exhibited varying trends at different measurement points. At point C1, the maximum horizontal displacement of the slope surface decreased significantly from an outward protrusion of 1.3 mm to 0.25 mm. At point C2, the maximum horizontal displacement decreased from an outward protrusion of 0.35 mm to an inward depression of 0.15 mm. Conversely, at point C3, the maximum horizontal displacement increased from an inward depression of 0.05 mm to 0.15 mm. However, at points C4 and C5, there were no significant changes in the maximum horizontal displacement of the slope surface.

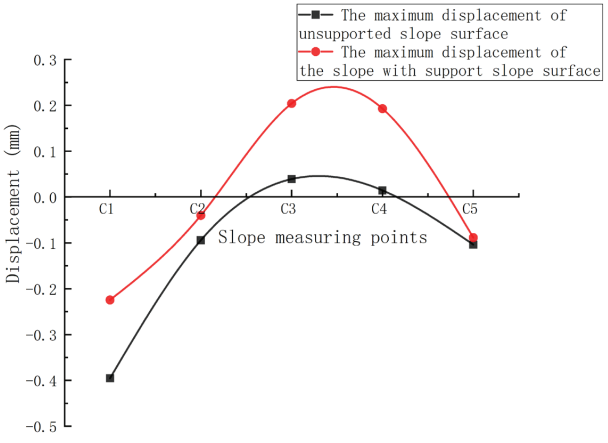

Figure 11. Maximum horizontal displacement of slope surface with loading frequency 4 Hz.

As shown in Figure 12, with the increase in the peak-to-peak crest loading, the maximum surface displacement at various measurement points demonstrated different trends. At point C1, the maximum surface displacement slightly increased and then remained relatively stable. At point C2, the maximum surface displacement decreased from an inward depression of 0.1 mm to 0 mm. Meanwhile, at point C3, the maximum surface displacement increased from

0.15 mm to 0.2 mm. At point C4, the maximum surface displacement slightly increased before stabilizing. Additionally, at point C5, the maximum surface displacement initially remained unchanged and then slightly increased to an outward protrusion of 0.15 mm.

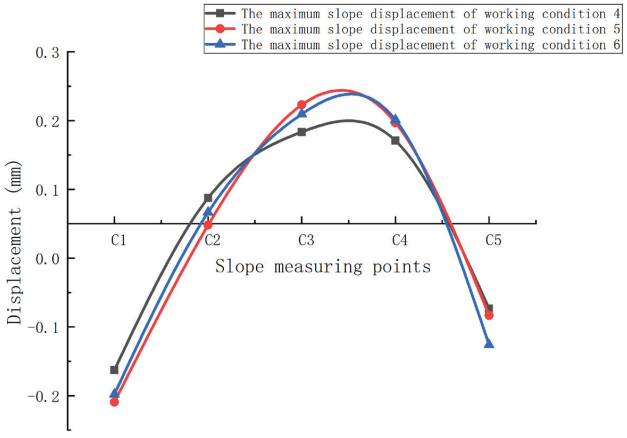

Figure 12. Maximum displacement of different up and down peak slopes.

As depicted in Figure 13, with the increase in the peak value differential of the crest loading, the maximum surface displacement at various measurement points showed distinct changes. At point C1, the maximum surface displacement decreased from an outward protrusion of 0.23 mm to 0.18 mm. At point C2, the maximum surface displacement increased from an inward depression of 0.2 mm to 0.7 mm. However, at points C3, C4, and C5, the maximum surface displacement remained relatively unchanged and maintained a consistent pattern.

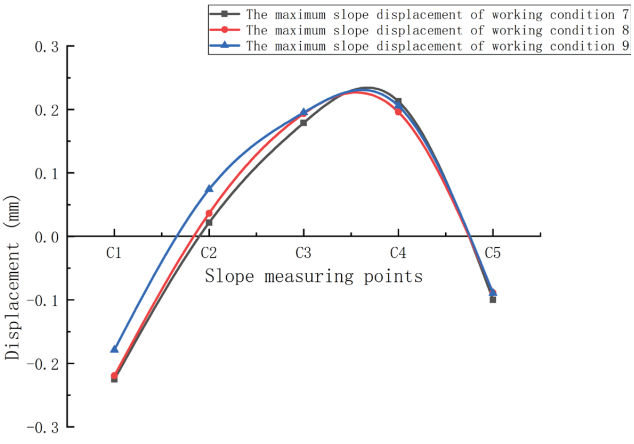

Figure 13. Maximum displacement of slope surface with different upper peaks.

Under crest loading, the slope surface exhibits outward protrusion at the slope crest and slope toe regions, while it shows inward depression in the middle section of the slope. Compared to the unsupported slope, significant reductions in the maximum horizontal surface displacement are observed at various measurement points when the slope is supported. Point C1 at the crest experiences the most substantial decrease in the maximum surface displacement, followed by slightly smaller reductions at points C2 (crest) and C5 (toe), whereas points C3 and C4 in the middle section show no significant variation. This could

be attributed to the proximity of point C1 to the loading area, leading to a more pronounced effect of the crest load. Therefore, in practical applications, particular attention should be given to reinforcing and monitoring the support at the crest and toe positions, emphasizing the comprehensive implementation of the wooden frame beam–bamboo anchor support. The considerable reduction in the maximum horizontal surface displacement on the slope surface with the wooden frame beam–bamboo anchor support demonstrates the feasibility of using this system as temporary support for railway embankment slopes.

3.3. Bamboo Anchor Shaft Force Variation Law

As shown in Figure 14, the bamboo anchor rods are installed at an angle of 105 degrees with respect to the slope surface. The anchoring end is embedded within the slope, while the anchor head is connected to the wooden frame beam, forming an integrated support system. According to Formula (1), the normal stress on the cross-sectional area of the bamboo anchor rod is represented, where the axial force of the bamboo anchor rod is the cross-sectional area, and is the modulus of elasticity of the bamboo anchor rod. By employing Formulas (1) and (2), the axial force of the bamboo anchor rod can be determined as shown in Equation (3).

$$\sigma = \frac{F_N}{S_0} \tag{1}$$

$$E = \frac{\sigma}{\varepsilon} \tag{2}$$

$$F_N = E\varepsilon S_0 \tag{3}$$

$$\text{Anchor bending moment : } M = EW\varepsilon_M \tag{4}$$

where W is the flexural section modulus of the bamboo anchor taken as $\frac{3\pi d}{16}$, and ε_M is $\frac{1}{2}$ of the measured strain due to the bending moment using the half-bridge wiring method.

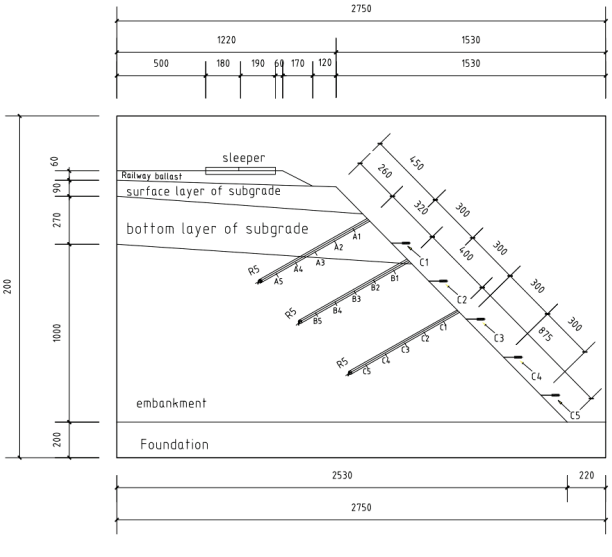

Figure 14. Bamboo anchor arrangement position.

The axial forces at various measurement points for Rod A and Rod B under different loading frequencies are illustrated in Figure 15. For Rod A, except at point A2 where it experiences compression, the other measurement points endure tension. Among these points, A4 exhibits the maximum tensile force, while A3 shows the minimum tensile force

across all conditions. When the frequency escalates to 3 Hz, apart from points A2 and A3, the axial forces at the remaining points increase to varying degrees. However, with the frequency further increased to 4 Hz, the axial forces in Rod A slightly diminished instead.

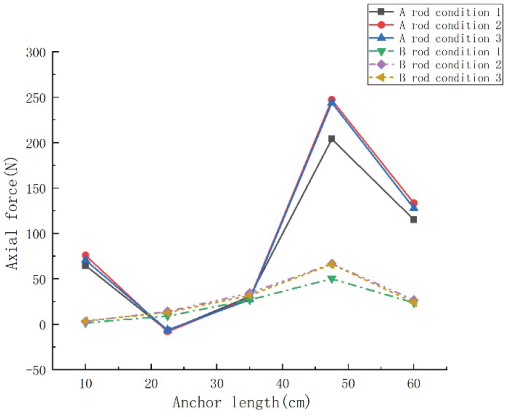

Figure 15. Axial force of anchor rod with different loading frequency.

On the other hand, the overall axial force in Rod B is smaller than that in Rod A. Rod B experiences tension at all measurement points under loading, except for point B1, which transitions from tension to compression at 4 Hz loading. Throughout all conditions, B4 manifests the maximum tensile force among the measurement points for Rod B. As the loading frequency increases to 3 Hz, the axial forces at different points in Rod B increase to varying extents, with the most significant increment observed at point B4. However, when the loading frequency rises to 4 Hz, there is no noticeable change in the axial forces.

The axial forces at various measurement points for Rod A and Rod B under different peak-to-peak loading conditions are depicted in Figure 16. In all scenarios, except at point A2, all measurement points for Rod A experience tension, with A4 exhibiting the maximum tensile force. When the peak-to-peak loading increases to condition 5, the axial force at A4 noticeably increases; however, with further increments in the peak-to-peak loading, the axial force slightly decreases.

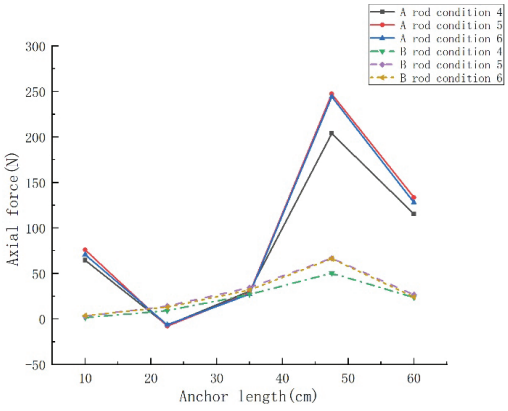

Figure 16. Different upper and lower peak anchor shaft forces.

In comparison to Rod A, all measurement points for Rod B experience tension, with the axial force gradually increasing from the anchor head to the anchoring end until point B4, where it decreases. Notably, B4 exhibits the maximum tensile force. With the increase

in the peak-to-peak loading, the axial forces in Rod B initially show a certain degree of augmentation, followed by a trend toward stabilization.

The axial forces at various measurement points for Rod A and Rod B under different peak differential loading conditions are illustrated in Figure 17. For Rod A, except at point A2, all measurement points experience tension. The maximum axial force for Rod A is consistently observed at A4 in all conditions. The distribution pattern of axial forces along the rod reveals a trend where the force gradually decreases from the anchor head towards the anchoring end, initially exhibiting compression and then transitioning to tension, reaching its peak at point A4. As the upper peak value increases to condition 8, the axial force in the rod shows no significant change; however, upon reaching condition 9, there is a sudden drop in the rod's axial force.

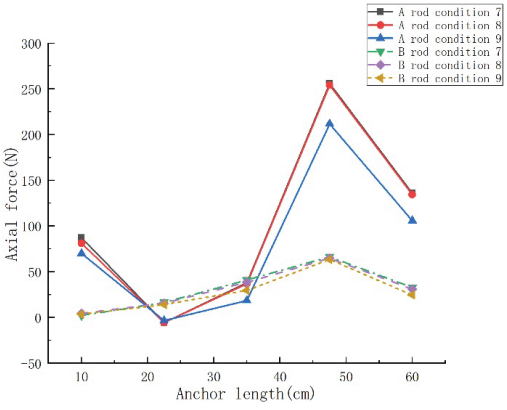

Figure 17. Different upper peak anchor shaft forces.

In comparison to Rod A, all measurement points for Rod B experience tension, with the maximum axial force occurring at B4. The axial force distribution along the rod gradually increases from the anchor head towards the anchoring end, reaching its peak at position B4, and subsequently decreasing. Interestingly, in Rod B, as the upper peak value increases, the axial forces at all measurement points decrease.

In various conditions, the axial force in Rod A at the slope top is significantly larger than that in Rod B at the slope middle. The closer the rod is to the top of the slope, the greater the axial force distribution along the rod. This indicates that the effect of Rod A at the slope top on slope support is more pronounced. The axial forces in the anchor rods show a pattern of larger forces at the anchoring end and smaller forces at the anchor head. Therefore, it is deemed unreasonable in engineering practice to assume a uniform distribution of axial force along the length of the anchor rod.

Within the support system, Rod A, situated closer to the loading point near the slope top, takes the lead in providing support, transitioning subsequently to the anchor rods at the slope middle and slope angle. The maximum value of axial force in the rod appears at measurement point 4, closer to the anchoring end. This phenomenon is due to the anchoring end's proximity to the potential slip surface of the slope, causing the axial force in the anchor rod to reach its maximum as a result of shear displacement along the potential slip surface.

The axial force in the anchor rod shows an initial positive correlation in increase, both in frequency and upper and lower peak values, followed by no significant increase in the later stage. However, when only the upper peak value increases, the axial force on the anchor rod decreases. This reduction may be attributed to the transition of axial force in the anchor rod as the upper peak value increases, gradually distributing the force across the entire support system, collectively resisting slope movement.

3.4. Bamboo Anchor Bending Moment Analysis

Under different frequency loadings, the bending moments at various points of Rods B and C are shown in Figure 18. The lower parts of Rod segments B1–B3 experience tension, resulting in positive bending moments, while the upper parts of Rod segments B3–B5 are under tension, creating negative bending moments. There is a tendency for the surrounding soil to slide downwards, with the maximum bending moment occurring at the anchor head.

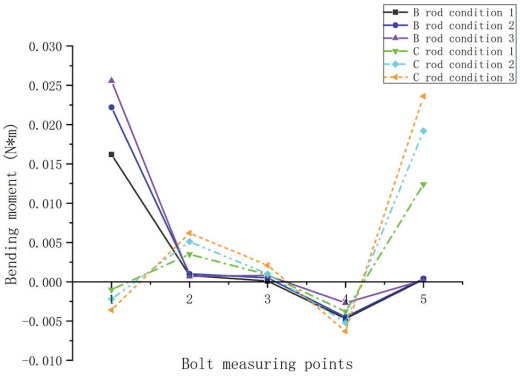

Figure 18. Anchor bending moment with different loading frequencies.

The bending moments in Rod C exhibit an alternating tensile pattern, resembling a wave-like bending behavior. Rod segments C1–C3 and the lower part near the anchoring end experience tension, generating positive bending moments and causing the soil around these segments to compact. Conversely, from Rod segment C3 to the upper part near the anchoring end, tension results in negative bending moments, leading to a tendency for the surrounding soil to slide downward. The maximum bending moment is observed at Rod C5.

The bending moments at various points of Rods B and C increase with the rise in frequency, but in comparison to axial forces, the overall bending moments in these rods are relatively small.

According to the statements in academic journals, the bending moments at various measuring points for Bars B and C under different peak loads are shown in Figure 19. At the lower section of Bars B1–B2, tension generates positive bending moments, while at the upper section of B2–B5, tension creates negative bending moments. The soil around the body bars of B near the anchor head is compacted, indicating a tendency for possible slippage of the soil near the anchor head.

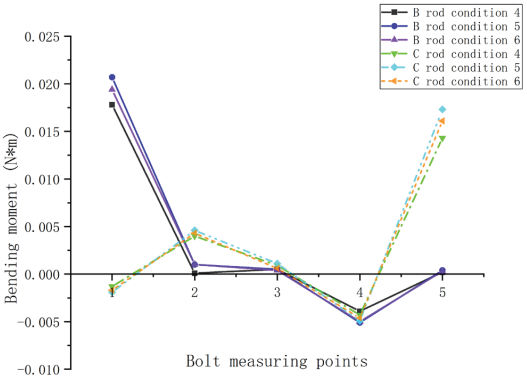

Figure 19. Different upper and lower peak anchor bending moments.

For Bar C, segments C1–C3 and the lower part near the anchor end experience tension, resulting in positive bending moments, whereas from C3 to the upper part near the anchor end, tension generates negative bending moments. The maximum bending moment for Bar B occurs at the anchor head, whereas for Bar C, it appears at the anchor end. With an increase in the peak values of loading, both Bars B and C exhibit only a slight increase in bending moments.

Under different maximum peak loadings, the bending moments at various points of Rods B and C are illustrated in Figure 20. The lower sections of Rod B segments B1–B3 are under tension, resulting in positive bending moments and leading to soil compaction around the rod tip. Conversely, the upper parts of Rod segments B3–B5 are under tension, generating negative bending moments and causing a tendency for the surrounding soil to slide.

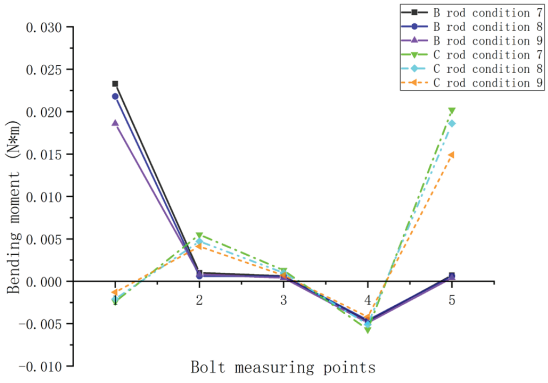

Figure 20. Anchor bending moment with different peak differences.

Rod C exhibits an alternating tensile pattern, resembling a wave-like bending behavior. Rod segments C1–C3 and the lower part near the anchoring end experience tension, generating positive bending moments, while from Rod segment C3 to the upper part near the anchoring end, tension results in negative bending moments. Rod C might exhibit significant bending deformation at C3, where the surrounding soil around the front part of C3 is compacted, while the soil around the rear part shows signs of sliding. The maximum bending moment occurs at point B1 for Rod B and at point C5 for Rod C.

As the maximum peak loading increases, only the maximum bending moment point, B1 in Rod B, decreases. In contrast, the bending moments at various points in Rod C decrease as the maximum peak loading increases.

Compared to the axial forces on the anchor rods, the bending moments on the anchor rods are considerably smaller. With an increase in depth, the point of maximum bending moment on the anchor rods also shifts from the anchor head towards the anchoring end. The bending moments along the length of the anchor rods exhibit an alternating tensile pattern resembling waves. Near measurement point 3, the soil around the segment close to the anchor head is compacted, while in the vicinity of the segment close to the anchoring end, there is a tendency for the soil to slide, indicating the potential presence of a slip surface near the anchoring end of the anchor rods.

The bending moments are significantly influenced by the loading frequency, increasing with higher loading frequencies. However, the influence of varying maximum peak loads on the bending moments is relatively small, showing only minor fluctuations in the bending moments. The impact of the maximum peak load on the bending moments is more evident, with the bending moments decreasing as the maximum peak load increases.

3.5. Wooden Frame Beam Bending Moment Analysis

The bending moments at various measuring points of the frame beams under different loading frequencies are illustrated in Figure 21. For the horizontal frame beams subjected to top loading, the lower sections of measuring points H1, H3, H5, and H7 are under tension, indicating positive bending moments, while the upper sections of measuring points H2, H4, and H6 are under tension, indicating negative bending moments. As the frequency increases, the bending moments at each measuring point gradually increase, with larger amplitudes at higher frequencies.

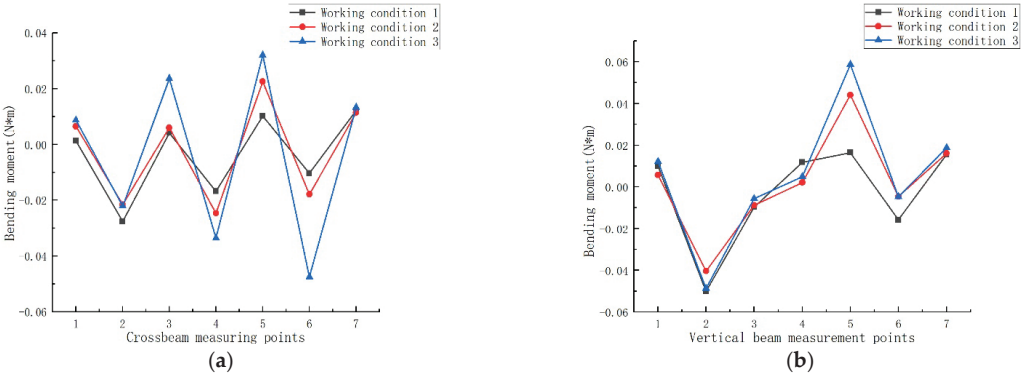

Figure 21. Bending moments of frame beams with different loading frequencies. (**a**) Cross beam; (**b**) vertical beam.

Regarding the vertical frame beams under loading, the lower sections of segments S4–S7 are under tension, indicating positive bending moments, whereas the upper sections of segments S1–S4 are under tension, indicating negative bending moments. With the frequency increase, segment S5 exhibits a significant increase in bending moment, reaching the maximum, while segments S2, S4, and S6 show slight increases in bending moments, and the remaining measuring points remain relatively stable.

Comparing the two diagrams, both horizontal and vertical frame beams exhibit an alternating pattern of tension in bending moments. The bending moments of the horizontal beams are more affected by the loading compared to the vertical beams.

The bending moments at various measuring points of the frame beams under different upper and lower peak values of loading are illustrated in Figure 22. The overall bending moments exhibit an alternating pattern of tension, resembling a wave-like shape. With the increase in upper and lower peak values, except for H3, the bending moments at the remaining measuring points significantly increased. The bending moments at the sides of the beam are relatively smaller and show less variation.

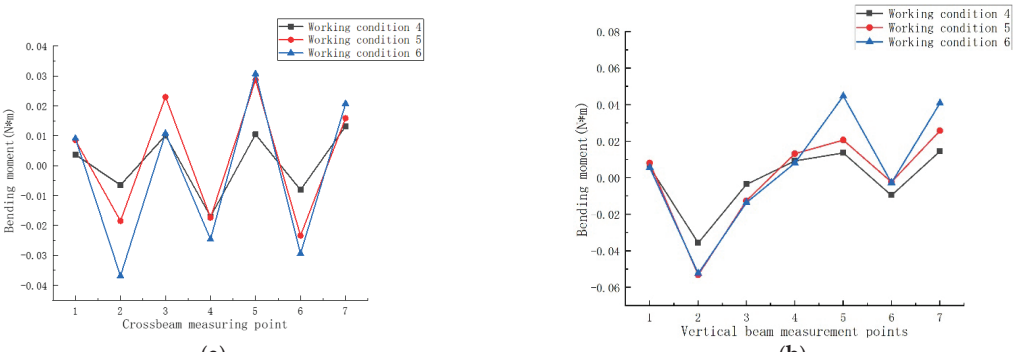

(**a**) (**b**)

Figure 22. Different upper and lower peak frame beam bending moments. (**a**) Cross beam; (**b**) vertical beam.

For the vertical frame beams under loading, the lower sections of segments S4–S7 are under tension, indicating positive bending moments, while the upper sections of segments S1–S4 are under tension, indicating negative bending moments. With the increase in upper and lower peak values, the bending moments at each measuring point notably increase.

The bending moments at various measuring points of the frame beams under different upper peak values of loading are illustrated in Figure 23. Under the loading conditions, the lower parts of the horizontal beam at points H1, H3, H5, and H7 are under tension, while the upper parts at points H2, H4, and H6 are also under tension. With the increase in upper peak values, there is a significant increase in bending moments at points H3, H4, and H6, while the bending moments at points H1, H2, and H7 decrease. For the vertical beam, the lower sections of segments S4–S7 are under tension, and the upper sections of segments S1–S4 are under tension. The change in bending moments with the increase in upper peak values is minimal.

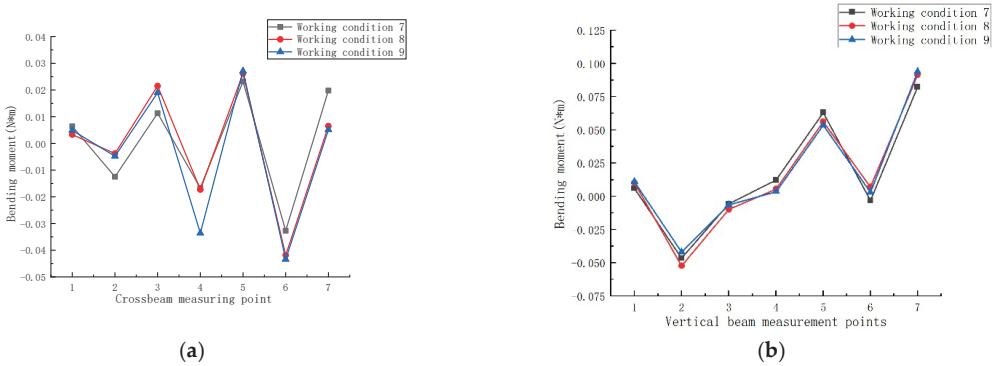

(**a**) (**b**)

Figure 23. Different upper peak frame beam bending moments. (**a**) Cross beam; (**b**) vertical beam.

Both the horizontal beam and the vertical beam of the wooden frame beams exhibit a wave-like pattern of alternating tension and compression. This behavior resembles the actual structural bending observed in frame beams in engineering practice. Within the combined system of slope soil, bamboo anchor rods, and frame beams, the frame beams experience a dual compression–tension stress pattern. The horizontal beam mainly experiences bending stress in the middle and anchor head sections, suggesting a need for reinforced support in the midsection for engineering purposes. The vertical beam shows upward tension and outward bending in the upper section, while the lower section experiences downward tension and inward bending toward the slope face. The horizontal

beam is notably affected by changes in frequency, upper and lower peak values, and peak value differences.

4. Stability Analysis of the Slope of Roadbed Supported by Timber-Frame Beam–Bamboo Anchor Rod

The slope model is divided into five soil layers, consistent with the parameters of the indoor physical model test, comprising the foundation layer, embankment layer, sub-base bottom layer, sub-base surface layer, and ballast layer. The experimental slope's dimensions were scaled up at a similarity ratio of 1:7 to establish a full-scale model of the road slope supported by wooden frame beams and bamboo anchor rods. The bamboo anchor rods were arranged in a pattern of three rows and three columns, embedded at an angle of 105 degrees, while the wooden frame beams were arranged in four rows and five columns, both using 1D embedded beam elements. The slope soil adopted the Mohr–Coulomb model, and the bamboo anchor rods and wooden frame beams were modeled using elastic elements. After generating the solid and dividing it into grids, the model is depicted in Figure 24.

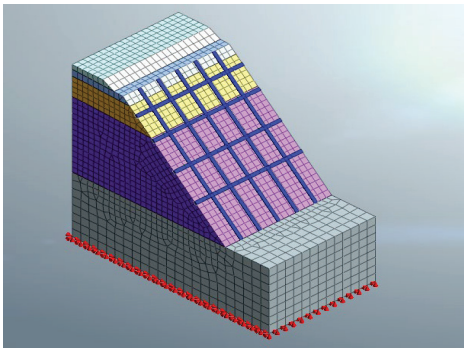

Figure 24. A 3D numerical model of bamboo anchor–wood frame beam roadbed slope.

4.1. Slope Safety Factor

The slope safety factor is an essential indicator of slope stability. Midas GTS NX calculates the slope safety factor by iteratively reducing the internal friction angle and cohesion of the slope soil using the strength reduction method. When the slope approaches the critical point of failure, the value by which the slope is reduced represents the safety factor of the slope.

Table 4 shows the safety factor of the roadbed slope under different numbers of bamboo anchor supports in loading condition 2. Under the action of train loads, the safety factor of the roadbed slope significantly increases with the presence of wooden framework beams and bamboo anchor supports. Compared to the safety factor of the roadbed slope without wooden framework beams and bamboo anchor support, there is a 20.13% increase in the safety factor of the slope. This result indicates that the supporting structure effectively reduces the impact of cyclic train loads on the roadbed slope, thereby enhancing its stability.

Table 4. Coefficient of safety of slopes with different number of rows.

Side Slopes	Safety Factor K	Safety Factor Improvement Rate
Unsupported slope	1.103	-
Three rows and three rows of bamboo anchor slope	1.325	20.13%

4.2. Maximum Shear Strain of the Slope

The maximum shear strain of the slope is an important index to measure the force condition of the soil body of the slope, and the dynamic response of the soil body of the

slope under train loading can be inferred from the maximum shear strain of the slope to infer the potential slip surface or damage location of the slope. After calculation by Midas GTS NX 2016 finite element software, the cloud diagrams of the maximum shear strains of the embankment slopes under train loads were extracted for different arrangements of bamboo anchors and wooden frame beam support arrangements. Figure 25a shows that the maximum shear strain of the slope is distributed at the foot of the slope when there is no wood frame beam–bamboo anchor support, and the potential slip surface is formed with the bed surface at the top of the slope, and the slope is most prone to shear damage at the foot of the slope. Figure 25b shows that when the slope is supported by bamboo anchors and wooden frame beams, the maximum shear strain of the slope appears below the loading place at the top of the slope, and the maximum shear strain of the slope gradually spreads and expands to the slope body from the loading place at the top of the slope, and the shear strain decreases greatly. The maximum shear strain at the foot of the slope is very small, and a potential slip surface is not formed in the body of the slope.

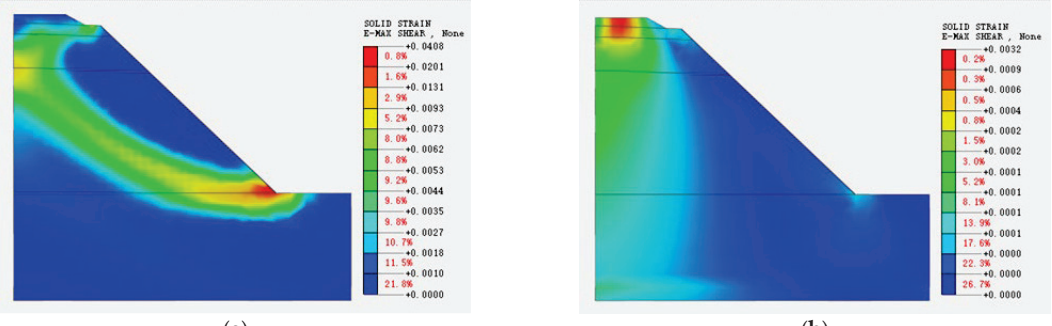

(**a**) (**b**)

Figure 25. Maximum shear strain on the slope. (**a**) Unsupported slope; (**b**) bamboo anchors for slope support.

In summary, compared with the maximum shear strain cloud diagram of the unsupported embankment slope, the maximum shear strain is obviously smaller when the slope is supported, and the maximum shear strain is also very small in the area of the slope supported by bamboo anchors and wooden frame beams; the maximum shear strain at the foot of the slope decreases significantly, and there is no through maximum shear strain slip surface formed in the slope, and the range of the distribution is also reduced. This shows that the maximum shear strain distribution range and size of the slope can be greatly reduced in the wooden frame beam–bamboo anchor support, reducing the probability of shear damage at the foot of the slope, effectively supporting the slope, and improving the stability of the slope.

4.3. Maximum Shear Stress on the Slope

The maximum shear stress of the slope is also one of the important indices to judge the stability of the slope. Figure 26a shows that when the slope is unsupported, the maximum shear stress peak is mainly concentrated in the ballast layer, and the top and foot of the slope are also subject to large shear stresses according to the potential sliding surface of the slope. At this time, the foot of the slope and the top of the slope are susceptible to shear damage. Figure 26b shows that when the slope is supported by bamboo anchors, the maximum shear stress of the slope decreases abruptly, and the peak shear stress decreases by 34.7%. In the slope supported by bamboo anchors, the maximum shear stress decreases abruptly, and the shear stress is mainly concentrated at the top of the slope below the loading point. It is an arc-shaped downward decay; the foot of the slope and the top of the

slope shear stress decrease abruptly, and the probability of occurrence of shear damage is greatly reduced.

In summary, when the slope is unsupported, the maximum shear stress distribution range fills the whole slope, shear damage easily occurs at the top and foot of the slope, and the stability of the slope is poor. Further, when the slope is supported by bamboo anchors and wooden frame beams, the maximum shear stress distribution range of the slope is rapidly reduced and mainly concentrates in the arc-shaped spreading attenuation below the loading point and attenuation mainly concentrates in the ballast layer and the foundation layer, the foot of the slope and the top of the slope shear stress is suddenly reduced, and the probability of shear damage is greatly reduced.

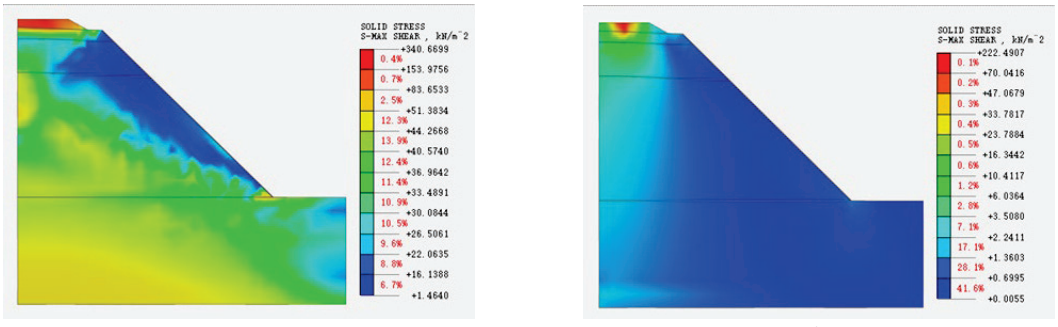

(**a**) (**b**)

Figure 26. Maximum shear stress on the slope. (**a**) Unsupported slope; (**b**) bamboo anchors for slope support.

5. Conclusions

This paper conducted model experiments on roadbed slopes that were supported by wooden framework beams and bamboo anchor systems under train loads. Three-dimensional numerical simulations were performed to analyze the effect of train load frequency, peak difference, and peak value on the soil pressure of the roadbed slope. They also analyzed the horizontal displacement of the slope surface, the internal forces within the supporting structure, and the slope safety factor. The relevant conclusions are as follows:

(1) When the loading frequency increases from 2 Hz to 3 Hz, there is a considerable increase in soil pressure; however, further increments in the loading frequency result in a smaller increase in soil pressure. The increase in dynamic load shows a positive correlation with soil pressure.

(2) In indoor slope model experiments, the axial force on the anchor rods is not uniformly distributed. Therefore, in engineering design, the assumption of uniform axial force distribution along the length of the anchor rods is deemed unreasonable. Across various conditions, the axial force on the rod tends to be greater closer to the top of the slope. The support system primarily operates with the top-slope anchor rods and then gradually transitions to the anchor rods in the middle and at the foot of the slope. The combined action of the anchor rods and wooden framework beams forms an integral support system that resists slope movement, thereby enhancing slope stability.

(3) The point of maximum bending moment in the anchor rods gradually transitions from the anchor head to the anchored end with increased burial depth. The bending moment is significantly influenced by loading frequency, increasing with higher loading frequencies. It shows minor fluctuations with variations in upper and lower peak values. Notably, the bending moment is prominently influenced by increased upper peak values, exhibiting a decrease with their rise. This phenomenon might be due to the larger peak difference, causing the combined wooden framework beam–bamboo anchor support system to resist slope movement.

(4) When employing the wooden framework beam–bamboo anchor support as temporary support in engineering applications for roadbed slopes, it is crucial to monitor and protect the positions at the slope's top and bottom. Additionally, enhancing the overall integrity of the wooden framework beam–bamboo anchor support is recommended.
(5) Under the influence of train loads, the roadbed slope with wooden framework beam–bamboo anchor support effectively mitigates the impact of dynamic train loads. The safety factor of the roadbed slope is increased by 20.13% compared to the unsupported condition, significantly enhancing slope stability.

Author Contributions: All authors contributed to this study's conception and design. Investigation, writing—original draft preparation, and writing—review and editing, G.H.; supervision and validation, H.Y.; data curation and formal analysis, Z.W.; conceptualization and funding acquisition, X.J.; resources, Z.C. All authors commented on previous versions of the manuscript. All authors have read and agreed to the published version of the manuscript.

Funding: This study was supported by the Special Projects in Key Fields of Higher Education in Guangdong Province (Grant No.: 2023ZDZX4044), the Special Projects in Key Fields of Higher Education in Guangdong Province (Grant No.: 2023ZDZX4045), the Research Capacity Enhancement Project of Key Construction Discipline in Guangdong Province (Grant No.: 2022ZDJS092), the National Natural Science Foundation of China (31971727), and the Forest Science and Technology Innovation Program of Hunan Province (XLK202105-3).

Data Availability Statement: The raw data supporting the conclusions of this article will be made available by the authors on request.

Conflicts of Interest: Author Zhengyi Cao was employed by the company Nuclear Industry Jinhua Survey and Design Institute Co., Ltd. The remaining authors declare that the research was conducted in the absence of any commercial or financial relationships that could be construed as a potential conflict of interest.

References

1. Wang, Y.; Liu, X. Plant slope protection in highway engineering. In Proceedings of the IOP Conference Series: Earth and Environmental Science, Ordos, China, 28–29 April 2018; p. 052038.
2. Ng, C.W.W.; Leung, A.K.; Kamchoom, V.; Garg, A. A Novel Root System for Simulating Transpiration-Induced Soil Suction in Centrifuge. *Geotech. Test. J.* **2014**, *37*, 733–747. [CrossRef]
3. Yi-bing, W.; Wen-qi, Y.; Cheng, Z.; Qun, C.J. Numerical analysis of hydraulic characteristics of slopes reinforced by vertical geotextile belts and vegetation. *Chin. J. Geotech. Eng.* **2020**, *42*, 238–243.
4. Lin, D.-G.; Liu, W.-T.; Lin, S.-H. Estimating the effect of shear strength increment due to root on the stability of Makino bamboo forest slopeland. *J. GeoEngineering* **2011**, *6*, 73–88.
5. Zhou, B.; Wang, B.; Liang, C.; Wang, Y.J. Study on load transfer characteristics of wholly grouted bolt. *Chin. J. Rock Mech. Eng.* **2017**, *36*, 3774–3780.
6. Mira, E.; Rousteau, A.; Tournebize, R.; Robert, M.; Evette, A. Evaluating the suitability of neotropical trees and shrubs for soil and water bioengineering: Survival and growth of cuttings from ten Caribbean species. *Ecol. Eng.* **2022**, *185*, 106808. [CrossRef]
7. Li, Y.; Fu, J.; Yu, D.; Hu, X.; Zhu, H.; Li, G.; Hu, X.J. Mechanical effects of halophytes roots and optimal root content for slope protection in cold and arid environment. *Chin. J. Rock Mech. Eng.* **2015**, *34*, 1370–1383.
8. Vergani, C.; Chiaradia, E.A.; Bassanelli, C.; Bischetti, G.B. Root strength and density decay after felling in a Silver Fir-Norway Spruce stand in the Italian Alps. *Plant Soil* **2013**, *377*, 63–81. [CrossRef]
9. Yang, H.; Zhu, Y.; Jiang, X.; Fan, W.; Liu, K.; Zhao, S.; Huang, L.J. Study on the Supporting Effect of Bamboo anchor and wood Frame Beam Reinforcing Cohesive Soil Slope. *Indian Geotech. J.* **2023**, *53*, 844–858. [CrossRef]
10. Zhu, Y.; Yang, H.; Liu, Y.; Jiang, X.; Deng, R.; Huang, L.; Yin, P.; Lai, G. Numerical Simulation of the Combined Slope Protection Effect of Living Stump and Bamboo Anchor. *Geotech. Geol. Eng.* **2021**, *40*, 635–645. [CrossRef]
11. Jiang, X.; Qian, Y.; Yang, H.; Xiao, Z.; Fan, W.; Zhu, Y.; Liu, W.; Guo, J. Model Test Studies on Slope Supported by Bamboo Anchor and Timber Frame Beam. *Geotech. Geol. Eng.* **2022**, *40*, 4327–4344. [CrossRef]
12. Yan, S.; Su, X. Dynamic Characteristics and Dynamic Response of Subgrade Slopes under Dynamic Loads. In Proceedings of the 2010 International Conference on E-Product E-Service and E-Entertainment, Henan, China, 7–9 November 2010; pp. 1–4.
13. Ye, S.; Fang, G.; Zhu, Y. Model establishment and response analysis of slope reinforced by frame with prestressed anchors under seismic considering the prestress. *Soil Dyn. Earthq. Eng.* **2019**, *122*, 228–234. [CrossRef]
14. Islam, M.; Gnanendran, C. Slope stability under cyclic foundation loading-Effect of loading frequency. In Proceedings of the Geo-Congress 2013: Stability and Performance of Slopes and Embankments III, San Diego, CA, USA, 3–7 March 2013; pp. 750–761.

15. Qiu, H.Z.; Kong, J.M.; Zhang, Y.J. Analysis on dynamic response of the foundation pit supporting structure under vehicle loads. *Adv. Mater. Res.* **2013**, *790*, 638–642. [CrossRef]
16. Zhi-jia, W.; Jian-jing, Z.; Xiao, F.; Kong-ming, Y.; Ming-yuan, W.; Sheng-en, P. Isolated similar design method for a scaled model test and its application to slope-anchor cable-lattice beam system. *Rock Soil Mech.* **2016**, *37*, 2617–2623.
17. Zhang, F.; Ma, G.; Liu, X.; Tao, Y.; Li, R.; Feng, D. Experimental Analysis of the Ratio of Similar Materials by Similarity Model Test on Raw Coal. *Curr. Sci.* **2017**, *113*, 2174–2179. [CrossRef]
18. Hongguang, J.; Xuecheng, B.; Yunmin, C. Full-scale Accel-erated Testing for Simulation of Train Moving Loads in Track-subgrade System of High-speed Railways. *China Civ. Eng. J.* **2015**, *9*, 85–95.

applied sciences

MDPI

Article

Application of Direct Shear Test to Analysis of the Rate of Soil Improvement with Polyester Fibres

Giang Nguyen [1,2,*], Soňa Masarovičová [1], Filip Gago [1] and Joanna Grzybowska-Pietras [2]

[1] Faculty of Civil Engineering, University of Žilina, Univerzitná 8215/1, 010 26 Žilina, Slovakia; sona.masarovicova@uniza.sk (S.M.); filip.gago@uniza.sk (F.G.)
[2] Faculty of Materials, Civil and Environmental Engineering, University of Bielsko-Biala, Willowa 2, 43-309 Bielsko-Biala, Poland; jpietras@ubb.edu.pl
* Correspondence: giang.nguyen@uniza.sk or gnguyen@ubb.edu.pl; Tel.: +421-41-513-5759

Featured Application: Based on confirmed significant improvement of the shear strength parameters of soil using tested polyester fibres, there is a potential application of fibres in increasing the subsoil bearing capacity, increasing the slope stability or decreasing the soil pressure.

Abstract: When improving soil shear strength using various materials, determination of the improvement rate is a key issue and can be carried out using a direct shear test (DST). However, many standards for DST require only three specimens in the test and do not deal with test result uncertainty. In this study, shear strength parameters of clay of intermediate plasticity (CI) and sandy clays (CS1, CS2) improved with the addition of polyester fibres of 70 mm in length in amounts of 0.5%, 1.0%, and 1.5% of dry soil mass were obtained using DST with a shear box of size 0.3 m × 0.3 m × 0.08 m. The results show that using fibres provides significant improvement and the number of tested specimens (three or four) in DST has a significant impact on the obtained values of shear strength parameters. It is not recommended to carry out DST with only three specimens. The analysis of uncertainty shows that covariance between correlated input quantities (normal stresses and shear stresses) has a negligible influence on result uncertainty. The worst-case estimated uncertainties are very high and should not be applied. Analysis of the state of the fibre surface before and after shearing using scanning electron microscopy (SEM) shows that suitable fibre scratch resistance may be the reason for the large improvement.

Keywords: direct shear test; number of specimens; uncertainty of shear strength parameters; covariances; worst-case estimated uncertainties; fibre scratch resistance

Citation: Nguyen, G.; Masarovičová, S.; Gago, F.; Grzybowska-Pietras, J. Application of Direct Shear Test to Analysis of the Rate of Soil Improvement with Polyester Fibres. *Appl. Sci.* **2024**, *14*, 4601. https://doi.org/10.3390/app14114601

Academic Editors: António Alberto Santos Correia and Paulo José da Venda Oliveira

Received: 30 April 2024
Revised: 24 May 2024
Accepted: 25 May 2024
Published: 27 May 2024

1. Introduction

In practice, in many cases, an improvement of soil properties proves necessary. Since soil shear strength is one of the most important properties, it is often required to be improved. To evaluate the improvement rate of soil shear strength, despite some shortcomings (predefined shear plan, uneven distribution of shear stress, small shear box, etc.) of the direct shear test (DST), many authors apply the DST in their research due to its simplicity. The DST has been used, e.g., to evaluate soil improvement with fibres [1–5], lime and fly ash [6], and palm oil fuel ash (POFA)-based geopolymer [7]. In addition to the use of DST in evaluation of the improvement rate of soil shear strength, DST has been used, e.g., for evaluation of the reinforcement effects of conventional geotextiles, geogrids, and novel geotextiles [8], evaluation of the influence of the scale effect on the shear strength of scaled coarse-grained soil (CGS) [9], and analysis of coarse-grained soil behavior during shearing [10]. Moreover, DST has been used, e.g., for the determination of soil shear strength parameters, which are further used in machine learning (ML) models built for their predicting for other soils without the need to carry out DST [11].

Tang et al. [1] investigated the effects of discrete short polypropylene fibre (PP-fibre) on the strength and mechanical behaviour of uncemented and cemented clayey soil (CL). In the presented investigation, 12 groups of soil samples were prepared at three different percentages of PP-fibre content (i.e., 0.05%, 0.15%, and 0.25% by weight of soil) and two different percentages of cement content (i.e., 5% and 8% by weight of soil), and unconfined compression and direct shear tests were carried out after 7-, 14-, and 28-day curing periods. The specimens for DST were shaped in a cylindrical mould of 20 mm in height with an inner diameter of 61.8 mm. The tests were performed at four vertical normal stresses, 50, 100, 200, and 300 kPa, in order to define the shear strength parameters. The authors stated that the test results indicated that the inclusion of fibre reinforcement within uncemented and cemented soil caused an increase in shear strength. The introduced increase in the values of the angle of internal friction was very small. So, e.g., after curing for 28 days, the values of the angle of internal friction of soil with 5% cement content and 0.05%, 0.15%, and 0.25% fibre content were 35.1°, 36.3°, and 36.7°, respectively (differences of 1.2° and 0.4°); the values of the angle of internal friction of soil with 8% cement content and 0.05%, 0.15%, and 0.25% fibre content were 37.0°, 37.5°, and 39.3°, respectively (differences of 0.5° and 1.8°). Since the differences were very small, it was also possible that such small changes could be smaller than the result uncertainty; therefore, uncertainty analysis could be useful.

Valipour et al. [3] investigated the effects of recycled tire polymer fibres (RTPFs) and glass fibres (GFs) on enhancing the strength/deformation properties of clays. A series of compaction, unconfined compression, and DST were performed on precisely prepared composite soils comprising clay with different amounts (0.5, 1.0 and 1.5%) of RTPFs and GFs having varying lengths (5 and 10 mm). For the clay reinforced with GFs and RTPFs, the shear strength was measured by a direct shear apparatus implementing the method of ASTM D3080 [12]. All specimens were sheared under constant vertical stresses of 55, 105, and 205 kPa. The differences between the peak friction angle of soil and soil composite were very small (from 0.1° to 3.3°; smaller than 1° in four cases). Similar small differences between the peak friction angle of composite with various amounts of RTPFs and GFs could be seen (from 0.4° to 2.7°; smaller than 1° in six cases). Small changes in both the peak friction angle and cohesion could be seen between 0.5% and 1% composite, e.g., 1° and 0.2 kPa (RTPF—L 10 mm), and 0.4° and 2.6 kPa (GF—L 5 mm). Therefore, it was also possible in this case that such small changes could be smaller than the result uncertainty, so uncertainty analysis could be useful.

Urian et al. [4] studied the mechanical characteristics of clay improved with shredded polyethylene terephthalate (PET). PET was provided by a local plastic waste repository. It comes from recycled water, beer, and soda bottles and was cleaned using specific methods for cleaning and recycling plastic waste. PET was shredded into irregular shapes with sizes ranging from 3 mm to 12 mm and was randomly distributed in percentages of 2%, 4%, and 6%. DST was performed according to the Romanian standard STAS 8942/2-82 [13] applying three normal stresses (100 kPa, 200 kPa, and 300 kPa). The values of the peak angle of internal friction of soil with 2%, 4%, and 6% PET were 20.93°, 20.20°, and 24.40°, respectively, so the improvement could be 2.10°, 1.37° and 5.57°, respectively (the peak angle of internal friction of soil without PET was 18.83°). Values of the residual angle of internal friction of soil with 2%, 4% and 6% PET were 12.21°, 11.33°, and 11.92°, respectively, so the improvement could be −0.17°, −1.04°, and −0.45°, respectively (the residual angle of internal friction of soil without PET was 12.37°). It was also possible in this case that such small changes could be smaller than the result uncertainty; therefore, uncertainty analysis could be useful.

Tang et al. [6] studied the mechanical properties of Xinyang red clay improved by lime and fly ash. The dry red clay soil that passed through the 2 mm sieve was divided into four groups. The first group was the single lime group, adding lime by 2%, 5%, 8%, and 11%. The second group was the single fly ash group, adding fly ash by 5%, 10%, 15%, and 20%. The third group was the mixed lime–fly ash group, and the mass ratios of lime–fly ash to dry soil were 1:2:7, 1:3:6, and 1:4:5. The fourth group was the control group, without lime

or fly ash. DST was used to determine the soil shear strength parameters of the improved soil, applying three normal stresses (100 kPa, 200 kPa, and 300 kPa). The values of the angle of internal friction of soil with 2%, 5%, 8%, and 11% lime content were 14°, 14°, 15°, and 17°, respectively, so the improvement could be 1.5°, 1.5°, 2.5°, and 4.5°, respectively (angle of internal friction of soil was 12.5°). The values of the angle of internal friction of soil with 5%, 10%, 15%, and 20% fly ash content were 11°, 13°, 12°, and 10°, respectively, so the improvement could be −1.5°, 0.5°, −0.5°, and −2.5°, respectively. The values of the angle of internal friction of soil with lime–fly ash–dry soil ratios of 1:2:7, 1:3:6, and 1:4:5 were 12.8°, 10.2°, and 13°, respectively, so the improvement could be 0.3°, −2.3°, and 0.5°, respectively. Similarly, in this case, it was possible that such small changes could be smaller than the result uncertainty, so uncertainty analysis could be useful.

Zhu et al. [11] used the shear strength parameters obtained from DST (with four applied normal stresses of 100, 200, 300, and 400 kPa) as guide values for predicting soil shear strength parameters using combined data and three different machine learning models. In total, 83 values of the angle of internal friction and 83 values of cohesion were obtained. The measured values of the internal friction angle ranged from 8.66° to 32.16°, with mean and median values of 18.73° and 17.70°, respectively. The cohesion value ranged from 1.74 to 38.95 kPa, with a mean of 20.77 kPa and a median of 20.91 kPa. Since the reliability of the predicted values of the shear strength parameters obtained from the models depended on the reliability of the above-mentioned values of the shear strength parameters, their uncertainty should be taken into account.

In our opinion, there is a big limitation to DST that is not addressed by many researchers: a large amount of DST is carried out in accordance with ASTM D3080/D3080M [12], STAS 8942/2-82 [13], AASHTO T 236-08: 2008 [14], BS 1377: Part 7:1990 [15], and ISO 17892-10:2018 [16], where only three specimens are sufficient and no limit value of the correlation coefficient between shear stresses and normal stresses is prescribed. One can propose that, in such cases, different combinations of three normal stresses (e.g., the combination 50 kPa, 100 kPa, and 200 kPa and the combination 100 kPa, 200 kPa, and 300 kPa) can provide different DST results (but are valid for the same common interval of normal stress from 100 kPa to 200 kPa). In contrast to the mentioned standards, STN 72 1030: 1988 [17] prescribes at least four specimens and PN-88/B-04481 [18] requires at least five specimens. Even in cases where researchers applied DST using four specimens, the improvement of shear strength parameters is small in some cases, but no uncertainty of the DST results is provided, so the improvement could not be confirmed.

DST was also applied in the evaluation of soil improvement using PES fibres TEXZEM PES 200 [19–21]. Nguyen et al. [19] reported the results of DST of soil improved by the mentioned fibres, TEXZEM PES 200, in amounts of 0.5%, 1.0%, and 1.5% of soil dry mass. Soil SC was used. DST was carried out using a fully automatic large shear box apparatus, SHEARMATIC 300 (Wykeham Farrance, CONTROLS Group, Milan, Italy). It was found that the optimal amount of fibres was 1%, at which the increase in the angle of internal friction measured was 6.1° (from 45.2° to 51.3°, corresponding to 13.5%) and the increase in cohesion obtained was 17.5 kPa (from 0 kPa to 17.5 kPa). The results of DST of soil CS mixed with the previously mentioned fibres, TEXZEM PES 200, can be also seen in the study by Nguyen [20]. DST was carried out using the above-mentioned large shear box apparatus, SHEARMATIC 300. The results showed that fibres in the amount of 0.5% significantly increased the angle of internal friction (by 8.7°, corresponding to 28.8%) as well as cohesion (by 14.4 kPa, corresponding 48.2%). Jakubík [21] also introduced a significant improvement of soil CS mixed with the previously mentioned fibres, TEXZEM PES 200. DST was carried out using the previously mentioned large shear box apparatus, SHEARMATIC 300. The results showed that fibres in the amount of 0.5% increased both the angle of internal friction by 16.1° (corresponding 86.0%) and cohesion by 32.3 kPa (corresponding 211.2%).

Ungureanu et al. [22], after analysing various possible methods for the estimation of DST uncertainty, came to the conclusion that a hybrid ordinary least squares method, denoted as HOLS, which they presented, provided better results in both cases of ho-

moscedastic and heteroscedastic data compared to the ordinary least squares (OLS), iterative weighted least square (IWLS), and weighted line of organic correlation (WLOC) approaches, as OLS largely overestimated measurement uncertainties (MUs) while IWLS and WLOC strongly underestimated MUs. The HOLS simulations of the MU values of the DST outcomes, depending on the correlation coefficient values of the DST measurands, clearly showed that when these correlations were stated as zero, then the MUs were underestimated. Also, the simulations proved that the greatest MU values were obtained when the DST measurands were totally negatively correlated. Therefore, the authors stated that further research was needed for accurate estimation of the correlation coefficient values.

Concerning the use of scanning electron microscopy (SEM) in an analysis of specimens after shearing, Cai et al. [23], on the basis of the micrographs of the shear plane of a polypropylene fibre–lime specimen, stated that it was clearly seen that, after shearing, some fibres were left in the soil with part of the length exposed to the air and, on the other hand, some threadlike grooves appeared in the shear plane. This was likely due to the strong resistance of the fibres against tension. Part of the fibre was pulled out from the soil when shearing occurred and the fibre itself was not sheared off. From the abrasion trace in the fibre surface, it was indicated that the fibres strengthened the soil due to friction between the fibres and soil particles.

To evaluate the factors affecting the interfacial strength properties of polypropylene fibre-reinforced soil, Tang et al. [24] carried out a single fibre pull-out test using a modified special apparatus. The SEM image taken from a single fibre-reinforced specimen after the pull-out test showed a number of visible scratches along the fibre's longitudinal direction on the surface. The authors stated that this may have resulted from the plowing of angular hard particles into the fibre body during the shear process. It confirmed that an interlock forc developed between the soil particles and the fibre surface.

Rivera-Gómez et al. [25] introduced an analysis of the influence of the fibre type on the polymer matrix/fibre bond using a natural organic polymer stabiliser. The study compared the effect of polypropylene and wool fibres on the mechanical properties of natural polymer-based stabilised soils. The authors stated that SEM proved to be a useful tool for the direct study of polymer–soil matrix interfaces. According to the authors, the main factors that affected the adhesion between the fibres and the soil were: (a) the cohesive properties of the polymer–soil matrix; (b) the compression friction forces appearing on the surface of the reinforcing fibre due to the shrinkage of the soil; and (c) the shear resistance of the polymer–soil matrix due to the surface form and roughness of the fibre. The authors also came to the conclusion that the loss of strength observed was not only caused by the variation in the fibre type but was more importantly the result of the effect of the differing properties of different soil types.

Liu et al. [26] applied X-ray diffraction and SEM analyses to reveal the micromechanics of the deformation and strength of grout. In the paper cited, the SEM results of concrete grout in sand for 28 days under 0 kPa, 100 kPa, and 200 kPa are presented. In the case of a pressure of 0 kPa, one can see that there was a large amount of pores and many pores were connected. In the case of a pressure of 100 kPa, there were fewer pores that were less connected. The maximal pore size was about 25 μm. The SEM images of the grout under a pressure of 200 kPa showed many fewer pores that had smaller pore sizes (about 7–15 μm). The authors stated that when the pressure was increased, the grout material particles became denser and the amount of hydration products rose, resulting in an increase in the consolidation deformation and UCS of the grout.

Another significant study showing the importance of the roughness of the fibre surface for improving the properties of the soil–cement–fibre composite is presented in [27]. To investigate the influence of the roughness of the fibre surface on improvement, cylindrical specimens of stabilised sandy soil, unreinforced and reinforced with polypropylene and sisal fibres, were tested. The fibres had the same length (12 mm), but the sisal fibres had a larger diameter (140 μm in comparison with 32 μm of the polypropylene fibre), larger tension strength (558 MPa in comparison with 250 MPa of the polypropylene fibre), and

higher surface texture roughness in comparison with the polypropylene fibres. The results of the unconfined compression strength tests carried out with and without the application of cyclic loading showed that the inclusion of fibres induced a decrease in the accumulated permanent axial strain, and this reduction was more significant for the use of sisal fibres due to the greater roughness and higher mechanical properties of this type of fibre. Analysing the obtained values of axial strain and unconfined compressive strength, it could be stated that, independent of the application of cyclic loading, reinforcement with sisal fibres was more effective than the use of polypropylene fibres. The greater roughness and better mechanical properties of sisal fibres promoted more effective anchorage and mobilisation of a higher tensile strength. Furthermore, the larger diameter of the sisal fibres provided a larger contact area between the fibres and surrounding material for the same strain level in comparison with the polypropylene fibres, so the anchorage was more effective and higher tensile strength was mobilised.

From the above-mentioned literature review, it can be stated that there are many studies dealing with soil improvement using DST, but most of them applied only three specimens and the test result uncertainty was not provided, so improvement could not be confirmed. The application of the fibres TEXZEM PES 200 improves the soil shear strength parameters considerably. The surface condition of the fibres significantly affects the characteristics of the reinforced soil and it is useful to deal with this issue.

In this study, DST has been carried out for three different soils improved by the mentioned fibres and four specimens have been tested in DST, applying four different normal stresses. The shear strength parameters were determined for all four specimens and various combinations of three specimens so that the influence of specimen number on test results could be analysed. The uncertainty of shear strength parameters was determined, also considering covariance between correlated input quantities (normal stresses and shear stresses) and a worst-case strategy. The obtained values of uncertainty enabled us to confirm the improvement rate and deepen the understanding of DST uncertainty. The applied SEM uncovered the possible reason for the significant improvement.

2. Materials and Methods

Soil from a cut slide and excavated soil at the highway construction site near Žilina, Slovakia, and soil from a cut slide in Przybędza, Poland, were used, see Figure 1.

(**a**) (**b**) (**c**)

Figure 1. Highways under construction near Žilina, Slovakia and in Przybędza, Poland. (**a**) Location No. 1: cut slide (soil CI), near Žilina, Slovakia; (**b**) Location No. 2: excavated soil, about 360 m from location No. 1 (soil CS1); (**c**) Location No. 3: cut slide (soil CS2), Przybędza, Poland [28].

BS 1377: 1990. Part 2 [29] was applied to obtain soil particle size distribution, water content (w), liquid limit (w_L), and plastic limit (w_P), and British Standard BS 5930:2015 [30] was applied to classify the soils. The grain size distribution of the soils is presented in Figure 2 and the soil properties can be seen in Table 1.

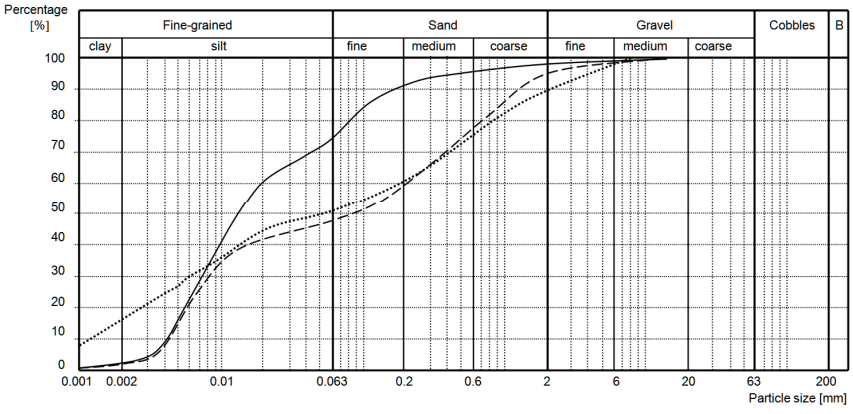

Figure 2. Grain size distribution diagram of soils: Full line is applied for CI; long dash line is applied for CS1; dotted line is applied for CS2.

Table 1. Soil properties.

Soil Parameters	CI	CS1	CS2
Water content (%)	18.1	21.6	10.2
Plastic limit (%)	20.6	27.8	19.7
Liquid limit (%)	44.2	54.7	40.2
Plasticity index (%)	23.6	26.9	20.5
Optimum water content (%)	18.6	21.0	13.7
Maximum dry density (kg·m^{-3})	1717	1630	1925

Polyester fibres TEXZEM PES 200 were used and the fibre properties are presented in Table 2. A picture of the fibres is presented in Figure 3a.

Table 2. Properties of polyester fibre [20].

Polyester Fibre Parameters	TEXZEM PES 200
Length (mm)	70
Colour	White
Density (g·cm^{-3})	1.38
Mass density (dtex)	2200
Tensile strength (cN/dtex)	7.77
Elongation at break (%)	10.6

Slovak technical standard STN 72 1030: 1988 on DST [17] was applied to determine the shear strength parameters of the soil and soil mixed with fibres. DST was carried out using a fully automatic large shear box apparatus, SHEARMATIC 300 (Wykeham Farrance, CONTROLS Group, Milan, Italy), presented in Figure 3b. The fibres were mixed with soils of optimum water content and maximum dry density in amounts of 0.5%, 1.0% and 1.5% (ratio of fibres to dry soil) and compacted in a box of size 0.3 m × 0.3 m × 0.08 m. The consolidation time was 5 h, and the shear speed was 0.05 mm/min. Normal stresses of 50 kPa, 100 kPa, 200 kPa, and 300 kPa were applied and tests were terminated at a horizontal displacement 35 mm (11.6% of the width of the specimen). A picture of a specimen of soil and fibres in the amount of 0.5% after testing under a normal stress of 50 kPa can be seen in Figure 3c.

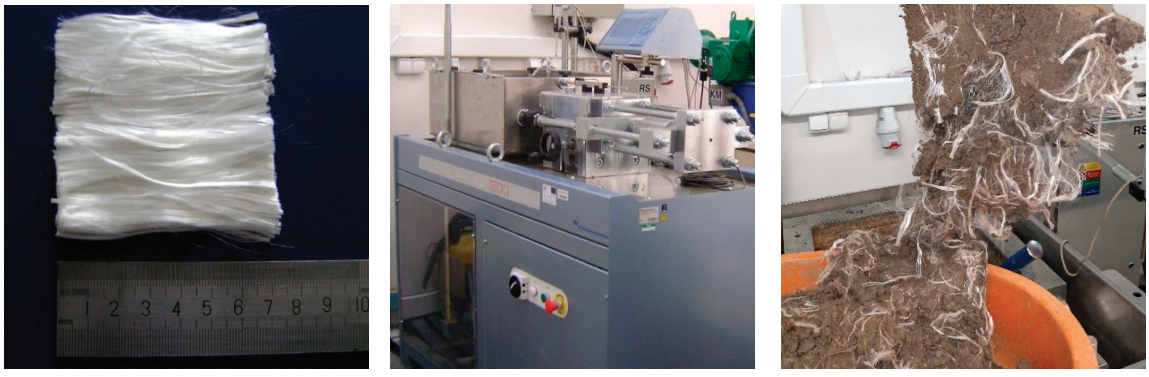

(**a**) (**b**) (**c**)

Figure 3. Test device and tested fibres: (**a**) Polyester fibres TEXZEM PES 200 before testing; (**b**) Automatic large shear box apparatus SHEARMATIC 300; (**c**) Specimen of soil and fibre after testing (0.5% fibre, normal stress 50 kPa).

The shear strength parameters were calculated using formulae:

$$\tan\phi = \frac{n\sum \tau\sigma_{ef} - \sum \tau \sum \sigma_{ef}}{n\sum {\sigma_{ef}}^2 - \left(\sum \sigma_{ef}\right)^2} \quad (1)$$

$$c = \frac{\sum \tau \sum {\sigma_{ef}}^2 - \sum \sigma_{ef} \sum \tau\sigma_{ef}}{n\sum {\sigma_{ef}}^2 - \left(\sum \sigma_{ef}\right)^2} \quad (2)$$

where τ and σ_{ef} (kPa) are the pair of stresses obtained from each specimen and n is the number of specimens.

STN 72 1030: 1988 requires the test to be carried out with at least four specimens for the test of peak strength and requires the value of the correlation coefficient r calculated using Formula (3) to be larger than 0.9500:

$$r = \frac{n\sum \left(\tau\sigma_{ef}\right) - \sum \tau \sum \sigma_{ef}}{\sqrt{\left[n\sum {\sigma_{ef}}^2 - \left(\sum \sigma_{ef}\right)^2\right].\left[n\sum \tau^2 - (\sum \tau)^2\right]}} \quad (3)$$

Determination of uncertainty was carried out in accordance with EUROLAB Technical Report 1/2006 [31]. Here, only the most important issues are presented. So, e.g., a procedure to determine the uncertainties of normal stress $u(\sigma)$ and shear stress $u(\tau)$ is introduced. Determination of the uncertainties of the angle of internal friction and cohesion could be performed applying the same principle.

Based on our experience, the standard uncertainty of the shear box was proposed to be u_a = 0.2% and u_b = 0.2% (for dimensions a and b of the shear box). Based on calibration protocols and the magnitude of force measured, the standard uncertainties u_N = 0.141% of normal force and u_T= 0.158% of shear force were applied.

The normal stress is a function of normal force N and box size parameters a and b. The parameters N, a, and b are not dependent on one another (not correlated); the standard uncertainty of the normal stress σ in kPa was obtained using the formula:

$$u(\sigma) = \sqrt{[c_N.u(N)]^2 + [c_a.u(a)]^2 + [c_b.u(b)]^2} \quad (4)$$

where c_N, c_a, and c_b are the sensitivity coefficients relating to the particular parameters N, a, and b, respectively, and will be obtained by the partial derivative of the model function f, step by step, of N, a, and b. So, e.g., the sensitivity coefficient for N was determined as follows:

$$c_N = \frac{\partial f}{\partial N} = \frac{\partial\left(\frac{N}{a.b}\right)}{\partial N} = \frac{1}{a.b}\Bigg|_{a=0.30, b=0.30} \tag{5}$$

In the same way, c_a and c_b were determined.

The absolute value of the standard uncertainty of the particular parameter, e.g., of the normal force $u(N)$, was calculated by multiplying its estimated value by the standard uncertainty of the force transducer:

$$u(N) = N.u_N \tag{6}$$

In the same way, $u(a)$ and $u(b)$ and then $u(\sigma)$ were determined based on Formula (4).

Regarding the uncertainty of the shear stress $u_c(\tau)$, inconformity of the specimen can give different shear stresses at the same normal stress even if the same test procedure is applied. Therefore, in this case, it was proposed that the standard uncertainty of the type A $u_A(\tau)$ of shear stress existed but did not exceed 0.5%. The value $u_A(\tau)$ was used to calculate the combined standard uncertainty of the shear stress, applying the following formula:

$$u_c(\tau) = \sqrt{u_A(\tau)^2 + u_B(\tau)^2}, \tag{7}$$

where $u_B(\tau)$ is determined in the same way as in the case of $u(\sigma)$.

In order to determine the uncertainty as precisely as possible, a further source of uncertainty was considered, namely, the covariances between correlated input quantities (normal stresses and shear stresses). In the case of DST, covariances between stresses exist since they are calculated using a common specimen area A. So, e.g., covariance $u(\sigma_i, \tau_j)$ could be obtained using the formula:

$$u(\sigma_i, \tau_j) = \left(\frac{\partial \sigma_i}{\partial A}\right).\left(\frac{\partial \tau_j}{\partial A}\right).u(A)^2 \tag{8}$$

Then, the correlation coefficient $r(\sigma_i, \tau_j)$ could be obtained using the formula:

$$r(\sigma_i, \tau_j) = \frac{u(\sigma_i, \tau_j)}{u(\sigma_i).u(\tau_j)} \tag{9}$$

Applying a similar procedure, the correlation coefficients $r(\sigma_i, \sigma_j)$ and $r(\tau_i, \tau_j)$ could be calculated.

A standard uncertainty $u(tan\varphi)$ caused by parameters σ_i and τ_i and also their correlation was determined similarly as in the case of $u(\sigma)$, applying Equation (1), considering $tan\varphi$ as a function of eight parameters (four normal stresses and four shear stresses). A formula in [22] was used, as follows:

$$\begin{aligned} u(\tan\phi)^2 = u(\beta) = &\sum_{i=1}^{n} (c(\sigma_i)u(\sigma_i))^2 + \sum_{i=1}^{n} (c(\tau_i)u(\tau_i))^2 + \\ &+2.\sum_{i=1}^{n-1}\sum_{j=i+1}^{n} c(\sigma_i)c(\sigma_j)r(\sigma_i, \sigma_j)u(\sigma_i)u(\sigma_j) + \\ &+2.\sum_{i=1}^{n-1}\sum_{j=i+1}^{n} c(\tau_i)c(\tau_j)r(\tau_i, \tau_j)u(\tau_i)u(\tau_j) + \\ &+2.\sum_{i=1}^{n-1}\sum_{j=i+1}^{n} c(\sigma_i)c(\tau_j)r(\sigma_i, \tau_j)u(\sigma_i)u(\tau_j) \end{aligned} \tag{10}$$

The uncertainty range of the angle of friction φ is asymmetric [22] since uncertainty is defined for $tan\varphi$ (not for φ). According to [22], if one notes $\beta_0 = tan(\varphi_0)$, then β (slope of strength line) belongs to the $[\beta_0 - u(\beta);\ \beta_0 + u(\beta)]$ interval. Consequently, φ varies in the $[atan(\beta_0 - u(\beta)); atan(\beta_0 + u(\beta))]$ range. Thus, two components of $u(\varphi)$ can be differentiated, i.e.,

$$u_-(\phi) = atan(\beta_0) - atan(\beta_0 - u(\beta)), \tag{11}$$

which is the left-hand side of $u(\varphi)$, and

$$u_+(\phi) = atan(\beta_0 + u(\beta)) - atan(\beta_0) \tag{12}$$

which is the right-hand side of $u(\varphi)$.

The expanded uncertainty (using a coverage factor k = 2) of φ should be split in the right-hand interval $U_{\varphi+;95\%} = 2{\cdot}[atan(\beta_0 + u(\beta)) - \varphi_0]$ and the left-hand interval $U_{\varphi-;95\%} = 2 \cdot [\varphi_0 - atan(\beta_0 - u(\beta))]$. The larger values from them will be introduced in the paper as U_φ.

The standard uncertainty of cohesion $u(c)$ was determined in the same way as in the case of $u(tan\varphi)$, applying Equation (2), and the expanded uncertainty U_c was determined by multiplying the standard uncertainty $u(c)$ by the coverage factor k = 2.

To examine the influence of covariance between correlated input quantities (normal stresses and shear stresses), U_φ and U_c were calculated without using correlation coefficients, marked as case A, and using correlation coefficients, marked as case B (see Formulae (9) and (10)).

To explore the magnitude of the uncertainty in the case of the worst-case estimation, marked as case C, the uncertainty was calculated by adding linearly the uncertainty contributions $c(\sigma_i).u(\sigma_i)$ and $c(\tau_i).u(\tau_i)$ and not considering the correlation coefficients.

The morphology of the fibres before and after shearing under various normal stresses was investigated by SEM. Fibres were taken from the shear surface of the center ninth of specimens of size 10 cm × 10 cm (shear box of size 30 cm × 30 cm) after shearing under normal stresses of 50 kPa and 300 kPa, and their morphologies were compared. A JEOL JSM 5500 LV microscope (JEOL Ltd., Tokyo, Japan) operating in backscattered electron mode was used. The observations were carried out for fibres sputtered with gold using the JEOL JFC 1200 ionic sputter coater.

3. Results

3.1. Improvement of Soil Shear Strength Parameters

Maximal values of shear stress for various amounts of fibres can be seen in Table 3. Dependence of shear stress on normal stress in soil CI, CS1, and CS2 is introduced in Figures 4–6.

Table 3. Maximal values of shear stress for various amounts of fibres.

Soil	Maximal Values of Shear Stress for Various Amounts of Fibres (kPa)							
	0%		0.5%		1.0%		1.5%	
	Normal Stress σ (kPa)	Shear Stress τ (kPa)	Normal Stress σ (kPa)	Shear Stress τ (kPa)	Normal Stress σ (kPa)	Shear Stress τ (kPa)	Normal Stress σ (kPa)	Shear Stress τ (kPa)
CI	50.1	85.667	50.1	94.667	50.1	91.111	50.3	110.333
	100.3	125.889	100.2	123.778	100.2	143.889	100.3	168.889
	200.3	177.444	200.1	183.778	200.1	218.111	200.3	215.778
	300.4	246.778	300.1	241.556	300.2	**274.222**	300.3	257.444
CS1	50.2	74.556	50.1	**137.556**	50.3	131.000	50.3	125.444
	100.2	143.889	100.2	**182.444**	100.2	173.667	100.0	146.444
	200.1	171.111	200.1	**248.111**	200.1	207.556	200.2	183.778
	300.2	249.889	300.4	**319.556**	300.3	261.778	300.2	192.000

Table 3. *Cont.*

Soil	Maximal Values of Shear Stress for Various Amounts of Fibres (kPa)							
	0%		0.5%		1.0%		1.5%	
	Normal Stress σ (kPa)	Shear Stress τ (kPa)	Normal Stress σ (kPa)	Shear Stress τ (kPa)	Normal Stress σ (kPa)	Shear Stress τ (kPa)	Normal Stress σ (kPa)	Shear Stress τ (kPa)
CS2	50.3	71.111	50.3	80.333	50.3	75.889	50.3	72.222
	100.1	107.000	100.2	122.222	100.2	109.778	100.2	114.444
	200.1	151.000	200.3	184.778	200.2	196.667	200.2	189.444
	300.1	167.222	300.2	228.889	300.2	259.889	300.3	263.444

Note: Since there are many numbers in tables, bold and colour are applied to differ them. Generally, blue numbers indicate favourable values. Red numbers indicate unfavorable values. This rule is applied in further tables. More information is introduced and commented in the paper.

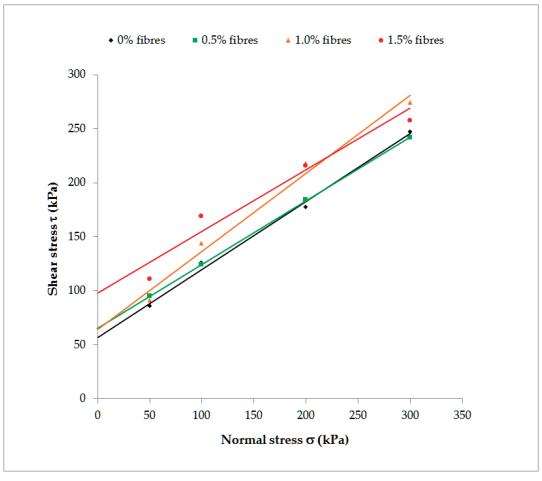

Figure 4. Shear stress versus normal stress in soil CI.

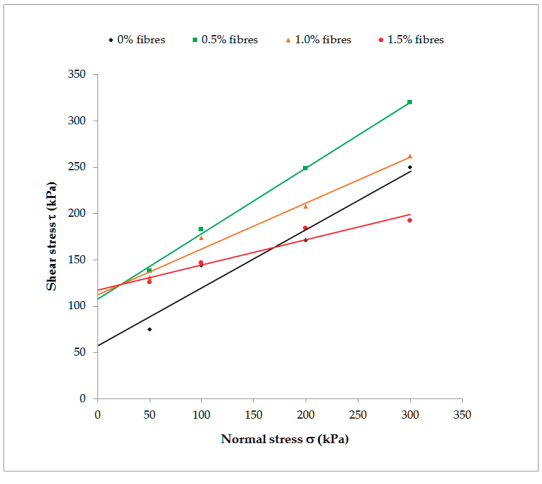

Figure 5. Shear stress versus normal stress in soil CS1.

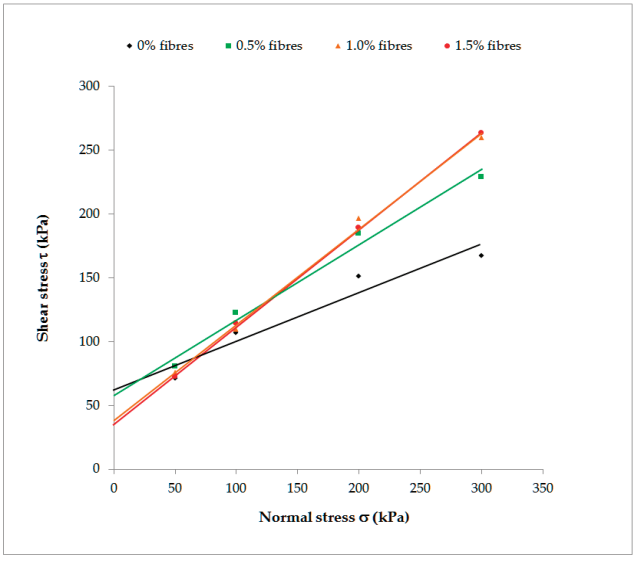

Figure 6. Shear stress versus normal stress in soil CS2.

Values of the shear strength parameters of soils and soils reinforced by fibres as well as their expanded uncertainty are introduced in Table 4 (soil CI), Table 5 (soil CS1), and Table 6 (soil CS2).

Table 4. Shear strength parameters of soils and soils reinforced by fibres and their expanded uncertainty (soil CI).

Soil	Case No.	Fibre Amount	Strength Parameters		R-Value	Expanded Uncertainty											
						Without Covariance (A)				With Covariance (B)				Worst-Case (C)			
			φ	c		U(φ)		U(c)		U(φ)		U(c)		U(φ)		U(c)	
		(%)	(°)	(kPa)		(°)	(%)	(kPa)	(%)	(°)	(%)	(kPa)	(%)	(°)	(%)	(kPa)	(%)
CI (4 specimens; No. 1, 2, 3, and 4)	1	0.0	32.019	57.158	0.99752	0.524	1.64	1.603	2.81	0.520	1.62	1.604	2.81	1.052	3.29	3.593	6.29
		0.5	30.502	65.141	0.99996	0.534	1.75	1.619	2.48	0.528	1.73	1.620	2.49	1.070	3.51	3.631	5.57
		1.0	35.842	64.344	0.99296	0.542	*1.51*	1.811	2.82	0.540	*1.51*	1.820	2.83	1.086	*3.03*	4.190	6.51
		1.5	29.097	97.507	0.97594	0.596	2.05	1.896	*1.94*	0.586	2.01	1.914	*1.96*	1.212	4.17	4.227	*4.34*
CI (3 specimens; No. 1, 2, and 3)	2	0.0	30.858	59.821	0.99305	0.734	2.38	1.741	2.91	0.722	2.34	1.720	2.88	1.296	4.20	3.745	6.26
		0.5	30.753	64.578	0.99997	0.760	2.47	1.814	2.81	0.746	2.43	1.784	2.76	1.328	4.32	3.829	5.93
		1.0	39.758	53.869	0.99575	0.724	1.82	2.035	3.78	0.718	1.81	2.022	3.75	1.280	3.22	4.451	8.26
		1.5	33.803	86.688	0.96794	0.842	2.49	2.214	2.55	0.828	2.45	2.186	2.52	1.506	4.46	4.750	5.48
CI (3 specimens; No. 2, 3, and 4)	3	0.0	31.139	62.338	0.99644	0.738	2.37	3.030	*4.86*	0.728	2.34	2.994	*4.80*	1.268	4.07	6.092	*9.77*
		0.5	30.506	65.122	0.99994	0.736	2.41	2.997	4.60	0.728	2.39	2.968	4.56	1.254	4.11	6.129	9.41
		1.0	33.090	81.638	0.99675	0.794	2.40	3.454	4.23	0.784	2.37	3.422	4.19	1.368	4.13	7.105	8.70
		1.5	23.883	125.349	0.99942	0.908	*3.80*	3.559	2.84	0.876	*3.67*	3.466	2.77	1.502	*6.29*	6.749	5.38

Note: The authors are aware of the unsuitable introduction of values of shear strength parameters with 3 digits after the decimal in this and further tables. The underlying reason is the necessity of comparison since, in some cases, there will be no difference if 1 or 2 digits after the decimal is (are) applied, leading to misunderstandings. Specimen No. 1 was loaded by normal stress of about 50 kPa; specimen No. 2 was loaded by normal stress of about 100 kPa; specimen No. 3 was loaded by normal stress of about 200 kPa; and specimen No. 4 was loaded by normal stress about of 300 kPa. The same is applied in further tables. In Tables 4–6, for every column, maximal absolute values are marked as red underlined numbers, maximal relative values are marked as italic red underlined numbers, minimal absolute values are marked as blue underlined numbers, and minimal relative values are marked as italic blue underlined numbers. More information is introduced and commented in the paper.

Table 5. Shear strength parameters of soils and soils reinforced by fibres and their expanded uncertainty (soil CS1).

Soil	Case No.	Fibre Amount	Strength Parameters		R-Value	Expanded Uncertainty											
						Without Covariance (A)				With Covariance (B)				Worst-Case (C)			
			φ	c		U(φ)		U(c)		U(φ)		U(c)		U(φ)		U(c)	
		(%)	(°)	(kPa)		(°)	(%)	(kPa)	(%)	(°)	(%)	(kPa)	(%)	(°)	(%)	(kPa)	(%)
CS1 (4 specimens; No. 1, 2, 3, and 4)	1	0.0	32.398	56.633	0.97043	0.526	*1.62*	1.634	2.89	0.522	*1.61*	1.636	2.89	1.066	*3.29*	3.616	6.39
		0.5	35.539	105.696	0.99886	0.634	1.78	2.245	2.12	0.622	1.75	2.250	2.13	1.276	3.59	4.953	4.69
		1.0	26.252	113.245	0.98957	0.638	2.43	1.997	1.76	0.618	2.35	2.002	1.77	1.288	4.91	4.239	3.74
		1.5	15.209	117.690	0.96082	0.568	3.73	1.693	*1.44*	0.540	3.55	1.712	*1.45*	*1.132*	7.44	3.525	*2.99*
CS1 (3 specimens; No. 1, 2, and 3)	2	0.0	30.589	60.788	0.90622	0.722	2.36	1.738	2.86	0.714	2.33	1.728	2.84	1.316	4.30	3.831	6.30
		0.5	35.968	104.608	0.99670	0.918	2.55	2.559	2.45	0.896	2.49	2.510	2.40	1.610	4.48	5.358	5.12
		1.0	25.942	113.888	0.96729	*0.960*	3.70	2.322	2.04	*0.926*	3.57	2.264	1.99	*1.684*	6.49	4.761	4.18
		1.5	21.144	106.703	0.99949	0.918	4.34	2.096	1.96	0.876	4.14	2.028	1.90	1.570	7.43	4.164	3.90
CS1 (3 specimens; No. 2, 3, and 4)	3	0.0	27.928	82.190	0.96292	0.800	2.86	3.187	*3.88*	0.778	2.79	3.104	*3.78*	1.382	4.95	5.975	*7.27*
		0.5	34.407	112.899	0.99973	0.900	2.62	4.120	3.65	0.880	2.56	4.050	3.59	1.520	4.42	*8.132*	7.20
		1.0	23.768	126.168	0.99135	0.924	3.89	3.612	2.86	0.886	3.73	3.500	2.77	1.532	6.45	6.659	5.28
		1.5	12.822	128.524	0.93839	0.798	*6.22*	2.913	2.27	0.754	*5.88*	2.814	2.19	1.308	*10.20*	5.337	4.15

Table 6. Shear strength parameters of soils and soils reinforced by fibres and their expanded uncertainty (soil CS2).

Soil	Case No.	Fibre Amount	Strength Parameters		R-Value	Expanded Uncertainty											
						Without Covariance (A)				With Covariance (B)				Worst-Case (C)			
			φ	c		U(φ)		U(c)		U(φ)		U(c)		U(φ)		U(c)	
		(%)	(°)	(kPa)		(°)	(%)	(kPa)	(%)	(°)	(%)	(kPa)	(%)	(°)	(%)	(kPa)	(%)
CS2 (4 specimens; No. 1, 2, 3, and 4)	1	0.0	20.755	62.443	0.96472	0.450	2.17	1.236	*1.98*	0.442	2.13	1.250	*2.00*	0.904	4.36	2.830	*4.53*
		0.5	30.510	58.150	0.99256	0.512	1.68	1.535	2.64	0.508	1.67	1.542	2.65	1.026	3.36	3.541	6.09
		1.0	36.933	38.232	0.99776	0.498	1.35	1.609	4.21	0.496	1.34	1.612	4.22	0.980	2.65	3.753	9.82
		1.5	37.257	36.098	0.99973	0.498	*1.34*	1.613	4.47	0.496	*1.33*	1.614	4.47	0.982	*2.64*	3.720	10.31
CS2 (3 specimens; No. 1, 2, and 3)	2	0.0	27.469	48.963	0.99123	0.668	2.43	1.476	3.02	0.660	2.40	1.460	2.98	1.184	4.31	3.191	6.52
		0.5	34.452	48.888	0.99703	0.704	2.04	1.742	3.56	0.698	2.03	1.728	3.53	1.244	3.61	3.791	7.76
		1.0	39.172	32.197	0.99835	0.622	1.69	1.744	5.42	0.658	1.68	1.734	5.39	1.148	2.93	3.796	11.79
		1.5	37.862	34.490	0.99953	0.662	1.75	1.706	4.95	0.660	1.74	1.698	4.92	1.162	3.07	3.746	10.86
CS2 (3 specimens; No. 2, 3, and 4)	3	0.0	16.758	81.488	0.96632	0.648	*3.87*	2.313	2.84	0.630	*3.76*	2.268	2.78	1.108	*6.61*	4.568	5.61
		0.5	28.074	71.832	0.99511	*0.736*	2.62	2.906	4.05	*0.726*	2.59	2.876	4.00	*1.268*	4.52	5.964	8.30
		1.0	36.890	38.516	0.99588	0.683	1.85	3.087	*8.01*	0.681	1.85	3.080	*8.00*	1.192	3.23	*6.646*	*17.25*
		1.5	36.672	40.012	0.99999	0.690	1.88	*3.108*	7.77	0.688	1.88	*3.098*	7.74	1.188	3.24	6.561	16.40

Differences in shear strength parameters for various amounts of fibres (i.e., improvement), considering all four specimens (case No. 1), are introduced in Table 7.

Table 7. Differences (improvement) in shear strength parameters for various amounts of fibres.

Soils	Improvement of Shear Strength Parameters by Various Amounts of Fibres	Differences in Strength Parameters			
		φ		c	
		(°)	(%)	(kPa)	(%)
CI	Differences between 0.5% and 0.0%	−1.517	−4.74	7.983	13.97
	Differences between 1.0% and 0.0%	**3.823**	**11.94**	**7.186**	**12.57**
	Differences between 1.5% and 0.0%	−2.922	−9.13	40.349	70.59
CS1	Differences between 0.5% and 0.0%	**3.141**	**9.70**	**49.063**	**86.63**
	Differences between 1.0% and 0.0%	−6.146	−18.97	56.612	99.96
	Differences between 1.5% and 0.0%	−17.189	−53.06	61.057	107.81
CS2	Differences between 0.5% and 0.0%	9.755	47.00	−4.293	−6.88
	Differences between 1.0% and 0.0%	**16.178**	77.95	**−24.211**	−38.77
	Differences between 1.5% and 0.0%	**16.502**	79.51	**−26.345**	−42.19

The SEM images of fibres before testing can be seen in Figure 7a (50× magnification) and Figure 7b (2000× magnification). The SEM images of fibres mixed with soil CI in

various amounts after shearing under normal stresses of 50 kPa and 300 kPa are posted in Figure 8. The SEM images of fibres mixed with soil CS1 in various amounts after shearing under normal stresses of 50 kPa and 300 kPa are posted in Figure 9. The SEM images of fibres mixed with soil CS2 in various amounts after shearing under normal stresses of 50 kPa and 300 kPa are posted in Figure 10.

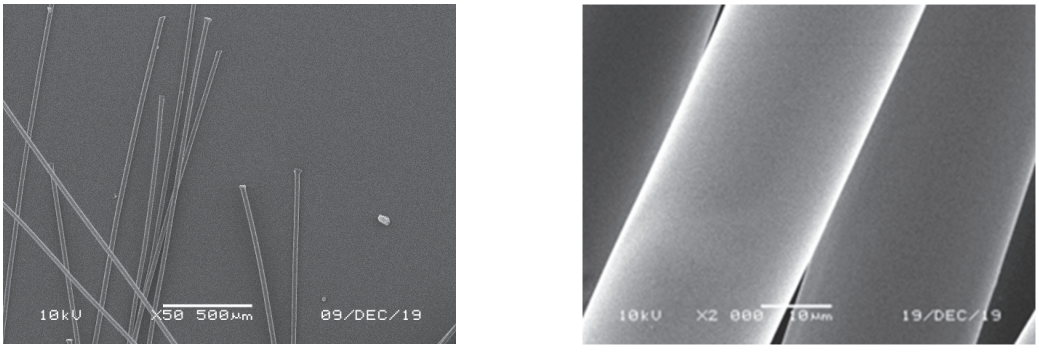

(**a**) (**b**)

Figure 7. The SEM images of fibres before testing: (**a**) 50× magnification; (**b**) 2000× magnification.

As can be seen in Table 7 (blue coloured numbers), fibres in the amount of 1.0% increased the angle of internal friction of soil CI by 3.823° (11.94%) and also increased cohesion by 7.186 kPa (12.57%). The increase in the angle of internal friction could be confirmed since 3.81° was larger than the uncertainty of 0.520° + 0.540° = 1.060° (see expanded uncertainty with covariance in Table 4 for 0% and 1% fibres; four specimens). The increase in cohesion could be also confirmed since 7.186 kPa was larger than the uncertainty of 1.604 kPa + 1.820 kPa = 3.424 kPa (see expanded uncertainty with covariance in Table 4 for 0% and 1% fibres; four specimens). The increases in both the angle of internal friction and cohesion in the case of fibres in the amount of 1.0% was caused by the fact that all shear stresses were higher in comparison with the case of 0% fibres (compare blue numbers with red numbers in Table 3 and see a yellow line in Figure 4) and there was the highest shear stress from all shear stress values (274.2 kPa, corresponding to a normal stress of 300 kPa). It is possible that such a high value of shear stress was reached due to friction between the soil particles and fibres (see a great number of depth scratches on the fibre surface in Figure 8d).

Regarding soil CS1 (see blue coloured numbers in Tables 3 and 7 and a green line in Figure 5), fibres in the amount of 0.5% increased the angle of internal friction of soil CS1 by 3.141° (9.70%) and also increased cohesion by 49.063 kPa (86.63%). The increase in the angle of internal friction could be confirmed since 3.141° was larger than the uncertainty of 0.522° + 0.622° = 1.144° (see expanded uncertainty with covariance in Table 5 for 0% and 0.5% fibres; four specimens). The increase in cohesion could be also confirmed since 49.063 kPa was much larger than the uncertainty of 1.636 kPa + 2.250 kPa = 3.886 kPa (see expanded uncertainty with covariance in Table 5 for 0% and 0.5% fibres; four specimens). These increases were caused by high values of all maximal shear stresses corresponding to all normal stresses. It should be noted that the mentioned maximal shear stresses were the highest in comparison with the maximal shear stresses obtained from other amounts of fibres (1.0% and 1.5%). It is possible that such high values of shear stresses were reached due to friction between the soil particles and fibres (see scratches on the fibre surface in Figure 9a,b). It is worth noting that the maximal shear stresses in the case of fibres in the amount of 1.5% were very low in comparison with the other amounts of fibres (see a red line in Figure 5). This could be caused by a specific behaviour of this soil CS1, which had a higher liquid limit, plastic limit, and optimal water content, but a lower maximum dry

density than soil CI (see Table 1). It can be proposed that the specific behaviour of this soil CS1 also caused more soil particles to attach to the fibre surface and less scratches on the fibre surface, as shown in Figure 9c–f.

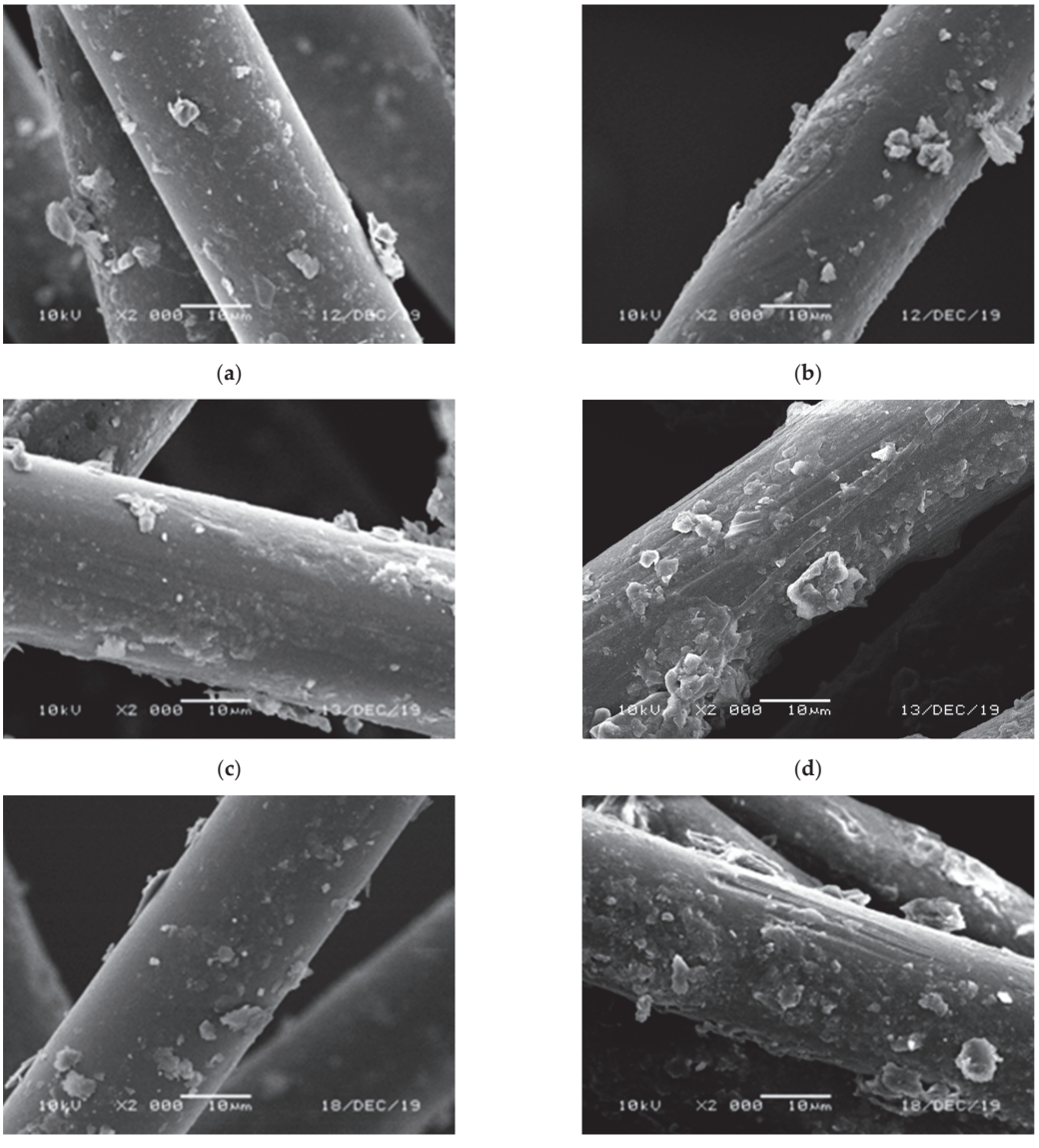

Figure 8. The SEM images of fibres applied in soil CI after shearing: (**a**) 0.5% fibres, normal stress of 50 kPa; (**b**) 0.5% fibres, normal stress of 300 kPa; (**c**) 1.0% fibres, normal stress of 50 kPa; (**d**) 1.0% fibres, normal stress of 300 kPa; (**e**) 1.5% fibres, normal stress of 50 kPa; (**f**) 1.5% fibres, normal stress of 300 kPa.

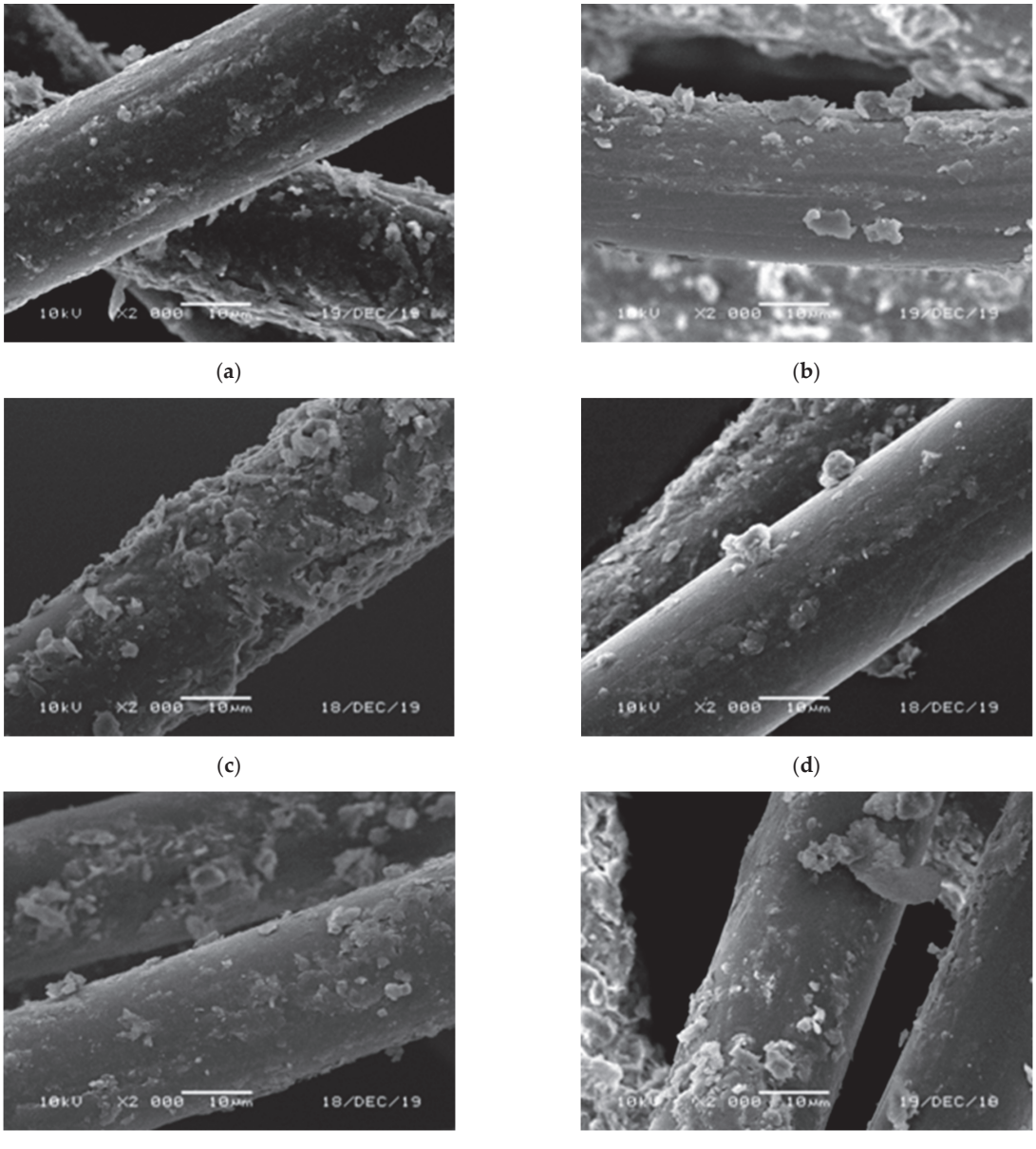

(**a**) (**b**)

(**c**) (**d**)

(**e**) (**f**)

Figure 9. The SEM images of fibres applied in soil CS1 after shearing: (**a**) 0.5% fibres, normal stress of 50 kPa; (**b**) 0.5% fibres, normal stress of 300 kPa; (**c**) 1.0% fibres, normal stress of 50 kPa; (**d**) 1.0% fibres, normal stress of 300 kPa; (**e**) 1.5% fibres, normal stress of 50 kPa; (**f**) 1.5% fibres, normal stress of 300 kPa.

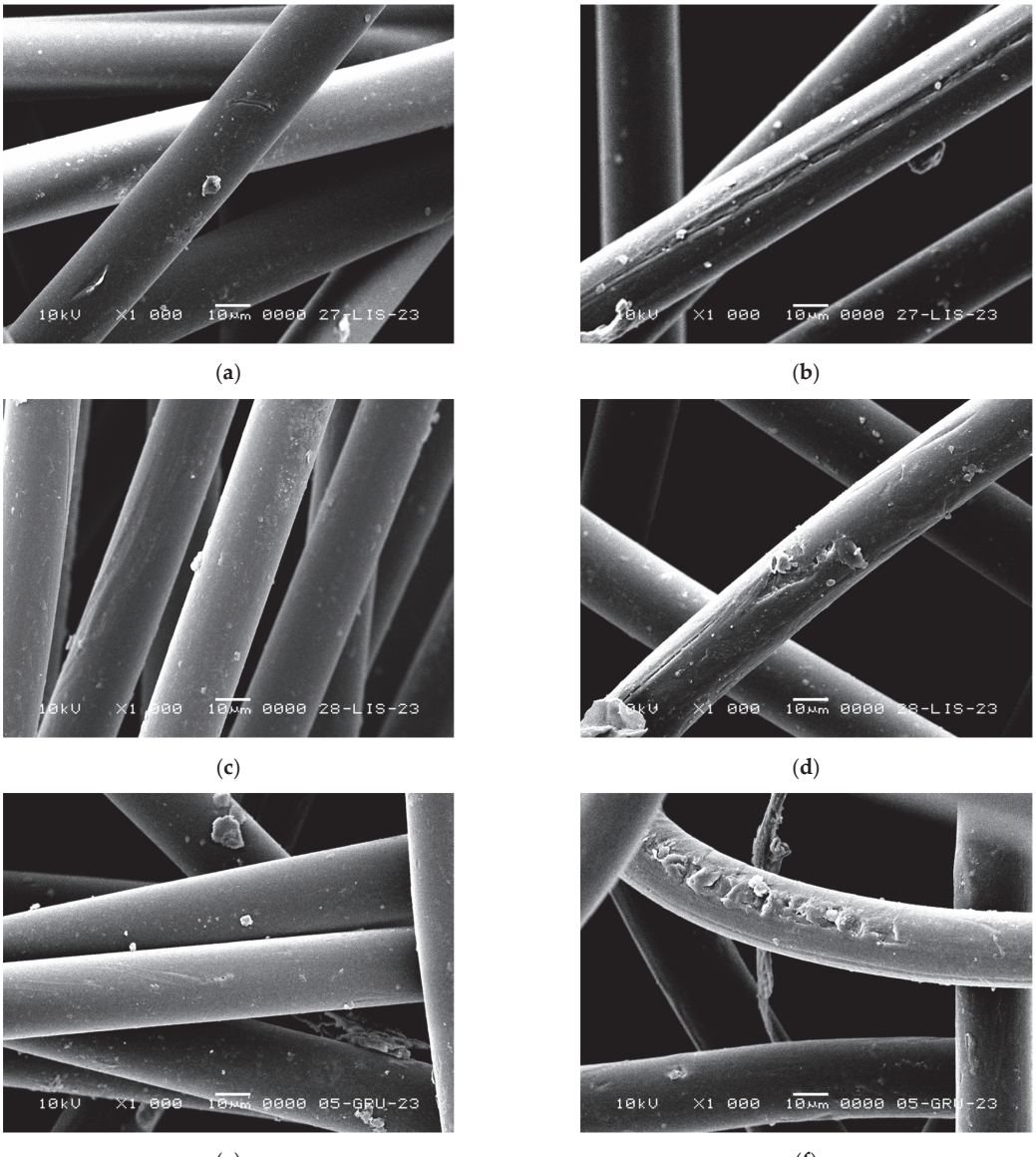

(**a**) (**b**)

(**c**) (**d**)

(**e**) (**f**)

Figure 10. The SEM images of fibres applied in soil CS2 after shearing: (**a**) 0.5% fibres, normal stress of 50 kPa; (**b**) 0.5% fibres, normal stress of 300 kPa; (**c**) 1.0% fibres, normal stress of 50 kPa; (**d**) 1.0% fibres, normal stress of 300 kPa; (**e**) 1.5% fibres, normal stress of 50 kPa; (**f**) 1.5% fibres, normal stress of 300 kPa.

The behaviour of soil CS2 was different in comparison with the aforementioned soils (see Tables 3, 6 and 7 and Figure 6). Fibres in the amount of 0.5% increased the angle of internal friction of soil CS2 by 9.755° (47.00%) but decreased cohesion by 4.293 kPa (6.88%). The increase in the angle of internal friction could be confirmed since 9.755° was larger than the uncertainty of 0.442° + 0.508° = 0.950° (see expanded uncertainty with covariance in Table 6 for 0% and 0.5% fibres; four specimens). The decrease in cohesion could be confirmed

since 4.923 kPa was larger than the uncertainty of 1.250 kPa + 1.542 kPa = 2.792 kPa (see expanded uncertainty with covariance in Table 6 for 0% and 0.5% fibres; four specimens). There were large increases in the angle of internal friction and large decreases in cohesion in the case of soil mixed with 1% and 1.5% fibres (see bold blue and red coloured numbers in Table 7 and a yellow and red line in Figure 6). This fact was caused by the high values of shear stress at a normal stress of 300 kPa but low values of shear stress at a normal stress 50 kPa, see blue and red numbers in Table 3. Soil CS2 without fibres had the lowest shear stress at a normal stress of 300 kPa in comparison with the above soils (only 167.222 kPa, see red coloured number in Table 3). It is proposed that high values of shear stress of soil mixed with fibres were reached due to the suitable composition of soil particle and fibre scratch resistance (see Figure 10b,d,f).

3.2. Influence of the Specimen Number on Test Results

An analysis of the influence of specimen number on the test results was also carried out. Values of the shear strength parameters of the soils and those reinforced by fibres evaluated from various combinations of specimens (all four tested specimens and chosen combinations of only three specimens) are introduced in Table 4 (for soil CI), Table 5 (for soil CS1), and Table 6 (for soil CS2). Values of the shear strength parameters were evaluated based on normal stresses and shear stresses, posted in Table 3, where specimen No. 1 was loaded by a normal stress of about 50 kPa, specimen No. 2—by a normal stress of about 100 kPa, specimen No. 3—by a normal stress of about 200 kPa, and specimen No. 4—by a normal stress of about 300 kPa. The reason for introducing these combinations of specimens No. 1, 2, and 3 and No. 2, 3, and 4 was that these two combinations had a common interval of normal stress from 100 kPa to 200 kPa; therefore the shear strength parameters obtained from them would be valid for the mentioned interval of normal stress (but they were very different), as can be seen later. Differences in shear strength parameters, obtained by various combinations, are introduced in Table 8 (for soil CI), Table 9 (for soil CS1), and Table 10 (for soil CS2).

Table 8. Differences in shear strength parameters between various specimen combinations (soil CI).

	Fibre Amount	**Differences in Strength Parameters**			
		φ		**c**	
	(%)	**(°)**	**(%)**	**(kPa)**	**(%)**
Case No. 1 (4 specimens: No. 1, 2, 3, and 4)—Case No. 2 (3 specimens: No. 1, 2, and 3) (° or kPa, %)	0.0	1.161	3.76	−2.663	−4.45
	0.5	−0.251	−0.82	0.563	0.87
	1.0	**−3.916**	**−9.85**	**10.475**	**19.45**
	1.5	**−4.706**	**−13.92**	**10.819**	**12.48**
Case No. 1 (4 specimens: No. 1, 2, 3, and 4)—Case No. 3 (3 specimens: No. 2, 4, and 4) (° or kPa, %)	0.0	0.88	2.83	−5.18	−8.31
	0.5	−0.004	−0.01	0.019	0.03
	1.0	**2.752**	**8.32**	**−17.294**	**−21.18**
	1.5	**5.214**	**21.83**	**−27.842**	**−22.21**
Case No. 2 (3 specimens: No. 1, 2, and 3)—Case No. 3 (3 specimens: No. 2, 4, and 4) (° or kPa, %)	0.0	−0.281	−0.90	−2.517	−4.04
	0.5	0.247	0.81	−0.544	−0.84
	1.0	**6.668**	**20.15**	**−27.769**	**−34.01**
	1.5	**9.920**	**41.54**	**−38.661**	**−30.84**

Note: in Tables 8–10, underlined red numbers show the worst case (extremely large differences in shear strength parameters, caused by different combinations of 3 specimens); no underlined red numbers show more favorable case, but there are still very large differences in shear strength parameters.

As can be seen in Tables 4–6, the values of the correlation coefficient R between shear stresses and normal stresses were high and the test results could be accepted since tests with only three specimens were in accordance with [12–16], where no prescribed value of the correlation coefficient was posted. As has been mentioned, many analyses in existing

research are carried out from data obtained from DST of only three specimens. However, various combinations of three specimens provided different results.

Table 9. Differences in shear strength parameters between various specimen combinations (soil CS1).

	Fibre Amount	Differences in Strength Parameters			
		φ		c	
	(%)	(°)	(%)	(kPa)	(%)
Case No. 1 (4 specimens: No. 1, 2, 3, and 4)—Case No. 2 (3 specimens: No. 1, 2, and 3) (° or kPa, %)	**0.0**	**1.809**	**5.91**	**−4.155**	**−6.84**
	0.5	−0.429	−1.19	1.088	1.04
	1.0	0.31	1.19	−0.643	−0.56
	1.5	**−5.935**	**−28.07**	**10.987**	**10.30**
Case No. 1 (4 specimens: No. 1, 2, 3, and 4)—Case No. 3 (3 specimens: No. 2, 4, and 4) (° or kPa, %)	**0.0**	**4.47**	**16.01**	**−25.557**	**−31.10**
	0.5	1.132	3.29	−7.203	−6.38
	1.0	**2.484**	**10.45**	**−12.923**	**−10.24**
	1.5	2.387	18.62	−10.834	−8.43
Case No. 2 (3 specimens: No. 1, 2, and 3)—Case No. 3 (3 specimens: No. 2, 4, and 4) (° or kPa, %)	**0.0**	**2.661**	**9.53**	**−21.402**	**−26.04**
	0.5	1.561	4.54	−8.291	−7.34
	1.0	2.174	9.15	−12.28	−9.73
	1.5	**8.322**	**64.90**	**−21.821**	**−16.98**

Table 10. Differences in shear strength parameters between various specimen combinations (soil CS2).

	Fibre Amount	Differences in Strength Parameters			
		φ		c	
	(%)	(°)	(%)	(kPa)	(%)
Case No. 1 (4 specimens: No. 1, 2, 3, and 4)—Case No. 2 (3 specimens: No. 1, 2, and 3) (° or kPa, %)	**0.0**	**−6.714**	**−24.44**	**13.48**	**27.53**
	0.5	**−3.942**	**−11.44**	**9.262**	**18.95**
	1.0	−2.239	−5.72	6.035	18.74
	1.5	−0.605	−1.60	1.608	4.66
Case No. 1 (4 specimens: No. 1, 2, 3, and 4)—Case No. 3 (3 specimens: No. 2, 4, and 4) (° or kPa, %)	**0.0**	**3.997**	**23.85**	**−19.045**	**−23.37**
	0.5	**2.436**	**8.68**	**−13.682**	**−19.05**
	1.0	0.043	0.12	−0.284	−0.74
	1.5	0.585	1.60	−3.914	−9.78
Case No. 2 (3 specimens: No. 1, 2, and 3)—Case No. 3 (3 specimens: No. 2, 4, and 4) (° or kPa, %)	**0.0**	**10.711**	**63.92**	**−32.525**	**−39.91**
	0.5	**6.378**	**22.72**	**−22.944**	**−31.94**
	1.0	2.282	6.19	−6.319	−16.41
	1.5	1.19	3.24	−5.522	−13.80

For example, for soil CI, see Table 4 (case No. 2, 1.5% fibres), based on the test results of the combination of specimens No. 1, 2, and 3, one can state that the angle of internal friction of soil with an amount of fibres of 1.5% was 33.803° and cohesion was 86.688 kPa. But based on the results from the combination of specimens No. 2, 3, and 4 (case No. 3), these values were 23.833° and 125.349 kPa. The differences were very high, up to 9.920° (41.54%) and −38.661 kPa (−30.84%), see underlined red number in Table 8 (Case No. 2 (three specimens: No. 1, 2, and 3)—Case No. 3 (three specimens: No. 2, 4, and 4)). The second largest differences were applied for 1% fibres: 6.668° (20.15%) and −27.769 kPa (−34.01%), see underlined red number in the immediate top line in Table 8.

Similar large differences could be also seen for soil CS1 and CS2, see Tables 9 and 10. Therefore, it is not recommended to carry out DST with only three specimens.

3.3. Uncertainty of Shear Strength Parameters

Values of the expanded uncertainties of the shear strength parameters are introduced in Table 4 (for soil CI), Table 5 (for soil CS1), and Table 6 (for soil CS2). In the mentioned tables, for every column, maximal absolute values of uncertainties are marked as red underlined numbers, maximal relative values of uncertainties are marked as italic red underlined numbers, minimal absolute values of uncertainties are marked as blue underlined numbers, and minimal relative values of uncertainties are marked as italic blue underlined numbers.

As can be seen in the tables, the lowest uncertainties were applied for DST with four specimens (case No. 1) and the highest uncertainties were applied for DST with three specimens (case No. 3). This fact supports the recommendation to not carry out DST with only three specimens, especially in the case of using DST to evaluate the rate of shear strength parameter improvement by various materials.

The values of the uncertainties of the shear strength parameters in case B (with covariances) were closest to the real uncertainties since covariances between correlated input quantities (normal stresses and shear stresses) were taken into account. In this case, for soil CI (see Table 4), the maximal absolute value of the uncertainty of the angle of internal friction max$U(\varphi)$ was 0.876° (3.67%) and the minimal absolute value of the uncertainty of the angle of internal friction min$U(\varphi)$ was 0.520° (1.62%). The maximal absolute value of the uncertainty of cohesion max$U(c)$ was 3.466 kPa (2.77%) and minimal absolute value of the uncertainty of cohesion min$U(c)$ was 1.604 kPa (2.81%). For soil CS1 (see Table 5), max$U(\varphi)$ = 0.926° (3.57%), min$U(\varphi)$ = 0.522° (1.61%), max$U(c)$ = 4.050 kPa (3.59%), and min$U(c)$ = 1.636 kPa (2.89%). For soil CS2 (see Table 6), max$U(\varphi)$ = 0.726° (2.59%), min$U(\varphi)$ = 0.442° (2.13%), max$U(c)$ = 3.098 kPa (7.74%), and min$U(c)$ = 1.250 kPa (2.00%). So, generally, in this study, the uncertainties of the angle of internal friction were under 1° and 4% and the uncertainties of cohesion were under 5 kPa and 8%. These values are not negligible and should be taken into account since, when evaluating improvement rate, the difference (improvement) in shear strength parameters should be larger than the uncertainties.

The uncertainties of the shear strength parameters in case C (worst-case estimated uncertainties) were very high. For soil CI (see Table 4), max$U(\varphi)$ = 1.506° (4.46%) and max$U(c)$ = 7.105 kPa (8.70%). For soil CS1 (see Table 5), max$U(\varphi)$ = 1.684° (6.49%) and max$U(c)$ = 8.132 kPa (7.20%), and for soil CS2 (see Table 6), max$U(\varphi)$ = 1.268° (4.52%) and max$U(c)$ = 6.646 kPa (17.25%). Therefore, it is not recommended to apply the worst-case estimation of uncertainty.

For easier comparison, differences in expanded uncertainty between various cases (case A: without covariance; case B: with covariance; and case C: worst-case) were calculated and are presented in Table 11 (for soil CI), Table 12 (for soil CS1), and Table 13 (for soil CS2). The manner of marking and colouring the numbers is the same as in the case of the numbers in Tables 4–6. As can be seen, for all soils, differences in expanded uncertainty between case B and case A were minimal, so covariances between correlated input quantities (normal stresses and shear stresses) had a negligible influence on result uncertainty. On the contrary, differences in expanded uncertainty between case C and case A and also between case C and case B were very high, even much more than 100% in many cases.

Table 11. Differences in expanded uncertainty between various cases (case A: without covariance; case B: with covariance; and case C: worst-case), soil CI.

Soil	Case No.	Fibre Amount	Differences in Expanded Uncertainty											
			Case B—Case A				Case C—Case A				Case C—Case B			
			ΔU(φ)		ΔU(c)		ΔU(φ)		ΔU(c)		ΔU(φ)		ΔU(c)	
		(%)	(°)	(%)	(kPa)	(%)	(°)	(%)	(kPa)	(%)	(°)	(%)	(kPa)	(%)
CI (4 specimens; No. 1, 2, 3, and 4)	1	0.0	−0.004	−0.76	0.001	0.06	0.528	100.76	1.990	124.14	0.532	102.31	1.989	124.00
		0.5	−0.006	−1.12	0.001	*0.06*	0.536	100.37	2.012	124.27	0.542	102.65	2.011	124.14
		1.0	**−0.002**	***−0.37***	0.009	0.50	0.544	100.37	2.379	***131.36***	0.546	101.11	2.37	***130.22***
		1.5	−0.010	−1.68	0.018	0.95	0.616	***103.36***	2.331	122.94	0.626	***106.83***	2.313	120.85

Table 11. *Cont.*

Soil	Case No.	Fibre Amount	Differences in Expanded Uncertainty											
			Case B—Case A				Case C—Case A				Case C—Case B			
			ΔU(φ)		ΔU(c)		ΔU(φ)		ΔU(c)		ΔU(φ)		ΔU(c)	
		(%)	(°)	(%)	(kPa)	(%)	(°)	(%)	(kPa)	(%)	(°)	(%)	(kPa)	(%)
CI (3 specimens; No. 1, 2, and 3)	2	0.0	−0.012	−1.63	−0.021	−1.21	0.562	76.57	2.004	115.11	0.574	79.50	2.025	117.73
		0.5	−0.014	−1.84	−0.030	−1.65	0.568	74.74	2.015	111.08	0.582	78.02	2.045	114.63
		1.0	−0.006	−0.83	−0.013	−0.64	0.556	76.80	2.416	118.72	0.562	78.27	2.429	120.13
		1.5	−0.014	−1.66	−0.028	−1.26	0.664	78.86	2.536	114.54	0.678	81.88	2.564	117.29
CI (3 specimens; No. 2, 3, and 4)	3	0.0	−0.010	−1.36	−0.036	−1.19	0.530	71.82	3.062	101.06	0.540	74.18	3.098	103.47
		0.5	−0.008	−1.09	−0.029	−0.97	0.518	70.38	3.132	104.50	0.526	72.25	3.161	106.50
		1.0	−0.010	−1.26	−0.032	−0.93	0.574	72.29	3.651	105.70	0.584	74.49	3.683	107.63
		1.5	−0.032	−3.52	−0.093	−2.61	0.594	65.42	3.190	89.63	0.626	71.46	3.283	94.72

Note: In Tables 11–13, for every column, maximal absolute values are marked as red underlined numbers, maximal relative values are marked as italic red underlined numbers, minimal absolute values are marked as blue underlined numbers, and minimal relative values are marked as italic blue underlined numbers. More information is introduced and commented in the paper.

Table 12. Differences in expanded uncertainty between various cases (case A: without covariance; case B: with covariance; and case C: worst-case), soil CS1.

Soil	Case No.	Fibre Amount	Differences in Expanded Uncertainty											
			Case B—Case A				Case C—Case A				Case C—Case B			
			ΔU(φ)		ΔU(c)		ΔU(φ)		ΔU(c)		ΔU(φ)		ΔU(c)	
		(%)	(°)	(%)	(kPa)	(%)	(°)	(%)	(kPa)	(%)	(°)	(%)	(kPa)	(%)
CS1 (4 specimens; No. 1, 2, 3, and 4)	1	0.0	−0.004	−0.76	0.002	0.12	0.540	102.66	1.982	121.30	0.544	104.21	1.980	121.03
		0.5	−0.012	−1.89	0.005	0.22	0.642	101.26	2.708	120.62	0.654	105.14	2.703	120.13
		1.0	−0.020	−3.13	0.005	0.25	0.650	101.88	2.242	112.27	0.670	108.41	2.237	111.74
		1.5	−0.028	−4.93	0.019	1.12	0.564	99.30	1.832	108.21	0.592	109.63	1.813	105.90
CS1 (3 specimens; No. 1, 2, and 3)	2	0.0	−0.008	−1.11	−0.010	−0.58	0.594	82.27	2.093	120.43	0.602	84.31	2.103	121.70
		0.5	−0.022	−2.40	−0.049	−1.91	0.692	75.38	2.799	109.38	0.714	79.69	2.848	113.47
		1.0	−0.034	−3.54	−0.058	−2.50	0.724	75.42	2.439	105.04	0.758	81.86	2.497	110.29
		1.5	−0.042	−4.58	−0.068	−3.24	0.652	71.02	2.068	98.66	0.694	79.22	2.136	105.33
CS1 (3 specimens; No. 2, 3, and 4)	3	0.0	−0.022	−2.75	−0.083	−2.60	0.582	72.75	2.788	87.48	0.604	77.63	2.871	92.49
		0.5	−0.020	−2.22	−0.070	−1.70	0.620	68.89	4.012	97.38	0.604	72.73	4.082	100.79
		1.0	−0.038	−4.11	−0.112	−3.10	0.608	65.80	3.047	84.36	0.646	72.91	3.159	90.26
		1.5	−0.044	−5.51	−0.099	−3.40	0.510	63.91	2.424	83.21	0.554	73.47	2.523	89.66

Table 13. Differences in expanded uncertainty between various cases (case A: without covariance; case B: with covariance; and case C: worst-case), soil CS2.

Soil	Case No.	Fibre Amount	Differences in Expanded Uncertainty											
			Case B—Case A				Case C—Case A				Case C—Case B			
			ΔU(φ)		ΔU(c)		ΔU(φ)		ΔU(c)		ΔU(φ)		ΔU(c)	
		(%)	(°)	(%)	(kPa)	(%)	(°)	(%)	(kPa)	(%)	(°)	(%)	(kPa)	(%)
CS2 (4 specimens; No. 1, 2, 3, and 4)	1	0.0	−0.008	−1.78	0.014	1.13	0.454	100.89	1.594	128.96	0.462	104.52	1.58	126.40
		0.5	−0.004	−0.78	0.007	0.46	0.514	100.39	2.006	130.68	0.518	101.97	1.999	129.64
		1.0	−0.002	−0.40	0.003	0.19	0.482	96.79	2.144	133.25	0.484	97.58	2.141	132.82
		1.5	−0.002	−0.40	0.001	0.06	0.484	97.19	2.107	130.63	0.486	97.98	2.106	130.48
CS2 (3 specimens; No. 1, 2, and 3)	2	0.0	−0.008	−1.20	−0.016	−1.08	0.516	77.25	1.715	116.19	0.524	79.39	1.731	118.56
		0.5	−0.006	−0.85	−0.014	−0.80	0.540	76.70	2.049	117.62	0.546	78.22	2.063	119.39
		1.0	−0.040	−0.60	−0.010	−0.57	0.526	84.57	2.052	117.66	0.490	74.47	2.062	118.92
		1.5	−0.002	−0.30	−0.008	−0.47	0.500	75.53	2.040	119.58	0.502	76.06	2.048	120.61
CS2 (3 specimens; No. 2, 3, and 4)	3	0.0	−0.018	−2.78	−0.045	−1.95	0.460	70.99	2.255	97.49	0.478	75.87	2.300	101.41
		0.5	−0.010	−1.36	−0.030	−1.03	0.532	72.28	3.058	105.23	0.542	74.66	3.088	107.37
		1.0	−0.002	−0.29	−0.007	−0.23	0.509	74.52	3.559	115.29	0.511	75.04	3.566	115.78
		1.5	−0.002	−0.29	−0.010	−0.32	0.498	72.17	3.453	111.10	0.500	72.67	3.463	111.78

It was found that, in this study, correlation coefficient $r(\sigma_i, \sigma_j)$ had a value of 0.80095, $r(\sigma_i, \tau_j)$ had a value of 0.42487, and $r(\tau_i, \tau_j)$ had a value of 0.22537. Covariance between correlated input quantities (normal stresses and shear stresses) decreased the uncertainties of the angle of internal friction and increased the uncertainties of cohesion for all tested soils in the case of DST using all four specimens (see differences in expanded uncertainty

in columns "Case B—Case A" in Tables 11–13). In the case of DST using three specimens, covariance decreased the uncertainties of the angle of internal friction and decreased the uncertainties of cohesion for all tested soils (see differences in expanded uncertainty in columns "Case B—Case A" in Tables 11–13). However, the changes were very small (the largest change in φ was −0.044° (−5.51%), see Table 12, CS1, Case 3) and had no impact on geotechnical design since the obtained values of the shear strength parameters from DST should be rounded (e.g., according to [17,18], the obtained value of the angle of internal friction φ should be rounded to 0.1° and the value of cohesion c should be rounded to 1 kPa).

4. Discussion

The obtained values of the shear strength parameters of soils CI and CS1 improved with fibres TEXZEM PES 200, showing significant improvement. Similarly as in previous studies [18–20], the optimal amounts of fibres were 0.5% or 1%, depending on the type of soil. In the case of soil CS2, even if there was no simultaneous increase in both shear strength parameters, it is proposed that, in many cases, regarding subsoil bearing capacity, slope stability, and soil pressure, an increase in the angle of internal friction of soil CS2 by 9.755° (47.00%) and decrease in cohesion by 4.293 kPa (6.88%) can be considered as an improvement. However, a calculation check is required. It is also necessary to note that the mentioned improvement only applies to the cases of static loads. In the cases of dynamic loads induced from, e.g., urban vibration, industrial machinery, earthquakes, wind loads, and sea waves, among others [27], further tests should be carried out. In any case, based on the findings presented in [27], the issue regarding the specific strain level required for mobilisation of the tensile strength of the fibers should be investigated.

The SEM images taken in this study showed visible scratches on the fibre surface, which were present not only locally but also along the fibre's longitudinal direction on the surface, similarly as presented in [24]. It can also be proposed that this may result from the plowing of angular hard particles into the fibre body during the shear process, due to the suitable scratch resistance of the tested fibres. The SEM images also confirmed the conclusion presented in [25] that soil properties are very important since the surfaces of the fibres were very different after shearing in soil CI and CS1. The contact area between the soil and fibres is also important since, as can be seen in [26], higher consolidation stress makes the tested material denser with less pores of smaller size. So, it is proposed that higher normal stress provides larger contact area between the soil and fibres compared to lower normal stress; therefore, in the case of higher normal stress, there are more scratches of larger depth. However, the issues presented above are very complex and require further study. It is planned to test the same soil with fibres TEXZEM PES 200 and other fibres.

In this study, the minimal uncertainty of the angle of internal friction φ was 0.422° (see expanded uncertainty with covariance in Table 6; 0% fibres; four specimens) and the minimal uncertainty of cohesion c was 1.250 kPa (see expanded uncertainty with covariance in Table 6; 0% fibres; four specimens). When comparing improvement, the difference between two cases should be calculated and the difference (improvement) should be larger than the sum of the uncertainties of two cases, e.g., larger than 2.0.422° = 0.844° and 2. 1.250 kPa = 2.500 kPa. In this study, the differences should be larger than the mentioned values 0.844° and 2.500 kPa since the values of 0.422° and 1.250 kPa were minimal (specific values to be compared are calculated and presented in the Section 3.1). It is therefore useful to check if the difference (improvement) in shear strength parameters of 0.5° [1]; 0.1° and 0.4°, 0.2 kPa [3]; −0.17° and −0.45° [4]; 0.3° and 0.5° [6] can be confirmed based on result uncertainty analysis.

Taking into account the above-mentioned values of 0.422° and 1.250 kPa, in our opinion, it would also be useful to determine the uncertainty of the shear strength parameters presented in [11] with 2 digits after the decimal (values of φ from 8.66° to 32.16°, with mean and median values of 18.73° and 17.70°, and values of c from 1.74 to 38.95 kPa, with a mean of 20.77 kPa and a median of 20.91 kPa), which were used as guide values for the pre-

diction of soil shear strength parameters using combined data and three different machine learning models.

It was found that in DST, correlation coefficients between normal stresses and shear stresses can be determined precisely since they are calculated using the same shear surface. Correlation coefficient r(σi,σj) had a value of 0.80095, r(σi,τj) had a value of 0.42487, and r(τi,τj) had a value of 0.22537. These values enabled a more precise determination of the uncertainty of shear strength parameters by considering the covariance between normal stresses and shear stresses, so it does not call for the worst-case strategy to be applied, implying totally negative error correlation so increasing uncertainty by up to 28% [22].

Since in practice, in some cases, the worst-case strategy, considering the linearly added uncertainty contributions $c(\sigma_i).u(\sigma_i)$ and $c(\tau_i).u(\tau_i)$ and not considering correlation coefficients, can be accepted, the magnitude of the uncertainty for this case was also explored. It was found that, in DST, this procedure gave very high uncertainty and, in many cases, it was higher than 100% in comparison with the uncertainty considering squared uncertainty contributions $c(\sigma_i).u(\sigma_i)$ and $c(\tau_i).u(\tau_i)$ and the real obtained correlation coefficients presented above. The maximal relative differences were 109.63% for φ (see Table 12; CS1; Case C—Case B; Case 1) and 132.82% for c (see Table 13; CS2; Case C—Case B; Case No.1). The minimal relative differences were still very high, which were 71.46% for φ (see Table 11; CI; Case C—Case B; Case 3) and 89.66% for c (see Table 12; CS1; Case C—Case B; Case No.3). Therefore, this procedure is highly not recommended.

5. Conclusions

From the obtained results, the following conclusions can be made:

1. The tested fibres improved the soil shear strength parameters differently; both the angle of internal friction and cohesion were increased for soil CI using 1.0% fibres and for soil CS1 using 0.5% fibres. For soil CS2, the angle of internal friction increased but cohesion decreased.
2. SEM is a useful tool for exploring the fibre surface after shearing. Suitable fibre scratch resistance can significantly increase the shear strength parameters, but there are additional fibre properties contributing to the improvement rate, such as fibre surface roughness, adhesion of soil particles to the fibre surface, etc., which requires further study.
3. It is not recommended to carry out DST with only three specimens since different combinations of three specimens provide different results.
4. Improvement rates of shear strength parameters of soil using various materials require determination of their uncertainty so that the improvement can be confirmed. Determination of the uncertainty of shear strength parameters is also important in the case when they are used as guide values for the prediction of soil shear strength parameters using machine learning models.
5. In this study, correlation coefficients between normal stresses and shear stresses existed and were not negative. Covariance between normal stresses and shear stresses has a negligible influence on shear strength parameter uncertainty.
6. The worst-case strategy, considering linearly added uncertainty contributions $c(\sigma_i).u(\sigma_i)$ and $c(\tau_i).u(\tau_i)$ and not considering correlation coefficients, provides too high uncertainty and is not recommended.
7. This study also has various limitations. The tests were carried out only for clayey soils with insufficient shear strength. It will be useful to carry out further tests for silty soils and sandy soils.
8. A further limitation of this study is the focus of the research only on shear strength parameters, without dealing with deformation properties. Since soil mixed with fibres can be compacted to reach a maximum dry soil density obtained from a standard Proctor test, it is proposed that there will not be a problem with excessive deformation. It is planned to carry out an oedometer test of soil mixed with fibres using an

oedometer with a diameter of 30 cm so that the deformation in practical applications can be quantified.

9. This study presents the results of laboratory tests where the preparation of specimens can be different from the preparation of soil in practical applications. Using a modern soil stabiliser with a powerful milling and mixing rotor can minimise the difference. In the case of soil where the preparation of soil in practical applications does not provide similar conditions as in the laboratory, verification using in situ testing is required.

Author Contributions: Conceptualization, G.N., S.M., F.G. and J.G.-P.; methodology, G.N., S.M., F.G. and J.G.-P.; formal analysis, G.N., S.M., F.G. and J.G.-P.; investigation, S.M., F.G. and J.G.-P.; writing—original draft preparation, G.N.; writing—review and editing, G.N., S.M., F.G. and J.G.-P.; project administration, F.G.; funding acquisition, F.G. All authors have read and agreed to the published version of the manuscript.

Funding: This research was funded by the Operational Programme Integrated Infrastructure: Application of innovative technologies focused on the interaction of engineering constructions of transport infrastructure and the geological environment, ITMS2014+ code 313011BWS1, and the project was cofounded by the European Regional Development Fund. The APC was funded by 313011BWS1.

Institutional Review Board Statement: Not applicable.

Informed Consent Statement: Not applicable.

Data Availability Statement: The original contributions presented in the study are included in the article, further inquiries can be directed to the corresponding author.

Conflicts of Interest: The authors declare no conflicts of interest.

References

1. Tang, C.S.; Shi, B.; Gao, W.; Chen, F.; Cai, Y. Strength and mechanical behavior of short polypropylene fiber reinforced and cement stabilized clayey soil. *Geotext Geomembr.* **2007**, *25*, 194–202. [CrossRef]
2. Sarli, J.M.; Hadadi, F.; Bagheri, R.-A. Stabilizing Geotechnical Properties of Loess Soil by Mixing Recycled Polyester Fiber and Nano-SiO_2. *Geotech. Geol. Eng.* **2020**, *38*, 1151–1163. [CrossRef]
3. Valipour, M.; Shourijeh, P.; Mohammadinia, A. Application of recycled tire polymer fibers and glass fibers for clay reinforcement. *Transp. Geotech.* **2021**, *27*, 100474. [CrossRef]
4. Urian, A.-M.; Ilies, N.-M.; Nemes, O.; Nagy, A.-C. Clayey Soil Improvement with Polyethylene Terephthalate (PET) Waste. *Appl. Sci.* **2023**, *13*, 12081. [CrossRef]
5. Bao, X.; Bao, Z.; Li, L.; Li, Y.; Peng, P.; Chen, X. Investigation of the Water-Retention Characteristics and Mechanical Behavior of Fibre- Reinforced Unsaturated Sand. *Appl. Sci.* **2023**, *13*, 11337. [CrossRef]
6. Tang, H.; Yang, Z.; Zhu, H.; Dong, H. Experimental Study on the Mechanical Properties of Xinyang Red Clay Improved by Lime and Fly. *Ash. Appl. Sci.* **2023**, *13*, 6271. [CrossRef]
7. Khasib, I.A.; Daud, N.N.N.; Nasir, N.A.M. Strength Development and Microstructural Behavior of Soils Stabilized with Palm Oil Fuel Ash (POFA)-Based Geopolymer. *Appl. Sci.* **2021**, *11*, 3572. [CrossRef]
8. Liu, W.; Li, H.; Yang, Y.; Xu, P.; Dai, Z.; Yang, G.; Wang, H.; Wang, Z. Study on Improvement Characteristics of a Novel Geotextile with Stitched Transverse Ribs. *Appl. Sci.* **2023**, *13*, 1536. [CrossRef]
9. Li, S.; Wang, T.; Wang, H.; Jiang, M.; Zhu, J. Experimental Studies of Scale Effect on the Shear Strength of Coarse-Grained Soil. *Appl. Sci.* **2022**, *12*, 447. [CrossRef]
10. Stacho, J.; Sulovska, M. Shear strength properties of coarse-grained soils determined using large-size direct shear test. *Civ. Environ. Eng.* **2022**, *18*, 244–257. [CrossRef]
11. Zhu, L.; Liao, Q.; Wang, Z.; Chen, J.; Chen, Z.; Bian, Q.; Zhang, Q. Prediction of Soil Shear Strength Parameters Using Combined Data and Different Machine Learning Models. *Appl. Sci.* **2022**, *12*, 5100. [CrossRef]
12. *ASTM D3080/D3080M-11*; Standard Test Method for Direct Shear Test of Soils under Consolidated Drained Conditions. ASTM International: West Conshohocken, PA, USA, 2012.
13. *STAS 8942/2-82*; Foundation Ground. Determination of Earth Strength. By Direct Shearing. Romanian Institute for Standardization: Bucharest, Romania, 1982.
14. *AASHTO T 236-08*; Standard Method of Test for Direct Shear Test of Soils under Consolidated Drained Conditions. American Association of State Highway and Transportation Officials: Washington, DC, USA, 2008.
15. *BS 1377: Part 7:1990*; British Standard Methods of Test for Soils for Civil Engineering Purposes. Part 7: Shear Strength Tests (Total Stress). British Standards Institution: London, UK, 1990.

16. *ISO 17892-10:2018*; Geotechnical Investigation and Testing—Laboratory Testing of Soil—Part 10: Direct Shear Tests. International Organization for Standardization: Geneva, Switzerland, 2018.
17. *STN 72 1030: 1988*; Laboratory Direct Shear Box Drained Test of Soils. ÚNM publishing house: Prague, Czech Republic, 1988.
18. *PN-88/B-04481*; Building Soils—Laboratory Tests. Alfa Publishing House: Warsaw, Poland, 1988.
19. Nguyen, G.; Hrubešová, E.; Voltr, A. Soil improvement using polyester fibres. *Proceedia Eng.* **2015**, *111*, 596–600. [CrossRef]
20. Nguyen, G. Laboratory study of soils shear strength improvement by polyester fibers. *Fibres Text East Eur.* **2019**, *27*, 91–99. [CrossRef]
21. Jakubík, L. Laboratory Testing of Mechanical Properties of Soil with Added Synthetic Material. Master's Thesis, University of Žilina, Žilina, Slovakia, 2019.
22. Ungureanu, C.; Priceputu, A.; Nguyen, G.; Pencea, I.; Turcu, R.N.; Popescu-Argeş, A.C. Hybrid OLS for uncertainties estimation in direct shear testing. *Measurement* **2021**, *185*, 110018. [CrossRef]
23. Cai, Y.; Shi, B.; Ng, C.W.W.; Tang, C. Effect of polypropylene fibre and lime admixture on engineering properties of clayey soil. *Eng. Geol.* **2006**, *87*, 230–240. [CrossRef]
24. Tang, C.S.; Shi, B.; Zhao, L.Z. Interfacial shear strength of fiber reinforced soil. *Geotext. Geomembr.* **2010**, *28*, 54–62. [CrossRef]
25. Rivera-Gómez, C.; Galán-Marín, C.; Bradley, F. Analysis of the Influence of the Fiber Type in Polymer Matrix/Fiber Bond Using Natural Organic Polymer Stabilizer. *Polymers* **2014**, *6*, 977–994. [CrossRef]
26. Liu, W.; Liang, J.; Xu, T. Tunnelling-induced ground deformation subjected to the behavior of tail grouting materials. *Tunn. Undergr. Space Technol.* **2023**, *140*, 105253. [CrossRef]
27. Oliveira, P.J.V.; Anunciação, G.R.; Correia, A.A.S. Effect of cyclic loading frequency on the behavior of a stabilized sand reinforced with polypropylene and sisal fibers. *J. Mater. Civ. Eng.* **2022**, *34*, 06021008. [CrossRef]
28. Beskid Air. Available online: https://www.youtube.com/watch?v=3v_0rdgTyWc (accessed on 29 April 2024).
29. *BS 1377: 1990*; Part 2: Methods of Test for Soils for Civil Engineering Purposes. Part 2. Classification Tests. British Standards Institution: London, UK, 1990.
30. *BS 5930:2015*; Code of Practice for Ground Investigations. British Standards Institution: London, UK, 2015.
31. EUROLAB. *Technical Report 1/2006—Guide to the Evaluation of Measurement Uncertainty for Quantitative Test Results*; EUROLAB: Paris, France, 2006.

applied sciences

MDPI

Article

A New Method for Constructing the Protection and Seepage Control Layer for CSGR Dam and Its Application

Yangfeng Wu [1,2], Jinsheng Jia [1,2,*], Cuiying Zheng [2], Baozhen Jia [2], Yang Wang [2] and Wambley Adomako Baah [2]

[1] State Key Laboratory of Hydraulic Engineering Simulation and Safety, Tianjin University, Tianjin 300072, China; wuyangfeng_0211@tju.edu.cn
[2] State Key Laboratory of Simulation and Regulation of Water Cycle in River Basin, China Institute of Water Resources and Hydropower Research (IWHR), Beijing 100038, China; zhengcy@iwhr.com (C.Z.); jiabaozhen1987@sohu.com (B.J.); wangyang7078@foxmail.com (Y.W.); wambleybaah@gmail.com (W.A.B.)
* Correspondence: jiajsh@iwhr.com

Abstract: Effective seepage control is crucial for maintaining the structural integrity of Cemented Sand, Gravel and Rock (CSGR) dams. Traditional methods using conventional concrete (CVC) or grout-enriched roller-compacted concrete (GERCC) are costly and disruptive. This paper presents a novel technique for constructing the protection and seepage control layer in Cemented Sand, Gravel and Rock (CSGR) dams. The method involves grouting and vibrating the loosened Cemented Sand, Gravel and Rock (CSGR) material to create vibrated grout-enriched Cemented Sand, Gravel and Rock, which performs similarly to concrete. A new surface water stop structure has also been developed for the structural joints. Laboratory tests revealed that Cemented Sand, Gravel and Rock (CSGR) with a vibrating–compacted (VC) value of 2–6 s and a compressive strength of 4 MPa meets design requirements for medium and low dams when the slurry addition rate is 8–12%. The T-shaped surface water stop demonstrated a bonding strength of over 1.8 MPa, withstanding a water pressure of 1.6 MPa. This method, integrated with dam body construction, reduces material costs by about 50% and eliminates construction interference. Specialized equipment for this technique has been developed, with a capacity of 12 m^2/h. Implemented in the Minjiang Navigation and Hydropower Qianwei Project and Shaping I Hydropower Station, it has shown significant economic, environmental and safety benefits, promoting sustainable dam construction.

Keywords: cemented sand, gravel and rock dam; protection and seepage control layer; vibrated grout-enriched cemented sand, gravel and rock; T-shaped surface water stop; grouting and vibrating equipment

Citation: Wu, Y.; Jia, J.; Zheng, C.; Jia, B.; Wang, Y.; Baah, W.A. A New Method for Constructing the Protection and Seepage Control Layer for CSGR Dam and Its Application. *Appl. Sci.* **2024**, *14*, 5423. https://doi.org/10.3390/app14135423

Academic Editors: António Alberto Santos Correia and Paulo José da Venda Oliveira

Received: 30 April 2024
Revised: 18 June 2024
Accepted: 19 June 2024
Published: 22 June 2024

1. Introduction

The Cemented Material Dam (CMD), is a new type of dam featuring characteristics lying between those of embankment dams and concrete dams. Jinsheng Jia of China introduced the concept of the CMD in 2009 and subsequently published a paper on the topic in 2012 [1]. In response, the International Committee on Large Dams (ICOLD) formed a technical committee dedicated to CMD in 2013. The following year, Chinese technical guidelines for CMD, prepared by Liu et al. were published [2]. It is categorized into Cemented soil dam, HCC (including Hardfill dam, Cemented Sand and Gravel (CSG) dam, Cemented Sand, Gravel and Rock (CSGR) dam) and Cemented rockfill dam [3]. The CSGR dam has been developed drawing upon the design principles of both the Hardfill dam and the CSG dam. In comparison to these predecessors, it relaxes the requirements for aggregate size further, eases control over fine particle content and composition, and proposes new methods for quality control in supporting construction [4,5]. The anti-seepage system of the CSGR dam primarily depends on the upstream protection provided by the protection and seepage control layer, although there is currently no durability requirement for the internal dam's anti-seepage capabilities. The material strength and aggregate gradation needed for

the internal dam are low, allowing for a wider selection of aggregate with relaxed screening and washing requirements. This enables the use of riverbed sand and gravel directly in construction, reducing costs and promoting environmental friendliness. The protection and seepage control layer typically follows the construction methods of Hardfill and CSG dams, commonly utilizing conventional concrete (CVC) or grout-enriched roller-compacted concrete (GERCC) [6–8]. During the construction phase, materials such as CSGR, CVC, and GERCC are typically employed and built simultaneously. However, the construction of this structure entails complexity and potential interferences. This complexity arises due to notable differences between CSGR and CVC or GERCC in expansion coefficient, elastic modulus, and hydration heat parameters. Consequently, ensuring quality control during construction is often a cause for concern [9–11]. Hence, a novel approach is suggested: incorporating vibrated grout-enriched CSGR in constructing the protection and seepage control layer of the CSGR dam. This innovation promises to enhance construction efficiency significantly while simultaneously reducing project costs.

The grouting and vibrating technology of the roller-compacted concrete (RCC) dam projects involves adding an appropriate amount of cement slurry (generally between 4% and 8% of the total volume of GERCC) to the newly mixed dry-hard roller-compacted concrete mixture, then using an immersible vibrator to compact and form an anti-seepage material with similar flow characteristics to CVC [12]. This material replaces the commonly used CVC as the impervious barrier on the upstream surface of the dam. This method not only reduces the production and transportation costs but also solves the problem of effective transition and combination of different materials between RCC and CVC, enhancing continuity and integrity [13]. Therefore, in theory, it is feasible to use this technology as a protective layer for CSGR dams. Compared to concrete, CSGR material has a more complex gradation and uses less cementitious material. The amount of slurry grout directly affects the construction work of the vibrated grout-enriched CSGR, as well as the properties and durability after hardening. Therefore, experimental research is necessary.

The typical arrangement for the split water stop in the protection and seepage control layer of Hardfill and CSG dams usually involves buried water stops [14–16]. The surface water stop for concrete face rockfill dams was also pioneered by Jinsheng Jia [17]. This innovation has seen extensive adoption in concrete face rockfill dams exceeding 200 m in height [18,19]. It typically consists of a rubber rod, plastic filler, and anchoring rubber plate. This design addresses the drawbacks of buried water stops, yet its structure is intricate and its cost is elevated [20]. The subsequent advancement in coated surface water stops optimized the anchorage cover plate by incorporating a polyurea coating film [21]. This innovation eliminated the need for an anchorage system, simplifying construction processes. However, the heightened efficiency came at the expense of increased costs [22]. Consequently, there is a need to develop a new type of surface water stop that balances safety, cost-effectiveness, and ease of construction for CSGR dams.

The construction of CSGR dams differs significantly from that of RCC dams. This contrast is particularly evident in medium and low dams, where narrow construction sites and faster filling speeds are common requirements. The grouting and vibrating equipment designed for RCC dams [23–25] cannot be directly applied to CSGR dams because, unlike RCC, CSGR dam materials exhibit variation depending on the available material type for excavation in the reservoir area or nearby locations, and typically lack a fixed gradation. The maximum particle size is 150 mm for dams and up to 300 mm for cofferdam construction; hence, there is high fluctuation in mud and water content during mixing. Consequently, there is a need to develop grouting and vibrating equipment tailored to the characteristics of CSGR materials and the specific requirements of construction site conditions.

In this paper, a novel concept is introduced, suggesting the utilization of vibrated grout-enriched CSGR materials as the protection and seepage control layer for CSGR dams. The proposed configuration method is tailored to the vibrated grout-enriched CSGR. Additionally, a new type of T-shaped surface water stop is devised, along with the determination of supporting construction parameters. Furthermore, efficient grouting and

vibrating mechanical equipment suitable for narrow warehouse surfaces is developed. The feasibility of the proposed idea is validated through its application in the Tangba Protection Dam of the Qianwei Navigation and Hydropower Hub Project on the Minjiang River and Shaping I Hydropower Station on the Dadu River.

2. A New Idea for the Construction of the Protection and Seepage Control Layer for the CSGR Dam

The construction of the protection and seepage control layer for the CSGR dam must fulfill the objectives of anti-seepage effectiveness and durability and strength, while also addressing challenges such as minimizing construction interference between CVC, RCC, and CSGR components within the dam body, as well as overcoming difficulties related to accessibility for rolling machinery near the boundary areas. Combined with the construction experience from Tangba Protection Dam and Shaping I Hydropower Station, a novel approach has been devised: employing vibrated grout-enriched CSGR as the protection and seepage control layer for the CSGR dam, as illustrated in Figure 1. This method also introduces a redesigned water stop structure. Additionally, to address challenges encountered in constructing CSGR dams on non-rock foundations, it is proposed to relocate the cutoff wall to the upstream side of the dam. The key features of this innovative concept include:

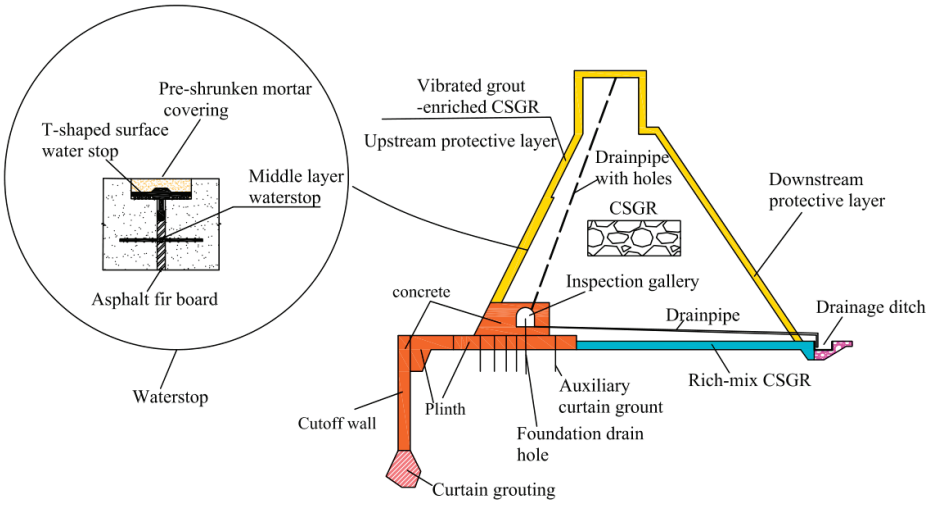

Figure 1. New cross-section of CSGR dam.

(1) The anti-seepage and drainage zoning design of the CSGR dam.

The protection and seepage control layer of the CSGR dam includes the upstream, downstream and top areas. Its function is considered according to the concrete face rockfill dam, which undertakes the anti-seepage under the action of high-pressure water. The dam body is designed according to the bearing body, which mainly meets the requirements of stability against sliding and compressive strength. Drainage is set between the protection and seepage control layer and the bearing body, and it is discharged in time when water leakage occurs, which can further relax the restrictions on the dam material. When the CSGR dam is constructed on the sandy pebble foundation and the dam height is low, the drainage can be canceled because the sandy pebble foundation itself has drainage capacity.

(2) The vibrated grout-enriched CSGR is used as the material of protection and seepage control layer.

Combined with the sand, gravel and rock of the Tangba protection dam riverbed, according to the design requirements of the protection and seepage control layer, a suitable admixture was selected to develop a vibrated grout-enriched CSGR with a 90-day compres-

sive strength greater than 15 MPa, an impermeability grade of W8 and a frost resistance grade of F100 (Fn, F represents the frost resistance grade of concrete and n represents the frost resistance grade value. Fn indicates that the specimen is damaged after n freeze–thaw cycles of concrete, where n = 100) Combined with the sand, gravel and rock of the Shaping I Hydropower Station riverbed, a suitable admixture was selected based on a series of laboratory trial compatibility tests to develop a vibrated grout-enriched CSGR that can meet the compressive strength of more than 20 MPa, the impermeability grade of W12 (Wp, W represents the impermeability grade, *p* represents the concrete impermeability grade value. Wp indicates that the test sample can withstand hydrostatic pressure of P/10 MPa without any water seepage, where *p* = 12), and the frost resistance grade of F225, as shown in Table 1. The properties of the vibrated grout-enriched CSGR material can reach the indexes of CVC and RCC materials, and it is safe and reliable as the protection and seepage control layer material of the dam body. Because it is CSGR, the construction technology is consistent with the bearing body of the dam body, so the construction equipment and construction technology have been further simplified, avoiding the interference caused by the simultaneous construction of conventional concrete as the protection and seepage control layer and CSGR as the dam body material. It is proposed to add a slurry rate of 8–12% in the fresh CSGR materials, so that its workability can be changed from dry and rolling CSGR to slump and vibratable CSGR, whose compactness can be further improved by full vibration.

Table 1. Mixing ratio of vibrated grout-enriched CSGR.

Project	Design Index	Quantity for 1 m^3 Slurry (kg)				Slurry Rate (%)	Quantity for 1 m^3 Vibrated Grout-Enriched CSGR (kg)				Slump (cm)	90 d Compressive Strength	Impermeability Grade	Frost Resistance Grade
		Water	Cement	Water Reducing Admixture	Air Entraining Admixture		Water	Cement	Fly Ash	Aggregate				
*A**	C_{90}15W6F50	540	1270	12.7	0.127	8	153.6	138.6	36.8	2200.3	6.0	22.5	W8	F100
*B**	C_{90}20W6F50	540	1270	1.0	0.127	7	126.7	135.4	46.5	2264.5	8.5	24.2	W12	F225

*A** refers to Tangba Protection Dam; *B** refers to Shaping I Hydropower Station.

(3) For the Tangba protection dam, the structural form of separating the cut-off wall from the dam body is proposed, which avoids the mutual interference between the cut-off wall construction and the dam construction, and facilitates the repair and reinforcement when problems occur during the period of operation.

(4) A new T-shaped surface water stop structure (Figure 2) is proposed, which has a simple structure, convenient construction and can adapt to large deformation [26].

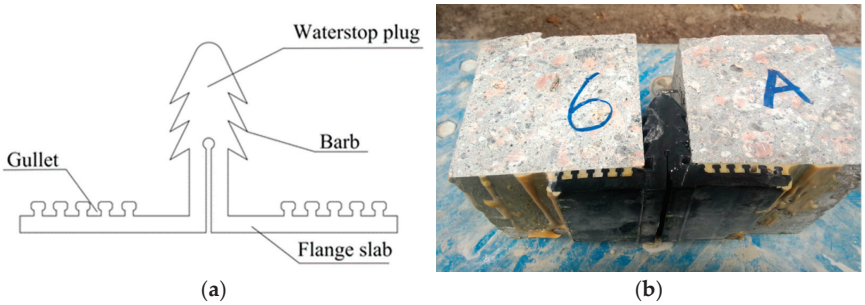

Figure 2. New T-shaped surface water stop structure: (**a**) schematic diagram; (**b**) object picture.

3. Experimental Study on Vibrated Grout-Enriched CSGR Material of Tangba Protection Dam

The new idea has been fully applied to the Tangba Protection Dam of Qianwei Navigation and Hydropower Hub Project on the Minjiang River. For this reason, the Tangba Protection Dam is taken as an example for a detailed introduction.

3.1. Project Background

The Qianwei Navigation and Hydropower Hub Project is located in the lower reaches of the Minjiang River in Sichuan Province, China. It is the third step of shipping and hydropower planning in the lower reaches of the Minjiang River (Leshan–Yibin). The project grade is second-class and the project scale is large (2) type [27]. Its primary development objective is to prioritize navigation while integrating power generation, water supply, and irrigation to foster local economic and social advancement. The hub's normal water level stands at 335 m, with a total reservoir capacity of 228 million cubic meters. Positioned approximately 2 km upstream of the hub's right bank, the protection dam or dike spans around 2.76 km in length, reaching a maximum height of 15 m. Engineered to withstand a 20-year flood standard, the project is designated as Grade 4. The construction of the protection dam necessitates placement atop a 13-m-thick layer of sand and gravel cover. Originally, a solution involving a geotextile membrane core wall and rockfill dam was proposed. However, concerns regarding potential leakage failure and overtopping risks prompted the proposal of an alternative solution: the CSGR dam depicted in Figure 3. This design features a trapezoidal cross-section with a symmetrical profile, boasting a slope ratio of 1:0.5 on the upstream face and 1:0.7 on the downstream face. The primary body of the dam is constructed from Cemented Sand, Gravel and Rock, boasting a design strength of $C_{180}4$ (that is 180-day compressive strength of 4 MPa). As a protective measure against seepage, cemented and compacted gravel material is employed on the upstream side, adhering to the design specifications of $C_{90}15W6F50$ (that is, a 90-day compressive strength (C) of 15 MPa, and impermeability and frost resistance grades of W6 and F50, respectively). To ensure watertightness, T-shaped surface water stops are deployed for joint sealing along the dam body and between the plinth and the cutoff wall. Also, due to the low height of the dam and its foundation consisting of sand and gravel, it possesses a drainage capacity. Consequently, the drainage setting between the protective anti-seepage layer and the main body of the dam is canceled.

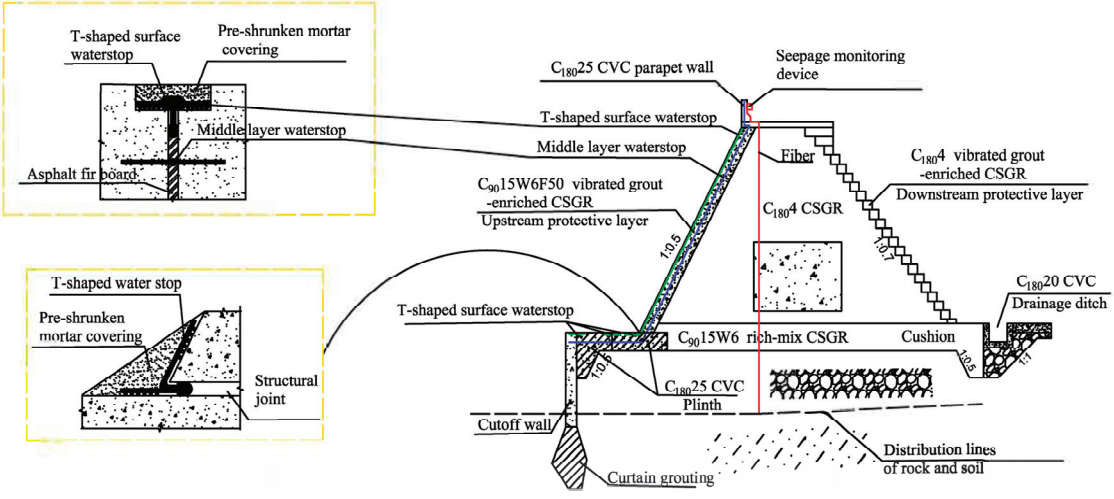

Figure 3. The cross-section of Tangba protection dam.

3.2. Raw Materials

3.2.1. Cement

The cement is P.O 42.5 ordinary Portland cement produced by Sichuan Qianwei Baoma Cement Co., Ltd. (Leshan, China), and its physical and chemical composition is shown in Table 2.

Table 2. Chemical and physical parameters of the cement.

Chemical			Physical									
SO_3 (%)	MgO (%)	Cl^- (%)	Density (g/cm^3)	Fineness (%)	Specific Surface Area (cm^2/g)	Standard Consistency (%)	Setting Time (min)		Compressive Strength (MPa)		Flexural Strength (MPa)	
							Initial	Final	3 d	28 d	3 d	28 d
2.87	2.5	0.015	3.16	6.6	3610	27.2	140	190	30.6	49.5	5.7	7.8

3.2.2. Fly Ash

The fly ash is grade II ash provided by Leshan Runsen Waste Recycling Co., Ltd. (Leshan, China), and its physical and chemical characteristics are shown in Table 3. According to Table 3, the fineness is achieved by screening fly ash through a 45 μm square hole sieve, and the fineness of the fly ash samples is expressed by the mass percentage of the sieve residue on the sieve. The water demand ratio is the ratio of the water demand of CSGR materials prepared with fly ash compared to specimens without fly ash (control). These are supported by ASTM C618 [28]. With strength activity index, the compressive strength of the test mortar and the control mortar is measured after 28 days, and the activity of the test mortar was determined by the ratio of the compressive strength of the two [29].

Table 3. Chemical and physical parameters of the fly ash.

Chemical		Physical				
SO_3 (%)	f-CaO (%)	Density (g/cm^3)	Fineness (%)	Water Demand Ratio (%)	Moisture Content (%)	Strength Activity Index (%)
2.42	2.6	2.47	20.0	98	0.5	70.6

3.2.3. Admixture

The GK-4A water-reducing admixture and GYQ air-entraining admixture were provided by Shijiazhuang Mayor An Yucai Building Materials Co., Ltd. (Shijiazhuang, China), and the performance test was carried out using the cement in Table 2. According to Table 4, the results indicated that the admixture and cement exhibited good compatibility. Also in Table 4, the difference in setting time refers to the difference between the setting time of the CSGR with admixture and those without admixture [30]. The ratio of compressive strength refers to the ratio between the compressive strengths of samples with admixture to those without admixture at different ages [31].

Table 4. Chemical and physical parameters of the admixtures.

Product	Chemical				Physical							
	pH	Cl^-	Na_2SO_4 (%)	Alkali (%)	Density (g/cm^3)	Bleeding Rate Ratio (%)	Water Reduction (%)	Difference in Setting Time (min)		Ratio of Compressive Strength (%)		
								Initial	Final	3 d	7 d	28 d
GK-4A	7.0–8.0	0.02	10	1.5	0.6	43.0	25.4	110	90	180	160	155
GYQ	7.0–8.0	0.03	13	1.3	0.8	25	6.2	90	115	100	98	94

3.2.4. Natural Aggregate

The riverbed sand, gravel and rock aggregate near the upstream of the Qianwei Navigation and Hydropower Hub Project was selected for the test. A total of 22 groups of particle screening tests were conducted based on gradations ranging from 150~80 mm, 80~40 mm, 40~20 mm, 20~5 mm, and below 5 mm. The gradation envelope of the gravel aggregate is depicted in Figure 4 (*S*1 to *S*22 represent the gradation of the material, *M*1, *M*2, and *M*3 represent the finest, average and coarsest gradation, respectively). Among these gradations, the proportion of extra-large stones (80~150 mm) ranges from 16% to 32%, averaging 22.3%. The proportion of boulders or large stones (40~80 mm) ranges

from 23% to 33%, with an average of 28.9%. Medium stones (20~40 mm) constitute 17% to 19%, averaging 18.9%. Small stones (5~20 mm) represent 7% to 14%, with an average of 11.1%. The proportion of sand (less than 5 mm) varies from 10% to 29%, averaging 18.8%. The coarsest gradation's sand ratio within the envelope line is 10.3%, while the finest gradation's sand ratio is 28.1%. The average fineness modulus of the sand is 1.44, indicating it is super fine sand, with an average mud content of 2.3%.

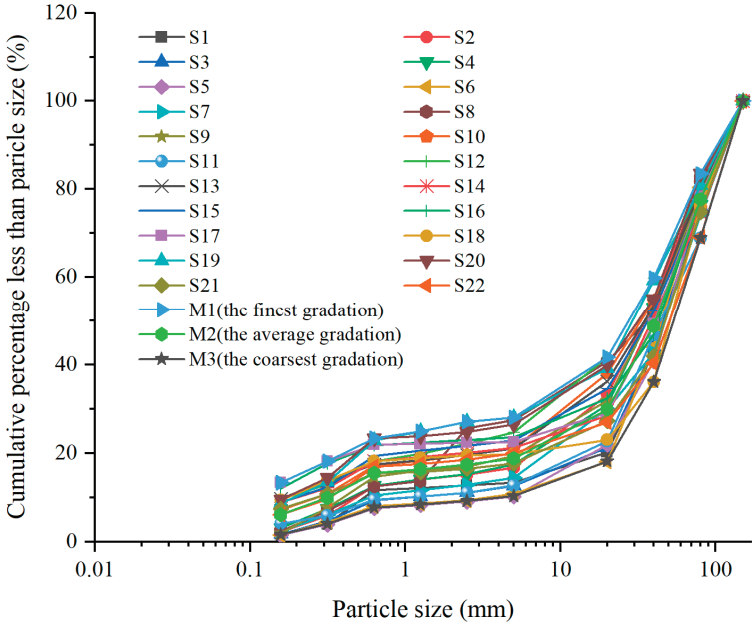

Figure 4. Particle size distribution curve of aggregate (Cumulative Sieve Residue).

3.3. The Mix Proportion of CSGR

According to the principle of 'double gradation and double strength' proposed by Jia Jinsheng, the mixing material is prepared and controlled [2]. In this process, the maximum particle size of coarse aggregate is set at 150 mm, with a cementitious material content of 80 kg/m^3. The vibrating–compacted (VC) value at the mixer's exit is regulated between 2 to 8 s without any admixture. The specific details are outlined in Table 5, where the schemes A1 and A2 represent *M*1 aggregate (the finest gradation, sand ratio is 28.1%, extra-large stones: large stones: medium stones: small stones = 27.5: 35.6: 23.3: 13.6) and *M*2 aggregate (the average gradation, sand ratio is 18.8%, extra-large stones: large stones: medium stones: small stones = 22.9: 33.0: 25.2: 18.9), respectively, for producing CSGR materials with the lowest strength, denoted as $C_{180}4$.

Table 5. Mix proportion of CSGR.

Scheme	Sand Ratio (%)	W/Cm Ratio	VC Value(s)	Quantity for 1 m^3 CSGR (kg)					Compressive Strength (MPa)		
				Water	Cement	Fly Ash	Coarse Aggregate	Fine Aggregate	28 d	90 d	180 d
*A*1	28.1	1.43	3.5	114	40	40	1649.39	644.61	2.7	5.5	6.5
*A*2	18.8	1.06	6.0	85	40	40	1942.30	449.70	6.0	11.2	12.4

3.4. The Vibrated Grout-Enriched CSGR

3.4.1. Slurry

The slurry material must exhibit excellent rheological properties and be capable of rapid diffusion within the laid CSGR, ensuring that the grouted and mixture attain the required degree of compaction to meet the design specifications for the anti-seepage protective layer. Typically, a higher water–cement ratio in the slurry enhances its rheological performance, but this necessitates a greater volume of slurry to achieve the desired design criteria. Therefore, a method was adopted by Feng et al. [32] to optimize the slurry mix ratio by minimizing the water–binder ratio, considering both slurry diffusion within the uniform mixture and its spread across the vibrating surface. The recommended slurry mix ratios are presented in Table 6. The rheology of the slurry is regulated through Marsh fluidity, maintained within the range of 6 to 12 s. Additionally, the specific gravity of the slurry, measured using a specific gravity meter, serves as a control index for the water–cement ratio during mixing.

Table 6. Mix proportion of slurry.

No.	1 m^3 Slurry Material Dosage (kg^3)				Marsh Fluidity (s)	Density (kg/L)
	Water	Cement	Water Reducing Admixture	Air Entraining Agent		
*A*580	540	1270	12.9	1.29	11	1.884

3.4.2. Determination of the Amount of Grouting

Utilizing the slurry compositions listed in Table 6 as the grouting material and incorporating the *A*1 and *A*2 CSGR mixtures from Table 4, six distinct slurry addition rates were established: 5%, 6%, 8%, 10%, 12%, and 14%, respectively. The prepared vibrated grout–enriched CSGR is marked as *GA*1 and *GA*2. Following the guidelines outlined in "Test code for hydraulic concrete" (SL/T 352-2020) [33], the 'indoor mixing and forming method of GERCC', was executed using a vibrating table. Various volumes of the specified slurry, as detailed in Table 6, were added to the machine-mixed CSGR. After undergoing three rounds of manual mixing, specimens were formed. Wet sieving ensured particles larger than 40 mm were not retained, and subsequent tests were conducted to measure the slump and air content of the resulting specimens.

The test results are depicted in Figure 5. Figure 5a indicates that the slump of the mixture post slurry addition ranges between 10 and 60 mm, while the indoor air content falls within the 4% to 5.8% range, signifying improved workability of the mixture. In Figure 5b, it is evident that the compressive strength of vibrated grout-enriched CSGR escalates with increasing slurry rate. At an 8% slurry rate, with a total cement content of 176 kg/m^3, the 90-day compressive strength exceeds 15 MPa, meeting design specifications (where *GA*1 surpasses a design strength of 15 MPa at an 80% strength guarantee rate, and *GA*2 exceeds a preparation strength of 17.9 MPa). Concurrently, the impermeability grade reaches W8 and the frost resistance grade reaches F100, as illustrated in Figure 5c,d, satisfying the requirements for impervious layer materials for dams with heights below 30 m (with a minimum allowable impermeability grade of W4). However, at a 12% slurry addition rate, the resulting vibrated grout-enriched CSGR contains a total cementitious material of 223 kg/m^3, achieving a 90-day compressive strength surpassing 20 MPa, with an impermeability grade of W11 and a frost resistance grade of F125. This meets the design criteria for impervious layer materials for dams, with heights ranging from 30 to less than 70 m (with a minimum allowable impermeability grade of W6). Notably, a 14% slurry addition rate increases the cementitious material content to 247 kg/m^3, significantly impacting economic feasibility and raising the risk of cracking, hence not recommended.

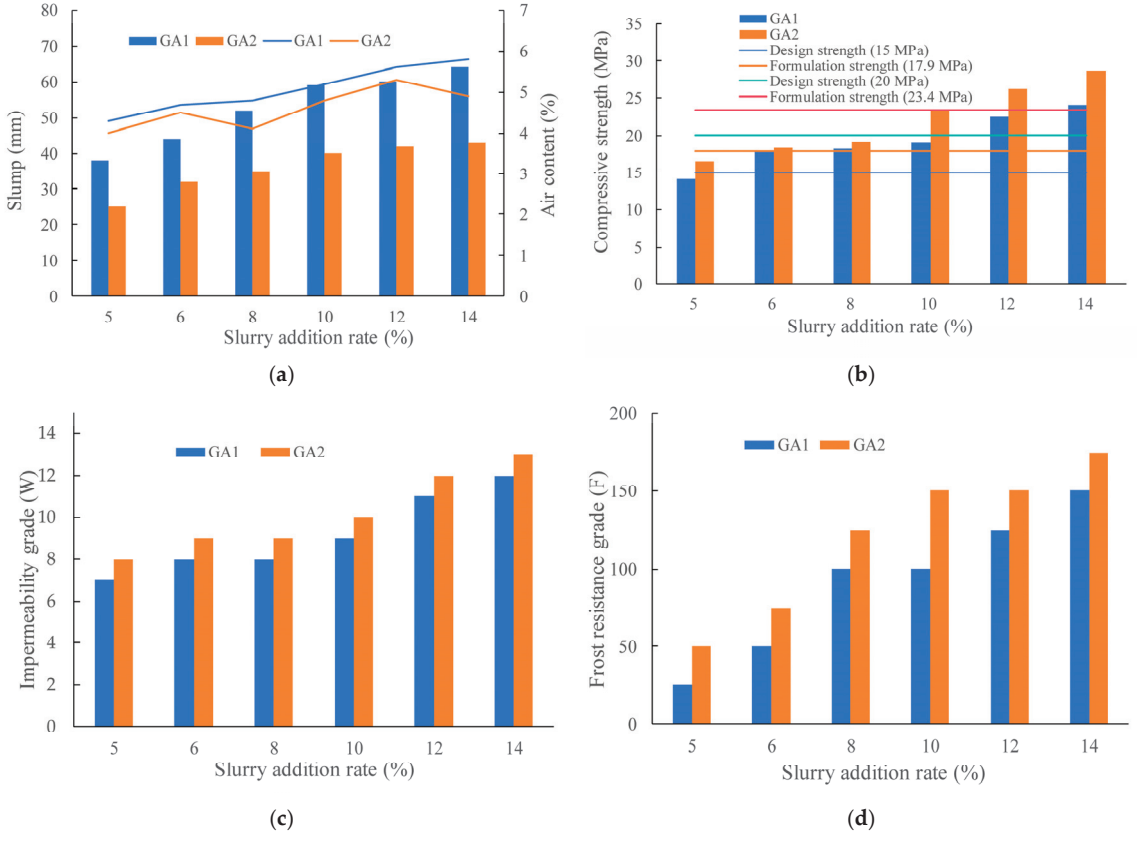

Figure 5. Test results of different slurry addition rates: (**a**) slump and air content; (**b**) 90-day compressive strength; (**c**) 90-day impermeability grade; (**d**) 90-day frost resistance grade.

4. Test of T-Shaped Surface Water Stop

4.1. Bond Strength Test

The pull-out test, according to "Test methods for building waterproofing coatings" (GB/T 16777-2008) [34], was utilized to examine the bonding efficacy of a T-shaped surface water stop and a protective anti-seepage layer surface.

4.1.1. Test Conditions

Concrete prism specimens measuring 400 mm × 100 mm × 100 mm were prepared for surface treatment using structural adhesive under various conditions, including air drying, surface brushing, and application of an interfacial agent after 24 h of drying and soaking. The pull-out test was conducted after 180 days under outdoor natural conditions (refer to Figure 6). Eight distinct working conditions were established for the test, each comprising three specimens and undergoing 12 pull-out tests, as outlined in Table 7. Notably, the interfacial agent used is a substance aimed at enhancing the bonding performance between the structural adhesive and wet concrete.

(**a**) (**b**)

Figure 6. Pull-out test of structural adhesive: (**a**) Pull-out test; (**b**) Typical case after failure.

Table 7. Pull-out test results under different working conditions.

No.	Specimen Situation	Brushed Surface	Applied Surface Coating Agent	Average Drawing Strength (MPa)	Destructed Sites
1	*A* [1]	✓	✓	2.32	Specimen body
2	*B* [2]	✓	×	3.87	Specimen body
3	*B*	✓	✓	3.91	Specimen body
4	*A*	×	✓	2.34	50% of the specimen body, 50% of the interface between the agent and the specimen
5	*A*	×	×	1.82	Between the interface agent and the specimen
6	*B*	×	✓	2.78	Between the interface agent and the specimen
7	*A*	✓	×	1.83	Specimen body
8	*B*	×	×	3.11	Between the interface agent and the specimen

[1] *A* is soaked in water for 24 h, and the surface is dried; [2] *B* is a dry specimen; ✓ means specified condition satisfied; × means specified condition not satisfied.

4.1.2. Test Results

The results are presented in Table 7. Across various conditions, the bonding strength of the structural adhesive exceeds 1.8 MPa. Applying an interfacial agent to the surface of wet specimens enhances the bonding strength to some degree, though it remains lower than that achieved under dry conditions. The presence of contaminants like surface debris on the concrete surface diminishes bonding strength with the structural adhesive, compromising the effectiveness of water sealing. The pull-out failure strength of the T-shaped water stop measures approximately 0.6 MPa, with failures typically occurring at the interface between the water stop and the structural adhesive. Hence, before the T-shaped water stop installation, it is crucial to brush or clean surface contaminants like debris and ensure dryness before applying the structural adhesive, followed by proper sealing post-installation.

4.2. Water Resistance Test

To the surface of precast concrete specimens with cracks, T-shaped surface water stops were adhered, and hydraulic pressure tests, according to "Hydrophilic expansion waterproofing sealant " (JG/T 312-2011) [35], were conducted on both the upstream and downstream sides to study the water pressure resistance of the water stops.

4.2.1. Test Scheme

The experiment was conducted in a test tank, with an inner diameter of 47.5 cm and a height of 50 cm, capable of withstanding internal pressures of over 2 MPa. The T-shaped surface water stop was installed in the penetrating seams of concrete specimens measuring 45 cm in diameter and 25 cm in height. The concrete specimens were placed into the test tank, and the surrounding seams were filled and sealed with sealant. The experimental

setup is depicted in Figure 7. After the structural adhesive had fully cured, the tank was filled with water, and hydraulic pressure was applied using automatic pressure loading equipment to maintain a stable pressure throughout the test period.

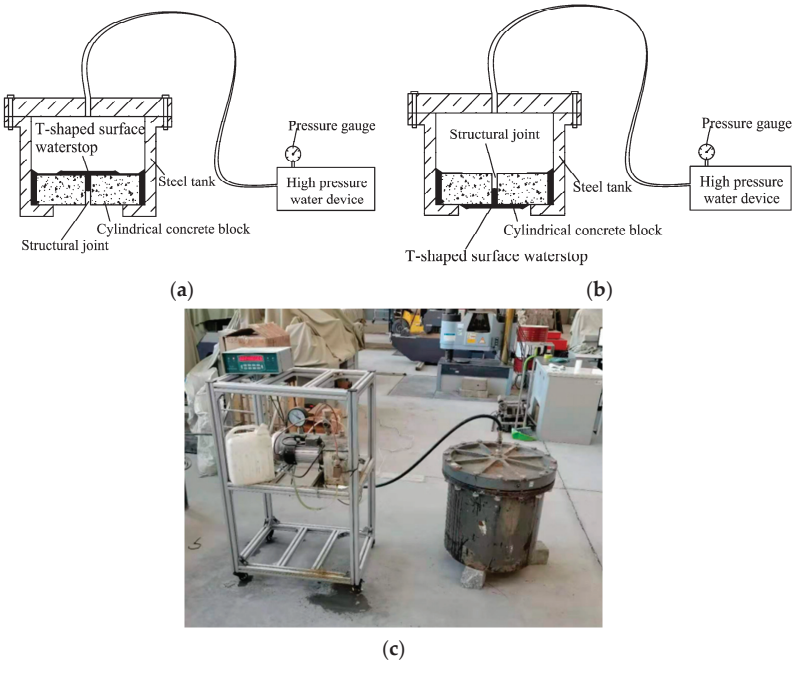

Figure 7. Water pressure test of T-shaped surface water stop: (**a**) Upstream water pressure test (**b**) Downstream water pressure test (**c**) Test device.

During the upstream water pressure test, the pressure was incrementally increased by 0.2 MPa each time, while during the downstream water pressure test, it was incremented by 0.1 MPa. Each pressure level was maintained for 2 h to stabilize. The water pressure was continuously increased until failure and leakage occurred in the water stop, or until reaching the pressure limit of 2 MPa, at which point the test was stopped. The maximum water pressure reached during the test was recorded. Three sets of tests were conducted, and the average value was calculated as the maximum load-bearing water pressure of the T-shaped water stop.

4.2.2. Test Results

The results of the water pressure resistance test are shown in Table 8. The test indicates that the T-shaped surface water stop exhibits a minimum resistance to an upstream water pressure of 1.6 MPa, providing excellent water sealing effectiveness for structural joints in medium and low CSGR dams with a dam height H < 70 m. The minimum resistance to downstream water pressure is 0.4 MPa. For safety considerations, a buried water stop design is also required after the installation of the T-shaped surface water stop.

Table 8. Results of the water pressure resistance test for the T-shaped surface water stop.

Test Classification	Failure Water Pressure/MPa		
	First Group	Second Group	Third Group
Upstream water pressure	1.6	2.0	2.0
Downstream water pressure	0.4	0.5	0.4

5. Research and Development of Special Grouting and Vibrating Equipment for CSGR

To address the practicality of specialized equipment, the developed equipment needs to possess features such as flexibility in movement, rapid grouting and vibrating from multiple directions and angles, as well as simultaneous grouting and vibrating capabilities. The grouting and vibrating capacity of a single device should reach 12 m^2/h. Therefore, a piece of specialized equipment, as shown in Figure 8, has been designed and developed. This equipment includes a control system, grouting and vibrating system, rail-type vibrating head, laser ranging system, etc. Construction can be divided into five stages, as shown in Figure 9. The first to the second stage requires 5 s (rapid insertion); the second to the third stage lasts for 40 s, including 20 s of grouting and 15 s of vibrating; the third to the fourth stage lasts for 19 s (slow extraction of vibrating); the fourth to the fifth stage takes 5 s. For typical CSGR levees with a paving area of 50 m long, 70 cm wide, and 70 cm thick, construction can be completed within 2 h using this equipment, significantly improving construction efficiency.

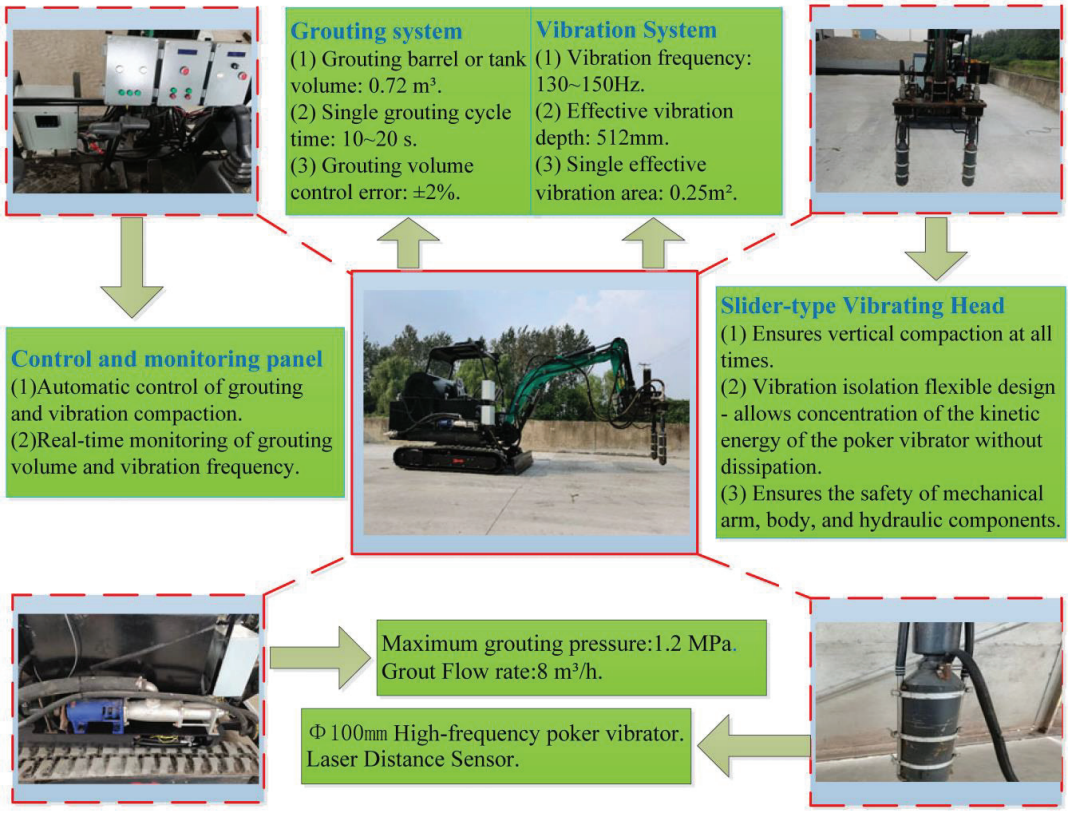

Figure 8. The grouting and vibrating equipment of CSGR.

The equipment is built upon a micro crawler hydraulic excavator platform, with the entire body occupying a footprint of 2.3 m in length and 1.35 m in width. Leveraging its mobility, rotation capability, hydraulic system, and work apparatus, it can maneuver flexibly on the dam surface without disrupting the compacting process of the dam body. The grouting and vibrating system composition and working principle of the equipment are shown in Figure 10. The equipment boasts a total engine power of 35 KW, which powers actions such as grouting, vibrating, and movement during construction. Grouting can be achieved through either automated quantified grouting or interactive human–machine

control for uniform grout distribution. A stable hydraulic drive is employed, controlled by a microcontroller that actuates electromagnetic directional valves to enable the forward rotation of hydraulic motors, propelling the screw pump to discharge grout. A rotary encoder monitors the pump's rotation speed, regulating the grout output accordingly. To prevent slurry sedimentation and pipe blockage, a microcontroller governs a three-way actuator for slurry circulation, facilitating both injection and backflow. Additionally, a low-speed stirring device is installed within the slurry tank to maintain slurry consistency. Vibrating is executed using a dual-head high-frequency vibrator with an adjustable vibration frequency, driven by an engine-powered belt drive system for frequency control. Moreover, grouting pipes are directly welded and integrated on both sides of the poker vibrator. During operation, the vibrator is inserted vertically into the loosened CSGR, enabling simultaneous vibrating and grouting. Laser distance measurement is utilized during the vibrating to maintain a safe distance between the template and the vibrating rod, thereby preventing damage to the template. After each grouting and vibrating work, the whole slurry pipeline should be cleaned in time by pumping clear water to avoid slurry precipitation and pipe blockage, and the pulley group with vibrating head should be deeply cleaned and lubricated. Regularly inspect and maintain the lubrication system, filtration system, hydraulic system and electrical system of the entire equipment, replace worn parts in a timely manner, ensure that all safety functions are functional, and maintain detailed maintenance activity logs.

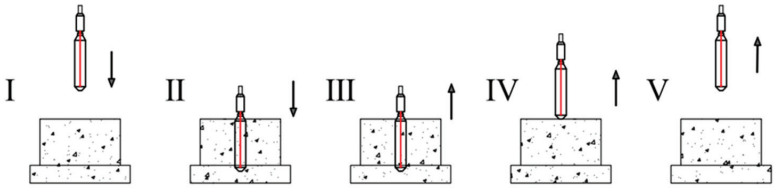

Figure 9. Working state of grouting and vibrating equipment (I is the ready stage, II is the insertion stage, III is the grouting and vibrating stage, IV is the redraw stage and V is back to the ready stage for the repetitions of the cycle).

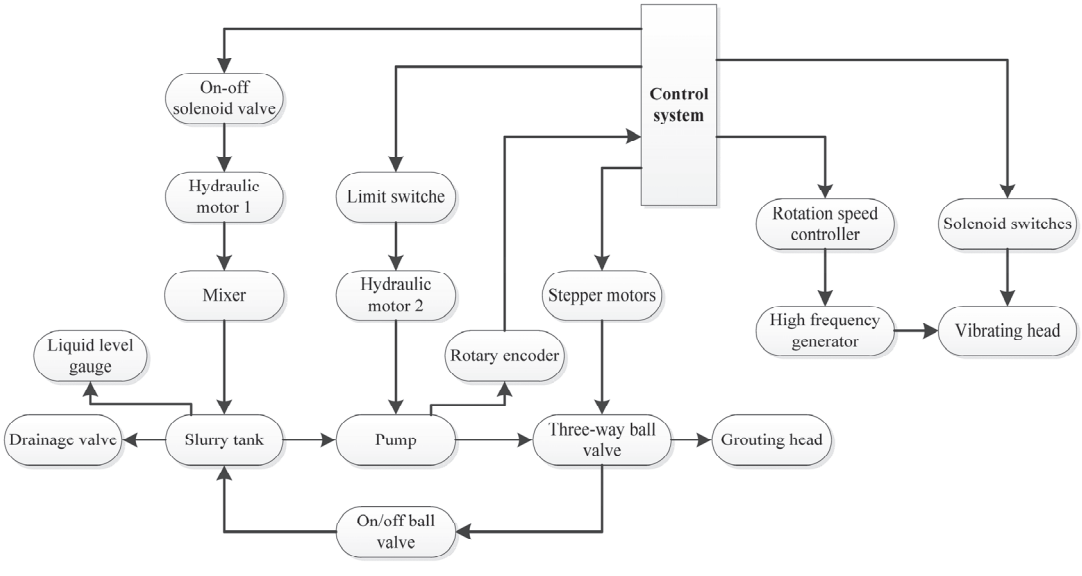

Figure 10. Design system composition and working principle of the equipment.

6. On-Site Constructions of the Vibrated Grout-Enriched CSGR

6.1. On-Site Test

The dam aggregate consists of the natural sand, gravel and rock material excavated from the riverbed. During construction, it is not subjected to screening or washing, and particles larger than 150 mm are removed. To ensure safe construction practices, digital mixing and intelligent control techniques can be employed [6]. Previous indoor testing has demonstrated that when the slurry addition rate is 8%, the vibrating–compacted slurry CSGR material meets the design requirements of $C_{90}15W6F50$. However, in actual construction, the characteristics and construction nuances of CSGR materials often result in deviations from indoor test results. Hence, field testing is conducted to determine the optimal slurry addition rate.

The field rolling test section is situated along the dam axis, spanning from pile number K2 + 330.38 to K2 + 425.38 within the dam body. Upon the completion of the test, this section is directly integrated into the CSGR dam for permanent structures. The specific area for the vibrated grout-enriched CSGR test is delineated in Figure 11a, focusing on the dam between pile numbers K2 + 330.38 and K2 + 360.38. The test procedure employs full-section flat paving, with a paving layer thickness of approximately 50 cm.

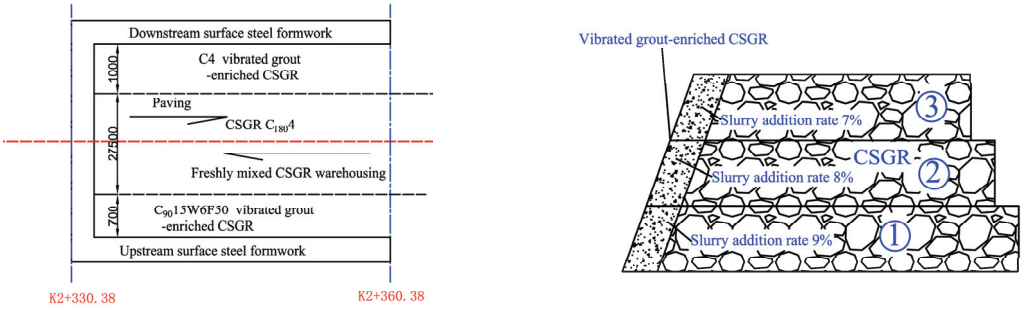

Figure 11. The layout of the field test of vibrated grout-enriched CSGR: (**a**) test area (**b**) slurry adding test scheme.

For the vibrated grout-enriched CSGR test area, which constitutes the upstream protective layer, the width measures 70 cm. The special grouting and vibrating equipment operates according to the configuration depicted in Figure 9. From bottom to top, the slurry rates are set at 9%, 8%, and 7%, as illustrated in Figure 11b.

The test results are presented in Table 9, indicating that the on-site strength of CSGR meets the design specifications for Cemented Material Dam (CMD) engineering. Table 10 displays the test results for CSGR with added slurry and vibration. It is observed from Table 10 that the slurry mix ratio prepared indoors aligns with the engineering requirements for vibrated grout-enriched CSGR. When determining the amount of slurry for construction cost considerations, a preference should be given to an 8% grouting ratio. However, if quality assurance is prioritized, a 9% slurry addition rate is recommended. At this rate, the total cementitious material quantity is 187 kg/m^3, with a total water demand ranging from 126 kg/m^3 to 152 kg/m^3.

Table 9. Test results of CSGR mixture.

Layer Number	VC Value/s	Compressive Strength /MPa	
		Minimum Value	Mean Value
①	10.3	5.6	7.6
②	8.7	4.2	7.1
③	6.0	4.5	8.3

Table 10. Test results of different slurry addition rate.

Slurry Addition Rate (%)	Surface Quality	Compressive Strength (MPa)		Impermeability Grade	Freeze Resistance Grade
		Minimum Value	Mean Value		
7%	surface less slurry	12.2	15.8	W8	F50
8%	the surface can be slurried, the slurry is suitable	14.4	17.4	W9	F50
9%	the surface can be slurried, the slurry is rich	15.2	19.8	W11	F75

6.2. Application

The Tangba Protection dam has a total length of 2.7 km, with a crest elevation of 336.10 m and the filling volume of CSGR material reached 373,000 m^3. The vibrated grout-enriched CSGR with a slurry rate of 9% was used in the protection and seepage control layer on both the upstream and downstream areas. Through sequential rolling and layer-by-layer construction, the total amount of vibrated grout-enriched CSGR used is 20,867 m^3. Figure 12 illustrates the completed Tangba Protection Dam. The quality test results in the construction process are presented in Table 11. The protective layer of the dam meets the design requirements of C_{90}15W6F50. The T-shaped surface water stop totals 10,163 m. Its installation and fixation were straightforward, ensuring fast construction speed, easy replacement and repair in subsequent stages (Figure 13).

Figure 12. The completion of Tangba CSGR dam.

Table 11. Quality test results of vibrated grout-enriched CSGR.

	Types of CSGR	Vibrated Grout-Enriched CSGR C_{90}15W6F50
Design index	Impermeability grade	W6
	Compressive strength guarantee rate/%	80
	Compressive strength/MPa	15
	Frost resistance grade	F50
Measured value	Impermeability grade	>W6
	Compressive strength guarantee rate/%	88
	Minimum strength/MPa	11.8
	Average strength/MPa	18.6
	The standard deviation of compressive strength	3.8
	The qualified rate of frost resistance at design age/%	100

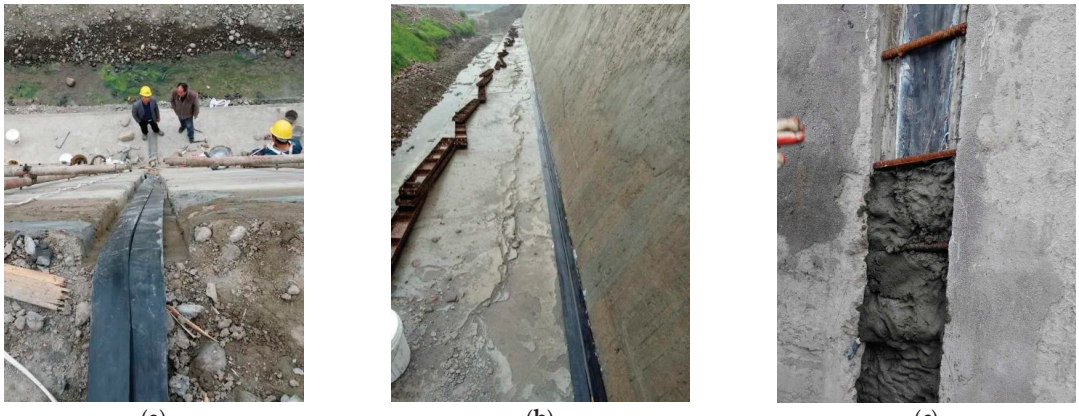

(**a**) (**b**) (**c**)

Figure 13. The installation of the T-shaped surface water stop: (**a**) transverse joint water stop (**b**) water stop between protection layer and toe slab (**c**) mortar cover protection.

From 15 to 16 May 2020, the first phase of water storage was completed, with the water level rising from 326 m to 330 m. Subsequently, from 15 to 16 September 2021, the second phase of water storage concluded, resulting in the water level increasing from 330 m to 335 m (see Figure 14). The water storage operations have been ongoing for nearly four years. Notably, optical fiber leakage measuring devices installed after the transverse joint have detected no leakage points, indicating the commendable comprehensive anti-seepage performance of the dam body. It is worth highlighting that during the impoundment period, the levee endured the '8 18' catastrophic flood in 2020. Despite the large-scale disaster in Leshan and Qianwei, it effectively withstood the excessive flood, ensuring the safety of life and property for over 11,000 residents and more than ten major enterprises in Tangba Township. The safety and reliability of the dam have met the anticipated standards.

Figure 14. The impoundment of the flood control levee to an elevation of 335 m.

7. Discussion

The costs of utilizing conventional concrete (CVC), grout-enriched roller-compacted concrete (GERCC), and vibrated grout-enriched CSGR, solely in terms of factory material costs (reference unit price: P.O 42.5 grade ordinary Portland cement 450 yuan/t, fly ash 120 yuan/t, high-efficiency water reducing agent 8000 yuan/t, air-entraining agent 13,000 yuan/t.), excluding expenses like transportation and mixing, are compared in Table 12. From this comparison, it becomes evident that CVC and GERCC are the most expensive options, whereas vibrated grout-enriched CSGR stands out for its significantly lower cost attributed to the use of on-site gravel materials. The cubic meter cost of vibrated

grout-enriched CSGR is less than 50% of CVC, and vibrated grout-enriched CSGR and its construction benefits from the streamlined process of rolling out the CSGR dam body, which reduces interference and enhances promotional advantages.

Table 12. Cost comparison of different protection and seepage control layers.

Material	The Amount of Cementitious (kg/m^3)		Cost per Cubic Meter (Yuan)	Construction Technology	Remarks
	Cement	Fly Ash			
CVC	140	60	310	Vibration, needs grading of aggregate and has interference with CSGR rolling construction.	The average aggregate is 90 yuan per ton
GERCC	151	36	293	Grouting and vibrating, needs grading of aggregate and has interference with CSGR rolling construction	The average aggregate is 90 yuan per ton
Vibrated grout-enriched CSGR	151	36	142	Grouting and vibrating, needs grading of aggregate and has less interference (high seamless transition) with CSGR rolling construction.	The average aggregate is 20 yuan per ton

The vibrated grout-enriched CSGR is produced by grouting and vibrating directly onto the pre-paved CSGR material. In contrast to CVC, it plays a pivotal role in coordinating transition deformations at the interface between the impermeable layer and the main dam. This not only bolsters the continuity and integrity of the dam structure but also mitigates the local damage and stripping caused by abrupt shifts in material characteristics. Moreover, vibrated grout-enriched CSGR minimizes the variety of materials required at batching plants, thereby boosting production efficiency and decreasing construction interference. As a result, it emerges as an optimal choice for future CSGR dam protection and seepage control layers. However, ongoing research is essential to comprehensively understand its long-term material performance and engineering applications. The successful deployment of vibrated grout-enriched CSGR at the Tangba Protection Dam serves as a promising case study for similar projects.

This study delves into the influence of slurry quantity on properties of vibrated grout-enriched CSGR material and construction efficacy, refining conventional joint sealing methods and investigating water sealing effectiveness. Nonetheless, challenges remain in utilizing this technology in 100-m-high dams, prompting the consideration of external flexible geomembrane installation for taller structures. Variations in geographical applicability underscore the need for further research into more frost-resistant types of cemented sand, gravel and rock. These considerations highlight avenues for future advancements in CSGR technology to enhance dam construction practices.

8. Conclusions

This paper introduces a newly developed and successfully applied method for utilizing vibrated grout-enriched CSGR as the protective and seepage control layer in CSGR dams, in conjunction with a T-shaped water stop structure. Additionally, specialized construction equipment for slurry addition and CSGR vibration has been developed. The main conclusions are as follows:

(1) Using the cement slurry with a water–cement ratio of 0.42, under the grouting rates of 8% and 12%, the $C_{180}4$ dry-hard cemented sand, gravel and rock with a VC value of 2~8 s can be changed into the vibro-cemented sand, gravel and rock with a slump of 10–60 mm grade $C_{90}15W8F100$ and $C_{90}20W11F125$, respectively.

(2) A strong bonding effect exists between the new T-shaped surface water stop and the protective layer, with a bonding strength exceeding 1.8 MPa. The water stop surface

exhibits an anti-water pressure ability greater than 1.6 MPa, effectively sealing joints in CSGR dams.

(3) Specially developed CSGR grouting and vibrating equipment can be adapted for use in the construction of the upstream and downstream impermeable protective layers of CSGR under conditions characterized by limited surface area and large particle size.

(4) When the height of the dam is low, Cemented Sand, Gravel and Rock dams can be constructed on non-rock foundations. To ensure project safety, a design approach is employed that separates the cutoff wall from the dam body, and utilizes a T-shaped surface water stop design to prevent mutual interference.

The novel technique has demonstrated significant economic, environmental, and safety advantages in the Minjiang Navigation and Hydropower Qianwei Project and the Shaping I Hydropower Station on the Dadu River. The developed technique will offer immense sustainability when adopted in subsequent projects: Firstly, it will reduce construction costs by replacing traditional concrete with a vibrated grout-enriched CSGR mixture, utilizing locally available materials and reducing cement usage through fly ash substitution. Secondly, it will optimize construction processes by simplifying the construction of the protection and impermeable layer, thereby reducing time and disruptions. Thirdly, it will provide environmental benefits by minimizing the carbon footprint, thus promoting eco-friendly practices. Lastly, safety shall be enhanced through specialized equipment automation and the use of the developed T-shaped surface water stop, ensuring greater stability of dam structures.

Author Contributions: Formal analysis, W.A.B.; Investigation, Y.W. (Yang Wang); Resources, B.J.; Writing—original draft, Y.W. (Yangfeng Wu); Writing—review and editing, Y.W. (Yangfeng Wu) and J.J.; Supervision, J.J. and C.Z.; Funding acquisition, J.J. All authors have read and agreed to the published version of the manuscript.

Funding: This research is financially supported by the National Key Research and Development Plan of China under Grant No. 2018 YFC0406801 and by State Key Laboratory of Simulation and Regulation of Water Cycles in River Basins.

Institutional Review Board Statement: Not applicable.

Informed Consent Statement: Not applicable.

Data Availability Statement: The original contributions presented in the study are included in the article, further inquiries can be directed to the corresponding author.

Conflicts of Interest: The authors declare no conflicts of interest.

Abbreviations

The following abbreviations are used in this manuscript:

CSGR	Cemented Sand, Gravel and Rock
CVC	Conventional concrete
GERCC	Grout-Enriched Roller-compacted concrete
VC	Vibrating–compacted
CMD	Cemented Material Dam
CSG	Cemented Sand and Gravel
(ICOLD)	International Committee on Large Dams
CMD	Cemented Material Dam
HCC	Hardfill, Cemented Sand and Gravel (CSG), Cemented Sand, Gravel and Rock (CSGR)
RCC	Roller-compacted concrete

References

1. Jia, J.; Zheng, G.; Ma, F. Studies on cemented material dam and its application in China. In Proceedings of the 6th International Symposium on Roller Compacted Concrete (RCC) Dams, Zaragoza, Spain, 23–25 October 2012.
2. *Chinese Standards SL678-2014*; Technical Guideline for Cemented Granular Material Dams SL678. China Water & Power Press: Beijing, China, 2014. (In Chinese)

3. Jia, J.; Lino, M.; Jin, F.; Zheng, C. The Cemented Material Dam: A New, Environmentally Friendly Type of Dam. *Engineering* **2016**, *2*, 490–497. [CrossRef]
4. Londe, P.; Lino, M. The faced symmetrical hardfill dam: A new concept for RCC. *Int. Water Power Dams Constr.* **1992**, *44*, 19–24.
5. Sakamoto, T.; Yoshida, H.; Yasuda, N.; Maeda, K.; Takei, A. The design and construction of trapezoidal CSG dams in Japan. *Hydropower Dams* **2017**, *24*, 68–75.
6. Jia, J.; Ding, L.; Wu, Y.; Zhao, C.; Zhao, L. Research and application of cemented sand and gravel technology based on soft rock. *Appl. Sci.* **2023**, *13*, 4626. [CrossRef]
7. Sina, K.; Farshbaf, A. A new solution for water-tightening of the cemented sand-gravel (CSG) hardfill dams. *Innov. Infrastruct. Solut.* **2023**, *8*, 173.
8. Chen, J.; Liu, P.; Xu, Q.; Li, J. Seismic analysis of hardfill dams considering spatial variability of material parameters. *Eng. Struct.* **2020**, *211*, 110439. [CrossRef]
9. Ding, Z.; Xue, J.; Zhu, X.; Wang, J. Optimization of CSG dam profile based on response surface methodology. *Case Stud. Constr. Mater.* **2022**, *17*, e01430. [CrossRef]
10. Guo, L.; Zhang, J.; Guo, L.; Wang, J.; Shen, W. Research on Profile Design Criteria of 100 m CSG Dams. *Case Stud. Constr. Mater.* **2022**, *16*, e01137. [CrossRef]
11. Cai, X.; Zhang, Y.; Guo, X.; Zhang, X.; Li, F.; Zhang, T. Review on research progress of cemented sand and gravel dam. *Sci Eng Compos Mater.* **2022**, *29*, 438–451. [CrossRef]
12. *Chinese Standards DL/T 5788-2019*; Construction Specification for Hydraulic Grout Enriched Vibrated Concrete DL/T 5788. China Electric Power Press: Beijing, China, 2019. (In Chinese)
13. Musselman, E.; Flynn, R.; Zimmer, G.; Young, J. Field Trial for Air Entrained Grout Enriched Roller Compacted Concrete. In Proceedings of the 2nd International Seminar on Dam Protection against Overtopping, Fort Collins, CO, USA, 7–9 September 2016.
14. Amir, A.; Ali, N.; Mohsen, G.; Seyed, H. Seismic evaluation of cemented material dams—A case study of Tobetsu Dam in Japan. *Earthq. Struct.* **2016**, *10*, 717–733.
15. Kim, S.; Choi, W.; Kim, Y.; Shin, J.; Kim, B. Investigation of Compressive Strength Characteristics of Hardfill Material and Seismic Stability of Hardfill Dams. *Appl. Sci.* **2023**, *13*, 2492. [CrossRef]
16. Guillemot, T.; Lino, M. Design and Construction Advantages of Hardfill Symmetric Dam—Case Study: Safsaf Dam in Eastern Algeria. In Proceedings of the 6th International Symposium on Roller Compacted Concrete (RCC) Dams, Zaragoza, Spain, 23–25 October 2012.
17. Xu, Y.; Hao, J. Development and prospect of slab joint waterstop technology of CFRDs. *J. China Inst. Water Resour. Hydropower Res.* **2018**, *16*, 457–465. (In Chinese)
18. Cho, B.H.; Nam, B.H.; Seo, S.; Kim, J.; An, J.; Youn, H. Waterproofing performance of waterstop with adhesive bonding used at joints of underground concrete structures. *Constr Build Mater.* **2019**, *221*, 491–500. [CrossRef]
19. Ma, H.; Chi, F. Technical Progress on Researches for the Safety of High Concrete-Faced Rockfill Dams. *Engineering* **2016**, *2*, 332–339. [CrossRef]
20. Sun, Z.; Li, J.; Fei, X. Flexible water stop structure with flat cover on the surface of concrete face joint in cold area. *Water Power* **2019**, *45*, 50–53. (In Chinese)
21. Zeinizadeh, A.; Mirzabozorg, H.; Noorzad, A.; Amirpour, A. Hydrodynamic pressures in contraction joints including waterstops on seismic response of high arch dams. *Structures* **2018**, *14*, 1–14. [CrossRef]
22. Wu, Y.; Jia, J.; Wang, Y.; Zheng, C.; Zhao, L.; Jia, B. Investigation on Hydraulic Fracturing and Flexible Anti-Hydrofracturing Solution for Xiaowan Arch Dam. *Appl. Sci.* **2023**, *13*, 9302. [CrossRef]
23. Wang, C.; Luo, W.; Xu, B. The Control System Design of Concrete Mixing Station based on PLC. In Proceedings of the 2020 IEEE International Conference on Information Technology, Big Data and Artificial Intelligence (ICIBA), Chongqing, China, 6–8 November 2020; pp. 1498–1501.
24. Nagy, P.B.; Pistrol, J.; Kopf, F.; Adam, D. Integrated compaction control based on the motion behavior of a deep vibrator. *Transp. Geotech.* **2021**, *28*, 100539. [CrossRef]
25. Wan, D.; Guan, T.; Yang, S. Intelligent monitoring of concrete vibration quality under the integrated perception of space-air-ground. *J. Chin. Ceram. Soc.* **2023**, *51*, 1219–1227. (In Chinese)
26. Wang, Y.; Jia, J.; Zheng, C.; Jia, Y.; Liu, Z. A Water Stop Structure and Its Construction Method. CN 105019404A, 29 June 2015. (In Chinese).
27. Chen, Z.; Feng, J.; Li, R.; Wang, Y.; Peng, F.; Li, K. Field observation and numerical modelling of supersaturated dissolved gas at river confluence. *Ecol. Model.* **2022**, *471*, 110017. [CrossRef]
28. *ASTM C 618-03*; Standard Specification for Coal Fly Ash and Raw or Calcined Natural Pozzolan for Use in Concrete. ASTM International: West Conshohocken, PA, USA, 2023.
29. *ASTM C109*; Standard Test Method for Compressive Strength of Hydraulic Cement Mortars (Using 2-in. or [50-mm] Cube Specimens). ASTM International: West Conshohocken, PA, USA, 2023.
30. *ASTM C403/C403M*; Standard Test Method for Time of Setting of Concrete Mixtures by Penetration Resistance. ASTM International: West Conshohocken, PA, USA, 2016.
31. *ASTM C39/C39M*; Standard Test Method for Compressive Strength of Cylindrical Concrete Specimens. ASTM International: West Conshohocken, PA, USA, 2021.

32. Feng, W.; Jia, J.; Ma, F. Study on durability of dam materials and new-type protective materials for cemented sand and gravel dam. *Shuili Xuebao* **2013**, *44*, 500–504. (In Chinese)
33. *Chinese Standards SL/T 352-2020*; Test Code for Hydraulic Concrete SL/T 352. China Water & Power Press: Beijing, China, 2020. (In Chinese)
34. *Chinese Standards GB/T 16777-2008*; Test Methods for Building Waterproofing Coatings GB/T 16777. Standards Press of China: Beijing, China, 2008. (In Chinese)
35. *Chinese Standards JG/T 312-2011*; Hydrophilic Expansion Waterproofing Sealant JG/T 312. Standards Press of China: Beijing, China, 2011. (In Chinese)

applied sciences

MDPI

Article

An Evolutionary Neural Network Approach for Slopes Stability Assessment

Joaquim Tinoco [1,*], António Gomes Correia [1], Paulo Cortez [2] and David Toll [3]

[1] Department of Civil Engineering, Advanced Production and Intelligent Systems (ARISE), Institute for Sustainability and Innovation in Structural Engineering (ISISE), University of Minho, 4800-058 Guimarães, Portugal; agc@civil.uminho.pt
[2] Department of Information Systems, ALGORITMI Research Center, University of Minho, 4800-058 Guimarães, Portugal; pcortez@dsi.uminho.pt
[3] Department of Engineering, University of Durham, Durham DH1 3LE, UK; d.g.toll@durham.ac.uk
* Correspondence: jtinoco@civil.uminho.pt

Abstract: A current big challenge for developed or developing countries is how to keep large-scale transportation infrastructure networks operational under all conditions. Network extensions and budgetary constraints for maintenance purposes are among the main factors that make transportation network management a non-trivial task. On the other hand, the high number of parameters affecting the stability condition of engineered slopes makes their assessment even more complex and difficult to accomplish. Aiming to help achieve the more efficient management of such an important element of modern society, a first attempt at the development of a classification system for rock and soil cuttings, as well as embankments based on visual features, was made in this paper using soft computing algorithms. The achieved results, although interesting, nevertheless have some important limitations to their successful use as auxiliary tools for transportation network management tasks. Accordingly, we carried out new experiments through the combination of modern optimization and soft computing algorithms. Thus, one of the main challenges to overcome is related to the selection of the best set of input features for a feedforward neural network for earthwork hazard category (EHC) identification. We applied a genetic algorithm (GA) for this purpose. Another challenging task is related to the asymmetric distribution of the data (since typically good conditions are much more common than bad ones). To address this question, three training sampling approaches were explored: no resampling, the synthetic minority oversampling technique (SMOTE), and oversampling. Some relevant observations were taken from the optimization process, namely, the identification of which variables are more frequently selected for EHC identification. After finding the most efficient models, a detailed sensitivity analysis was applied over the selected models, allowing us to measure the relative importance of each attribute in EHC identification.

Keywords: slope stability condition; soft computing; genetic algorithms; imbalanced data

Citation: Tinoco, J.; Gomes Correia, A.; Cortez, P.; Toll, D. An Evolutionary Neural Network Approach for Slopes Stability Assessment. *Appl. Sci.* **2023**, *13*, 8084. https://doi.org/10.3390/app13148084

Academic Editor: Arcady Dyskin

Received: 6 June 2023
Revised: 5 July 2023
Accepted: 8 July 2023
Published: 11 July 2023

1. Motivation and Background

Transportation infrastructures are a key and strategic asset in our day-to-day life. In fact, nations frequently spend money maintaining or improving their transportation networks in an effort to create more secure and effective infrastructure. The main issue currently facing nations with highly developed transportation systems is how to keep it running in all circumstances. How to identify the crucial network components that need funding to be allocated for their upkeep or repair is a crucial issue from the perspective of managing a transportation network. As a result, and in order to maximize the budget that is available, decision support tools are needed to assist decision makers in identifying such key network components and selecting the optimal course of action for allocating the budget that is available. Slopes are possibly the component in the framework of transportation networks, particularly for railways, for which their failure can have the

largest effects on a number of levels, including potentially significant economic damage and loss of life. As a result, it is critical to create techniques to spot possible issues before they become failures.

Many models and approaches have been proposed over time to identify slope failures. However, since the majority were designed for natural slopes, they have considerable drawbacks when used on constructed (human-made) slopes. Additionally, they have limited network level applicability because the majority of the current systems were developed using small databases or based on individual case studies. The need for data from complex tests or costly monitoring systems represents an extra obstacle to the application of the majority of current slope stability assessment systems. Below, we summarize some approaches found in the literature for slope failure detection.

The current methods for evaluating slope stability were compiled by Pourkhosravani and Kalantari [1], which they classify as limit equilibrium (LE) methods, numerical analysis methods, artificial neural networks, and limit analysis methods. Recently, Ullaha et al. [2] also published a brief review of the actual methods for slope stability assessments, having dived them into five distinct groups instead of four. Among all these approaches, the literature has emphasizedthe finite elements methods [3], reliability analysis [4,5], and those approaches based on machine learning algorithms [6–25]. More recently, some new approaches have been proposed based on the vector sum method [26,27]. In 2015, Pinheiro et al. [28] developed a new and versatile statistical system based on the evaluation of various factors affecting the stability of a given slope. By weighting the different factors, a final indicator of the slope stability can be determined. Later, in 2016, an evidence-based asset management strategy was proposed by Power et al. [29], which is comprised of the establishment of a risk-based prioritization matrix for all earthwork assets and the quantification of the probability of earthwork failure.

These and numerous other approaches that can be found in the literature, from the perspective of large-scale network management, are constrained to a limited applicability domain and reliant on information that can be difficult and expensive to obtain. In addition, determining whether a slope will fail or not is frequently a difficult task involving many variables and high dimensionality. In order to work around these kinds of restrictions and aid in the decision-making process for large-scale network management, a first endeavor was recently made [30,31] by comparing two popular types of data mining (DM) algorithms: artificial neural betworks (ANNs) [32,33] and support vector machines (SVMs) [34]. When compared with other simpler learning models (e.g., multiple regression or logistic regression models), the ANN and SVM models are more flexible learners, being capable of learning complex input-to-output mappings. We particularly note that the two initial slope stability prediction studies [30,31] assumed a fixed set of selected input variables that could easily be collected during routine inspection activities. The main goal was to compare two learning models (ANN and SVM) for both regression and classification tasks. The preliminary studies [30,31] provided some useful insights that helped to design the approach proposed in this work. Firstly, the best predictive results in both works were produced by the ANN model when performing a nominal classification. Secondly, while interesting predictive results were achieved by the ANN model, the performance was far from ideal. In particular, a high error was obtained for the infrequent EHC (earthwork hazard category) classes (which are related to more hazardous conditions). Thirdly, although the implementation of resampling techniques to handle the imbalanced data issue (which arises as the majority of slopes are in perfect condition) has not always been effective; in some instances, it aided the algorithms in better learning the problem. Such an asymmetric distribution of the data represents a key challenge of the work since it affects the model's response over all four EHC classes. Fourthly, it was observed that the identification of slope stability is governed by a specific group of characteristics. Figure 1 compares the performance of ANN models when identifying the slope stability of rock and soil cuttings as well as soil embankments based on recall, precision, and $F_{1-score}$ metrics. More information about the achieved performance can be found in the published works [30,31]. As demonstrated, and taking

recall measure as a benchmark, an exceptional prediction ability was observed for class "A". Class "B" also exhibited strong accuracy. Nevertheless, for classes "C" and "D", which had a higher probability of failure, the attained performance fell short of expectations, specifically for rock cuttings.

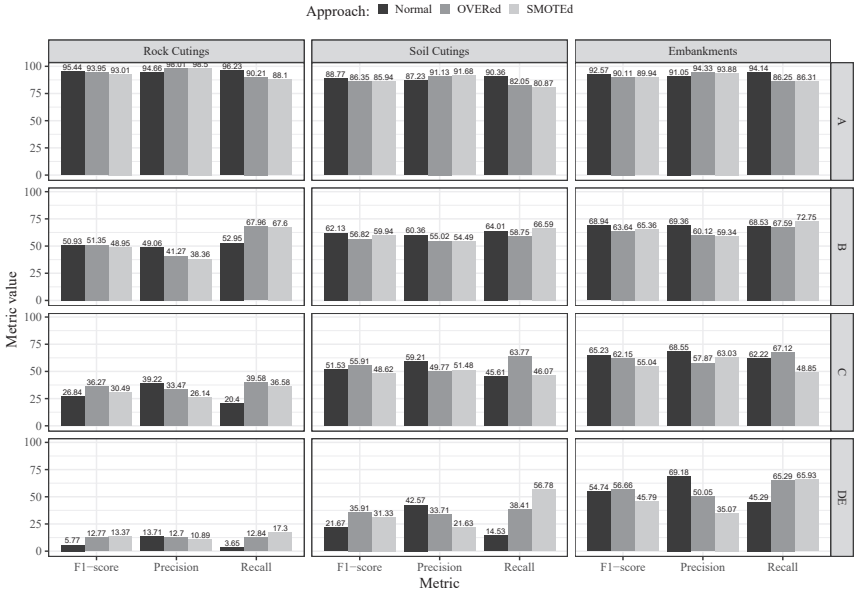

Figure 1. Comparison of ANN models based on recall, precision, and $F_{1-score}$ according to a nominal classification strategy for predicting slope stability of rock and soil cuttings and soil embankments (adapted from [30,31]).

Following the same strategy adopted during the first attempt (i.e., the use of information that can be readily obtained through routine visual inspections [30,31]), the researchers conducted additional tests. In this research, we propose a novel method to improve the performance of models identifying the stability of rock and soil cuttings, as well as embankments. Thus, this paper combines two artificial intelligence (AI) techniques: genetic algorithms (GA), which are popular metaheuristics methods for optimization, and ANNs, which have non-linear learning capabilities. This combination, known as an evolutionary neural network (ENN), allows us to gain interesting capabilities from both AI techniques. In particular, GA is used to perform a search of the best set of input features, which represents one of the major challenges of this work, thus performing automatic feature selection. When compared with other GA input feature optimization works (e.g., [35]), the novelty of our GA approach is that we adopt Pareto curve optimization, allowing us to simultaneously optimize performance measures for all four EHC classes (and not just a single overall performance measure). We note that Pareto curve optimization methods need to keep track of a population of diverse solutions, and GAs are a natural and popular approach for such multi-objective optimization tasks [36]. As for the ANN, it uses a selected set of features as inputs and performs a non-linear mapping with the target output, allowing us to automatically obtain data-driven multi-class classifiers. As underlined above, it is expected that by using a reduced number of features to feed the ANNs, their predictive performance will improve. Finally, a detailed sensitivity analysis was applied to the best ENN models for each one of the three types of slopes, allowing us to identify the key variables in the identification of slope stability.

In conclusion, the primary objective of this study is to develop a simple and rapid method to identify the stability level of a given slope based on visual information that can

be readily obtained during routine inspections. However, it is important to note that, from a network management perspective, the use of visual data is enough for the identification of critical network zones, for which additional information can be later collected to conduct a more detailed stability analysis, which is beyond the scope of this study. This innovative approach aims to aid the administrative organizations of railway networks in allocating existing resources to rank assets based on their stability.

2. Data Characterization

As was already indicated, this work combines ANNs and GA with the goal of creating novel models to identify their stability, from this point referred to as EHC [29], of rock and soil cuttings as well as soil embankments.

The EHC system is composed of four levels, "A", "B", "C", and "D", where the probability of failures increases from class "A" to "D". Three distinct databases were compiled for training and testing purposes, each containing information gathered during routine inspections and supplemented with geometric, geological, and geographic data for each slope. All three databases were compiled by NetworkRail employees and are related to the UK railway network. On the basis of their experience, NetworkRail engineers attributed a class of the EHC system to each slope, which was taken as a stand-in for the slope's actual stability conditions for the year 2015.

Figure 2 represents the distribution of EHC levels. Its analysis reveals a significant number of available records for all three types of slopes, namely 5945 and 10,928 records for rock and soil cuttings, respectively, and 25,673 records for embankment slopes. We also noted a high asymmetric distribution (imbalanced data) of the records for each EHC class. For example, taking as reference the database for embankments, more than 63% of the data are classified as class "A", and only 2.5% belongs to class "D".

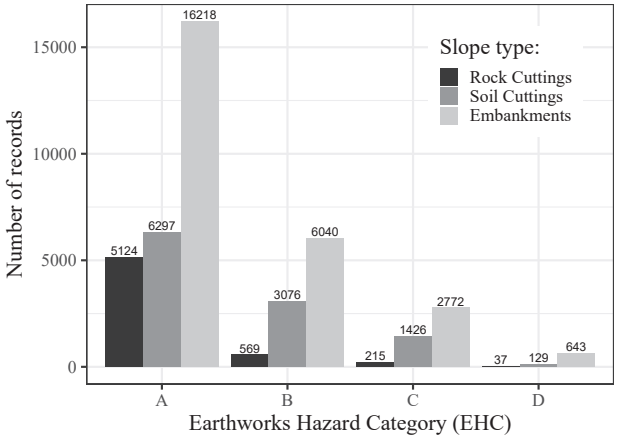

Figure 2. The data distribution of rock and soil cuttings from slopes and embankments by EHC class.

Although this type of asymmetric distribution, where the majority of the slopes have a low failure probability (class "A"), is typical and desirable from the perspective of slope network management and slope safety, it can pose a significant learning challenge for DM models. In fact, when dealing with imbalanced classification tasks in which at least one target class label has fewer training samples than other target class labels, the straightforward application of a DM training algorithm frequently results in data-driven models with improved prediction accuracy for the majority classes and decreased classification accuracy for the minority classes. Thus, methods such as oversampling and the synthetic minority oversampling technique (SMOTE), which modify the data to be used for training purposes with the aim of balancing the target class, are frequently adopted to

handle datasets where the classes are not equally distributed (imbalanced). In particular, oversampling is a straightforward strategy that balances the final training set by adding random samples (with repetition) of the classes with fewer training data. SMOTE is a more advanced method that generates "new data" by establishing a neighborhood by examining the nearest neighbors and then sampling from that neighborhood. It assumes that the proximity of the original data makes it comparable. By creating synthetic instances, SMOTE helps to increase the representation of the minority class, making the dataset more balanced. This can lead to improved model performance, especially when the class imbalance is significant. It is important to note that SMOTE should be applied only to the training set and not the entire dataset. Also, it is recommended to combine SMOTE with other techniques, such as undersampling the majority class or using more advanced algorithms, such as the SMOTE-ENN (SMOTE with edited nearest neighbors) method, to further enhance the effectiveness of the resampling process. Under the SMOTE approach, regarding the nearest neighbours' k values, different values were tested before settling on $k = 3$, which achieved the highest performance.

More than 50 variables were taken into consideration as model features, including information typically gathered during routine inspections, as well as data from geometric, geographic, and geological sources. To be precise, 65, 51, and 53 variables were considered, respectively, in the study of rock and soil cuttings and embankment slopes. A complete list of all variables considered in each study can be found in Tinoco et al. [31] and Tinoco et al. [30].

3. Methodology

3.1. Artificial Neural Networks

As shown above in Figure 1, which illustrates the models' performance in EHC prediction that was achieved during the first experiments [30,31], the ANN algorithms produced the most effective overall results. Accordingly, only ANNs were trained for EHC prediction in this new attempt.

It should be noted that ANNs are among the most effective DM algorithms for resolving challenging issues across a variety of knowledge domains [37–39], including in civil engineering [40–43]. In slope stability problems, several applications of ANNs can be found in the literature [13,44,45]. Another important point of evidence underlying the huge potential of ANNs is their recent developments under the deep learning field, which have significantly advanced the state of the art in speech recognition, visual object recognition, object detection, and numerous other fields, including drug discovery and genomics [46–48].

In spite of these important advances, in this work, we adopt the "traditional" neural networks. In a nutshell, ANNs are learning systems that originally were driven by how human brains work [49]. They process information iteratively by multiple neurons. ANNs are reliable when exploring data with noise and are capable of modeling intricate non-linear mappings. This research adopted the following parameters for the ANN:

- A multilayer perceptron with only feedforward connections;
- One hidden layer containing H processing units;
- A grid search of $\{0, 2, 4, 6, 8\}$ to determine the optimal value of H;
- A logistic function applied to the neural function of the hidden nodes $1/(1 + e^{-x})$;
- The BFGS technique [50] as an optimizer for the ANN.

The BFGS technique is a quasi-Newton method (also referred to as a variable metric algorithm) that was published simultaneously in 1970 by Broyden, Fletcher, Goldfarb, and Shanno [50]. It uses function values and gradients to construct a representation of the optimized surface [51].

3.2. Genetic Algorithms

In a data-driven undertaking, it is common practice to employ heuristic search methods, such as GA [52], for feature selection. In fact, when compared to exhaustive search methods, which can become computationally intensive for larger datasets [52], iterative algorithms such as sequential search or evolutionary algorithms (e.g., GA) [53] are more likely to produce interesting optimization outcomes with a moderate use of computational resources.

As stated in Section 2, models can be fed with a substantial number of input features (more than 50 variables). Feeding all of these attribute features to the learning models will increase the model's complexity and decrease the accuracy of its predictions, as some of these features may not be particularly relevant. However, the search space for all possible input combinations is excessively large (2^{50}). Thus, we employed a GA in this study to identify the optimal set of input features that improve EHC prediction. These modern and versatile optimization techniques stand out as some of the most potent optimization tools due to their ability to handle large search spaces with minimal computational overhead and their simplicity of interpretation and application.

Supported by AI and natural selection, a GA starts by coming up with random answers to a problem, which are then improved step by step until they are optimal or close to optimal. Based on that, the GA [53] can be used to determine the subset of features [54,55] where the bits on the chromosome show whether or not the feature is present. Finding the global maximum for the objective function will yield the finest suboptimal subset. In this case, the objective function is the predictor's performance.

GAs can do more than just optimize a single goal. This is very important because there is often not a single best trade-off answer, but a set of trade-offs with different goals. When addressing slope stability assessments, the capability to predict well in all four classes of the EHC classification system, and not in just one, is of the utmost importance. Due to the asymmetrical distribution of the data, which could result in a high overall performance based solely on a high level of accuracy for class "A" (the most common class), this characteristic is of the utmost importance.

Consequently, for multi-criteria optimization tasks, optimizing a Pareto front of solutions is one of the most effective strategies. Thus, each solution is deemed non-dominated, or Pareto optimal, if none of the objectives can be improved in value without deteriorating the others [56]. In the context of slope management, all Pareto optimal solutions can be assumed to be equivalent, and the decision maker or project manager can establish the primary selection criteria for choosing one solution over another based on the characteristics of the via (e.g., urban or rural location) through which a network of slopes is connected.

Since Pareto front multi-optimization requires keeping an eye on a population of solutions, population-based meta-heuristics, such as evolutionary multi-objective optimization (EMO), have become common solutions. Evolutionary computational methods, such as GA and EMO, operate by sustaining a population of individuals (potential solutions), where a chromosome represents an individual data representation of a solution and a gene represents a value position within such a representation. The design of the chromosome is a crucial aspect of adopting evolutionary approaches, as it defines the problem's search space. In this research, each chromosome is a sequence of 1 and 0 genes, with each gene indicating whether a characteristic is present (1) or absent (0).

This study implements a well-known EMO search engine, the non-dominated sorting genetic algorithm-II (NSGA-II [57], to address the slope stabilization identification multi-criteria optimization problem. The NSGA-II algorithm was adopted due to two major factors. Firstly, NSGA-II is a popular and state-of-the-art multi-objective evolutionary algorithm (MOEA) method that tends to obtain state-of-the-art results when the number of objectives is lower than 5. For instance, in [36], the NSGA-II algorithm outperformed other multi-objective methods such as S metric selection (SMS-EMOA) and aspiration set (AS-EMOA). Second, R software allows NSGA-II to be implemented with low computational effort [58] by taking advantage of the mco [59] package.

For NSGA-II parameterization, the standard values as defined in the R software were adopted, as follows:

- Population size: 100;
- Stop criteria: after 100 generations;
- Crossover probability: 0.7;
- Mutation probability: 0.2.

The default parameterization was selected for two main reasons. First, a single run of the hybrid NSGA-II and ANN combination is computationally costly. For instance, under the default parameterization, each GA generation requires the training of 100 ANNs, each trained with thousands of data records. Thus, tuning all NGSA-II hyperparameters (e.g., via grid search [60–62]) would require a prohibitive computational effort. Secondly, NSGA-II works as a second-order optimization procedure since it it selects the input variables that feed the ANN training algorithm (the first-order optimization method). Thus, the tuning of NSGA-II's internal parameters is not a critical issue. In preliminary tests, smaller population sizes (i.e., 20, 30, and 50) and various values for crossover and mutation probabilities were examined. However, the obtained results were inferior to the default values. As the *mco* package of the R tool employs a real-value representation of the NSGA-II method, all genes were initially rounded to the nearest integer (1 or 0) for the initial fitness function step.

The optimization was executed on a Linux server machine with an Intel Xeon 2.27 GHz. The total computational effort for the optimization depended significantly of the size of the database, but was never below than 672 h (around one month).

3.3. Model Evaluation

When handling unbalanced multi-class datasets (such as our EHC case), single classification measures can result in misleading predicted values. For instance, if there are four classes, "A", "B", "C", and "D", where 95% of the examples are related to class "A", then a classifier with a 95% classification accuracy might correspond to a "dumb" predictor that always outputs the "A" class. Thus, in this work, rather than assuming a single measure, we computed performance measures for all four EHC classes.

When evaluating the prediction quality for a particular class, there are two types of errors, false positives and false negatives, each of which correspond to different costs (specific to the domain problem). In order to better measure the prediction performance for each of the four EHC classes, rather than focusing on one type of error (e.g., just false positives), we computed classification metrics that are widely used in multi-class tasks and that consider both types of errors [63]:

- Recall;
- Precision;
- $F_{1-\text{score}}$.

The first measure takes into account false negatives, the second one considers false positives, and the third score provides a trade-off between both measures. The recall, also known as the true-positive rate or sensitivity, assesses the proportion of instances of a particular class that the model correctly identified. In other words, the recall of a certain class is given by the formula $TruePositives/(TruePositives + FalseNegatives)$. The precision metric, also known as the positive predictive value, measures the accuracy of the model when it predicts a particular class. Specifically, the precision of a particular class is determined by the formula $TruePositives/(TruePositives + FalsePositives)$. We further note that there is another measure that considers false positives, the false-positive rate. However, using precision or the false-positive rate would essentially lead to the same quality measurement (i.e., assess the value of false positives). Thus, in this work, we opted to use recall since it is commonly used as a complementary measure that is associated with precision. As for the third measure, the $F_{1-\text{score}}$ corresponds to the harmonic mean of precision and recall accord-

ing to the following expression: $2 \cdot (precision \cdot recall)/(precision + recall)$. All three metrics can range from 0% to 100%, with a higher value indicating a more accurate predictor.

The generalization capability of the ANN models was evaluated using a 5-fold cross-validation method with 5 runs [64], with the exception of the optimization phase, in which a 3-fold cross-validation method with 2 runs was used. This means that each modelling setup was trained $3 \times 5 = 15$ (optimization step) or $5 \times 5 = 25$ (modelling step) times. When compared with the simpler holdout method (single split between training and testing), the *k*-fold cross-validation procedure has the advantage of obtaining predictions for all the data. Under this approach, the data are randomly split into *k* mutually exclusive subsets with the same length. Then, a cycle with *k* iterations is executed, where all data except a differently selected fold are used for training. Once the model is trained, predictions are performed for the selected fold (unseen data). In the end, a total of *k* models are trained and tested. Thus, the measured performance measures on unseen data are more robust. The k-fold cross-validation procedure ensured that all three prediction metrics (recall, prediction, and $F_{1-score}$) were always computed on the unseen test data.

3.4. Sensitivity Analysis

A model's interpretability is of paramount importance, particularly from an engineering point of view, to obtain a detailed understanding of what has been learned by the models. Indeed, data-driven models, namely those based on ANN algorithm, are usually designed as black box models. Explainable artificial intelligence (xAI) [65,66] is a well-established domain with a thriving community that has developed a number of highly effective methods to explain and interpret the predictions of complex machine learning models, such as deep neural networks. In this study, a comprehensive sensitivity analysis (SA) [67] was conducted on the final models (i.e., the Pareto optimal solutions). SA is a simple method that was implemented following the training phase and measured the model's responses when a given input was modified, thereby allowing one to quantify the relative importance of each attribute.

The SA approach is inspired by experimental design [68], which is often used to identify causal relationships. There are other approaches to obtain knowledge from trained ANNs, such as the extraction of rules from trained ANNs. However, such approaches tend to discretize or simplify the predictive model's responses, leading to rules that do not accurately represent the original model or that consider just single-input interactions. The advantage of the SA approach is that it accurately measures the trained ANN's responses (even if the class decision boundaries are complex) under a computationally efficient mapping approach. In effect, and in accordance with the findings of Cortez and Embrechts [69], in this research, we employed a global sensitivity analysis (GSA) technique that is capable of detecting interactions among all combinations of input attributes. In this context, F inputs are changed at same time. F can range from one, as in a one-dimensional SA, denoted as 1-D, to I, as in an I-D SA. Iteratively, each input assume different values withing its range by L levels. The other inputs are held constant at the baseline, b. Seven levels ($L = 7$) were adopted in this research, which allowed an interesting amount of detail to be added at a reasonable computational effort. For the baseline b, the average value of each input was considered.

In short, the ANN was initially calibrated to the entire dataset. The fitted model was then subjected to the GSA algorithm, and the respective sensitivity responses were stored. Next, significant visualization techniques were computed using these responses. Specifically, the input importance bar graph illustrates the relative impact of each input variable (from 0% to 100%). The rationale behind SA is that the input is more significant the greater the changes observed in the output. Following the recommendation of Cortez and Embrechts [69], the gradient metric was chosen to measure this effect:

$$g_a = \sum_{j=2}^{L} |\hat{y}_{a,j} - \hat{y}_{a,j-1}| / (L-1) \quad (1)$$

where a denotes the input variable under analysis and $\hat{y}_{a,j}$ is the sensitivity response for $x_{a,j}$. We note that in [69], other SA measures were tested, including range and variance. However, in that study, it was shown that the gradient measure is more theoretically sound and provided better experimental evidence when compared with the range and variance measures (e.g., the variance tended to overemphasize the importance of the most relevant input, while the range provided an identical value for linear or high-frequency wave responses that produced the same range). Having computed the gradient for all inputs, the relative importance (R_a) was then calculated using:

$$R_a = g_a / \sum_{i=1}^{I} g_i \cdot 100(\%) \quad (2)$$

3.5. Modelling Procedure

A nominal classification approach showed the highest overall response on EHC prediction during the first attempt [30,31]. Accordingly, the same modelling strategy was adopted in this new attempt. In addition, as mentioned before, only ANN algorithms were trained, as they showed superior performance in the EHC problem. SMOTE, oversampling, and no resampling were also tested in these new experiments (only during the modelling step) in order to address the issue of imbalanced data [70,71], as no conclusive conclusion could be drawn from the first attempt regarding the optimal resampling technique. We note that the three resampling approaches are reasonably diverse. The no resampling option did not change the training data; thus, it was used as a baseline to check if the other resampling approaches provided a modelling value. Since the minority classes occurred very infrequently, it made more sense to apply oversampling rather than undersampling (if this last method was applied, the training data would be too small). Finally, SMOTE is a state-of-the-art resampling technique that generates synthetic samples for minority classes.

The overall proposed procedure was comprised of two main steps, as illustrated in Figure 3 and as described below:

1. **Optimization:** The objective of applying GA is to identify the optimal set of variables that minimizes the objective function. Consequently, our GA began by randomly defining an initial population in which each individual (a sequence of 1 and 0 indicating whether a feature was included or not) represented a potential solution (set of variables) to the problem. The objective function corresponded to the maximization of the recall metric for all four EHC classes (a multi-objective problem). The fitness function corresponded to an ANN algorithm-based predictive model. Two ANNs were fitted to the database using the methodology outlined in Section 3.1 (i.e., a feedforward network with one hidden layer, a logistic function for hidden nodes, and a grid search of $\{0, 2, 4, 6, 8\}$ for H definition using a 3-fold cross-validation schema as the validation procedure). Then, for each EHC class, a recall metric (the average of both ANNs) was calculated, which was then utilized by the GA to optimize the optimal set of attributes for EHC identification.
2. **ANN training:** After optimization, five ANNs were fitted to the database for each Pareto optimal solution (set of optimal variables) using the methodology described in Section 3.1. Here, in addition to the standard approach (no resampling), ANNs were trained with a resampled database using the SMOTE and oversampling approaches. Notably, the various sampling methods were only applied to the training data, which were used to fit the data-driven models, and the test data (as provided by the 5-fold cross-validation procedure) were not altered. This means that $3 \times (5 \times 5) = 75$ ANNs were trained for each Pareto optimal solution. Each model was then subjected to a sensitivity analysis to determine the relative relevance of each attribute for EHC prediction.

As presented and discussed in the next sections, it was possible to identify the average number of input variables considered for EHC prediction. In addition, the variables selected more frequently by the GA were determined. In the end, based on the overall performance

of each model (measured by the recall, precision, and $F_{1-score}$ for all four EHC classes) and the results of the sensitivity analysis, a single model was chosen and thoroughly analyzed.

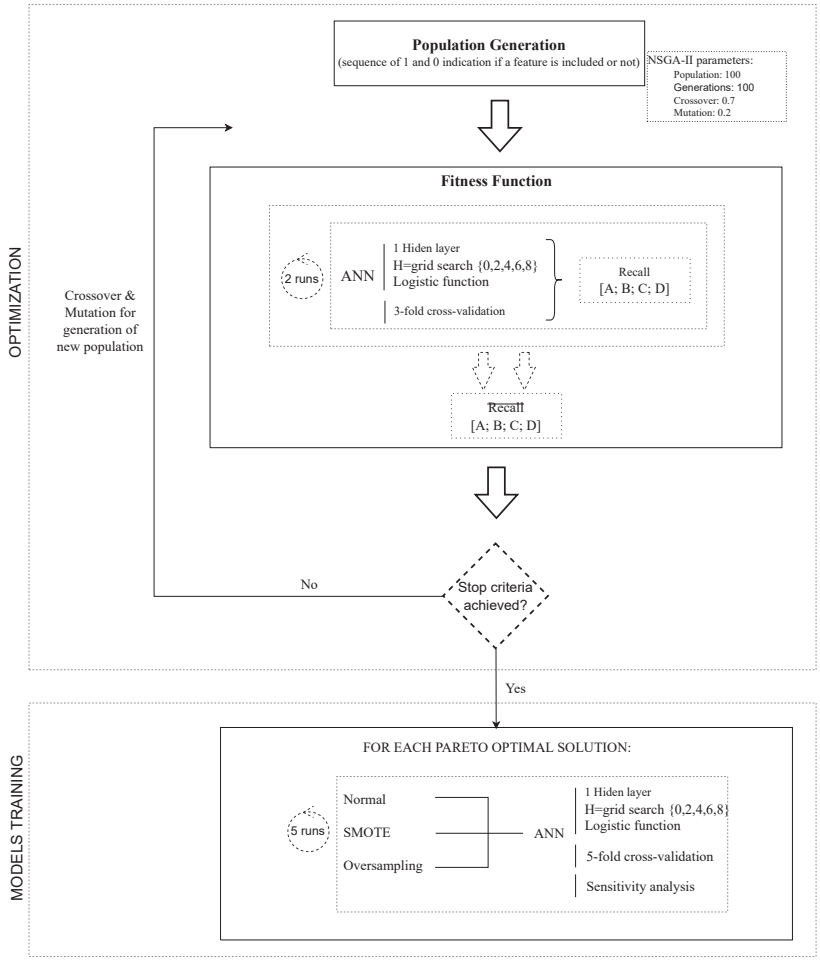

Figure 3. Flowchart of the applied methodology.

Although not presented in the paper, it should be mentioned that some other experiments were also carried out following a regression strategy, where, in addition to the optimization of the best set of attributes, a numeric regression scale was also optimized at the same time.

The R statistical environment [58] was adopted to implement all experiments conducted in this research. Moreover, to facilitate the implementation of ANNs and NSGA-II algorithms, as well as validation techniques such as cross-validation, the rminer [51] and mco [59] packages were used.

4. Results and Discussion

This section summarizes the main achievement in the EHC prediction of rock and soil cuttings from slopes and embankments by combining the learning capabilities of the ANN and the optimization power of the GA.

4.1. Feature Selection

Figure 4 depicts the trade-off between recall values for each one of the four EHC class for all Pareto optimal solutions covering the three case studies, that is, rock and soil cuttings and embankments. Although putting all this information in a single graph is somewhat confusing, for the purposes of analysis, itis more than enough, as it aims at providing an overview of the performance for each EHC class.

From its analysis, and as expected, the best solution is always a performance commitment between all EHC classes. This commitment is particularly evident between class "A" and classes "B", "C", and "D". For example, to obtain a high performance for class "A", the response for the other classes must be compromised in some way. The same behavior is also observed for the other possible EHC class combinations, although in some instances, specifically between the "B" and "C" classes, commitment is not as evident. In fact, there are some solutions that maximise the response for such classes. In addition to the performance commitment between EHC classes, Figure 4 also demonstrates the inferior performance of all Pareto optimal solutions for classes "C" and "D", namely for rock cuttings (below 0.4) when compared to class "A" (above 0.9).

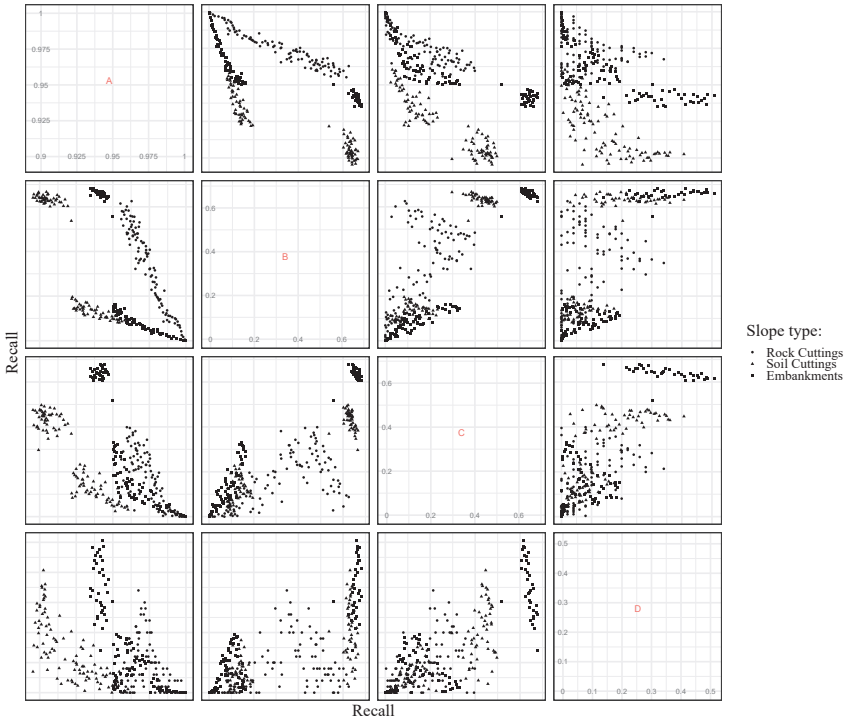

Figure 4. Recall correlation matrix for each Pareto-optimal solution.

As previously stated, GAs were applied in this study for feature selection purposes; in other words, they were used to find the best model (set of input variables) that maximized EHC prediction. However, some additional and useful information was extracted from the achieved results, which was useful to obtain a better understanding of the behavior of the stability of slopes. Specifically, they provided information regarding the optimal number of inputs for the accurate determination of slope stability, as well as the variables that should be used as model attributes.

Figure 5 demonstrates that, with the exception of embankments, all Pareto optimal solutions evaluated fewer than ten features and no more than forty inputs. There are some

solutions for embankments that considered fewer than ten inputs, with a minimum of five attributes. Still, in regards to embankments, it is interesting to observe that most of the solutions have considered, on average, 15 or 34 inputs. Moreover, for the rock and soil cuttings' slopes, although this was not so evident, the number of variables considered by a significant part of the solutions ranged between 10 and 20 or between 30 and 40. These observations indicate that only about half of the more than 50 features available for model training were simultaneously considered as input to a model. In fact, the majority of Pareto optimal solutions in the study of rock cuttings considered between sixteen and seventeen features, while some were fed by as many as thirty-one features. Regarding soil cutting, the most frequent number of variables taken by the Pareto optimal solutions was 12, and for embankments, that number was 15.

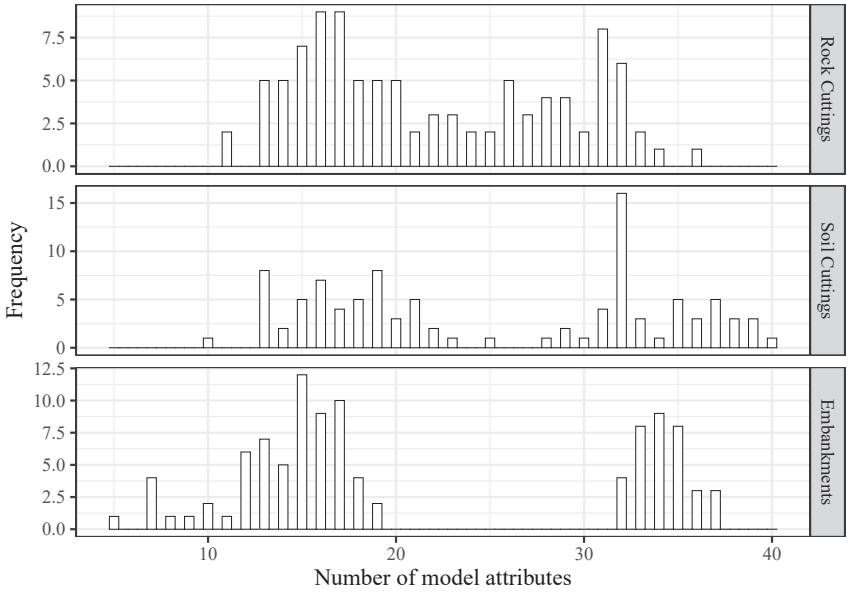

Figure 5. Number of features used as model attributes over all Pareto optimal solutions.

From Figure 6, which shows the variables present in at least half of all Pareto optimal solutions, it can be observed that slopes categorized as "high" and "angle" are common to the three types of slopes. Moreover, it can also be observed that only three variables were considered as model attributes by all Pareto optimal solutions among the three slope types. Comparing the three slope types, higher variability was observed for embankments in terms of the model attributes considered by any Pareto optimal solution. In fact, only a restricted group of 14 variables are present on 50% of all Pareto optimal solutions. When considering rock and soil cuttings, this number becomes almost twice higher, particularly for soil cuttings, where a group of 23 variables were used by 50% of all solutions.

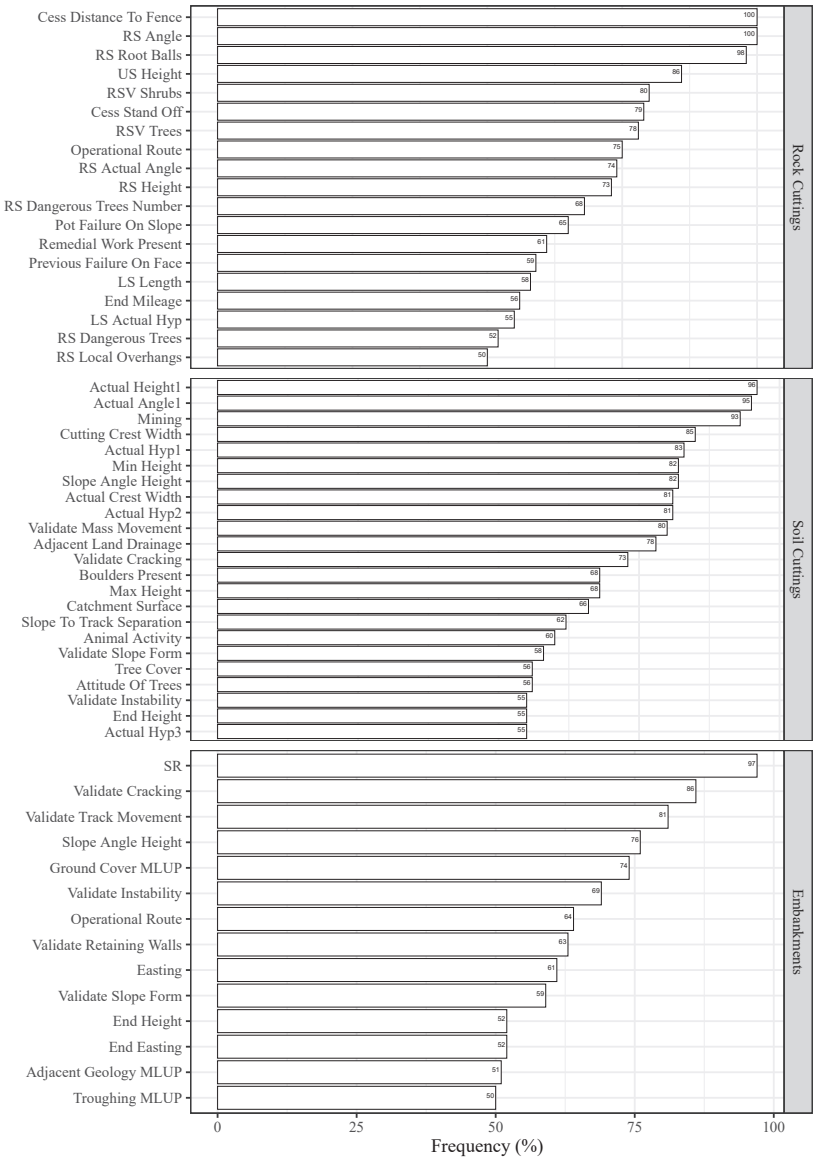

Figure 6. Number of times that each input feature is selected as model attribute over all Pareto optimal solutions.

4.2. Model Performance

A single model was chosen from all Pareto optimal solutions for aeach slope type on the basis of the recall, precision, and $F_{1-\text{score}}$ performance metrics across all EHC classes. As summarized in Section 3.5, all Pareto optimal solutions were retrained using the SMOTE and oversampling techniques, as well as without resampling (normal). The efficacy of these Pareto optimal solutions for each slope type is presented and discussed in the following sections.

Using the recall, precision, and $F_{1-\text{score}}$ metrics as benchmarks, Figure 7 compares ANNs models from the first ANN models (from now referred to as the "old" models [30,31])

and the best ANN models selected among all Pareto optimal solutions (referred to from now on as the "updated" models). This comparison was made by calculating the difference between the metrics of the "updated" and "old" models. Hence, positive values correspond to the superior performance of the "updated" models. Despite the fact that the overall difference between the "updated" and "old" models is not statistically significant, the "updated" models have several key advantages over the "old" ones. On the one hand, using the recall metric as a benchmark, the "Updated" models, particularly those following a SMOTE approach, demonstrate a significant improvement in the prediction of classes "C" and "D". On the other hand, this "updated" model utilizes a significantly reduced number of features. On average, less than 30 variables were considered instead of the more than 50 considered in the "Old" models. These two aspects represent a significant accomplishment from a practical standpoint. First, less information is required to accomplish the same overall performance, which represents significant time and cost savings. Second, a better performance on classes "C" and "D" prediction was achieved with almost no performance penalization for the remaining classes.

This trade-off between the models' responses for the major and minority classes is a consequence of the highly asymmetric distribution of the database. However, it should be noted that the "updated" models achieved a better balance by increasing their performance for the minority classes, for which the probability of failure is higher, without significantly compromising their responses for the major classes.

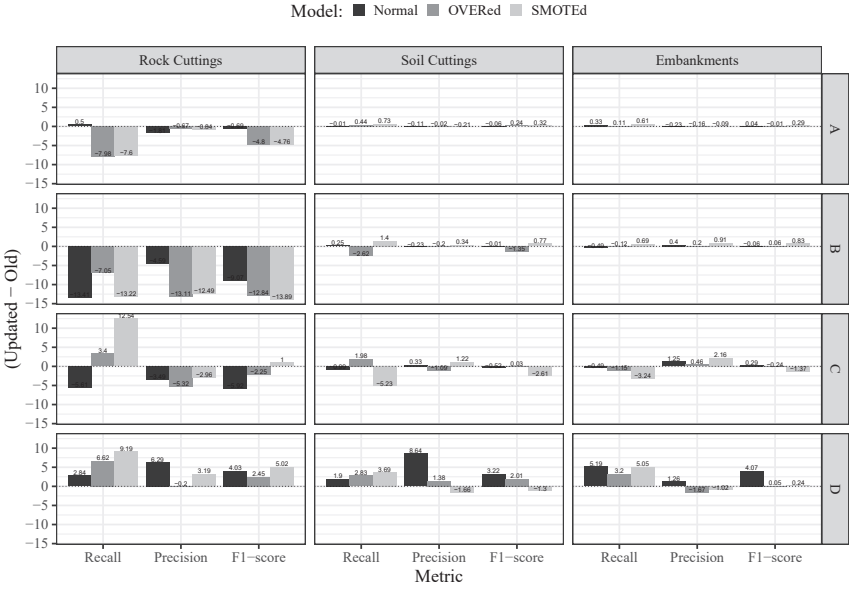

Figure 7. Comparison of the best ANN models ("updated" vs. "old") based on recall, precision and $F_{1-score}$ according to a nominal classification strategy in slope stability prediction of rock and soil cuttings, slopes, and embankments.

When analyzing the effect of the training sampling approaches (oversampling and SMOTE), some effectiveness can be observed for classes "C" and "D", for which the probability of failure is higher (as these are minority classes), particularly for rock cuttings. Concerning classes "A" and "B", the implementation of a sampling approach does not produce the same effectiveness. When comparing SMOTE and oversampling, the effectiveness of the first method seems to be slightly superior. These results are in line with those observed during the first iteration, as reported in [30,31].

Figure 8 depicts the relationship between the observed and predicted EHC classes based on the "updated" SMOTE-based ANN model. Its superior performance on classes "A" and "B" is evident from its analysis. Particularly for soil cuttings and embankments, we can also observe a very interesting response for class "D" (more than 60% of the slopes belonging to class "D" were correctly identified). Furthermore, one can observe that when a slope's class is not correctly identified, it is categorized as belonging to the closest class. For instance, a slope of class "D" that is not predicted as "D" is typically classified as "C". These results are encouraging and drive new experiences toward improvements in the performance of models, particularly for minority classes.

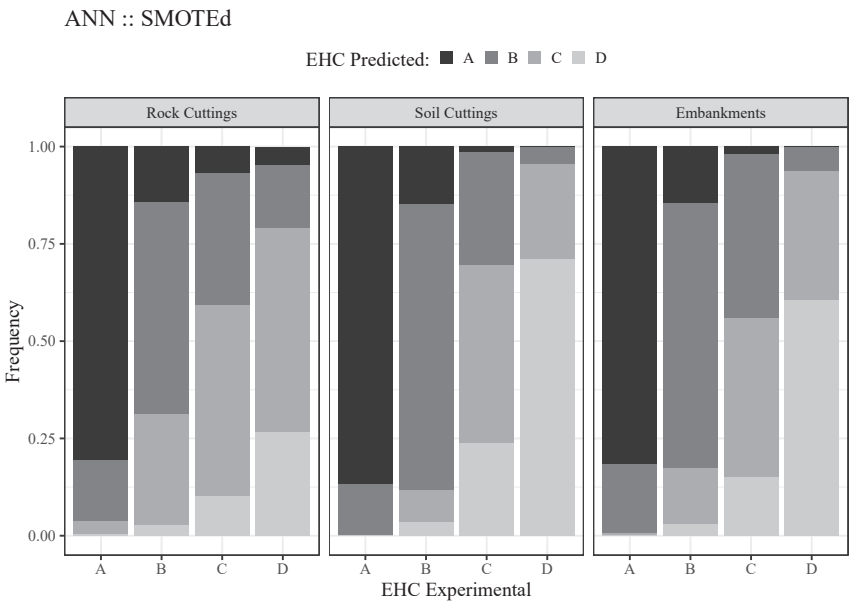

Figure 8. Best performance of ANN models ("updated" models) in EHC prediction of rock and soil cuttings, slopes, and embankments according to a nominal classification strategy and following a SMOTE approach.

4.3. Model Interpretation

As important as the performance of a model is, its interpretability is also highly important, particularly when it is based on complex algorithms, such as ANNs. Due to their mathematical complexity, these models are typically difficult to understand and usually referred to as "black boxes". Therefore, it is essential to "open" such models in order to comprehend what they have learned. In this study, a GSA methodology [67] was used to identify the most important parameters (1-D SA, input importance bar plot).

Figure 9 shows the relative importance of the twenty more relevant variables according to the best "updated" models, as described above.

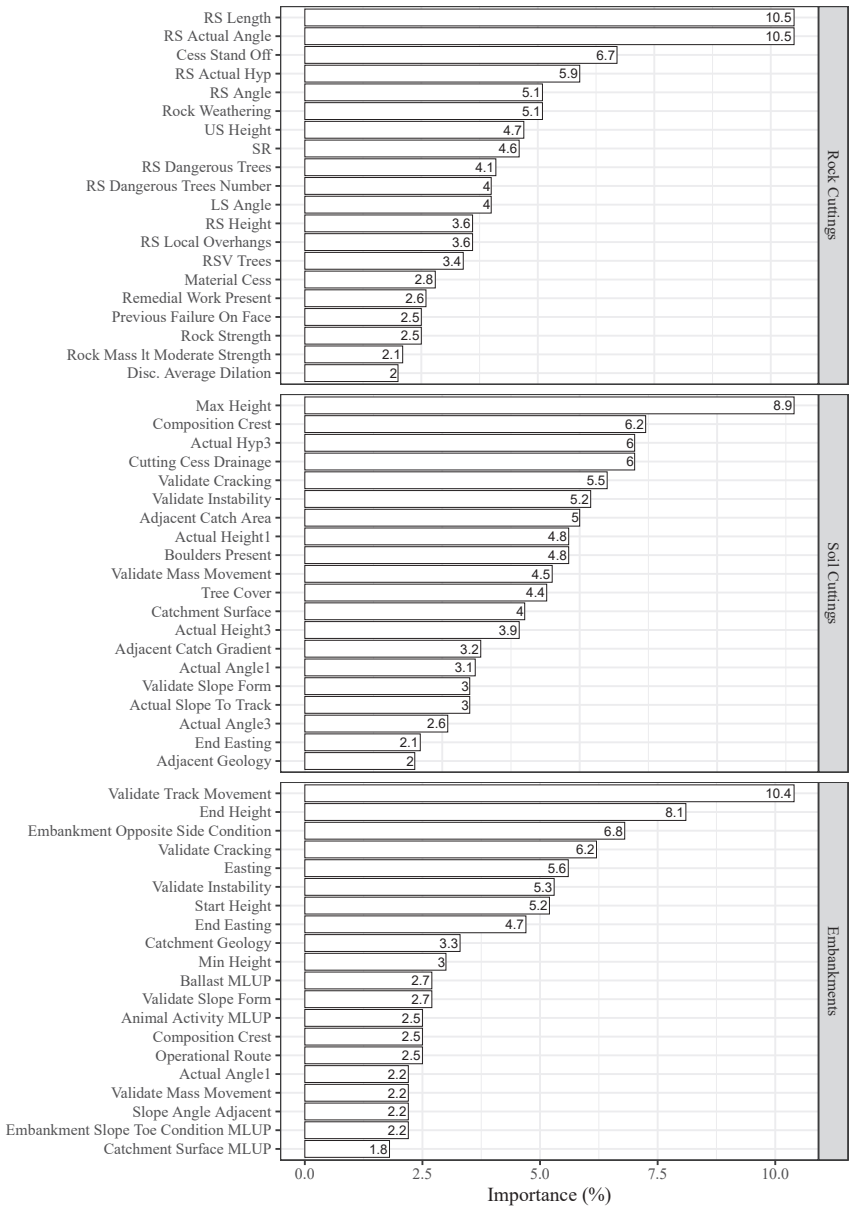

Figure 9. Relative importance bar plot for each variable according to the best ANN model ("updated" models) following a nominal classification strategy in predicting the slope stability of rock and soil cuttings and embankments.

Comparing this ranking with the "old" models reported on [30,31], it can be observed that both rankings share around half of the more relevant features. The exceptions are the rock cuttings, where only 6 of the 20 more relevant variables were also identified as such in the "updated" models.

Focusing only on the 20 more relevant variables according to the "updated" models for each of the slope types, it can be observed that any variable has an individual influence

higher than 10.5 %. Concerning the rock cuttings, the variables "RS Length" and "RS Actual Angle" present a relative importance of 10.5%. In the case of soil cuttings, the variable "Max Height" stands out from the others, with an influence of 8.9%. Relating to embankments, the variable "Validate Track Movement" presents a relative influence of 10.4%, which is closely followed by "End Height", with 8.1%. Moreover, it can also be observed that at least one variable related to the slope angle or slope height appears at the top of the ranking.

Overall, these rankings follow what is known regarding the main factors relating to slope stability [2,15,20,21,27]. Several empirical studies have shown that a high slope and its angle are among the key factors that mostly contribute to the stability of a given slope [1,14,22,28].

5. Final Remarks

After a first attempt to identify the stability of rock and soil cuttings and embankments using machine learning algorithms and taking into account the visual features that are usually collected during routine inspections, a second attempt was made by combining artificial neural networks (ANNs) and genetic algorithms (GA), a combination also known as an evolutionary neural network (ENNs), for feature selection and slope stability classification purposes. This innovative approach allows ANNs and GAs to work together to assess the stability of a slope. Although the overall performance did not improve significantly, the new models presented some important advantages. First, to achieve the same overall performance, the number of input variables decreased to less than 30. This is a key point from a practical point of view since it endows the model with more flexibility when less information is available. Furthermore, this can allow the railway infrastructure management companies to collect less information to determine the stability level of their slope network, which, in turn, will allow them to reduce costs related to routine inspections. Second, better performance is achieved for the identification of classes "C" and "D", which correspond to a higher probability of failure, without significantly compromising the model's performance on the remaining classes. From a safety point of view, this represents a significant improvement, allowing for the strategic investment of the available budget on critical slopes. In addition, such a strategic maintenance plan can reduce traffic constraints due to slope failures and, consequently, the probability of severe incidents. In summary, these results are encouraging and consist of a promising research direction towards a more efficient identification of the stability of slopes, particularly for minority classes. Thus, as a future development, we intend to explore other feature selection approaches as well as different strategies to handle imbalanced data (e.g., the usage of Tomek links or Gaussian copula transformations [72]). In addition, considering the high number of data available for each of the three slope types, a deep learning approach may provide an important contribution toward the prediction models' efficiency.

Despite the fact that new attempts are still necessary, this study demonstrates once more the extreme difficulty of such a task, namely by considering only visual features. Nonetheless, this difficult task is of the utmost importance, especially for developed nations that must maintain large-scale transportation networks despite limited budgets for maintenance and network operations.

Author Contributions: All authors contributed to the study conception and design. Material preparation, data collection, and analysis were performed by J.T., A.G.C., P.C. and D.T. The first draft of the manuscript was written by J.T., and all authors commented on previous versions of the manuscript. All authors have read and agreed to the published version of the manuscript.

Funding: This work was supported by FCT, the "Fundação para a Ciência e a Tecnologia", within the Institute for Sustainability and Innovation in Structural Engineering (ISISE), project UID/ECI/04029/2013, as well as Project Scope: UID/CEC/00319/2013 and through the post-doctoral grant fellowship with reference SFRH/BPD/94792/2013. This work was also partly financed by FEDER (Fundo Europeu de Desenvolvimento Regional) funds through the Competitivity Factors Operational Programme—COMPETE and by national funds through FCT within the scope of the project POCI-01-0145-FEDER-007633. This work has also been supported by COMPETE: POCI-01-0145-FEDER-007043.

Institutional Review Board Statement: Not applicable.

Informed Consent Statement: No human participants were involved in this research.

Data Availability Statement: The data that support the findings of this study are not publicly available due to privacy issues.

Acknowledgments: This work was partly financed by FCT/MCTES through national funds (PIDDAC) under the R&D Unit Institute for Sustainability and Innovation in Structural Engineering (ISISE) under reference UIDB/04029/2020 and under the Associate Laboratory Advanced Production and Intelligent Systems ARISE under reference LA/P/0112/2020, as well as through the post-doctoral Grant fellowship with reference SFRH/BPD/94792/2013. A special thanks goes to Network Rail, who kindly made available the data (basic earthworks examination data and the Earthworks Hazard Condition scores) used in this work.

Conflicts of Interest: The authors declare no conflict of interest.

References

1. Pourkhosravani, A.; Kalantari, B. A Review of Current Methods for Slope Stability Evaluation. *Electron. J. Geotech. Eng.* **2011**, *16*, 1245–1254.
2. Ullaha, S.; Khanb, M.U.; Rehmana, G. A Brief Review of the Slope Stability Analysis Methods. *Geol. Behav.* **2020**, *4*, 61–65.
3. Suchomel, R.; Mašı, D. Comparison of different probabilistic methods for predicting stability of a slope in spatially variable $c - \varphi$ soil. *Comput. Geotech.* **2010**, *37*, 132–140. [CrossRef]
4. Sivakumar Babu, G.; Murthy, D. Reliability analysis of unsaturated soil slopes. *J. Geotech. Geoenviron. Eng.* **2005**, *131*, 1423–1428. [CrossRef]
5. Husein Malkawi, A.I.; Hassan, W.F.; Abdulla, F.A. Uncertainty and reliability analysis applied to slope stability. *Struct. Saf.* **2000**, *22*, 161–187. [CrossRef]
6. Gavin, K.; Xue, J. Use of a genetic algorithm to perform reliability analysis of unsaturated soil slopes. *Geotechnique* **2009**, *59*, 545–549. [CrossRef]
7. Wang, H.; Sassa, K. Comparative evaluation of landslide susceptibility in Minamata area, Japan. *Environ. Geol.* **2005**, *47*, 956–966. [CrossRef]
8. Cheng, M.Y.; Hoang, N.D. Slope Collapse Prediction Using Bayesian Framework with K-Nearest Neighbor Density Estimation: Case Study in Taiwan. *J. Comput. Civ. Eng.* **2016**, *30*, 04014116. [CrossRef]
9. Ahangar-Asr, A.; Faramarzi, A.; Javadi, A.A. A new approach for prediction of the stability of soil and rock slopes. *Eng. Comput.* **2010**, *27*, 878–893. [CrossRef]
10. Lu, P.; Rosenbaum, M. Artificial neural networks and grey systems for the prediction of slope stability. *Nat. Hazards* **2003**, *30*, 383–398. [CrossRef]
11. Sakellariou, M.; Ferentinou, M. A study of slope stability prediction using neural networks. *Geotech. Geol. Eng.* **2005**, *23*, 419–445. [CrossRef]
12. Cheng, M.Y.; Wu, Y.W.; Chen, K.L. Risk Preference Based Support Vector Machine Inference Model for Slope Collapse Prediction. *Autom. Constr.* **2012**, *22*, 175–181. [CrossRef]
13. Yao, X.; Tham, L.; Dai, F. Landslide susceptibility mapping based on support vector machine: A case study on natural slopes of Hong Kong, China. *Geomorphology* **2008**, *101*, 572–582. [CrossRef]
14. Kang, F.; Han, S.; Salgado, R.; Li, J. System probabilistic stability analysis of soil slopes using Gaussian process regression with Latin hypercube sampling. *Comput. Geotech.* **2015**, *63*, 13–25. [CrossRef]
15. Kang, F.; Xu, Q.; Li, J. Slope reliability analysis using surrogate models via new support vector machines with swarm intelligence. *Appl. Math. Model.* **2016**, *40*, 6105–6120. [CrossRef]
16. Kang, F.; Li, J. Artificial bee colony algorithm optimized support vector regression for system reliability analysis of slopes. *J. Comput. Civ. Eng.* **2016**, *30*, 04015040. [CrossRef]
17. Kang, F.; Li, J.s.; Li, J.j. System reliability analysis of slopes using least squares support vector machines with particle swarm optimization. *Neurocomputing* **2016**, *209*, 46–56. [CrossRef]
18. Kang, F.; Li, J.S.; Wang, Y.; Li, J. Extreme learning machine-based surrogate model for analyzing system reliability of soil slopes. *Eur. J. Environ. Civ. Eng.* **2017**, *21*, 1341–1362. [CrossRef]
19. Das, S.K.; Biswal, R.K.; Sivakugan, N.; Das, B. Classification of slopes and prediction of factor of safety using differential evolution neural networks. *Environ. Earth Sci.* **2011**, *64*, 201–210. [CrossRef]
20. Suman, S.; Khan, S.; Das, S.; Chand, S. Slope stability analysis using artificial intelligence techniques. *Nat. Hazards* **2016**, *84*, 727–748. [CrossRef]
21. Koopialipoor, M.; Armaghani, D.J.; Hedayat, A.; Marto, A.; Gordan, B. Applying various hybrid intelligent systems to evaluate and predict slope stability under static and dynamic conditions. *Soft Comput.* **2019**, *23*, 5913–5929. [CrossRef]
22. Naidu, S.; Sajinkumar, K.; Oommen, T.; Anuja, V.; Samuel, R.A.; Muraleedharan, C. Early warning system for shallow landslides using rainfall threshold and slope stability analysis. *Geosci. Front.* **2018**, *9*, 1871–1882. [CrossRef]

23. Zhang, W.; Gu, X.; Hong, L.; Han, L.; Wang, L. Comprehensive review of machine learning in geotechnical reliability analysis: Algorithms, applications and further challenges. *Appl. Soft Comput.* **2023**, *136*, 110066. [CrossRef]
24. Soranzo, E.; Guardiani, C.; Chen, Y.; Wang, Y.; Wu, W. Convolutional neural networks prediction of the factor of safety of random layered slopes by the strength reduction method. *Acta Geotech.* **2023**, *18*, 3391–3402. [CrossRef]
25. Wang, L.; Wu, C.; Gu, X.; Liu, H.; Mei, G.; Zhang, W. Probabilistic stability analysis of earth dam slope under transient seepage using multivariate adaptive regression splines. *Bull. Eng. Geol. Environ.* **2020**, *79*, 2763–2775. [CrossRef]
26. Fu, X.; Sheng, Q.; Zhang, Y.; Chen, J.; Zhang, S.; Zhang, Z. Computation of the safety factor for slope stability using discontinuous deformation analysis and the vector sum method. *Comput. Geotech.* **2017**, *92*, 68–76. [CrossRef]
27. Liu, G.; Zhuang, X.; Cui, Z. Three-dimensional slope stability analysis using independent cover based numerical manifold and vector method. *Eng. Geol.* **2017**, *225*, 83–95. [CrossRef]
28. Pinheiro, M.; Sanches, S.; Miranda, T.; Neves, A.; Tinoco, J.; Ferreira, A.; Gomes Correia, A. A new Empirical System for Rock Slope Stability Analysis in Exploitation Stage. *Int. J. Rock Mech. Min. Sci.* **2015**, *76*, 182–191. [CrossRef]
29. Power, C.; Mian, J.; Spink, T.; Abbott, S.; Edwards, M. Development of an Evidence-based Geotechnical Asset Management Policy for Network Rail, Great Britain. *Procedia Eng.* **2016**, *143*, 726–733. [CrossRef]
30. Tinoco, J.; Gomes Correia, A.; Cortez, P.; Toll, D. Data-Driven Model for Stability Condition Prediction of Soil Embankments Based on Visual Data Features. *J. Comput. Civ. Eng.* **2018**, *32*, 04018027. [CrossRef]
31. Tinoco, J.; Gomes Correia, A.; Cortez, P.; Toll, D. Stability Condition Identification of Rock and Soil Cutting Slopes Based on Soft Computing. *J. Comput. Civ. Eng.* **2018**, *32*, 04017088. [CrossRef]
32. Fan, Y.; Xu, K.; Wu, H.; Zheng, Y.; Tao, B. Spatiotemporal modeling for nonlinear distributed thermal processes based on KL decomposition, MLP and LSTM network. *IEEE Access* **2020**, *8*, 25111–25121. [CrossRef]
33. Taormina, R.; Chau, K.W. ANN-based interval forecasting of streamflow discharges using the LUBE method and MOFIPS. *Eng. Appl. Artif. Intell.* **2015**, *45*, 429–440. [CrossRef]
34. Faizollahzadeh Ardabili, S.; Najafi, B.; Shamshirband, S.; Minaei Bidgoli, B.; Deo, R.C.; Chau, K.w. Computational intelligence approach for modeling hydrogen production: A review. *Eng. Appl. Comput. Fluid Mech.* **2018**, *12*, 438–458. [CrossRef]
35. Tahir, M.; Tubaishat, A.; Al-Obeidat, F.; Shah, B.; Halim, Z.; Waqas, M. A novel binary chaotic genetic algorithm for feature selection and its utility in affective computing and healthcare. *Neural Comput. Appl.* **2022**, *34*, 11453–11474. [CrossRef]
36. Cortez, P. *Modern Optimization with R*, 2nd ed.; Springer: New York, NY, USA, 2021.
37. Liao, S.; Chu, P.; Hsiao, P. Data mining techniques and applications. A decade review from 2000 to 2011. *Expert Syst. Appl.* **2012**, *39*, 11303–11311. [CrossRef]
38. Garg, A.; Garg, A.; Tai, K.; Sreedeep, S. An integrated SRM-multi-gene genetic programming approach for prediction of factor of safety of 3-D soil nailed slopes. *Eng. Appl. Artif. Intell.* **2014**, *30*, 30–40. [CrossRef]
39. Javadi, A.A.; Ahangar-Asr, A.; Johari, A.; Faramarzi, A.; Toll, D. Modelling stress–strain and volume change behaviour of unsaturated soils using an evolutionary based data mining technique, an incremental approach. *Eng. Appl. Artif. Intell.* **2012**, *25*, 926–933. [CrossRef]
40. Tinoco, J.; Gomes Correia, A.; Cortez, P. A Novel Approach to Predicting Young's Modulus of Jet Grouting Laboratory Formulations over Time using Data Mining Techniques. *Eng. Geol.* **2014**, *169*, 50–60. . [CrossRef]
41. Tinoco, J.; Gomes Correia, A.; Cortez, P. Support Vector Machines Applied to Uniaxial Compressive Strength Prediction of Jet Grouting Columns. *Comput. Geotech.* **2014**, *55*, 132–140. [CrossRef]
42. Gomes Correia, A.; Cortez, P.; Tinoco, J.; Marques, R. Artificial Intelligence Applications in Transportation Geotechnics. *Geotech. Geol. Eng.* **2013**, *31*, 861–879. [CrossRef]
43. Miranda, T.; Gomes Correia, A.; Santos, M.; Sousa, L.; Cortez, P. New Models for Strength and Deformability Parameter Calculation in Rock Masses Using Data-Mining Techniques. *Int. J. Geomech.* **2011**, *11*, 44–58. [CrossRef]
44. Wang, H.; Xu, W.; Xu, R. Slope stability evaluation using back propagation neural networks. *Eng. Geol.* **2005**, *80*, 302–315. [CrossRef]
45. Cheng, M.Y.; Roy, A.F.; Chen, K.L. Evolutionary risk preference inference model using fuzzy support vector machine for road slope collapse prediction. *Expert Syst. Appl.* **2012**, *39*, 1737–1746. [CrossRef]
46. LeCun, Y.; Bengio, Y.; Hinton, G. Deep learning. *Nature* **2015**, *521*, 436. [CrossRef] [PubMed]
47. Farabet, C.; Couprie, C.; Najman, L.; LeCun, Y. Learning Hierarchical Features for Scene Labeling. *IEEE Trans. Pattern Anal. Mach. Intell.* **2013**, *35*, 1915–1929. [CrossRef]
48. Goodfellow, I.; Bengio, Y.; Courville, A. *Deep Learning*; MIT Press: New York, NY, USA, 2016.
49. Kenig, S.; Ben-David, A.; Omer, M.; Sadeh, A. Control of Properties in Injection Molding by Neural Networks. *Eng. Appl. Artif. Intell.* **2001**, *14*, 819–823. [CrossRef]
50. Venables, W.; Ripley, B. *Modern Applied Statistics with S*, 2nd ed.; Springer: Berlin/Heidelberg, Germany, 2003.
51. Cortez, P. Data Mining with Neural Networks and Support Vector Machines using the R/rminer Tool. In *Advances in Data Mining: Applications and Theoretical Aspects*; Perner, P., Ed.; Springer: Berlin/Heidelberg, Germany, 2010; pp. 572–583.
52. Chandrashekar, G.; Sahin, F. A survey on feature selection methods. *Comput. Electr. Eng.* **2014**, *40*, 16–28. [CrossRef]
53. Golberg, D.E. Genetic algorithms in search, optimization, and machine learning. *Addion Wesley* **1989**, *1989*, 36.

54. Sun, Y.; Babbs, C.; Delp, E. A comparison of feature selection methods for the detection of breast cancers in mammograms: Adaptive sequential floating search vs. genetic algorithm. In Proceedings of the 2005 IEEE Engineering in Medicine and Biology 27th Annual Conference, Shanghai, China, 17–18 January 2006; pp. 6532–6535.
55. Alexandridis, A.; Patrinos, P.; Sarimveis, H.; Tsekouras, G. A two-stage evolutionary algorithm for variable selection in the development of RBF neural network models. *Chemom. Intell. Lab. Syst.* **2005**, *75*, 149–162. [CrossRef]
56. Bonissone, P.P.; Subbu, R.; Lizzi, J. Multicriteria decision making (MCDM): A framework for research and applications. *IEEE Comp. Int. Mag.* **2009**, *4*, 48–61. [CrossRef]
57. Chou, J.; Tseng, H. Establishing expert system for prediction based on the project-oriented data warehouse. *Expert Syst. Appl.* **2011**, *38*, 640–651. [CrossRef]
58. R Team. *R: A Language and Environment for Statistical Computing*; R Foundation for Statistical Computing: Viena, Austria, 2009. Available online: http://www.r-project.org/ (accessed on 7 July 2023).
59. Mersmann, O.; Trautmann, H.; Steuer, D.; Bischl, B.; Deb, K. Package "mco": Multiple Criteria Optimization Algorithms and Related Functions. 2014. Available online: https://cran.r-project.org/package=mco (accessed on 7 July 2023).
60. Ali, Y.A.; Awwad, E.M.; Al-Razgan, M.; Maarouf, A. Hyperparameter search for machine learning algorithms for optimizing the computational complexity. *Processes* **2023**, *11*, 349. [CrossRef]
61. Anggoro, D.A.; Mukti, S.S. Performance Comparison of Grid Search and Random Search Methods for Hyperparameter Tuning in Extreme Gradient Boosting Algorithm to Predict Chronic Kidney Failure. *Int. J. Intell. Eng. Syst.* **2021**, *14*. [CrossRef]
62. Alibrahim, H.; Ludwig, S.A. Hyperparameter optimization: Comparing genetic algorithm against grid search and bayesian optimization. In Proceedings of the 2021 IEEE Congress on Evolutionary Computation (CEC), Kraków, Poland, 28 June–1 July 2021; pp. 1551–1559.
63. Witten, I.; Frank, E.; Hall, M.; Pal, C. *Data Mining: Practical Machine Learning Tools and Techniques*, 4th ed.; Morgan Kaufmann: New Your, NY, USA, 2017.
64. Hastie, T.; Tibshirani, R.; Friedman, J. *The Elements of Statistical Learning: Data Mining, Inference, and Prediction*, 2nd ed.; Springer: New York, NY, USA, 2009.
65. Holzinger, A.; Saranti, A.; Molnar, C.; Biecek, P.; Samek, W. Explainable AI methods-a brief overview. In *xxAI—Beyond Explainable AI;* Springer: Cham, Switzerland, 2022; pp. 13–38.
66. Confalonieri, R.; Coba, L.; Wagner, B.; Besold, T.R. A historical perspective of explainable Artificial Intelligence. *Wiley Interdiscip. Rev. Data Min. Knowl. Discov.* **2021**, *11*, e1391. [CrossRef]
67. Cortez, P.; Embrechts, M. Using Sensitivity Analysis and Visualization Techniques to Open Black Box Data Mining Models. *Inf. Sci.* **2013**, *225*, 1–17. [CrossRef]
68. Brook, R.J.; Arnold, G.C. *Applied Regression Analysis and Experimental Design*; CRC Press: New York, NY, USA, 2018.
69. Cortez, P.; Embrechts, M. Opening Black Box Data Mining Models Using Sensitivity Analysis. In Proceedings of the 2011 IEEE Symposium on Computational Intelligence and Data Mining, CIDM 2011, Paris, France, 11–15 April 2011; IEEE: Paris, France, 2011; pp. 341–348.
70. Kaur, H.; Pannu, H.S.; Malhi, A.K. A systematic review on imbalanced data challenges in machine learning: Applications and solutions. *ACM Comput. Surv. (CSUR)* **2019**, *52*, 1–36. [CrossRef]
71. Carrington, A.; Fieguth, P.; Qazi, H.; Holzinger, A.; Chen, H.; Mayr, F.; Manuel, D. A new concordant partial AUC and partial c statistic for imbalanced data in the evaluation of machine learning algorithms. *BMC Med. Inform. Decis. Mak.* **2020**, *20*, 4. [CrossRef]
72. Pereira, P.J.; Pereira, A.; Cortez, P.; Pilastri, A. A Comparison of Machine Learning Methods for Extremely Unbalanced Industrial Quality Data. In *Progress in Artificial Intelligence;* Lecture Notes in Computer Science; Springer: Cham, Switzerland, 2021; Volume 12981.

applied sciences

MDPI

Article

Assessing the Sustainability of Alternative Shaft Construction Methods

António M. G. Pedro [1,*], Lucas Repsold [2] and Jorge Almeida e Sousa [3]

[1] ISISE, ARISE, Department of Civil Engineering, University of Coimbra, 3030-788 Coimbra, Portugal
[2] COBA Group, 1649-011 Lisbon, Portugal; lucasrepsold@gmail.com
[3] Department of Civil Engineering, University of Coimbra, 3030-788 Coimbra, Portugal; jas@dec.uc.pt
* Correspondence: amgpedro@dec.uc.pt; Tel.: +351-23-979-7224

Abstract: Reducing carbon dioxide (CO_2) emissions is a global priority. The concrete industry has a major role in this reduction since it accounts for about 8% of global CO_2 emissions. Despite significant improvements in the sustainability of the production of concrete, one of the best solutions is still to improve the design and construction methods, such that the required quantities of concrete are reduced. Using, as a reference, a real case study, this study compares alternative shaft construction methodologies from engineering and sustainability points of view, highlighting the advantages and drawbacks of each solution. To achieve this purpose, a back analysis is performed to ensure that the numerical model is accurately calibrated and the shaft construction methods can be adequately assessed. The results show that, while the considered methods are applicable and satisfy engineering requirements, the characteristics of the lining of the shaft could have been optimized, resulting in a reduction in CO_2 emissions by at least 50% without compromising the safety of the construction.

Keywords: sustainability; shaft excavation method; numerical modelling

Citation: Pedro, A.M.G.; Repsold, L.; Almeida e Sousa, J. Assessing the Sustainability of Alternative Shaft Construction Methods. *Appl. Sci.* **2024**, *14*, 4476. https://doi.org/10.3390/app14114476

Academic Editor: Syed Minhaj Saleem Kazmi

Received: 24 April 2024
Revised: 20 May 2024
Accepted: 23 May 2024
Published: 24 May 2024

1. Introduction

With the aim of creating a more sustainable world, politicians, under the umbrella of United Nations (UN), set up Agenda 2030, where 17 Sustainable Development Goals (SDGs) were established [1]. These SDGs have the ambition of ending poverty and inequality in the world, improving health and education, and spurring economic growth while tackling climate change and preserving nature. Whitin the objective of solving the climate crisis (UN-SDG 13), reducing carbon dioxide (CO_2) emissions is one of the most important aspects, which led, at the United Nations Climate Change Conference in 2015, to the Paris Agreement, where 196 parties signed a treaty, which aims to hold "the increase in the global average temperature to well below 2 °C above pre-industrial levels" [2]. To achieve that goal, it is fundamental to promote a major transformation in the construction sector (UN-SDG 9), where concrete manufacturing contributes to its massive carbon footprint, being responsible for at least 8% of global carbon emissions [3,4], with the ingredient cement accounting for most of this [4–7]. Moreover, its production consumes large amounts of raw materials and freshwater, causing high strain on the environment [8,9].

However, the concrete industry assumes major importance in the economy and growth of any country as it produces an essential material for infrastructure development. As a result, it is expected that the rising global population and urbanization will drive up the demand for cement and concrete by 12–23% by 2050 from current levels [10], with the increase being particularly relevant in countries and regions like China, India, and Africa [5,11]. Hence, improving the sustainability of concrete production and use can have a significant global impact on the climate.

To tackle this objective, the concrete industry has been incorporating various sustainability initiatives into all aspects associated with the production and utilization of concrete [5,7,8,12,13]. An in-depth review of the numerous contributions that have been

made to adapt and transform concrete into a sustainable material can be found in Hasanbeigi et al. [7], Adesina [8] and Chen et al. [12]. These new technologies are mainly focused on replacing part of the cement in the production of concrete with low-carbon concrete materials (LCCMs) [12], such as ground granulated blast-furnace slag (GGBF) and fly ash (FA), among others [14,15]. Other strategies consist of improving the energy efficiency of the production of concrete [7] and exploiting the potential of concrete recycling to increase the rate of CO_2 uptake [13]. Naturally, one of the best options for reducing concrete emissions is simply using concrete more rationally and efficiently in construction, which requires a better optimization of structures at the design stage and also an improvement in the construction methods employed [16,17]. As pointed out by Basu et al. [18] and Song et al. [19], this optimization should also include geotechnical works, where the comparison of different solutions through life cycle assessments (LCAs) would highlight the most climate-friendly design for that specific structure [19,20]. Following that approach, a few studies have been published on the topic. For instance, Luo et al. [21] analyzed the impact on carbon emissions of installing driven precast and bored piles; Sandanayake et al. [22] evaluated the emissions released by constructing two types of foundations of residential buildings, while Berndt [23] presented a study on the optimization of the concrete mixture in order to reduce the CO_2 emissions for large wind turbine foundations; Inui et al. [24], Damians et al. [25], and Pons et al. [26] performed LCAs of different types of retaining walls, trying to establish the most eco-friendly solution for particular scenarios; Chau et al. [27] calculated the emissions for two sections of the UK Channel Tunnel Rail Link; Sauer [28] and Aldrian et al. [29] discussed, in detail, the emissions caused by different types of linings usually adopted in tunnels; and Hu et al. [30] and Von der Tann et al. [31] evaluated the emissions for different design solutions of deep excavations.

In all cases, it is evident that performing an LCA analysis can be very complex, particularly at the design stage, where there is no clear definition of all aspects involved, mainly those associated with construction works. The gap between design, construction methods and sustainability can be bridged by performing back-analysis studies, where the performance of the adopted design and of possible alternative solutions is evaluated to provide suggestions for better design in future projects. Naturally, this process is highly dependent on the quality of the back analysis and on the amount of data available to calibrate and validate the numerical model. Following this methodology, this study assesses the impact of adopting alternative shaft construction methods from both engineering and sustainability points of view. Using, as a reference, the case of the WA2 shaft, built as part of the Dublin Port Tunnel project (DPT) [32], a numerical model is developed incorporating all the geotechnical information available at the shaft site. After a rigorous calibration of the constitutive model adopted for the soil layers and its validation against instrumentation data, alternative sequences for shaft excavation are assessed. These include the simulation of the excavation employing the SBE (Support Before Excavation) technique—where the support, such as diaphragm walls, is installed prior to the excavation—and of the EBS method (Excavation Before Support)—where the support is only installed once excavation is completed, such as in the case of shotcrete lining or precast concrete segments (PCL) [33].

2. The WA2 Shaft

The construction of the DPT, completed in 2006, was a major engineering infrastructure projects in Ireland and aimed to establish a quick connection between the Dublin harbor and the C-ring (M50) and M1 motorways, allowing for a quick transfer of heavy goods, while reducing heavy traffic congestion in the city center, contributing to a more sustainable environment with better air quality and noise reduction [32]. The project comprised the construction of twin-bored tunnels with 12.5 m of external diameter and 2.6 km long. To speed up the construction process, it was decided to build shaft WA2 (concluded in 2001), which served as a launching platform for the twin tunnel excavation. As explained by Cabarkapa et al. [34], after early design optimization studies, the final geometry of the circular shaft was established, consisting of an internal diameter of 56.6 m and a depth of

around 29.0 m. The construction followed the SBE method [35], with the support consisting of a 1.5 m thick diaphragm wall. A total of 26 panels were constructed, each being slightly over 7 m wide and approximately 32.5 m deep, with this dimension depending on the position of the top of the bearing stratum, a limestone layer. In addition to the capping beam at the top of the shaft, a ring beam, made of concrete with a section of 2.5 × 2.5 m^2 with its top at a depth of 10.5 m, was also executed. The concrete base slab was 1 m thick in the general section and 2 m thick around the breakouts of the tunnels [34]. The geometry and support system installed in the WA2 shaft are illustrated in Figure 1.

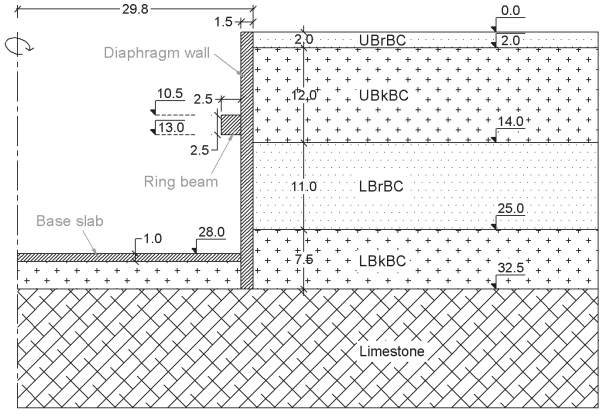

Figure 1. Scheme of the stratigraphy and geometry of WA2 shaft.

At the shaft location, the geology comprised the well-known Dublin boulder clays (DBCs) overlying a carboniferous limestone layer [36]. A detailed assessment of the geological features and geotechnical characteristics of that formation and its units can be found in Skipper et al. [36] and Long and Menkiti [37], respectively. The stratigraphy comprised 2 m of the weathered Upper Brown (UBrBC) unit, followed by the Upper Black (UBkBC) unit, which had a thickness of around 12 m. The third layer was the Lower Brown (LBrBC) unit, with a thickness of 11 m, and, finally, the 7.5 m thick Lower Black (LBkBC) unit was found (see Figure 1). Approximately hydrostatic conditions with a groundwater table located about 2 m below ground level (bottom of UBrBC) were measured by piezometers installed at the site.

3. Numerical Model

3.1. Details of the Analysis

To provide insights into the sustainability of the construction method employed in the excavation of the WA2 shaft, a numerical model was created using PLAXIS 2D v22.02 [38]. To incorporate all aspects of the problem in the simulation, a coupled consolidation analysis was performed while taking advantage of the axisymmetric nature of the problem. 15-noded triangular elements with 12 Gaussian integration points were employed for determining the displacements and stress states, respectively, in the solid elements, while for the diaphragm wall, 5-noded plate elements were employed. As can be seen in Figure 2, the mesh employed in the SBE analysis had a higher concentration of elements surrounding the diaphragm wall, where higher stress and strain variations are expected. Interface elements were used to simulate the soil–structure interaction and to prevent water flow through the diaphragm wall.

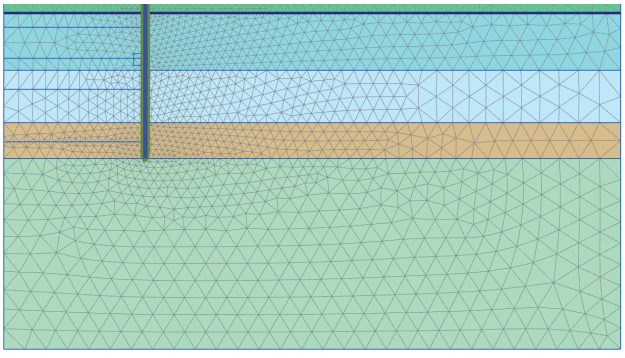

Figure 2. Mesh employed in the SBE analyses.

According to the information provided by the DPT administration [39], the WA2 shaft took approximately 5 months to excavate. To replicate the excavation process adequately, a linear advance rate was assumed in the numerical model, resulting in a value of 5 days per meter of excavation. An additional 15 days were assumed for the construction of the ring beam, which resulted in a total duration of 160 days. The simulation of the shaft excavation involved the following stages:

1. Generation of the initial stress state (assumed as geostatic with K_0-conditions);
2. Construction of the diaphragm wall ("wished in place");
3. Excavation to 14 m depth at a rate of 5 days/m;
4. Installation of the concrete ring beam (15 days);
5. Excavation to 29 m depth (base of the shaft) at a rate of 5 days/m.

The initial ground conditions were generated using, as a reference, the parameters proposed by Cabarkapa et al. [34]. A hydrostatic pore water pressure profile with the ground water table located at a depth of 2 m (bottom of UBrBC) was considered, together with the values of bulk unit weight (γ) and at-rest coefficient of earth pressure (K_0), as presented in Table 1. As suggested by Cabarkapa et al. [34] and Kovacevic et al. [40], the isotropic permeability (k) was considered for all layers, with values of 10^{-8} m/s for the Dublin Brown Boulder Clay and 10^{-9} m/s for all the other materials.

Table 1. General soil parameters adopted in the analysis.

Material	γ (kN/m^3)	K_0	k (m/s)
UBrBC	21.0	1.50	1×10^{-8}
UBkBC	22.5	1.50	1×10^{-9}
LBrBC	22.0	1.35	1×10^{-8}
LBkBC	22.5	1.20	1×10^{-9}
Limestone	26.0	1.00	1×10^{-9}

In agreement with Cabarkapa et al. [34], the behavior of the limestone was assumed to be linear elastic-perfectly plastic, with its stiffness being described by E = 3 GPa and $\nu = 0.3$, and its strength given by the Mohr–Coulomb failure criterion, with $\varphi' = 45^\circ$ and $c' = 50$ kPa, with non-associated plasticity characterized by $\psi = 0^\circ$.

Similar to the model suggested by Kovacevic et al. [40] and Kovacevic et al. [41], and in contrast with the linear elastic-perfectly plastic model employed by Cabarkapa et al. [34], the mechanical response of DBC units was described herein using an expanded generalized version of the Modified Cam-Clay (MCC) model [42]. In the present case, this model introduces the nonlinear Hvorslev surface of Tsiampousi et al. [43] on the dry side and is combined with the nonlinear small strain stiffness formulation of Taborda et al. [44]. As in

the original MCC formulation, the virgin compression line has a linear shape in ln $p' - \nu$ plane, being defined by:

$$\nu = \nu_1 - \lambda \cdot \ln p' \tag{1}$$

where p' is the mean effective stress, $\nu = 1 + e$ is the specific volume, and ν_1 and λ are model parameters. The stress ratio in the critical state is defined by the angle of shear resistance (ϕ'), while the nonlinear Hvorslev surface is controlled by four additional parameters, where α_{HV} and n control the shape of the surface and β_{HV} and m that of the plastic potential.

In terms of elastic behavior, the formulation established by the original MCC model for the tangent bulk stiffness, K_{tan}, is adopted:

$$K_{tan} = \frac{\nu \cdot p'}{\kappa} \tag{2}$$

where κ is the slope of the isotropic swelling line in the ln $p' - \nu$ space. Conversely, for the tangent shear modulus, G_{tan}, a modified hyperbolic expression is adopted [44]:

$$G_{tan} = G_{max} \cdot R_G = \underbrace{G_{ref}\left(\frac{p'}{p'_{ref}}\right)^{m_G}}_{(1)} \cdot \underbrace{\left[R_{G,min} + \frac{1 - R_{G,min}}{1 + \left(\frac{E_d}{a}\right)^b}\right]}_{(2)} \tag{3}$$

where G_{max} is the shear stiffness at very small strains, R_G is the stiffness reduction factor, p'_{ref} is a reference pressure (taken as 100 kPa), G_{ref} is the small-strain shear modulus at $p' = p'_{ref}$, E_d is the generalized deviatoric strain (i.e., the second invariant of the strain tensor), and m_G, a, b and $R_{G,min}$ are model parameters. This model, denoted as IC MAGE M06, was implemented as a User-Defined Soil Model (UDSM) into PLAXIS2D, which is described in Tsiampousi et al. [45]. The model is integrated using a modified Euler sub-stepping algorithm with automatic error control, as proposed by Sloan [46] and Sloan et al. [47], with the specific implementation for PLAXIS UDSMs detailed in Taborda et al. [48]. The derivation of the model parameters for all DBC layers is explained in detail in the next section, while the numerical simulations of the laboratory tests that validate the use of this constitutive model are reproduced in Appendix A.

In terms of excavation support, the diaphragm wall and the capping and ring beams were modelled as linear elastic with their stiffness described by E = 25.0 GPa, ν = 0.15 and with the dimensions presented in Figure 1. Lastly, the interaction between the support and the adjacent ground was modelled using interface elements with a strength reduced to two-thirds of that of the adjacent soil. The stiffness of these elements was set to $k_N = k_T = 10^6$ kN/m^3, where the subscripts N and T denote the normal and tangential directions, respectively.

3.2. Calibration of the Dublin Boulder Clay Units

The calibration of IC MAGE M06 [45,48] followed a hierarchical approach, where each parameter was estimated sequentially and the order was set by its physical relevance and by its independency from other values [49–51]. The first aspect of the model to calibrate is determining the shear stiffness at very small strains (term (1) in Equation (3)). Using as a reference the results plotted in Figure 3a of different field tests (MASW, seismic refraction and cross-holes), performed at the WA2 shaft site and in other locations in Dublin with a similar profile [37,52], the evolution with the depth of the shear stiffness at very small strains (G_{max}) was interpreted, allowing for the definition of parameters G_{ref} and m_G for all DBC units. Given the variability observed in the field tests, it was decided to adjust the parameters so that the average stiffness was reproduced. It should be noted that given the weathered nature of the UBrBC, and in agreement with the field tests results, a constant G_{ref} of 220 MPa was adopted for this unit (i.e., $m_G = 0$).

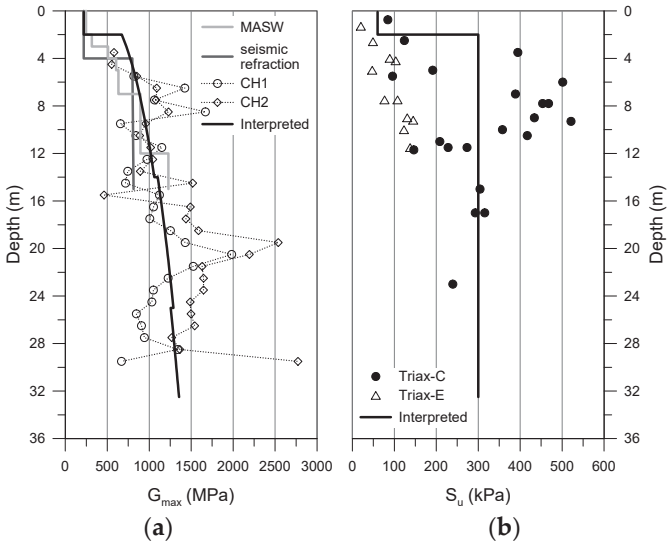

Figure 3. Experimental and interpreted (**a**) G_{max} and (**b**) S_u profiles.

Based on the results of conventional triaxial compression and extension tests, and as suggested by Long and Menkiti [37], a value $\varphi' = 36^{\circ}$ was adopted for the strength at the critical state of all units. The parameters of the compression and swelling lines were adopted following the revisited analysis performed by Kovacevic et al. [41], where the authors defined a set of different values for Brown and Black Boulder Clay units, regardless of their position (Upper or Lower) in the ground profile. Finally, the Hvorslev surface (shape and potential) and the shear stiffness degradation (term (2) in Equation (3)) were calibrated against the triaxial data presented by Long and Menkiti [37]. It is worth mentioning that since no test results were available to calibrate the LBkDC unit, it was assumed that its parameters were identical to those of the UBkBC unit, with the exception of G_{ref}, which had a higher value, reflecting the deeper position of that layer.

Table A1 in Appendix A summarizes all parameters of the IC MAGE M06 model adopted for all the DBC units considered in the analysis. Moreover, numerical reproductions of the oedometer and triaxial (compression and extension) tests that were used to calibrate the constitutive model are also shown in Appendix A. The results demonstrate a very good agreement between the numerical and measured data for all units, validating the adopted calibration process.

A final aspect required for the numerical simulation is related to the definition of the OCR profile at the WA2 shaft site. Unfortunately, there are no records of this state parameter available in the literature, and its estimation had to be performed indirectly based on the undrained shear strength (S_u) profile. Figure 3b presents the S_u values measured in triaxial compression and extension tests performed on DBC samples [37]. Although scatter and some discrepancies between compression and extension can be observed, the Irish practice usually considers an isotropic undrained shear strength defined by the profile presented by the solid black line [37]. A value of 60 kPa in the weathered UBrBC is generally assumed, and in the remaining units, a value of 300 kPa is commonly adopted. Based on this S_u profile, an equivalent OCR profile was derived using the closed-form solution of IC MAGE M06 [45] and introduced into the model as an initial state condition.

3.3. Validation of the Numerical Model against Intrumentation Data

The lateral deflections caused by the WA2 shaft excavation were measured by 10 inclinometers, 9 of which were installed in the diaphragm wall panels, while 1 was installed in the soil behind the shaft. Cabarkapa et al. [34] presented the records of the

horizontal displacements at four depths of the excavation (5.0, 11.5, 18.0, and 25.0 m), as can be seen in Figure 4. Unfortunately, the data available are not directly associated with the location of the inclinometer and, consequently, only a general characterization of the shaft behavior can be performed. As expected, the movements caused by the shaft excavation increase with the depth of excavation. However, it should be noted that the registered displacements can be considered as very small, not surpassing 8 mm in any inclinometer. Prior to the construction of the ring beam (Figure 4a,b), the shaft deflected, almost like a cantilever, with its rotating point below the base of the excavation, suggesting that the panels might have deformed, at least to some extent, independently. After the construction of the ring beam (Figure 4c,d), it is possible to observe some bulging in the middle and lower portions of the diaphragm wall, while the displacements in the upper part remained approximately constant, which is typical of this type of structure [53].

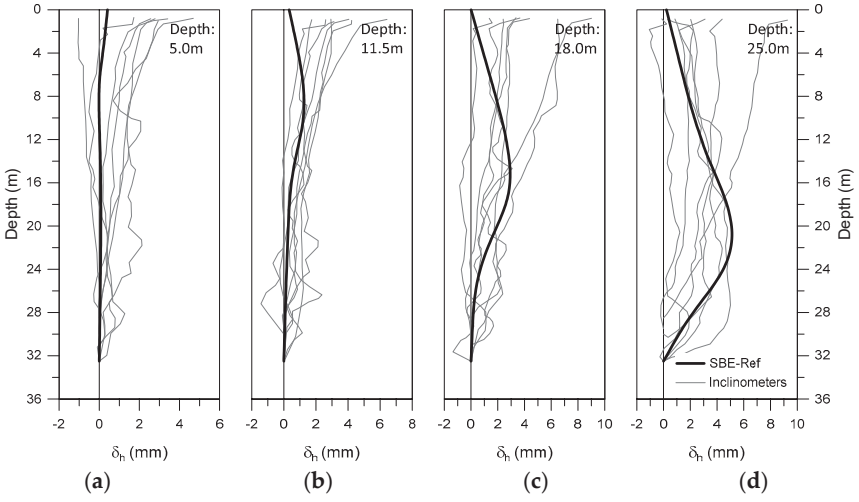

Figure 4. Comparison of predicted and observed diaphragm wall deflections at different shaft excavation depths: (**a**) 5.0 m; (**b**) 11.5 m; (**c**) 18.0 m; (**d**) 25.0 m.

Superimposed on the figure are the horizontal displacements predicted by the numerical model for the reference analysis (SBE-Ref). The results obtained for all excavation depths are in reasonable agreement with the average movement observed for the shaft. For a depth of excavation of 5.0 m, the model captures the cantilever movement, while for larger depths, bulging for the lower portion of the shaft, particularly below the ring beam, is also predicted adequately. Near the surface, the model predicts smaller displacements than those recorded, although still inside the envelope of horizontal displacements recorded. Based on the results, it can be concluded that the numerical model is able to reasonably predict the behavior of the shaft excavation.

4. Shaft Construction Methods

4.1. SBE Shaft Excavation

Despite the optimization of the design of the shaft support, which, accordingly with Cabarkapa et al. [34], significantly reduced the thickness of the diaphragm wall, the solution adopted for the shaft includes substantial structural elements, with its 1.5 m thick diaphragm wall complemented by the 2.5 × 2.5 m^2 concrete ring beam. To evaluate to what extent the adopted support could be reduced, thus potentially leading to more sustainable designs, two additional analyses were performed. In the first one, the ring beam was not modelled (SBE-Ring), while in the second one, in addition to disregarding the ring beam, the thickness of the diaphragm wall was reduced by half to 0.75 m (SBE-0.75).

Figure 5 presents, for the last excavation stage (29 m depth), the horizontal movements and forces (in terms of hoop and bending moment envelopes) obtained in the diaphragm wall for the various SBE analyses. The results show that the ring beam has an almost negligible effect, contributing only to a slight reduction in the horizontal displacements at its location. Similarly, only local variation is predicted in terms of structural forces, with a slight increase in both hoop forces and bending moments. In contrast, the reduction in the wall thickness leads to a considerable decrease in the associated bending moments (by a factor of more than 60%) and hoop forces (factor of 15%). However, the reduction in terms of forces is associated with an increase in horizontal movements, which now reach a maximum of 9.5 mm, an increase of 120% compared with the reference analysis (4.3 mm). The influence of reducing the stiffness of the diaphragm wall by half is also noticeable in the estimated settlements at the surface (Figure 6), where an increase of about 45% is observed. Nevertheless, even after such increases, the magnitude of the ground movements induced by excavation of the shaft can still be considered small.

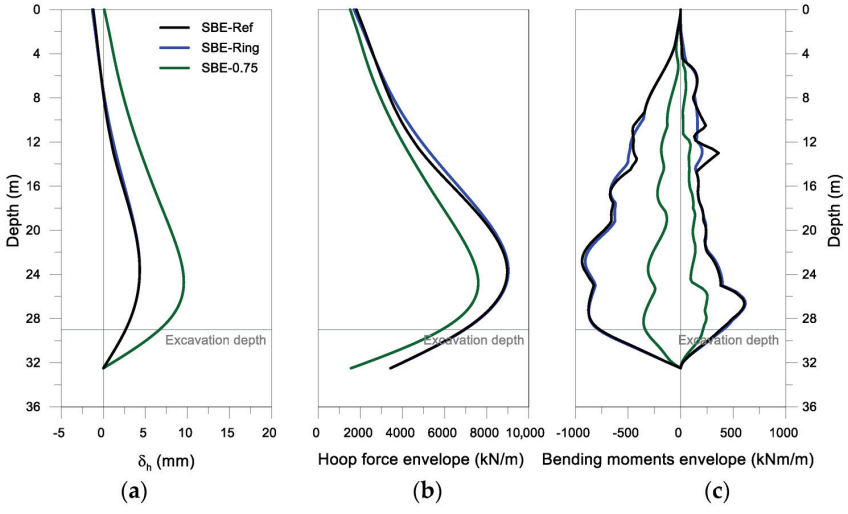

Figure 5. Influence of the SBE shaft excavation method: (**a**) horizontal displacements; (**b**) hoop force; (**c**) bending moments.

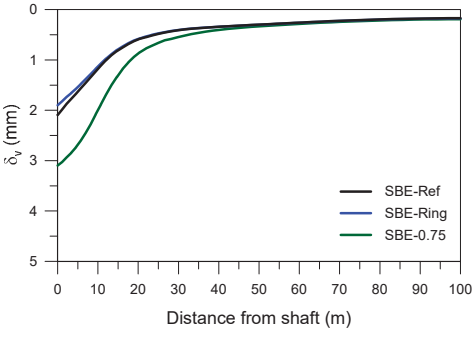

Figure 6. Influence of the SBE shaft excavation method on the settlements.

4.2. EBS Shaft Excavation

To further assess the influence of the shaft construction method, additional analyses following the principles of EBS, i.e., support only installed after excavation, were carried

out. The support provided by the diaphragm wall was replaced by shotcrete or pre-cast segmental lining, which are, isolated or combined, the typical lining solutions installed in EBS methodology [35]. In the performed analyses, the thickness of the shotcrete was reduced from 1.50 m to 0.35 m, with the latter value being in agreement with the thicknesses usually employed in shafts excavated with a similar methodology and in comparable materials [35]. For the segmental lining, a standard thickness of 0.35 m was adopted [35]. For ease of comparison, the elastic properties of the shotcrete were considered equal to those of the diaphragm wall, while for the segmental lining, a Young's modulus of 37 GPa was employed, reflecting the characteristics of prefabricated concrete. In the EBS methodology, a key factor is the size of the excavation step, since lager values of this quantity will cause larger soil decompression, leading to increased movements and instabilities (local or even global), while small steps introduce significant constraints in the excavation process, requiring higher construction time and costs, while diminishing the overall advantages of using EBS principles. To evaluate the effects of the type of support and of the excavation step, six analyses were performed, as outlined in Table 2.

Table 2. Details of the EBS analyses.

Designation	Thickness (m)	Excavation Step (m)	E (GPa)
EBS-1.50	1.5	1.0	25
EBS-0.75	0.75	1.0	25
EBS-0.35	0.35	1.0	25
EBS-0.35-2 m	0.35	2.0	25
EBS-0.35-3 m	0.35	3.0	25
EBS-0.35-Seq	0.35	1.0	37

To simulate the EBS analyses, the construction sequence adopted in the numerical model was modified. Hence, after the generation of the initial stress state, the first excavation step was performed. In the following stage, a new excavation step was performed while installing the lining supporting the previously excavated step. This sequence was carried out until the full excavation depth was reached. The duration of each stage was adapted so that the whole excavation process would take the same 160 days defined for the SBE analyses.

The horizontal displacements and lining forces obtained for the last excavation stage are plotted in Figure 7. As expected, the reduction in thickness of the shotcrete from 1.50 m to 0.35 m increased the horizontal displacements by a factor of 1.7, reaching a maximum of 37.5 mm in EBS-0.35 in comparison with 21.9 mm in EBS-1.50. For the analysis with a 0.75 m thick shotcrete support, the maximum displacement was 27.8 mm. In contrast, a significant reduction in the bending moments was observed, with an absolute maximum of 1395 kNm/m in the thicker case, in comparison to just 190 kNm/m in EBS-0.35. A reduction but of a smaller magnitude was also observed in the hoop forces (7025 kN/m against 6450 kN/m). The use of the stiffer segmental lining (EBS-035-Seg) leads to smaller horizontal displacements (29.9 mm) but slightly higher lining forces (6670 kN/m and 220 kNm/m) in comparison with the shotcrete analysis with the same thickness (EBS-0.35). The results also confirm that the excavation step is an important aspect. When its value is increased from 1 m to 3 m, an increase in horizontal displacements of about 35% is observed. In contrast, a reduction of approximately 7% in the hoop force and about 46% in bending moments is predicted. A similar behavior can be observed in terms of settlements (Figure 8), as a reduction in stiffness or an increase in the excavation step will increase the magnitude of the deformations, which can reach a maximum of 47 mm in the analysis where the support is less stiff and the excavation step larger (EBS-0.35-3 m).

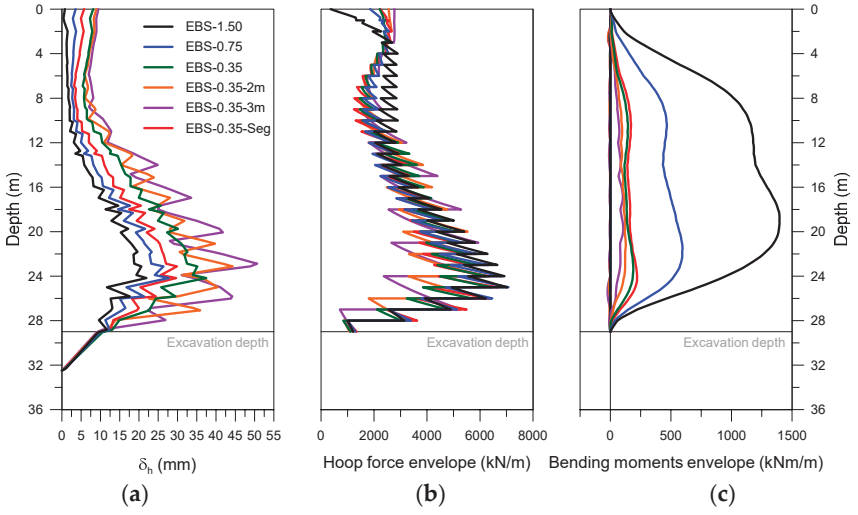

Figure 7. Influence of the EBS shaft excavation method: (**a**) horizontal displacements; (**b**) hoop force; (**c**) bending moments.

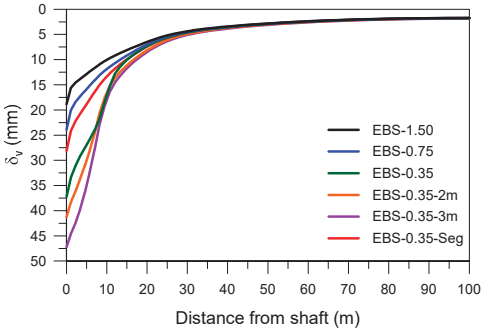

Figure 8. Influence of the EBS shaft excavation method on the settlements.

5. Discussion Regarding Sustainability

Until recently, the optimal design of a structure was defined as that which met the safety requirements at minimum cost. Due to the climate emergency, sustainability considerations have become increasingly important. Indeed, nowadays, it is indispensable to consider this perspective in the design stage, with the optimal solution being a compromise between cost and sustainability while meeting all safety requirements. However, this evaluation is difficult to perform since the quantification of costs, and particularly of CO_2 emissions, at the design stage requires knowledge of several factors. These include those whose associated prices/emissions are very volatile, such as fuel and human labor, which can only be adequately defined closer to the start of construction [30]. Moreover, there is still scarce and scattered information regarding the evaluation of CO_2 emissions related to specific activities, rendering their quantification even more difficult. Nevertheless, with the implementation, standardization [54–56], and generalization of LCA in different accessible platforms [19,20,31], this task, which is key when evaluating the sustainability of different construction processes, is becoming easier to perform. Using as a reference those platforms and previous studies [28,30], it was possible to define a reasonable range of unit CO_2 emissions (i.e., in ton per m^3) associated with the construction of diaphragm walls, application of shotcrete, and installation of PCL. Those values are presented in Table 3 and were used to calculate the CO_2 emissions associated with each of the solutions studied in the previous

section. As expected, the unit values regarding the diaphragm walls are substantially higher, being mostly affected by the steel reinforcement required. The difference between shotcrete and PCL is mostly related to the concrete composition and with the rebound of material associated with the shotcrete application, which produces higher emissions when compared to the PCL. The CO_2 results presented in Table 3 reflect those differences, with the SBE analyses presenting much higher CO_2 emissions, with a maximum of 16,835 t being estimated for the worst-case scenario, which corresponds to the reference analysis (SBE-Ref). In contrast, the PCL solution (EBS-Seg) is responsible for the minimum CO_2 emissions (maximum of 1267 t), as can be more easily seen in Figure 9.

Table 3. Summary of the results.

Analysis	CO_2 Emissions			Displacements		Lining Forces	
	Volume (m^3)	CO_2 (t CO_2/m^3)	CO_2 (t CO_2)	δ_h/H(%)	δ_v/H(%)	Hoop Force	Bending Moments
SBE-Ref	16,033	0.70–1.05	11,223–16,835	0.015	0.007	A	A
SBE-Ring	15,675	0.70–1.05	10,972–16,459	0.015	0.007	A	A
SBE-0.75	7786	0.70–1.05	5450–8175	0.033	0.011	A	A
EBS-1.50	15,675	0.35–0.50	5486–7837	0.076	0.065	A	NA
EBS-0.75	7786	0.35–0.50	2725–3893	0.096	0.083	A	NA
EBS-0.35	3621	0.35–0.50	1267–1810	0.129	0.128	A	A
EBS-0.35-2 m	3621	0.35–0.50	1267–1810	0.153	0.142	A	A
EBS-0.35-3 m	3621	0.35–0.50	1267–1810	0.175	0.163	A	A
EBS-0.35-Seq	3621	0.25–0.35	905–1267	0.103	0.097	A	A

A—Acceptable; NA—Not Acceptable.

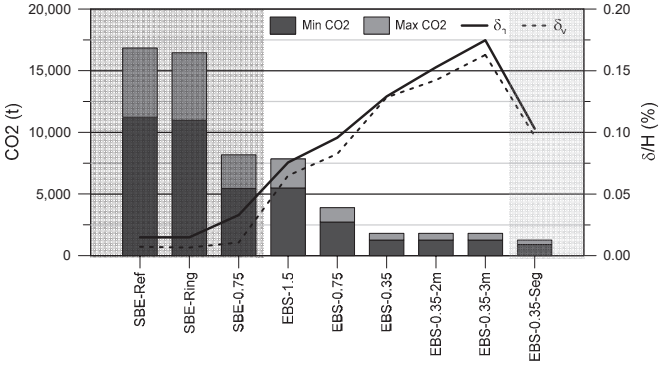

Figure 9. Comparison of the results of all analysis.

Also, in Table 3, the engineering requirements related to the displacements (vertical and horizontal) and the lining forces (hoop force and bending moments) are presented. According to a review performed by Long [57], all analyses met the displacement thresholds for both vertical and horizontal movements, with the highest values predicted being smaller than 0.25% and 0.20% of the shaft height (H) for vertical and horizontal displacements, respectively. However, analyses where an excavation step higher than 1 m (EBS-0.35-2 m and EBS-0.35-3 m) was applied exceeded the recommendations of Clough and O'Rourke [58], which defined a threshold of 0.15% for horizontal movements. In terms of lining forces, it is also clear that the analyses with a shotcrete thickness of 0.75 (EBS-0.75) and 1.5 m (EBS-1.50) are not acceptable since the magnitude of the predicted bending moments far exceeds the capacity of the shotcrete, which is usually just reinforced with fibers. The forces predicted for all other cases are within the capacity of the support solutions considered in this study.

Figure 9 summarizes the obtained data regarding CO_2 emissions and displacements. As expected, the SBE analyses present the best performance in terms of displacements due to the initial installation of the diaphragm wall (i.e., prior to any excavation taking place) but have a very detrimental impact in terms of CO_2 emissions. In contrast, the EBS methodology is much more environmentally friendly, particularly if PCL is employed, but it induces higher deformations, which increase with a reduction in the stiffness of the lining and/or with an increase in the excavation step. As a result, and given the small displacements precited in all cases, it would have been more acceptable to use EBS methods to construct the shaft or, at least, to reduce the thickness of the diaphragm wall to 0.75 m, which would itself lead to a reduction of 50% in the associated CO_2 emissions. Although the economical aspect was not analyzed in this study, it should be mentioned that, typically, the costs and the duration of works associated with EBS methods are smaller than those associated with SBE, which would make the decision to adopt EBS even more suitable for the present case.

6. Conclusions

Despite its complexity, the evaluation of sustainability at the design stage for all geotechnical works is becoming imperative. However, its inclusion at an early stage of the design process can be difficult, and often the best solution to achieve sustainability is to optimize the design by comparing different construction solutions using, as a reference, previous case studies. By performing back-analysis studies with adequately calibrated and validated numerical models, it is possible to assess the advantages and shortcomings of different design and construction methods. The outcome of such studies addresses UN-SDGs 9 (Industry, Innovation and Infrastructure) and 13 (Climate Change) and can be used as a reference in the development of future infrastructure. An example of this methodology is shown in this paper, where the excavation of the WA2 shaft was analyzed in detail. After adequate calibration based on field and laboratory testing and validation against monitoring data, the numerical model enabled the assessment of the potential impact of the selected excavation method (SBE or EBS). The results show that, while the excavation method employed (SBE) had the best performance in terms of minimizing the displacements in the ground, it had the greatest environmental impact in terms of CO_2 emissions. In contrast, the EBS analyses, particularly when PCL was installed, had the smallest CO_2 emissions, and, although the displacements were higher than in the SBE analyses, this could represent an acceptable engineering solution, meeting commonly accepted safety thresholds. As a result, it is clear that the characteristics of the lining of the shaft could have been optimized, resulting in a reduction in CO_2 emissions by at least 50% without compromising the safety of the construction.

Author Contributions: Conceptualization, A.M.G.P. and L.R.; methodology, A.M.G.P.; software, A.M.G.P.; validation, L.R. and J.A.e.S.; writing—original draft preparation, A.M.G.P.; writing—review and editing, L.R. and J.A.e.S. All authors have read and agreed to the published version of the manuscript.

Funding: This work was partly financed by FCT/MCTES through national funds (PIDDAC) under the R&D Unit Institute for Sustainability and Innovation in Structural Engineering (ISISE), under reference UIDB/04029/2020, and under the Associate Laboratory Advanced Production and Intelligent Systems ARISE under reference LA/P/0112/2020.

Institutional Review Board Statement: Not applicable.

Informed Consent Statement: Not applicable.

Data Availability Statement: The raw data supporting the conclusions of this article will be made available by the authors on request.

Conflicts of Interest: Author Lucas Repsold was employed by the company COBA Group. The remaining authors declare that the research was conducted in the absence of any commercial or financial relationships that could be construed as a potential conflict of interest.

Appendix A

The model parameters adopted for all DBC units employed in the numerical analyses are presented in Table A1. Figure A1 compares the measured and simulated $e - \sigma'_v$ curves obtained for an oedometer test performed on a UBkBC sample [59]. The model, apart from the initial part of the curve, which is usually affected by soil disturbance, predicts with reasonable accuracy the reduction in volume with an increase in vertical stress and is also capable of accurately reproducing the unloading performed at the end of the test. Figure A2 compares the measured and simulated effective stress paths, stress–strain curves, excessive pore water pressure–strain curves, and undrained Young's modulus degradation obtained for conventional undrained compression and extension triaxial tests performed in three of the four units of DBC (no results were available for the Lower Black Boulder Clay) [37]. The model predicts, with good accuracy, the stress path and the mobilization of deviatoric stresses for all units, as well as the evolution of excess pore pressures from initially positive to negative at high strains, as would be expected for an over-consolidated clay. The shear stiffness degradation is also accurately captured by the model in all cases reproduced.

Table A1. Parameters adopted for reproducing the stress–strain behavior of the Dublin Boulder Clays units.

Component	Parameter	UBrBC	UBkBC	LBrBC	LBkBC
Strength	ϕ' (°)	36.0	36.0	36.0	36.0
Compression line	ν_1	1.565	1.480	1.565	1.480
	λ	0.04	0.03	0.04	0.03
Swelling line	κ	0.002	0.002	0.002	0.002
Hvorslev surface	α_{HV}	1.0	1.0	1.0	1.0
	n	0.8	0.8	0.8	0.8
	β_{HV}	0.05	0.1	0.05	0.1
	m	1.5	1.2	1.5	1.2
Shear stiffness	G_0 (MPa)	220	800	850	850
	m_G	0.0	0.3	0.3	0.3
	a	3.5×10^{-5}	0.1×10^{-5}	3.5×10^{-5}	0.1×10^{-5}
	b	1.0	1.7	1.0	1.7
	$R_{G,min}$	0.02	0.02	0.02	0.02

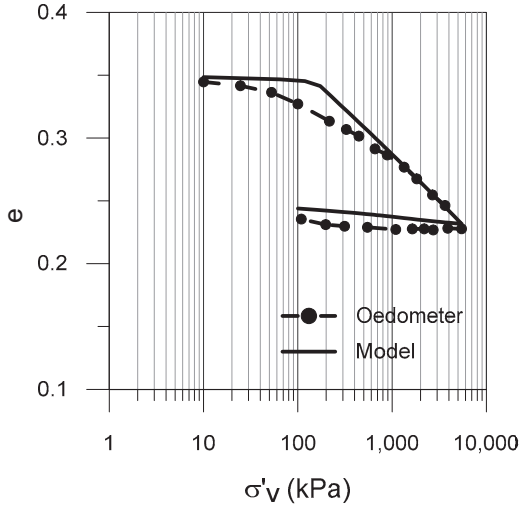

Figure A1. Experimental and modelled oedometer test of UBkBC.

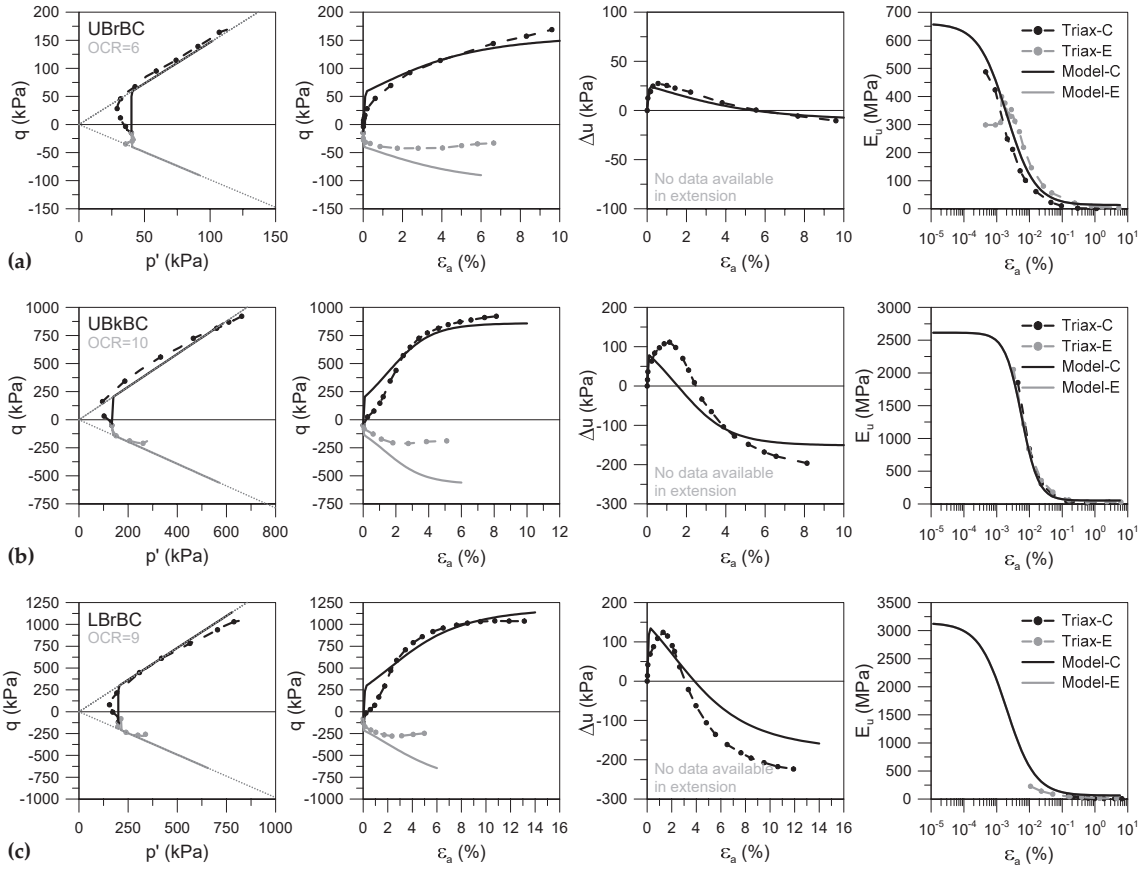

Figure A2. Experimental and modelled triaxial tests—effective stress paths; stress-strain curves; excessive pore water pressure-strain curves; undrained modulus degradation: (**a**) UBrBC; (**b**) UBkDC; (**c**) LBrDC.

References

1. Project Everyone. The Global Goals. Available online: https://www.globalgoals.org/ (accessed on 10 April 2024).
2. UNFCCC. The Paris Agreement. Available online: https://unfccc.int/process-and-meetings/the-paris-agreement (accessed on 10 April 2024).
3. Lehne, J.; Preston, F. Making concrete change. In *Innovation in Low-Carbon Cement and Concrete*; Chatham House: London, UK, 2018.
4. Monteiro, P.J.M.; Miller, S.A.; Horvath, A. Towards sustainable concrete. *Nat. Mater.* **2017**, *16*, 698–699. [CrossRef] [PubMed]
5. Worrell, E.; Price, L.; Martin, N.; Hendriks, C.; Ozawa-Meida, L. Carbon Dioxide Emission from the Global Cement Industry. *Annu. Rev. Energy Env.* **2001**, *26*, 303–329. [CrossRef]
6. Flower, D.J.M.; Sanjayan, J.G. Green house gas emissions due to concrete manufacture. *Int. J. Life Cycle Assess.* **2007**, *12*, 282–288. [CrossRef]
7. Hasanbeigi, A.; Price, L.; Lin, E. Emerging energy-efficiency and CO_2 emission-reduction technologies for cement and concrete production: A technical review. *Renew. Sustain. Energy Rev.* **2012**, *16*, 6220–6238. [CrossRef]
8. Adesina, A. Recent advances in the concrete industry to reduce its carbon dioxide emissions. *Environ. Chall.* **2020**, *1*, 100004. [CrossRef]
9. Purnell, P. The carbon footprint of reinforced concrete. *Adv. Cem. Res.* **2013**, *25*, 362–368. [CrossRef]
10. IEA. *Technology Roadmap—Low-Carbon Transition in the Cement Industry*; IEA: Paris, France, 2014.
11. Wu, P.; Song, Y.; Zhu, J.; Chang, R. Analyzing the influence factors of the carbon emissions from China's building and construction industry from 2000 to 2015. *J. Clean. Prod.* **2019**, *221*, 552–566. [CrossRef]

12. Chen, S.; Teng, Y.; Zhang, Y.; Leung, C.K.Y.; Pan, W. Reducing embodied carbon in concrete materials: A state-of-the-art review. *Resour. Conserv. Recycl.* **2023**, *188*, 106653. [CrossRef]
13. Damtoft, J.S.; Lukasik, J.; Herfort, D.; Sorrentino, D.; Gartner, E.M. Sustainable development and climate change initiatives. *Cem. Concr. Res.* **2008**, *38*, 115–127. [CrossRef]
14. Tait, M.W.; Cheung, W.M. A comparative cradle-to-gate life cycle assessment of three concrete mix designs. *Int. J. Life Cycle Assess.* **2016**, *21*, 847–860. [CrossRef]
15. Grist, E.R.; Paine, K.A.; Heath, A.; Norman, J.; Pinder, H. The environmental credentials of hydraulic lime-pozzolan concretes. *J. Clean. Prod.* **2015**, *93*, 26–37. [CrossRef]
16. Jannik, G.; John, B.; Peter, T. Scenario analysis of embodied greenhouse gas emissions in UK construction. *Proc. Inst. Civ. Eng. Eng. Sustain.* **2018**, *171*, 178–190. [CrossRef]
17. Guggemos, A.A.; Horvath, A. Decision-support tool for assessing the environmental effects of constructing commercial buildings. *J. Archit. Eng.* **2006**, *12*, 187–195. [CrossRef]
18. Basu, D.; Misra, A.; Puppala, A.J. Sustainability and geotechnical engineering: Perspectives and review. *Can. Geotech. J.* **2015**, *52*, 96–113. [CrossRef]
19. Song, X.; Carlsson, C.; Kiilsgaard, R.; Bendz, D.; Kennedy, H. Life Cycle Assessment of Geotechnical Works in Building Construction: A Review and Recommendations. *Sustainability* **2020**, *12*, 8442. [CrossRef]
20. Kendall, A.; Raymond, A.J.; Tipton, J.; DeJong, J.T. Review of life-cycle-based environmental assessments of geotechnical systems. *Proc. Inst. Civ. Eng. Eng. Sustain.* **2018**, *171*, 57–67. [CrossRef]
21. Luo, W.; Sandanayake, M.; Zhang, G. Direct and indirect carbon emissions in foundation construction—Two case studies of driven precast and cast-in-situ piles. *J. Clean. Prod.* **2019**, *211*, 1517–1526. [CrossRef]
22. Sandanayake, M.; Zhang, G.; Setunge, S. Environmental emissions at foundation construction stage of buildings—Two case studies. *Build. Environ.* **2016**, *95*, 189–198. [CrossRef]
23. Berndt, M.L. Influence of concrete mix design on CO_2 emissions for large wind turbine foundations. *Renew. Energy* **2015**, *83*, 608–614. [CrossRef]
24. Inui, T.; Chau, C.; Soga, K.; Nicolson, D.; O'Riordan, N. Embodied Energy and Gas Emissions of Retaining Wall Structures. *J. Geotech. Geoenviron. Eng.* **2011**, *137*, 958–967. [CrossRef]
25. Damians, I.P.; Bathurst, R.J.; Adroguer, E.G.; Josa, A.; Lloret, A. Environmental assessment of earth retaining wall structures. *Environ. Geotech.* **2017**, *4*, 415–431. [CrossRef]
26. Pons, J.J.; Penadés-Plà, V.; Yepes, V.; Martí, J.V. Life cycle assessment of earth-retaining walls: An environmental comparison. *J. Clean. Prod.* **2018**, *192*, 411–420. [CrossRef]
27. Chau, C.; Soga, K.; O'Riordan, N.; Nicholson, D. Embodied energy evaluation for sections of the UK Channel Tunnel rail link. *Proc. Inst. Civ. Eng. Geotech. Eng.* **2012**, *165*, 65–81. [CrossRef]
28. Sauer, J. Ecological Considerations on the Sustainability of Tunnel Structures in the Transport Infrastructure. Ph.D. Thesis, Technical University of Munich, Munich, Germany, 2016.
29. Aldrian, W.; Bantle, A.; Juhart, J. CO_2 reduction in tunnel construction from a material technology point of view. *Geomech. Tunn.* **2022**, *15*, 799–810. [CrossRef]
30. Hu, H.; Li, C.; Xu, Z.; Gui, Y.; Zong, L.; Shi, J. Calculation example of full cycle carbon emission of super deep foundation pit and carbon reduction measures. *Low-Carbon Mater. Green Constr.* **2023**, *1*, 11. [CrossRef]
31. Von der Tann, L.; Størdal, I.F.; Ritter, S.; Feizi, S. First steps in the development of standardised processes for life cycle assessments of geotechnical works. *IOP Conf. Ser. Earth Environ. Sci.* **2022**, *1122*, 012046. [CrossRef]
32. Dublin Tunnel. About the Dublin Tunnel. Available online: https://dublintunnel.ie/about-dublin-tunnel/ (accessed on 10 April 2024).
33. Faustin, N.; Elshafie, M.; Mair, R. Modelling the excavation of elliptical shafts in the geotechnical centrifuge. In *Physical Modelling in Geotechnics*; CRC Press: Boca Raton, FL, USA, 2018; Volume 2, pp. 791–796.
34. Cabarkapa, Z.; Milligan, G.W.E.; Menkiti, C.O.; Murphy, J.; Potts, D.M. Design and performance of a large diameter shaft in Dublin Boulder Clay. In Proceedings of the BGA International Conference on Foundations: Innovations, Observations, Design and Practice, Dundee, UK, 2–5 September 2003; pp. 175–185.
35. Faustin, N.E.; Elshafie, M.Z.; Mair, R.J. Case studies of circular shaft construction in London. *Proc. Inst. Civ. Eng. Ground Improv.* **2018**, *171*, 391–404. [CrossRef]
36. Skipper, J.; Follett, B.; Menkiti, C.; Long, M.; Clark-Hughes, J. The engineering geology and characterization of Dublin Boulder Clay. *Q. J. Eng. Geol. Hydrogeol.* **2005**, *38*, 171–187. [CrossRef]
37. Long, M.; Menkiti, C.O. Geotechnical properties of Dublin boulder clay. *Géotechnique* **2007**, *57*, 595–611. [CrossRef]
38. Bentley Systems. *CONNECT Edition V22.02 PLAXIS 2D—Reference Manual*; Bentley Systems: Exton, PA, USA, 2022.
39. Dublin Tunnel. Press. Available online: https://dublintunnel.ie/wp-content/uploads/pdf/dublin-tunnel-press-pack.pdf (accessed on 10 April 2024).
40. Kovacevic, N.; Miligan, G.W.E.; Menkiti, C.O.; Long, M.; Potts, D.M. Finite element analyses of steep man-made cuts in Dublin boulder clay. *Can. Geotech. J.* **2008**, *45*, 549–559. [CrossRef]
41. Kovacevic, N.; Menkiti, C.O.; Long, M.; Potts, D.M. Finite element analyses of a cantilever wall in Dublin Boulder Clay. In *Geotechnical Engineering for Infrastructure and Development*; Emerald Publishing Ltd.: Bingley, UK, 2015; pp. 3983–3988.

42. Roscoe, K.H.; Burland, J. On the generalized stress-strain behaviour of wet clay. In *Engineering Plasticity*; Cambridge University Press: Cambridge, UK, 1968; pp. 539–609.
43. Tsiampousi, A.; Zdravković, L.; Potts, D.M. A new Hvorslev surface for critical state type unsaturated and saturated constitutive models. *Comput. Geotech.* **2013**, *48*, 156–166. [CrossRef]
44. Taborda, D.M.G.; Potts, D.M.; Zdravković, L. On the assessment of energy dissipated through hysteresis in finite element analysis. *Comput. Geotech.* **2016**, *71*, 180–194. [CrossRef]
45. Tsiampousi, A.; Kontoe, S.; Taborda, D.M.G. *IC MAGE Model 06—Modified Cam-Clay Model with a Non-Linear Hvorslev Surface and Isotropic Small Strain Shear Stiffness, Version 1.6*; Zenodo: Geneva, Switzerland, 2023. [CrossRef]
46. Sloan. Substepping schemes for the numerical integration of elastoplastic stress–strain relations. *Int. J. Numer. Methods Eng.* **1987**, *24*, 893–911. [CrossRef]
47. Sloan, S.W.; Abbo, A.J.; Sheng, D. Refined explicit integration of elastoplastic models with automatic error control. *Eng. Comput.* **2001**, *18*, 121–194. [CrossRef]
48. Taborda, D.M.G.; Kontoe, S.; Tsiampousi, A. *IC MAGE UMIP—Universal Model Interface for PLAXIS, Version 3.5*; Zenodo: Geneva, Switzerland, 2023. [CrossRef]
49. Loukidis, D.; Salgado, R. Modeling sand response using two-surface plasticity. *Comput. Geotech.* **2009**, *36*, 166–186. [CrossRef]
50. Gallipoli, D.; D'Onza, F.; Wheeler, S.J. A sequential method for selecting parameter values in the Barcelona basic model. *Can. Geotech. J.* **2010**, *47*, 1175–1186. [CrossRef]
51. Pedro, A.M.G.; Zdravković, L.; Potts, D.; Almeida e Sousa, J. Derivation of model parameters for numerical analysis of the Ivens shaft excavation. *Eng. Geol.* **2017**, *217*, 49–60. [CrossRef]
52. Donohue, S.; Gavin, K.; Long, M.; O'Connor, P. Gmax from multichannel analysis of surface waves for Dublin boulder clay. In Proceedings of the 13th European Conference on Soil Mechanics and Geotechnical Engineering, Prague, Czech Republic, 3 September 2003; Volume 2, pp. 515–520.
53. Pedro, A.; Zdravkovic, L.; Potts, D.; Sousa, J.A.E. Numerical modelling of the Ivens shaft construction in Lisbon, Portugal. In *Geotechnical Engineering*; Emerald Publishing Ltd.: Bingley, UK, 2019; Volume 172, pp. 263–282. [CrossRef]
54. *ISO 14044:2006*; Environmental Management—Life Cycle Assessment—Requirement and Guidelines. International Organization for Standardization: Geneva, Switzerland, 2006.
55. *ISO 14040:2006*; Environmental Management—Life Cycle Assessment—Principles and Framework. International Organization for Standardization:: Geneva, Switzerland, 2006.
56. *EN 15804:2012+A2:2019*; Sustainability of Construction Works—Environmental Product Declarations—Core Rules for the Product Category of Construction Products. iTeh Standards: Etobicoke, ON, Canada, 2019.
57. Long, M. Database for retaining wall and ground movements due to deep excavations. *J. Geotech. Geoenviron. bEng.* **2001**, *127*, 203–224. [CrossRef]
58. Clough, G.W.; O'Rourke, T.D. Construction induced movements of insitu walls. In *Proceedings of the Design and Performance of Earth Retaining Structures*; American Society of Civil Engineers: Reston, VA, USA, 1990; pp. 439–470.
59. Brangan, C. Behaviour of Deep Excavation in Dublin Glacial Till. Ph.D. Thesis, Department of Civil Engineering, University College Dublin, Dublin, Ireland, 2007.

applied sciences

MDPI

Article

Long-Term Durability of Cement-Treated Soil Used in Offshore Airport Island Construction

Hidenori Takahashi [1,*], Itsuki Sato [1], Yoshiyuki Morikawa [1] and Akira Ozawa [2]

[1] Geotechnical Engineering Department, Port and Airport Research Institute, National Institute of Maritime, Port and Aviation Technology, 3-1-1 Nagase, Yokosuka 2390826, Japan
[2] Facility Service, Central Japan International Airport Co., Ltd., 1-1 Centrair, Tokoname 4798703, Japan
* Correspondence: takahashi-h@p.mpat.go.jp

Abstract: In port and harbour areas, soft soils such as dredged soil can be solidified by mixing them with cement and other solidifiers in a pumping pipe. This method is known as pneumatic flow mixing. In this method, the soil and solidifiers are stirred and mixed using the turbulence effect of the plug flow generated in the pipe. The authors investigate the long-term durability of the treated soil on the artificial island where this method was first fully introduced. This paper summarises the results of five investigations on the island immediately after construction and 4, 10, 15, and 20 years after construction. No reduction in the unconfined compressive strength or needle penetration gradient was observed in the treated soil. Some degradation was observed at the top and bottom exposed surfaces of the treated soil, similar to that of soil subjected to other treatments. In addition to needle penetration and chemical tests, elemental mapping using an electron beam microanalysis was performed to determine the degree of degradation. The depth of degradation 20 years after construction was 18–25 mm. Although the amount of cement added in the pneumatic flow mixing method was relatively small, this value was within the range of degradation depths over time investigated in previous studies and did not represent a significant degradation.

Keywords: long-term durability; deterioration; cement-treated soil; pneumatic flow mixing; reclaimed island; strength; electron beam microanalysis

Citation: Takahashi, H.; Sato, I.; Morikawa, Y.; Ozawa, A. Long-Term Durability of Cement-Treated Soil Used in Offshore Airport Island Construction. *Appl. Sci.* **2023**, *13*, 8081. https://doi.org/10.3390/app13148081

Academic Editors: Paulo José da Venda Oliveira and António Alberto Santos Correia

Received: 16 June 2023
Revised: 5 July 2023
Accepted: 6 July 2023
Published: 11 July 2023

1. Introduction

When building civil engineering structures, soft soils are often improved using cement or other solidifiers to increase their stiffness and strength. It is also important to ensure that there is no impact to the environment, as an elevated pore water pH and leaching of hexavalent chromium have been noted in the immediate vicinity of cement-treated soil. In port and harbour areas, in addition to the deep mixing method, in which solidifiers are stirred and mixed into soft subsoil, lightweight mixing methods, in which solidifiers are mixed into soil collected from the field, are used effectively [1]. In the pneumatic flow mixing method, solidifiers are also added to the dredged soft soil in the pumping pipe, where they are pumped by a pneumatic pumping vessel using a dredger, and the dredged soil and solidifier are stirred and mixed using the turbulent effect of the plug flow generated in the pumping pipe [2]. The applications of treated soil include reclamation material, backfill material behind seawalls, and temporary embankments to demarcate reclaimed lands. It is also used directly behind quay walls to reduce the earth pressure and prevent liquefaction. This method was tested at the Port of Nagoya in Japan in 1998 and subsequently used extensively in the reclamation of airport islands at Central Japan International Airport and Tokyo International Airport. This method can continuously improve the quantities of soft soil; thus, it can effectively use large stockpiles of dredged soil in port areas and assist in rapidly constructing large-scale reclamation works such as airport islands. The use of dredged soil rather than soil transported from mountains in the

pneumatic flow mixing method contributes to sustainability. Ground improvement with a little cement is also useful in terms of reducing carbon dioxide emissions. In recent years, this method has been adopted in coastal construction projects not only in Japan, but also in North America and other parts of Asia, and its use is progressing worldwide [3].

Cement treatment methods are useful because they can significantly improve the physical properties of soft soils in the short term. However, treated soils deteriorate in the long term, starting from the exposed surface [4–13]. The pneumatic flow mixing method is no exception; the surface of the treated soil exposed to the untreated soil deteriorates, albeit slowly. The deep mixing method, which was developed in the 1970s as a pioneering solidification method, requires a large amount of cement, and the strength of the treated soil is high, at 1500 kN/m^2 or more (when solidifying clayey soil). Even after 50 years, no problematic deterioration has occurred in the field. In contrast, in the pneumatic flow mixing method, the mixing of soil and cement occurs via a plug flow in the pumping pipe, and the strength of the treated soil is not very high, ranging from 100 to 500 kN/m^2. In addition, this method has only been applied onsite for approximately 20 years, and there is no track record regarding its degradation characteristics. Therefore, it is important to understand the degree of deterioration from the perspective of the long-term service of structures. If geomaterials in civil engineering structures do not deteriorate, do not require energy or materials for repair, and can remain in service, they can offer many environmental, social, and economic benefits and consequently increase sustainability. Therefore, the condition of the treated soil should be continuously checked, and its long-term durability should be considered.

The authors investigate the long-term durability of cement-treated soil on an artificial island of Central Japan International Airport, where the pneumatic flow mixing method was first fully introduced. This paper summarises the results of four investigations [14–16], including those conducted at the time of reclamation (2002), and four (2006), ten (2012), and fifteen (2017) years after the reclamation, as well as the results of a detailed investigation in the 20th year (2022). In 2022, in addition to the strength properties of the treated soil, the degradation characteristics near the surfaces exposed to the untreated soil were also investigated. Needle penetration tests, chemical tests, and surface analyses (elemental mapping) using an electron beam microanalysis (EPMA) were implemented to determine the degree of degradation near the exposed surfaces.

2. Pneumatic Flow Mixing Method and Construction of Airport Island

2.1. Overview of Pneumatic Flow Mixing Method

The pneumatic flow mixing method is a solidification method in which soil is solidified by chemical treatment to increase its shear strength and improve its compressibility, liquefaction resistance, and impermeability. Solidification methods can be divided into those that solidify the ground in situ and those that mix a chemical stabiliser (solidifier) with the soil as a pretreatment for backfill or reclamation materials; the pneumatic flow mixing method is classified as the latter. In this method, the soil and solidifier are stirred and mixed in a pumping pipe. This allows the equipment to be simplified, with a solidifier-adding device connected to the existing pneumatic pumping equipment. There are two methods for adding solidifiers to the pumping pipe: the 'pumping system', in which solidifiers are added before compressed air is injected, and the 'line system', in which solidifiers are added after compressed air is injected (Figure 1). Depending on the properties of the solidifier, the addition method can be classified as the 'slurry method' or the 'powder method'.

When attempting to pump only soil in a pumping pipe, friction with the pipe wall causes a large pressure reduction and the pressure in the pipe is high, making pumping difficult. Pneumatic pumping is a technology in which compressed air is continuously injected into a pumping pipe to generate a multiphase flow of dredged soil and air to transport the dredged soil to the outlet. Figure 2 shows an image of pneumatic pumping and kneading. In the multiphase flow generated by the compressed air injection, the dredged soil is broken up and forms a plug. During pumping, this plug of dredged soil

constantly changes shape owing to friction with the pipe wall and intermittently collapses and reforms. The pneumatic flow mixing method utilises this change in plug shape to mix the dredged soil and solidifier. The pneumatic flow mixing method has been applied to cohesive soils with sand and gravel contents of 50% or less. This method uses pneumatic pumping; thus, clayey soils with sand and gravel contents of less than 30% and water contents of 90–110% (approximately 1.3–1.5 times the liquid limit) are the most suitable.

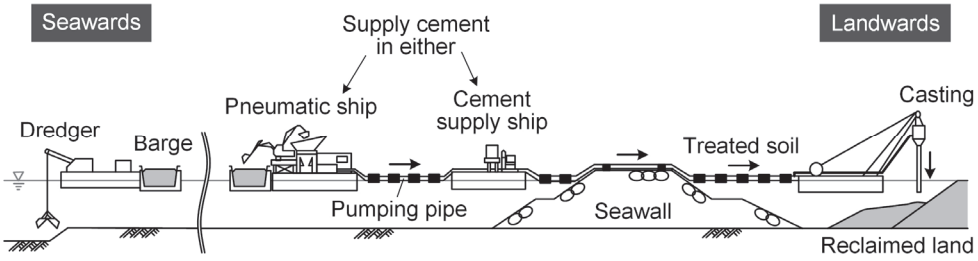

Figure 1. System used to implement the pneumatic flow mixing method.

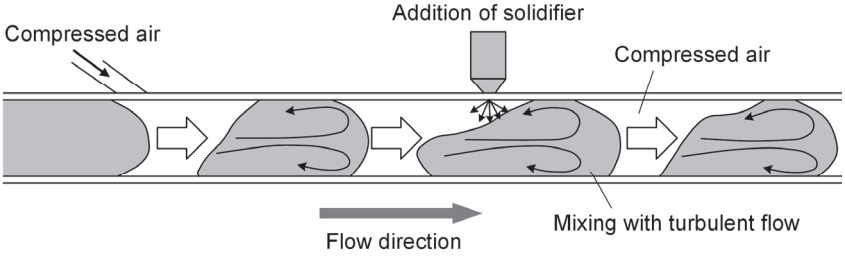

Figure 2. Schematic view of mixing in a pneumatic pipe.

Soil is not mechanically stirred in the pneumatic flow mixing method; thus, there is concern regarding variations in the strength of the treated soil. It is a common practice to allow for a certain degree of heterogeneity in treated soil based on experience, including the results of field trials. The strength of the soil treated by the pneumatic flow mixing method is set by assuming that the strength in the field follows a normal distribution and considering the variability and failure rate. The failure rate is defined as the percentage of the unconfined compressive strength of the in situ-treated soil that is below the design strength. The failure rate should be set according to the intended use of the treated soil; however, it is generally set at 25%. The actual amount of solidifier added is determined based on the results of laboratory mixing tests, considering the quality required by the design and the need to ensure fluidity during pumping. Variations in the strength of the in situ-treated soil and its ratio to the laboratory mix strength (strength ratio) are also considered. If the strength variation and strength ratio of the in situ-treated soil are not determined by field trails, a coefficient of variation of 0.35 and a strength ratio of 0.5 are used as guides when the amount of solidifier added is approximately 50–100 kg/m^3, based on past performance data. When treated soil is used as a landfill material, the amount of solidifier added is usually approximately 50–70 kg/m^3 and the design strength is often set at 100–200 kN/m^2. For a more detailed description of the pneumatic flow mixing method, please refer to [2].

2.2. Construction Work on Airport Island

The area around the city of Nagoya in Japan has a population of 20 million and a thriving automobile and other industries, and a full-fledged international hub airport was desired for both passenger and cargo traffic. The airport is the fourth largest international

hub airport after the international airports in Tokyo and Osaka (Haneda, Narita, and Kansai International Airports), and was constructed over a five-year period from 2000 to 2005. Central Japan International Airport (nicknamed Centrair, IATA airport code: NGO) was built as an artificial island 2–3 km off the coast of Tokoname City, Aichi Prefecture. In this area, relatively shallow water (less than 7 m in depth) extends 3–5 km offshore. Although the island construction area includes an alluvial clay layer with a maximum thickness of 20 m, the thickness of this layer is less than 5 m in most areas, and the Tokoname Formation, which has an *N* value of more than 50 and can be regarded as a good bearing stratum, exists below the alluvial clay layer. By improving the alluvial clay layer using the sand drain method, which is a type of vertical drain method, it was possible to reduce the residual settlement to a few centimetres at the time of the airport opening.

Of the approximately 5,800,000 m^2 of the airport island, 4,700,000 m^2 is used for the airport, which required approximately 52,000,000 m^3 of reclaimed soil to create. Approximately 10,000,000 m^3 of dredged soil from the nearby Port of Nagoya was effectively utilised (Figure 3). The physical properties of the dredged soil used in the project were as follows: soil particle density 2.68–2.72 g/cm^3, sand and gravel contents 2–18%, fine grain contents 82–98%, liquid limit 55–88%, and ignition loss 5.3–7.8%. It was difficult to promote consolidation at a low cost after reclamation and to put it into service early in the short construction period; therefore, the pneumatic flow mixing method was applied. Some of the basic facilities of the airport are located on the ground formed by the treated soil. Thus, the design strength of the treated soil was set based on the condition that it had the strength required for the subgrade of a roadbed and would not settle under consolidation. Specifically, based on the relationships between the unconfined compressive strength, CBR value, and consolidation yield stress, which were determined in advance by laboratory tests, the design strength was set to satisfy the CBR value based on the Japanese airport pavement structural design guidelines, and to ensure that no consolidation yield stress occurred at the bottom of the improved soil. The design strength was 120 kN/m^2. The failure rate, coefficient of variation, and strength ratio were set as 25%, 0.35, and 0.5, respectively. The calculated average in situ strength was 157 kN/m^2. The construction of the Central Japan International Airport is described in detail in [17–19], and the reader can refer to these works for further details.

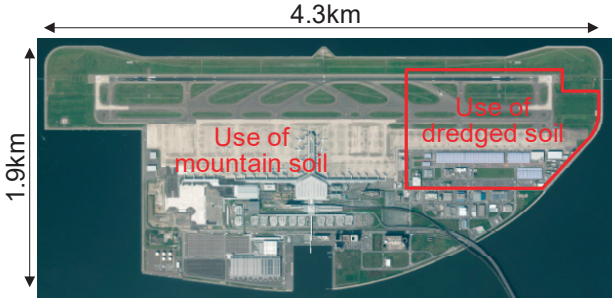

Figure 3. Central Japan International Airport and areas where dredged soil was used.

3. Survey Locations and Methods

Five borehole investigations (with 25 boreholes drilled immediately after the reclamation and two drilled in each of the other investigations) were conducted on the improved ground over a period of 20 years (2002, 2006, 2012, 2017, and 2022). A planar survey location map and a schematic of the columnar sections are presented in Figure 4. In 2002, the airport was not in service, which made it possible to survey a wide area. After the airport was put into service, the survey locations were limited owing to the operational constraints of the airport, and the survey locations after 2006 were different from those immediately after the reclamation was completed. The location was an unpaved area adjacent to a taxiway. As

shown in the sampling columnar sections, the lower part of the treated soil produced by the pneumatic flow mixing method consisted of fine-to-medium-grained sands, whereas the upper part was a reclaimed soil layer consisting of sand and gravel mixed with cobbles. Although the elevation varied slightly depending on the borehole drilled, the treated soil lay at a depth of approximately 2–7 m, which was below the residual water level (at a depth of approximately 1.4 m). The residual water level is higher than that of the treated soil; thus, it can be said to be in a non-drying condition.

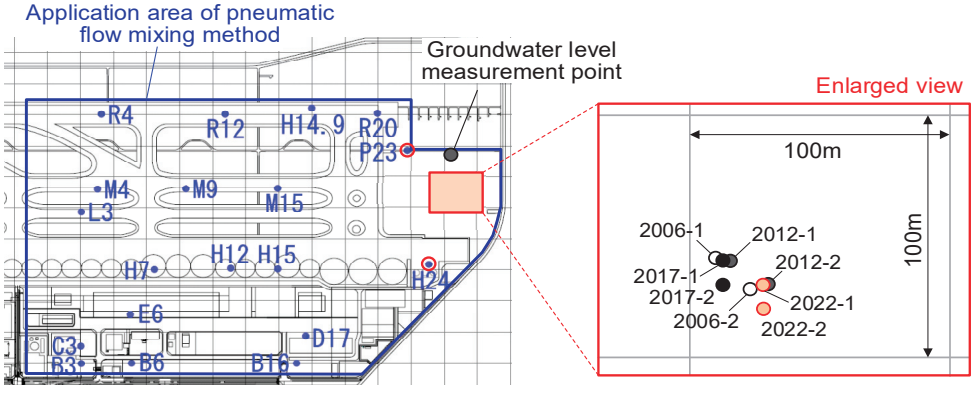

(**a**)

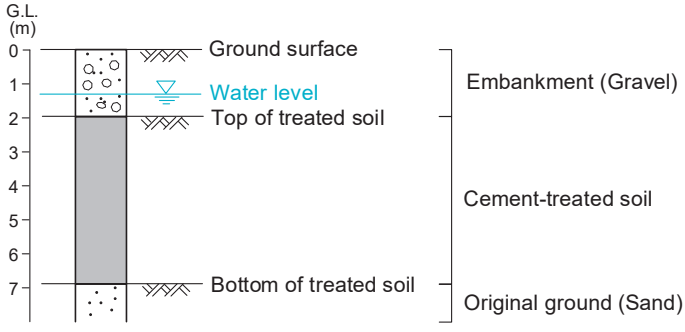

(**b**)

Figure 4. Survey points and schematic columnar sections: (**a**) survey points (left: immediately after construction; right: second and subsequent surveys); (**b**) schematic of columnar section.

Specimens were collected at each site using double-tube samplers with built-in sleeves and triple samplers at the boundary between the overburden (sand and gravel) layer and treated soil. Examples of the bores and treated soil samples are shown in Figure 5. As shown in the photograph, the sampling caused cracks at several positions, but the number of cracks was small enough to ensure that a 132 mm specimen was obtained for the unconfined compression test. The laboratory tests for the sampled soil are listed in Table 1. Continued tests included water content and wet density tests, as well as unconfined compression tests, with two–three test specimens per metre of sample being taken for compression testing. Needle penetration tests were also conducted up to 2012 on the cut surface inside the treated soil and in 2017 and 2022 on the nearby treated soil exposed to the untreated soil. In addition, chemical tests and areal analyses (elemental mapping) using EPMA were implemented. The location maps of the tests are shown in Figure 6. Groundwater

samples were collected in 2012, and chloride ion concentrations were measured using ion chromatography.

(**a**) (**b**)

Figure 5. Boring and sampling: (**a**) boring operation; (**b**) core sample.

Table 1. List of tests conducted on samples.

Test	Part	2002	2006	2012	2017	2022
Water content test	Interior	x	x	x	x	x
Test for bulk density of soil	Interior	x	x	x	x	x
Unconfined compression test	Interior	x	x	x	x	x
	Interior		x	x		
Needle penetration test	Surface				x	x
	Near surface					x
Chemical analysis of suspension	Near surface				x	x
EPMA	Near surface					x
Analysis of groundwater	Boring hole			x		

x: test implemented.

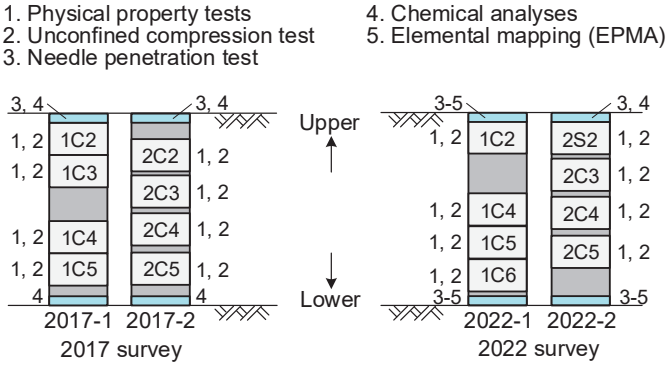

Figure 6. Tested parts of cores.

Unconfined compression and needle penetration tests were conducted according to the Japanese Geotechnical Society Standards [20,21]. The purpose of these tests was to investigate the continuous changes in strength (strength development and reduction). The specimens used for the unconfined compression tests were approximately 66 mm (diameter) × 132 mm (height). The treated soil samples were hard and difficult to shape into the standard 50 mm

diameter for compaction tests; thus, the diameter was taken as sampled (approximately 66 mm), and the height was twice that. In surveys up to 2012, no signs of strength reductions were observed in the treated soil, whereas in the 2017 and 2022 surveys, needle penetration tests were conducted against the surface exposed to the untreated soil. It was difficult to determine the exact exposure surface for the treated soil sampled in the field; however, after lightly removing the surface sand and gravel with a finger, the surface that seemed to be solidified was considered the exposure surface. In some samples, gravel was embedded in the exposed surface of the treated soil and needle penetration tests were conducted on the surface after removing this gravel. Two types of needle penetration tests were conducted near an exposure surface: one in which the needle penetrated the exposure surface perpendicularly and the other in which the needle penetrated the sample from the side at several depths. In the former method, the penetration resistance can be continuously determined from the exposed surface; however, the measurable depth is limited. With the latter method, there is no limit to the depth at which the penetration resistance can be measured; however, the data are discrete in the depth direction. In the 2022 survey, the latter method was also utilised because the former method did not provide a clear degradation depth.

For chemical analyses, soil suspensions were prepared and analysed according to the Japanese Geotechnical Society Standards [22,23]. The four measurement parameters were the pH, calcium ion concentration, sodium ion concentration, and electrical conductivity, which were determined using Horiba compact instruments. The pH and calcium ion concentration decreases with the progressive degradation of the treated soil, and the electrical conductivity decreases accordingly. According to a previous study [13], there is a correlation between these parameters, and chemical analyses were performed to determine the signs of deterioration. The test locations are shown in Figure 7. In the 2017 survey, only one measurement was made near each end of the borehole, whereas in the 2022 survey, the specimen was divided into smaller sections from the exposure surface and analysed. However, the upper and lower ends of core 2022-2 (especially the upper end) contained large amounts of gravel, were brittle, and collapsed during cutting. Therefore, the soil was analysed in batches of a few centimetres.

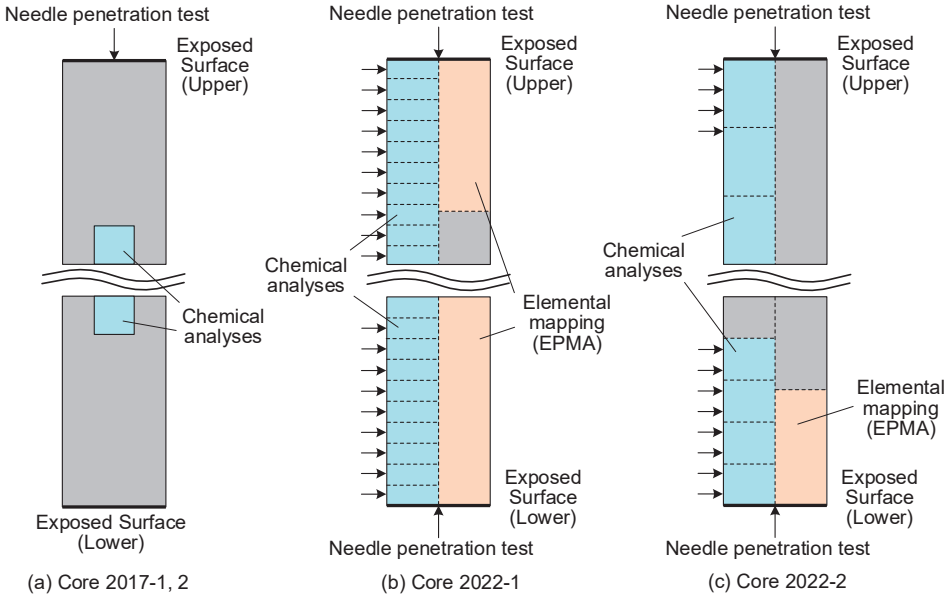

Figure 7. Testing near exposed surfaces.

In the 2022 survey, an EPMA of the surface (elemental mapping) was implemented on samples near the exposed surface. This type of analysis provides a more detailed picture of the calcium concentration, and EPMAs have been used in the concrete engineering field to investigate calcium excursions and determine the state of neutralisation. Calcium, magnesium, silicon, and aluminium were measured. The specimens for photography were cut with a saw, freeze- or vacuum-dried, and then hardened with resin. After dry-polishing, carbon was deposited to provide a surface with conductivity for surface analyses. The instrument used for the analysis was an electron microanalyser manufactured by JEOL. The following settings were used: an acceleration voltage of 15 kV, a sample current of 50 nA, a measurement time of 40 ms/pixel, a beam diameter of 50 μm, and a pixel size of 100 × 100 μm. The concentration was calculated as a mass percentage using the proportionality method based on the X-ray intensity of a standard sample. It should be noted that the upper part of core 2022-2 was brittle, and cutting it did not allow the sampling of the treated soil in blocks; therefore, EPMA imaging could not be performed for that part.

4. Long-Term Properties of the Interior of Cement-Treated Soil

4.1. Groundwater, Water Content, and Wet Density of Soil

The groundwater level was higher than the top of the treated soil, which was submerged in water. Groundwater was collected from the borehole, and the chloride ion concentration was examined. The results indicated that the chloride ion concentration was 98 mg/L. The chloride ion concentration in seawater is generally approximately 19,000 mg/L. Thus, the measured groundwater concentration was considerably lower than that of typical seawater. The groundwater characteristics were different from those of seawater, although the artificial island was located offshore, and the seawall was as close as 150 m. Previous studies [4,8,10,12] have shown that treated soil deteriorates faster when exposed to seawater. Thus, these test results indicated a favourable subsurface environment in terms of the long-term durability of the treated soil.

Figure 8 shows the distributions of the water content and wet density in the depth direction. As a result of the large number of test results immediately after reclamation, only the results for samples collected at sites P23 and H24 are shown, because these sites were close to the survey locations used since 2006. The figures show the changes in groundwater levels (highest and lowest values) measured between April 2011 and January 2012, together with the regression lines of the water content ratio and wet density against the depth. The water content ratio immediately after reclamation had little variation for depths shallower than 1.1 m, but for depths deeper than 1.1 m, the variation was in the range of 70–110%. The water level in the embankment at the time of reclamation was at a depth of 1.1 m, and it is possible that the water content ratio varied because the soil was cast into the water at depths deeper than this. Uniform values were obtained at depths shallower than 1.1 m, where casting was implemented in air, and the quality control in the field was considered successful to a certain extent. The difference in water content in the depth direction was slightly higher at deeper depths; however, this difference was not significant. The wet density of the samples was approximately 1.44 g/cm^3, with little variation and almost no difference in the depth direction. These results show that the properties of the improved soil were uniform and stable, with no differences between the investigations conducted in different years.

4.2. Unconfined Compressive Strength and Needle Penetration Resistance

The distributions of the unconfined compressive strength of the treated soil in the depth direction obtained from the five surveys are shown in Figure 9, along with the mean variation over time. For the 2002 survey, only the results for the samples collected at sites P23 and H24 are shown. Figure 9a shows that although the results varied, they were generally distributed in the range of 100–500 kN/m^2, with most of the data exceeding the design strength of 120 kN/m^2. The average value of the variation was also higher than

the average value of 157 kN/m^2 estimated at the time of the design. The figure shows the regression line of the unconfined compressive strength in relation to the depth. According to the regression line, the strength tended to decrease with an increase in depth. The above-mentioned distribution of water content showed that the water content tended to be slightly higher at deeper depths, suggesting that some water may have been taken in by the submerged casting. However, considering the design strength, the difference in strength in the depth direction was not a problem. Figure 9b, which shows the change in strength over time, indicates that there was no long-term decrease in strength, although small and large values were observed depending on the year of investigation. The range of standard deviations (1σ) from the mean value is shown by error bars, and it can be seen that the mean value minus the standard deviation was larger than the design strength for all the survey years. From these results, it can be concluded that overall, the strength properties of the treated soil were almost stable.

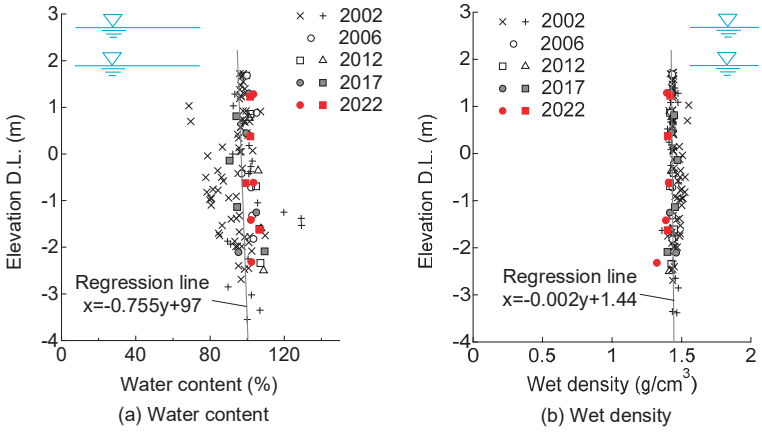

Figure 8. Distributions of water content and wet density in the depth direction.

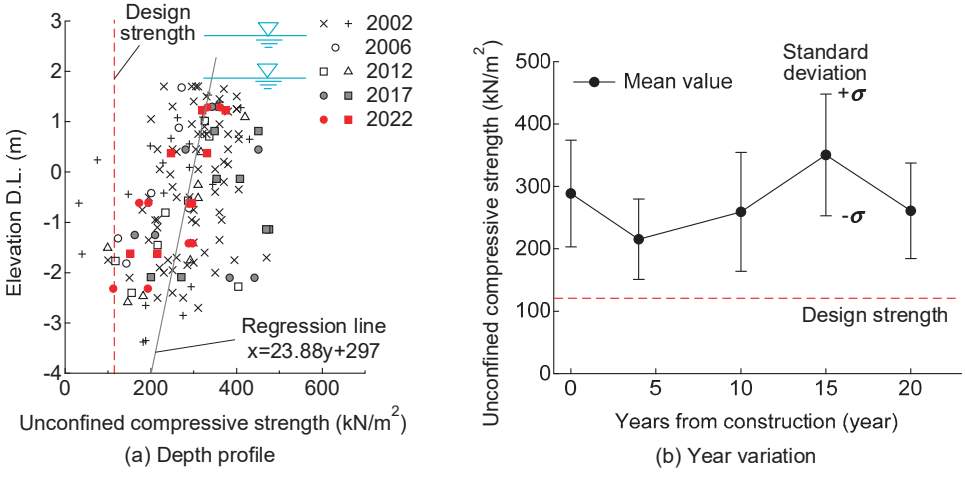

Figure 9. Depth distribution and ageing of unconfined compressive strength.

In the 2006 and 2012 surveys, needle penetration tests were conducted on cuttings from the interiors of the treated soil samples. As representative examples, Figure 10 shows the results of the 2012 survey, which was conducted ten years after construction. These results

demonstrate the relationship between the penetration depth and penetration resistance. For the uniformly treated soil, the relationship is proportional, as shown in the figure, and this gradient represents the stiffness and strength of the treated soil. If the strength had been reduced by deterioration, the gradient would be smaller. Conversely, in areas where the strength was higher, the gradient would be larger. No changes in these gradients were observed in the results presented in the examples, indicating that the strength of the treated soil was uniform. According to the Japanese Geotechnical Society Standards [21], a gradient up to a penetration of 10 mm is referred to as the needle penetration gradient. The relationship between this value and the unconfined compressive strength of a specimen in the vicinity of the needle penetration test is shown in Figure 11. This figure also shows the correlation between the two obtained in previous studies [24]. The plotted data show that the correlations did not deviate significantly from those obtained in a previous study and were typical of cement-treated soils.

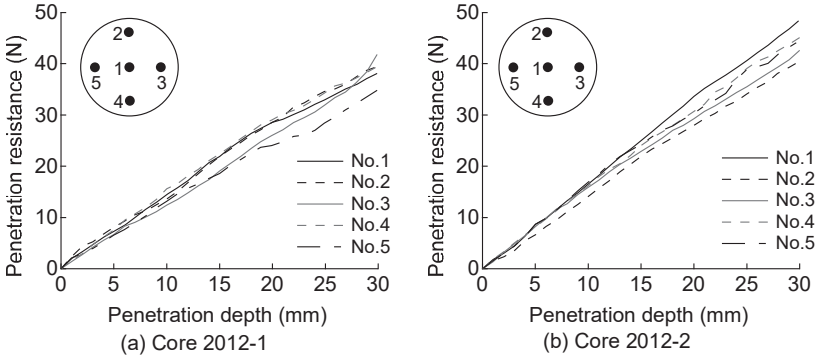

Figure 10. Needle penetration resistance at the inner surface of cement-treated soil (10 year survey).

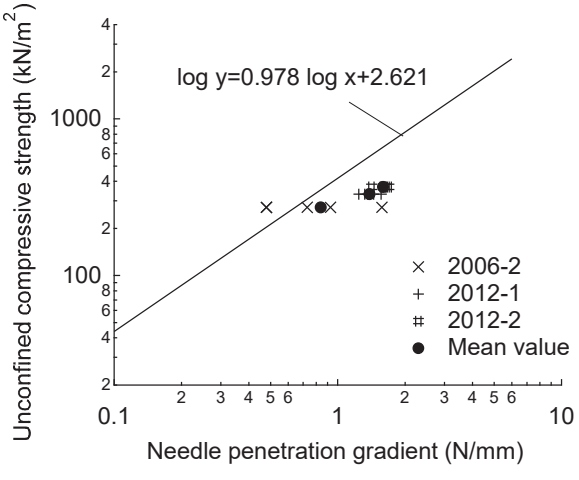

Figure 11. Relationship between unconfined compressive strength and needle penetration gradient.

5. Long-Term Properties of the Surface of Cement-Treated Soil

5.1. 15 Year Survey Results

No signs of strength reductions were observed in the interiors of the treated soil samples during the investigations up to 2012, needle penetration tests were conducted on the surfaces exposed to the untreated soil from the 2017 survey onwards. The results of the 2017 survey, 15 years after construction, are shown in Figure 12. The test results were

obtained from vertical needle penetration tests against the exposed top surfaces of two cores (2017-1 and 2017-2). The results for core 2017-1 showed that penetration resistance was encountered immediately after penetration, with a large variation in values. The results varied depending on the penetration point. Visual observations of the specimens suggested that this was because the treated soil contained gravel. On the other hand, the results for core 2017-2 showed that the penetration resistance values were relatively stable, and it was possible to identify areas with a constant gradient. With the exception of penetration no. 3, points of change in the gradient can be seen, and their locations are indicated by arrows in the figure. The slope is smaller in the shallow section and larger in the deeper section. In other words, the strength of the shallow part was low, and this part was considered to have deteriorated. Consequently, the strength was considered to have decreased in the range from the boundary to a depth of approximately 16–25 mm.

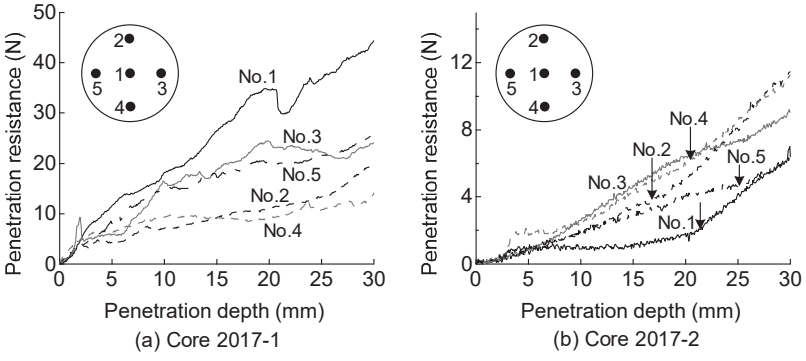

Figure 12. Needle penetration resistances at the surface of cement-treated soil samples (15 year survey).

In the 2017 survey, suspensions were prepared from samples subjected to needle penetration tests, which were then chemically analysed. The results are summarised in Table 2. The suspension was prepared from soil obtained at a depth of approximately 80–100 mm below the exposure surface, where the cement-treated soil was not considered to be degraded. As shown in the table, the cement-treated soil had a low pH. However, an alkaline atmosphere was maintained and calcium remained, which was consistent with the fact that the strength of the soil did not deteriorate.

Table 2. Results of the chemical analysis of suspensions (15 year survey).

Core	Part	pH	Ca^{2+} (ppm)	EC (mS/cm)
2017-1	Upper	9.0	160	2.7
	Lower	8.9	200	4.2
2017-2	Upper	8.9	190	2.0
	Lower	8.7	130	2.6

5.2. 20 Year Survey Results

The results of the needle penetration tests conducted in 2022, 20 years after construction, are shown in Figure 13. The results were obtained by vertically penetrating the exposed surfaces at the tops and bottoms of cores 2022-1 and 2022-2. In the upper part of core 2022-1, the gradient was relatively large; however, there were differences in the gradients between penetrations. The arrows in the figure may be seen as points of change in the gradients at 8 and 25 mm, although these were difficult to determine because of the large variation. In the upper part of core 2022-2, there was a sudden increase in the penetration resistance, possibly due to the needle hitting gravel. In addition, the gradient was small and it was difficult to determine the point of change. Similarly, in the lower part

of core 2022-1, the gradient was small and there was no point of change, except where the needle struck gravel. Constant gradients were identified in the lower part of core 2022-2, and the points of change were at approximately 18 mm. However, the point of change of the gradient in these tests was unclear and, with the exception of the upper part of core 2022-1, the gradients were small, and the possibility could not be ruled out that the degradation had progressed deeper than the 30 mm penetration of the needle. Therefore, it was decided to implement lateral needle penetration tests at several depths in the sample, elemental mapping by EPMA, and a chemical analysis to investigate the degradation at a deeper depth.

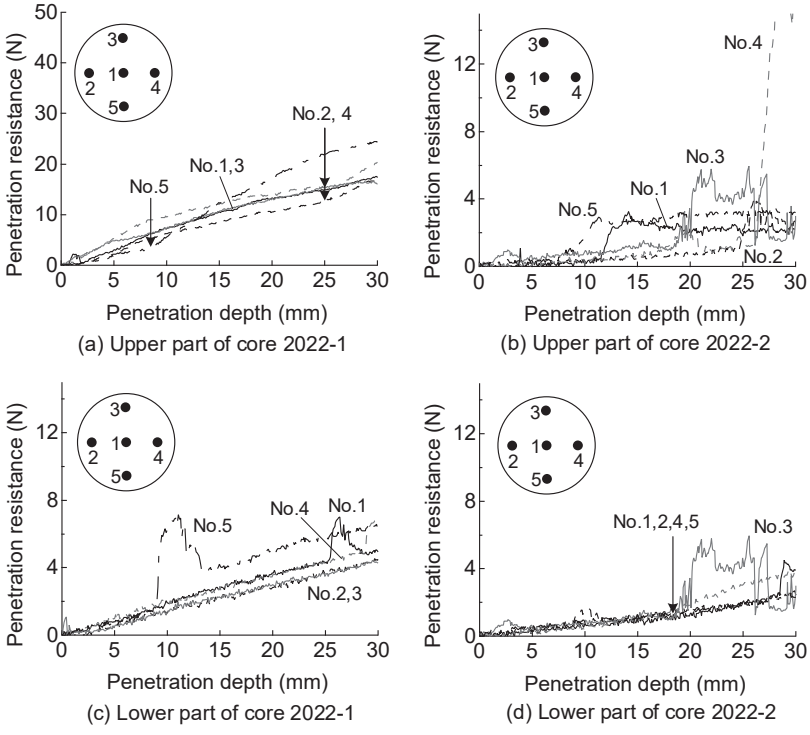

Figure 13. Needle penetration resistances at the surface of cement-treated soil samples (20 year survey).

The results of needle penetration tests on the lateral side of a sample are shown in Figure 14. These are the needle penetration gradients for each depth from the exposure surface and are the average gradients up to a penetration depth of 10 mm. In the upper part of core 2022-1, the gradients were generally large; however, in the range of 10–20 mm near the exposure surface, the penetration gradients tended to decrease. On the other exposure surfaces, the gradients were generally small, and no tendency for the gradient to decrease was observed in the vicinity of the exposure surface. However, there was no sudden change in the needle penetration gradient up to a depth of 70–100 mm. It is unlikely that the treated soil had deteriorated at this depth. It can be concluded that the deterioration did not progress deeper than 30 mm, and the strength of the soil was low from the time it was cast. The results of the elemental mapping by EPMA are shown in Figure 15. An examination of the calcium content, which is correlated with the strength of the cement-treated soil, shows that the calcium content in the upper part of core 2022-1 was high, which was consistent with the high needle penetration gradient at that location. However, the calcium content was low in the lower parts of cores 2022-1 and 2022-2, which was consistent with the small needle penetration gradients at these locations. These analyses also suggested that the

cement-treated soil did not deteriorate at any depth, but that there was an overall variation in the strength of the treated soil from the beginning of construction, with localised areas of low strength.

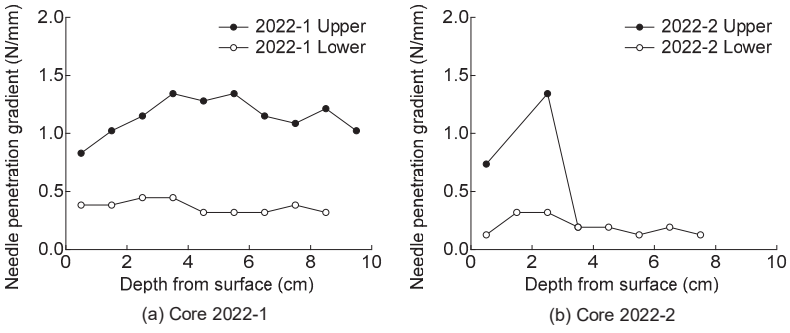

Figure 14. Needle penetration gradients near the surface of samples (20 year survey).

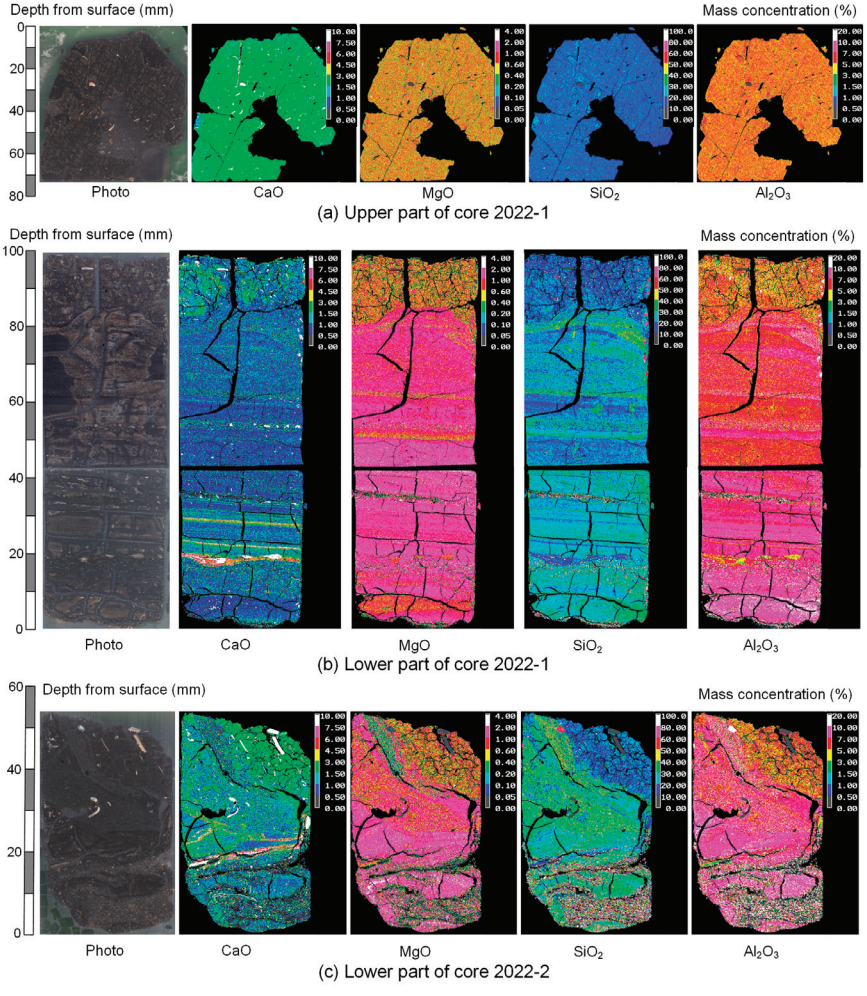

Figure 15. Elemental mapping results from an EPMA.

In the 2022 survey, the treated soil taken from several points on the exposed surface was ground and used to make suspensions, which were chemically analysed. The amount of soil collected in this survey was small, and the prescribed soil volume indicated by the Japanese Geotechnical Society Standards [23,24] could not be ensured. Therefore, the suspensions were prepared by maintaining a fixed ratio between the amount of soil and water. In core 2022-1, suspensions were made using soil collected at 1 cm intervals, whereas in core 2022-2, the amount of soil available for making the suspension was small, owing to gravel and other reasons, and the soil collected from an area of a few centimetres had to be used. The results of the chemical tests are presented in Table 3. An alkaline atmosphere was maintained and calcium remained, albeit at a lower pH, in the treated soil. In the upper and lower parts of core 2022-1, there was a trend towards lower calcium contents within several centimetres of the exposed surface, which may indicate degradation from the exposed surface. The overall results for the specimens indicated that the lower parts of cores 2022-1 and 2022-2 contained more sodium and therefore had higher electrical conductivity values. The calcium and sodium contents were low in the upper part of core 2022-2, where there was more gravel, and the treated soil was more brittle, suggesting that the treated soil had different characteristics from the rest of the specimen. Thus, the change in the depth direction from the exposed surface was small; however, the values differed significantly from specimen to specimen. It is reasonable to assume that the low calcium contents in some specimens did not indicate degradation but that the chemical properties were different from the beginning. In other words, the results of the chemical analyses did not indicate that the treated soil had deteriorated at any depth. Signs of deterioration were only observed within several centimetres of the exposed surface.

Table 3. Results of a chemical analysis of suspensions (20 year survey).

Core and Part	Depth from Exposed Surface (cm)	pH	Ca^{2+} (ppm)	Na^{+} (ppm)	EC (mS/cm)
2022-1 (Upper)	0–1	9.1	150	79	1.0
	1–2	9.1	170	80	1.0
	2–3	9.4	190	90	1.1
	3–4	9.4	190	90	1.1
	4–5	9.5	190	88	1.1
	5–6	9.4	190	83	1.1
	6–7	9.4	190	86	1.1
	7–8	9.4	190	85	1.1
	8–9	9.4	190	86	1.1
	9–10	9.7	200	87	1.1
2022-1 (Lower)	0–1	8.3	130	660	4.3
	1–2	8.1	120	640	4.4
	2–3	8.3	150	730	5.0
	3–4	8.2	160	770	5.2
	4–5	8.1	150	720	4.8
	5–6	8.2	160	830	5.3
	6–7	8.3	110	500	3.5
	7–8	8.2	150	730	4.8
	8–9	8.4	170	770	4.9
	9–10	8.4	180	860	5.1
2022-2 (Upper)	0–3.3	9.2	45	40	0.46
	3.3–6.6	9.2	39	28	0.30
	6.6–10	9.3	31	19	0.22
2022-2 (Lower)	0–2	8.4	320	1400	8.4
	2–4	8.9	340	1400	8.2
	4–6	8.3	320	1400	8.0
	6–8	8.5	330	1500	7.7

Based on the results of the needle penetration tests from the side of the sample described above, along with the EPMA images and chemical analysis results, only the area around the exposed surface of the treated soil was degraded. Based on the results of the needle penetration tests perpendicular to the exposed surface, a depth of approximately 18–25 mm could be considered as the depth of degradation.

5.3. Deterioration from the Surface of Treated Soil

The treated soils deteriorated from the exposed surface over the long term. The deterioration of treated soils from exposed surfaces has been demonstrated in previous studies [4–13]. The mechanism of this degradation is thought to be as shown in Figure 16. The calcium ion concentration in the pore water decreases owing to diffusion from the exposed surface. Calcium is supplied spontaneously to the pore water from the cement hydrates and other materials to increase the calcium ion concentration in the pore water. This supply breaks down the hydrates. The hydrates reinforce the structural framework; thus, the breakdown of the hydrates leads to a reduction in the strength of the treated soil. Previous studies have confirmed that the calcium concentration near the exposed surface decreases, and a correlation between the decrease in strength and calcium concentration has been obtained. However, this degradation is slow and takes years. The authors confirmed that the calcium ion concentration was reduced by forcibly replacing the pore water, which degraded the treated soil [25]. It has also been found that when treated soil is exposed to seawater, the magnesium salts in the seawater react with the cement hydrates, resulting in faster deterioration of the treated soil [4,8,10,12].

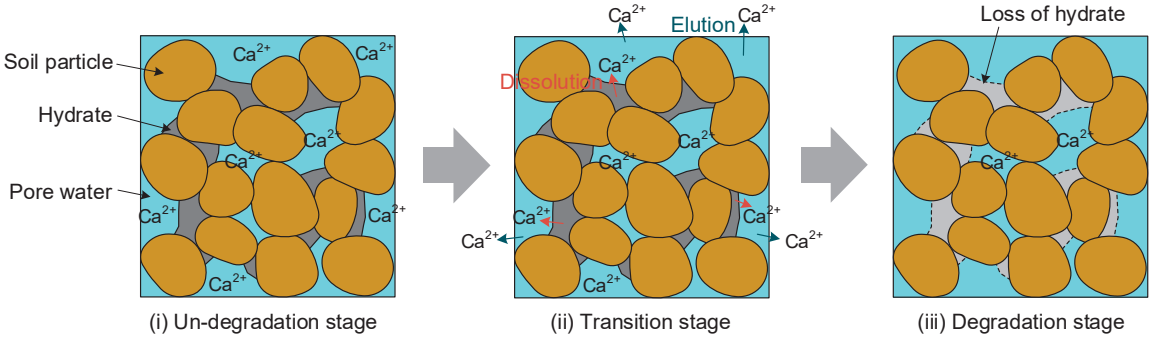

Figure 16. Deterioration mechanism of treated soil due to calcium dissolution and diffusion.

Takahashi et al. [13] graphically summarised the relationship between the duration of the exposure and the depth of the degradation, which was linear in a double logarithmic graph, as shown in Figure 17. This figure shows the results of the present study, which fall within the range of variation of the results of previous studies. Although the figure includes the results for both specimens of treated soil cured in laboratories and those produced by the deep mixing method in situ, the differences in the depth of degradation owing to different soils, cements, and improvement methods are within the range of variability. In practice, the rate of degradation should vary depending on the properties of the treated soil and the exposure conditions; however, within a realistic range of conditions, the rate of degradation is likely to fall within the range of variation. The treated soil in the pumping pipe at the site did not deteriorate rapidly, although its strength was not high.

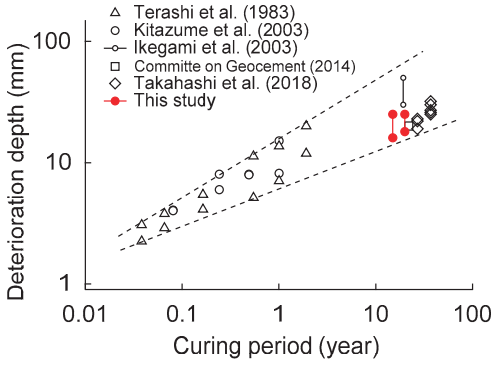

Figure 17. Relationship between duration of exposure and depth of degradation (Addendum to [13]).

6. Conclusions

The long-term durability of treated soil was investigated on an artificial island at Central Japan International Airport, where the pneumatic flow mixing method was first fully introduced. The results of five investigations conducted immediately after construction and 4, 10, 15, and 20 years after construction were summarised. The results obtained and conclusions are as follows:

(1) No reduction in the unconfined compressive strength or needle penetration gradient was observed in the interiors of treated soil samples, and there was no sign of deterioration.
(2) Some degradation was observed on the top and bottom exposed surfaces of the treated soil, similar to that of soil after other treatments. In addition to needle penetration and chemical tests, elemental mapping using an EPMA was performed to determine the degree of degradation. The depth of degradation 20 years after construction was approximately 18–25 mm.
(3) Although the amount of cement added in the pneumatic flow mixing method was relatively small, the degradation depth was within the range of the degradation depth over time investigated in previous studies and was not significant.
(4) The artificial island at Central Japan International Airport has a 2 m thick soil cover on top of the improved soil, and a reduction in strength of this magnitude would not affect the stability of the ground as a whole. In other words, it was confirmed to be durable at least during the first 20 years of construction.
(5) Based on the results to date, it is unlikely that the degree or extent of strength reductions of the treated soil will change abruptly; however, from the perspective of the long-term maintenance of the airport facilities, it is important to continuously investigate the long-term behaviour of the improved ground. Airport facilities demand high performance from the ground, and if there is an accelerated deterioration trend, measures need to be taken.
(6) There are only a few examples and reports on the long-term strength and durability of treated soils in the field; therefore, this study provides valuable data. The test results are particularly important for understanding the durability of the pneumatic flow mixing method. This method contributes to sustainability in terms of the effective use of dredged soil and less cement addition, and it would be more sustainable if it has long-term durability.

Author Contributions: Investigation, I.S. and A.O.; project administration, H.T.; validation, Y.M.; writing—original draft preparation, H.T. All authors have read and agreed to the published version of the manuscript.

Funding: This research received no external funding.

Institutional Review Board Statement: Not applicable.

Informed Consent Statement: Not applicable.

Data Availability Statement: Data is contained within the article.

Acknowledgments: Kawasaki Geological Engineering Co., Ltd. cooperated with the field investigations and tests. The authors would also like to acknowledge the persons in charge of Central Japan International Airport and Masaki Kitazume of the Tokyo Institute of Technology (formerly the Port and Airport Research Institute), who initiated the ongoing investigations from the time of the airport's construction.

Conflicts of Interest: The authors declare no conflict of interest.

References

1. Takahashi, H. *Ground Improvement for Coastal Engineering*; CRC Press: Boca Raton, FL, USA, 2023; pp. 1–196.
2. Kitazume, M. *The Pneumatic Flow Mixing Method*; CRC Press/Balkema: London, UK, 2017; pp. 1–233. [CrossRef]
3. Maher, A.; Kitazume, M.; Janbaz, M.; Miskewitz, R.; Douglas, S.; Yang, D. Utilization of pneumatic flow tube mixing technique (PFTM) for processing and stabilization of contaminated harbor sediment. *Mar. Georesources Geotechnol.* **2016**, *36*, 271–279. [CrossRef]
4. Shihata, S.A.; Baghdadi, Z.A. Long-term strength and durability of soil cement. *J. Mater. Civ. Eng.* **2001**, *13*, 161–165. [CrossRef]
5. Kitazume, M.; Nakamura, T.; Terashi, M.; Ohishi, K. Laboratory tests on long-term strength of cement treated soil. In Proceedings of the 3rd International Conference on Grouting and Ground Treatment, New Orleans, LA, USA, 10–12 February 2003; pp. 586–597.
6. Hayashi, H.; Nishikawa, J.; Ohishi, K.; Terashi, M. Field observation of long-term strength of cement treated soil. In Proceedings of the 3rd International Conference on Grouting and Ground Treatment, New Orleans, LA, USA, 10–12 February 2003; pp. 598–609.
7. Ikegami, M.; Ichiba, T.; Ohishi, K.; Terashi, M. Long-term strength change of cement treated soil at Daikoku Pier. In Proceedings of the Soft Ground Engineering in Coastal Areas, Yokosuka, Japan, 28–29 November 2002; pp. 241–246.
8. Rajasekaran, G. Sulphate attack and ettringite formation in the lime and cement stabilized marine clays. *Ocean Engineering* **2005**, *32*, 1133–1159. [CrossRef]
9. Nakamura, T.; Kitazume, M. Laboratory tests on durability of cement treated soils. In *Technical Note of the Port and Airport Research Institute*; No. 1128; Port and Airport Research Institute: Yokosuka, Japan, 2006; pp. 1–13. (In Japanese)
10. Hara, H.; Suetsugu, D.; Hayashi, S.; Matsuda, H. Deterioration mechanism of cement-treated soil under seawater. *J. Jpn. Soc. Civ. Eng. Ser. C (Geosph. Eng.)* **2013**, *69*, 469–479. (In Japanese)
11. Committee on Geocement. A study on long term stability of soil–cement columns improved by geocement, cement and concrete. *Cem. Concr.* **2014**, *804*, 9–14. (In Japanese)
12. Cui, X.; Zhang, N.; Li, S.; Zhang, J.; Tang, W. Deterioration of soil-cement piles in a saltwater region and its influence on the settlement of composite foundations. *J. Perform. Constr. Facil.* **2016**, *30*, 04014195. [CrossRef]
13. Takahashi, H.; Morikawa, Y.; Fujii, N.; Kitazume, M. Thirty-seven-year investigation of quicklime-treated soil produced by deep mixing method. *Ground Improv.* **2018**, *171*, 135–147. [CrossRef]
14. Kitazume, M.; Joyo, T.; Mizoguchi, M. Characteristics of soil improved by pneumatic flow mixing method after 4 years (translated by authors). In Proceedings of the 61st Annual Conference of the Japan Society of Civil Engineers, Kusatsu, Japan, 20–22 September 2006; pp. 305–306. (In Japanese).
15. Morikawa, Y.; Yokoe, S.; Kito, J. Characteristics of soil improved by pneumatic flow mixing method after 10 years (translated by authors). In Proceedings of the 67th Annual Conference of the Japan Society of Civil Engineers, Nagoya, Japan, 5–7 September 2012; pp. 451–452. (In Japanese).
16. Morikawa, Y.; Takahashi, H.; Yokoe, S.; Kito, J. Characteristics of soil improved by pneumatic flow mixing method after 15 years (translated by authors). In Proceedings of the 73rd Annual Conference of the Japan Society of Civil Engineers, Sapporo, Japan, 29–31 August 2018; pp. 451–452. (In Japanese).
17. Sato, T.; Kato, H. Application of the pneumatic flow mixing method to land development for Central Japan International Airport. In Proceedings of the 2002 International Symposium on Underwater Technology, Tokyo, Japan, 16–19 April 2002; pp. 93–98. [CrossRef]
18. Kitazume, M.; Satoh, T. Development of a pneumatic flow mixing method and its application to Central Japan International Airport construction. *Ground Improv.* **2003**, *7*, 39–148. [CrossRef]
19. Sato, T. Development and application of pneumatic flow mixing method to reclamation for offshore airport. In *Technical Note of the Port and Airport Research Institute*; No. 1076; Port and Airport Research Institute: Yokosuka, Japan, 2004; pp. 1–81. (In Japanese)
20. Japanese Geotechnical Society. Method For Unconfined Compression Test of Soils (JIS A1216). In *Japanese Geotechnical Society Standards—Laboratory Testing Standards of Geomaterials*; JGS 0511; Japanese Geotechnical Society: Tokyo, Japan, 2015; pp. 1–6.
21. Japanese Geotechnical Society. Method For Needle Penetration Test. In *Japanese Geotechnical Society Standards–Geotechnical and Geoenvironmental Investigation Methods*; JGS 3431; Japanese Geotechnical Society: Tokyo, Japan, 2018; pp. 1–5.

22. Japanese Geotechnical Society. Test Method for Ph of Suspended Soils. In *Japanese Geotechnical Society Standards–Laboratory Testing Standards of Geomaterials*; JGS 0211; Japanese Geotechnical Society: Tokyo, Japan, 2018; pp. 1–5.
23. Japanese Geotechnical Society. Test Method for Electric Conductivity of Suspended Soils. In *Japanese Geotechnical Society Standards–Laboratory Testing Standards of Geomaterials*; JGS 0212; Japanese Geotechnical Society: Tokyo, Japan, 2018; pp. 1–4.
24. Maruto Co., Ltd. *Penetrometer for Soft Rock: Model SH-70 Instruction Manual*; Maruto Co., Ltd.: Tokyo, Japan, 2006; pp. 1–3. (In Japanese)
25. Takahashi, H.; Morikawa, Y.; Uemura, T. Trial tests to promote degradation of cement treated soil by percolation technique. In Proceedings of the Deep Mixing, Online, 1–17 June 2021; pp. 15–17.

applied sciences

MDPI

Perspective

Recent Case Histories of Carbon-Neutral Activity Using Ground Improvement Technology in Japan

Masaki Kitazume

Kitazume Geotechnics, 2-43-2 Nakashirane, Asahi, Yokohama 241-0004, Japan; kitz.geotechnics@gmail.com

Abstract: Global warming due to greenhouse gas emissions has led to record-breaking heat waves, torrential rains and droughts on a global scale in recent years. For this reason, people around the world are more keenly aware of the need to reduce greenhouse gas emissions. The construction industry is one of these sources of greenhouse gas emissions. A lot of ground improvement techniques have been developed and applied to improve the physical and mechanical properties of soil in order to achieve stability improvement, ground settlement control, reinforcement, liquefaction prevention, etc. These techniques use a lot of natural materials such as sand and crushed stone and industrial products such as cement. In order to reduce their environmental impact and to economize these techniques, many kinds of industrial waste and by-products have been beneficially used in many types of ground improvement techniques. In response to the growing awareness of carbon neutrality in recent years, it is necessary to further promote initiatives such as the beneficial use of the industrial materials that have been used so far and the development of new materials and construction methods to reduce carbon dioxide emissions. It is expected that various biomass materials will be applied in ground improvement techniques to enhance "negative emission technology". In this paper, recent developments and applications of certain sorts of environmentally friendly ground improvement techniques, soil densification techniques and soil stabilization techniques are briefly introduced. It is to be expected that these will be further developed and applied to contribute to the reduction in carbon dioxide emissions.

Keywords: ground improvement techniques; carbon dioxide; case history

Citation: Kitazume, M. Recent Case Histories of Carbon-Neutral Activity Using Ground Improvement Technology in Japan. *Appl. Sci.* **2023**, *13*, 8985. https://doi.org/10.3390/app13158985

Academic Editors: Andrea Carpinteri, Paulo José da Venda Oliveira and António Alberto Santos Correia

Received: 13 June 2023
Revised: 19 July 2023
Accepted: 1 August 2023
Published: 5 August 2023

1. Introduction

The Earth's average surface temperature has shown unusually rapid increases over the past century, primarily due to the greenhouse gases released as people burn fossil fuels. Greenhouse gases, including not only carbon dioxide (CO_2) but also methane (CH_4), dinitrogen monoxide (N_2O) and chlorofluorocarbon (CCl_3F) gases, accounted for about 50,000 million tons of CO_2 globally in 2018, and 1240 million tons in Japan [1]. This global warming has led to record-breaking heat waves, torrential rains and droughts on a global scale in recent years. For this reason, people around the world are more keenly aware of the need to reduce greenhouse gas emissions.

The construction industry is one of these sources of greenhouse gas emissions, and accounts for about 43% of Japan's carbon dioxide (CO_2) emissions. Since cement, one of the most frequently used materials in construction, is a relatively inexpensive, mass-produced, safe and durable material, it has been used in building and infrastructure for more than 100 years. It is made of limestone, which contains a large amount of carbon dioxide. In the cement manufacturing process, a large amount of carbon dioxide is emitted during the firing of the limestone. More than 30% of Japan's carbon dioxide is emitted in the entire course of construction works during the production of cement and concrete in Japan.

A lot of ground improvement techniques have been developed and applied to improve the physical and mechanical properties of soil to achieve stability improvement, ground settlement control, reinforcement, liquefaction prevention, etc. These techniques use a lot of

natural materials such as sand and crushed stone and industrial products such as cement. In order to reduce the environmental impact and to economize the techniques, many kinds of industrial waste and by-products have been beneficially used in many types of ground improvement techniques since the 1980s. At that time, they were not recognized as having contributed to CO_2 reduction. In response to the growing awareness of carbon neutrality in recent years, it is necessary to further promote initiatives such as the beneficial use of the industrial waste and by-products that have been in use so far and the development of new materials and construction methods to reduce CO_2 emission.

In this paper, recent developments in and applications of environmentally friendly ground improvement techniques are briefly introduced.

2. The Classification and Historical Development of Ground Improvement Techniques

When any type of infrastructure is constructed and soft soil is encountered, over an area, high levels of ground settlement and problems of stability failure and liquefaction are anticipated. Many types of ground improvement techniques have been developed and applied to many infrastructures as a countermeasure to these problems. Figure 1 shows the historical evolution of major ground improvement methods and the historical transactions in the field of geotechnical subjects in Japan [2]. Historically, a major geotechnical subject was the "stability problem" in the 1940s and the 1950s. It is not an exaggeration to say that the stability problem was the only issue that could be dealt with at that time due to insufficient development in geotechnical engineering and construction machinery. Replacement methods were frequently applied for stability problems, where the soft clayey soil stratum was entirely or partially excavated and replaced by sandy material prior to construction of the superstructure. After the development of consolidation theories in the 1940s, "ground settlement" became one of the main geotechnical subjects of discussion, together with the stability problem in the 1950s. In order to accelerate the consolidation process and to reduce the residual settlement, several improvement methods, which may be categorized into "consolidation", were developed in the 1950s and the 1960s. Among them, the sand drain method was first applied at Nagasaki Port in 1952, which was followed by several applications in the 1950s to the 1960s. In order for ground settlement and deformation control to be applied, several densification methods were developed in the 1950s and the 1960s. In 1956, the first type of sand compaction pile (SCP) machine with a hammering device was developed in Japan for the densification of sandy ground (Figure 2). After various developments in machinery, the SCP method with a vibro-hammer was developed in 1959. Following its successful application to marine clay deposits, the SCP method has been applied not only to sandy ground but also to clay ground in many marine as well as on-land construction projects [3]. After the Niigata Earthquake in 1964, the dynamic behavior and liquefaction of sandy soil became one of the key issues in the field of geotechnical engineering. A lot of research efforts have been carried out on the dynamic properties of soil and countermeasures for liquefaction since then. In the period of rapid economic growth in the 1970s, the introduction of soil admixture stabilization was desirable for a rapid strength gain and high stiffness. In the 1970s, the deep mixing method (DMM), one of the in situ soil admixture techniques, was developed and put into practice (Figure 3). Due to the rapid strength increase of the soil, the DMM has been frequently applied to improve many kinds of foundation in marine and on-land construction [4]. In the 1970s and the 1980s, soil and groundwater contamination became one of the most pressing social problems. Since then, the management of waste landfill and contaminated sites has been a serious concern for those working in the discipline of geotechnical and geo-environmental engineering. This required the development of new ground improvement techniques to construct impermeable barriers for disposal sites and the enhanced beneficial use of dredged soft soil, subsoil and industrial waste, and also of any by-products. Many soil admixture stabilization techniques, such as the liquefied soil method, the light-weight soil method [5] and the pneumatic flow mixing method (ref. [6]) were developed and put into practice in the 1990s and the 2000s.

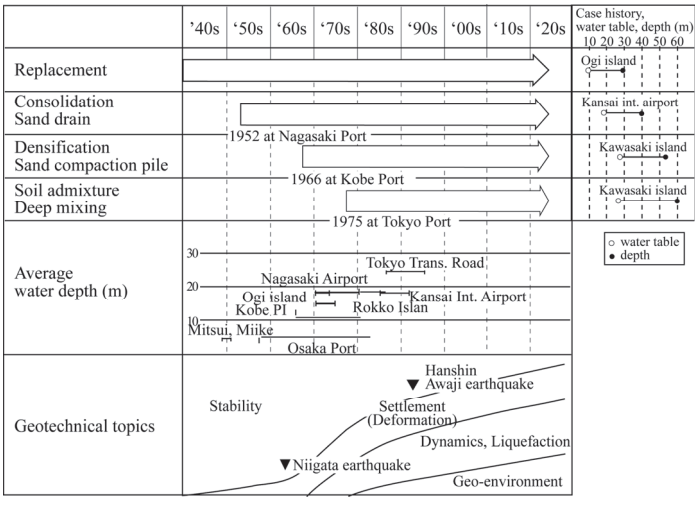

Figure 1. Historical evolution of major ground improvement methods and the historical transactions in the field of geotechnical subjects in Japan [2].

Figure 2. Sand compaction pile machine in the 1950s (courtesy of the Fudo Tetra Corporation).

Figure 3. Deep mixing machine in the 1970s.

Many kinds of industrial waste materials and by-products have been beneficially used in many types of improved ground methods since the 1990s. In response to the growing awareness of carbon neutrality in recent years, it is necessary to further promote initiatives, and these include the use of materials with a low carbon footprint, the underground embedding of materials emitting carbon dioxide, the reduction in the amount of construction material used and the consequent reduction in the amount of construction energy used.

3. Recent Developments in and Application of Environmentally Friendly Ground Improvement Techniques

3.1. Soil Densification Techniques

(1) Use of industry waste

The sand compaction pile method (SCP) is one of the densification techniques, in which many compacted sand piles are constructed in the ground to improve stability, for reducing ground settlement, and for preventing liquefaction [3]. Sand has been used in this method, but since the 1990s, many types of granular materials, including construction by-products such as slag [7], granular coal fly ash [8] and granular stabilized soil [9], have been beneficially used in this method. By promoting the beneficial use of these materials, these methods can provide a reduction in natural materials that can produce CO_2 emission.

(2) Discharge of biochar into the ground together with granular material

Recently, a new type of SCP method has been developed to achieve carbon dioxide reduction, in which biomass is discharged into the ground together with sand [10,11]. The sand is expected to increase the strength of the compacted pile, and the biomass is expected to store CO_2 in the ground. Since the amount of carbon dioxide stored in the ground is overwhelmingly larger than the CO_2 emitted in ground improvement work, this new technology can be described as being a "negative emission technology". A field test revealed the high applicability of the biomass material, bamboo chips, in which the strength and shape were confirmed to be equivalent to those of conventional sand piles (Figures 4 and 5 [11]). In the SCP method, a total of 5 kg CO_2 per m^3 of improved ground is emitted in construction when natural sand is used. In this new SCP method, however, carbon dioxide can be stored in the ground and the amount of CO_2 emission can be decreased to −20 kg CO_2 due to a larger amount of stored CO_2 than the amount that was emitted during construction.

Figure 4. Sand and biomass material (bamboo chips) [11] (courtesy of the Fudo Tetra Corporation).

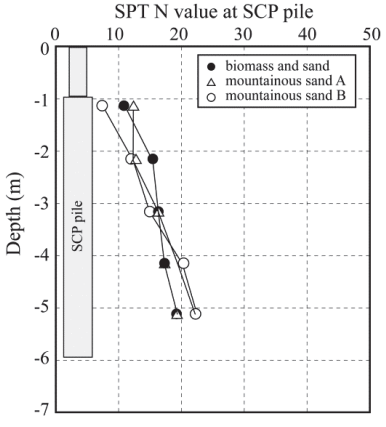

Figure 5. Strength profile along depth [11].

3.2. Soil Admixture Stabilization Techniques

Many soil admixture stabilization techniques have been developed and applied in many infrastructures since the 1970s due to their many benefits, such as rapid strength gain, wide applicability to many types of soil material, etc. In these techniques, cement is one of the materials most frequently used as a binder. However, about 800 kg of CO_2 is emitted during the manufacturing 1 ton of cement, and the energy consumption related to cement material and cement production is about 4% of the total CO_2 consumption in Japan. In cases where 200 kg cement per m^3 soil is used for stabilization, 160 kg of CO_2 is emitted. As the soil volumes to be stabilized are large in general, with the result that CO_2 emission should also be large, it is desirable to use new types of binder that can reduce CO_2 emission.

(1) Use of materials with a low carbon footprint

One of the new binders is high-furnace-slag cement [12,13], which replaces the ordinary Portland cement (OPC) content to 30% with CaO and to 10% with SiO_2 to compensate for the hydration reaction induced by the OPC. This new cement can reduce CO_2 emission by 30% compared to OPC and 50% compared to furnace-slag cement type B. This cement has been applied to the shallow mixing method and the deep mixing method, in which the amount of CO_2 emission can be reduced by about 51%, about 78 kg/m^3 to 40 kg/m^3, respectively.

The other new material is calcia, one of the by-products of the steel slag convertor. The calcia material is composed of calcia as the mother material, has a controlled chemical composition and is graduated. The calcia material can achieve a strength gain to about 200 kN/m^2 through the dewatering effect and the calcium hydration effect. It has been applied to stabilize dredged soft soil for backfilling, shallow stabilization and land reclamation [14,15].

(2) Mixing of biochar in the ground together with chemical binder

Recently, a new ground improvement method has been developed in which molten slag and biochar, as well as cement, are mixed with soil in situ [16–18]. The molten slag is produced by incinerating ash melted at a high temperature and cooled down, which is expected to improve the soil properties of clayey soil and can then reduce the required amount of cement for stabilization. The Japanese Industrial Standards (JIS) specified the quality and environmental safety requirements of the molten slag in 2006 to promote its utilization in civil engineering work and to prevent adverse impacts on the environment. Biochar is a material carbonized by the incomplete combustion of biomass raw materials, and functions to aid in the storage of carbon dioxide in the ground. By increasing the amount of biochar mixed, it is expected that carbon negativity will be achieved, in which the sum of CO_2 emission reductions and fixed amounts exceeds the emissions, which can bring about a sort of decarbonized ground improvement method. In construction, molten slag, biochar and cement are spread on the ground and mixed and compacted to build a stiff, shallow layer (Figure 6 [17]). The amounts of molten slag and biochar are 550 to 1750 kg/m^3 and 10 to 30 kg/m^3, which can reduce the amount of cement that needs to be used to about 60% of the cement used in the existing methods, as shown in Figure 7.

(3) Beneficial use of spoil

Another method is to reduce and beneficially use spoil, which can reduce the required amount of binder and reduce the construction energy used. A large amount of cement slurry is usually injected into the ground using soil admixture stabilization techniques. Cement slurry with a low water-to-cement ratio is preferable for strength increase. However, this leads to less fluidity of the slurry, which requires high-capacity pumping machinery to inject it into the ground. Several techniques have been developed to maintain high fluidity of the cement slurry with a low water-to-cement ratio, in which chemical additives are mixed with the slurry [19].

Figure 6. Shallow mixing machine [17] (courtesy of the SHIMIZU CORPORATION).

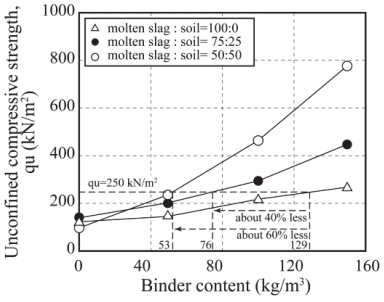

Figure 7. Relationship between amount of binder and strength [17].

Another method is the injection of an air bubble together with the cement slurry. The air bubble functions as a sort of ball bearing to increase the fluidity of the cement slurry The amount of cement slurry required can be reduced to achieve design strength, which can help to reduce the amount of cement, and the amount of energy used for cement production and transportation [20].

In the case of DMM, particularly the jet grouting method (Figure 8), a large amount of spoil, a mixture of in situ soil and cement slurry, flows out to the ground surface during construction. It is usually transported to a disposal site for dumping, which requires a lot of energy. In order to reduce the volume of spoil to be dumped, a new DMM is being developed in which the spoil is dissolved, separated and classified, and the soil particles in the fluid are used as mixing material, after adjusting its particle size distribution [21].

Figure 8. Jet grouting machine (courtesy of the Chemical Grouting Co., Ltd., Tokyo, Japan).

(4) Reduction in stabilized soil volume

Grid-type DM-improved ground is often applied for liquefaction mitigation [22]. In a single stroke of the deep mixing procedure, circular-shaped columns are constructed and they are overlapped together to create walls in a grid shape to improved the piece of the label, as shown in Figure 9. In the case of the jet grouting technique, the circular-shaped column is constructed by injecting high-pressure binder slurry, and its column diameter is

controlled by the air pressure and rotation speed of the mixing shaft; a low rotation speed creates a large-diameter column in the jet grouting method, and usually, they are kept constant to create a circular column shape. It is desirable to construct a rectangular-shaped column rather than a circular-shaped column for economic reasons. In the new jet grouting methods, the rotation speed of the shaft is controlled and changed to create an improved rectangular shape on the ground, as shown in Figure 10 [23–26].

Figure 9. Grid-type DM-improved ground.

Figure 10. Rectangular-shaped stabilized soil column constructed via jet grouting method (courtesy of the Chemical Grouting Co., Ltd.).

(5) Reduction in CO_2 emission during execution

Another effort has been made to reduce CO_2 emission by reducing the energy used in ground improvement works. The deep mixing method, for example, requires a large amount of energy to bring about the movement of mixing tools and the rotation of each mixing tool, and for producing cement slurry and pumping it into the ground. In order to reduce the construction energy expended, a new DM vessel was developed, as shown in Figure 11, which distributes the energy of an electric generator by installing a multiple-diesel engine; this transfers the generated energy through the downward movement of mixing tools, and beneficially uses exhaust heat in generating energy for air conditioning, and generates energy via solar power and wind turbines [27,28].

Figure 11. A new deep mixing vessel (courtesy of the Toa Corporation, Tokyo, Japan).

4. Concluding Remarks

In response to natural disasters such as earthquakes and landslides, many ground improvement techniques have been developed and applied to improve the physical and mechanical properties of soil to achieve stability improvement, ground settlement control, reinforcement, liquefaction prevention, etc. These techniques use a lot of natural materials and industrial products. In order to reduce the environmental impact and the costs of these methods, many kinds of industrial waste and by-products have been beneficially used in many types of improved ground methods. In response to the growing awareness of carbon neutrality in recent years, it is necessary to further promote initiatives such as the beneficial use of industrial waste and by-products, and the development of new materials and construction methods, to reduce CO_2 emission. It is also expected that various biomass materials will be used in the application of improved ground techniques to enhance "negative emission technology".

As the environmentally friendly ground improvement technologies introduced above are often a little more expensive than conventional technologies, it is necessary to reduce the costs of these techniques. On the other hand, society must also accept and share some of the costs for environmental protection.

In this paper, some of the recently developed ground improvement techniques are introduced briefly. It is to be expected that these will be further developed and applied to contribute to the reduction in carbon dioxide emissions.

Funding: This research received no external funding.

Institutional Review Board Statement: The study did not require ethical approval.

Conflicts of Interest: The author declares no conflict of interest.

References

1. Ministry of the Environment, Japan, Greenhouse Gas Inventory Office of Japan (GIO), CGER, NIES: National Greenhouse Gas Inventory Report of Japan. 2013, p. 782. Available online: https://www.enecho.meti.go.jp/en/category/special/article/detail_164.html (accessed on 31 July 2023).
2. Tsuboi, H. Ground Improvement Techniques for Marine Ground. In Proceedings of the 39th National Symposium on Geotechnical Engineering, Niigata, Japan, 7–9 July 1994; Japanese Society of Soil Mechanics and Foundation Engineering: Tokyo, Japan, 1994; pp. 13–18. (In Japanese)
3. Kitazume, M. *The Sand Compaction Pile Method*; CRC Press, Taylor & Francis: Boca Raton, FL, USA, 2005; 232p.
4. Kitazume, M.; Terashi, M. *The Deep Mixing Method*; CRC Press, Taylor & Francis Group: Boca Raton, FL, USA, 2013; 410p.
5. Tsuchida, T.; Egashira, K. *The Lightweight Treated Soil Method-New Geomaterials for Soft Ground Engineering in Coastal Areas*; CRC Press: Boca Raton, FL, USA, 2004; 136p.
6. Kitazume, M. *The Pneumatic Flow Mixing Method*; CRC Press, Taylor & Francis Group: Boca Raton, FL, USA, 2016; 233p.
7. Kitazume, M.; Minami, K.; Matsui, H.; Naruse, E. Field test on applicability of copper slag sand to sand compaction pile method. In Proceedings of the 3rd International Congress on Environmental Geotechnics, Lisboa, Portugal, 7–11 September 1988; Volume 2, pp. 643–648.
8. Okeno, K.; Saito, N.; Hyoudo, M.; Nakata, S.; Murata, M. Improved characteristics of granulated coal fly ash in marine SCP field test, Improvement effect. In Proceedings of the 60th Annual Conference of the Japan Society of Civil Engineers, Kyoto, Japan, 21–24 October 2001; pp. 400–401. (In Japanese)
9. Fujiwara, T.; Tanaka, H.; Kadota, M.; Ohiso, Y.; Kurata, T. Field test of static compaction improved method by granulated excavated-soil. In Proceedings of the 35th Annual Conference of the Japanese Society of Soil Mechanics and Foundation Engineering, Sapporo, Japan, 13–15 September 2000; pp. 1425–1426. (In Japanese)
10. Yamamoto, K.; Satou, K.; Watanabe, E.; Fijikawa, T.; Nunokawa, H.; Koga, C. Compaction and mechanical properties of bamboo chip and RC mixed material for SCP method. In Proceedings of the Annual Conference of Japan Society of Civil Engineers, Hiroshima, Japan, 14–15 September 2023; pp. 369–370. (In Japanese)
11. Home Page of Fudo Tetra Corporation. 2023. Available online: https://www.fudotetra.co.jp/news/ (accessed on 31 July 2023).
12. Yonezawa, T.; Sakai, E.; Koibuchi, K.; Kanda, T.; Dan, Y.; Sagawa, T. High-Slag Cement and Structures for Substantial Reduction of Energy and CO_2. In Proceedings of the 3rd International Conference on Sustainable Construction Materials and Technologies, Kyoto, Japan, 18–21 August 2013; pp. 1–10.
13. Kono, T.; Tsugawa, S.; Yoshida, T.; Sato, E.; Yonezawa, T.; Taki, S.; Kinoshita, M.; Nito, N. Characteristics of soil improvement using high-volume blast furnace slag cement (part 1). In Proceedings of the 45th Annual Conference of the Japanese Geotechnical Society, Matsuyama, Japan, 8–10 August 2010; pp. 565–566. (In Japanese)

14. Tanaka, Y.; Yamada, K.; Ookubo, Y.; Shibuya, T.; Nakagawa, M.; Akashi, Y.; Ichimura, M.; Yamagoshi, Y. Reclamation and evaluation of dredged soil with converter slag. *J. Geotech. Eng. Jpn. Soc. Civ. Eng.* **2021**, *68*, 486–491. (In Japanese)
15. Yamagoshi, Y.; Akashi, Y.; Nakagawa, M.; Kanno, H.; Tanaka, Y.; Tsuji, T.; Imamura, T.; Shibuya, T. Reclamation of the artificial ground made of dredged soil and converter slag by using pipe mixing method. *J. Geotech. Eng. Jpn. Soc. Civ. Eng.* **2013**, *69*, 952–957. (In Japanese)
16. Furuta, S.; Kinugawa, Y.; Takagi, S.; Tamura, S.; Nishida, M.; Nagasawa, M.; Tsuchiya, H.; Maeda, T. A decarbonizing soil improvement method using molten slag and biochar (No.1): Laboratory test. In Proceedings of the 78th Annual Conference of the Japan Society of Civil Engineers, Hiroshima, Japan, 11–15 September 2023. *submitted* (In Japanese)
17. Nishida, M.; Nagasawa, M.; Tsuchiya, H.; Maeda, T.; Furuta, S.; Kinugawa, Y.; Takagi, S.; Tamura, S. A decarbonizing soil improvement method using molten slag and biochar (No.2): In-situ test. In Proceedings of the 78th Annual Conference of the Japan Society of Civil Engineers, Hiroshima, Japan, 11–15 September 2023. *submitted* (In Japanese)
18. Home Page of Shimizu Corporation. Available online: https://www.shimz.co.jp/company/about/news-release/2023/2022061.html (accessed on 31 July 2023).
19. Hirano, S.; Mizutani, Y.; Nakamura, H.; Shimomura, S.; Sasada, H. Quality improvement of deep mixing method by dispersant additives. In Proceedings of the 50th Annual Conference of the Japanese Society of Soil Mechanics and Foundation Engineering, Matsuyama, Japan, 19–21 September 2015; pp. 881–882. (In Japanese)
20. Okabe, M.; Kawamura, K.; Masuda, K.; Seki, T. Ingenious device of site management in ground improvement work by CI-CMC method. *J. Jpn. Soc. Soil Mech. Found. Eng.* **2011**, *59*, 16–19. (In Japanese)
21. Kenbo, H. *Current Status, Issues and Prospects of Jet Grouting Method*; Kisoko, Sougou Doboku Kenkyusho. Co., Ltd.: Tokyo, Japan, 2017; pp. 7–10. (In Japanese)
22. Tokimatsu, K.; Mizuno, H.; Kakurai, M. Building damage associated with geotechnical problems. *Soils Found.* **1996**, *36*, 219–234. [CrossRef] [PubMed]
23. Shinsaka, T.; Yamazaki, J.; Nakanishi, Y.; Komiya, K. Quality Control and Shape Control Techniques in Jet Grouting. In Proceedings of the International Foundations Congress & Equipment Expo, IFCEE 2018, Orlando, FL, USA, 5–10 March 2018.
24. Shinsaka, T.; Yamazaki, J. Development of high-speed type jet grouting method. In Proceedings of the Geotechnics for Sustainable Development–Geotec Hanoi 2013, Hanoi, Vietnam, 28–30 November 2013.
25. Tsuchiya, T.; Abe, H.; Komatsu, K. A study on altering the cross-sectional shape and altering the quality of the jet grout column. In Proceedings of the Grouting 2017: Jet Grouting, Diaphragm Walls, and Deep Mixing, Honolulu, HI, USA, 9–12 July 2017; pp. 21–30.
26. Harada, K.; Ohbayashi, J.; Matsumoto, J.; Kubo, Y.; Akima, T. New ground improvement technologies under restricted conditions in Japan. In Proceedings of the 15th Asian Regional Conference on Soil Mechanics and Geotechnical Engineering, Fukuoka, Japan, 9–13 November 2015; pp. 1165–1170.
27. Imamura, K.; Ishiguro, K. Environmentally friendly deep mixing vessel, Kokaku. *Constr. Mech.* **2010**, 37–41. (In Japanese)
28. Saegusa, H.; Asada, H.; Taguchi, H.; Fukawa, H.; Hirota, S. Case study on application of deep mixing method in Kinjo area of Nagoya port. In Proceedings of the DFI Deep Mixing Conference 2021, Online, 1–17 June 2021; pp. 225–232.

MDPI AG
Grosspeteranlage 5
4052 Basel
Switzerland
Tel.: +41 61 683 77 34

Applied Sciences Editorial Office
E-mail: applsci@mdpi.com
www.mdpi.com/journal/applsci

Academic Open
Access Publishing

mdpi.com

ISBN 978-3-7258-2370-3